NASA Technical Paper 1072

The Mechanics of Atmospheric Systems Derived Through Vertical and Horizontal Analysis of Parametric Data

Robert E. Turner

NOVEMBER 1977

NASA

NASA Technical Paper 1072

The Mechanics of Atmospheric Systems Derived Through Vertical and Horizontal Analysis of Parametric Data

Robert E. Turner
George C. Marshall Space Flight Center
Marshall Space Flight Center, Alabama

National Aeronautics
and Space Administration

Scientific and Technical Information Office

1977

TABLE OF CONTENTS

LIST OF TABLES

LIST OF FIGURES

FIGURE PAGE

FIGURE PAGE

NOMENCLATURE

NASA	National Aeronautics and Space Administration
MSFC	Marshall Space Flight Center
NIMBUS	Earth Resources Technology Satellite (research satellite)
ATS	Atmospheric Technology Satellite
SMS	Synchronous Meteorological Satellite
NOAA	National Oceanic and Atmospheric Administration
IRIG	Inter-Range Instrumentation Group
SIRS-B	Satellite Infrared Spectrometer Model B
DMSP	Defense Meteorological Satellite Program
GMT	Greenwich mean time
RT_B	Resistance of baseline temperature ordinate
RK_1	Baseline ordinate temperature in degrees Kelvin
RM_1	Constant used in baseline reduction
RM_2	Constant used in baseline reduction
RM_3	Constant used in baseline reduction
RE	Radiosonde flight temperature in degrees Celsius
RM_4	Radiosonde flight temperature constant
TO	Negative temperature in degrees Celsius corresponding to an ordinate of 37.6 units
HC	Constants determined by type of humidity element used in the radiosonde
RH_B	Baseline humidity at a temperature of -40° Celsius and ordinate of 46.0 units
T_o	Temperature ordinate at the pressure contact

T_c	Temperature in degrees Celsius
TP_k	Potential temperature in degrees Kelvin
P	Pressure in millibars
TP_c	Temperature in degrees Celsius at the pressure contact
RH_o	Humidity ordinate at the pressure contact
E	Vapor pressure in millibars
w	Mixing ratio in gm Kg^{-1}
Cp	Specific heat of moist air cal^{-1} deg^{-1}
T_D	Dew point temperature in degrees Celsius
RD	Gas constant for dry air cal gm^{-1} deg^{-1}
EPT_k	Equivalent potential temperature in degrees Kelvin
Q	Latent heat of vaporization
TV_k	Virtual temperature in degrees Kelvin
YS	Height of radiosonde above GMD level in meters
YS^1	Height of radiosonde at the preceding contact
GMD	Ground meteorological direction finder
g	Acceleration of gravity m sec^{-2}
L, L-1	Current and preceding pressure contacts
R_E	Earth's radius, constant for a given location and dependent on station latitude
θ	Elevation angle in degrees
Y_G	Height of radiosonde above ground level
ϕ	Azimuth angle in degrees
W_{E-W}	East-west wind component m sec^{-1}
W_{N-S}	North-south wind component m sec^{-1}
WS	Scalar wind speed m sec^{-1}

WD	Wind direction in degrees from which the wind is coming, positive clockwise from true north
S_{E-W}	Smoothed east-west wind component m sec^{-1}
S_{N-S}	Smoothed north-south wind component m sec^{-1}
gpm	Geopotential meters
x	Coordinate of the radiosonde in x direction
y	Coordinate of the radiosonde in y direction
z	Coordinate of the radiosonde in z direction
RMS	Root mean square
σ	Root mean square error
σ_v	Root mean square error of the scalar wind
σ_D	Root mean square in wind direction
σ_{wx}, σ_{wy}	Root mean square of wind speed components

CHAPTER I

INVESTIGATION OF THE VARIABILITY OF THE ATMOSPHERIC MECHANISMS

I. INTRODUCTORY REMARKS

The science of meteorology has advanced rapidly toward the development of an understanding of large-scale atmospheric processes; however, the development of the understanding of meso- and micro-scale processes and their predictability has proceeded at a relatively slow pace. Almost all quantitative meteorological data above the surface of the Earth up to approximately the 30-kilometer level are obtained from balloon-borne instrumentation. The principal measurement system for acquiring these data is the rawinsonde system which provides soundings at 12-hour intervals primarily over continents, on some islands, and a few specially positioned ships. These data are scarce to nonexistent over vast ocean areas and over remote land areas (for example, the Amazon River Valley). In addition, the density of the stations is often inadequate for an analysis of the significant weather-producing systems. There is an urgent need for quantitative atmospheric data over ocean as well as land areas, and it would be highly desirable to obtain data on a smaller spatial and time scale to be able to diagnose and forecast weather-producing mesoscale

disturbances. One possibility for obtaining mesoscale data is the Earth satellite. However, before satellite data can be used effectively, satisfactory methods must be developed to obtain quantitative information from satellite data and to establish the creditability and representativeness of this information or data. Therefore, research needs to be performed to develop methods for obtaining and assessing quantitative data (for example, temperature, moisture, and wind) from satellite information.

Thus, extensive ground-based data are required for comparison and correlation with the satellite output.

This study describes an experiment designed to establish such ground-based data. The performance of the experiments and the representativeness and accuracy of the data are an important aspect of the research and are described in detail. A qualitative discussion of the meteorological forecasting information contained in the data is also given.

In its Second Annual Report to the President and the Congress, June 1973, the National Advisory Committee on Oceans and Atmospheres (NACOA) states:

> The United States has led in the remarkable advances of recent years in observing, describing, understanding, and simulating large-scale atmospheric behavior. NACOA finds it is now time to increase the relative effort on smaller-scale meteorological phenomena which nevertheless have large local impact--flash floods, tornadoes, severe hail, etc.--and to improve local forecasts. . . . Although we appear to stand on the threshold of practical weather modification, and some limited aspects are now operations, not enough is known about it to make it ready for

general operational use. In addition to unsatisfied questions in domestic and internation social, legal, and economic areas, a great deal of physical research still needs to be done. . . .

This status assessment substantiates:

1. A 1971 report entitled "The Atmospheric Sciences and Man's Needs: Priorities for the Future," by the Committee on Atmospheric Sciences, National Academy of Science (NAS) which recommends that:

> . . . emphasis should be placed on research on fronts, jet streams, organized convection, and other phenomena of mesoscale.

2. The Interdepartmental Committee for Atmospheric Sciences Report number 159a, June 1971, entitled "A National Program for Accelerating Progress in Weather Modification," which states:

> In addition to the special support for these National Projects, a significant increase in relevant broad background research and development support is also needed. This is particularly needed in the areas of microphysics and dynamics of mesoscale systems, meso-scale mathematical models . . . .

3. National Aeronautics and Space Administration (NASA) Earth Observation Office Environmental Program Retreat, March 4-5, 1974, which states:

> . . . purpose of considering in depth, but in an unstructured meeting, the programmatic 'drought' which faces NASA's Weather and Climatic Community in the five-year period between 1975 and 1980, and developing imaginative ideas for coping with the environmental problems of this period.
>
> . . . it will be possible to do detailed case-study analyses and to develop objective diagnostic and prediction techniques using statistical and perhaps numerical models of many mesoscale phenomena. In order to provide better forecasts of mesoscale systems and to reduce property loss and personal injuries . . . .

> . . . the needed improvement in mesoscale modeling could come through refinement of the models. . . .
>
> . . . Model sensitivity to changes in boundary conditions . . . model capability to utilize slowly changing secondary variables measured from remote sensing and conventional observations. . . .

II. BACKGROUND INFORMATION

Atmospheric motions range from very large dimensions down to the smallest scales of turbulence and molecular motion. Analysis of mid-tropospheric data reveals commonly occurring wave patterns with dimensions of 1,000-3,000 km or more which are called synoptic-scale features by Byers (1).[1] Superimposed on the synoptic-scale systems are mesoscale phenomena which are characterized by horizontal dimensions from about 10-1,000 km (see Reference (2) for additional information). Mesoscale systems include such phenomena as thunderstorms, flash floods, tornadoes, and sea breezes; they are responsible for a large portion of significant weather events.

Because of their small sizes and rapid changes with time, it is difficult to obtain adequate data on mesoscale systems. The national network of surface observing stations is not adequate to resolve many mesoscale phenomena in the horizontal, and the upper air network, containing stations about 300 km apart, with observations each 12 hours,

---

[1] Numbers in parentheses refer to similarly numbered references in the Bibliography.

provides even less resolution. Radar is an important source of data on mesoscale systems, and great strides are being made to obtain maximum use of this tool. It is hoped that satellites will provide better quantitative data on both mesoscale systems and synoptic-scale systems.

Until vast new quantities of data are available and can be handled by computers, it is necessary to study the mesoscale systems based on synoptic-scale data. It has been indicated that a hypothesis that is fundamental to all numerical models of the general circulation is that the effects of features of the atmosphere which have a scale smaller than 500 km (mesoscale) must be essentially determinable from larger-scale motions. Since House (3) has shown that synoptic data would have to be analyzed every two hours and preferably every hour in order to detect mesoscale phenomena, it is essential for meteorologists to understand the interrelationships between mesoscale and synoptic-scale systems.

Complex interactions between mesoscale and synoptic-scale systems occur over the entire Earth and are not well understood. Oort (4) has provided observational evidence on the atmospheric energy cycle which begins with a radiation excess in the equatorial region. This energy is thought to be carried into the upper troposphere in the cores of cumulonumbus clouds (mesoscale) instead of by large-scale vertical motion (synoptic scale), Riehl and Malkus (5). The convective systems are, in turn, related to synoptic-scale

equatorial waves. Available potential energy generated by a net heating of the tropics and cooling of polar regions is transformed into available eddy potential energy and kinetic energy by means of baroclinic eddies and their vertical motions. The baroclinic disturbances in turn maintain the mid-latitudes' zonal flow. Mesoscale systems influence these transformation processes. For example, Kreitzberg and Brown (6) investigated mesoscale systems associated with an occlusion and found that the mechanism directly governing the mesoscale thermal features and weather systems is the release of potential instability by the large-scale vertical motions within the cyclone. Reviews of research on severe convective storms may be found in papers by Palmen and Newton (7), Ludlum (8), and Fankhouser (9). These studies describe the storms and state the synoptic-scale conditions conducive to their formation. The precise physical mechanisms and interactions of phenomena and various scales of motion for the information of these storms are not known. Statistical methods are often used to infer the relationships between mesoscale phenomena and associated synoptic-scale parameters when an exact relationship is unknown. A better understanding of the interaction between these two scales of motion is one of the goals of Atmospheric Scientists.

It has been recognized for over a decade that meteorological satellites are capable of providing a platform to observe and measure changes in atmospheric variables

ranging from global patterns of clouds down to individual mesoscale systems. Initially, observations were of a photographic nature and a considerable effort was put forth simply to identify characteristic cloud fields with known synoptic features such as fronts, squall lines, cyclonic systems, etc. TIROS II provided the first medium resolution infrared data and initiated a series of studies on radiation balance, and cloud and surface temperatures, as well as estimates of water vapor content. Experiments using different wavelengths and different spectral bandwidths were carried out on the early TIROS series as well as NIMBUS satellites. The development of the synchronous satellites, ATS-I, ATS-III, and SMS-1 and SMS-2 in particular, opened up the potential for the determination of cloud motion from time-lapse photography from space as well as obtaining global views of cloud distributions at synoptic time periods.

The determination of three-dimensional cloud distribution from satellite data, although promising, quickly began to present disturbing problems. Although the overall distribution could be determined, resolution of the camera system prohibited a detailed portrayal of individual cloud elements or individual storms. Cloud-top temperature mapping was frustrated to some extent in early studies by sensor resolution and contributions from vertically spaced cloud layers contributing to the radiance measured by the satellite sensors. In addition, in the initial satellite studies, fragmented photographic mapping once a day made it

difficult to develop a coherent picture of the overall cloud distributions.

Determination of surface and cloud-top temperatures from the atmospheric window bands in early satellites were hampered by appreciable absorption due to water vapor in the intervening path between the cloud or surface, resulting in effective black body temperatures on the order of 10° Celsius lower than actually existed at the emitting surface. Absorption, as well as sensor resolution, prohibited detailed cloud-top temperature mapping with these early sensors.

With time, the resolution and absorption problems present in early meteorological satellite radiation data were overcome and additional sophisticated temperature profiling experiments were developed. The absorption problems present in the 8-12 micron wavelength used for early temperature determinations were essentially eliminated by going to narrower band widths at the 4- and 11-micron bands. Resolution was increased by developing high resolution and very high resolution radiometers. The feasibility of obtaining temperature profiles in the atmosphere with satellite was demonstrated with the Selective Chopper Radiometer (SCR), the Infrared Temperature Profile Radiometer (ITPR), and the Satellite Infrared Spectrometer (SIRS) of the NIMBUS satellites. The Temperature Humidity Infrared Radiometer (THIR) provided a reliable means to determine day

and nighttime surface and cloud-top temperature as well as mapping of atmospheric water vapor.

Results from the second generation medium spatial resolution scanning infrared radiometers on the NOAA 3 and 4 and NIMBUS 5 indicate that atmospheric temperature profile data can be obtained which will provide valuable supplements to conventional upper-level data. Profiles of temperature using the Vertical Temperature Profile Radiometer (VTPR) determined by measuring the thermal energy from the band center as well as in the wings of the absorption band provide a means for the interpretation of the variation of atmospheric temperature with altitude. By using curves, usually referred to as weighting functions, the layers most vividly sensed by the particular spectral channels can be defined. In the case of the Infrared Temperature Profile Radiometer on NIMBUS 5, four intervals of the 15 micron carbon dioxide band are used to develop an atmospheric temperature profile while two additional channels are used to detect clouds and surface temperatures. The temperature profile is obtained by solving the radiative transfer equation and, in the case of cloud contamination, these data are corrected to a zero-cloud amount to obtain a clear column radiance for the sounding. This specific cloud correction technique is discussed by Smith, Staelin, and Houghton (10).

Statistical approaches for obtaining maximum information about the atmosphere's thermal structure were examined

by Smith, Woolf, and Jacob (11) using the Satellite Infrared Spectrometer on NIMBUS 3. They showed that geopotential height profiles as well as temperature profiles could be expressed directly in terms of spectral radiance observations allowing useful estimates of pressure heights. To correct for clouds, a two-level cloud model was assumed with upper-level clouds randomly distributed with respect to lower clouds. Errors in the geopotential heights and temperatures of constant pressure surfaces were found to be seasonally dependent, but could become less than 40 meters and 1.5 to 2° Celsius for levels below 300 millibars in the summer season. Errors in radiance-calculated temperatures and heights, however, increased with increasing cloudiness.

The retrieval of atmospheric temperature profiles from satellite data using a solution of the radiative transfer equation through a first guess approach has been discussed by Smith, Woolf, and Fleming (12). Although successive iterations in the solution of the transfer equation above the cloud level lead to comparable temperatures which are independent of the initial first guess, below the true cloud level the solution of the transfer equation is dependent upon the guess profile of temperature. The necessity of determining cloud parameters from the radiance data to derive equivalent clear column radiance values also presents a complex problem.

The determination of the distribution of water vapor with height presents a similar problem to that of the

temperature structure. Although a multiband approach may be used such as that developed by Shen and Smith (13) for the NIMBUS 3 SIRS-B system, a single band approach can be used. In particular, the characteristics of the precipitable water profile are highly correlated with the saturated precipitable water given by the temperature profile. Through such an approach, the reduction of variance of the precipitable water above each mandatory level can be explained by the saturated precipitable water and variables defined from the radiance of one of two water vapor channels.

An exploration into the use of upper-level winds determined from vertical temperature profile observations was carried out by Endlich, Namcuso, Shigeishi, and Nagle (14). In this instance, data at the 250- and 300-millibar levels were used to determine geostrophic winds for application as initial estimates for the analysis of aircraft wings. Overall results were promising and indicated the potential of determining wind data from the satellite-derived geopotential height field.

Increased resolution and contamination-free windows now make mapping of cloud-top temperatures a feasible endeavor down to and including mesoscale cloud features. Problems still exist with the emissivity question of cirroform clouds. In this respect, Shenk and Curran (15) have suggested a procedure using a multispectral approach. Since the infrared emissivity depends upon the number of cloud particles in a vertical column, they examined the correlation

between the radiance measured at 11 microns and the normalized solar reflectance from the cloud surface. Although no specific values of emissivity could be given, a well defined correlation was present in the data between the normalized reflectance and the apparent black body temperature of the cirroform clouds.

The depiction of detailed cloud fields in three dimensions has recently become possible through the use of the data from the Air Force DMSP satellite. Here, very high resolution photographic data enables the mapping of cloud fields down to almost individual cloud elements. Use of these data enables a detailed picture of the cloud field to be developed which can then be used to evaluate and improve the analysis of the infrared radiation data used in determining cloud correction coefficients in the ITPR data.

III. ATMOSPHERIC VARIABILITY EXPERIMENT

In recent years, a major concentration of research has gone into the large and small ends of the atmospheric scales of motion, leaving a gap in the understanding of phenomena associated with the middle (mesoscale) scale. This gap includes the important processes involved with the onset and development of severe storm systems.

Therefore, an experiment was conducted utilizing a large network of rawinsonde stations acquiring data at intervals of every three hours when meteorological conditions were predicted to contain the particular mesoscale systems

of interest. This experiment was undertaken to acquire a unique data set which might yield fundamental new knowledge concerning the mechanisms for the formation, maintenance, and decay of severe storm systems as a function of their environment and provide a basis for relating the influence of severe storms on larger scale processes.

To provide the data for this research, an Atmospheric Variability Experiment (AVE) was conducted on April 24 and 25, 1975. Forty-two rawinsonde stations participated in the acquisition of rawinsonde data at three hour intervals over the United States, east of approximately 105 degrees west longitude, which are shown in Figure 1.1 and listed in Table 1.1. Flights were taken at nine time periods beginning April 23, 1975, at 2315 GMT, April 24, 1975, at 0515 GMT, 1115 GMT, 1415 GMT, 2015 GMT, 2315 GMT, and on April 25, 1975, at 0515 GMT, and 1115 GMT. During this period of time, photographs were taken of the experiment area at 30 minute intervals by the SMS-1 and SMS-2 satellites.

The objectives of this research experiment were to evaluate the accuracy and representativeness of quantitative satellite data, to investigate the variability of atmospheric parameters and systems of a scale smaller than that normally detected from data available at intervals of 12 hours, and to investigate the structure and dynamics of the atmosphere associated with severe weather.

The test plan required the experiment to be conducted when one or all of the following conditions were

Figure 1.1. Rawinsonde stations' location.

TABLE 1.1

RAWINSONDE STATIONS PARTICIPATING IN THE EXPERIMENT

Station Number	Location
208(CHS)	Charleston, South Carolina
211(TPA)	Tampa, Florida
213(AYS)	Waycross, Georgia
220(VPS)	Apalachicola, Florida
226(CKL)	Centerville, Alabama
232(BVE)	Boothville, Louisiana
235(JAN)	Jackson, Mississippi
240(LCH)	Lake Charles, Louisiana
248(SHV)	Shreveport, Louisiana
255(VCT)	Victoria, Texas
260(SEP)	Stephenville, Texas
261(DRT)	Del Rio, Texas
265(MAF)	Midland, Texas
304(HAT)	Hatteras, North Carolina
311(AHN)	Athens, Georgia
317(GSO)	Greensboro, North Carolina
327(BNA)	*Nashville, Tennessee
340(LIT)	*Little Rock, Arkansas
349(UMN)	*Monette, Missouri
363(AMA)	Amarillo, Texas
402(WAL)	Wallops Island, Virginia
405(IAD)	Sterling, Virginia (Dulles Airport)
425(HTS)	Huntington, West Virginia
429(DAY)	Dayton, Ohio
433(SLO)	*Salem, Illinois
451(DDC)	*Dodge City, Kansas
456(TOP)	*Topeka, Kansas
486(JFK)	Fort Totten, New York (Kennedy Airport)
518(ALB)	Albany, New York
520(PIT)	Pittsburg, Pennsylvania
528(BUF)	Buffalo, New York
532(PIA)	Peoria, Illinois
553(OMA)	Omaha, Nebraska
562(LBF)	North Platte, Nebraska
606(PWM)	Portland, Maine
637(FNT)	Flint, Michigan
645(GRB)	Green Bay, Wisconsin
654(HUR)	Huron, South Dakota
655(STC)	St. Cloud, Minnesota
662(RAP)	Rapid City, South Dakota
11001(MSF)	*Marshall Space Flight Center, Alabama
22001(FSI)	*Fort Sill, Oklahoma

*Selected stations for analyzing.

present: large horizontal temperature gradients, a jet stream, convective activity, a variety of cloud conditions, or rapid changes in weather patterns. The experiment was successful in that all of these conditions were realized during the effort.

In Chapter II, the data reduction process is described. Utilization is made of increased knowledge of parameters and techniques and of improved computational methods. The governing atmospheric equations, their solution procedure and computational process are briefly reviewed.

Chapter III deals with the data error analysis. Accuracy of the thermodynamic data and wind data are discussed. Equations and techniques are briefly reviewed. Estimates of errors in the data are given along with a discussion of how these errors affect the final product.

In Chapter IV, several types of analyses are presented and discussion of the atmospheric variability and mesoscale structure are reviewed. The nature of the horizontal and vertical wind field are presented. Constant pressure maps are plotted and analyzed to describe horizontal flow from the surface to higher altitude. Sounding data are plotted and analyzed for selected locations near severe thunderstorms and tornadoes. Comparison of satellite data with ground based data are made. The comparisons involve the application of densitometry techniques. It is believed that the application of these techniques to SMS-1 satellite

images is new and the results appear to show promise relative to locating severe storms with satellite images. Finally, the results of this effort are presented and discussed in the remainder of the chapter.

In Chapter V, major conclusions are made from the results of this effort and are presented.

CHAPTER II

DATA REDUCTION PROCESS

I. INTRODUCTORY REMARKS

This chapter describes the techniques and procedures that were used to process the experiment (AVE) data. The meteorological and statistical bases for the developments in this chapter are given in References (16, 17, 18, 19). The equations and data reduction techniques are applicable for rawinsonde measurements from equipment providing temperature, relative humidity, elevation and azimuth angles of radiosonde position as functions of pressure.

II. EQUATIONS AND DATA REDUCTION PROCEDURES

The evaluation of measurements by the rawinsonde systems with regard to conversion of ordinates for temperature and relative humidity to proper units and for computation of certain thermodynamic quantities are presented in this section. Figure 2.1 shows the steps of the data reduction process.

Data Extraction from Strip Charts

Angles, ordinates, and baseline data were extracted from the original records for all rawinsonde flights and punched into computer cards.

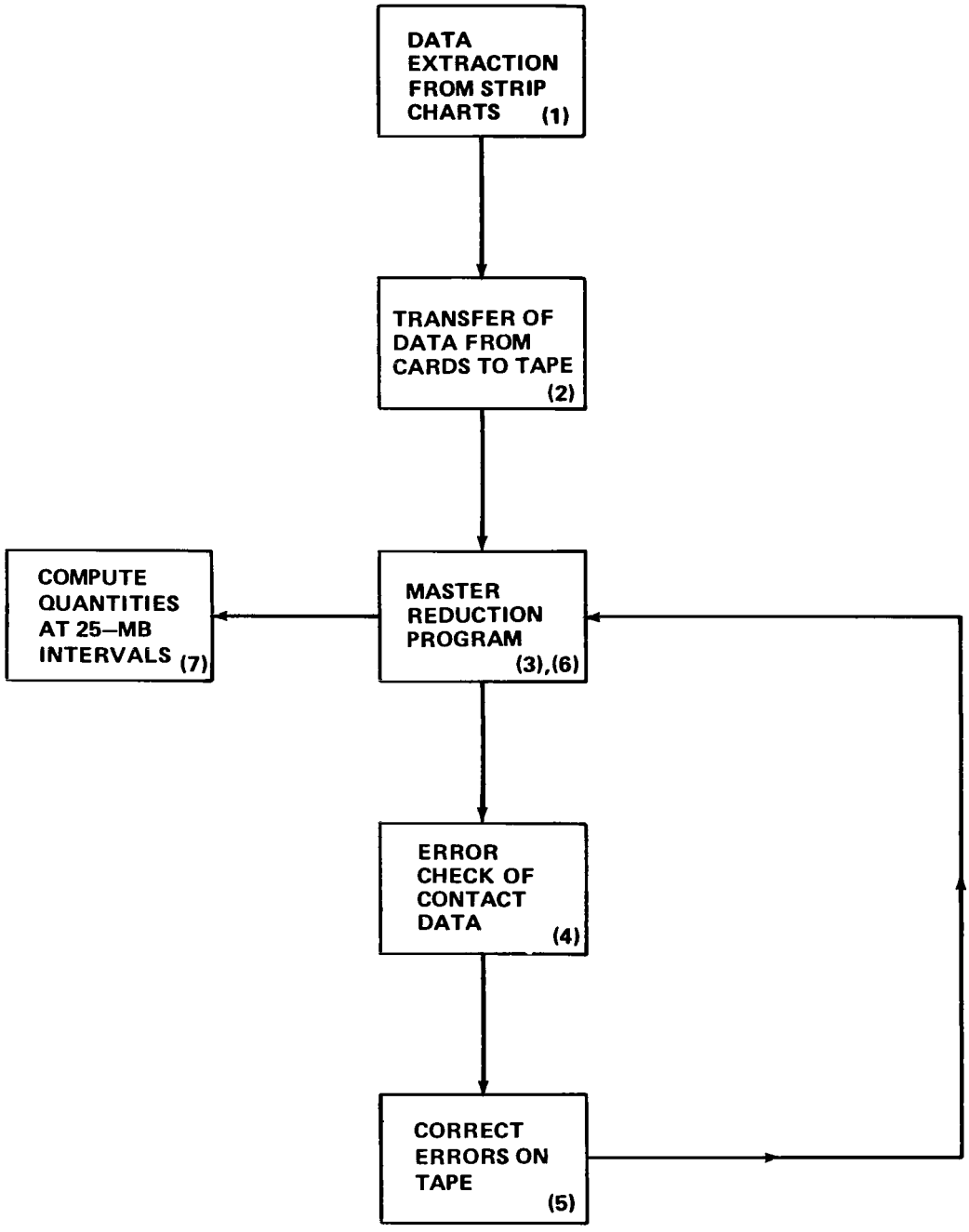

Figure 2.1. Data reduction process steps.

A baseline card was punched for each flight which contained surface data and thermodynamic calibration variables. Table 2.1 gives the name and column location of all data on the baseline cards. Figure 2.2 shows a sample baseline card. Missing data was indicated by a field of nines in the appropriate columns.

A series of data cards containing ordinate information was punched for each flight. A typical flight ascended to approximately 20 mb and contained about 160 ordinate cards. A list of the data contained on an ordinate card is given in Table 2.2, and a sample card is shown in Figure 2.2. Contact number and pressure were always indicated on the cards, but missing values of temperature ordinate, relative humidity ordinate, or time were indicated by filling the particular columns with nines. Information for the cards was obtained from the original strip chart of the flight and the pressure calibration chart for the individual radiosonde. If one wished to manually interpolate temperature ordinate or time, this could be done, and by punching a "1" in column 73 on the ordinate data cards, the fact would be indicated by an asterisk in the final output.

Angle data for each flight were punched on a separate deck of cards. In most cases, angles were available every 30 seconds by reading them directly from the recorder charts, but in some instances, either at 0000 GMT or 1200 GMT, the rawinsonde operators recorded angles at only 1 minute intervals. As shown in Table 2.1, this fact is

TABLE 2.1

BASELINE DATA CARDS

Columns	Variable
1	Rawin type
3-6	Station elevation in meters
8-11	Pressure contact number at the surface
13-18	Surface pressure in millibars
20-23	Surface temperature in degrees Celsius
25-28	Surface relative humidity in percent
30-33	Baseline temperature
35-38	Baseline relative humidity
40-43	Surface wind speed in meters per second
45-47	Surface wind direction in degrees
50-51	Month of flight
53-54	Year of flight
56-57	Day of flight
59-62	Time of flight in GMT
64-68	Station identification number
72	Angle identifier. A "1" indicates that angle data for the flight are given every minute and a blank indicates every 30 seconds

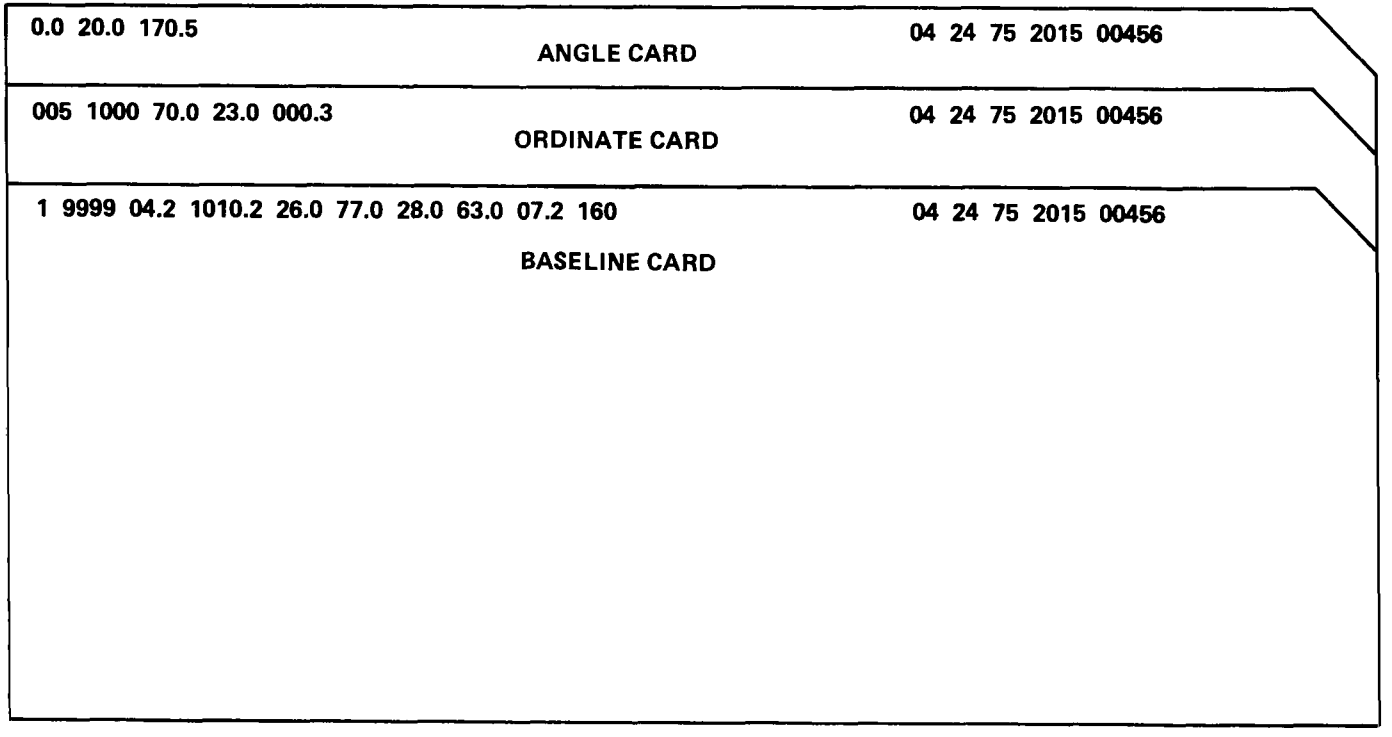

Figure 2.2. A sample computer card.

TABLE 2.2

ORDINATE DATA CARDS

Columns	Variable
1-3	Pressure contact number corresponding to the given pressure
5-8	Pressure at the given contact
10-13	Temperature ordinate
15-18	Humidity ordinate
20-24	Time from rawinsonde release
50-51	Month of rawinsonde release
53-54	Day of rawinsonde release
56-57	Year of rawinsonde release
59-62	Time of rawinsonde release in gmt
64-68	Station identification number
72	A "1" indicates the last card of the ordinate deck
73	A "1" indicates that either the temperature ordinate or the time from release have been manually interpolated

indicated on column 72 on the baseline data card. Table 2.3 describes the contents of the angle data cards and Figure 2.2 shows a sample card. After investigation, it was decided not to perform manual smoothing or to manually check angles, but instead to do this by use of the reduction program. Missing data was indicated by nines in the particular columns.

Transfer of Data from Cards to Tape

A complete flight deck consisting of a baseline data card, ordinate data cards, and angle data cards was created for each rawinsonde flight. The flight decks were then arranged according to increasing station identification number, and within the same station by increasing time, in preparation for transfer to magnetic tape for computation.

A leader card was created for each flight to precede the baseline information of each flight. The leader card contains the data, time, and station number of the flight that was found in columns 50-68 of the baseline data card, and also contains the total number of cards for the flight. This quantity enables one to quickly skip over a complete flight when using the tape. The format of the leader card is given in Table 2.4.

A simple program is used to print the contents of the raw data tape and simply reads each record and prints the contents as they appeared on the original cards. The data list produced by the program proved valuable in error checking procedures.

TABLE 2.3

ANGLE DATA CARDS

Columns	Variable
1-5	Time from rawinsonde release
7-10	Elevation angle
12-16	Azimuth angle
50-51	Month of rawinsonde release
53-54	Day of rawinsonde release
56-57	Year of rawinsonde release
59-62	Time of rawinsonde release in gmt
64-68	Station identification number
72	A "1" indicates the last card of the angle deck
74	A "1" indicates that the elevation angle was less than some given quantity

TABLE 2.4

FORMAT OF THE LEADER CARDS

Columns	Variable
1-2	Month of rawinsonde release
4-5	Day of rawinsonde release
7-8	Year of rawinsonde release
10-13	Time of rawinsonde release in gmt
15-19	Station identification number
21-24	Total number of cards comprising the flight

Master Reduction Process

This program was the most important in the data reduction process since it computed atmospheric parameters for each pressure contact from baseline, ordinate, and angle data that has been previously stored on tape. The program can be conveniently divided into several functional components. To facilitate its description, a flow chart of the program is given in Figure 2.3.

The first process of the program initializes the necessary arrays, defines functions to compute temperature and virtual temperature, and defines constants to be used in humidity determination. All variables that will be printed and transferred to magnetic tape as final output are initially defined to be zero. The station roster containing the station identification number, elevation, latitude, longitude and name is read from data cards followed by the number of flights to process or skip. All of the remaining data is read from magnetic tape.

The first record to be read from tape is the leader card described in Table 2.4. If one desires to compute consecutive flights beginning with the first flight, the information on the leader card is not used; however, if one wishes to calculate certain flights and skip others, the information is used to read raw flight data, skip the computation phase, and then begin with the next leader card until the desired station and time are located. The baseline data for the flight to be computed are read using the format

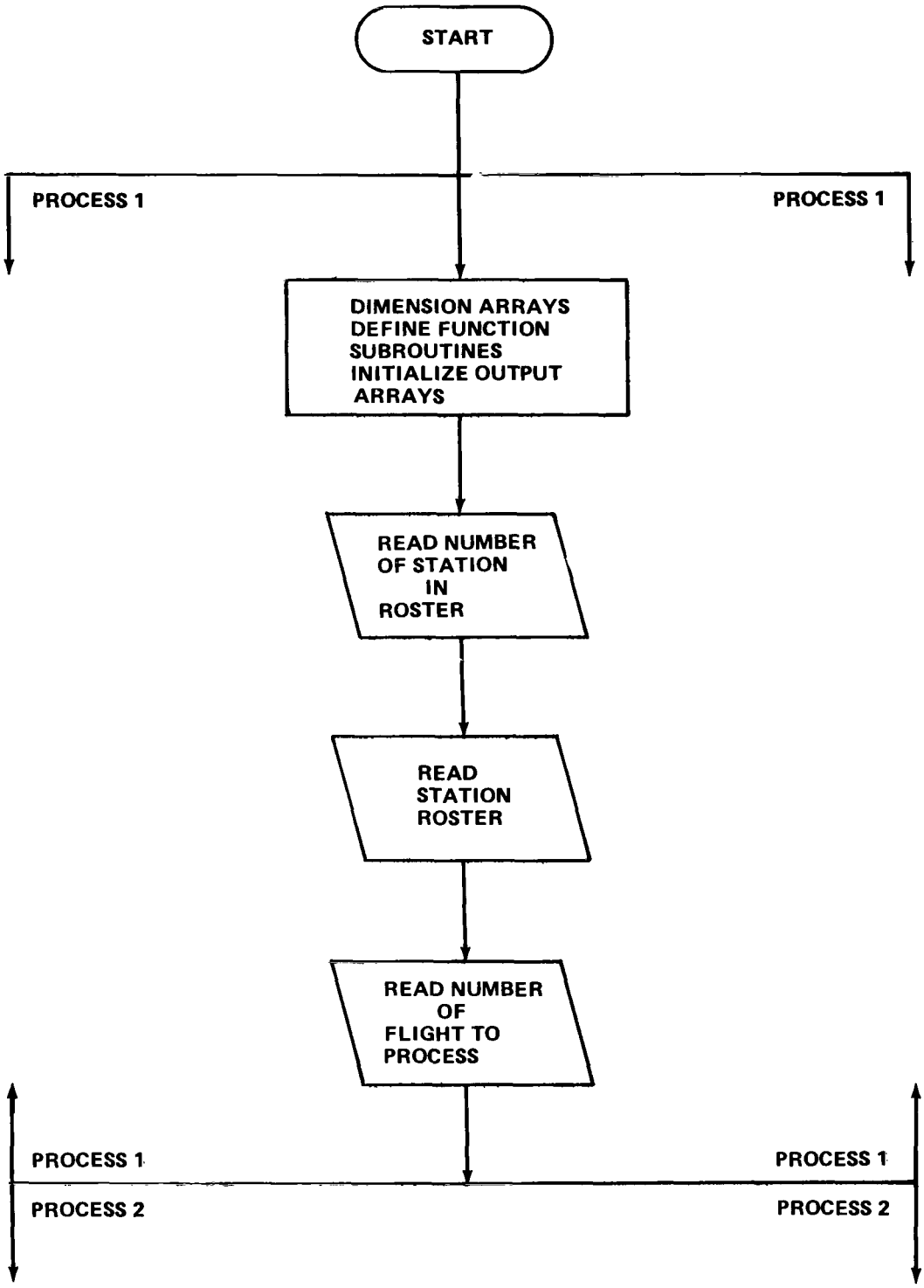

Figure 2.3. Flow chart of the master reduction process.

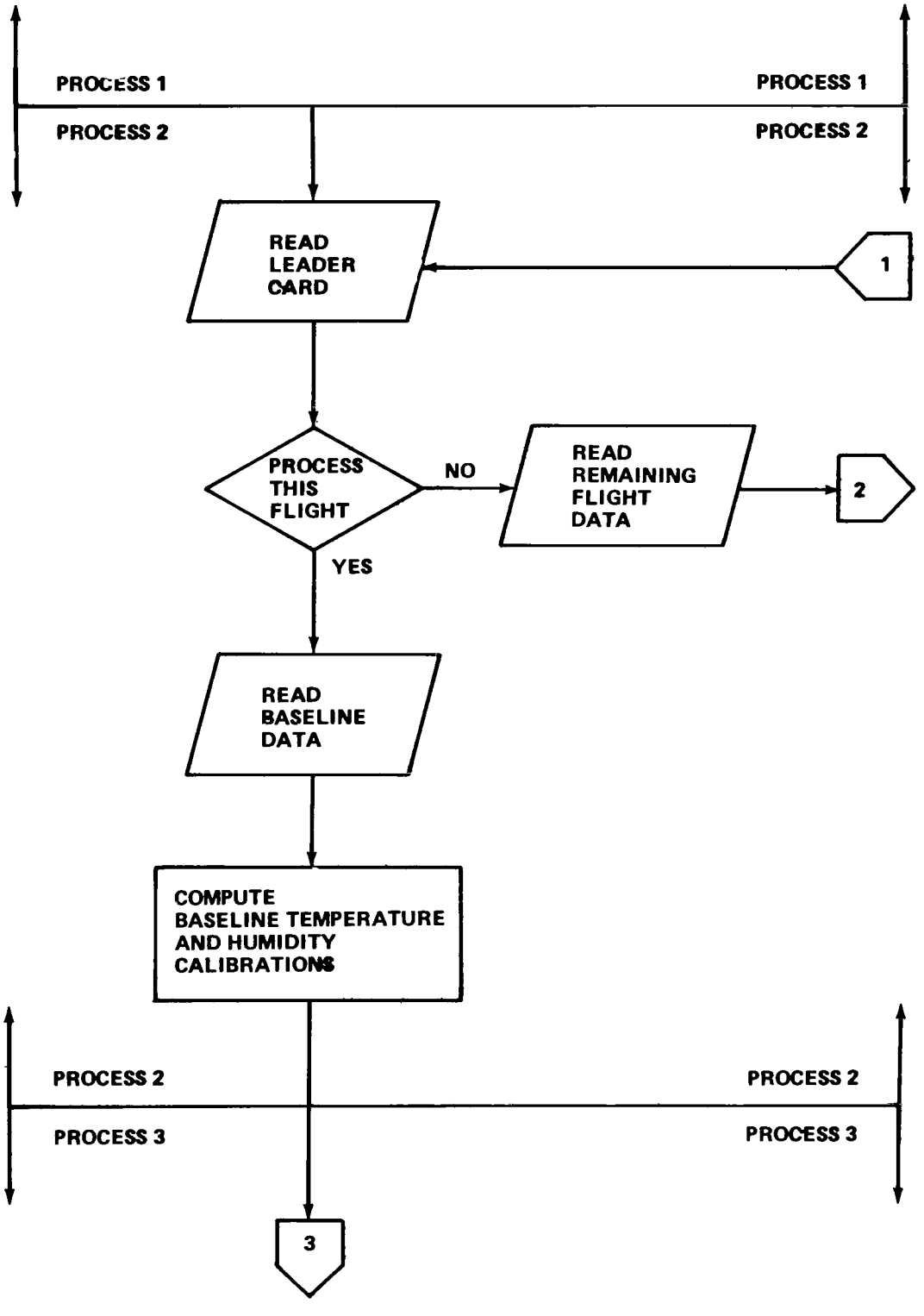

Figure 2.3. (continued)

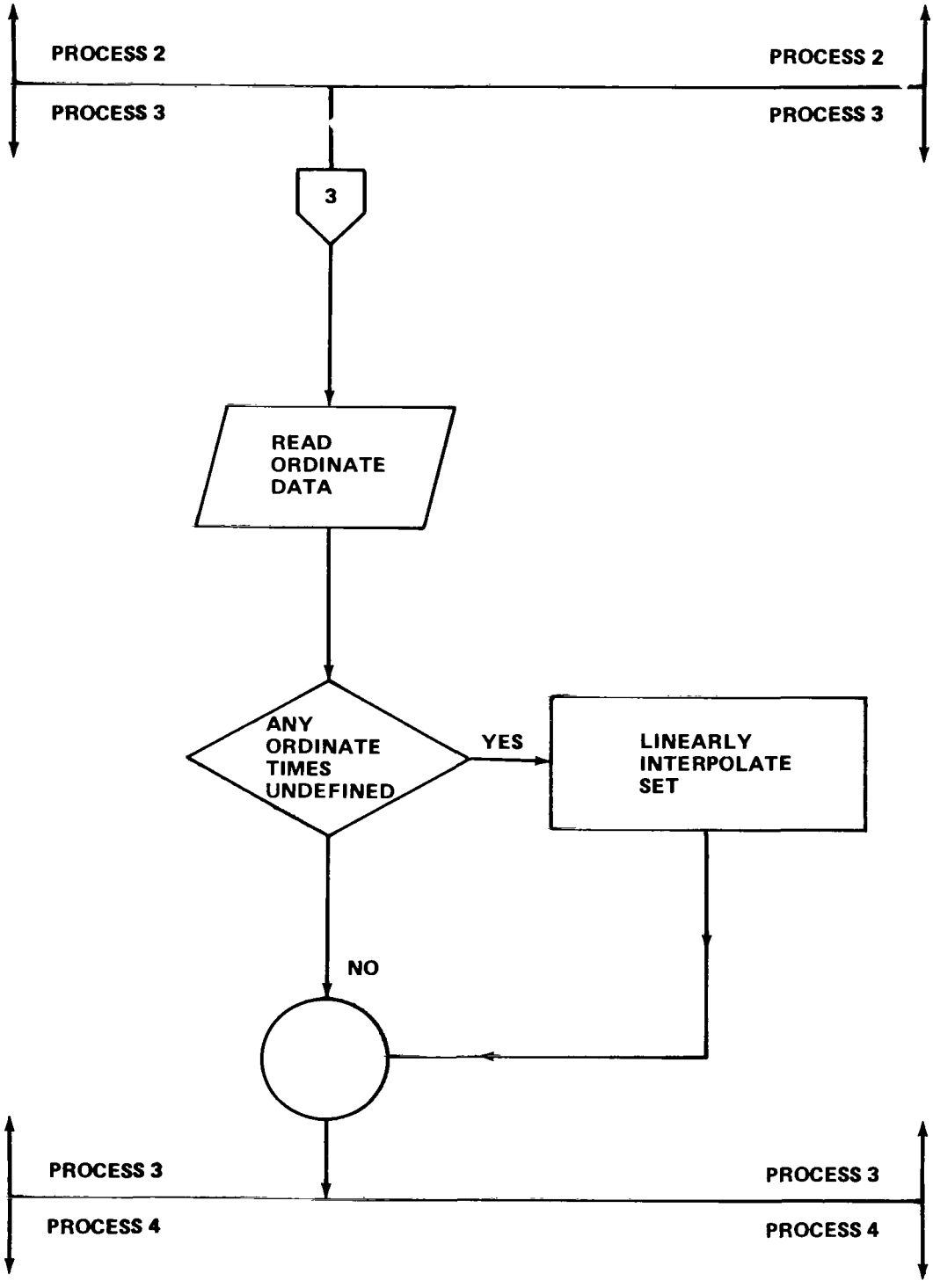

Figure 2.3. (continued)

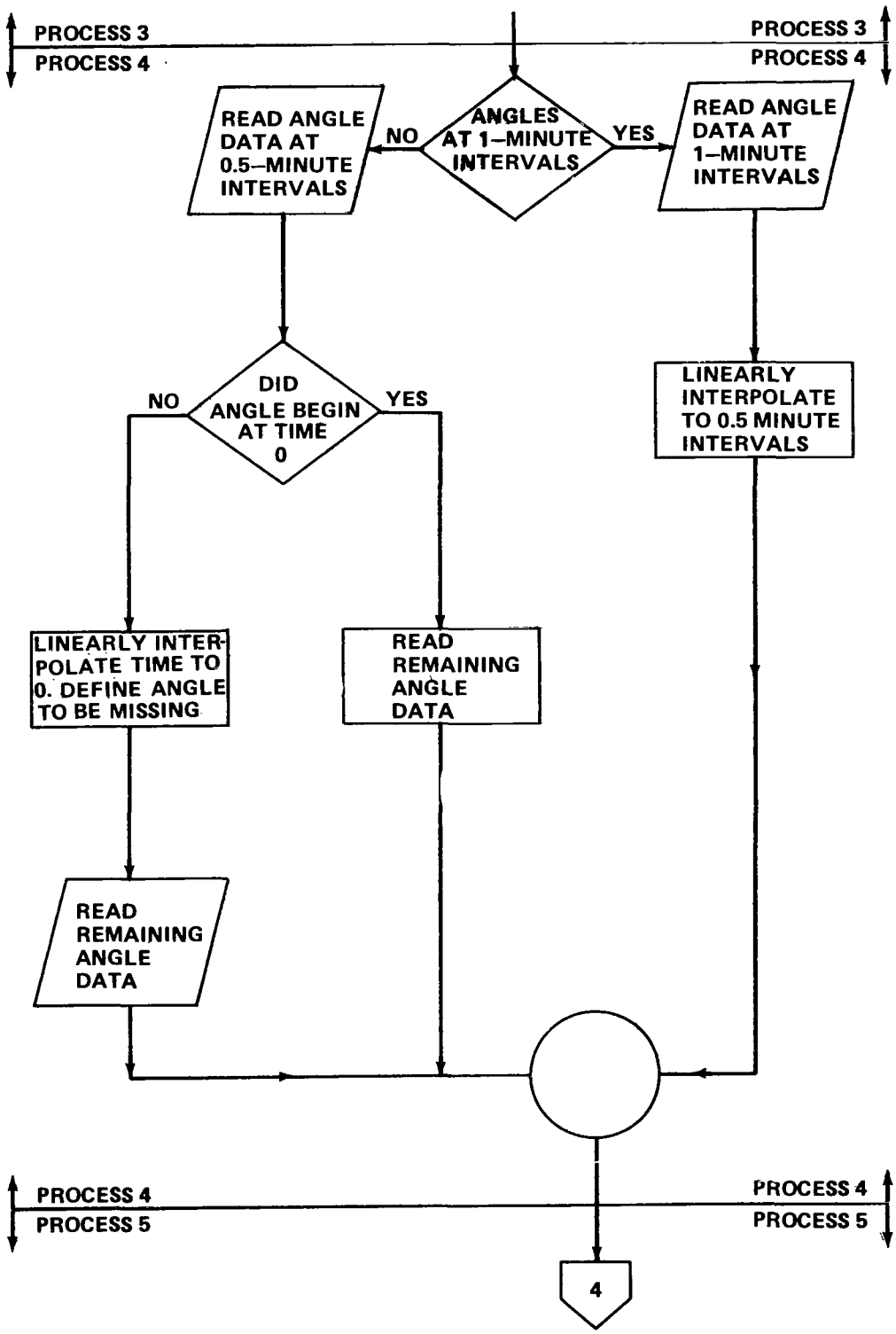

Figure 2.3. (continued)

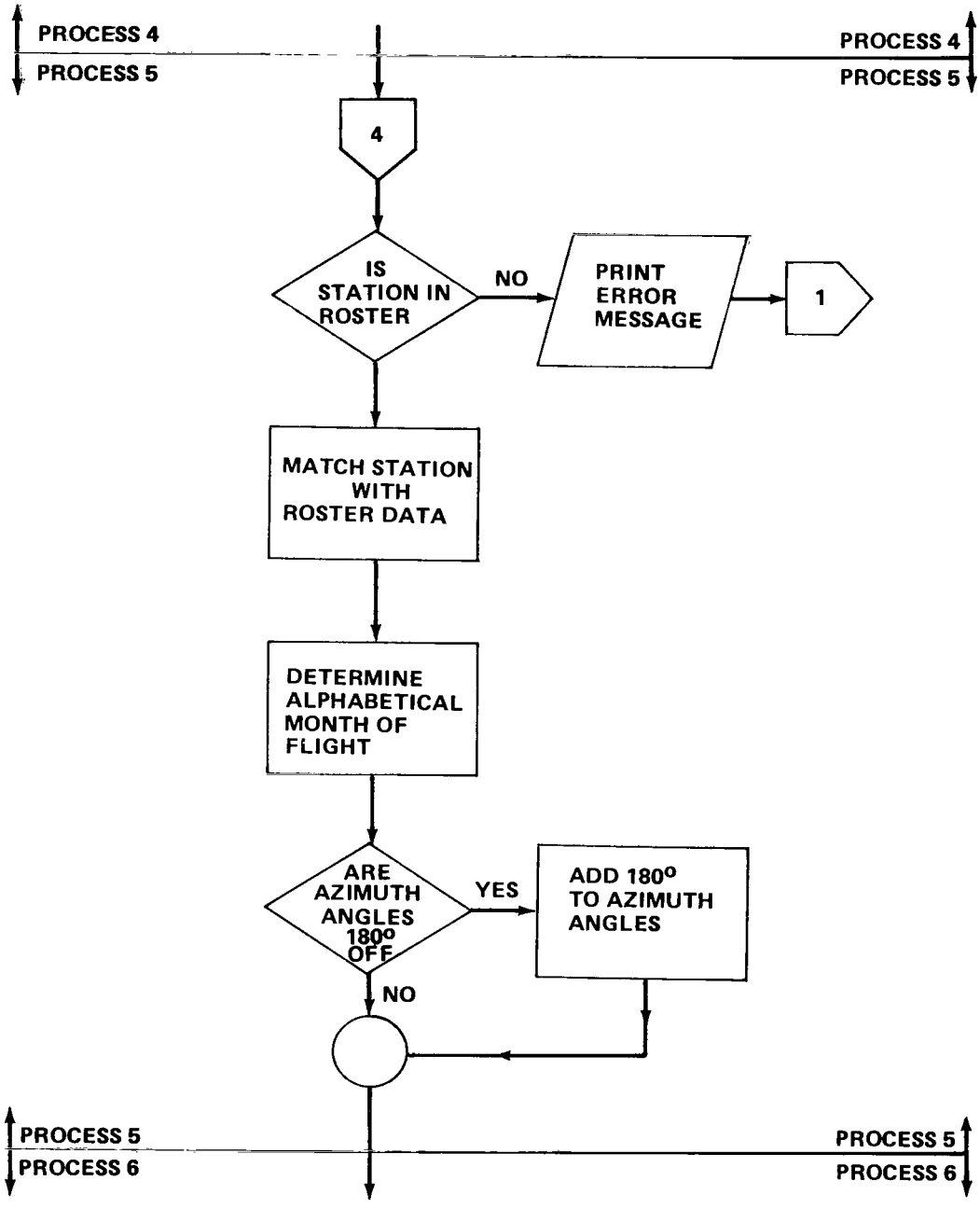

Figure 2.3. (continued)

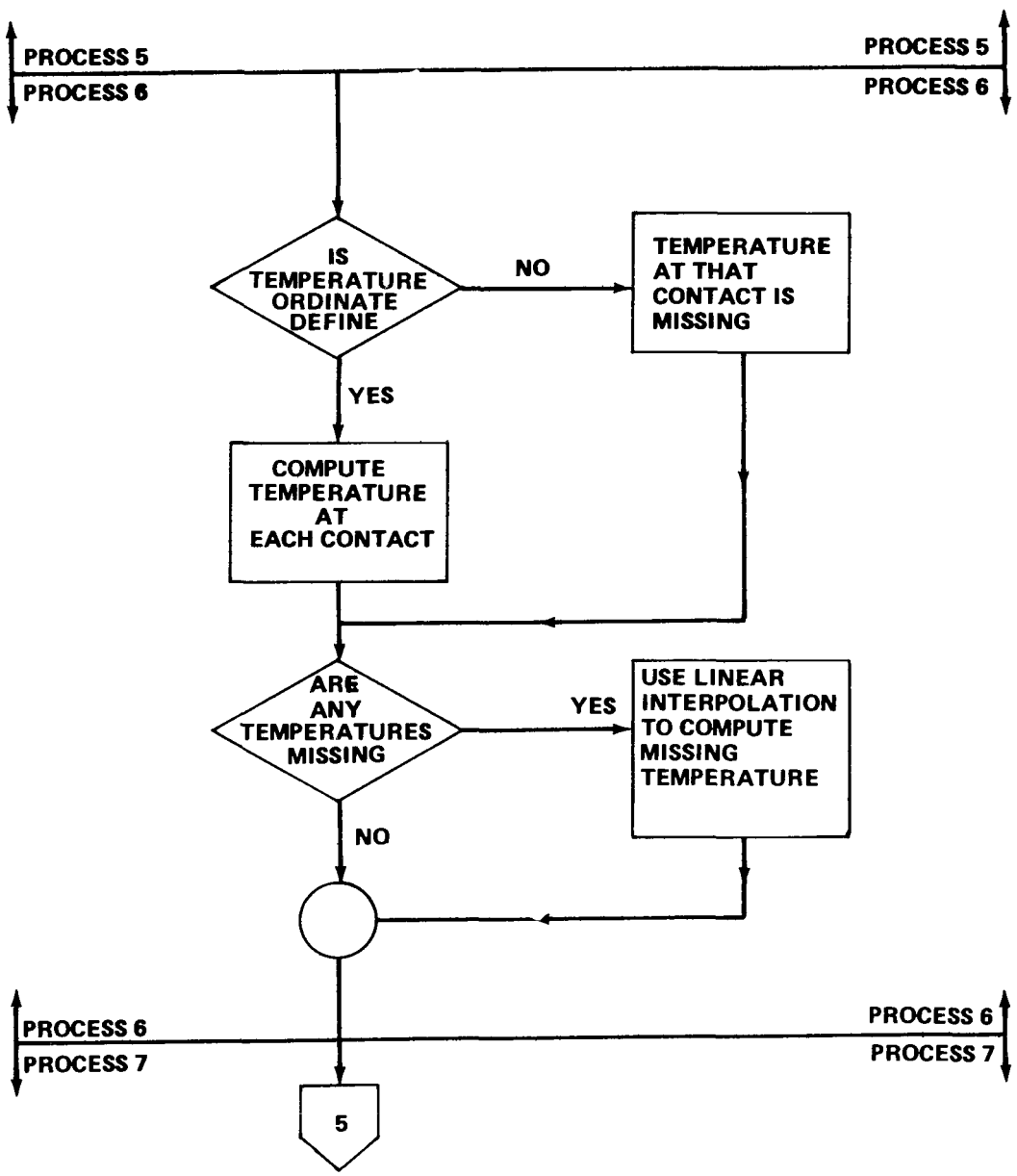

Figure 2.3. (continued)

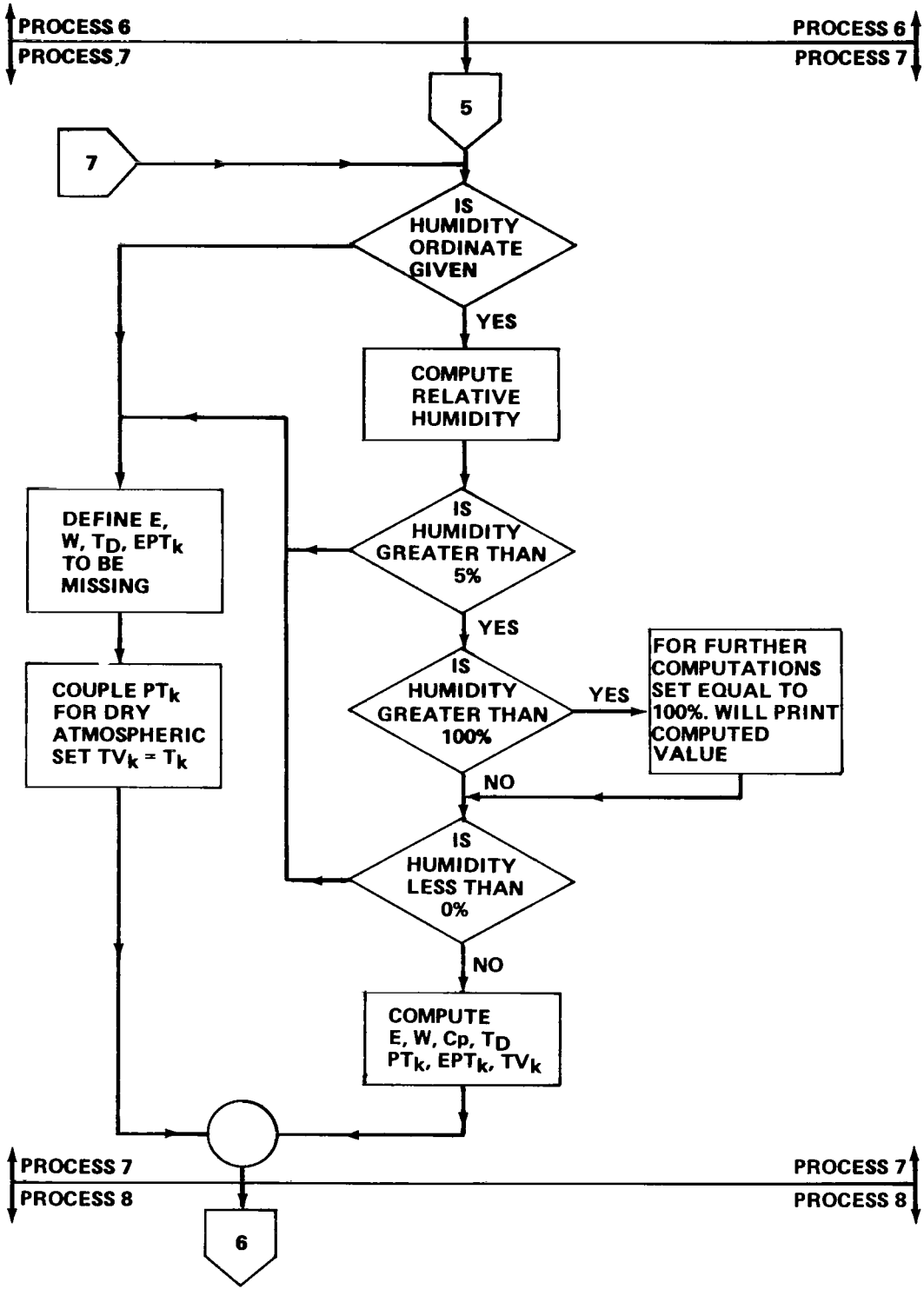

Figure 2.3. (continued)

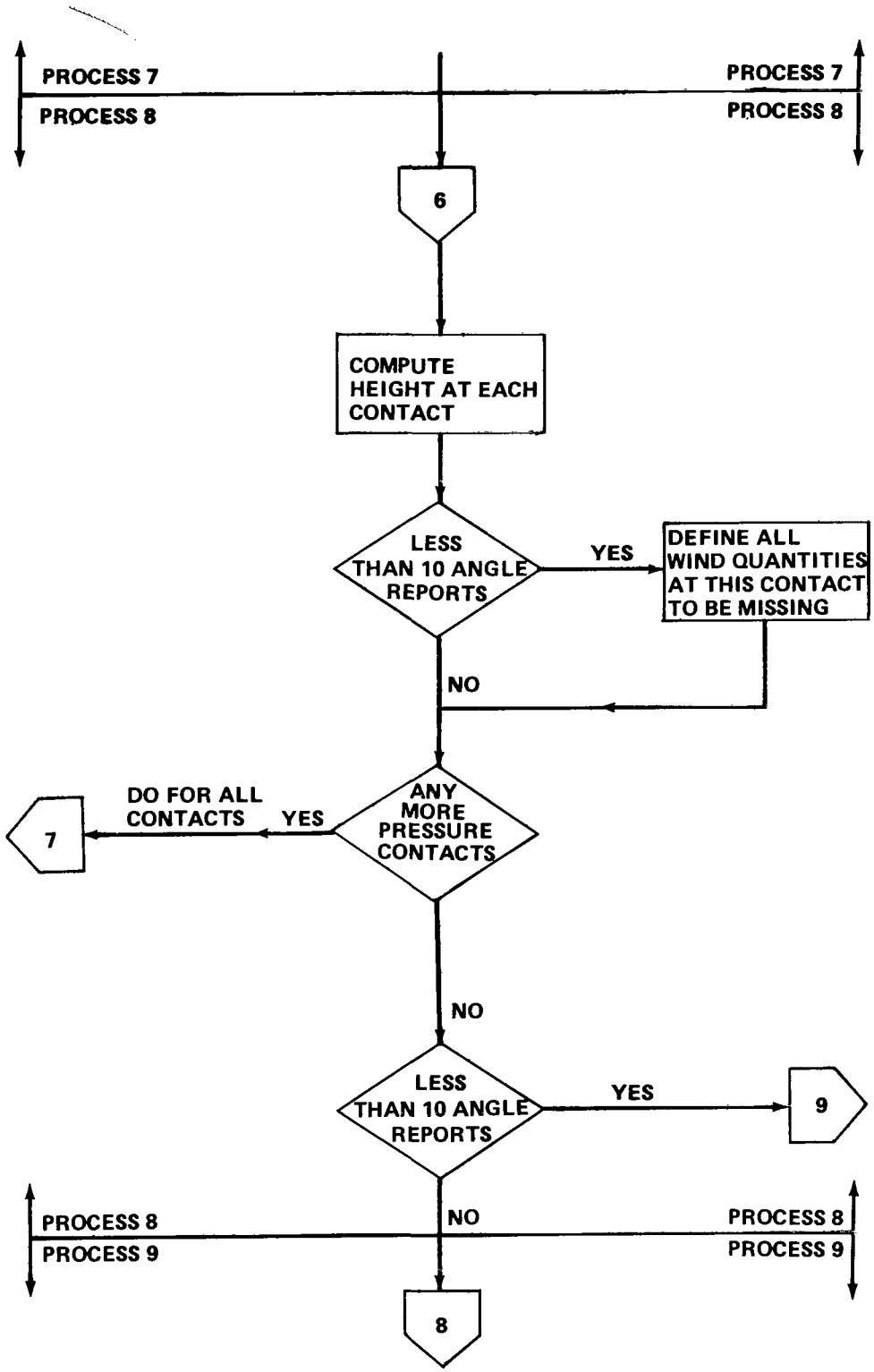

Figure 2.3. (continued)

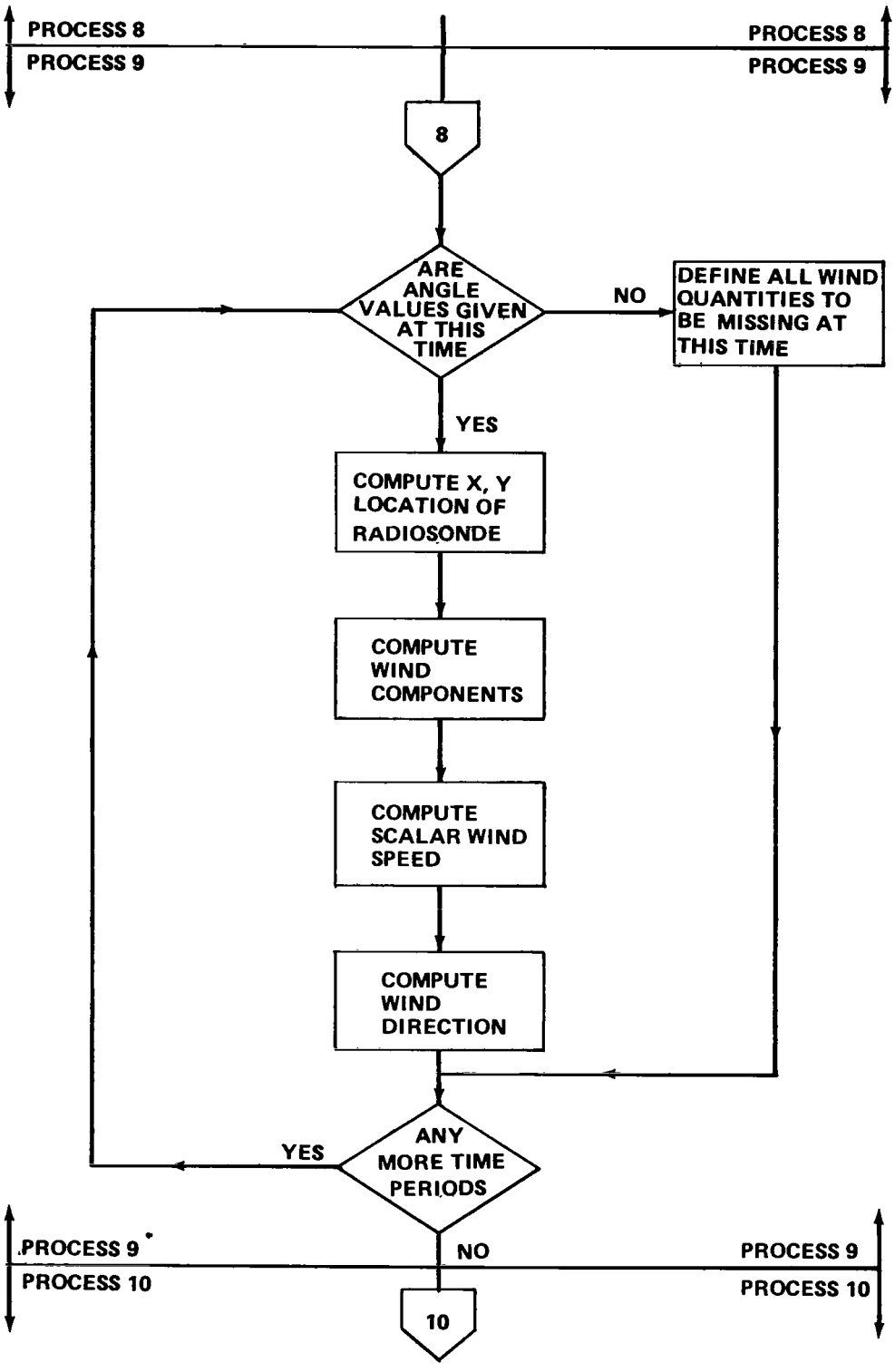

Figure 2.3. (continued)

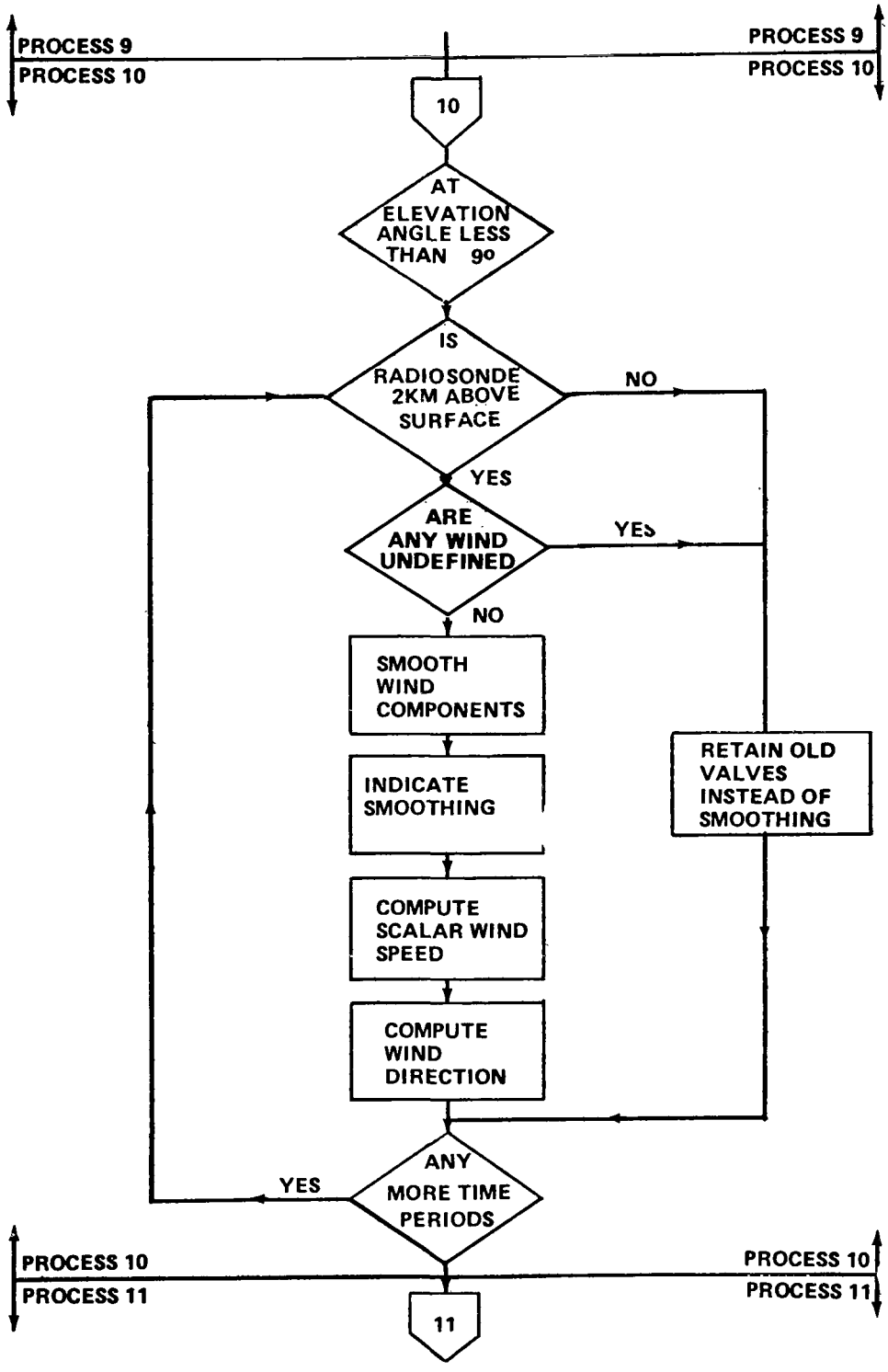

Figure 2.3. (continued)

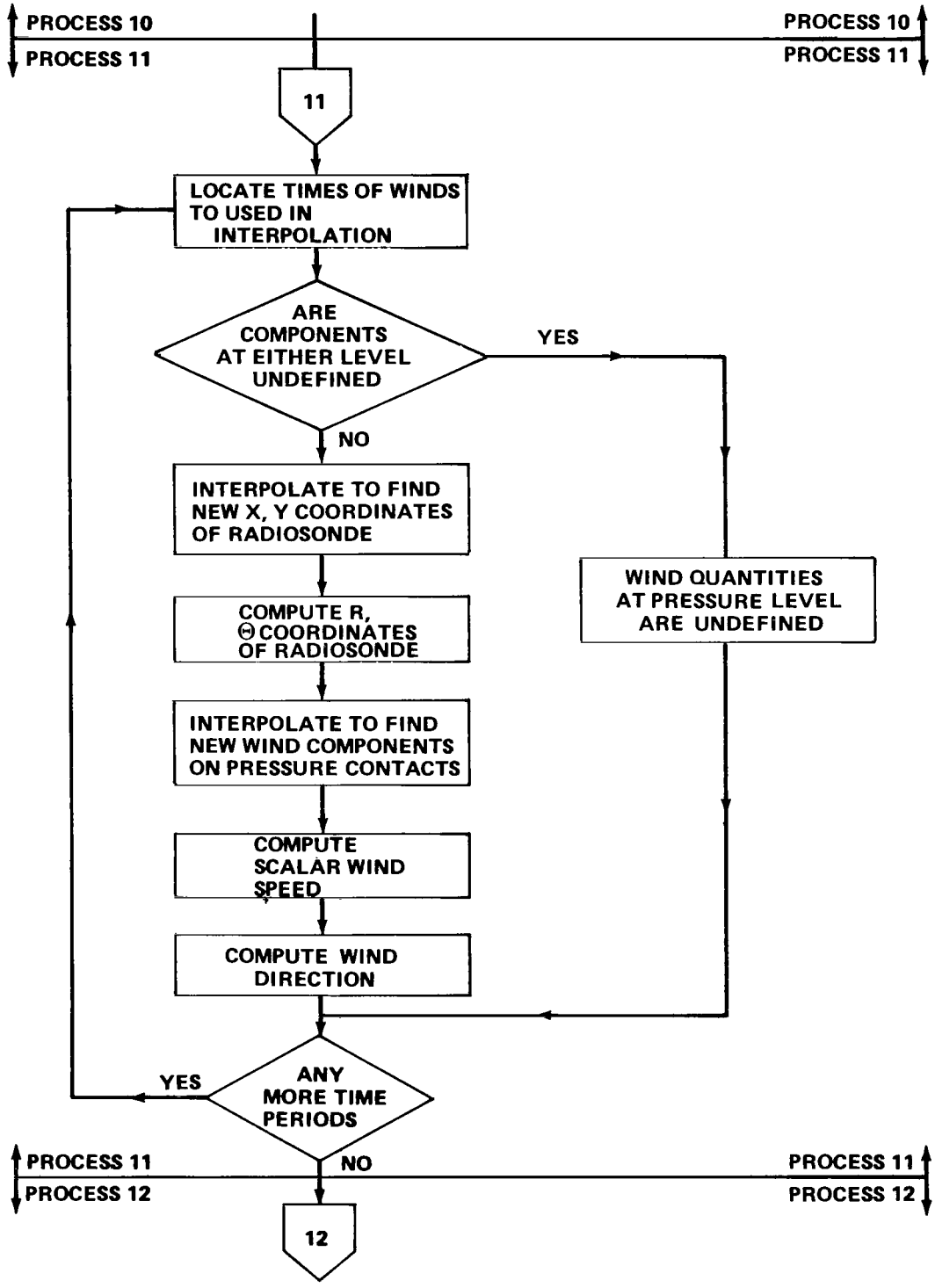

Figure 2.3. (continued)

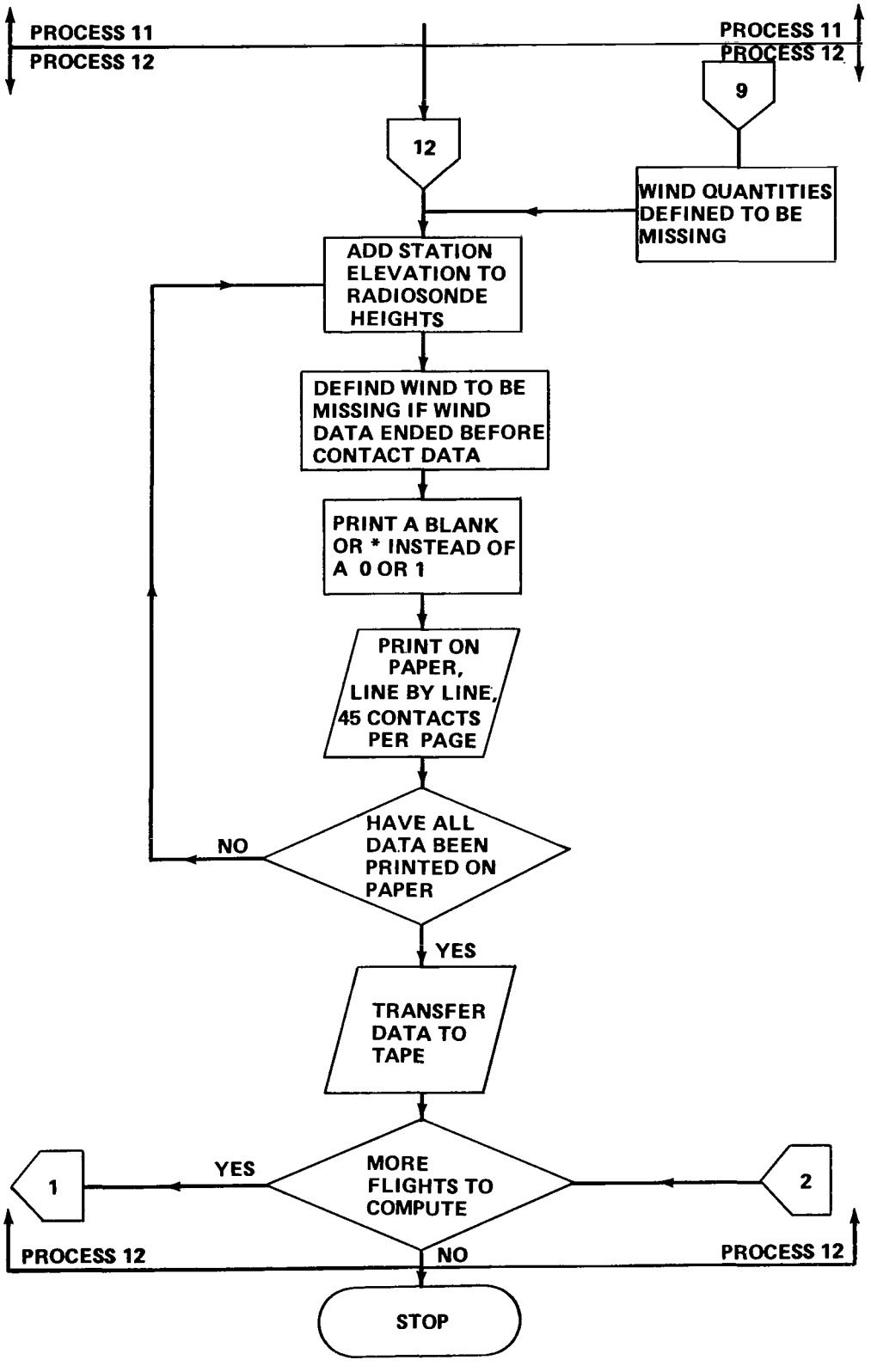

Figure 2.3. (concluded)

described in Table 2.1, page 21. Baseline temperature constants are set up at this stage for later use in computing temperature at each pressure contact. The equations used in this process of the program and the temperature computation process are identical to those currently used by the National Weather Service (NWS) and are described by Fuelberg (16) and Billions (17). The baseline equations are reproduced here:

$$RT_B = EXP[16.0082991 - 0.9966256 \cdot LOG_e(2 \cdot 37.6)] - 48000.0 \quad (2.1)$$

$$RK_1 = TO + 273.15 \quad (2.2)$$

$$RM_1 = 5.3018981\left(\frac{1.0}{303.0} - \frac{1.0}{RK_1}\right) \quad (2.3)$$

$$RM = \frac{-2.47991 \times 10^{-3} + [(2.47991 \times 10^{-3})^2 - 5.89986 \times 10^{-5} \cdot RM_1]^{1/2}}{2.0 \cdot 5.89986 \times 10^{-5}} \quad (2.4)$$

and

$$RM_3 = \frac{14000.0}{RT_B} \cdot EXP(RM_2) \quad (2.5)$$

TO is the negative temperature corresponding to an ordinate of 37.6 units. These constants are the manufactory calibration constants for the radiosondes.

Constants to be used later in the relative humidity computations are evaluated next. The scheme used in this program is based on a procedure described in IRIG Document 108-72 (18). The 20 constants for relative humidity

computation (HC1-HC20) are based on the following equations:

$$\begin{aligned} HC1 &= C1 + C2 \cdot RH_B \\ &\vdots \\ HC20 &= C39 + C40 \cdot RH_B \end{aligned} \qquad (2.6)$$

C1 through C20 are constants determined by the type of humidity element used in the radiosonde, while RH_B is the baseline humidity at a temperature of -40° Celsius and ordinate of 46.0 units.

The ordinate data described in Table 2.2, page 23, are read from magnetic tape. Although pressure contact number and the corresponding pressure are always available, time from release, temperature ordinates, and humidity ordinates may be missing. Since time at each pressure contact is necessary in the reduction scheme, a linear interpolation procedure is used to assign time where it is missing. If interpolation is performed, a locator array is used to mark this fact on the final output with an asterisk. Missing temperature values are interpolated in a later process, but relative humidity is not interpolated.

Most raw angle data were obtained at 30-second intervals, but the data at some stations were available at only 1 minute intervals. In many cases, the 30-second angle data did not begin at the time of release but began at some time after release; therefore, the first angle record is checked to determine if it begins at time equal zero. If

it does not begin at time equal zero, a linear interpolation scheme is used to fill in the missing time, but the missing angles themselves are not interpolated. The fact that interpolation was performed would appear in the final output as missing wind data. Once the angles are determined to begin at time of release, or after the missing times are interpolated back to the time of release, the angles are read without use of the procedure just described. This is possible because missing angle times are not encountered at any place in the data except at the beginning. The angles themselves may be missing, however.

The process of assignment of station parameters matches the station identification number of the flight being computed with that of a station number in the roster so that station elevation and name are retrieved for further use. A subroutine is called at this time to convert the numerical month of the flight to the alphabetical name of the month.

Temperature at each pressure contact is determined by use of the following equations according to Fuelberg (16) and Billions (17):

$$RE = EXP[16.0082991 - 0.9966256 \cdot LOG_e(2 \cdot T_o)] - 48000.0 \qquad (2.7)$$

$$RM_4 = LOG_e\left(\frac{RM_3 \cdot RE}{14000.0}\right) \qquad (2.8)$$

$$RK = \frac{1.0}{\left(\frac{1.0}{303.0}\right) + (4.6774 \times 10^{-5} \times RM_4) + [1.11278 \times 10^{-5} \cdot (RM_4)^2]} \qquad (2.9)$$

and

$$T_C = RK - 273.15 \tag{2.10}$$

T_O is the temperature ordinate at the pressure contact while RM_3 is a result of the baseline computation (Equation 2.5). T_C is temperature in degrees Celsius. If the temperature ordinate is missing at a particular contact, the temperature is first defined to be missing and then linear interpolation is used in a subsequent process to fill the gap. An array is used to mark the location of this interpolation in the final output.

The computation of other thermodynamic quantities at each pressure contact are made with relative humidity being the first quantity to be computed. If the humidity ordinate is missing, all other moisture-related quantities at the contact are defined to be missing. Potential temperature is computed according to this equation:

$$TP_k = T_k \left(\frac{1000.0}{P} \right)^{0.286} \tag{2.11}$$

where P is pressure and T_k is temperature in degrees Kelvin at the contact. Virtual temperature is set equal to the ambient temperature where relative humidity cannot be computed. This equation and many of the other thermodynamics equations to follow may be found in texts such as Hess (19) and IRIG Document 108-72 (18). If the humidity ordinate is given, relative humidity is computed using the procedure

described in IRIG Document 108-72 (18) and given by:

$$RH = (HC1 + HC2 \cdot TP_c)x^9 + (HC3 + HC4 \cdot TP_c)x^8 + \ldots + (HC17 + HC18 \cdot TP_c)x + (HC19 + HC20 \cdot TP_c) \quad (2.12)$$

The values of HC were obtained from the baseline calibration (Equation 2.6); TP_c is temperature at the contact in degrees Celsius while x is defined by the equation:

$$x = \frac{RH_o - 46}{41} \quad (2.13)$$

RH_o is the humidity ordinate at the pressure contact. If relative humidity is less than 5%, it and the other moisture variable are defined to be missing, then Equation 2.11 is used to compute potential temperature. In this situation, virtual temperature is again set equal to ambient air temperature.

The following equations are used to compute the remaining thermodynamic quantities based on relative humidity between 5% and 100%. Vapor pressure in millibars (E):

$$E = RH \cdot 0.0611 \times 10^{(7.5 \cdot TP_c)/(237.3+TP_c)} \quad (2.14)$$

Mixing ratio in gm/kg (w):

$$w = \frac{623.0 \cdot E}{P - E} \quad (2.15)$$

where P is pressure. The specific heat of moist air in

cal gm^{-1} deg^{-1} (Cp):

$$Cp = 0.24\left(1.0 + 0.84 \cdot \frac{W}{1000.0}\right) \tag{2.16}$$

The temperature of the dew point in degrees Celsius (T_D):

$$T_D = \frac{237.3 \cdot LOG_e(E) - 186.527}{8.286 - LOG_e(E)} \tag{2.17}$$

The potential temperature of moist air in degrees Kelvin (PT_k):

$$PT_k = T_k\left(\frac{1000.0}{P - E}\right)^{RD/Cp} \tag{2.18}$$

RD is the gas constant for dry air, namely 0.0687 cal gm^{-1} deg^{-1}.

Equivalent potential temperature in degrees Kelvin (EPT_k):

$$EPT_k = PT_k \cdot EXP\left(\frac{Q \cdot W/1000.0}{Cp \cdot TA_k}\right) \tag{2.19}$$

where Q is the latent heat of vaporization at the lifting condensation level of air at the pressure contact, and TA_k is the approximate temperature of air in degrees Kelvin at the lifting condensation level. Virtual temperature in degrees Kelvin (TV_k):

$$TV_k = \frac{T_k}{1.0 - \left(0.379 \cdot \frac{E}{P}\right)} \tag{2.20}$$

Computation of height at 30-second intervals of the radiosonde above ground level (YS) is computed using the hypsometric equation:

$$YS = YS' + \frac{RD}{g} \cdot \frac{TV_L + TV_{L-1}}{2} \cdot LOG_e\left(\frac{P_{L-1}}{P_L}\right) \qquad (2.21)$$

where YS' is the height of the radiosonde at the preceding contact, g is acceleration of gravity, and L and L-1 are the current and preceding pressure contacts, respectively.

The height of the radiosonde is determined at 30-second increments corresponding to the times of angle observations. This is achieved by a linear interpolation of height based on the time from release which is common to both the height and angle data.

Computation of wind at 30-second intervals are computed every 30 seconds until the angle data are depleted. If angle data are not available at some time within the flight, all quantities that are angle dependent at that time are defined to be missing. The distance of the radiosonde from the release point over a curved earth (S) is computed using a procedure by Danielson and Duquet (20). The equation is:

$$S = R_E\left[\cos^{-1}\left(\frac{\cos\theta}{1 \pm \frac{Y_G}{R_E}}\right) - \theta\right] \qquad (2.22)$$

where R_E is the earth's radius, θ is the elevation angle

between the release point and the radiosonde, and Y_G is the height of the radiosonde above ground level. The X and Y location coordinates of the radiosonde, X_s and Z_s respectively, are then determined from S and the azimuth angle ψ of the radiosonde using the equations:

$$X_s = S \text{ SIN } \psi \tag{2.23}$$

$$Z_s = S \text{ COS } \psi \tag{2.24}$$

Wind speed and direction at the surface are read from the baseline data card; the east-west component (W_{E-W}) and the north-south component (W_{N-S}) at the first level above the ground (30 seconds after release) are obtained by computing a forward difference of the radiosonde locations over a 30-second interval (DT = 30). After this time, centered differences over a 1 minute interval (DT = 60) are used to obtain the components; in both cases the following equations are used:

$$W_{E-W}(L-1) = \frac{X_s(L) - X_s(L-2)}{DT} \tag{2.25}$$

$$W_{N-S}(L-1) = \frac{Z_s(L) - Z_s(L-2)}{DT} \tag{2.26}$$

The scalar wind speed is given by:

$$WS(L-1) = \left[[W_{E-W}(L-1)]^2 + [W_{N-S}(L-1)]^2 \right]^{1/2} \tag{2.27}$$

Wind direction is obtained by first computing the value of A

from the equation:

$$A = \left[TAN^{-1} \left(\left| \frac{W_{E-W}(L-1)}{W_{N-S}(L-1)} \right| \right) \right] \cdot 57.29578 \qquad (2.28)$$

Since division by zero is undefined, steps must be taken to insure that this action is never attempted in Equation 2.28. Therefore, the absolute value W_{N-S} is never allowed to be smaller than 1.0×10^{-5}. After computing Equation 2.28, the following quadrant selections are applied to determine wind direction:

$$\frac{W_{E-W}}{W_{N-S}} \leq 0 \text{ and } W_{E-W} \leq 0; \quad DIR = 360° - A \qquad (2.29)$$

$$\frac{W_{E-W}}{W_{N-S}} \leq 0 \text{ and } W_{E-W} > 0; \quad DIR = 180° - A \qquad (2.30)$$

$$\frac{W_{E-W}}{W_{N-S}} > 0 \text{ and } W_{E-W} \leq 0; \quad DIR = A + 180° \qquad (2.31)$$

$$\frac{W_{E-W}}{W_{N-S}} > 0 \text{ and } W_{E-W} > 0; \quad DIR = A \qquad (2.32)$$

In order to have wind direction (WD) as that direction from which the wind blows, the following corrections are applied:

$$D = DIR + 180° \qquad (2.33)$$

$$D > 360°, \quad WD = D - 360° \qquad (2.34)$$

$$D \leq 360°, \quad WD = D \qquad (2.35)$$

Smoothing of the winds is performed on the wind components previously obtained at 30-second intervals by a five point smoothing process. The smoothing process does not begin until the time from release that corresponds to the radiosonde being 2 kilometers above the release point. Once begun, the smoothing process continues through the remaining time periods except that if any one of the five values to be used in the smoothing process is found to be missing no smoothing is performed at that time, and the original components are retained. When smoothing is performed, the following equations are used:

$$S_{E-W} = \sum_{L=1}^{5} W_{E-W}(L) \cdot CD(L) \tag{2.36}$$

$$S_{N-S} = \sum_{L=1}^{5} W_{N-S}(L) \cdot CD(L) \tag{2.37}$$

S_{E-W} is the smoothed east-west wind component, and S_{N-S} is the smoothed north-south wind component. The values of CD are the following binomial smoothing coefficients:

CD (1) = 0.06

CD (2) = 0.25

CD (3) = 0.38

CD (4) = 0.25

CD (5) = 0.06

The new components are used to determine a new wind direction and speed as was done in Equations 2.27-2.35.

Interpolation of the smoothed winds to pressure contacts is possible, since time from release is common to both ordinate and wind data. Therefore, it is possible to interpolate the smoothed winds and assign values to times corresponding to the pressure contacts. The X and Y coordinates of the radiosonde are first linearly interpolated and used to determine the range and azimuth angle of the radiosonde location. This is done in a manner similar to that of computing wind speed and direction except that coordinates and not wind components are used in this process. Wind components at the pressure contacts are determined by interpolation of the smoothed components which are then used to compute wind speed and direction at the contact according to Equations 2.27-2.35.

25-MB Increments Data

Meteorological charts are frequently plotted for a constant pressure surface; therefore, a process was used to interpolate the output onto surfaces that are 25 millibar apart. A flow chart is given in Figure 2.4. Since pressure contacts used in interpolation are only about 12 millibar apart near the surface and 3 millibar apart near the top of the flight, it is possible to use linear interpolation instead of logarithmic interpolation. If the particular 25 millibar level does not lie between the surface pressure value and the minimum pressure at the top of the flight, the data for that 25 millibar pressure surface are defined to be

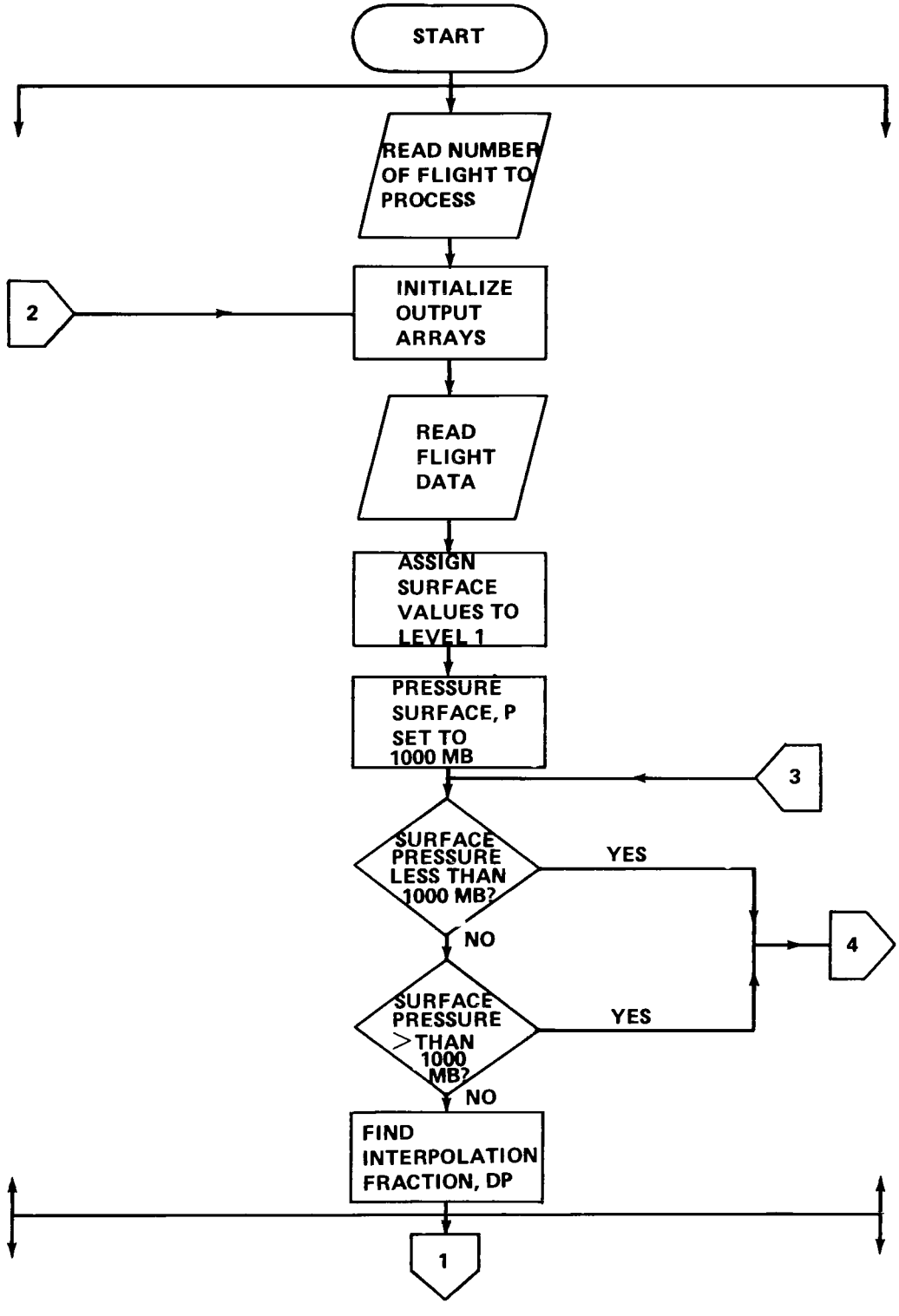

Figure 2.4. Flow chart of the 25-millibar increments data process.

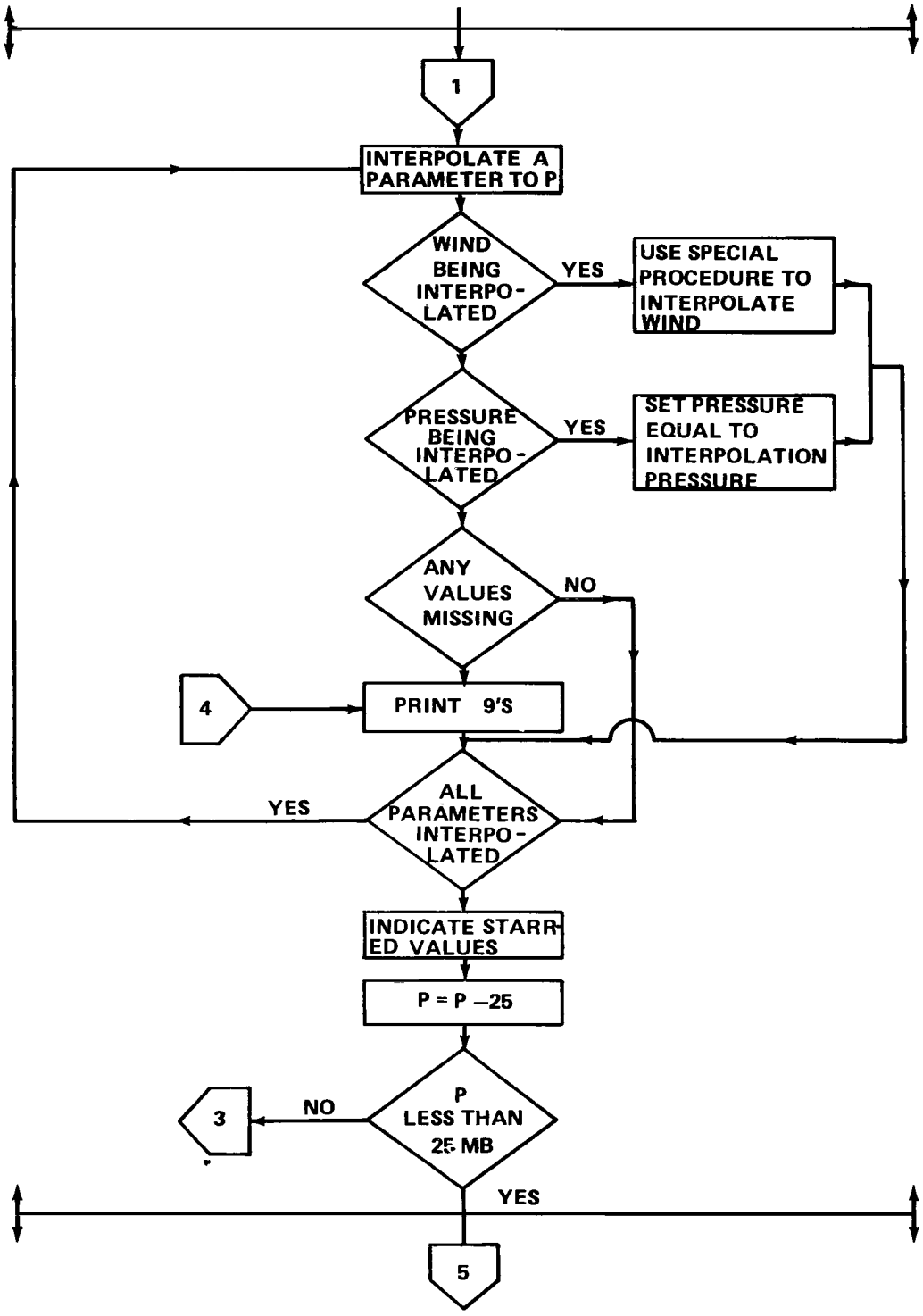

Figure 2.4. (continued)

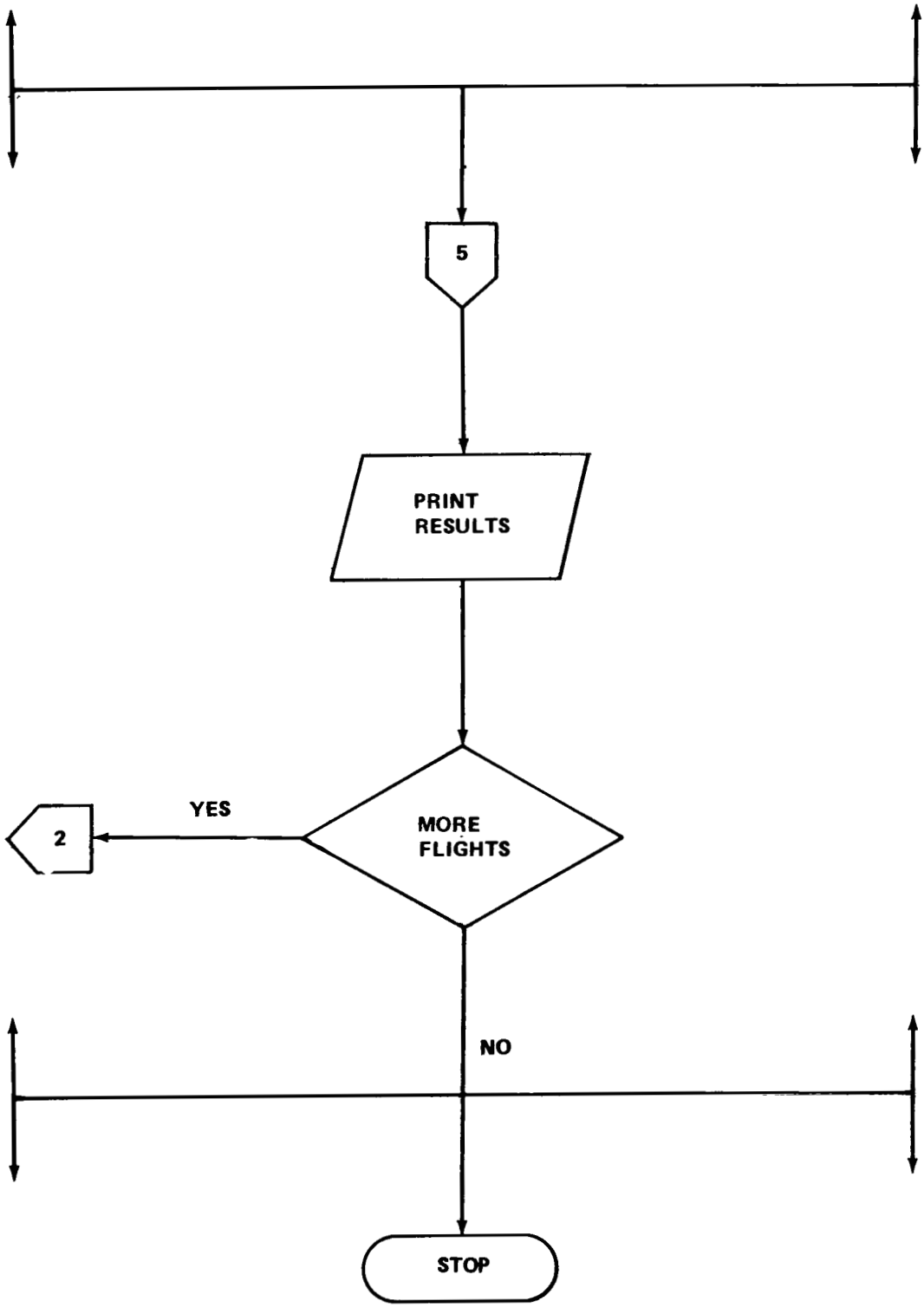

Figure 2.4. (concluded)

missing. Since wind direction may oscillate around 360 degrees, care must be taken to guard against fictitious directions. If data needed in the interpolation of a quantity are missing, the interpolated quantity is also defined to be missing.

CHAPTER III

DATA ERROR ANALYSIS

I. INTRODUCTORY REMARKS

Accuracy of atmospheric data is an important consideration in its use. This is especially true when small scale temporal and spatial features are being studied since these features may have amplitudes which approach the limit of accuracy of the data. The accuracy of data is dependent on several factors. These factors are the type of equipment being used, the reduction procedures used to process the data, human factors in calibrating and tracking the radiosonde, and reading the data. Current estimates of errors in the raw data are given in this chapter along with a discussion of how these errors affect the final processed data.

II. ACCURACY OF THE THERMODYNAMIC DATA

Temperature according to Case (21) adopts a root-mean square (rms) error of 0.7° Celsius based on laboratory determination, while Weidner and Chambers (22) believe that a value of 1.4° Celsius is more realistic operationally. Hodge and Harmantas (23) found rms differences between military and National Weather Service radiosondes to be about 0.5° Celsius under field conditions. It is believed that rms errors in the experiment temperature data are approximately 1.0° Celsius.

Radiosondes are calibrated after manufacture so that each pressure contact on the baroswitch corresponds to a certain atmospheric pressure. By comparing baroswitch pressure with those obtained hydrostatically using radiosonde temperatures and radiosonde heights measured by a high precision radar, Weidner and Chambers (22) found that baroswitch errors are generally small. The rms errors were determined to be approximately 1.3 mb from the surface to 400 mb, 1.1 mb from 400 to 100 mb, and 0.7 mb between 100 and 10 mb. These errors are considered representative of the experiment data.

A carbon strip element is used as the humidity sensor in radiosondes. Case (21) reports an error of 10% in the sensor. The current specifications for the humidity element are ±3% at 25° Celsius, ±5% at temperatures less than 25° Celsius plus an allowance for hysteresis of ±4% above a value 33% relative humidity, and ±5% at humidities between 10% and 33% according to Brousaides (24). Brousaides concludes that use of humidity sensor data at values below 20% is not valid except for the trend information. The humidity data from this investigation are thought to be generally within 10% of the true values.

Altitude of the radiosonde is determined by use of the hypsometric equation in which pressure, temperature, and relative humidity are variables. Errors in temperature, however, are the greatest source of error in height determination. The worst possible situation arises when

temperature errors are systematically of the same sign through great depths of the atmosphere. The height error at various pressures due to a systematic temperature error of 1.0° Celsius is given in Table 3.1. These errors are larger than would be expected in the experiment data inasmuch as the errors in temperature generally are of both signs. Scoggins and Smith (25), based on a study of simulate data, concluded that realistic rms errors in pressure altitude are on the order of 10 gpm at 500 mb, 20 gpm at 300 mb, and 50 gpm at 50 mb. An analysis of the experiment data suggests comparable errors.

III. ACCURACY OF THE WIND DATA

The experiment wind data were computed in several stages. These raw winds were smoothed, and the smoothed values were then interpolated to pressure contacts. The accuracy of the raw wind data will be described in detail, but the effects of smoothing and interpolation on accuracy must be described in more general terms.

Scoggins (26) developed a statistical technique for evaluating errors in wind data that will be used. According to Scoggins, if F is a function of X, Y, and Z, and if these are in error by ΔX, ΔY, and ΔZ, then F is in error by an amount ΔF which is given by the Taylor's series as:

$$\Delta F = \frac{\partial F}{\partial X} \Delta X + \frac{\partial F}{\partial Y} \Delta Y + \frac{\partial F}{\partial Z} \Delta Z \qquad (3.1)$$

The equation is valid if ΔX, ΔY, and ΔZ are small compared

TABLE 3.1

ERROR IN ALTITUDE DUE TO A SYSTEMATIC TEMPERATURE ERROR OF 1° CELSIUS

Pressure (mb)	Altitude (gpm)
50	87.7
100	67.5
200	47.1
300	35.3
400	26.8
500	20.7
600	15.3
700	10.7
800	6.7
900	3.1
1000	0

with $\partial F/\partial X$, $\partial F/\partial Y$, and $\partial F/\partial Z$; it was assumed that all terms involving squares, higher powers, and cross products of ΔX, ΔY, and ΔZ are negligible, and that higher derivatives are small in value. After squaring both sides of Equation 3.1 and replacing each term by its average value, the following equation is obtained when one assumes that errors in X, Y, and Z are independent:

$$\sigma_f^2 = \left(\frac{\partial F}{\partial x}\,\sigma_x\right)^2 + \left(\frac{\partial F}{\partial y}\,\sigma_y\right)^2 + \left(\frac{\partial F}{\partial z}\,\sigma_z\right)^2 \qquad (3.2)$$

The symbol σ denotes rms error.

Radio direction finding equipment is used to measure azimuth and elevation angles of the radiosonde while the hypsometric equation is used to determine its height. For the purpose of this discussion, a flat earth will be assumed although this was not done in the actual reduction process. The X, Y, and Z coordinates of the radiosonde are given by:

$$X = Z \text{ COT } \theta \text{ SIN } \psi \qquad (3.3)$$

$$Y = Z \text{ COT } \theta \text{ COS } \psi \qquad (3.4)$$

$$Z = \frac{R}{g}\,\overline{TV}\,\text{LOG}_e\left(\frac{P_1}{P_2}\right) \qquad (3.5)$$

where θ is elevation angle, ψ is azimuth angle, R is the gas constant, g is acceleration due to gravity, $\overline{TV}$ is mean virtual temperature, and P_1 and P_2 are pressure at two levels. Errors in X, Y, and Z can then be evaluated by use of Equation 3.2. The assumptions made are that errors in θ,

TV, and P are independent of each other, and that errors in each parameter are normally distributed. Results from Scoggins and Smith (25) indicate that there is some systematic component to the elevation angles at values below 10 degrees, but generally the above assumptions are thought to be valid for the experiment data which was recorded at 30-second intervals. Errors in Z are mostly due to errors in temperature and not errors in pressure or moisture. Application of the above equations yields:

$$\sigma_x^2 = [\sigma_z \cdot \text{COT}\ \theta \cdot \text{SIN}\ \psi]^2 + [\sigma_\theta \cdot Z \cdot \text{CSC}^2\theta \cdot \text{SIN}\ \psi]^2 + [\sigma \cdot Z \cdot \text{COT}\ \theta \cdot \text{COS}\ \psi]^2 \quad (3.6)$$

$$\sigma_y^2 = [\sigma_z \cdot \text{COT}\ \theta \cdot \text{COS}\ \psi]^2 + [\sigma_\theta \cdot Z \cdot \text{CSC}^2\theta \cdot \text{COS}\ \psi]^2 + [\sigma \cdot Z \cdot \text{COT}\ \theta \cdot \text{SIN}\ \psi]^2 \quad (3.7)$$

$$\sigma_z^2 = \left(\sigma_T \frac{R}{g} \text{LOG}_e \frac{P_1}{P_2}\right)^2 \quad (3.8)$$

Danielsen and Duquet (20) assumed that $\sigma = \sigma_\theta = 0.05$ degree for the radio direction finding equipment used in the experiment; however, Weiss and Georgian (27) indicate that these values are not equal, are larger than those generally assumed, and greatly dependent on elevation angle. A value of 1.0° Celsius is assumed for σ_T. If one assumes that $\psi = 90$ degrees, the value of σ_x will be a maximum, while if $\psi = 0$ degree, the value of σ_y is a maximum. The rms error of wind speed components σ_{wx} and σ_{wy} is given by:

$$\sigma_{wx} = \frac{[\sigma_{x_2}^2 + \sigma_{x_1}^2]^{1/2}}{\Delta t} \tag{3.9}$$

$$\sigma_{wy} = \frac{[\sigma_{y_2}^2 + \sigma_{y_1}^2]^{1/2}}{\Delta t} \tag{3.10}$$

where subscripts 2 and 1 refer to consecutive measurements. These equations can be simplified by assuming $\sigma_{x_2}^2 = \sigma_{x_1}^2$ and $\sigma_{y_2}^2 = \sigma_{y_1}^2$, which is reasonable over short time periods. The raw winds computed by the reduction program are based on angle measurements that are 60 seconds apart ($\Delta t = 60$). Finally, the rms error of the scalar wind ($\sigma_{|v|}$) is given by:

$$\sigma_{|v|} = [\sigma_{wx}^2 + \sigma_{wy}^2]^{1/2} \tag{3.11}$$

$\sigma_{|v|}$ is a maximum at either 0 degrees or 90 degrees.

Figure 3.1 shows the results of the computations at various elevation angles and pressure; heights used for corresponding pressure values are those of a standard atmosphere. RMS errors increase with increasing height and with decreasing elevation angle. Maximum rms errors for the experiment data at 700 mb range from 2.5 m sec^{-1} at an elevation angle of 10 degrees to about 0.5 m sec^{-1} at an elevation angle of 40 degrees. At 500 mb, the errors are 4.5 m sec^{-1} to about 0.8 m sec^{-1} at the same elevation angles; while at 300 mb, the errors are 7.8 m sec^{-1} to about 1.0 m sec^{-1}, respectively. One should remember that these

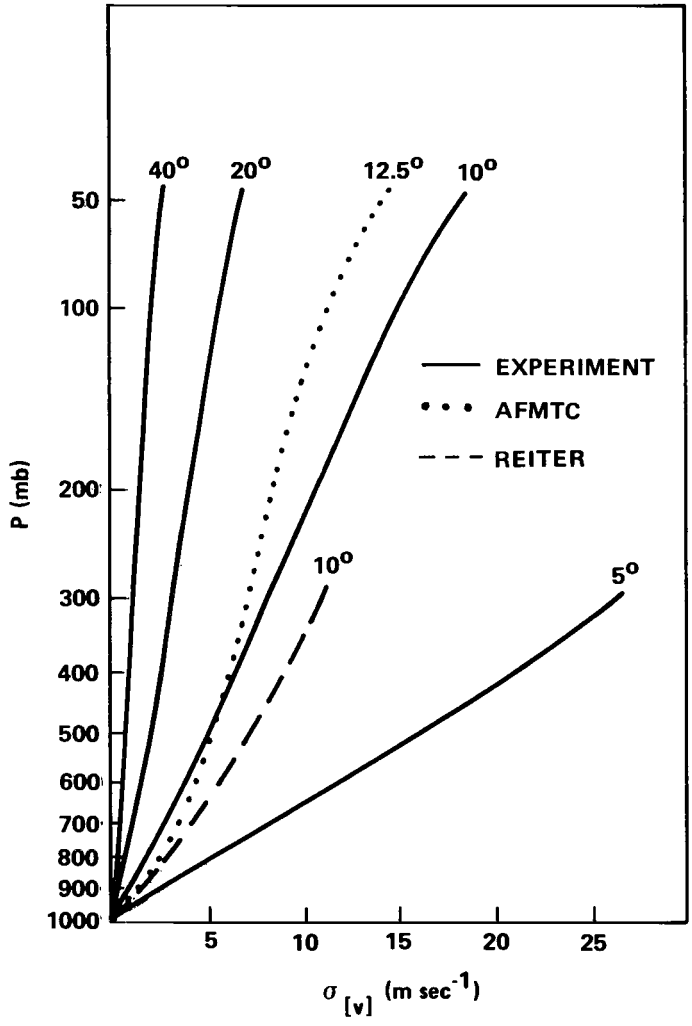

Figure 3.1. RMS errors of scalar wind speed as a function pressure and elevation angle.

values are maximum since the azimuth angle was assumed to be either 0 degrees or 90 degrees.

These errors of the raw wind are in agreement with those cited by Scoggins and Turner (28). Data published by the Air Force Missile Test Center (29) are also in good agreement with those of the experiment. RMS vector errors were given as a function of altitude and constant mean wind speed through a layer. Assuming an ascent rate of 5.0 m sec^{-1}, the elevation angle of the radiosonde at each altitude could be determined. RMS vector errors for an elevation angle of 12.5 degrees are shown in Figure 3.1. The results agree well with the experiment results. Results by Reiter (30), given in Figure 3.1 for an elevation angle of 10 degrees, are also consistent with those of the experiment. The errors cited by Reiter are based on a time interval of 2 minutes and an error in angle measurement of 0.075 degree.

When the elevation angle is small, $\sin \theta \approx \tan \theta$; therefore, rms errors in wind direction (σ_D) may be approximated by:

$$\sigma_D \approx \text{SIN}^{-1}\left(\frac{\sigma_{wy}}{|v|}\right) \tag{3.12}$$

where $|v|$ is the scalar wind speed. Since the error is dependent on the azimuth angle of the radiosonde, maximum errors can be given by making the azimuth angle equal to 0 degrees. Results for the experiment data are plotted as a

function of pressure and elevation angle in Figure 3.2. At 700 mb, the scalar wind speed is assumed to be 15 m sec^{-1}, while at 500 mb and 300 mb, it is assumed to be 20 m sec^{-1} and 25 m sec^{-1}, respectively. Errors from other geometric conditions and wind speeds would be different. The errors increase with decreasing pressure and decreasing elevation angle. Errors in the experiment wind direction at 700 mb range from about 9.5 degrees at an elevation angle of 10 degrees to about 1.3 degrees at an elevation angle of 40 degrees. At 500 mb, the errors are 13.4 degrees and 1.8 degrees at the same elevation angle, while at 300 mb, the errors are 18.0 degrees and 1.8 degrees, respectively. If one assumes that the rms vector errors given by the Air Force Missile Test Center (29) are maximum errors, the maximum rms direciton error will be given by:

$$\sigma_D = \text{TAN}^{-1}\left(\frac{\sigma_{\text{Vector}}}{|v|}\right) \tag{3.13}$$

RMS errors for an elevation angle of 12.5 degrees are plotted in Figure 3.2 for the same scalar wind speeds that were used previously. Good agreement can be seen between these values and those cited for the experiment data.

It may be stated that the rms errors cited for the raw winds are in general agreement with those obtained from other sources and are highly dependent on radiosonde location and ambient wind speed.

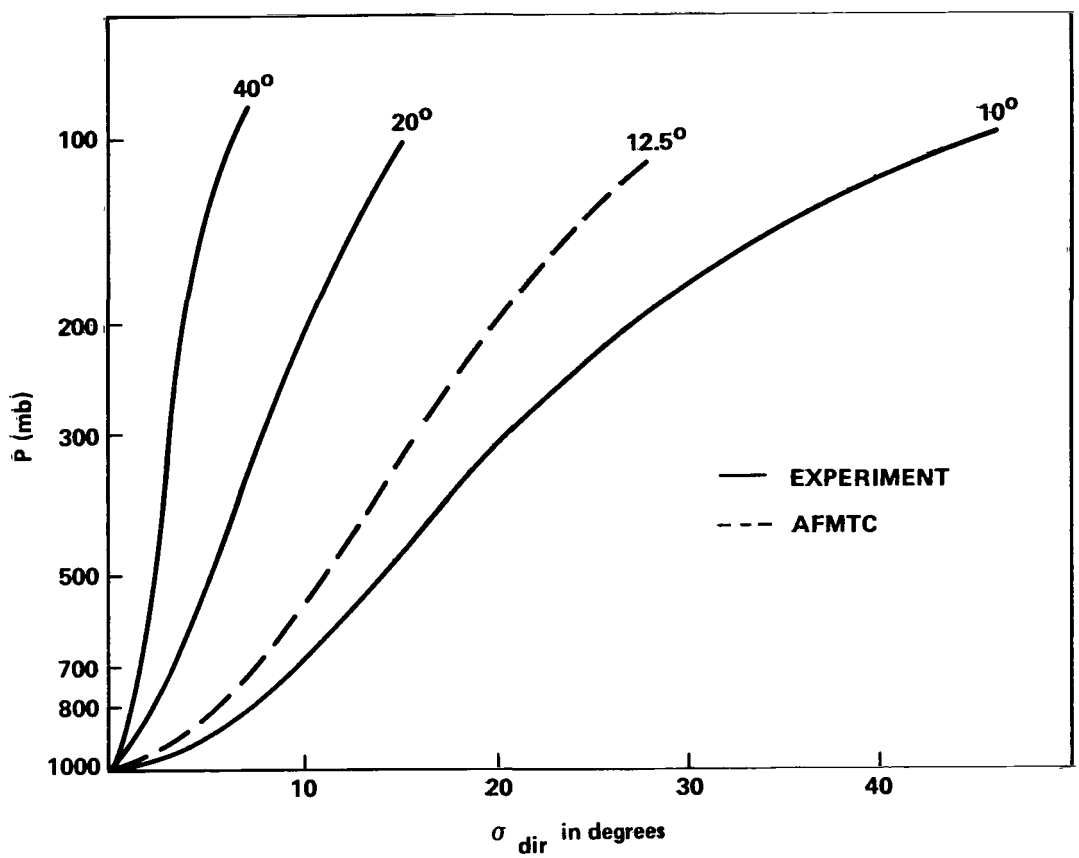

Figure 3.2. RMS errors of wind direction as a function of of pressure and elevation angle.

The experiment data indicates many small-scale variations in wind speed that become more apparent with increasing altitude. While some of these variations are indeed mesoscale meteorological phenomena, many are simply due to inaccuracies in the angle data which were truncated to the nearest 0.1 degree at 30-second intervals. It was felt desirable to smooth these winds so that very small scale features would be suppressed. The wind speeds are observed to become very erratic at elevation angles below 10.0 degrees with most of the fluctuations undoubtedly being nonmeteorological in nature. Danielsen and Duquet (20) found that errors in the elevation angles increase to 10 and 15 times the generally accepted rms error of 0.05 degree when the elevation angle is less than 10.0 degrees. They concluded that the increase in error was due to the inability of the tracking equipment to discriminate between direct and ground reflected or refracted signals. Therefore, some method of smoothing is clearly needed to suppress the large oscillations in wind speed associated with low elevation angles.

Several smoothing techniques were investigated in order to find a procedure which would perform the types of smoothing needed and lend itself to error analysis procedures. Smoothing the angle data by least square polynomial fitting was considered, but results obtained when this procedure was used by Scoggins and Smith (25) were not satisfactory. The application of smoothing functions to the

elevation angles and finite differencing over larger time intervals were considered but not used.

It was finally decided to apply five point binomial coefficients to the raw wind components that were obtained at 30-second intervals, and then to recompute scalar wind speeds and directions using the smoothed components. The response function for the five point weighted average is shown in Figure 3.3. Changes in speed with a frequency higher than 1.0 cycle minutes^{-1} are completely eliminated by the smoothing process while events of lower frequency are smoothed to a lesser extent. For example, 81 percent of the amplitude of changes in speed with a frequency of 0.2 cycle minutes^{-1} would be retained by the method, and 25 percent of the amplitude of changes in speed with a frequency of 0.5 cycle minutes^{-1} would be retained. Assuming an ascent rate of the radiosonde of 5 meters per second, this means that 81 percent of the measured shear in a 760 meter layer of the atmosphere would be retained by the smoothing method, and 25 percent of the measured shear in a 300 meter layer would be retained.

Smoothed wind components at 30-second intervals were interpolated on the basis of time from release to correspond to data given for the pressure contacts to determine the accuracy of pressure contact winds. New scalar wind speeds and directions were then computed. Near the surface, pressure contacts occur at approximately 0.5 minute intervals so that no great amount of smoothing is involved in matching

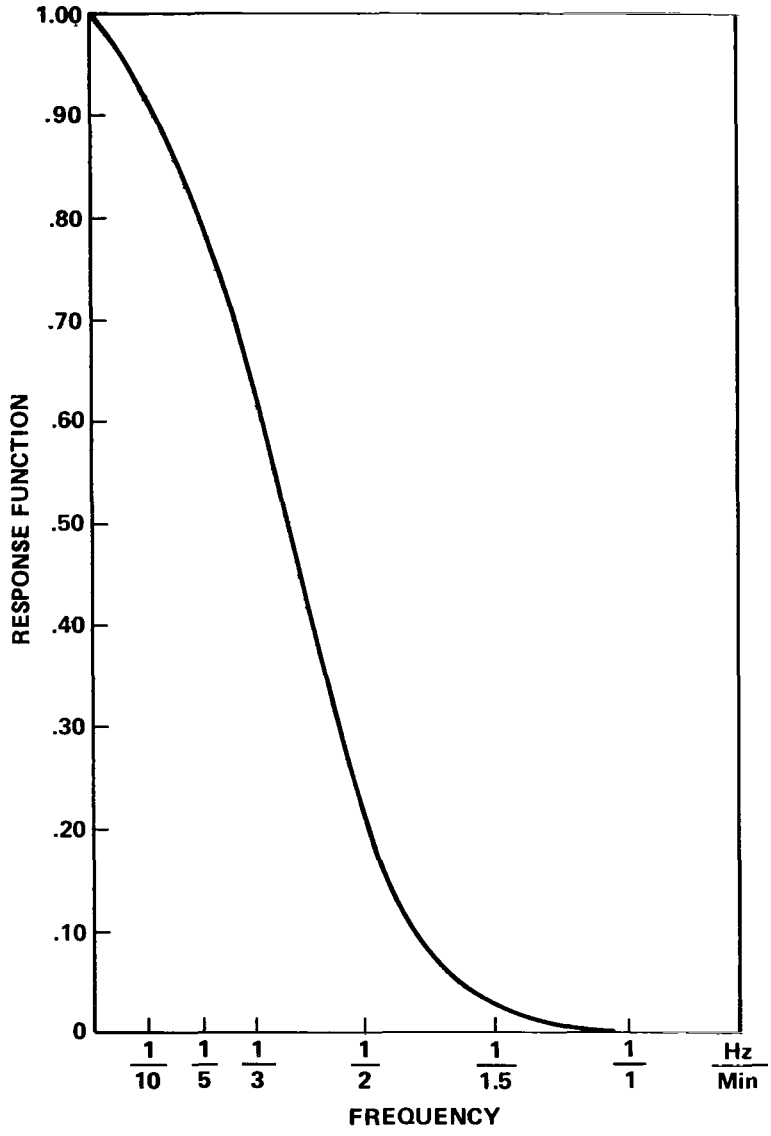

Figure 3.3. Response function for a five-point weighted average using binomial coefficients.

the winds with the contact data. At higher altitude, the difference in time between successive pressure contacts increases so that at 200 mb, the difference is about 0.6 minutes; at 50 mb, about 1.0 minutes; and at 25 mb, about 1.5 minutes. At these higher levels, more and more smoothing is involved in the interpolation process. The added smoothing due to larger time intervals between pressure contacts is evident near the top of the flight. This is not undesirable because the elevation angle generally decreases with altitude causing poorer quality wind data.

The accuracy of the experiment wind data on pressure contacts is greater than that for the raw winds because of the added smoothing and interpolation. In addition, errors cited for the raw winds were maxima for the stated elevation angles and pressure surfaces.

CHAPTER IV

ATMOSPHERIC VARIABILITY EXPERIMENT AND MESOSCALE STRUCTURE RESULTS

I. INTRODUCTORY REMARKS

The major results of the Atmospheric Variability Experiment are presented in this chapter. The results consist of maps, charts, and graphs which depict the kinematic and thermodynamic data up to the 200 mb level. Analysis of these data in the context of atmospheric variability are presented.

Before proceeding to a discussion of the AVE data, it is worthwhile to list some of the mechanisms by which severe storms are generated from a hydrostatically unstable atmosphere (local or finite amplitude instability). This will help to focus attention on the major result of the experiment which is a unique data set that documents an outbreak of extremely severe weather over the Midwest and Eastern United States. The set is characterized by the observed occurrence of 22 tornadoes.

Some of the following mechanisms believed responsible for mesoscale triggering of severe storms involve vertical lifting. The textbook mechanism for producing severe storm lines is the surface cold front. This mechanism is referred to as frontal uplift. In spite of limited research in this area, it is well known that cold fronts do produce violent

storms on occasion. The problem is that not all cold fronts have significant uplift associated with them, and when they do, the potential instability of the air ahead of the front in the warm air zone may have been exhausted by convective overturning triggered at earlier times.

A second mechanism related to severe storm formation is the dry line. The dry line is a discontinuity between moist air from the Gulf of Mexico and dry southwest desert air. Unlike the classic cold or warm front the dry line does not usually exhibit a significant density discontinuity across it, but it tends to develop certain front-like features, in the sense that a dew point discontinuity is present. There is evidence that when strong upper westerly currents from the desert interact with the deep convective layer which exists in the dry air during the daytime westerly momentum is rapidly brought down to the surface, creating low level flow in geostrophic balance and an associated convergence zone near the dry line. The events that occur are not fully understood and many mysteries remain to be unraveled.

A third mechanism unique to the Southern Plains states is the well known diurnally modulated low level southerly jet, which occurs as a climatic feature through the spring and summer. The basic dynamics of this phenomenon involve the strong accelerating effects of the Rocky Mountains as an elevated heat sink plus the atmospheric Ekman boundary layer diurnal oscillations which are

associated with diurnal variability of static stability. The result is a very strong low level jet which in turn is responsible for the initiation of severe weather.

A fourth mechanism responsible for mesoscale triggering is orographic lifting of air. The mesoscale features in the AVE experiment region in the opinion of the author are not believed to be sufficiently large to be considered as being a major factor in the analysis of the AVE data.

However, it should be kept in mind that local terrain features can induce finite amplitude gravity wave motion such that if the atmosphere is conditionally unstable and the amplitude of the wave is sufficiently large, the air parcels could become saturated and the conditional instability of the atmosphere could be realized. Other effects can be cited (such as the change of surface roughness effects, heat island effects and others).

A fifth and probably the most frequent impulse for triggering new convective storm cells is the low level outflow from earlier storms. This effect should be strongest at short distances from the previous cell and, thus, can be considered to be a part of the internal storm dynamics. The idea here is that once the large scale, mesoscale, and boundary layer forcing mechanisms have removed the inhibiting stable layer, buoyancy forces are then set free to transform large amounts of potential energy into the kinetic form.

The above major mechanisms as well as others cause severe storms and if the convection in these storms is of sufficient intensity to stretch the vortex tubes within the storm and concentrate vertical vorticity into a small area, then it is possible that tornadoes can result from the storm. Although relatively small, the tornado is one of the most locally destructive forces in nature. The tornado is characterized by a funnel cloud, accompanies an otherwise severe thunderstorm, is on the ground an average of 20 minutes, and damages an average area one-fouth miles wide along a path toward the northeast about 10 miles long, according to Kessler (30). While much damage is probably caused by winds above 125 miles per hour, the maximum winds of tornadoes (which have never been accurately measured) are probably between 175 and 250 miles per hour. Scientific observation of tornadoes is made very difficult because of their random occurrence, brief duration, small size, and great violence. The AVE data set provided herein is a unique set because it provides resolution of the synoptic grid at three hourly intervals in conjunction with an unusually severe outbreak of tornadoes. This is indeed remarkable because the ability to predict the occurrence of tornadoes at this time is relatively poor and the test time was selected 36 hours in advance.

In the following sections, the synoptic conditions and significant weather during the experiment are documented. The unusual severe weather phenomena with associated damage

and cost, small scale time variation of the atmosphere as revealed by the experiment, and finally, selected satellite photographs of the AVE network during the experiment will be presented. In the case of the latter, the application of the densitometry to the photographs in the visible and infrared bands will be discussed.

II. SYNOPTIC CONDITIONS AND SIGNIFICANT WEATHER DURING THE EXPERIMENT

In this section the synoptic conditions and significant weather events that occurred during the experiment are discussed. Figures 4.1 and 4.2 contain the surface map and associated 500 mb chart for the continental United States for 0000 GMT, April 24, 1975. These maps characterize the synoptic conditions that existed approximately half-way through the experiment.

At the beginning of the experiment on April 24, 1975, at 0000 GMT, three air mass types were distinguishable at the surface over the experiment area. A moist and warm maritime tropical (MT) air mass moved northward over the network with the strong southerly flow around a high pressure center ridge (1030 mb MSL central pressure) located about 500 kilometers off the coast of the Carolinas. Maritime tropical air covered almost two-thirds of the network extending from central Texas and Oklahoma eastward through all of the Gulf Coast and Middle Atlantic States and northeastward into the Ohio Valley.

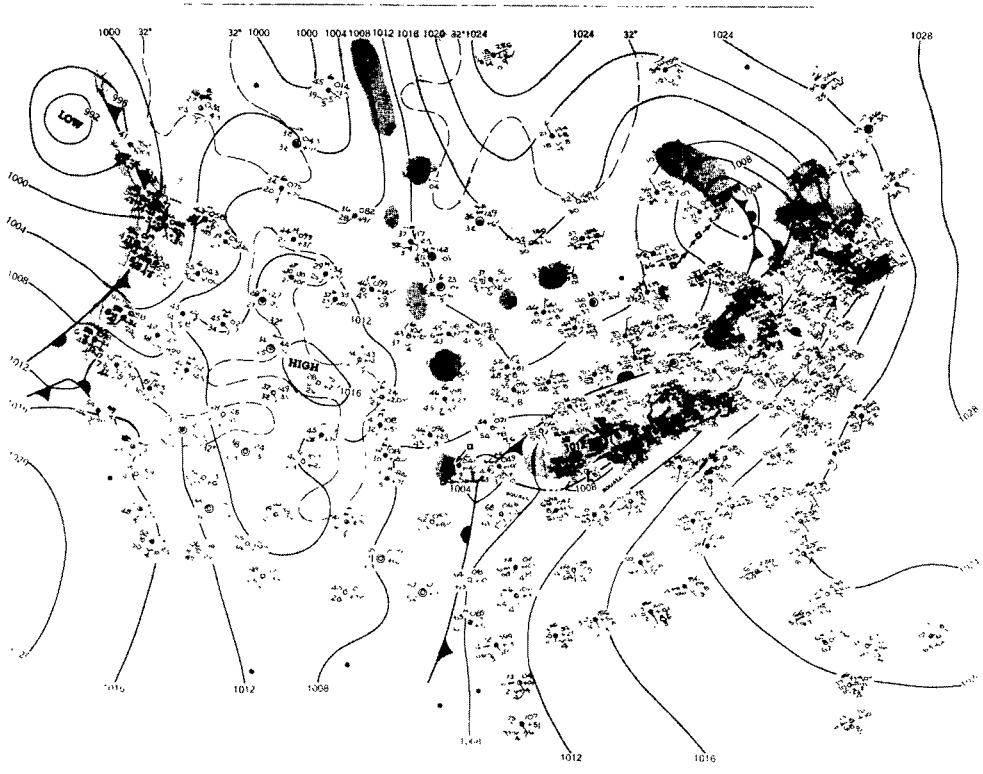

Figure 4.1. Surface weather map, April 24, 1975.

Source: Daily Weather Maps, Environmental Data Service, NOAA.

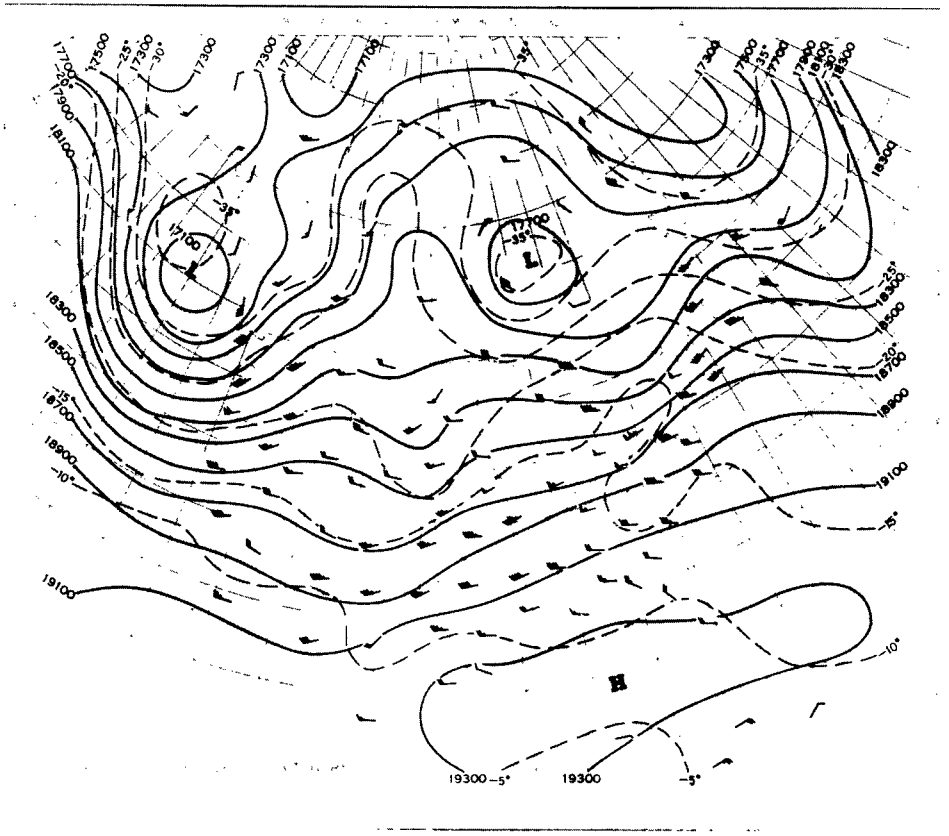

Figure 4.2. 500-millibar height contours chart, April 24, 1975.

Source: Daily Weather Maps, Environmental Data Service, NOAA.

A cold front, extending southwestward into Kansas from a moderately strong cyclone (1000 mb MSL central pressure) over northern Michigan, separated the maritime tropical air from the cooler and drier continental polar (CP) air moving southward over the Northern Plain States, while a warm front, extending southeastward from the cyclone into Pennsylvania, separated continental polar air over New England from maritime tropical air in the Ohio Valley. A second cyclone (1000 mb MSL central pressure) was located in central Kansas with a cold front or dry line extending southward into west Texas separating the very dry maritime polar (MP) air from the maritime tropical air in east Texas. A third weaker cyclone was just entering the network in western Nebraska and South Dakota.

Temperatures over the experiment area ranged from the upper seventies along the Gulf Coast to upper forties in the Northern Plain States, and dew point temperatures ranged from the upper sixties to the middle teens in the maritime tropical and maritime polar air masses, respectively.

The middle and upper tropospheric flow pattern was basically zonal during the entire experiment period with both the polar jet stream extending roughly west-east from the Northern Plain States to the Northeast United States, and the subtropical jet stream, located along the Gulf Coast States, well defined. Two clearly distinguishable short wave perturbations (wavelength $\simeq$ 1000 km) moved through the

basic zonal flow during the experiment and were responsible for creating most of the significant weather.

At the beginning of the experiment, the first short wave was associated with the cyclone over northern Michigan and the second with the developing cyclone in western Nebraska and South Dakota.

Light rain and rain showers with cloud tops below 25,000 feet occurred along and above the warm front associated with the first short wave as it moved eastward as a stable wave to a position about 250 kilometers off the coast of Maine at the end of the experiment. At 1200 GMT, on April 24, 1975, moderately strong thunderstorms formed in the Ohio Valley along the slowly southeastward moving cold front associated with the first short wave. By 2100 GMT, on April 24, 1975, a strong squall line had formed from central Tennessee northeast into western West Virginia. The radar revealed cloud tops to 46,000 feet and accordingly a tornado watch had been issued for this area three hours earlier. By 0000 GMT, on April 25, 1975, the severe thunderstorms had dissipated and only weaker shower and thundershower activity was present over the central Appalachians.

A second area of severe thunderstorm activity at 0000 GMT, on April 24, 1975, was associated with the cyclone in central Kansas and the warm front extending northeastward into northern Missouri. A tornado watch was issued in this area at 0000 GMT, on April 24, 1975, and the radar indicated cloud tops in excess of 60,000 feet. By 1500 GMT on

April 24, 1975, the thunderstorm area had moved about 200 kilometers to the south and decreased in intensity to only shower activity while the cyclone in central Kansas remained stationary.

A third area of severe convective activity developed at 0000 GMT on April 24, 1975, in western Nebraska and South Dakota in response to the eastward movement of the second short wave. The intensity of the thunderstorm activity decreased and the radar data indicated cloud tops up to 50,000 feet at 0000 GMT on April 24, 1975, with maximum cloud tops of only 30,000 feet at 1800 GMT on April 24, 1975, while the entire system and associated short wave moved slowly eastward into the central and eastern Dakotas and Nebraska.

At 2100 GMT on April 24, 1975, the cyclone in central Kansas began to intensify and move southeastward into northeast Oklahoma with the eastward movement of the second short wave. Severe thunderstorm activity developed rapidly within the intensifying low pressure region and southwestward along the trailing cold front or dry line. Three hours later, at 0000 GMT on April 25, 1975, the severe squall and tornado watch area was extended from central Oklahoma into southwest Missouri with maximum cloud tops at 56,000 feet.

Between 0000 GMT and 1200 GMT on April 25, 1975, the cyclone moved eastward into Kentucky with the eastward movement of the second short wave perturbation, while the

associated cold front extended southwestward into Texas. The severe squall line grew in intensity and length with maximum radar cloud tops exceeding 60,000 feet and, at 1200 GMT on April 25, 1975, extended along an arc almost 1000 kilometers long from eastern Kentucky southwestward into northern Alabama and westward into Arkansas. Both hail and tornadoes were reported along the path of the squall line.

At the end of the experiment, on April 25, 1975, at 1200 GMT, the major weather system was the strong squall line moving southeastward into the Southeast United States while the upper level flow pattern was developing a trough running north-south through the Northern Plains. With the developing trough, the surface anticyclone off the Carolinas had moved farther eastward out into the Atlantic and continental polar air was replacing maritime tropical air in the Ohio Valley and the Southeast United States with the southeastward movement of the cold front.

III. STUDIES OF LARGE SCALE FEATURES WITH THREE HOURLY DATA

In this section a discussion of the AVE data in the context of surface, 850, 700, 500, 400, 300, and 200 millibar charts shall be presented. The data summary maps are given at three hour intervals. The unique nature of the experiment data facilitates the study of atmospheric phenomena over a wide range of horizontal scales of motion. The high observational frequency together with the spatial and

temporal extensiveness of the data permit detailed study of the temporal evolution of meteorological features spatially resolvable with the current synoptic network. Although the data set is truly unique, it does have deficiencies relative to spatial content in both the wave number and frequency domains. However, the deficiencies may not be as severe as those associated with synoptic network station intervals. The Nyquist wavelength of the data set is typically 600 kilometers which corresponds to twice the typical distance between the network stations so that it appears the data only contains large mesoscale information. However, the Nyquist time period, T_N, is six hours which corresponds to twice the temporal observation interval and is characteristic of intermediate mesoscale phenomena. According to linear perturbation theory the radian frequency, ω, of a perturbation is related to the mean wind and cross mean wind radian wave numbers, k_x and k_y, respectively, by an equation of the form

$$\omega = \bar{u}k_x + F(k_x,k_y) \tag{4.1}$$

where $\bar{u}$ is the mean wind speed and $F(k_x,k_y)$ is a function which characterizes the dispersive motion of the perturbations. If for the sake of this argument one neglects the dispersive character of the perturbations, then the Nyquist period can be transformed to an effective Nyquist wavelength, λ_{Ne}, through the approximate equation

$$\lambda_{Ne} = \bar{u}\, T_N \qquad (4.2)$$

In the experiment $\bar{u}$ is on the order of 10 m sec^{-1} so that $\lambda_{Ne} \simeq 200$ km. Thus the decreased sampling time resulted in an effective Nyquist wavelength which is one-third of the Nyquist wavelength based on the network station intervals.

Temperature and pressure height analyses and data at each three hours for the period between 0000 GMT, April 23, 1975, to 1200 GMT, April 25, 1975, for six levels (850, 700, 500, 400, 300, and 200 millibar) are shown in Figures 4.3 to 4.11. The time of each chart is indicated on the associated figure title. The plotted data are from observations over the experiment area. Regular data outside the experiment region were used to aid in the analyses of these charts.

In the analysis of these charts, an effort was made to allow the data to suggest the patterns, but the acceptance of particular features in the analyses depended on their appearance at two successive times. Occasionally, it was found necessary to disregard some data and to interpolate for missing data. In addition, the principal of hydrostatic stability of the charts was applied in order to guarantee consistency between the analyses and the various levels.

As pointed out earlier, conditions prior to the experiment indicated a weak surface cold front formed east of the Rocky Mountains on April 23, 1975, with the strongest section of the front in the Northern Great Plains and Midwest where some upper level temperature gradient support was

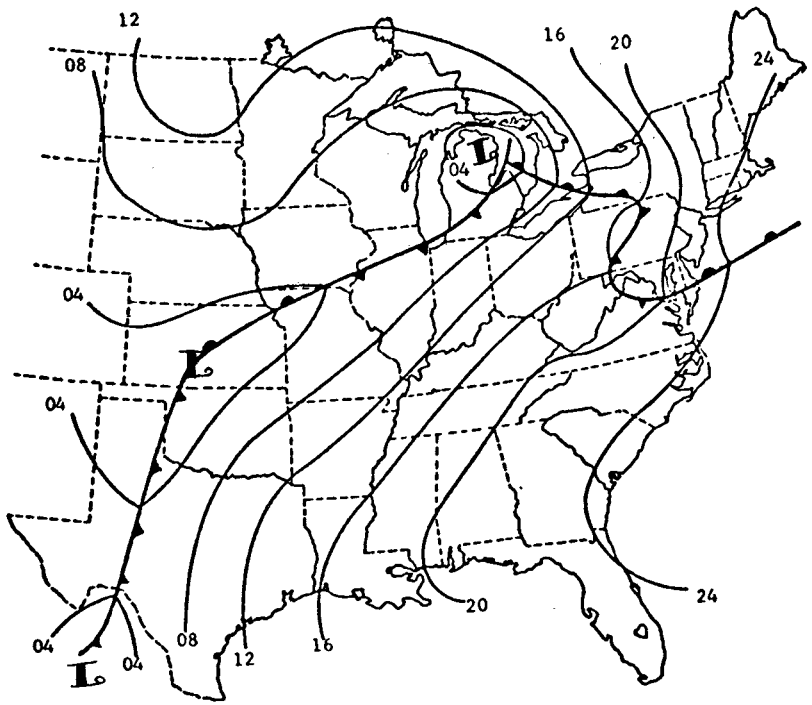

Surface

Figure 4.3. Synoptic charts for 0000 GMT, April 24, 1975.

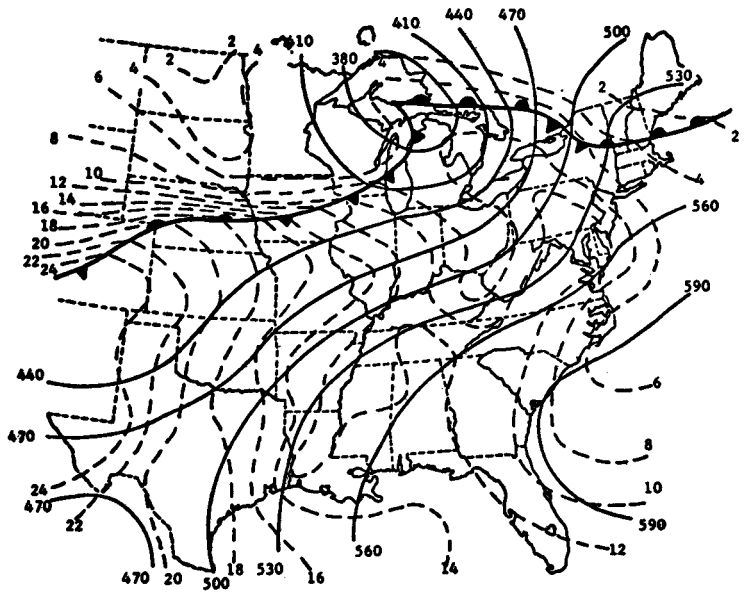

850 mb

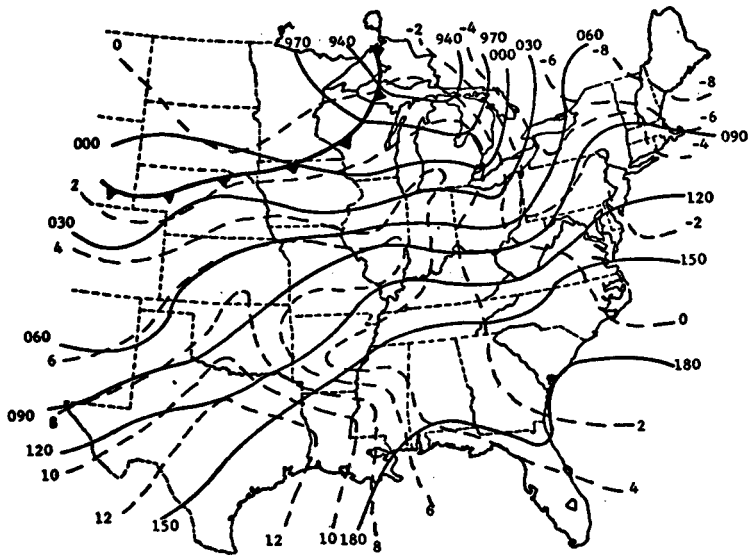

700 mb

Figure 4.3. (continued)

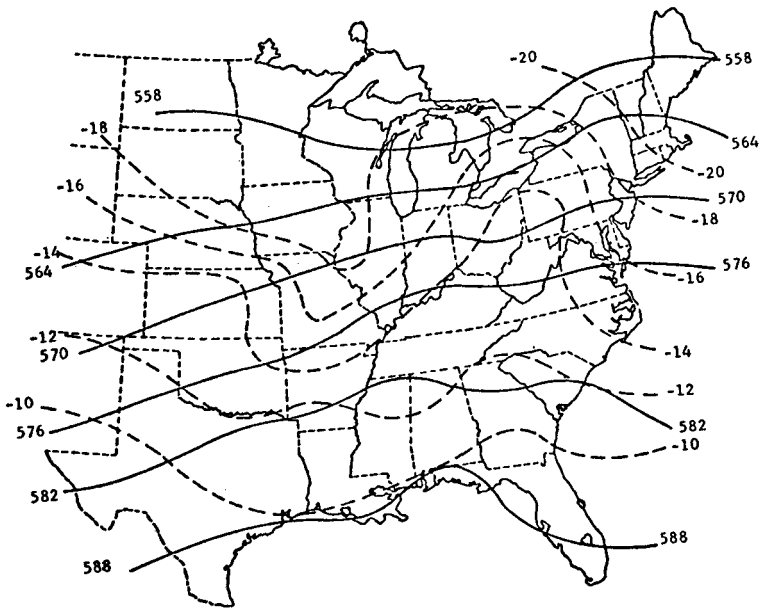

500 mb

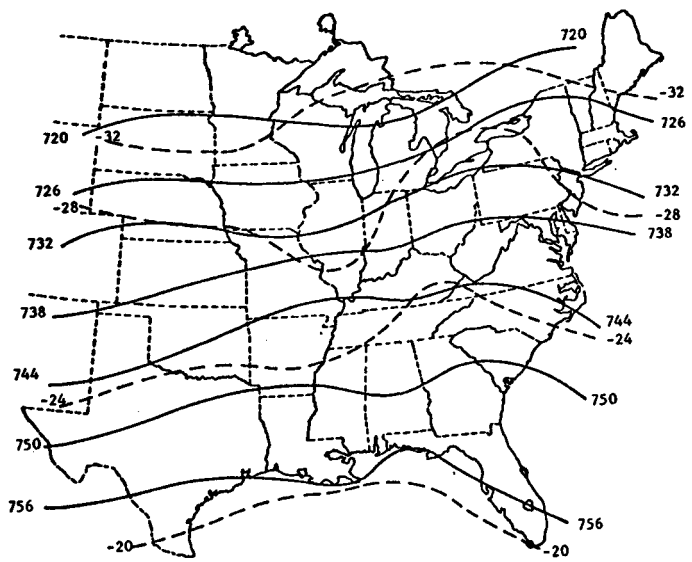

400 mb

Figure 4.3. (continued)

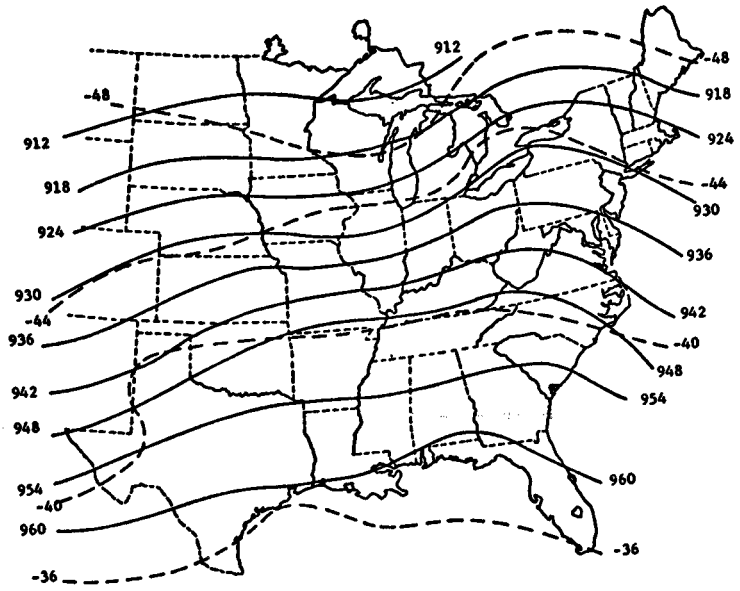

300 mb

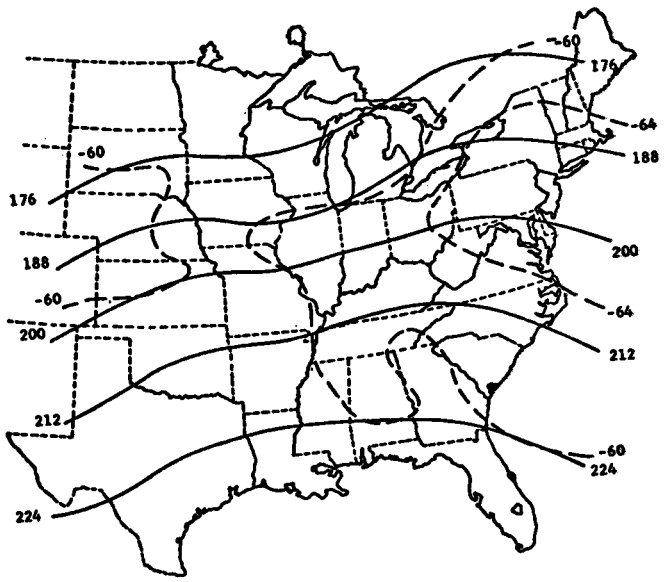

200 mb

Figure 4.3. (concluded)

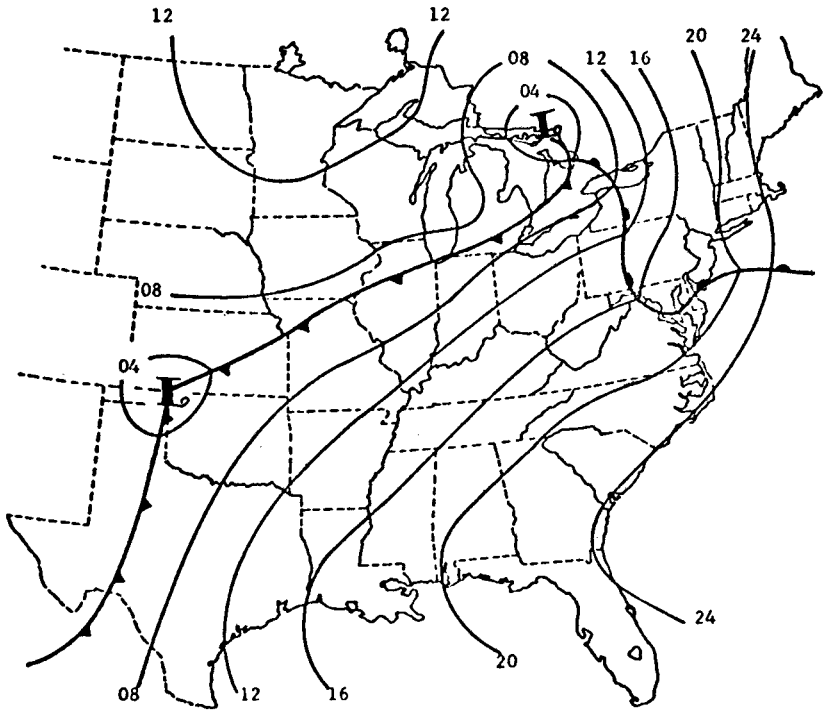

Surface

Figure 4.4. Synoptic charts for 0600 GMT, April 24, 1975.

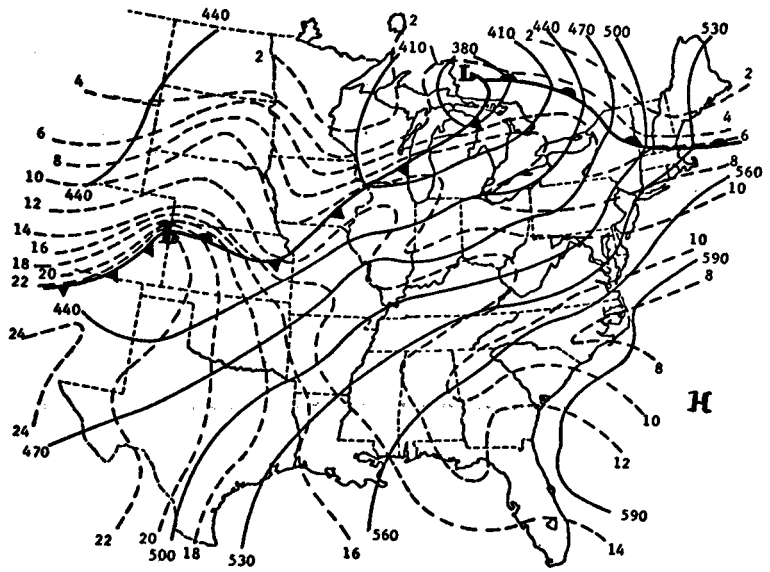

850 mb

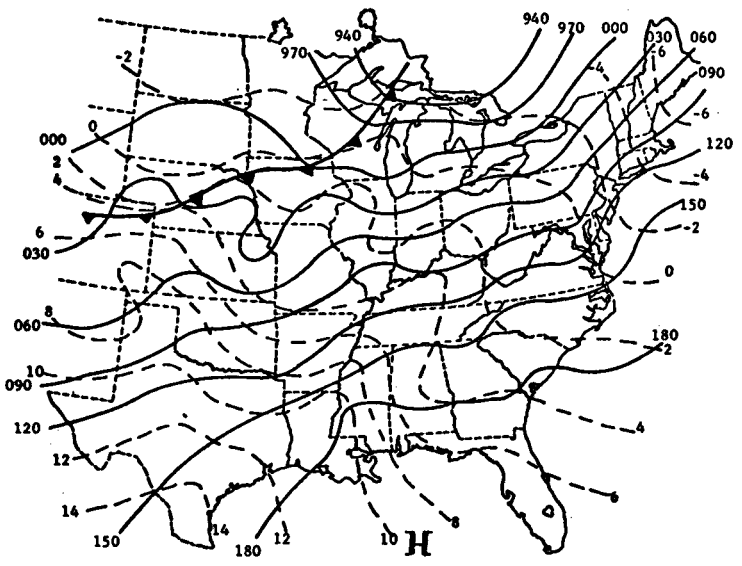

700 mb

Figure 4.4. (continued)

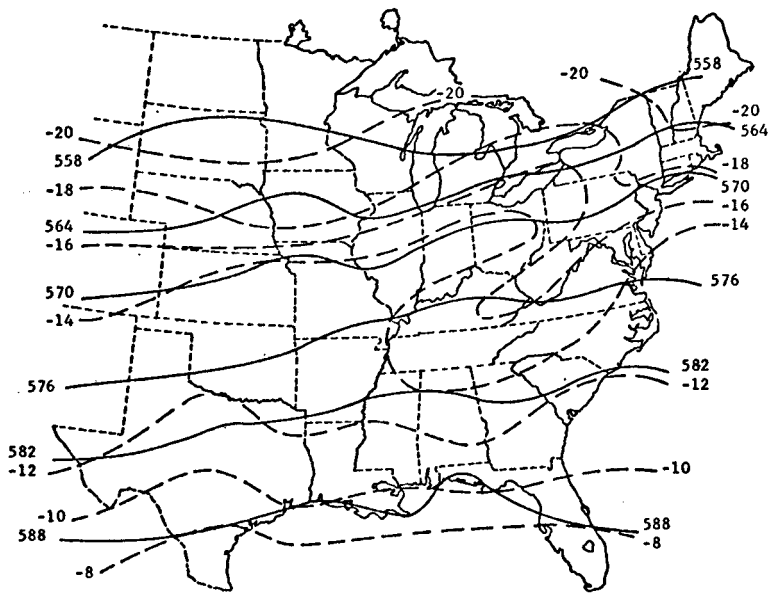

500 mb

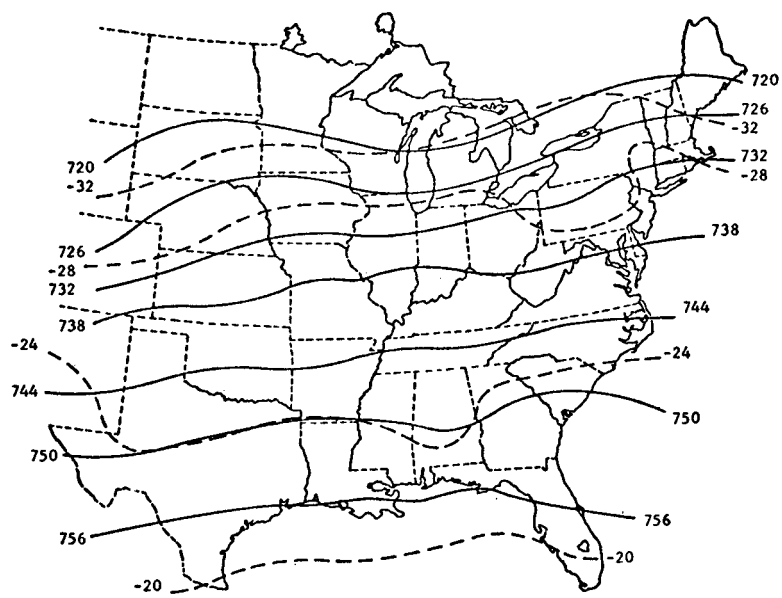

400 mb

Figure 4.4. (continued)

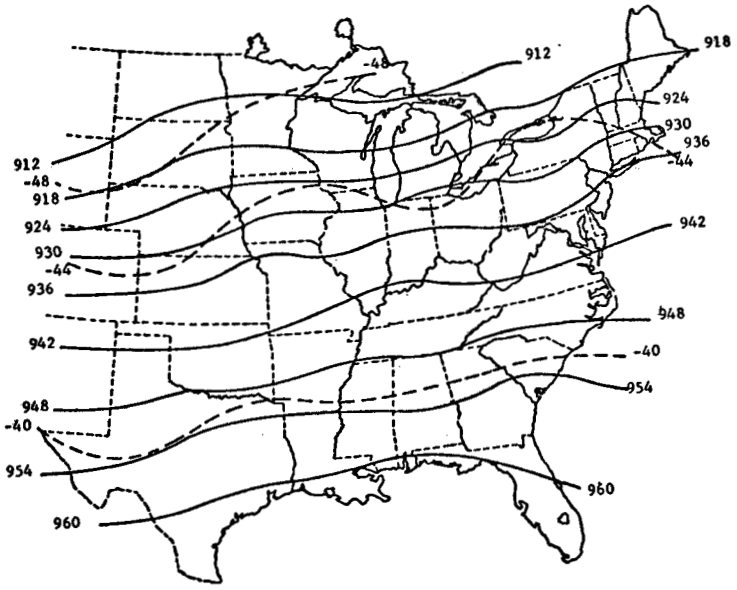

300 mb

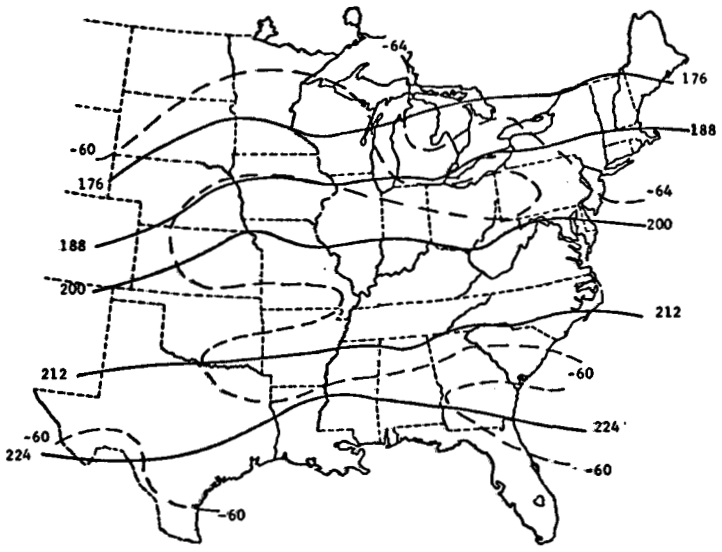

200 mb

Figure 4.4. (concluded)

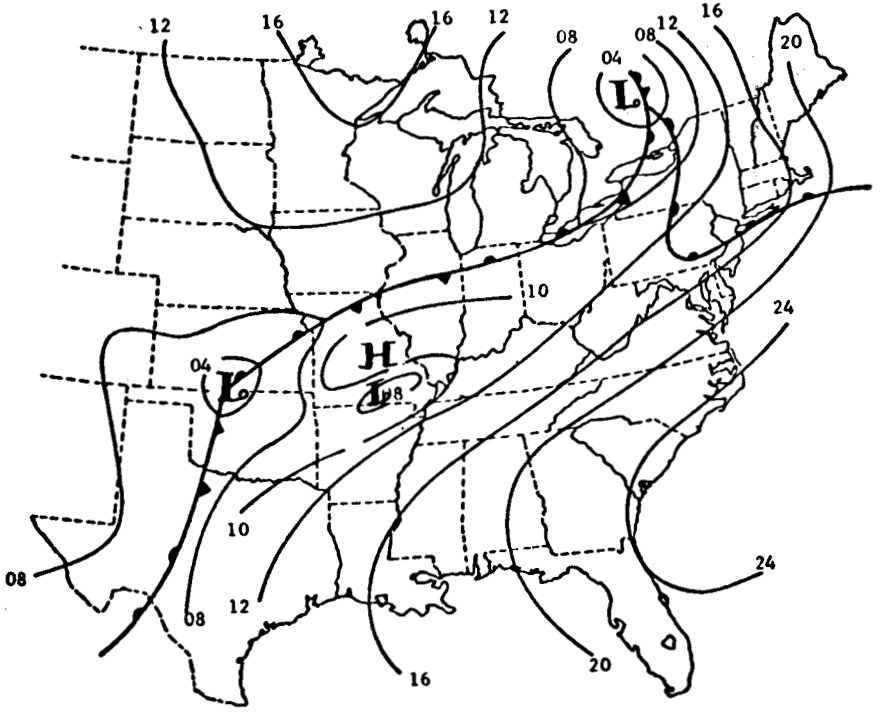

Surface

Figure 4.5. Synoptic charts for 1200 GMT, April 24, 1975.

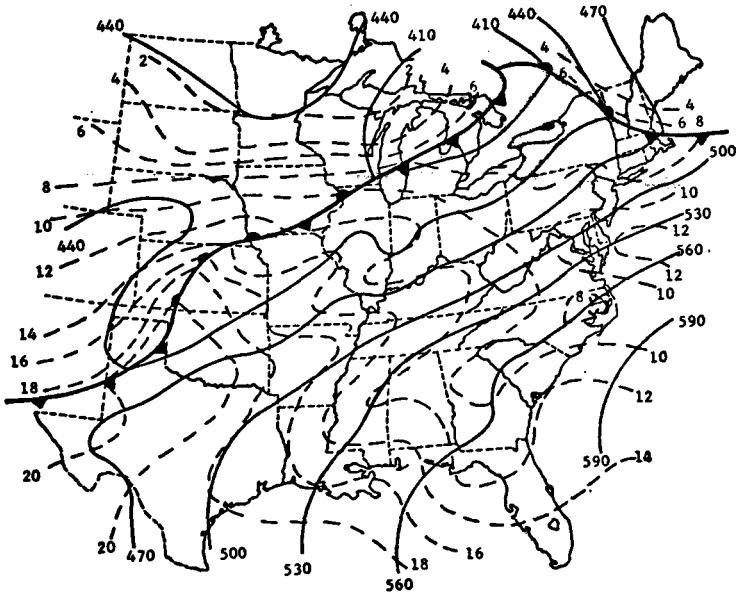

850 mb

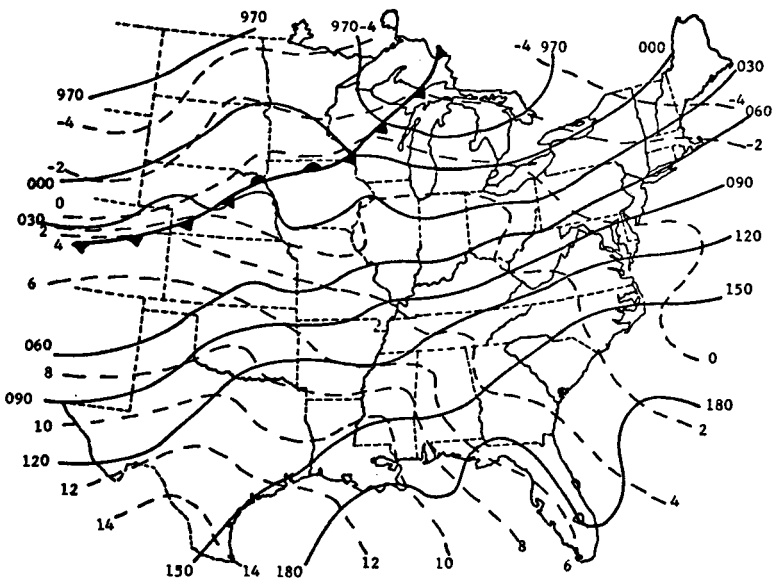

700 mb

Figure 4.5. (continued)

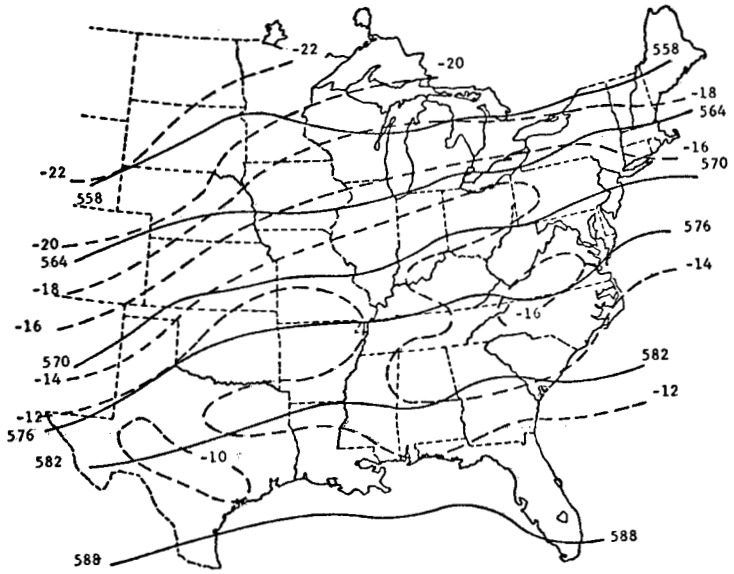

500 mb

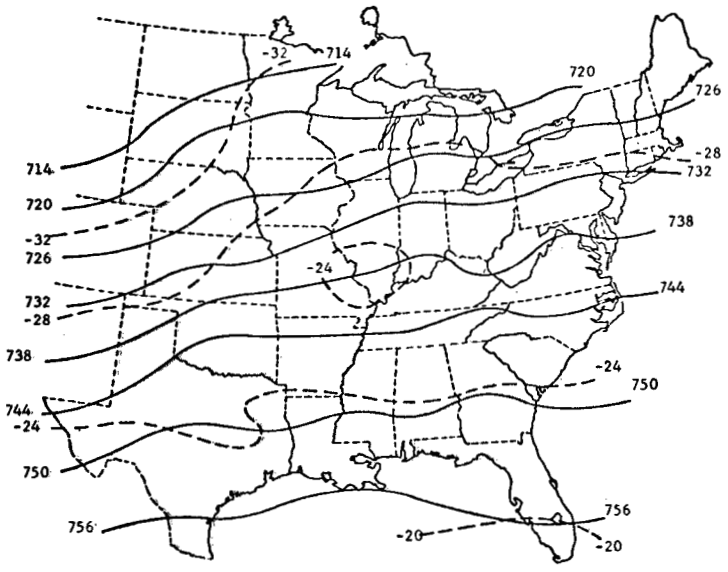

400 mb

Figure 4.5. (continued)

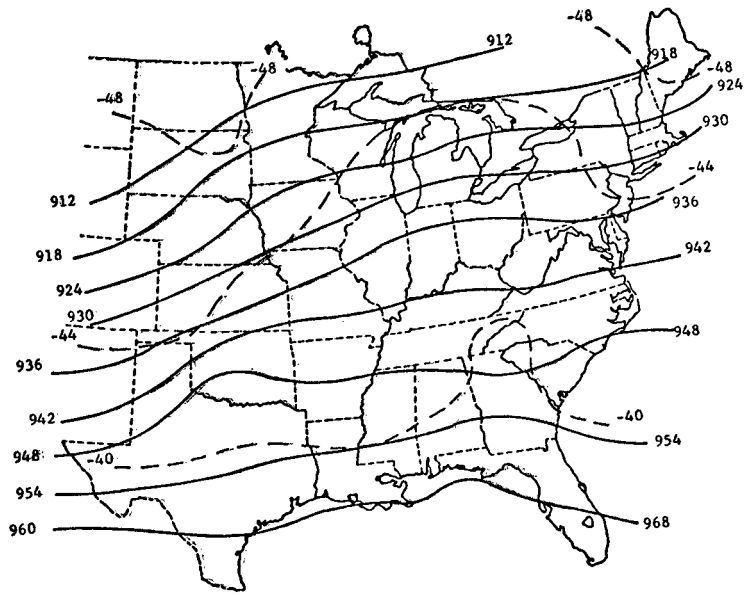

300 mb

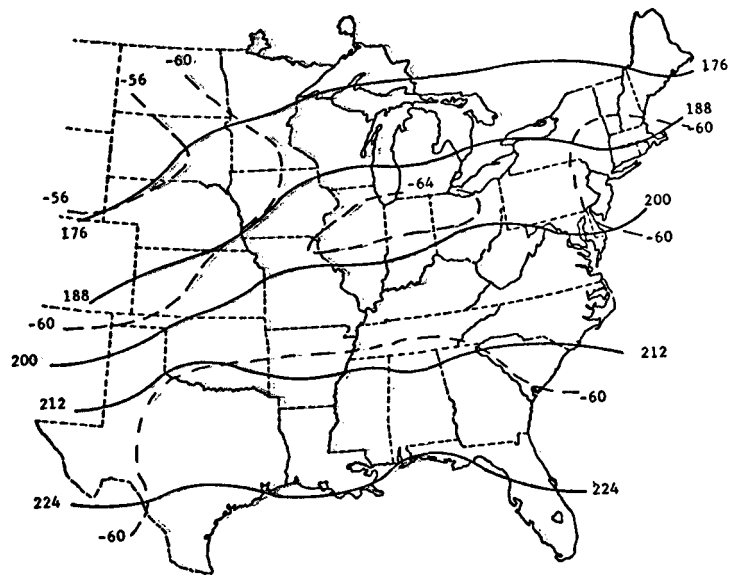

200 mb

Figure 4.5. (concluded)

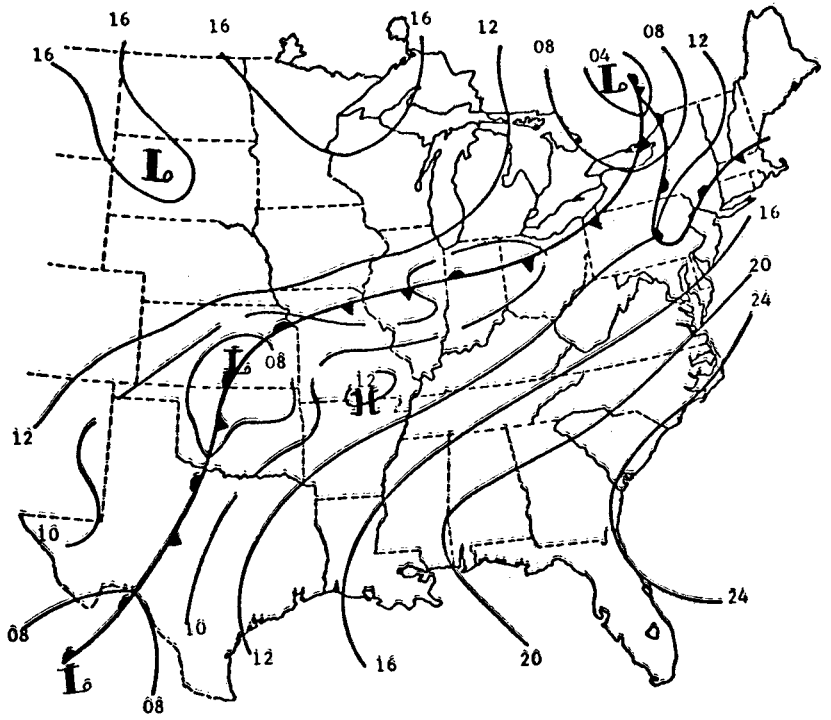

Figure 4.6. Synoptic charts for 1500 GMT, April 24, 1975.

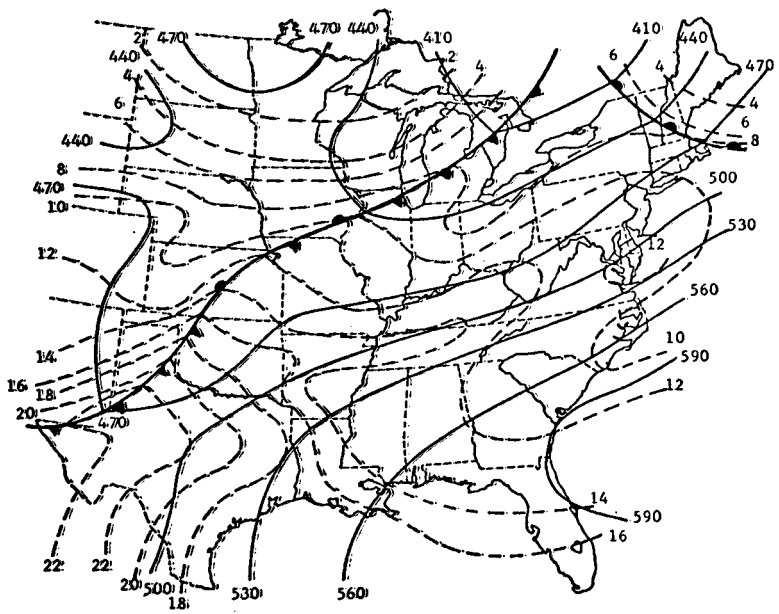

850 mb

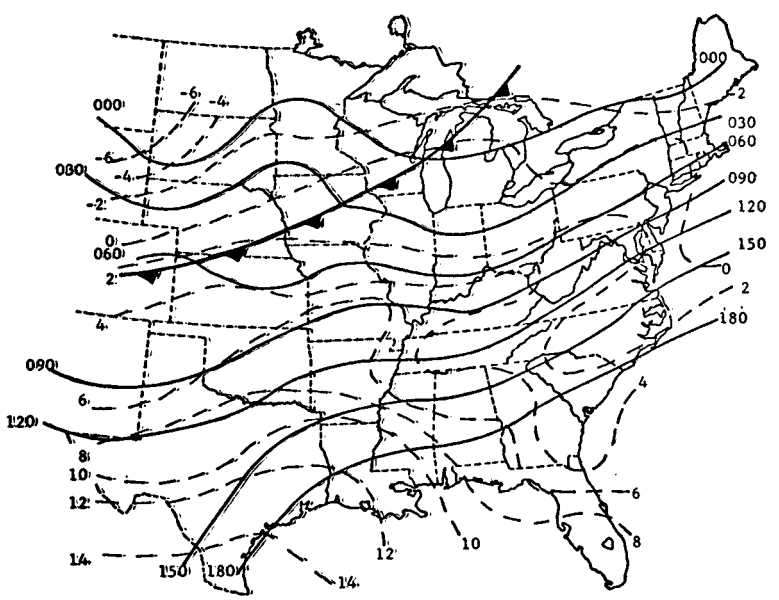

700 mb

Figure 4.6. (continued)

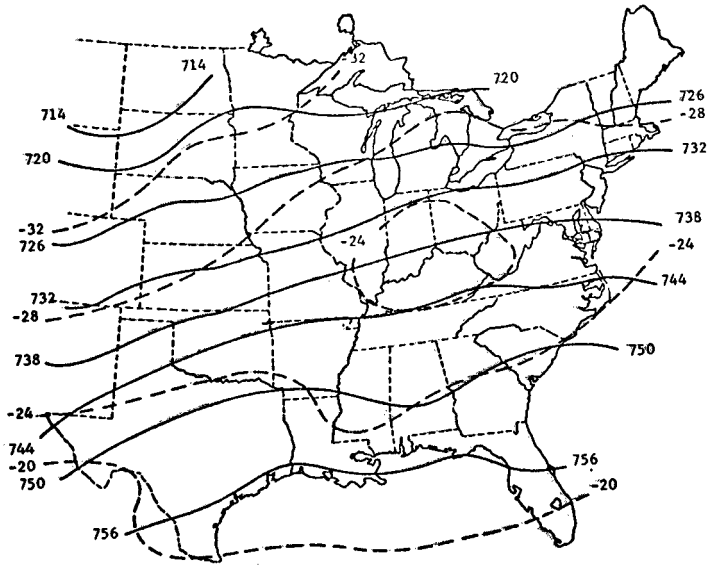

400 mb

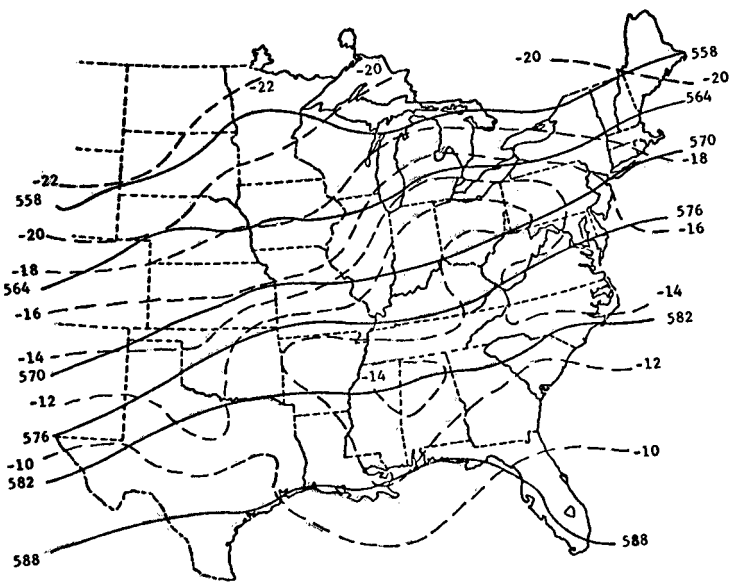

500 mb

Figure 4.6. (continued)

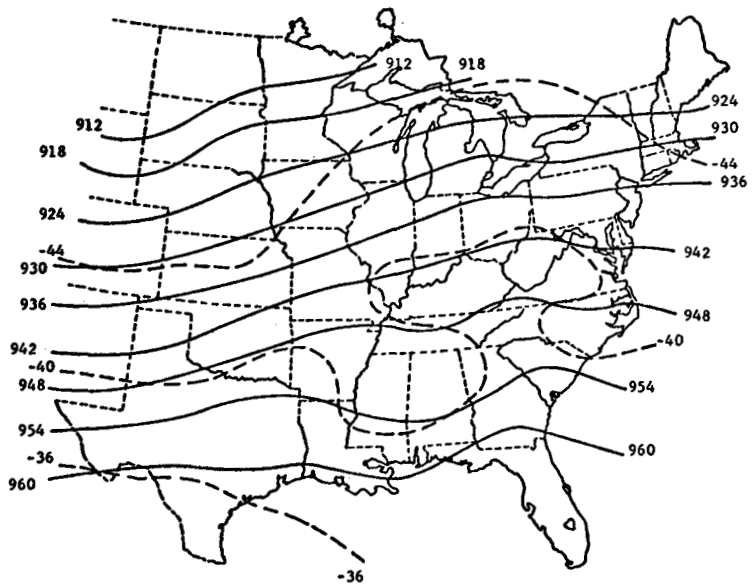

300 mb

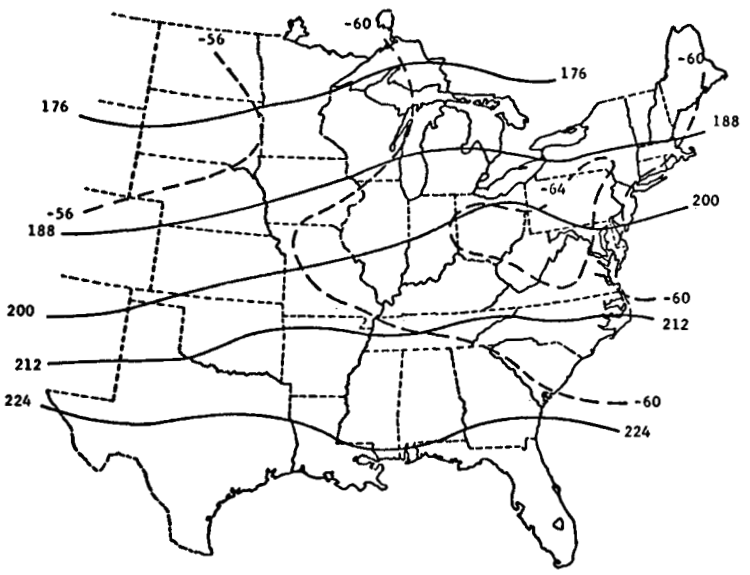

200 mb

Figure 4.6. (concluded)

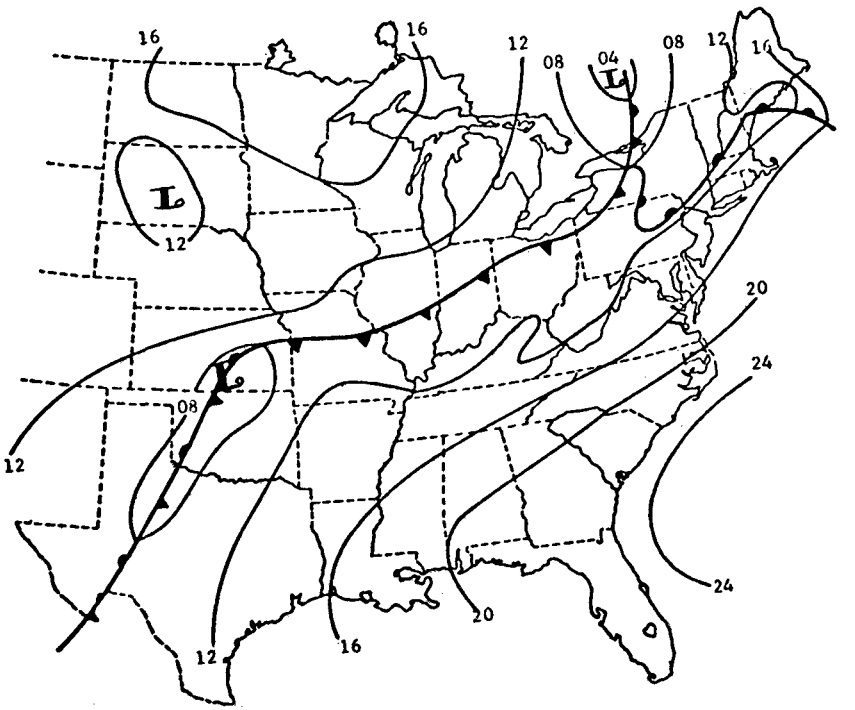

Surface

Figure 4.7. Synoptic charts for 1800 GMT, April 24, 1975.

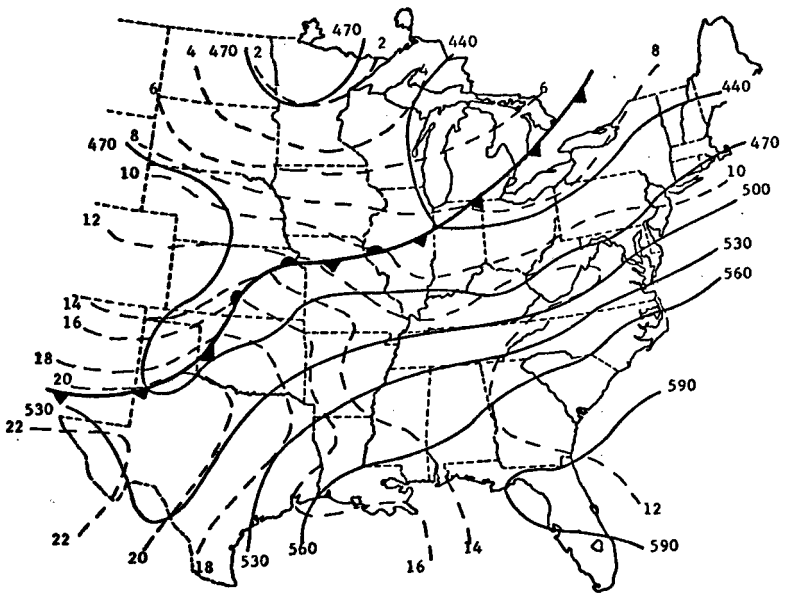

850 mb

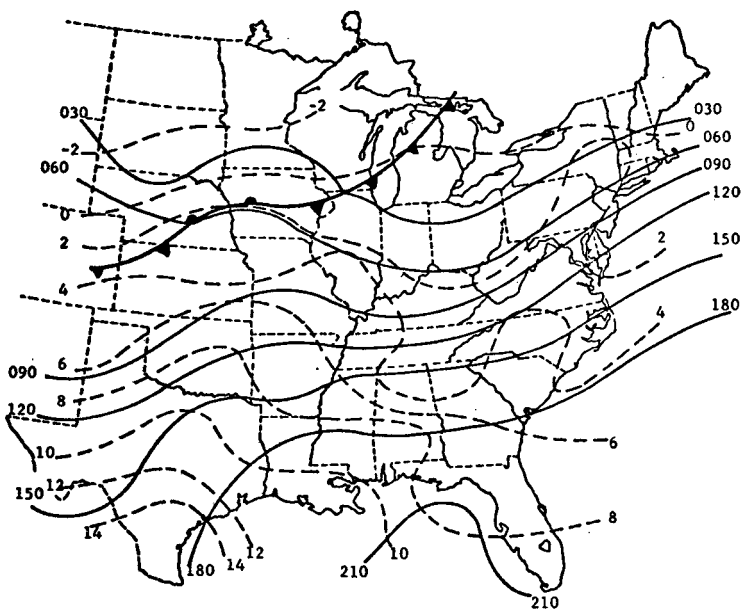

700 mb

Figure 4.7. (continued)

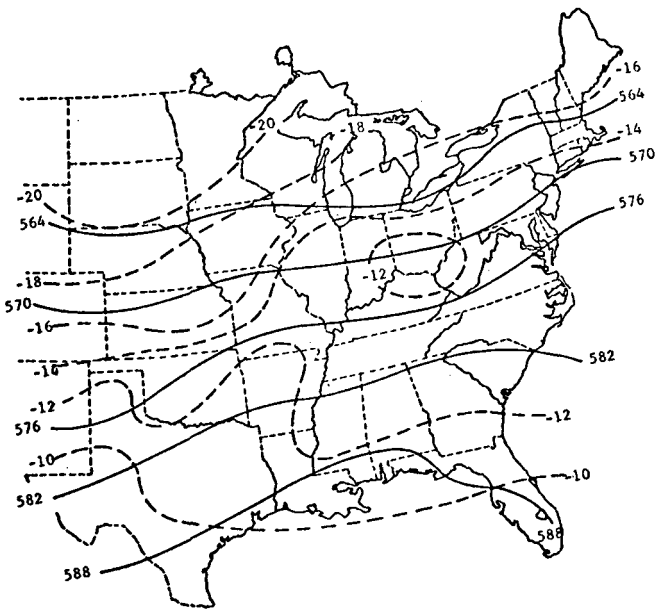

500 mb

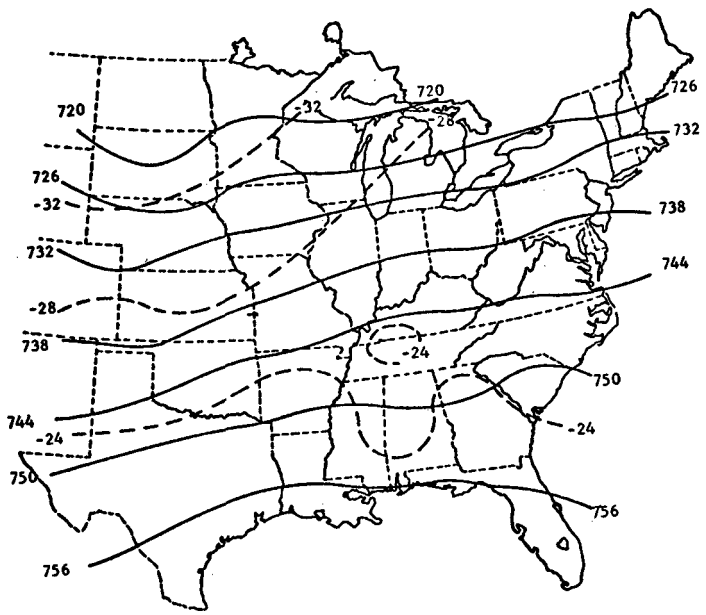

400 mb

Figure 4.7. (continued)

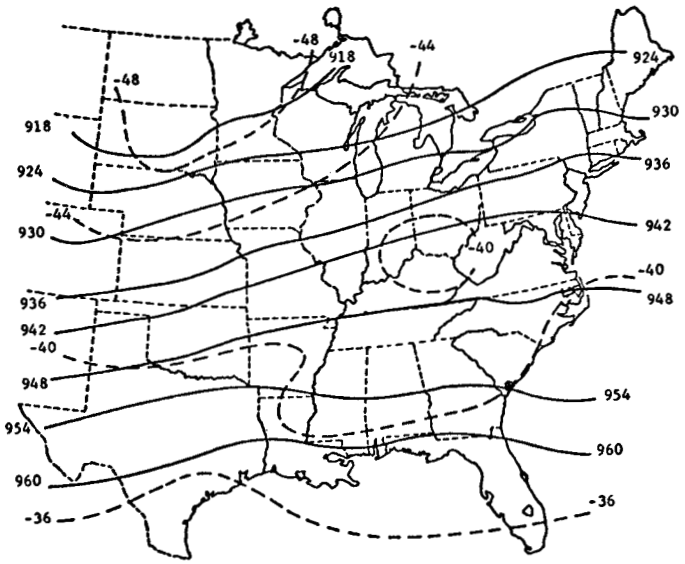

300 mb

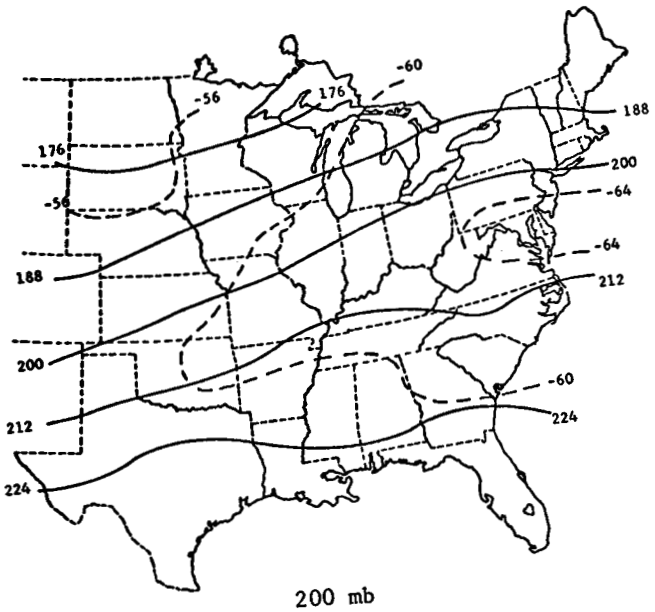

200 mb

Figure 4.7. (concluded)

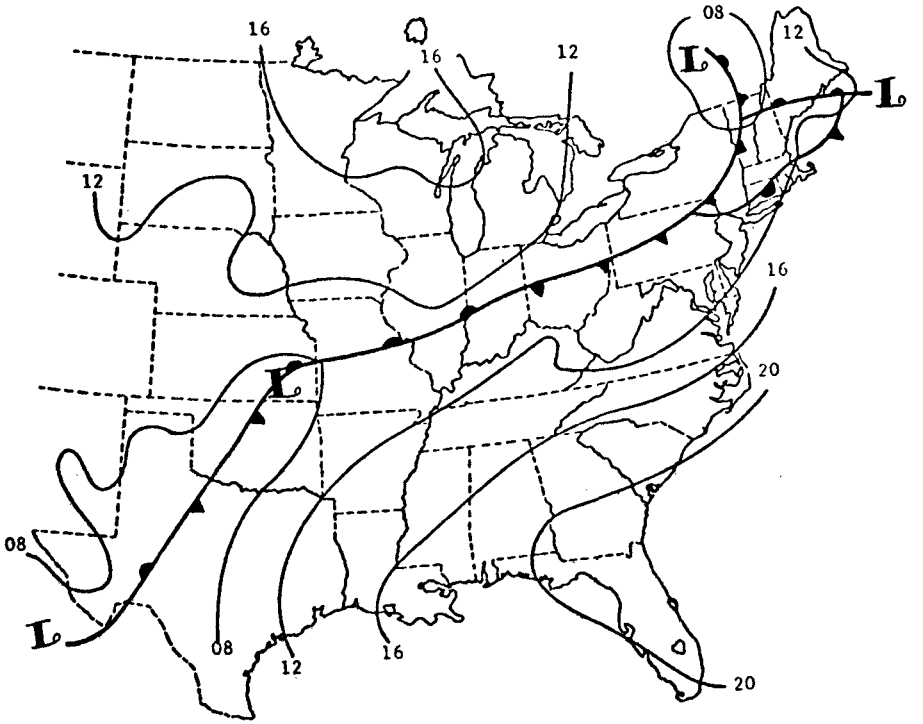

Surface

Figure 4.8. Synoptic charts for 2100 GMT, April 24, 1975.

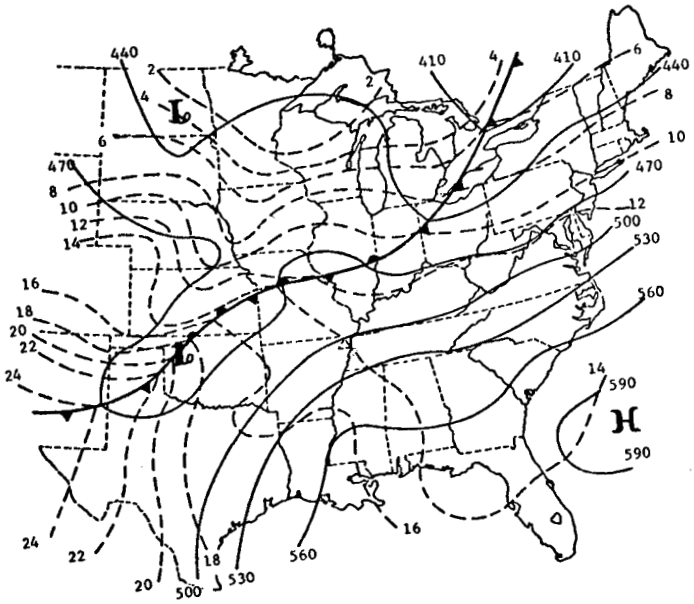

850 mb

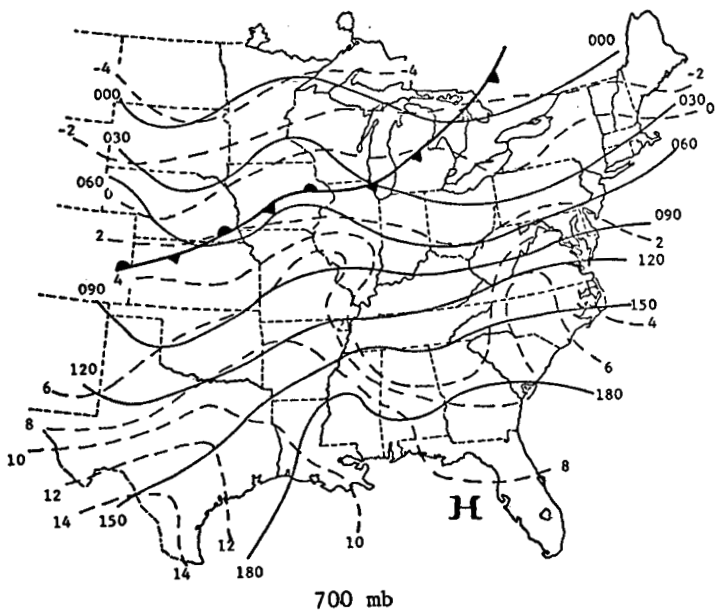

700 mb

Figure 4.8. (continued)

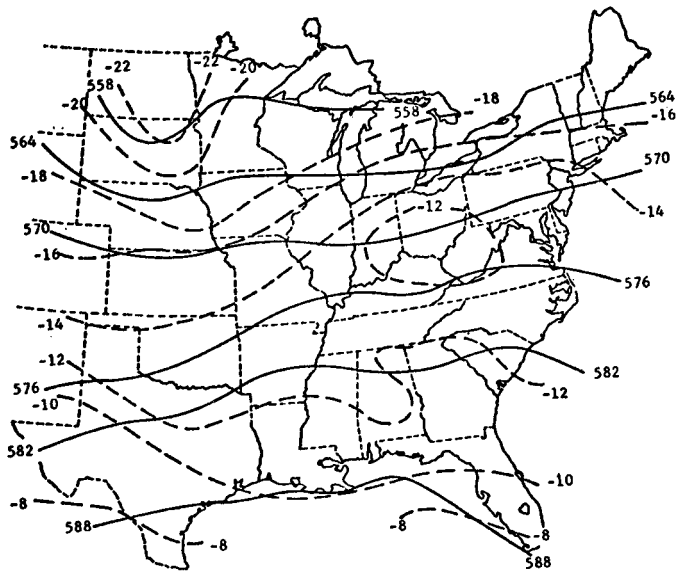

500 mb

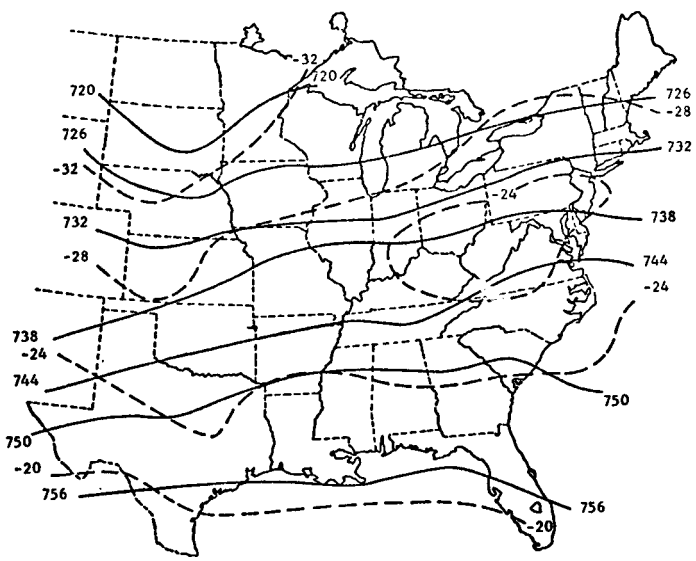

400 mb

Figure 4.8. (continued)

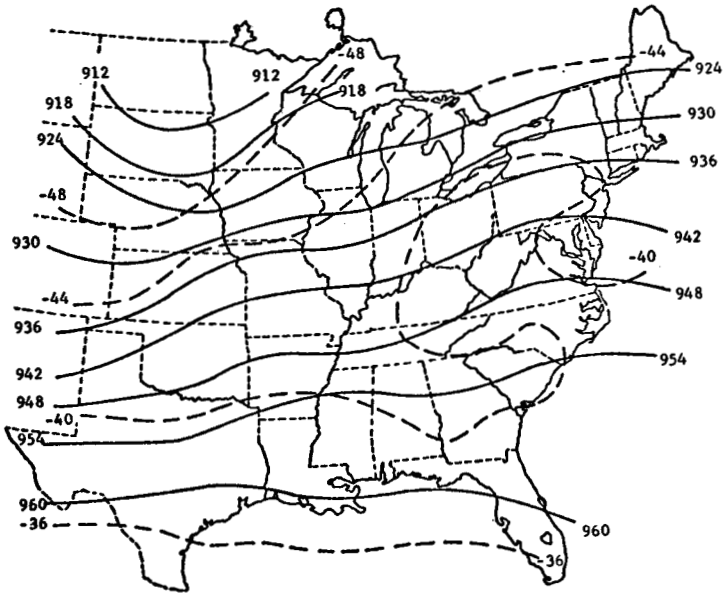

300 mb

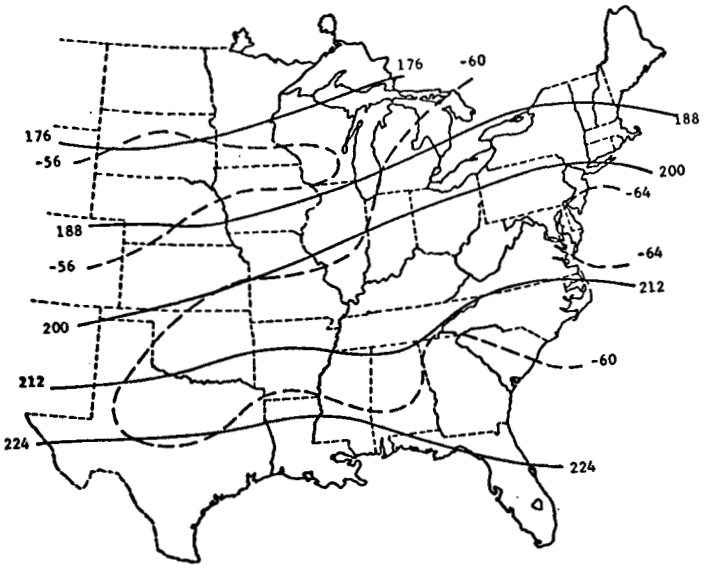

200 mb

Figure 4.8. (concluded)

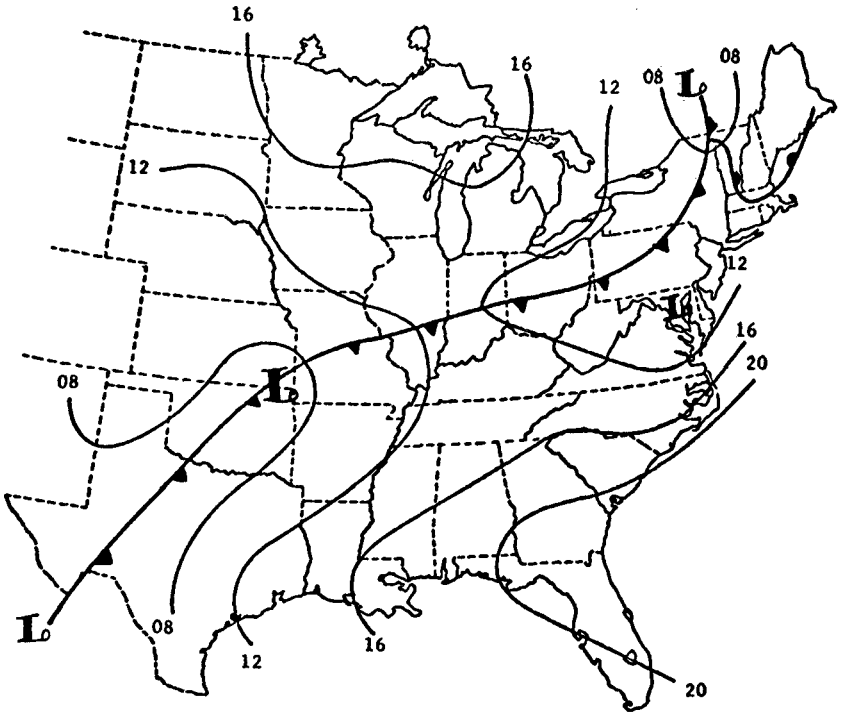

Surface

Figure 4.9. Synoptic charts for 0000 GMT, April 25, 1975.

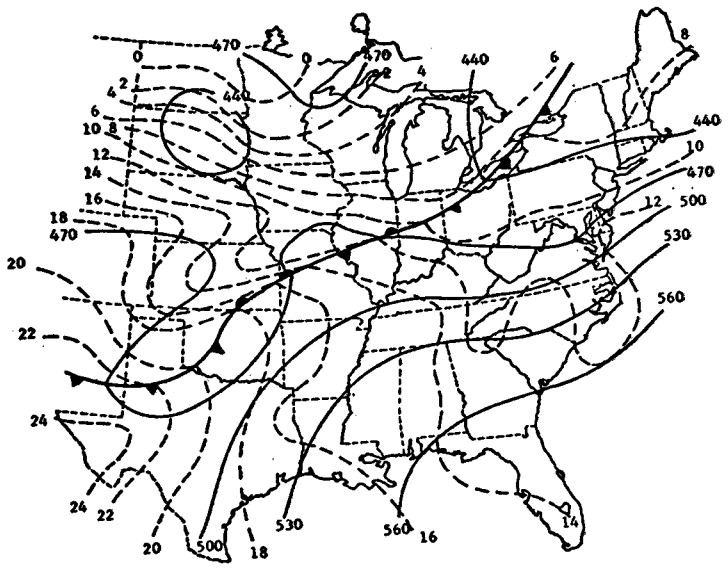

850 mb

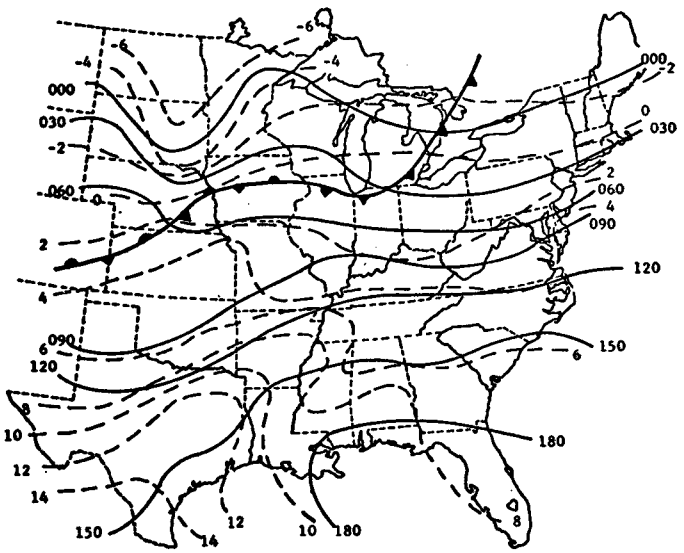

700 mb

Figure 4.9. (continued)

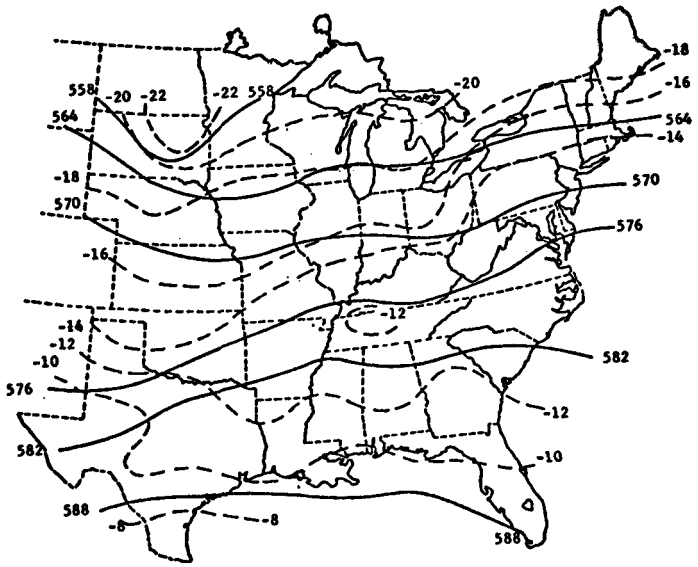

500 mb

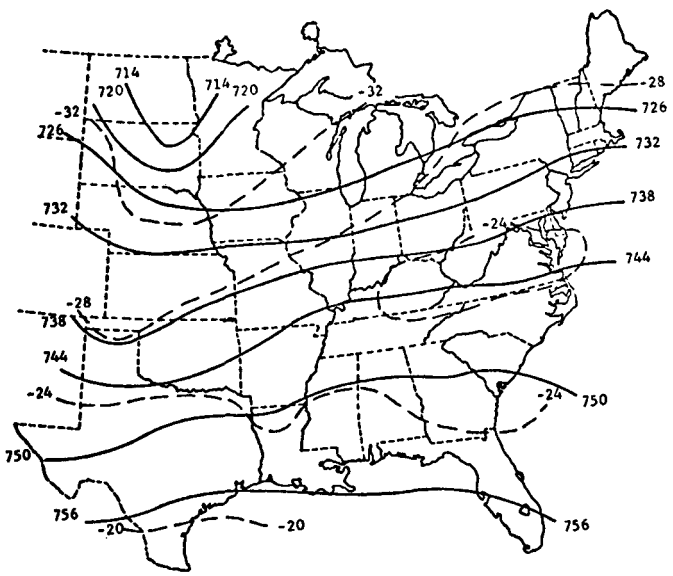

400 mb

Figure 4.9. (continued)

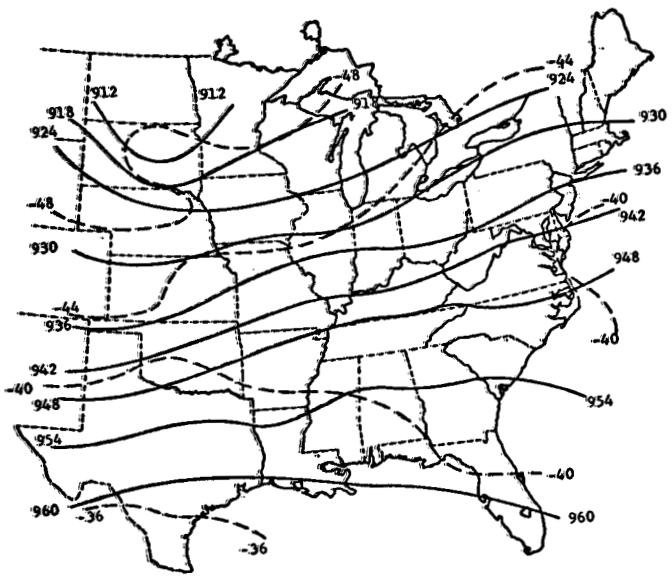

300 mb

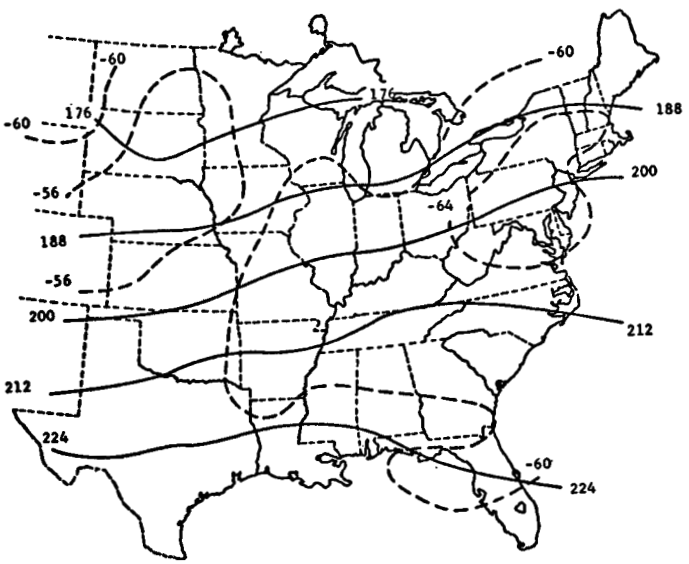

200 mb

Figure 4.9. (concluded)

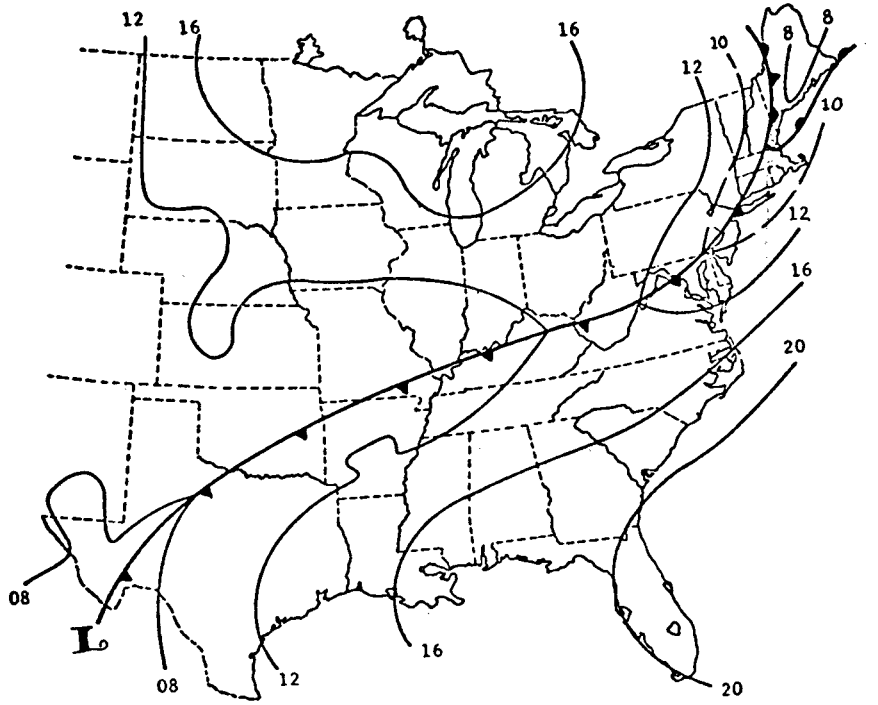

Surface

Figure 4.10. Synoptic charts for 0600 GMT, April 25, 1975.

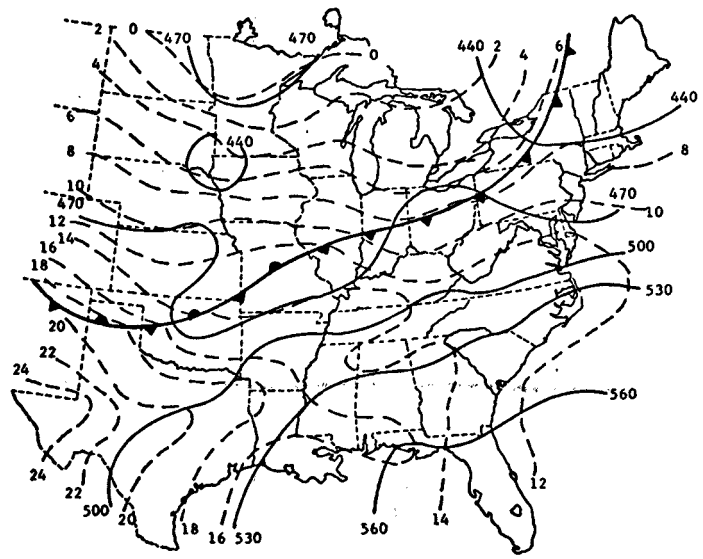

850 mb

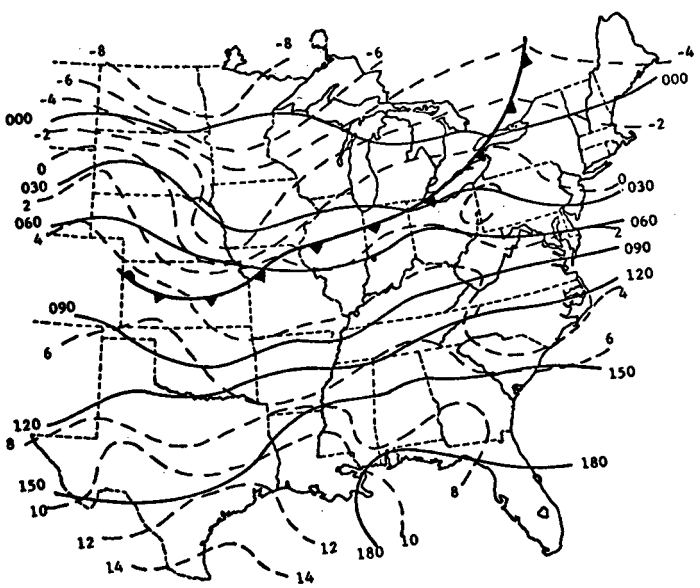

700 mb

Figure 4.10. (continued)

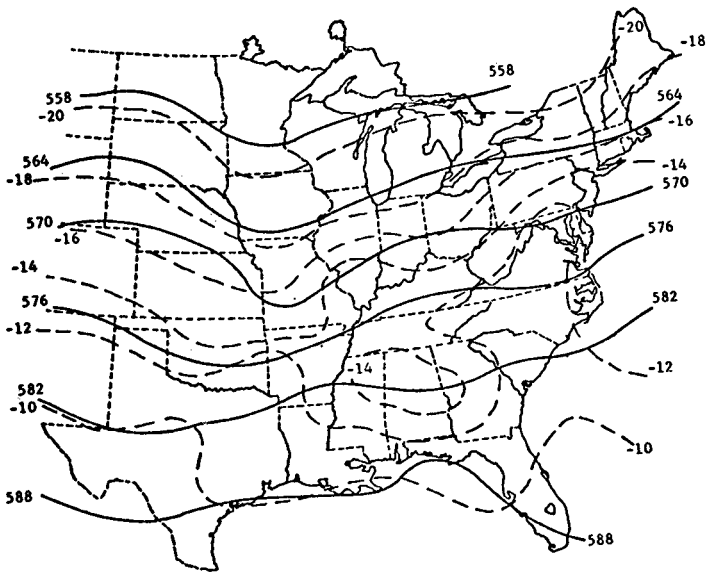

500 mb

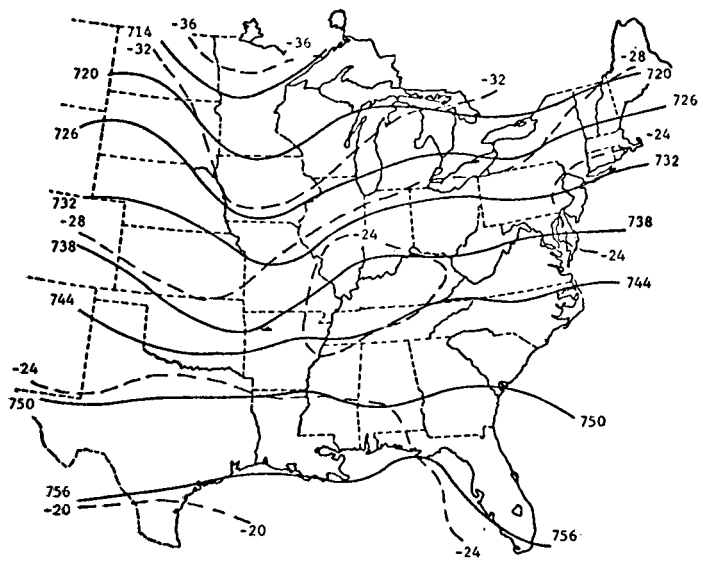

400 mb

Figure 4.10. (continued)

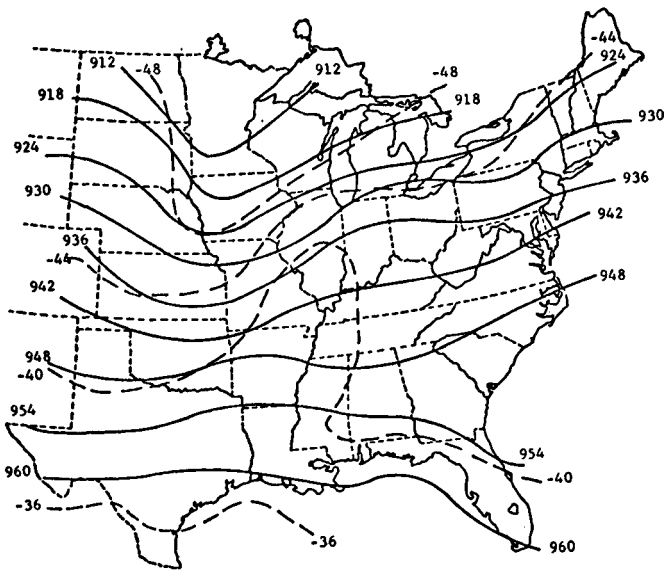

300 mb

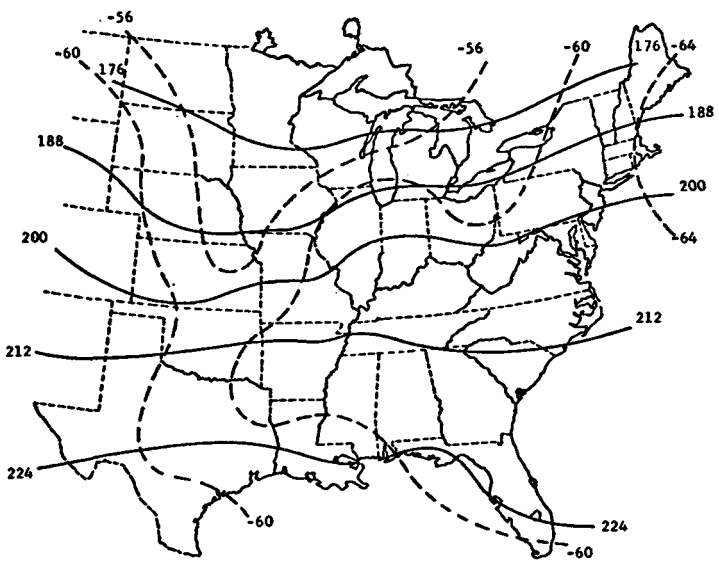

200 mb

Figure 4.10. (concluded)

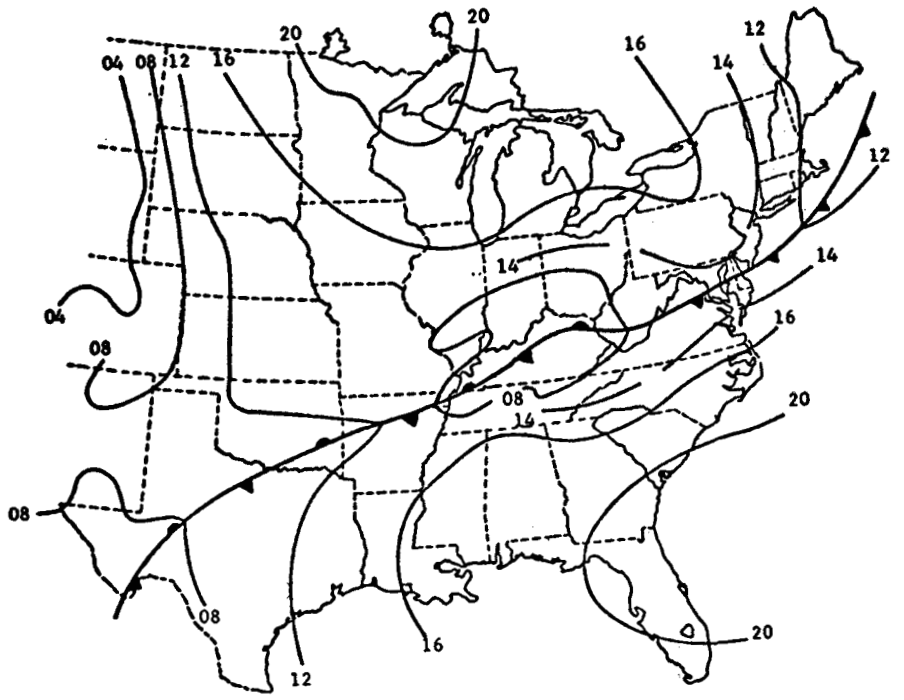

Figure 4.11. Synoptic charts for 1200 GMT, April 25, 1975.

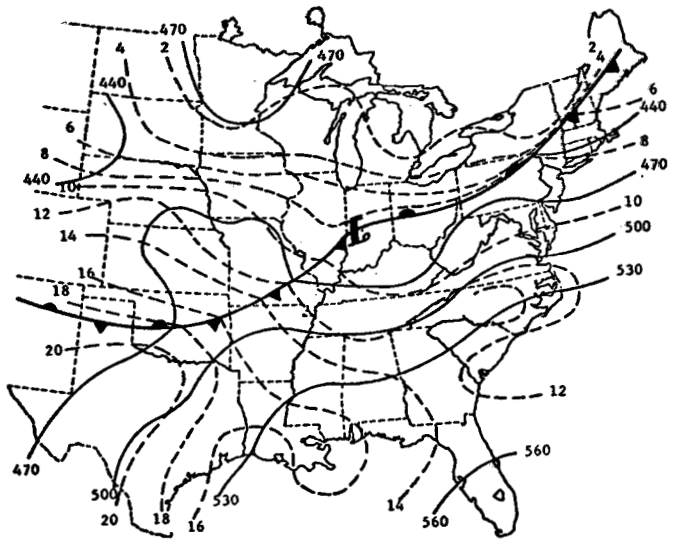

850 mb

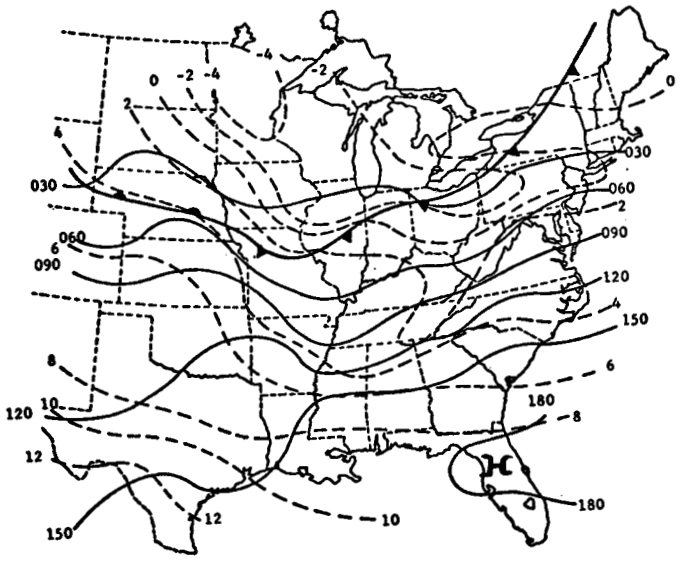

700 mb

Figure 4.11. (continued)

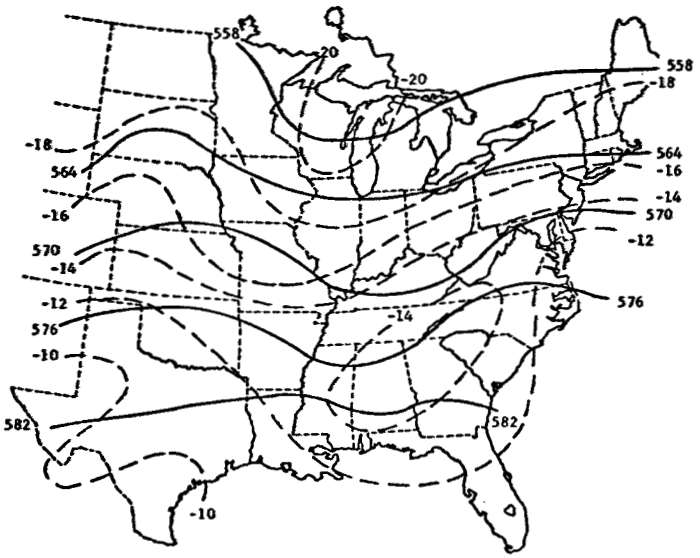

500 mb

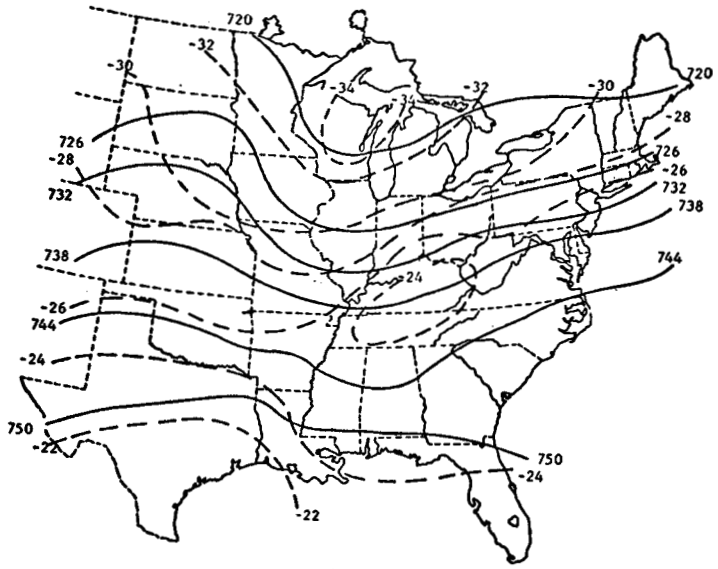

400 mb

Figure 4.11. (continued)

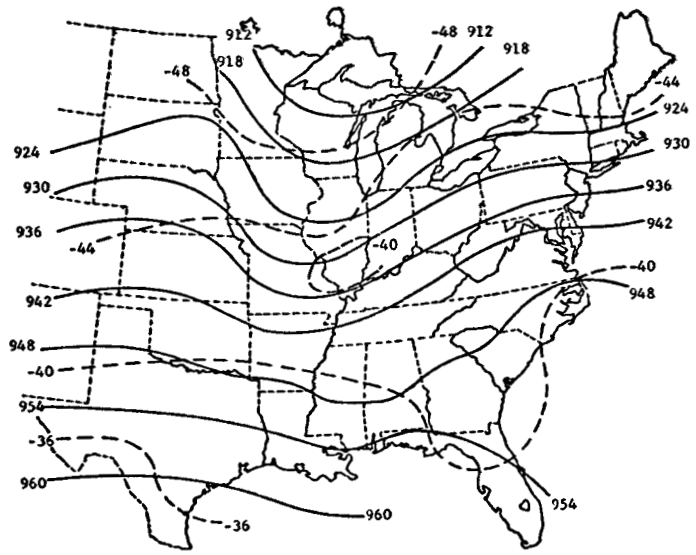

300 mb

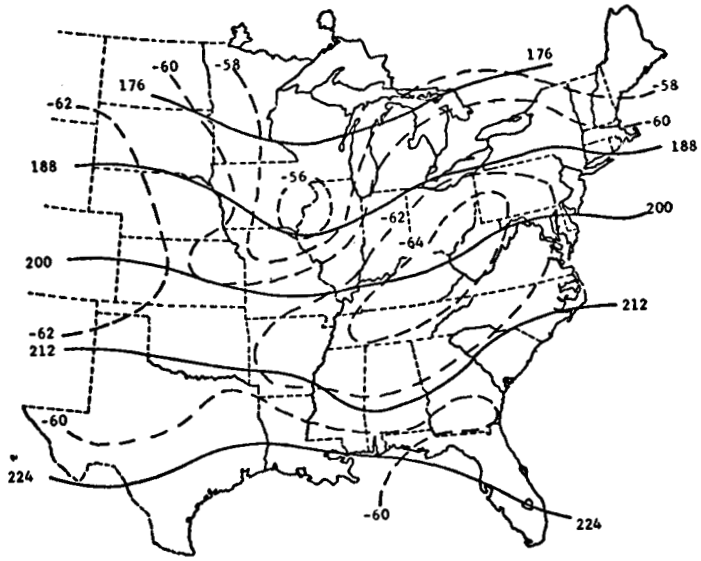

200 mb

Figure 4.11. (concluded)

evident. A small surface low pressure was centered over Iowa and southern Minnesota on April 23, 1975, which moved through the Great Lakes into Quebec by 1200 GMT, April 24, 1975. This northernmost frontal activity was associated with a short wave aloft which moved out of the long wave situated off the northwest coast of the United States.

At 0000 GMT, April 24, 1975, a second short wave upper trough produced by the long wave pattern off the United States west coast moved to the lee side of the Rocky Mountains and stimulated the development of a small surface low over southern Kansas as shown in Figure 4.3. The strongest thermal gradients, which are one measure of the support for the frontal system, were at the 850 millibar level over Nebraska and Iowa, as shown in Figure 4.3. A tongue of warm air is evident in Figure 4.3 at the 700 millibar level from southern Texas to the Great Lakes region. Cold air advection is seen at the 500 millibar level as shown in Figure 4.3 across Illinois. The features at levels above 500 millibar do not appear to be significant.

The cold frontal system with its boundary from southwest Texas to the low in Kansas was moving very slowly toward the east as shown in Figure 4.4. Some movement can be seen also with the northern portion of the front over the Great Lakes in conjunction with the surface low center north of Lake Huron. A low developed at the 850 millibar level (Figure 4.4) over northwest Kansas associated with the surface low as the upper level trough moved into that region.

The frontal system reflected at the 850 millibar level showed good temperature gradient support of as much as 10° Celsius per 100 nautical miles in the vicinity of the Kansas low. Warm advection continued over Texas and Oklahoma at the 700 millibar level. Other pressure levels do not indicate any significant features. Thunderstorms were occurring through Missouri, Illinois, and other surrounding states.

The intensification of the low pressure center at 1200 GMT, April 24, 1975, over Kansas was the dominant feature important to the potential development of severe weather as shown in Figure 4.5, page 90. Consequently, squall lines formed from southwestern Missouri to southern Indiana which is several hundred miles east of the front shown in Figure 4.5. No significant changes were noted in the major pressure patterns during the previous six hours. Although isotherm support was building in the upper level trough over Nebraska and western Kansas, they were most notably at the 500 millibar level in Figure 4.5.

The frontal system shown in Figure 4.6, page 94, continued to edge eastward at 1500 GMT, April 24, 1975. Strong thermal gradients can be seen at the 850 millibar level west of the trough lines from northwest Texas to the central Great Lakes. Warm air advection from southwest Texas through the Ohio Valley can be identified at the 850 millibar level by noting that the southwesterly wind flow over Oklahoma is almost perpendicular to the isotherms in

that region. Cold air advection shown by the flow of air across closely packed isotherms is clearly seen in the vicinity of the short wave trough over the upper Great Lakes and upper Midwest in Figure 4.6, page 94, at the 850, 700, and 500 millibar levels. It is less clear at the 400 millibar level because of the lack of detail in the thermal field.

The basic pattern at 1800 GMT, April 24, 1975, as shown in Figure 4.7, page 98, did not significantly change in the three hours from 1500 GMT. Severe thunderstorms were occurring in northwest Tennessee as a squall line moved into that region from Missouri.

At 2100 GMT, April 24, 1975, the short wave trough aloft had now become prominent at altitude pressure levels up to 300 millibar from the Dakotas to western Kansas as shown in Figure 4.8, page 102. The surface low had moved into southeast Kansas and the temperature gradients at the 850 millibar level indicated a strengthening of the system. Tornadoes were reported over north central Tennessee and West Virginia about this time as the pattern of convective instability began to spread across a large region from Texas to the Ohio Valley.

At 0000 GMT, April 25, 1975, the surface cold front stretched from southwest Texas to the weak low over extreme southwest Missouri as shown in Figure 4.9, page 106. The cold front continued from this low northeastward through the Central Midwest to the other low over Quebec. Severe

thunderstorms and tornadoes developed over northeast Oklahoma and southwest Missouri at this time in association with the frontal system which was moving slowly eastward. The cold air advection and associated thermal gradients identify the frontal boundary at the 850 millibar level, especially over Kansas. The short wave trough at the upper levels had moved to a position from the eastern Dakotas southward to northeast Texas. The severe weather developed in response to the short wave which helped to intensity the slowly moving surface front.

The cold front at 0600 GMT, April 25, 1975, had moved southeastward to southeast Oklahoma, northwest Arkansas, and western Kentucky with the surface low moving to the Ohio Valley, as shown in Figure 4.10, page 110. The short wave at the upper levels indicated signs of intensification from Minnesota, Iowa, Missouri, and eastern Oklahoma. Isotherms along the trough line support the short wave at all levels up to the 300 millibar level.

The surface frontal system, as shown in Figure 4.11, page 114, at 1200 GMT, April 25, 1975, had progressed to a line from southeast Oklahoma to the low over southern Indiana. Severe thunderstorms were occurring along a line from northern Alabama to eastern Kentucky in advance of the front. The height fields and isotherms identify the upper level trough from Mississippi, northward into Wisconsin.

The experience gained in the preparation of the charts, the above analyses, and a first look at the features

revealed the following conclusions. First, the experiment data are of sufficient quality so that, at least to the mid-troposphere, the evolution and movement of large scale features can be resolved on three hour time scales. Second, analysis of upper air data to one-half the tolerances cited for operational purpose reveal large scale, small amplitude features which exhibit space and time continuity. Reasonable tolerances in the temperature are ±0.5° Celsius to 400 millibar and ±1.0° Celsius above the 400 millibar level.

IV. UNUSUAL SEVERE WEATHER PHENOMENA DURING THE EXPERIMENT

In this section a discussion is given concerning the most severe weather events in the context of property damage and loss of life that occurred as a consequence of the severe storms. The most severe weather of the experiment occurred during the period of April 24 and 25, 1975. Also, a discussion is given concerning the pinpointing of unusual events by analysis of satellite photographs using the method of densitometry. Figure 4.12 shows a summary map which locates the significant severe weather events that occurred during the experiment.

Gove County, Kansas [1],[1] on the evening of April 24, 1975, received considerable hail, with some hailstones as large as tennis balls, which resulted in extensive damage to

[1]Numbers in brackets refer to the locations in Figure 4.12.

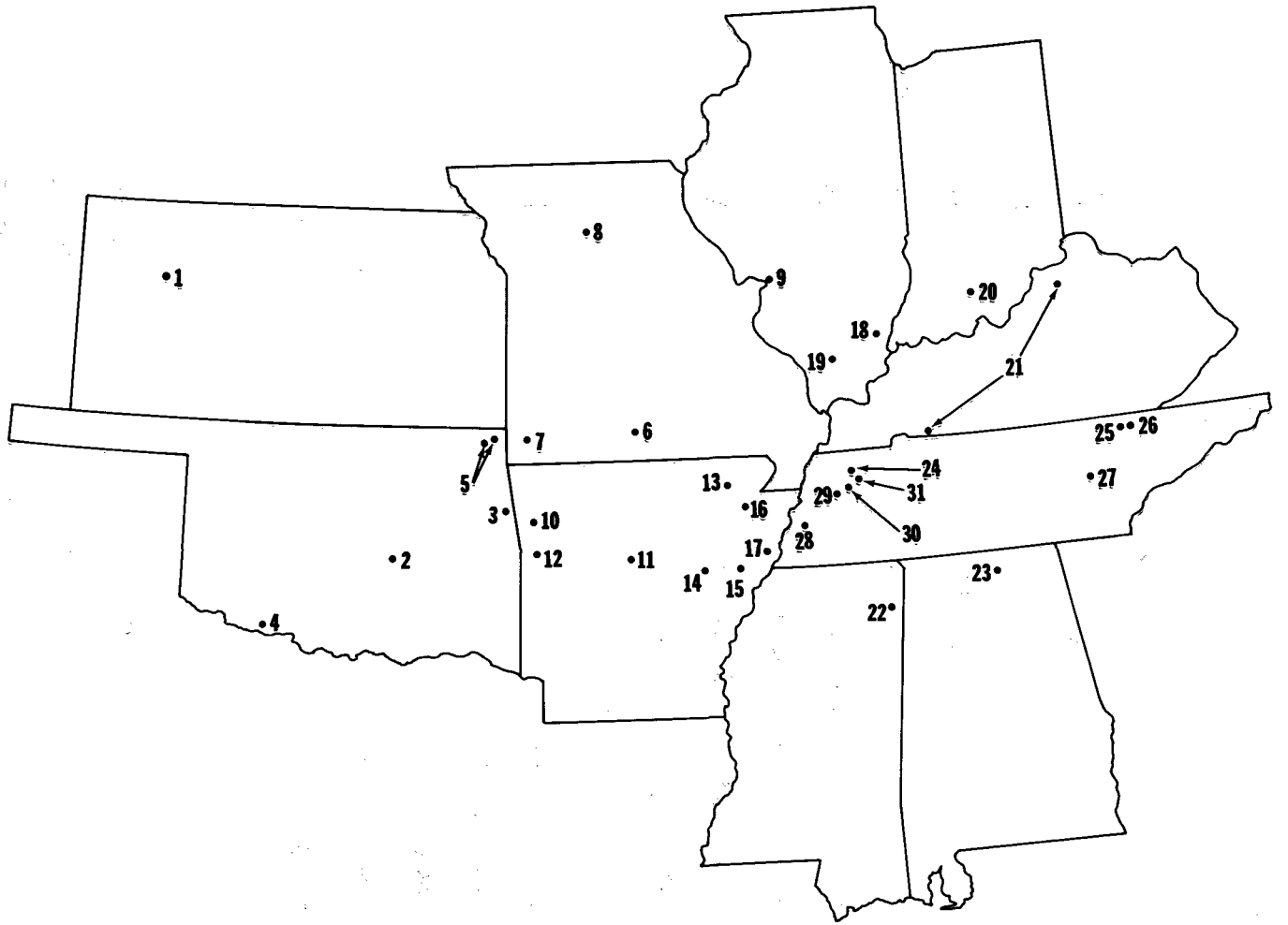

Figure 4.12. Location of unusual severe weather phenomena during the experiment.

automobiles, buildings, and crops. Property damage was estimated between $50,000 and $500,000.

In Oklahoma, a number of events occurred on April 24, 1975. At Wewoka, Seminole County [2], hail as large as baseballs accompanied a thunderstorm as it moved northeastward through Wewoka. Considerable damage to roofs and automobiles was reported. This event occurred at 2315 GMT (5:15 p.m.) and cut a path three miles wide and eight miles in length. Damage to property was estimated between $50,000 and $500,000. At Stilwell, Adair County [3], hail occurred at 2325 GMT (5:25 p.m.) and lasted for approximately 20 minutes. The damage to roofs caused by the hail was estimated between $50,000 and $500,000. In Cotton County [4], a thunderstorm producing hail over one inch in diameter moved eastward through the county. This event occurred at 0000 GMT (6:00 p.m.) and cut a path 3 miles wide and 20 miles in length. Heaviest damage was to grain crops in the Cookietown and Hastings area. Hail was reported up to two feet in some areas. Property damage was estimated between $5,000 and $50,000. In Craig and Ottawa Counties [5], a tornado touched down approximately two miles northeast of Blue Jacket, destroying a barn and damaging several farm buildings. The tornado moved eastward, destroying or damaging several buildings. Five homes and three mobile homes were destroyed in the Valley Mount community about five miles southwest of Miami. Three minor injuries were reported. The tornado touched down at 0000 GMT (6:00 p.m.)

and cut a path 75 yards wide and 7 miles in length. Property damage was estimated between $50,000 and $500,000.

In Missouri, a number of events occurred on April 24, 1975. At Nixa, Christian County [6], thunderstorms moving southeastwardly through northern Christian County in the early morning hours spawned some high winds and two small tornadoes shortly after 1100 GMT (5:00 a.m.). One tornado dipped down just east of Highway 65 and just north of Route 66, and another touched down in the Twin Acres subdivision. Only one woman was slightly injured when her trailer was demolished, just northwest of Nixa. Total damage was estimated at $250,000. In Newton County [7], a tornado developed at about 0040 GMT (6:40 p.m.) just east of Seneca and moved east along old Route 60 into South Neosho. It lifted just east of the city. The tornado cut a path 400 to 900 yards wide and 9 miles in length. Three persons were killed and 22 injured. Damage was estimated at $10,500,000. In Pettis County [8], a severe hailstorm occurred at 0000 GMT (6:00 p.m.). This storm moved from about 10 miles south of Sedalia northeastward, dumping golf ball hail in drifts between two to three feet deep. Damage was estimated between $50,000 and $500,000. In St. Louis and St. Louis County [9], between 0200 GMT (8:00 p.m.) and 0300 GMT (9:00 p.m.) severe thunderstorms moved through St. Louis. Golf ball size hail was reported at Highway 40 and Lindbergh Boulevard at 0238 GMT (8:38 p.m.), and winds gusted to 69

miles per hour with one-fourth inch hail at St. Louis University in the city.

In Arkansas, a number of events occurred on April 24 and 25, 1975. A funnel cloud moving in a northeasterly direction was reported from Cedarville, Crawford County [10], at 0330 GMT (9:30 p.m.) on April 24. Another funnel cloud moving toward the east was reported from Conway, Faulkner County [11], at 0548 GMT (11:48 p.m.) on April 24. Between 0500 GMT (11:00 p.m.) and 0555 GMT (11:55 p.m.) on April 24, 1975, lightning generated by thunderstorms moving through Waldron, Scott County [12], struck and set fire to a mobile home which was destroyed. Lightning also damaged a barn and its contents and a sign at the local Dairy Kreme. On April 25, 1975, funnel clouds were reported at 0608 GMT (12:08 a.m.) seven miles north of Walnut Ridge, Lawrence County [13], moving in an easterly direction; at 0630 GMT (12:30 a.m.) at Cotton Plant, Woodruff County [14], moving in an easterly direction; and at 0637 GMT (12:37 a.m.) five miles west of Forrest City, St. Francis County [15], moving toward the east. In Craighead County [16], at 0620 GMT (12:20 a.m.) on April 25, 1975, strong winds generated by a line of thunderstorms moving southeastward through the county heavily damaged several businesses, destroyed a mobile home, and damaged the Physical Education building at Arkansas State University. Total damage was estimated between $50,000 and $500,000. On April 25, 1975, at 0645 GMT (12:45 a.m.), a tornado moving toward the southeast briefly touched down in

the vicinity of Interstate 55 at Turrell, Crittenden County [17], heavily damaging two service stations before dissipating. It cut a path 40 yards wide and one-tenth mile in length.

In the southeast quarter of Illinois on April 24, 1975, between 0800 GMT (2:00 a.m.) and 1200 GMT (6:00 a.m.) torrential rains totaling as much as seven inches were caused by severe thunderstorms. Floodings were reported in Caral, Grayville, Norris City, and Fairfield. At Caral, White County [18], an earth dam collapsed, draining Pont-Ca Lake and flooding a 30-acre area to the east. Total damage was estimated between $5,000 and $50,000. In the southern third of Illinois [19], on April 24, 1975, between 0200 GMT (8:00 p.m.) and 0800 GMT (2:00 a.m.) thunderstorms produced hail and heavy rain. Damage was limited to trees and buildings and was estimated between $5,000 and $50,000.

On April 24 and 25, 1975, in the extreme southern section of Indiana [20], very heavy rain (as much as five inches) caused flash flooding that forced the evacuation of 100 families from their homes. Rain and flooding caused the worst soil erosion in the last 30 or 40 years in this area. Many homes and businesses suffered water damage, and the total damage was estimated between $500,000 and $5,000,000.

On April 24 and 25, 1975, in Kentucky [21], thunderstorms produced strong, damaging winds over the western and south central part of the state and heavy rains and flash flooding elsewhere. Four persons were injured in damaged

mobile homes near Bowling Green. A school was damaged extensively in Hickman, and one person was injured and 10 cows were killed in a barn that was destroyed in Henry County. Total damage was established between $500,000 and $5,000,000.

At Water Valley, Itawamba County, northern Mississippi [22], high winds caused considerable damage to roofs. These high winds occurred around 1030 GMT (4:30 a.m.) on April 25, 1975.

In the northern Alabama [23] counties of Madison, Limestone, Lawrence and Jackson, early morning thunderstorms occurred on April 25, 1975. These storms produced widespread damage as they moved eastward across the state. A small tornado dipped down at Redstone Arsenal, causing light damage. Five homes were damaged and three mobile homes destroyed. Several outbuildings and barns were also destroyed. Reports were received that a loud roar accompanied the severe weather. Total damage was estimated between $50,000 and $500,000.

A number of events occurred in Tennessee on April 24 and 25, 1975. At Meadowbrook, near Martin, Weakley County [24], a small tornado touched down briefly, causing roof damage to the Weakley High School and damaging several mobile homes. This touchdown occurred at 1630 GMT (10:30 a.m.) April 24, 1975, cutting a path 200 yards wide and one-half mile in length. One person was injured, and damage was estimated between $5,000 and $50,000. Strong winds were

reported at 2000 GMT (2:00 p.m.) April 24, 1975, in Lafayette, Macon County [25], which destroyed one mobile home, damaged another and caused roof damage to a few houses. Two persons were reported injured, and total damage was estimated between $5,000 and $50,000. Strong winds occurred at 2000 GMT (2:00 p.m.) April 24, 1975, in Red Boiling Springs, Macon County [26], causing damage to several mobile homes. Total damage was estimated between $5,000 and $50,000. In Crossville, community of Mayland, Cumberland County [27], a tornado touched down twice at 2230 GMT (4:30 p.m.) on April 24. Two mobile homes and a brick residence were destroyed. Other houses and businesses were damaged. One person was killed, four injured, and numerous trees were twisted and broken. The tornado cut a path 440 yards wide and 1-1/2 miles in length. Total damage was estimated between $50,000 and $500,000. On April 25, at 0700 GMT (1:00 a.m.) a tornado first touched down 1-1/2 miles southwest of Gilt Edge, Tipton County [28], and then again in Gilt Edge, destroying a mobile home and killing a five-month-old infant. Damage to other buildings also occurred, causing one person to be injured. The tornado cut a path 440 yards wide and 6 miles in length. Property damage was estimated between $5,000 and $50,000. A tornado touched down two miles west of Maury City [29], on April 25, 1975, at 0720 GMT (1:20 a.m.), causing roof damage. This tornado skipped along an 11-mile path through Cairo, Nance, and Quincy communities in Crockett County, destroying mobile

homes and damaging houses, barns, power lines and a silo before dissipating east of the Quincy community. Six people were injured in mobile homes. A path 440 yards wide and 11 miles in length was cut by the tornado. Property damage was estimated between $50,000 and $500,000. In Humboldt, Gibson County [30], high winds occurred on April 25, 1975, at 0740 GMT (1:40 a.m.), destroying one mobile home and damaging others. Several businesses, including the Humboldt Glass Company, Alton Box, Century Electric, Humboldt Shopping Center, and the local high school received roof damage. One person was injured, and property damage was estimated between $50,000 and $500,000. In Huntingdon, Smyrna community, Carrol County [31], high winds destroyed three mobile homes and injured five people on April 25, 1975, at 0800 GMT (2:00 a.m.). Also, nine farm buildings were destroyed and two others heavily damaged. Damage was estimated between $5,000 and $50,000.

It is interesting to compare some of these severe events with the satellite imagery and the ground base data.

The synchronous meteorological satellite (SMS) has the unique capability to observe meteorological phenomena on a mesoscale. SMS is in synchronous (stationary) orbit to obtain day and night information on the earth's weather by means of imaging instruments. The system includes viewing instruments capable of obtaining meaningful near-realistic data and a reliable subsystem for data relay from the spacecraft. Day and night views of the earth's cloud cover are

obtained by the visible and infrared spin scan radiometer (VISSR). The visible channels are capable of providing daytime images of the earth with a resolution of one-half nautical mile, and the infrared channels provide nighttime images with five nautical miles resolution.

It is proposed that satellite imagery can be used to observe the development of mesoscale phenomena in both time and space. This information should provide insight into the important mesoscale mechanisms responsible for triggering severe weather (tornadoes) and thus lead to a satellite forecasting system.

The purpose of this investigation is to demonstrate the time and space scales required of the satellite imagery to detect the mesoscale phenomena to be forecast. Toward this goal, satellite imagery taken from SMS-1 at 2300 GMT and 2330 GMT on April 24, 1975, was selected from the 226 visible and infrared photographs taken during the AVE IV experiment on April 23-25, 1975, for detailed analysis. These photographs were chosen somewhat arbitrarily but during the time when considerable severe storm activity was occurring over the central United States.

The transparencies of both the visible and infrared photographs were studied using a Model 703 Datacolor Densitometer. This device converts the various shades of gray (or photographic density) into a wide spectrum of colors. The color spectrum is displayed on a computer-type color display for quantitative analysis and image

enhancement. The result is a dynamic real-time display of brightness values corresponding to degrees of photographic density. The quantitative readings of brightness or density are made by placing a calibrated photographed step wedge in the picture for reference. An area in the image having a brightness corresponding to a step on the wedge will have the same color. The color wedge calibration used is shown in Table 4.1. The accuracy is limited only by the noise and shaping in the television camera.

TABLE 4.1

SMS-1 IMAGE TRANSPARENCY COLOR WEDGE CALIBRATION

Color	Shades	Density
Yellow	4	0.05
Cyan	4	0.20
Green	4	0.50
Orange	4	0.80
Magenta	4	1.10
Violet	4	1.14
Red	4	1.70
Blue	4	2.00

The results of the color coding are given in Figures 4.13 through 4.16. Each figure contains the black and white image, a 26 slice color coded image and a 32 slice color coded image. Figures 4.13 and 4.15 are the visible channels and Figures 4.14 and 4.16 are the infrared channels at 2300 GMT and 2330 GMT, respectively. Other representative photographs from the satellite imagery are assembled in the Appendix for the interested reader.

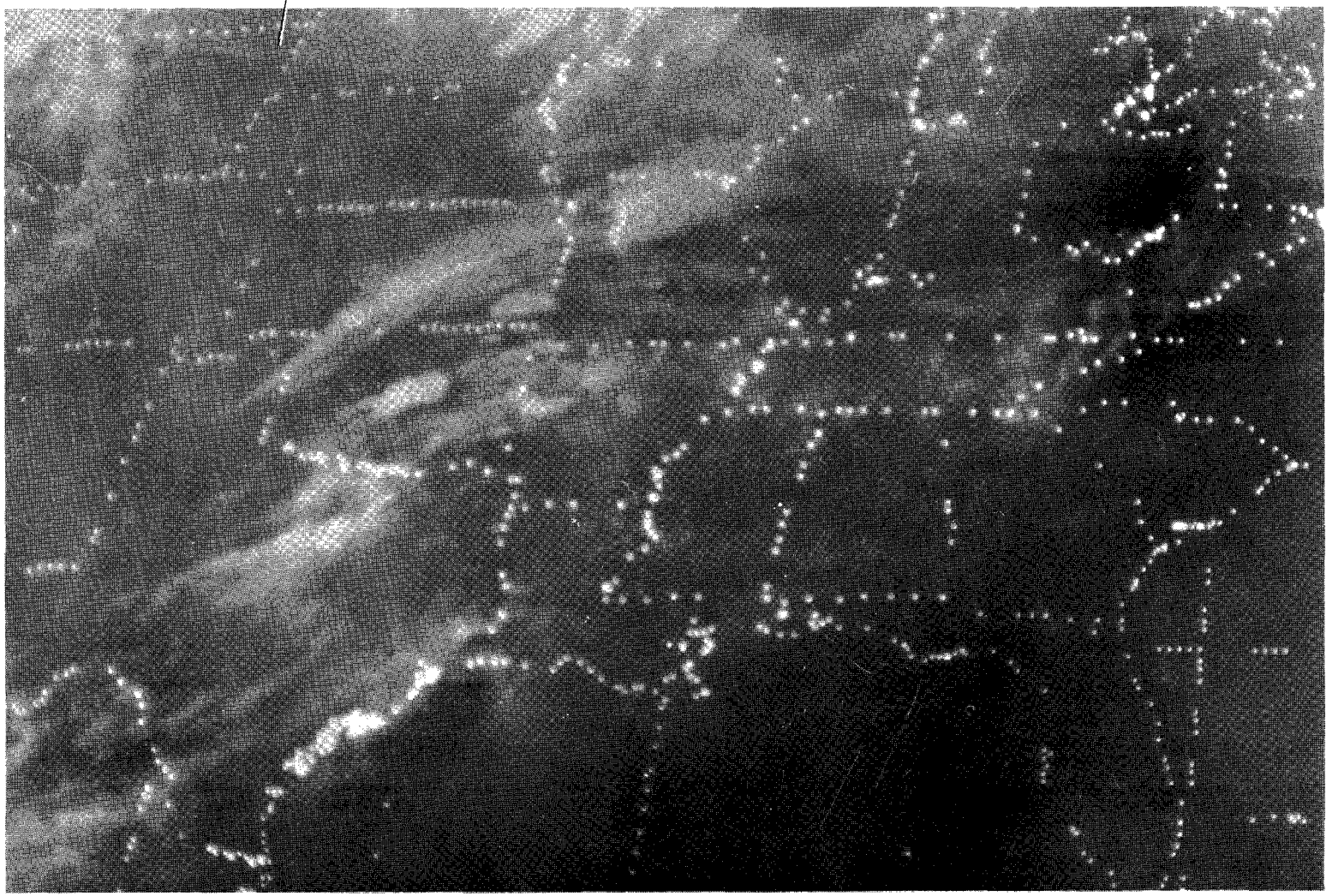

(Black and white)

Figure 4.13. SMS-1 visible channels, 2300 GMT, April 24, 1975.

(26 slice)

Figure 4.13. (continued)

(32 slice)

Figure 4.13. (concluded)

(Black and white)

Figure 4.14. SMS-1 infrared channels, 2300 GMT, April 24, 1975.

(26 slice)

Figure 4.14. (continued)

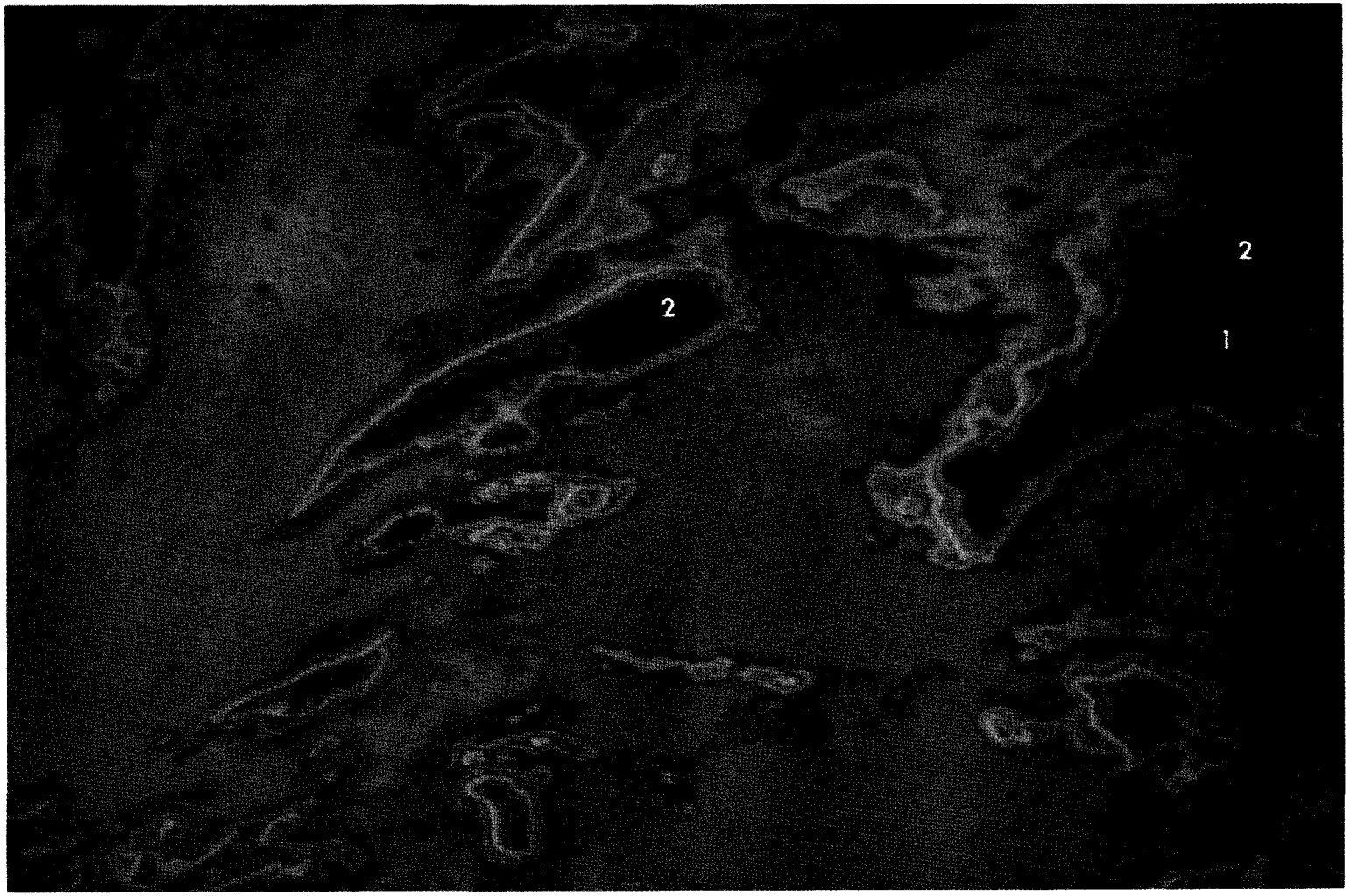

(32 slice)

Figure 4.14. (concluded)

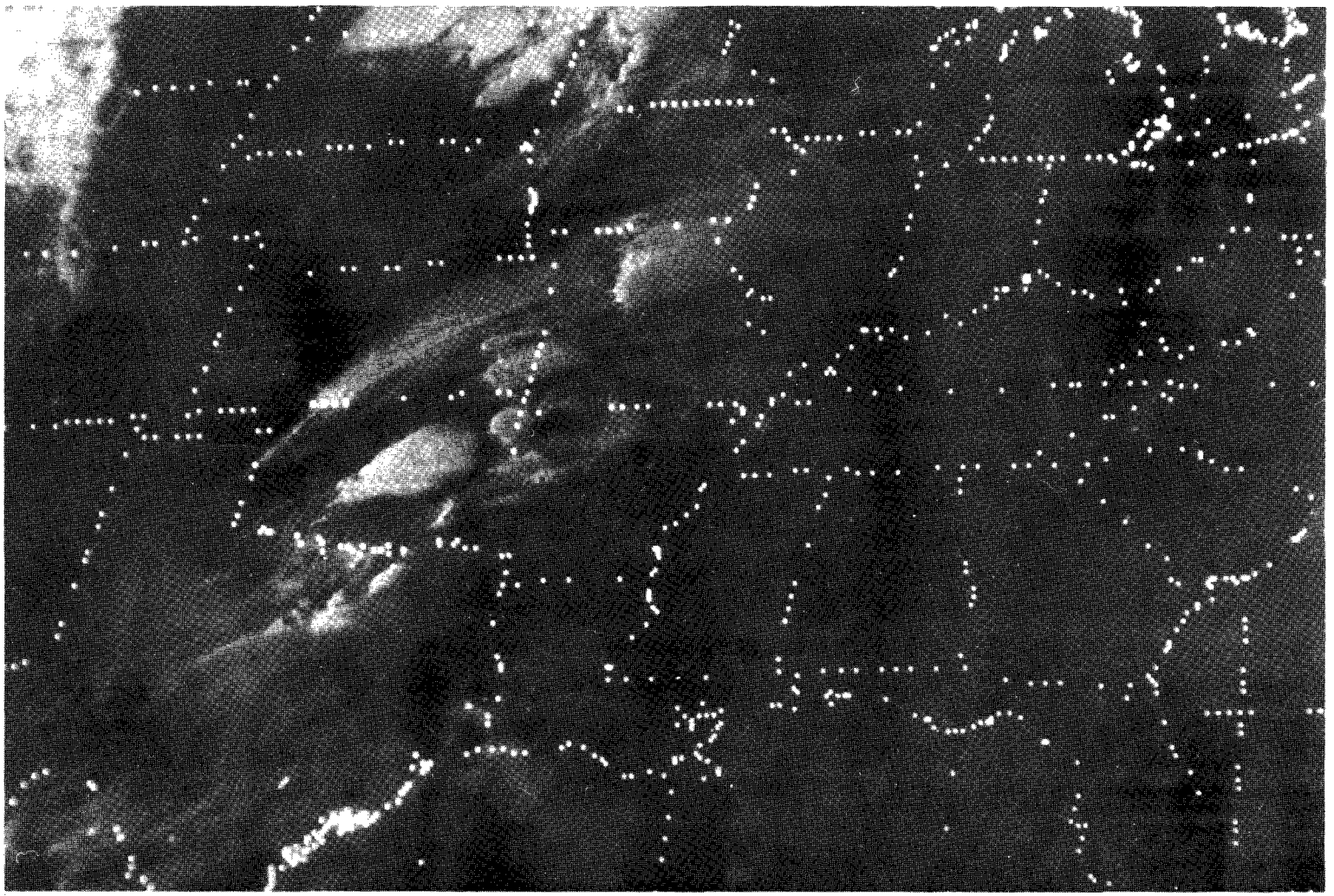

(Black and white)

Figure 4.15. SMS-1 visible channels, 2330 GMT, April 24, 1975.

(26 slice)

Figure 4.15. (continued)

(32 slice)

Figure 4.15. (concluded)

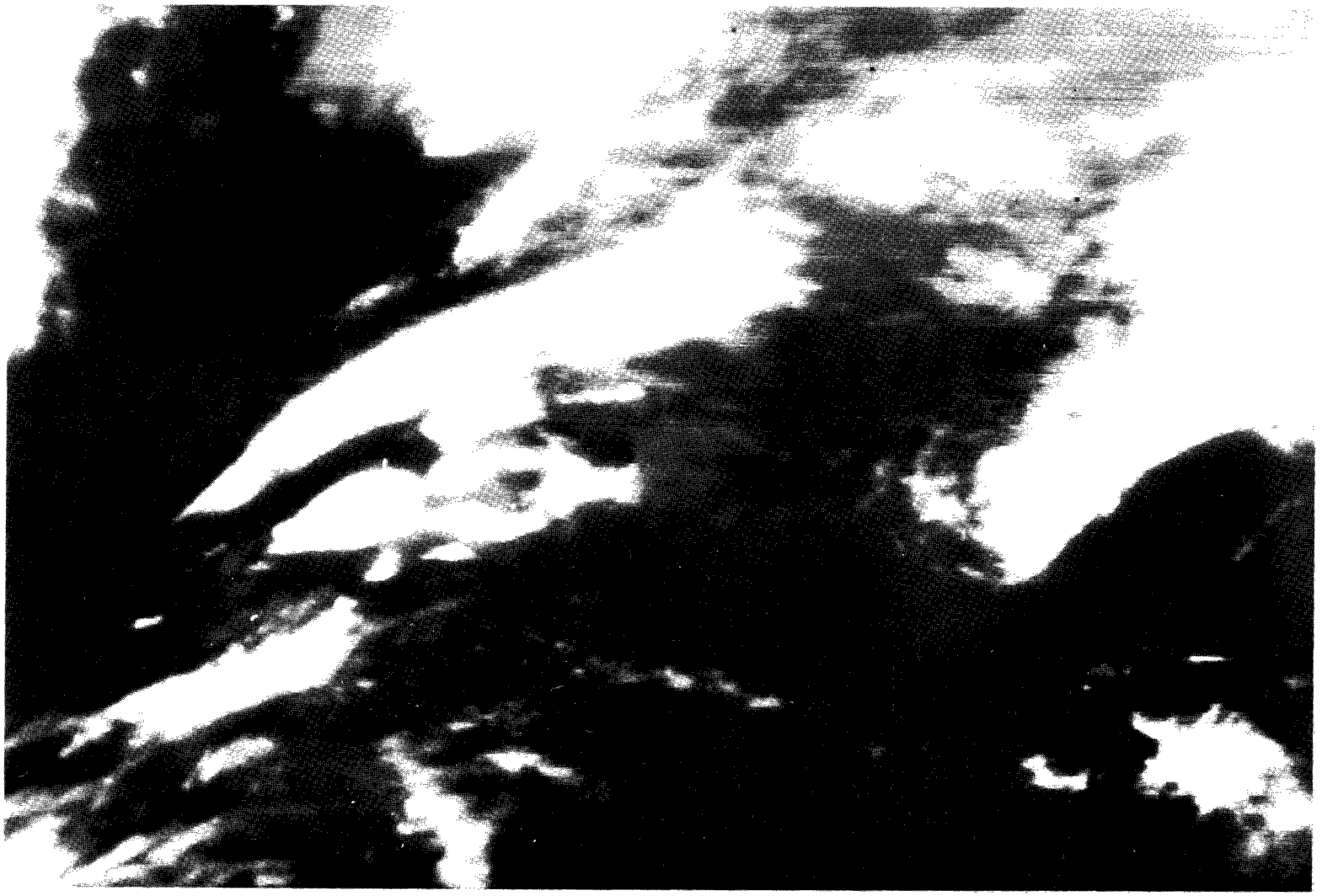

(Black and white)

Figure 4.16. SMS-1 infrared channels; 2330 GMT, April 24, 1975.

(26 slice)

Figure 4.16. (continued)

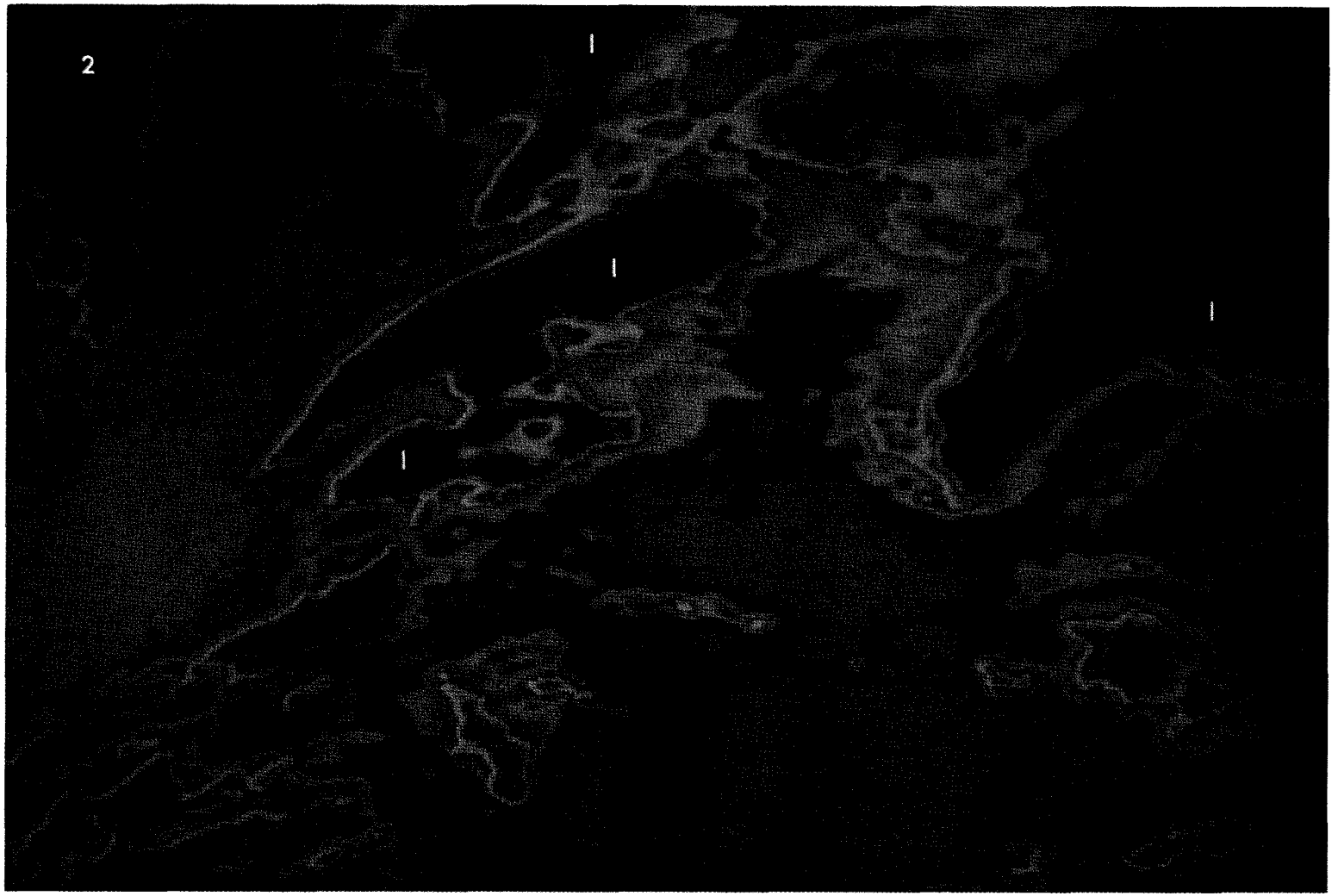

(32 slice)

Figure 4.16. (concluded)

Inspection of the preceding list of severe storm events reveals that three significant storm effects were reported at a time approximating the time of the photographs. These were events 2 (2315 GMT), 3 (2325 GMT) and event 27 (2230 GMT). Comparison of the locations of these events given in Figure 4.12 with the photographs lead to some interesting observations.

Event 2, which is a severe hailstorm, coincides exactly with the cloud formation marked (1) in Figures 4.13 and 4.15. The cloud formation obviously shows a build up between 2300 and 2330 associated with the reported severe thunder and hailstorm. The color coded photographs enhance the location of the storm also marked as (1). This appears to be one of the most dense portions of the photograph having a value of approximately 1.5, see Table 4.2.

TABLE 4.2

SMS-1 DENSITOMETRY MEASUREMENTS

Figure Number	Brightness Number	Density
4.13	1	1.409
	2	1.348
4.14	1	1.836
	2	1.775
4.15	1	1.348
4.16	1	1.897
	2	1.836

In interpreting the color coded, visible channel photographs one must be cognizant of the fact that the overlay of the outline of the states often gives the most dense spots, for example, the spot marked (E). These borders should not be confused with storm events.

Event 3 which was reported also as a hailstorm, labeled (2) on the photographs, occurred at 2325 almost simultaneously with the 2330 photographs and is clearly evident in Figure 4.15, page 139. The 32 slice color code appears to give better resolution of the storms than the 26 slice. Certainly Events 2 and 3 stand out rather dramatically in the 26 slice color coded photograph given in Figure 4.15 as does also Event 2 in the corresponding photograph in Figure 4.13, page 133.

A particularly striking feature of the color coded visible photographs is associated with Event 27 labeled (3) on the photographs. Inspection of the black and white image would suggest only modest storm activity in Tennessee. However, the color coded photograph in Figure 4.13 shows a very dense spot coinciding with the location of Event 27. This event was reported as a tornado touching down twice at 2230 GMT, 30 minutes before the photograph was taken. The remnants of this event are clearly visible in Figure 4.13 but have disappeared in Figure 4.15, one hour after the storm had passed.

Figure 4.13 and Figure 4.14, page 136, also indicate some type of activity at the location labeled (F). It is

possible that a storm did occur at that time but was unreported. No method of confirming this is available.

The infrared photographs in turn show higher density at the location of the three aforementioned storm events; however, they do not resolve the storm centers as clearly as the visible imagery. It is surprising that the visible photographs appear to show less cloud cover than the infrared and one might be tempted to conclude that the visible imagery has a decided advantage over the infrared. This set of photographs, however, was taken near dusk when the sunlight was at a decided angle and probably scattered from the cloud formation more effectively in the infrared wavelength than in the visible wavelength. This effect should be studied further in future satellite imagery applications.

The preceding arguments show that the satellite imagery taken at half-hour increments can resolve mesoscale activities. The ground based data, however, was taken at three-hour intervals. In the following, the ground based data are evaluated relative to the three events detected in the satellite imagery to ascertain if the time and space scale give meaningful information.

Ground Based Data

Ground based network stations surrounding Events 2 and 3 were Dodge City, Kansas; Monett, Missouri; Little Rock, Arkansas; and Fort Sill, Oklahoma. Unfortunately, Fort Sill, which was located nearest to the storm activity of interest, recorded at irregular intervals of approximately six hours.

The only measurement near the time of the hailstorm activity from Fort Sill was at 1850 GMT. Measurements taken at the other three stations were at 2015 GMT and 2315 GMT. The latter time essentially coincides with the reported occurrence of Event 2.

Data from the Dodge City station are given in Figures 4.17 through 4.21. They include vertical wind speed and direction profiles, vertical temperature profiles, and time cross sections of wind speed, wind direction and temperature. Figures containing data from all other stations, including the Monett, Little Rock and Fort Sill data, are given in the Appendix for convenient reference.

Inspection of the data taken at 2315 from the three stations do not appear to resolve any details of the storm other than those conventionally associated with frontal motion. This suggests that the spatial scale of the network is too large and perhaps needs refinement.

The time scale, however, would appear adequate in view of the fact that the time 2315 GMT at which the data were collected coincides exactly with the thunderstorm event and these events as interpreted from the previous photographs appear to persist over a half-hour period or more. A 12-hour interval would not likely have achieved this coincidence and much of the detail would be lost. This is graphically illustrated in Figure 4.20 and Figure 4.21. These plots show that sounding taken at the conventional time intervals of 1115 GMT and 2315 GMT miss

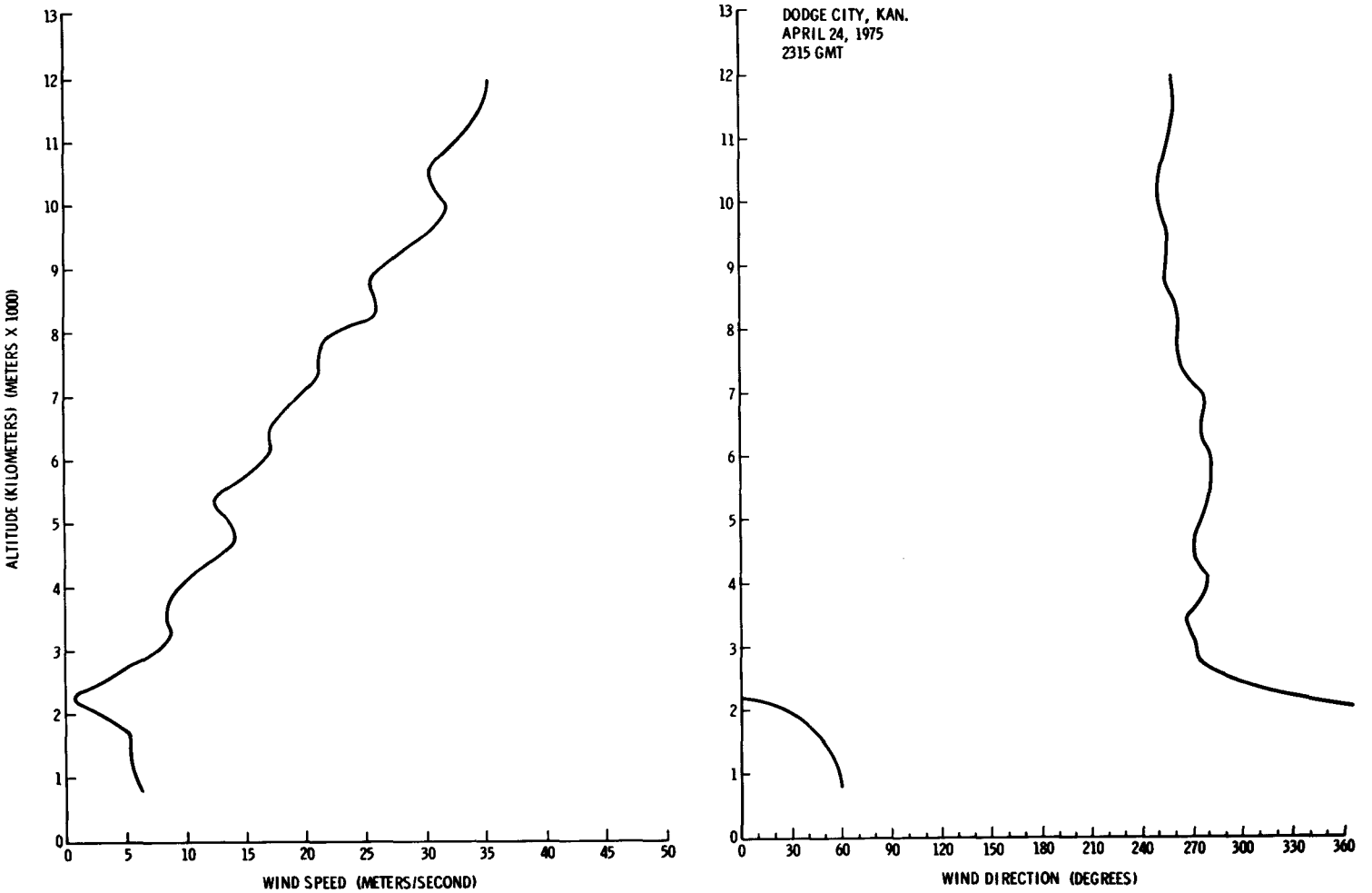

Figure 4.17. Vertical wind profile for 2315 GMT, April 24, 1975, over Dodge City, Kansas.

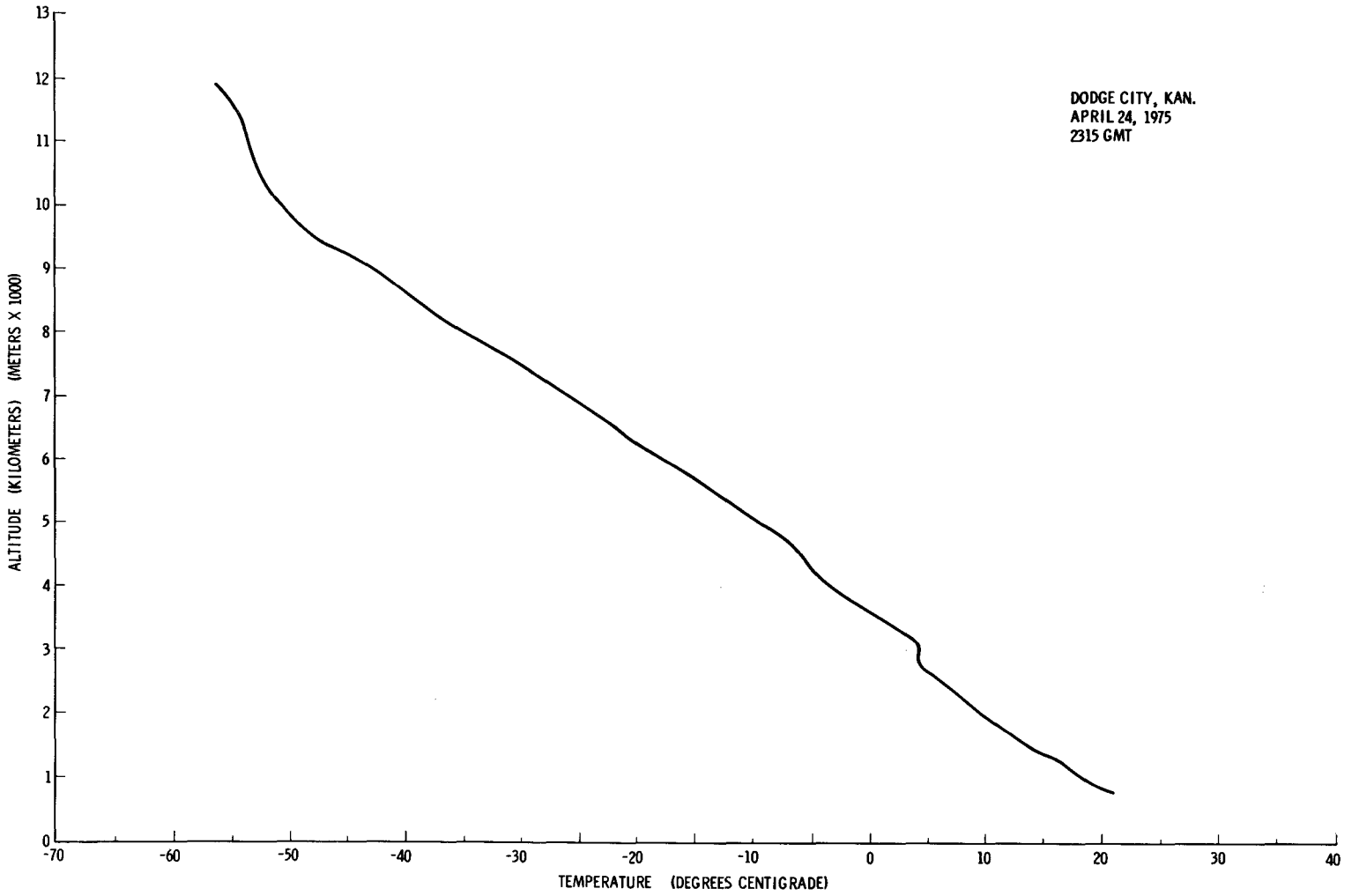

Figure 4.18. Temperature profile for 2315 GMT, April 24, 1975, over Dodge City, Kansas.

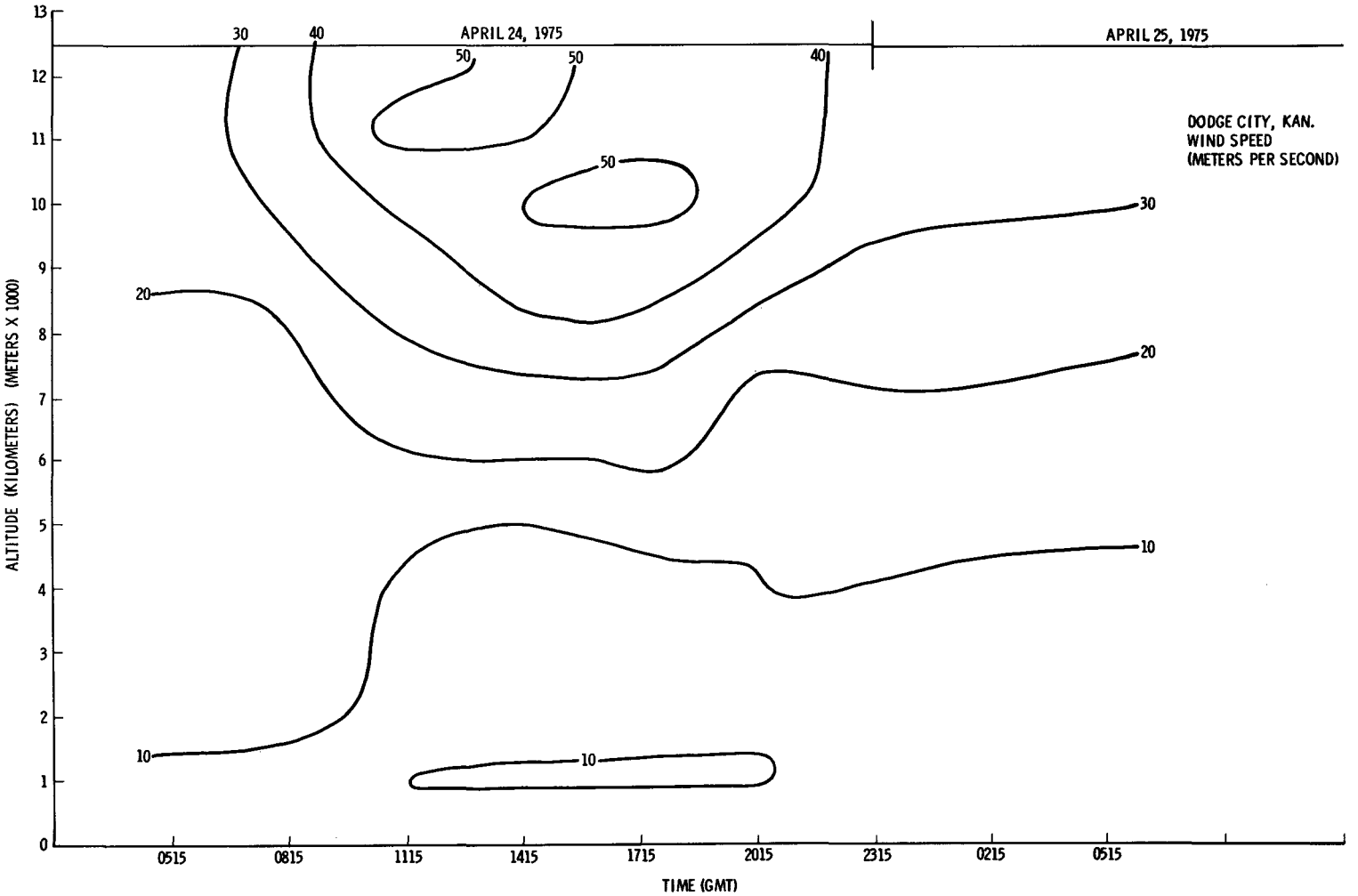

Figure 4.19. Time cross section of wind speed at Dodge City, Kansas.

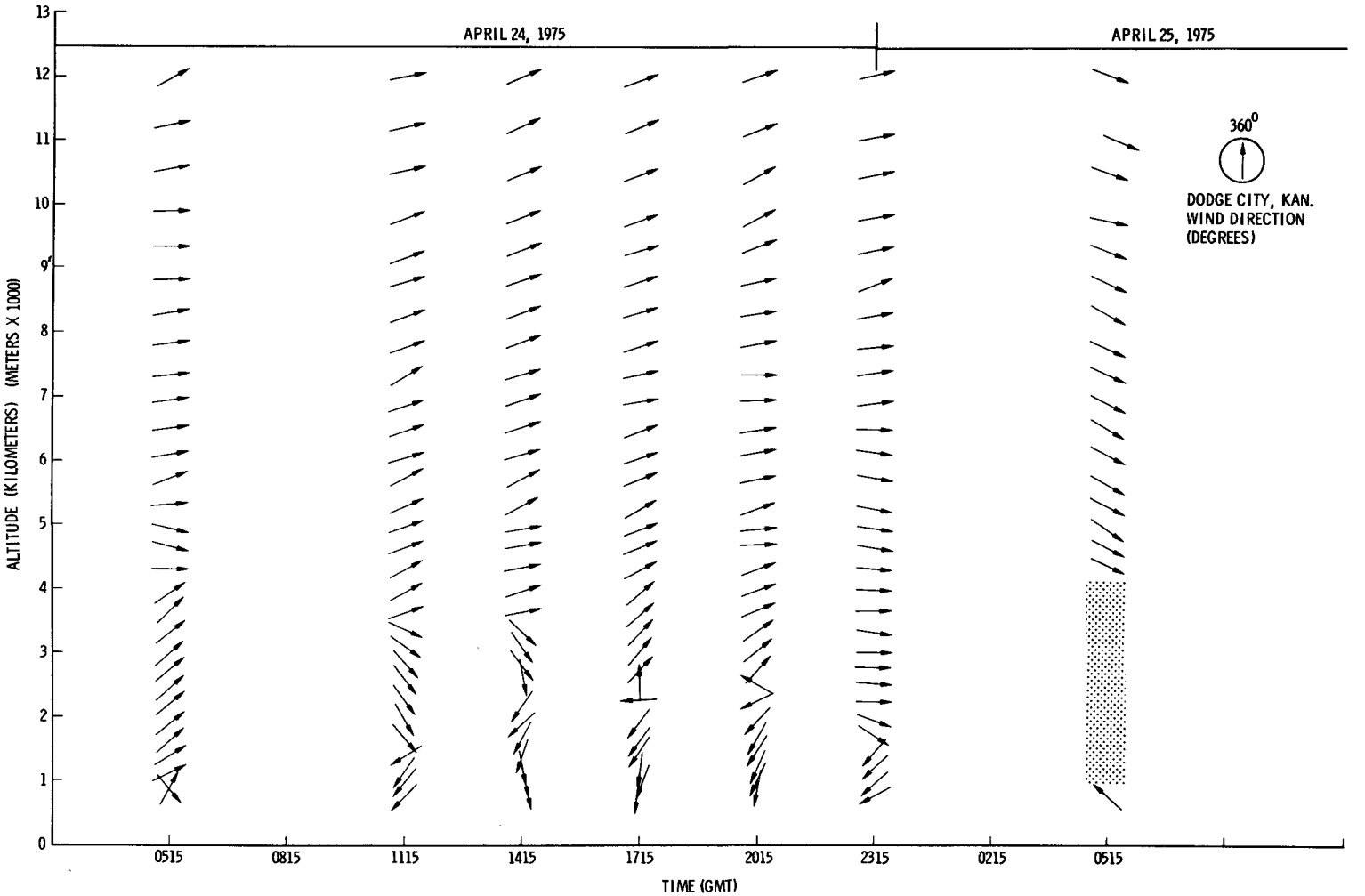

Figure 4.20. Time cross section of wind direction at Dodge City, Kansas.

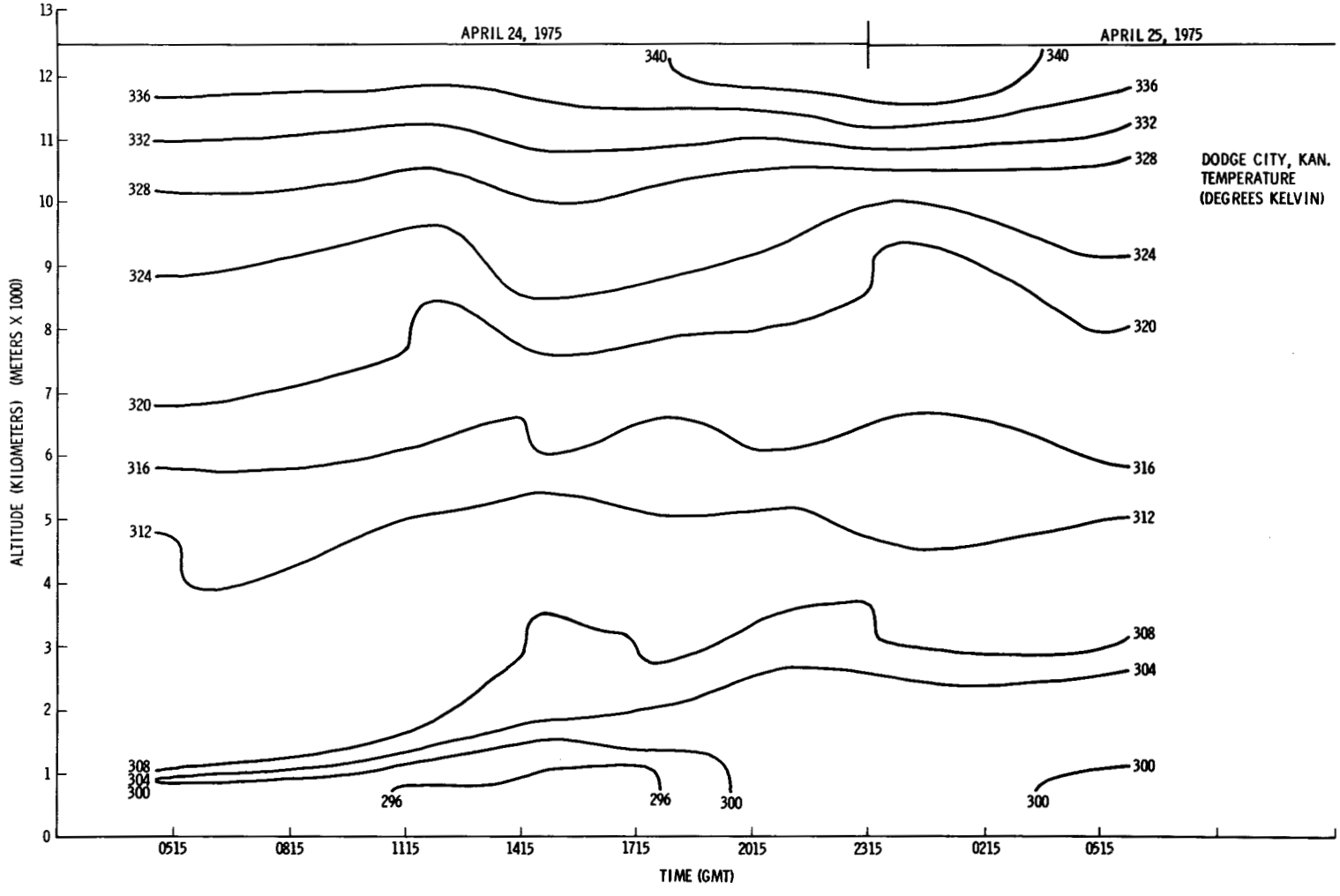

Figure 4.21. Time cross section of temperature at Dodge City, Kansas.

the complete reversal of the wind at Monett, Missouri, and the peculiar behavior of the wind between 2 and 3 km at 1715 GMT and 2015 GMT at Dodge City.

The above observation illustrates that entire features associated with mesoscale phenomena are completely lost with 12 hour sounding but are recorded with 3 hour soundings. Detailed ground based data such as reported herein is therefore expected to provide the necessary time resolution to develop and verify satellite forecasting techniques and also to support modeling studies of mesoscale phenomena. Further discussion of the resolution of mesoscale structure possible from the experimental data is given in the following section.

V. MESOSCALE STRUCTURE AS REVEALED BY THE EXPERIMENT DATA

The studies presented in this section concern the variability of important meteorological parameters plotted at individual stations. Actual vertical profiles of the three hourly values of height and wind speed and direction and temperature with time are presented in the Appendix for selected stations. These stations were chosen because of the unusual weather events which occurred during the time of the experiment. The hatched areas on the figures indicate missing data. Figure 4.12, page 123, shows the selected locations being discussed. Time cross sections of wind speed and direction and temperature for each of the selected

stations were plotted. Typical average and standard deviation values of the variability on the three hourly scales are seen generally to increase with height, apparently reflecting the increase in the amplitude of large scale features. The question as to what degree these observed tendencies represent real atmospheric variability on short time scales arises. Some degree of confidence can be placed in their reality only if they exceed the changes expected solely because of errors in individual measurements. Tendency uncertainties will depend on the degree of independence of measurement errors at successive observations, and the most appropriate assumption to be made here is uncertain. A reasonable significance criterion would be to require the three hourly changes to exceed errors in individual measurements. On the basis of this criterion, the temperature and height tendencies appear to be only marginally significant on the average, but the standard deviations indicate that occasionally real variability is reflected.

The meteorologist sometimes requires knowledge of atmospheric variables at times intermediate to the standard observation hours. To obtain them, subjective or objective interpolation of the standard observations is necessary. The simplest procedure is linear interpolation. Comparison of actual observations with linearly interpolated values will illustrate another aspect of atmospheric variability on small time scales. Referring again to the graphs, the

largest difference between actual and interpolated heights (~40 gpm), wind speeds (~15 ms^{-1}), wind direction (~20 degrees), and temperature (~6° Celsius) are found between the 0000 GMT, April 24 and 0000 GMT, April 25, 1975. Are these differences significant? Noting that the interpolated values will also be in error, a reasonable significance criterion is to require that the differences exceed double the observational uncertainty. On this basis, one would say that, to within limits determined by observational error, linear interpolation satisfactorily explains the variability in the height field, but only to a small degree in the other parameters.

These results, however, cannot be taken as a generality as it is apparent that the degree to which linear, or any, interpolation can explain observed variability is, in part, fortuitous. While the 12 hourly data happen to roughly delineate the large scale height variation, they do not at all describe that in the wind speed. In this latter case, no manner of interpolation would satisfactorily depict the true variation if based only on the standard observations. If the standard hours of observation were three hours earlier, however, a large part of the variability in the wind speed could be represented by linear interpolation. It can also be seen in the graphs that at certain levels and times, when there is little large scale variability, significant fluctuations exist on smaller scales which could frustrate one's best efforts at meaningful interpolation.

Previous analyses have shown that significant variability exists on small time scales. A scan of the graphs shows that much of the three hourly variability is related to the movement of the large scale trough, but significant oscillations of higher frequency are also evident. The question of whether these reflect the passage of organized systems of small scale arises. Kreitzburg and Brown (6), using 90 minute sounding data from a meso-network of stations, found such oscillations to possess space and time continuity. They associate them with mesoscale features in the 200 to 500 kilometer wavelength range.

To illustrate the relationship of temporal variability and mesoscale systems in the lower troposphere, time cross sections of the thermal and wind field over the selected stations are presented in graph form. Observations were available every three hours. The analyses were constructed from the 25 millibar data, the location of which at each observation time is indicated by the vertical profile. The isopleth intervals are 4° Kelvin in the thermal field and 10 meters per second and 10 degrees in the wind speed and direction fields.

Each of the fields shown in the figures display undulations and centers of maxima and minima on scales seldom revealed to the meteorologist. Many of these features have periods of at least three hours and receive independent confirmation from at least two consecutive observations. Much of the detail involved in the analyses

on the basis of single observations cannot be discounted entirely as due to observational uncertainty, but indicates the presence of features on scales smaller than those clearly resolved by this data.

In all fields the short term variability at some levels and times acquires magnitudes similar to those in the previous section (Section IV). Certainly the most spectacular changes would be observed in the wind direction in the first 1 or 2 kilometers. It appears that 1 kilometer is a characteristic vertical wavelength of the features displayed in the time sections so that one might expect appreciable differences in the variability over such depths.

Wind profiles in the lower stratosphere are found to contain considerable detail most notably of features with vertical wavelengths of 1/2 to 2 kilometers. Several soundings at single stations have shown these features to maintain their identity for periods ranging from several hours to perhaps as long as a day according to Weinstein, Reiter and Scoggins (31). These same authors feel that the perturbations are best explained as manifestations of passing inertial waves, while Danielsen (32) has found theoretical support for the idea that they are related to waves of the shear gravity or inertial gravity types. The high time resolution and spatial extensiveness of the experiment data presents the opportunity to study these wind features to the degree necessary to resolve their origin.

Some spatial aspects of these features received attention. Examination of the wind data at Little Rock, Arkansas, by means of profiles and cross section revealed that three wind maxima identifiable arrive at this station approximately 12 hours after their appearance at Topeka, Kansas. One might then infer a wavelength of about 600 kilometers (twice the distance between the stations), the term being used somewhat cautiously since the shape and orientation of the mesojet are unknown. However, Kreitzburg's (6) estimates of the scale of these features parallel to and across the mean flow bracket this value, and also indicate the orientation to be along the flow. The shape and orientation of these features as suggested by Kreitzburg's study together with the observations made are seen consistent with a general direction of movement along that of the mean flow of west to east. It does appear that the experiment winds will prove valuable in more extensive studies of these mesoscale wind features.

It is apparent that the above results of investigations of atmospheric variability and structure revealed by the unique data of the experiment are far from exhaustive. They do indicate that much of the interest awaits the detailed depiction of atmospheric structure with these data. The application of dynamic and numeric methods or models should aid in the understanding and description of the physical mechanisms responsible for and associated with the

mesoscale features. These in turn will indicate the proper approaches to prognostic techniques for prediction of various atmospheric parameters.

CHAPTER V

CONCLUSIONS

1. There is significant variability in the atmosphere observed at 3 hourly intervals that cannot be anticipated by interpolation between conventional 12 hourly observations.

2. There is considerable spatial variation of the temporal variability from station to station and level to level.

3. The experiment data are of sufficient quality so that, at least to the mid troposphere, the evolution and movement of large scale features can be resolved on three hourly time scales.

4. Satellite pictures provide a means of obtaining a better understanding of the factors involved in cloud motions. In turn once the motion is understood use can be made of satellite pictures for a successful production type scheme for forecasting severe weather.

5. Using the densitometry method, storms can be picked that have the greatest potential for causing tornadoes and storm centers can be resolved.

6. This investigation demonstrates that severe storms can be detected from satellite imagery. Development of an automatic technique for extracting cloud motions, tornado spots, and other meteorological phenomena from

visible and infrared images data on a real time must now be developed.

7. The research has demonstrated that features of mesoscale weather phenomena can be detected with 3 hourly sonde releases which cannot be resolved with the standard 12 hourly releases. Moreover, when coupled with radar and satellite imagery detailed movement of the storms with quantitative ground truth data provides an effective tool to study the basic physics of the mesoscale mechanisms responsible for triggering severe weather. Thus, the necessity to continue experiments on meso-spatial and time scales over large aerial extent is completely evidenced by this work. Many unresolved questions are still contained within the data reported. However, these data are now available for further efforts of the atmospheric scientific community to bring forth answers to advance the state of knowledge on severe weather of mesoscale proportions.

BIBLIOGRAPHY

BIBLIOGRAPHY

1. Byers, H. R. General Meteorology. New York: McGraw-Hill Book Company, Inc., 1959.

2. Fujita, T. "Analytical Mesometeorology: A Review," Meteorology Monographs, 5:121, 1963.

3. House, D. C. "The Problem of Detecting Mesoscale Motion Systems," Monthly Weather Review, 92:589-592, 1964.

4. Oort, A. H. "An Estimate of the Atmospheric Energy Cycle," Monthly Weather Review, 92:483-493, 1964.

5. Riehl, H., and J. S. Malkus. "On the Heat Balance of the Equatorial Trough Zone," Geophysica, 6:503-538, 1968.

6. Kreitzburg, C. W., and H. A. Brown. "Mesoscale Weather Systems Within an Occlusion," Journal of Applied Meteorology, 9:417-432, 1970.

7. Palmen, E., and C. W. Newton. Atmospheric Circulation Systems. New York: Academic Press, Inc., 1969.

8. Ludlum, F. H. "Severe Local Storms: A Review," Meteorology Monographs, 5:1-30, 1963.

9. Fankhouser, J. C. "Thunderstorm-Environment Interactions Determined from Aircraft and Radar Observations," Monthly Weather Review, 99:171-192, 1971.

10. Smith, W. L., D. H. Staelin, and J. T. Houghton. "Vertical Temperature Profiles from Second Generation Instruments Aboard NIMBUS 5." Paper presented at the COSPAR Symposium on Approaches to Earth Survey Problems through the Use of Space Techniques, Konstant, F.R. of Germany, May 23-June 6, 1973.

11. Smith, W. L., H. M. Woolf, and W. J. Jacob. "A Regression Method for Obtaining Real-Time Temperature and Geopotential Height Profiles from Satellite Spectrometer Measurements and Its Application to NIMBUS 3 SIRS Observations," Monthly Weather Review, 8:582-603, 1970.

12. Smith, W. L., H. M. Woolf, and H. E. Fleming. "Retrieval of Atmospheric Temperature Profiles from Satellite Measurements for Dynamical Forecasting," Journal of Applied Meteorology, 1:113-122, 1972.

13. Shen, W. C., and W. L. Smith. "Statistical Estimation of Precipitable Water with SIRS-B Water Vapor Radiation Measurements," Monthly Weather Review, 1:24-32, 1973.

14. Endlich, R. M., R. L. Namcuso, H. Shigeishi, and R. E. Nagle. "Computation of Upper Tropospheric Reference Heights from Winds for Use with Vertical Temperature Profile Observations," Monthly Weather Review, 11:808-818, 1972.

15. Shenk, W. E., and R. J. Curran. "A Multi-Spectral Method for Estimating Cirrus Cloub Top Heights," Journal of Applied Meteorology, 7:1213-1216, 1973.

16. Fuelberg, H. E. "Reduction and Error Analysis of the AVE II Pilot Experiment Data," NASA Contractor Report, CR-120496, NASA, Marshall Space Flight Center, 1974.

17. Billions, N. S. "Equations for Computer Processing U.S. Weather Bureau Radiosonde Temperature and Relative Humidity Data," U.S. Army Missile Command Report RR-TN-66-3, Redstone Arsenal, Alabama, 1965.

18. ANON. "IRIG Standards for Range Meteorological Data Reduction, Part 1: Rawinsonde," IRIG Document 108-72, White Sands Missile Range, 1972.

19. Hess, S. L. Introduction to Theoretical Meteorology. New York: Holt, Rinehart and Winston, 1959.

20. Danielson, E. F., and R. T. Duquet. "A Comparison of FP5-16 and GMD-1 Measurements and Methods for Processing Wind Data," NASA Contractor Report CR-61158, NASA, Marshall Space Flight Center, 1966.

21. Case, B. A. "Root-Mean-Square Error Analysis for Equations in Rawinsonde Evaluation Program," Report MTP-AERO-62-82, NASA, Marshall Space Flight Center, 1962.

22. Weidner, D. K., and J. Chambers. "Rawinsonde Comparison Project," NASA Contractor Report CR-61168, NASA, Marshall Space Flight Center, 1967.

23. Hodge, W. M., and C. Christos. "Compatibility of United States Radiosondes," Monthly Weather Review, 93:253-266, 1965.

24. Brousaides, F. J. "An Assessment of the Carbon Humidity Element in Radiosonde Systems," AFCRL-TR-73-0423, Air Force Cambridge Research Laboratories, Hanscom Field, Massachusetts, 1973.

25. Scoggins, J. R., and O. E. Smith. "Data for the First NASA Atmospheric Variability Experiment (AVE I), Part 1: Data Tabulation," NASA TM X-2938, NASA, Marshall Space Flight Center, 1973.

26. Scoggins, J. R. "An Evaluation of Detail Wind Data as Measured by the FPS-16 Radar/Spherical Balloon Technique," NASA TN D-1572, NASA, Marshall Space Flight Center, 1963.

27. Weiss, B. D., and E. J. Georgian. "AN/GMD-2A Rawin Set--AN/FPS-16 Radar Comparison," AFCRL-69-0522, Air Force Cambridge Research Laboratories, Hanscom Field, Massachusetts, 1969.

28. Scoggins, J. R., and R. E. Turner. "25-MB Sounding Data and Synoptic Charts for NASA AVE II Pilot Experiment Data," NASA TN D-7832, NASA, Marshall Space Flight Center, 1974.

29. ANON. "AMR Meteorological Handbook," AFMTC Pamphlet 105-1, Headquarters, Air Force Missile Test Center, Patrick Air Force Base, Florida, 1963.

30. Kessler, Edwin. "Tornadoes," Bulletin American Meteorology Society, 10:926-936, 1970.

31. Weinstein, A. L., E. R. Reiter, and J. R. Scoggins. "Mesoscale Structure of 11-20 Km Winds," Journal of Applied Meteorology, 5:49-57, 1966.

32. Danielsen, E. F. "The Laminar Structure of the Atmosphere and Its Relation to the Concept of a Tropopause," Journal of Meteorology Geophysics, 3:292-332, 1959.

APPENDIX

MICROFICHE ATTACHMENT

1. Report No.	2. Government Accession No.	3. Recipient's Catalog No.
NASA TP-1072		

4. Title and Subtitle	5. Report Date
The Mechanics of Atmospheric Systems Derived through Vertical and Horizontal Analysis of Parametric Data	November 1977
	6. Performing Organization Code
7. Author(s)	8. Performing Organization Report No.
Robert E. Turner	M-237
	10. Work Unit No.
9. Performing Organization Name and Address	
George C. Marshall Space Flight Center Marshall Space Flight Center, Alabama 35812	11. Contract or Grant No.
	13. Type of Report and Period Covered
12. Sponsoring Agency Name and Address	Technical Paper
National Aeronautics and Space Administration Washington, D. C. 20546	14. Sponsoring Agency Code

15. Supplementary Notes

Prepared by Space Sciences Laboratory, Science and Engineering

16. Abstract

For 36 hours during April 1975, an Atmospheric Variability Experiment was conducted. This research effort supported an observational program in which rawinsonde data, radar data, and satellite data were collected from a network of 42 stations east of the Rocky Mountains at intervals of 3 hours. This program presents data with a high degree of time resolution over a spatially and temporally extensive network.

Reduction of the experiment data is intended primarily as a documentation of the checking and processing of the data and should be useful to prospective users. Various flow diagrams of the data processing procedures are described, and a complete summary of the formulas used in the data processing is provided. A wind computation scheme designed to extract as much detailed wind information as possible from the unique experiment data set is discussed in detail. Estimates of the accuracy of the thermodynamic and wind data are presented. Estimates of errors in the thermodynamic and wind data are given together with a discussion of how these errors affect the final processed data.

Analysis of pressure, height, and temperature on constant pressure charts at 3-hour intervals shows that large-scale features with amplitudes only half the values of commonly cited observational uncertainties exhibit space and time continuity. Examination of 3-hour tendencies of important meterological variables indicates that they typically exceed measurement uncertainties, may often be inadequately represented by interpolation of 12-hour observations, and exhibit appreciable spatial variation. Time cross sections in the lower troposphere constructed from the 3-hour observations reveal features with scales of motion not seen by the meteorologist in routine operations (except for regional 3-hour surface maps); horizontal and temporal scales of motion encompass a major portion of the mesoscale, and vertical scales encompass variations as small as 0.3 km. The detailed wind profile data of the experiment resolve the mesoscale wind structure of the lower stratosphere consistent with the findings of other investigators.

An initial method of analysis of satellite image data is presented. It is based on the application of densitometry techniques whereby the field of density of the satellite image is correlated with the associated meteorological events. This work represents an initial attempt to analyze Synchronous Meteorological Satellite (SMS) images with the densitometry methods in the context of mesoscale phenomena.

17. Key Words (Suggested by Author(s))	18. Distribution Statement
	Cat. 47

19. Security Classif. (of this report)	20. Security Classif. (of this page)	21. No. of Pages	22. Price*
Unclassified	Unclassified	350	$10.00

*For sale by the National Technical Information Service, Springfield, Virginia 22161

APPENDIX

FIGURES

Figures A.1 through A.153 are additional data used in the analyses of mesoscale weather phenomena in this investigation.

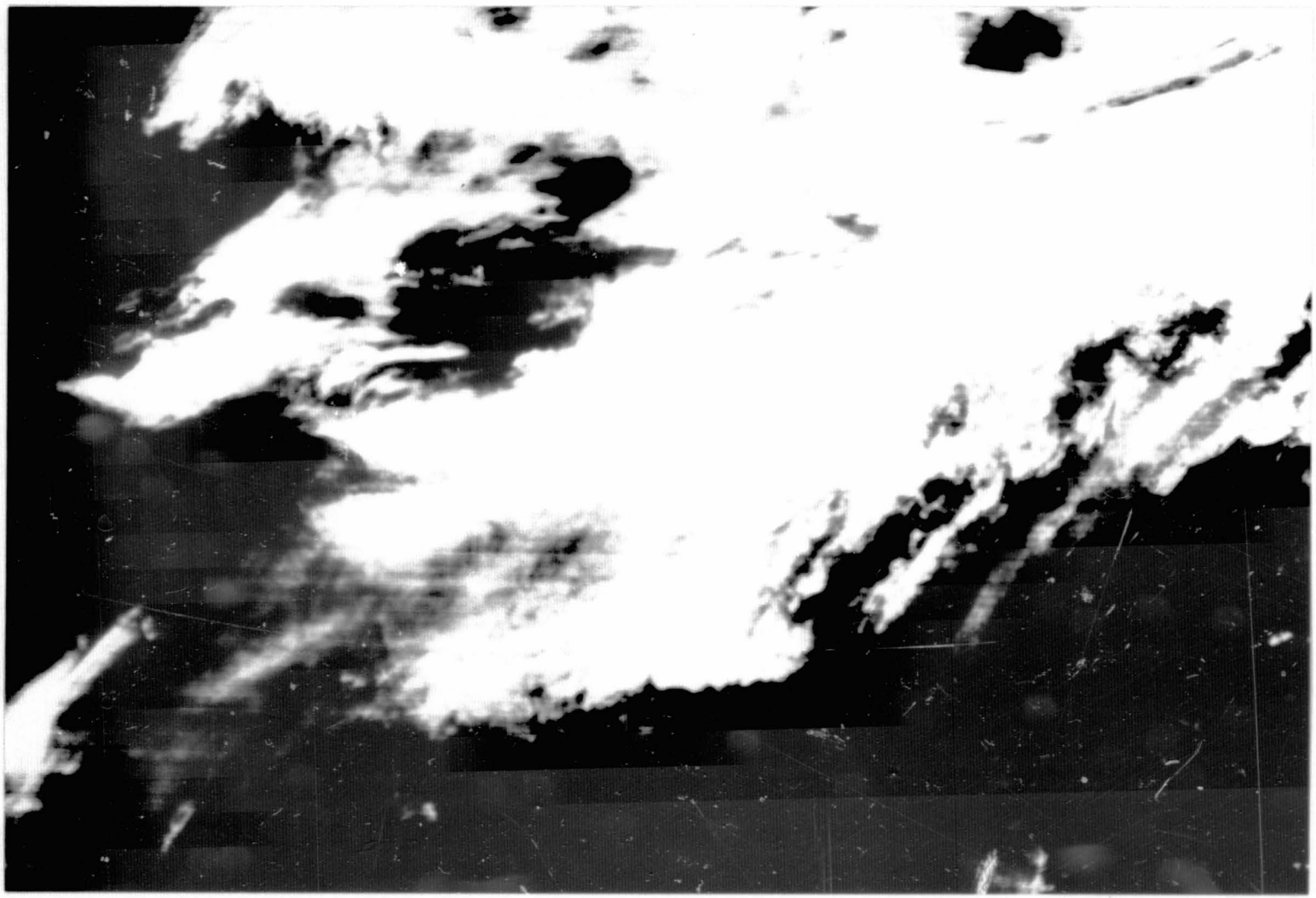

(Black and white)

Figure A.1. SMS-1 visible channels, 1530 GMT, April 24, 1975.

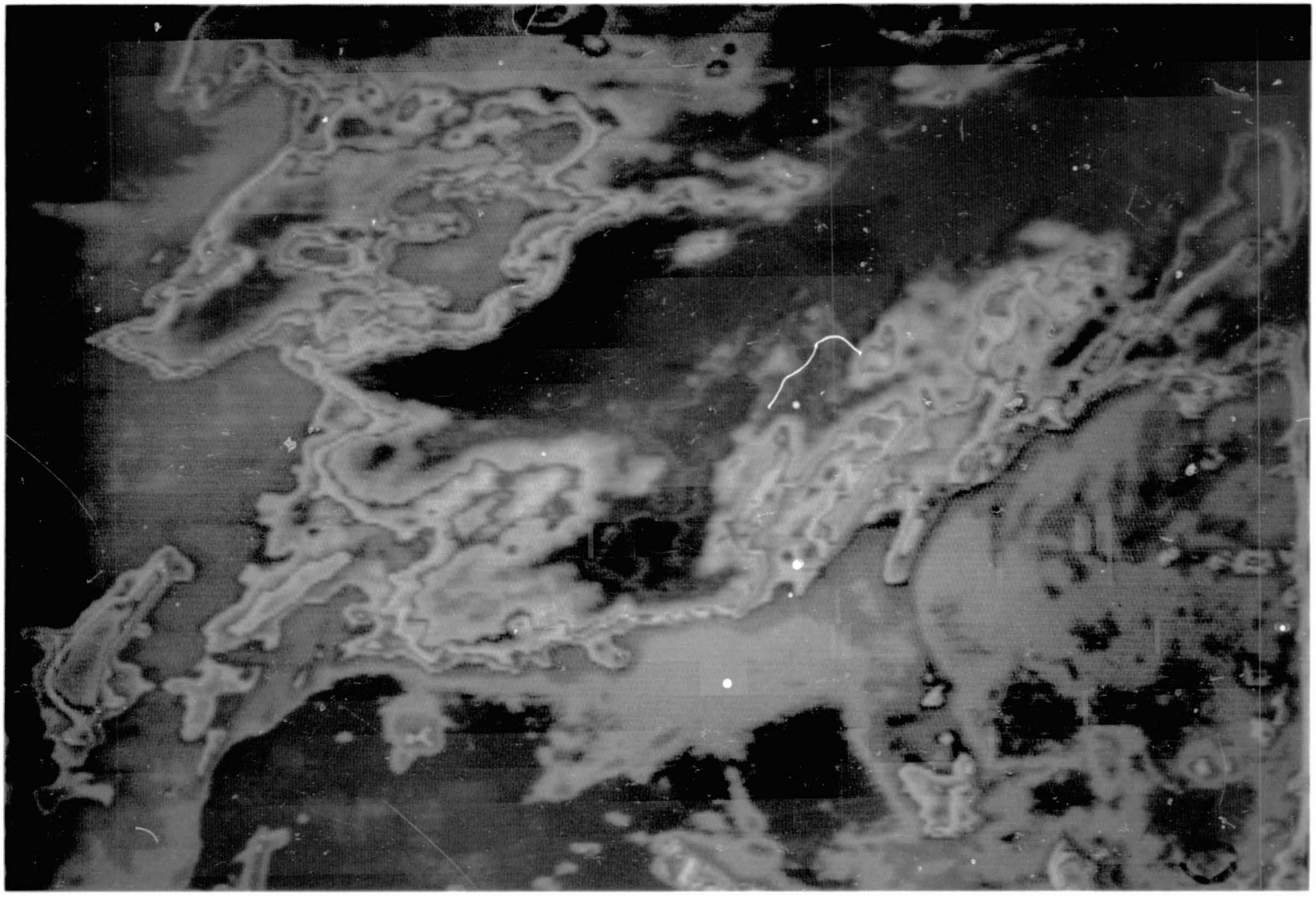

(26 color slice)

Figure A.1. (continued)

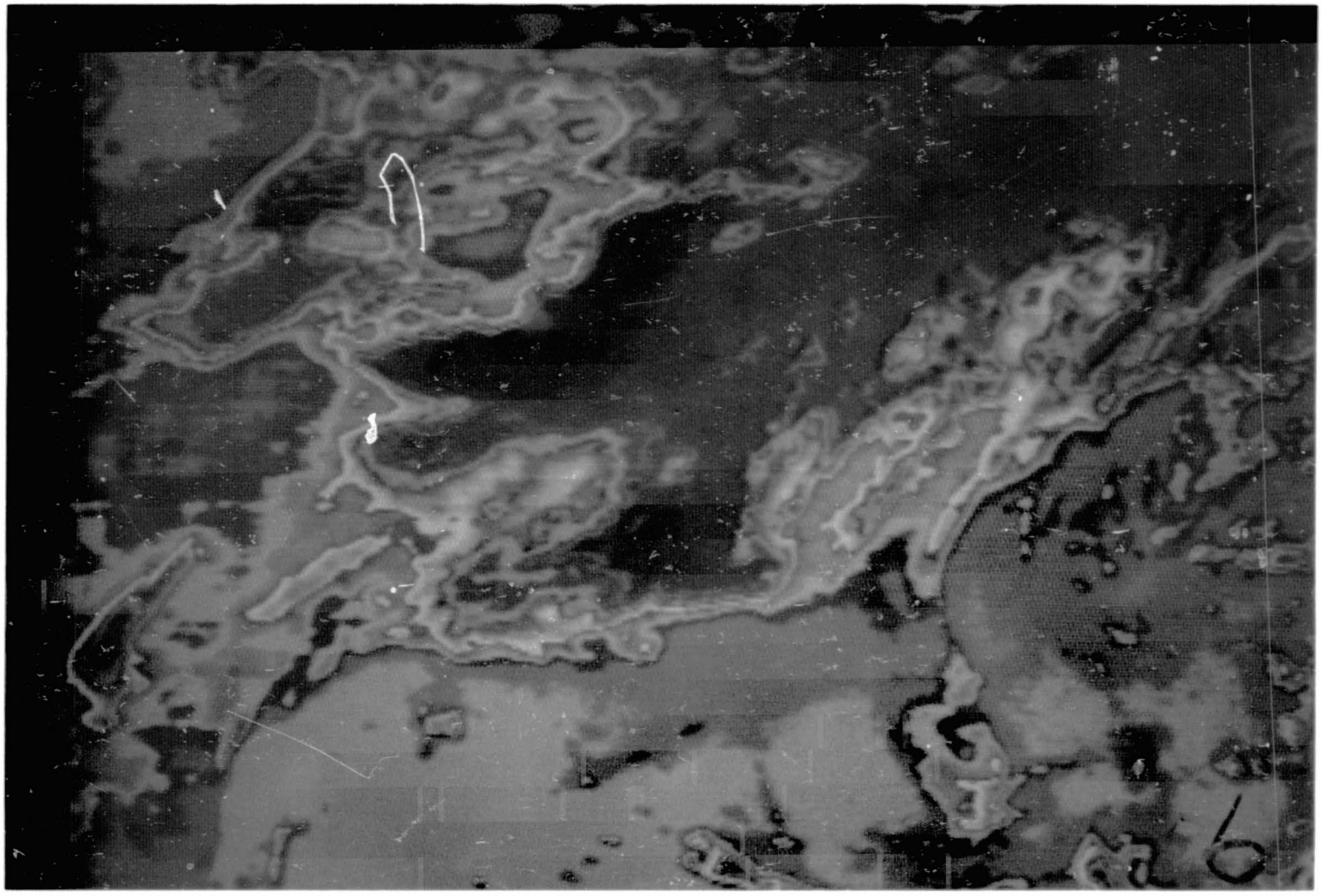

(32 color slice)

Figure A.1. (continued)

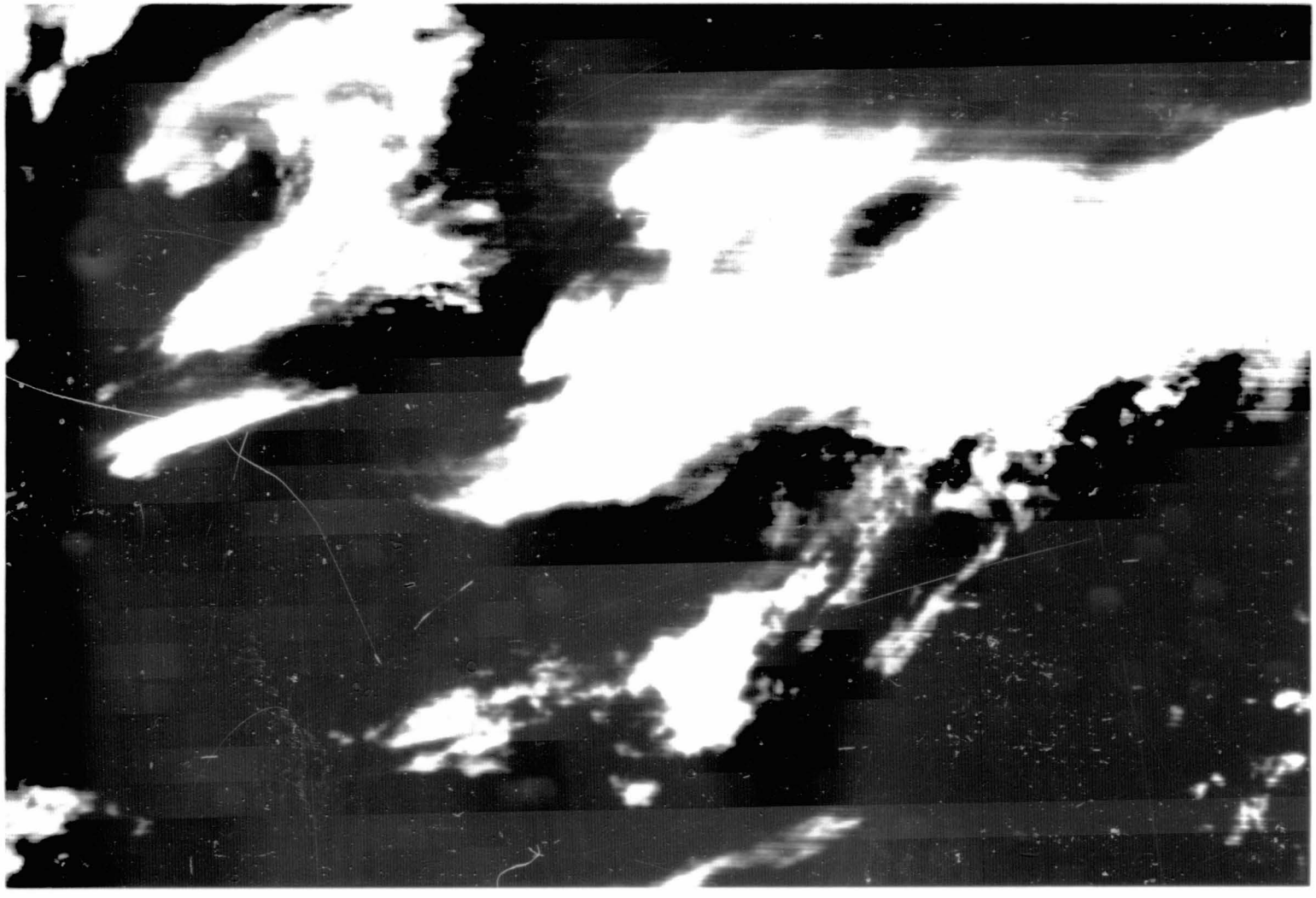

(Black and white)

Figure A.2. SMS-1 infrared channels, 1530 GMT, April 24, 1975.

(26 color slice)

Figure A.2. (continued)

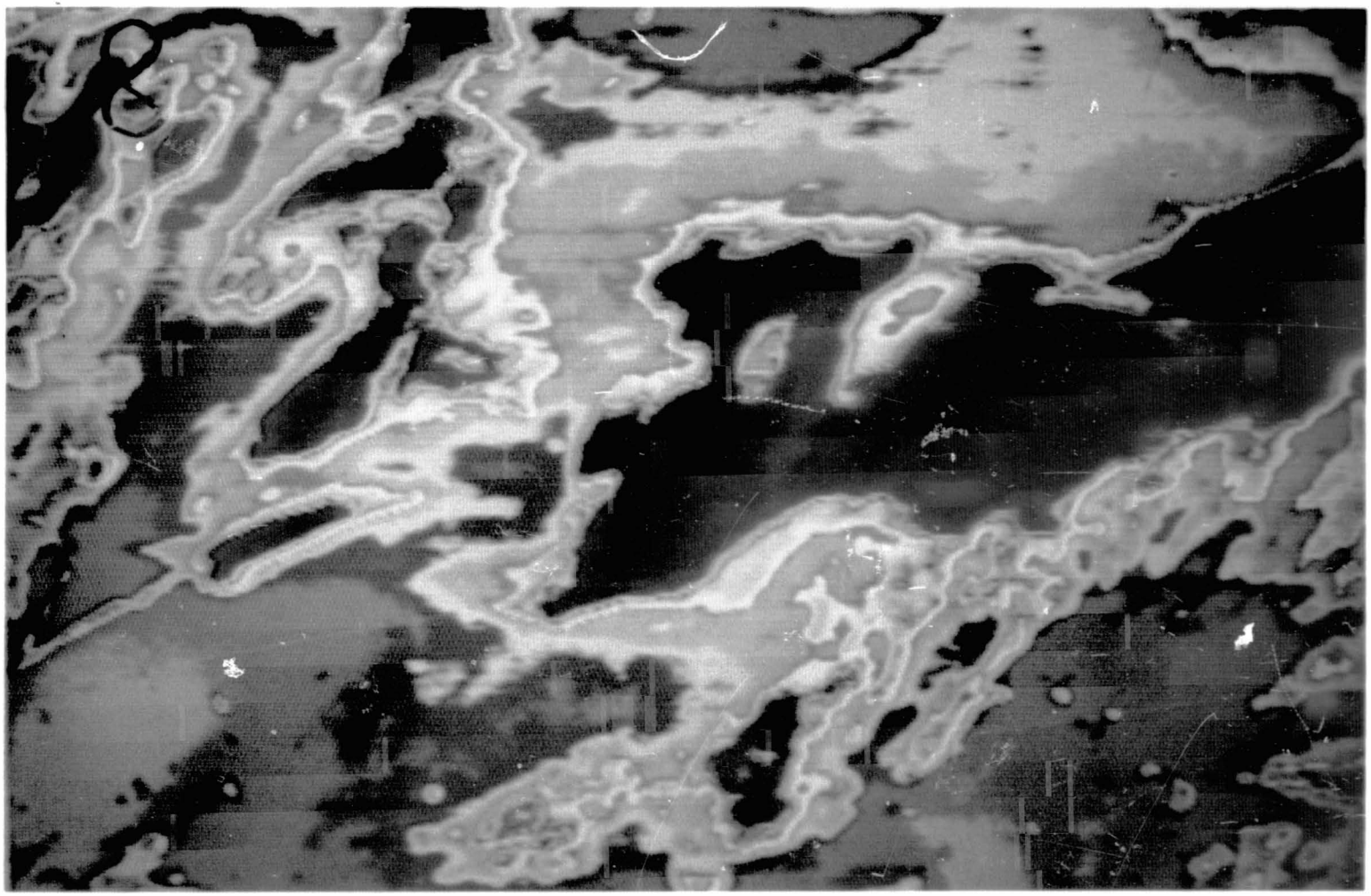

(32 color slice)

Figure A.2. (continued)

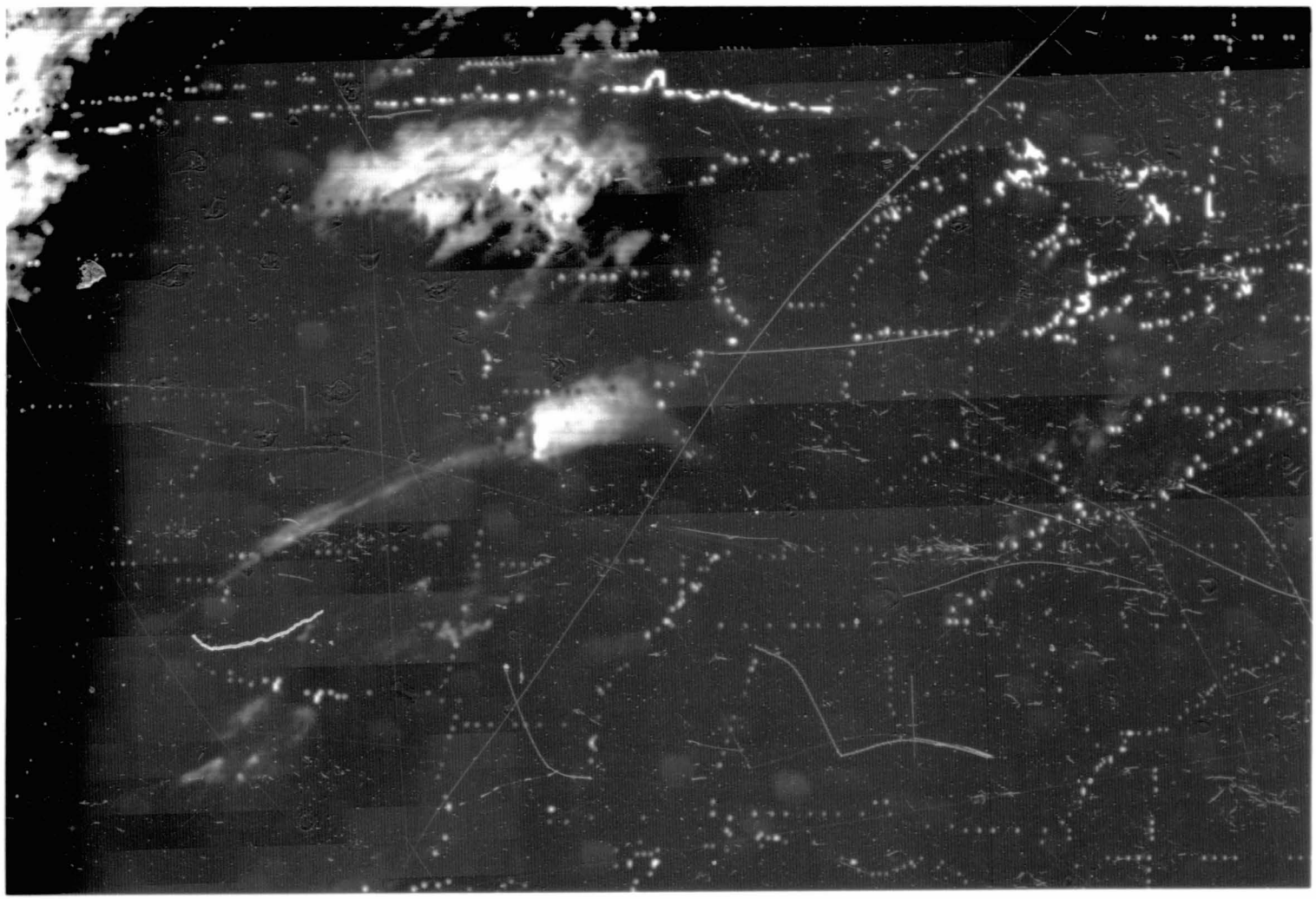

(Black and white)

Figure A.3. SMS-1 visible channels, 2230 GMT, April 24, 1975.

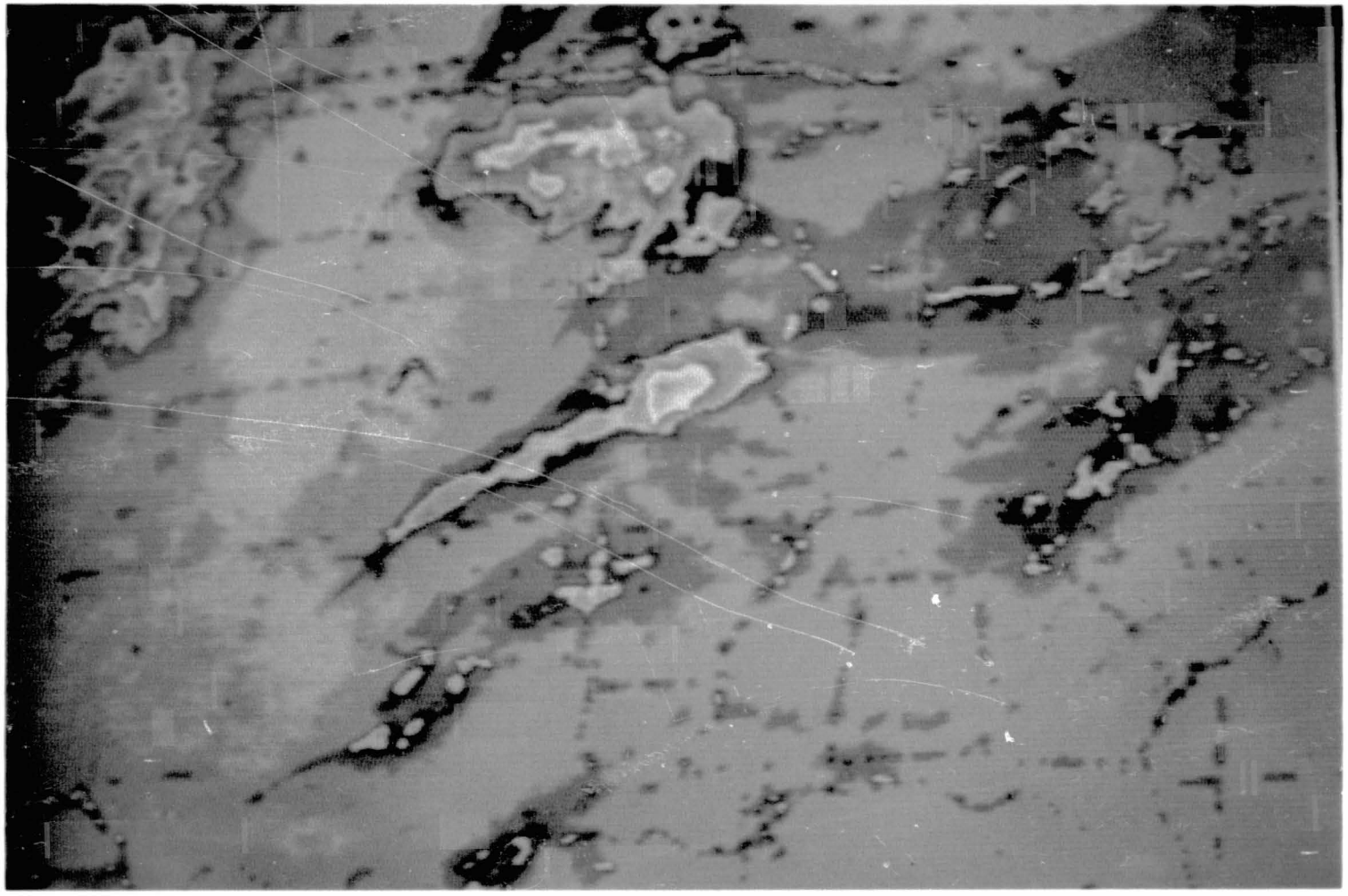

(26 color slice)

Figure A.3. (continued)

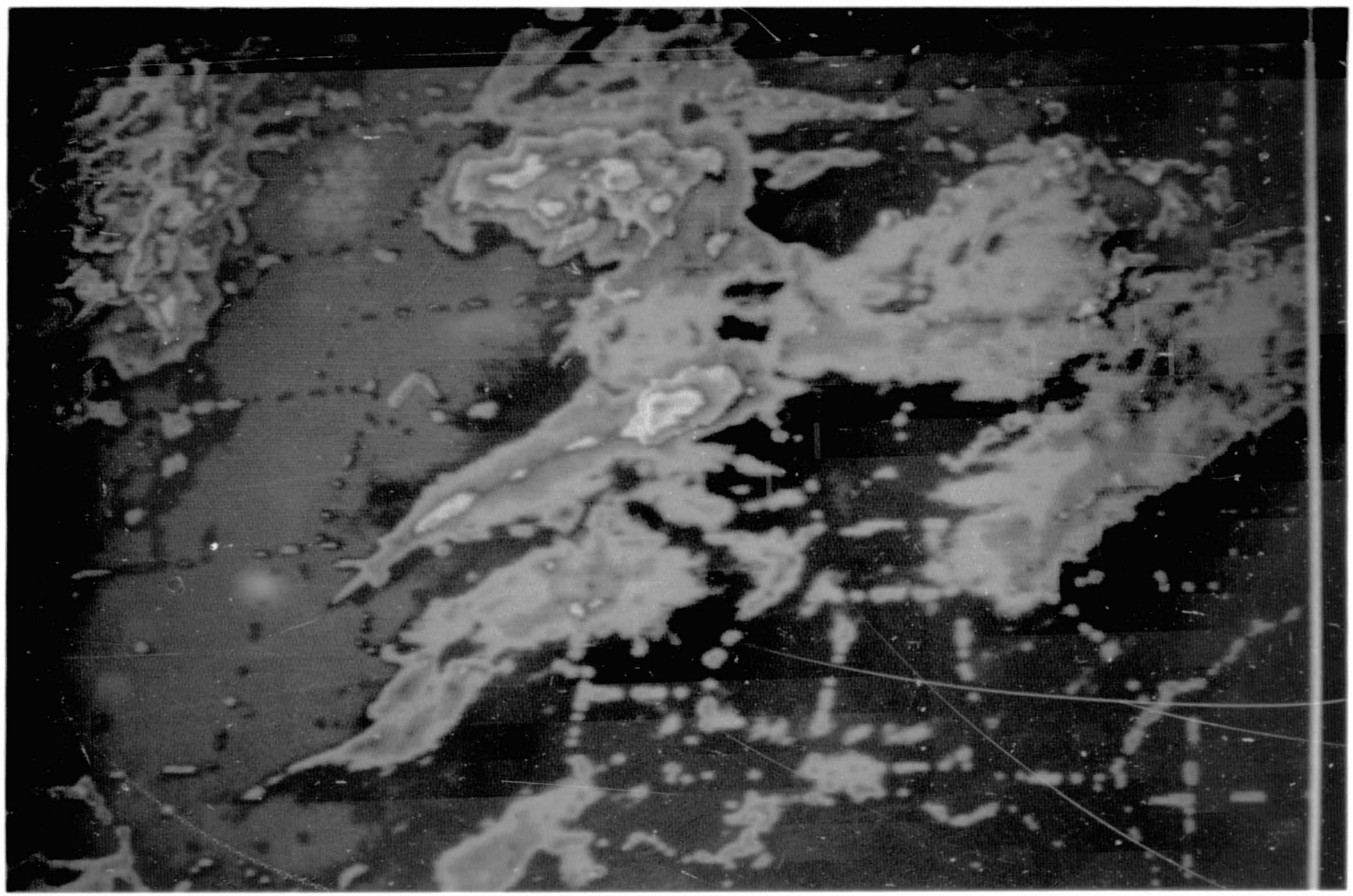

(32 color slice)

Figure A.3. (continued)

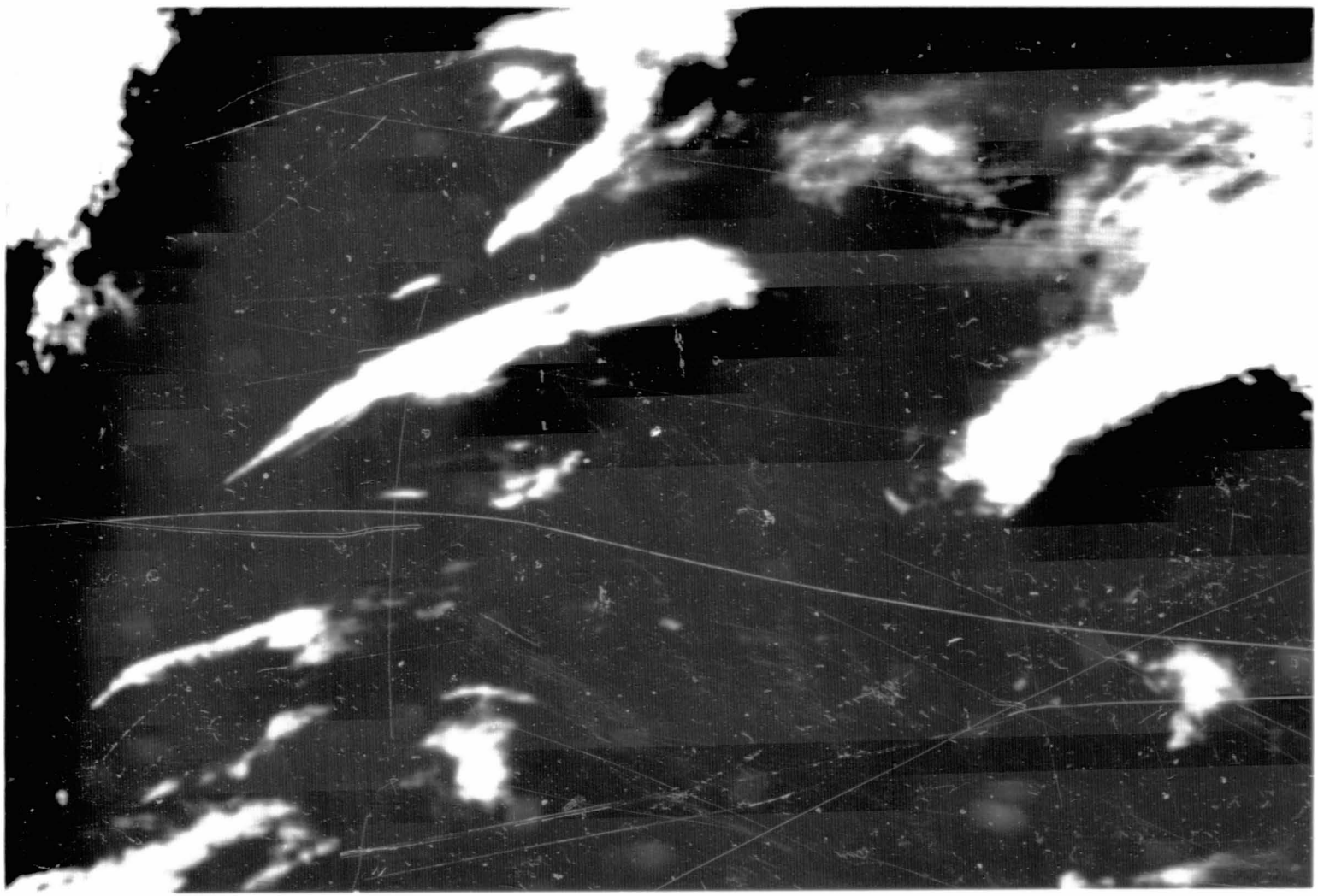

(Black and white)

Figure A.4. SMS-1 infrared channels, 2230 GMT, April 24, 1975.

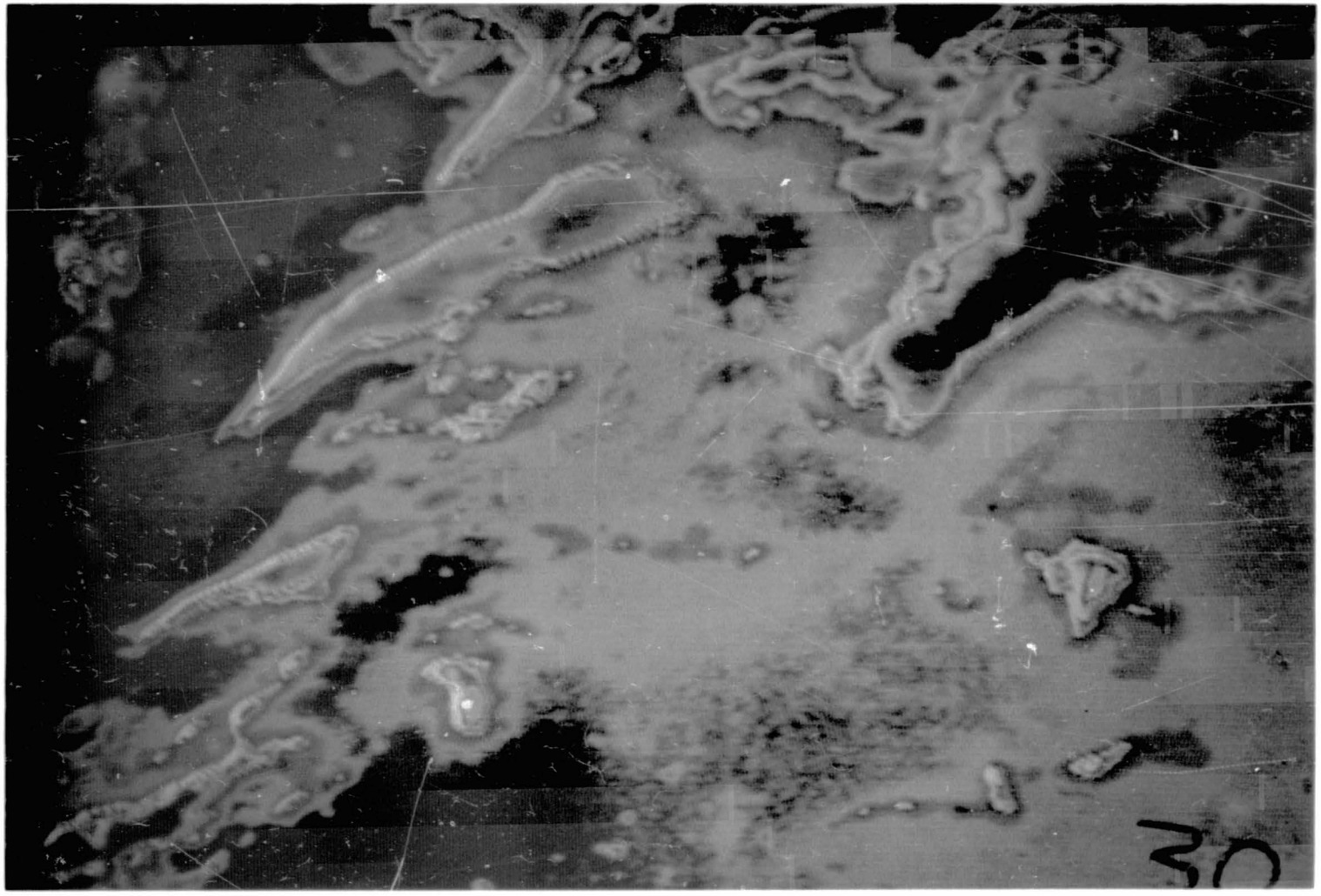

(26 color slice)

Figure A.4. (continued)

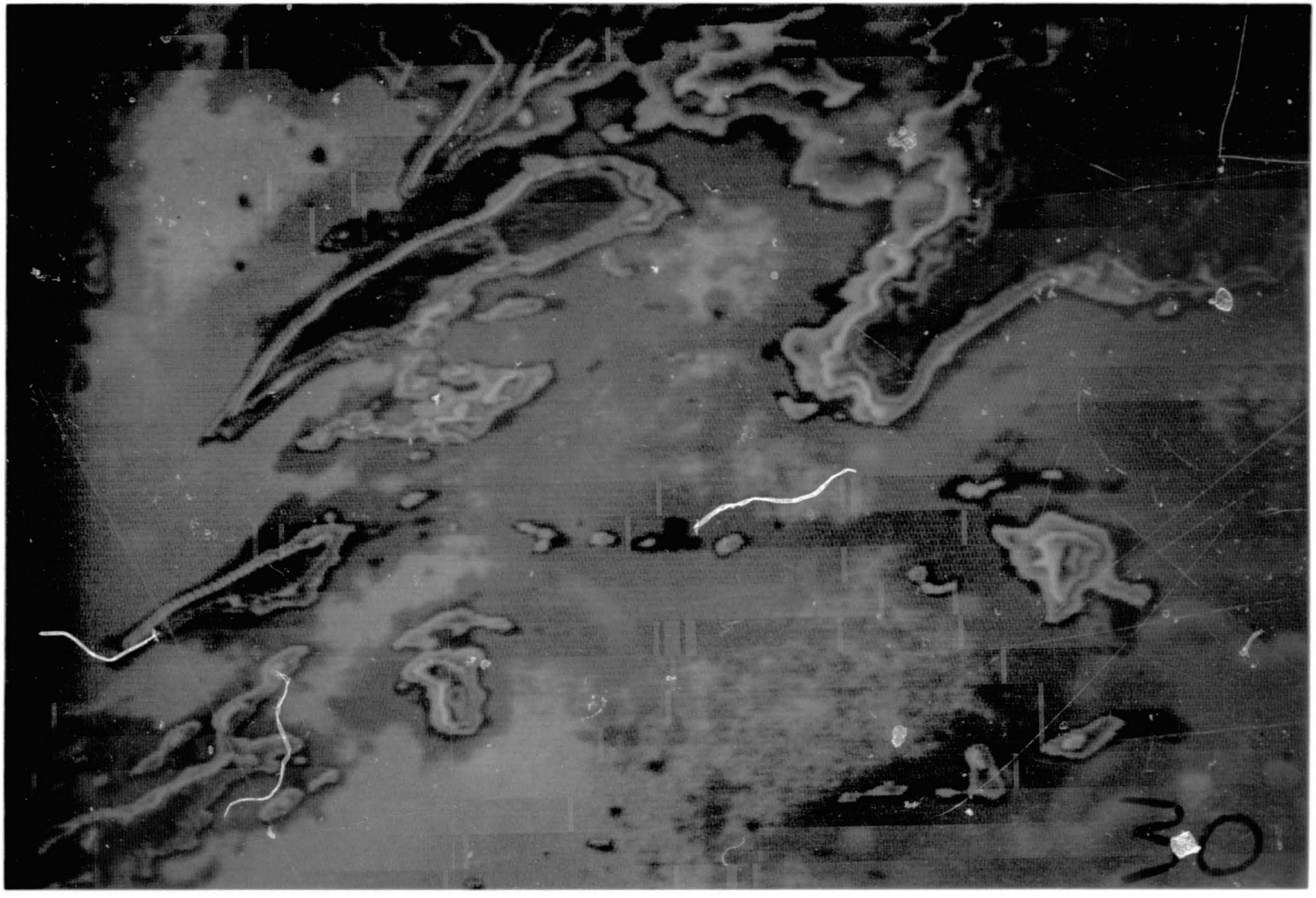

(32 color slice)

Figure A.4. (continued)

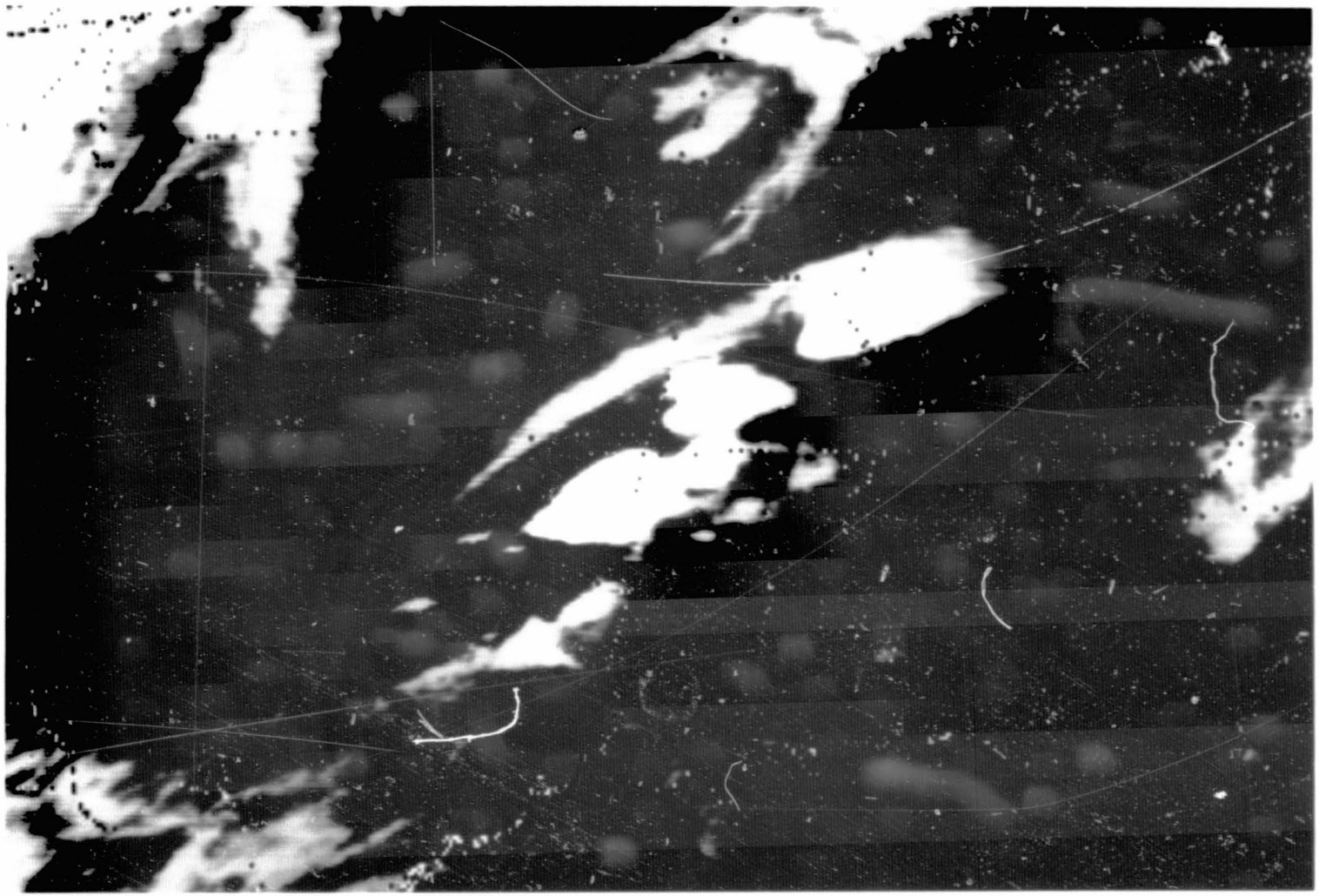

(Black and white)

Figure A.5. SMS-1 infrared channels, 0000 GMT, April 25, 1975.

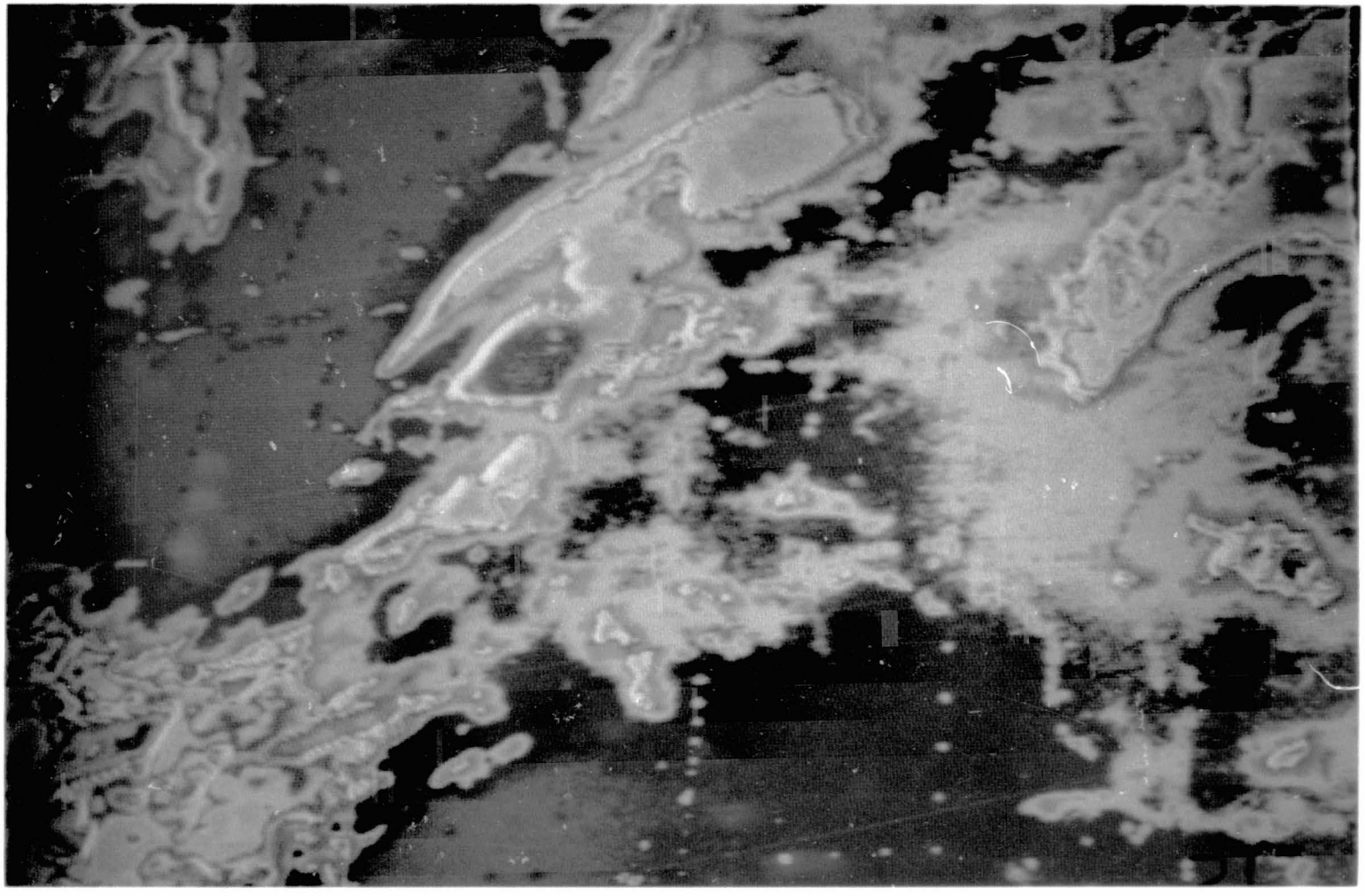

(26 color slice)

Figure A.5. (continued)

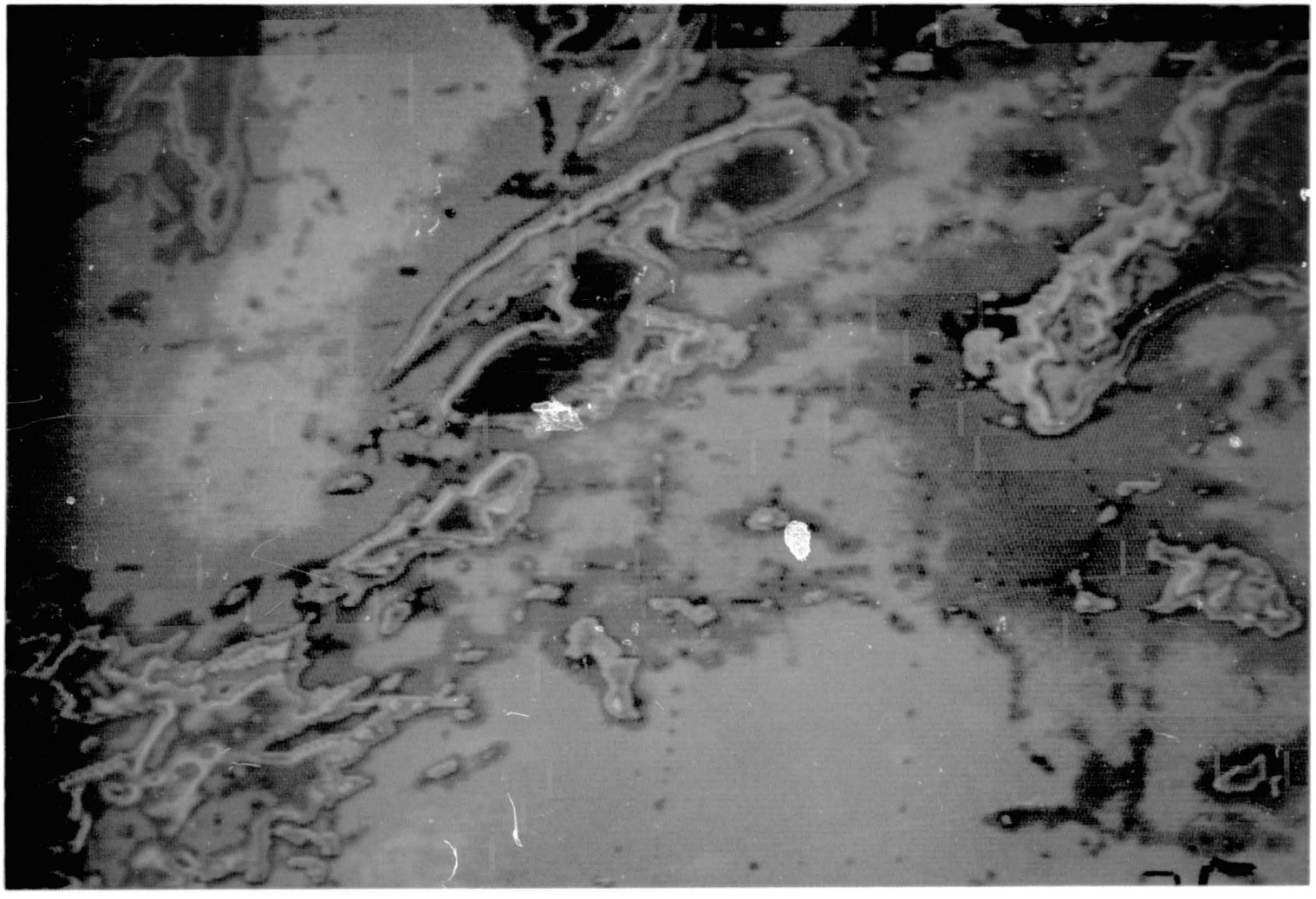

(32 color slice)

Figure A.5. (continued)

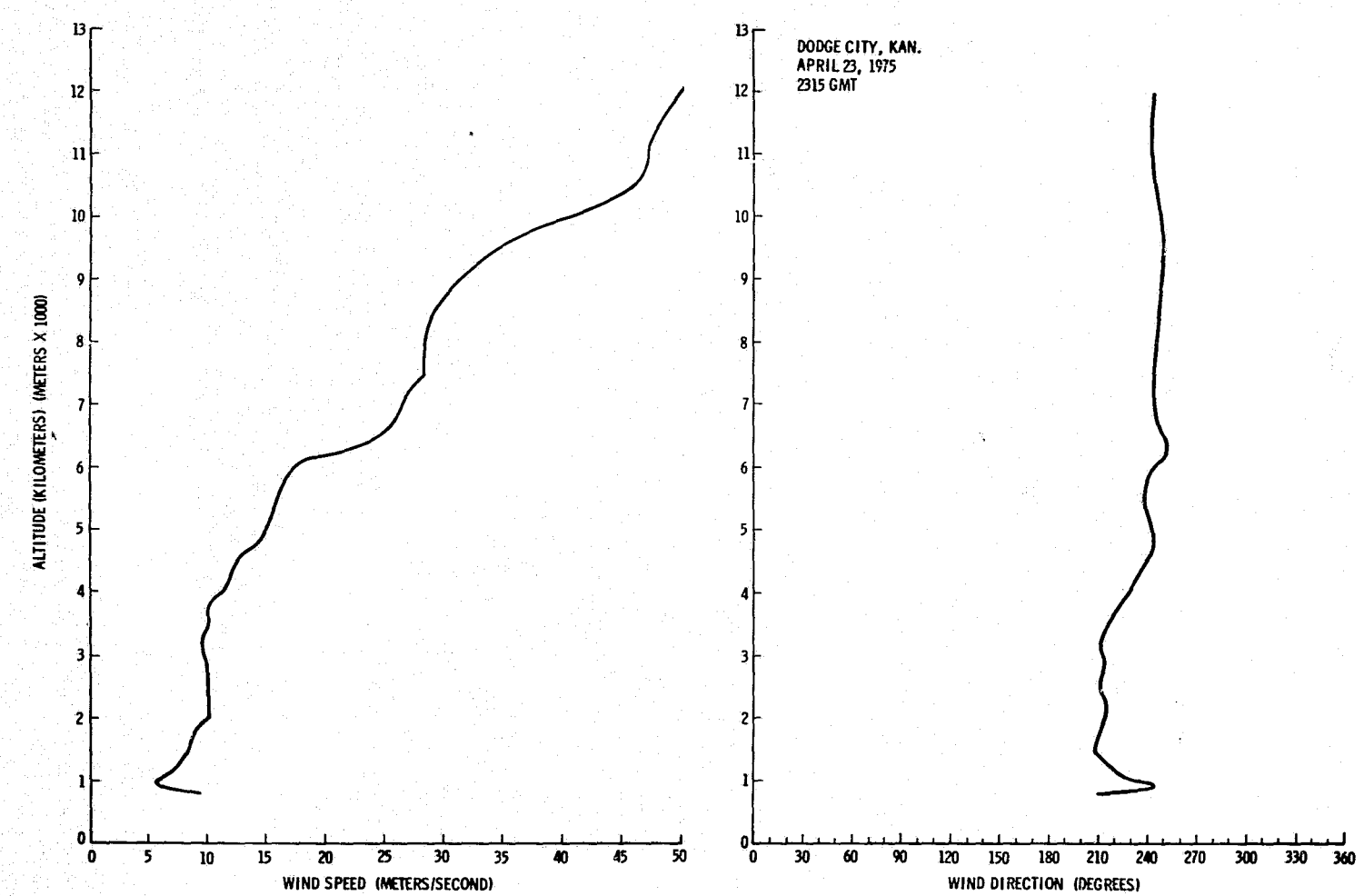

Figure A.6. Vertical wind profile for 2315 GMT, April 23, 1975, over Dodge City, Kansas.

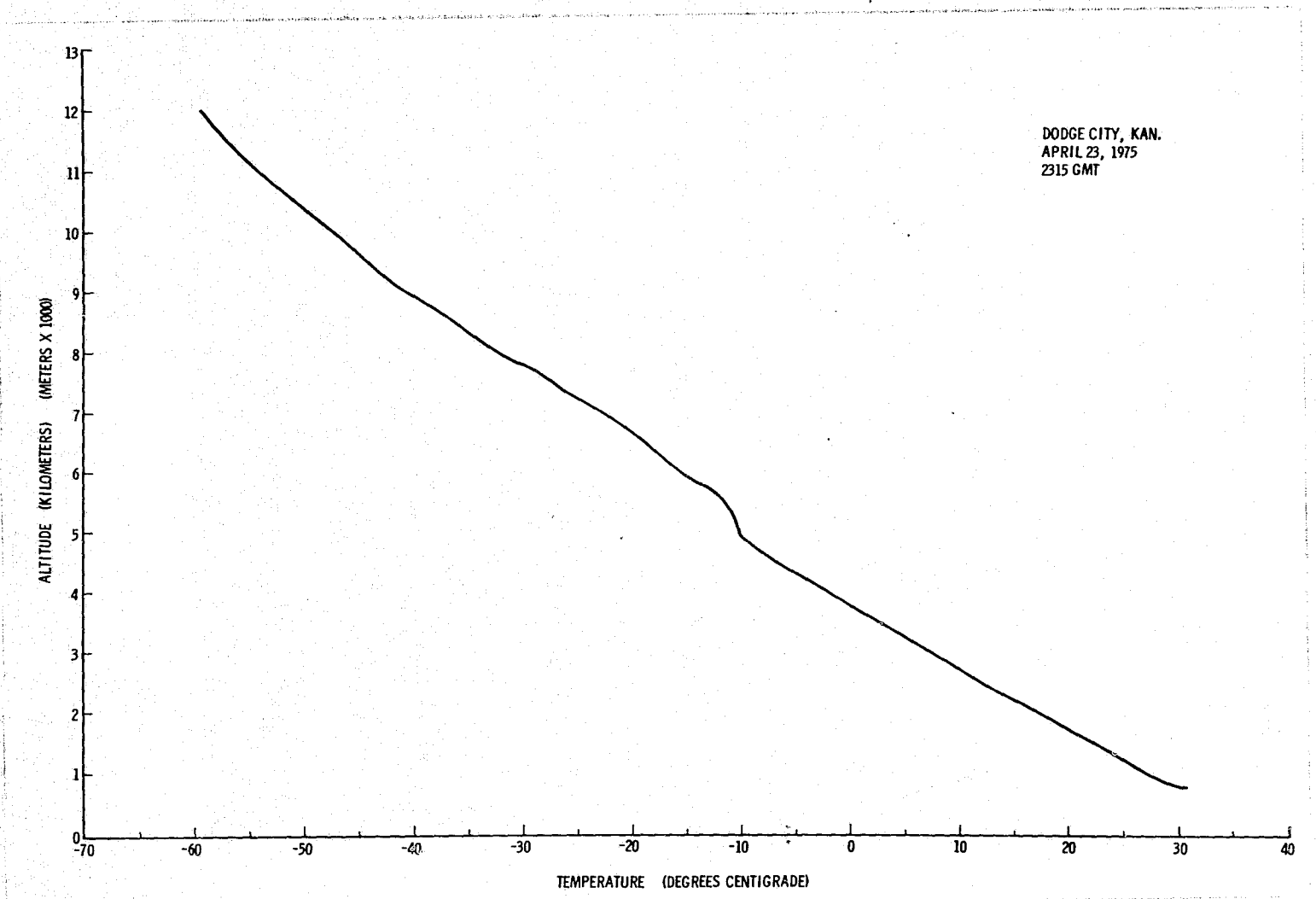

Figure A.7. Temperature profile for 2315 GMT, April 23, 1975, over Dodge City, Kansas.

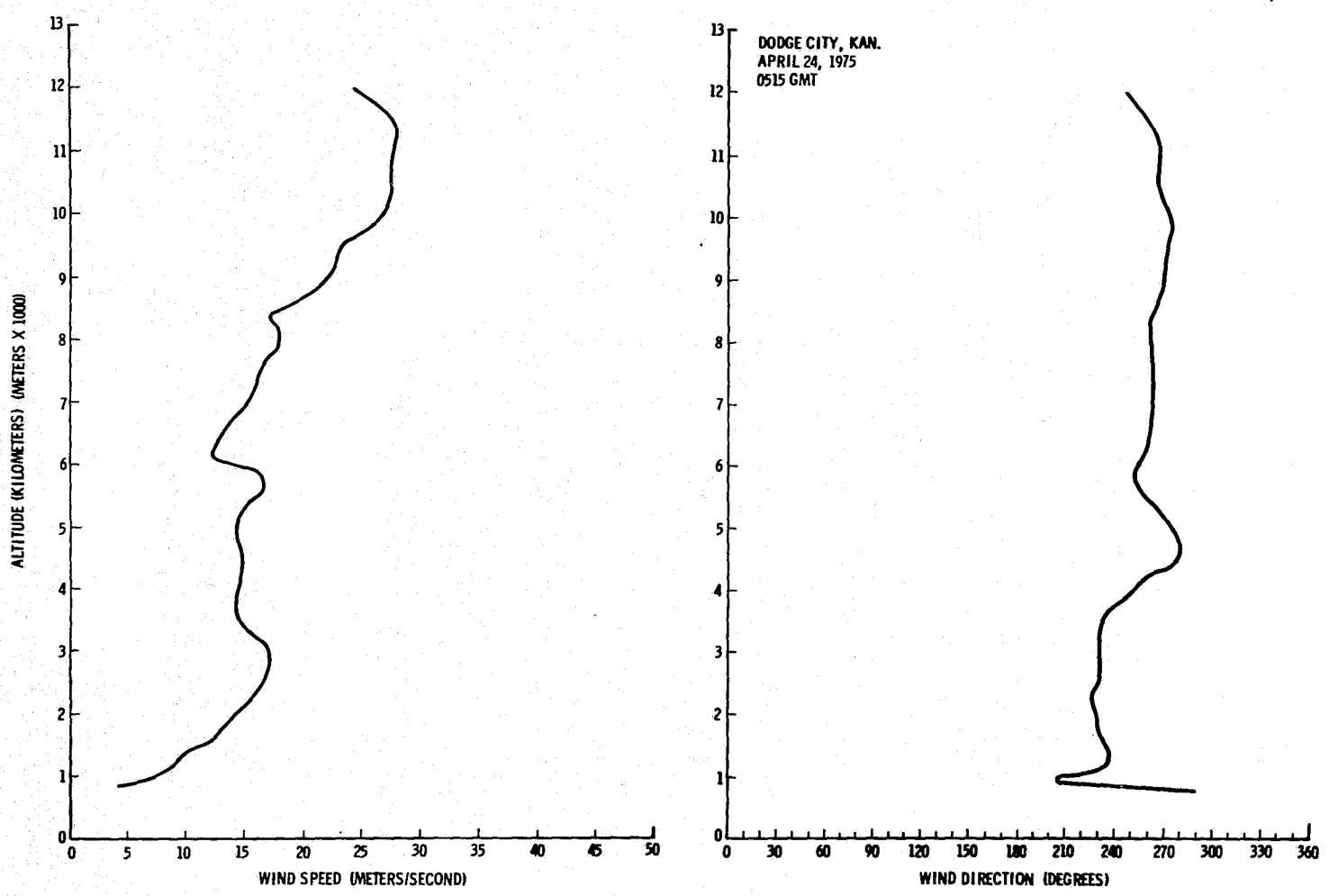

Figure A.8. Vertical wind profile for 0515 GMT, April 24, 1975, over Dodge City, Kansas.

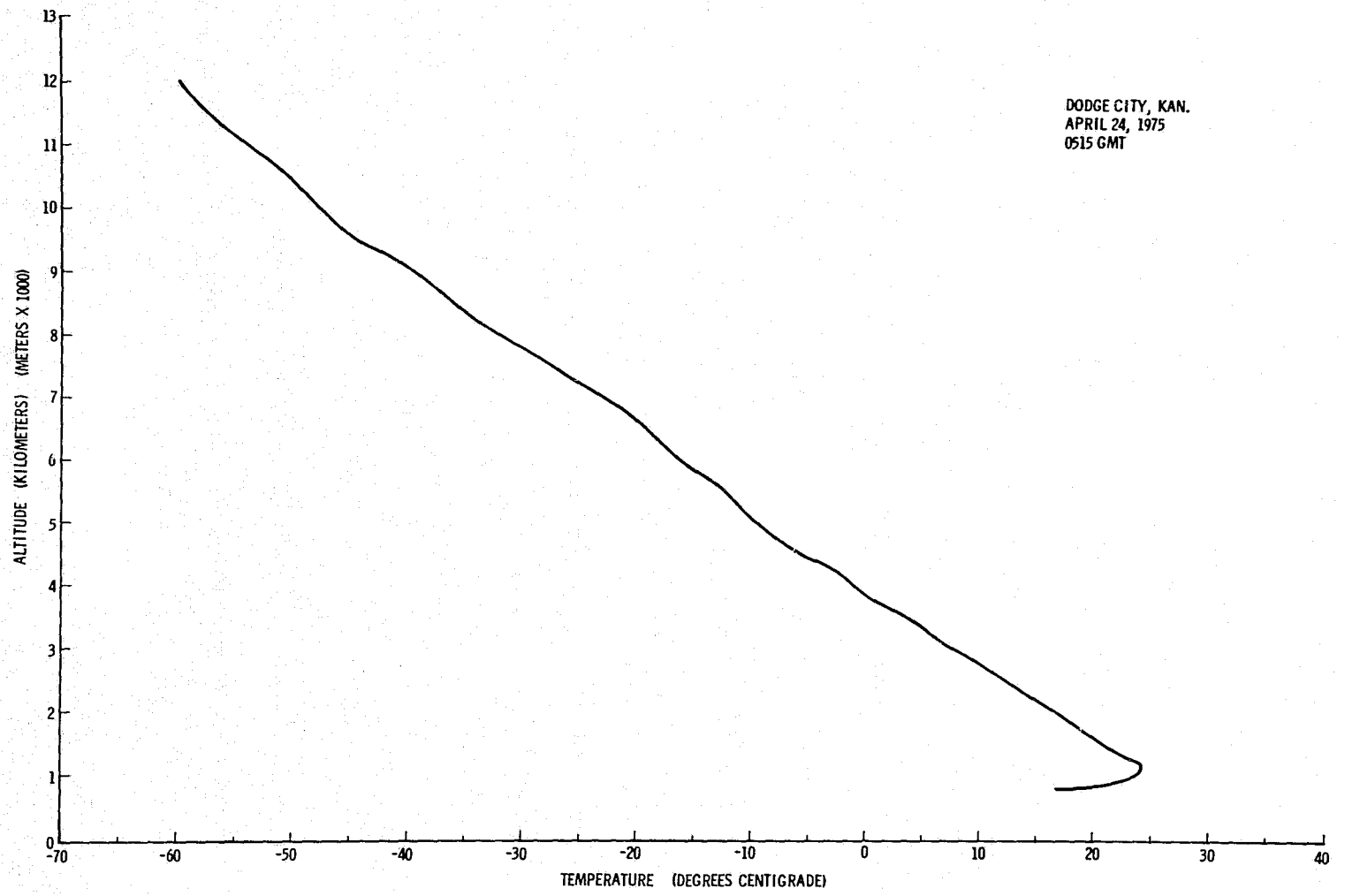

Figure A.9. Temperature profile for 0515 GMT, April 24, 1975, over Dodge City, Kansas.

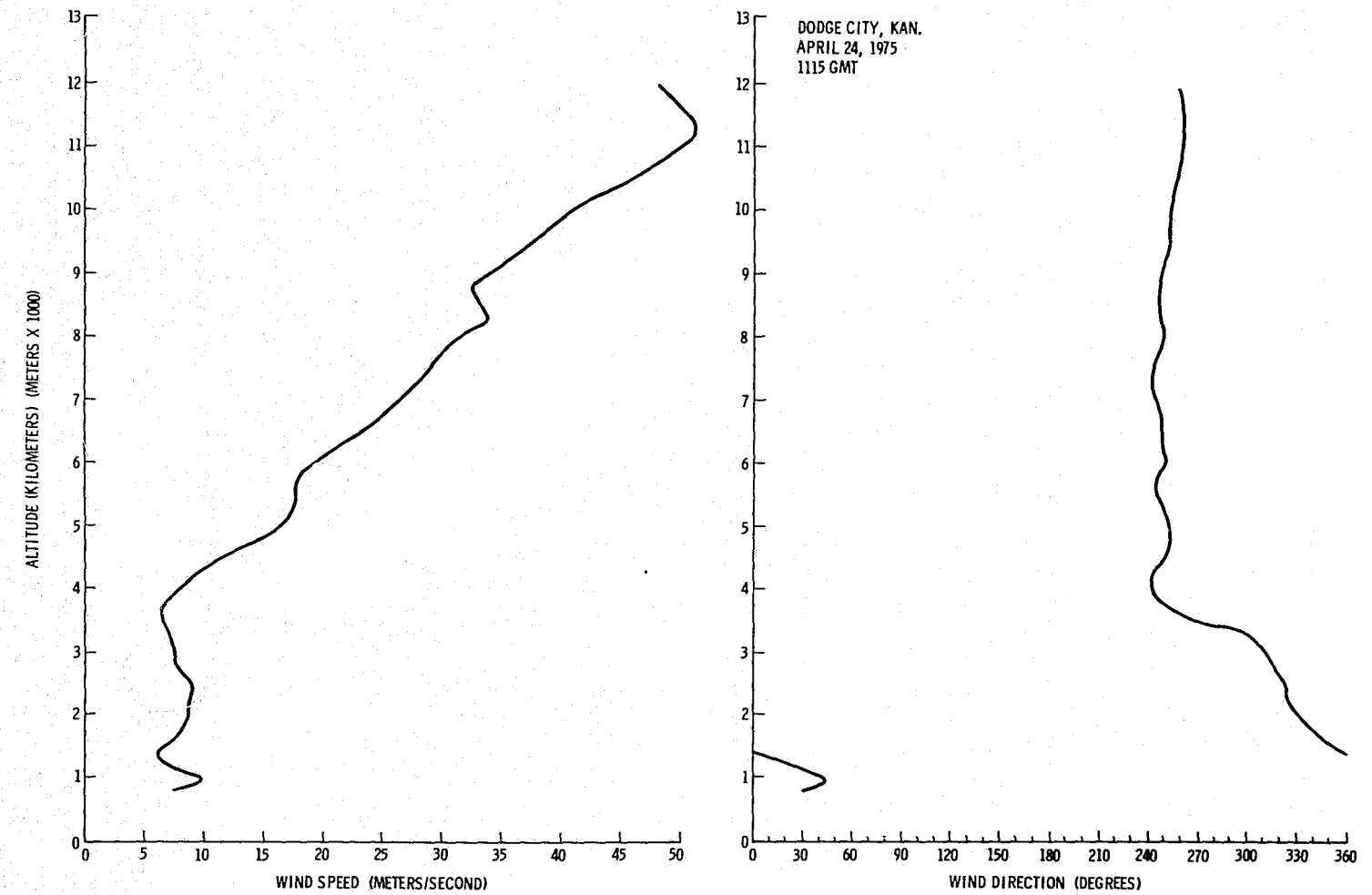

Figure A.10. Vertical wind profile for 1115 GMT, April 24, 1975, over Dodge City, Kansas.

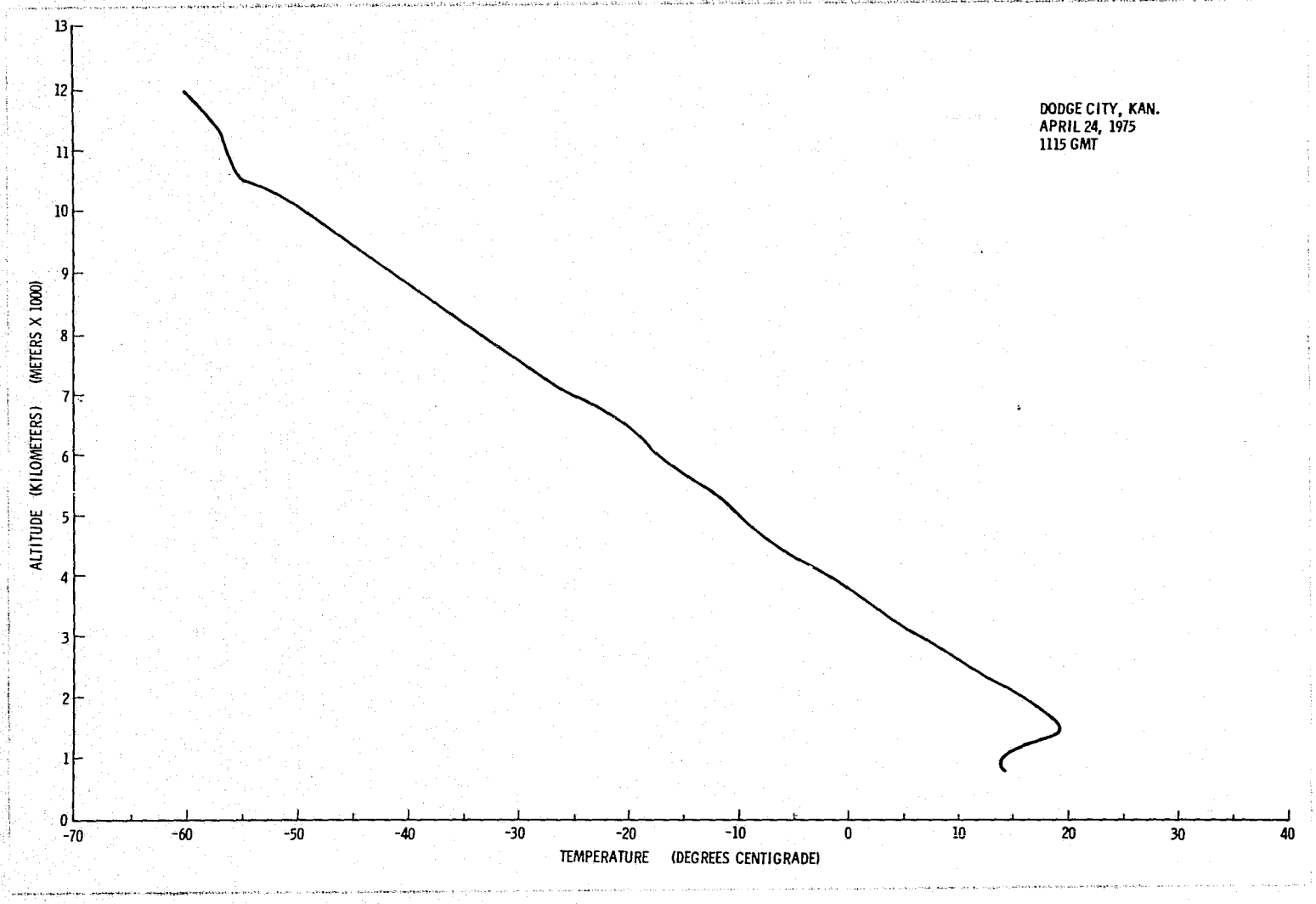

Figure A.11. Temperature profile for 1115 GMT, April 24, 1975, over Dodge City, Kansas.

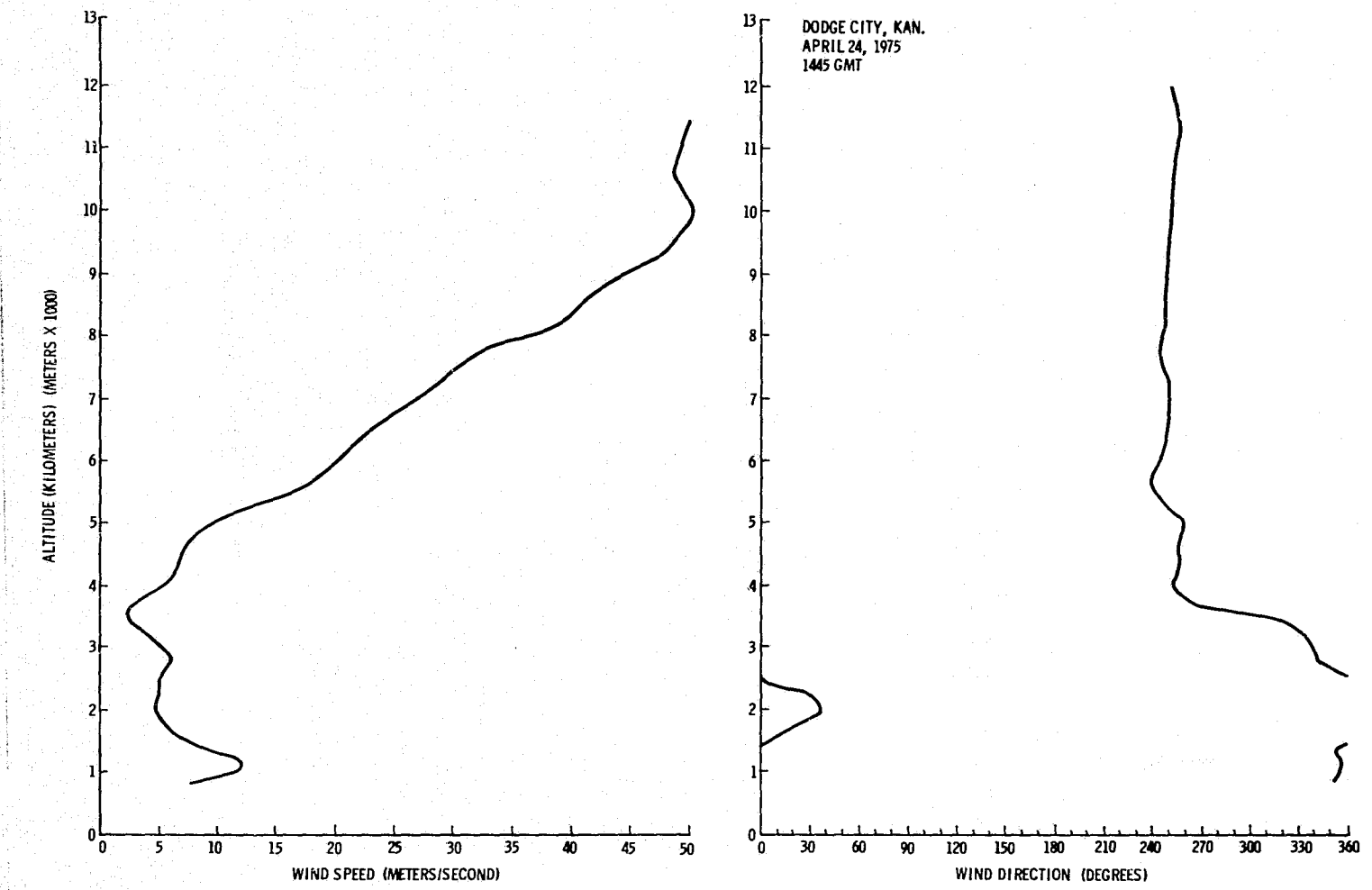

Figure A.12. Vertical wind profile for 1445 GMT, April 24, 1975, over Dodge City, Kansas.

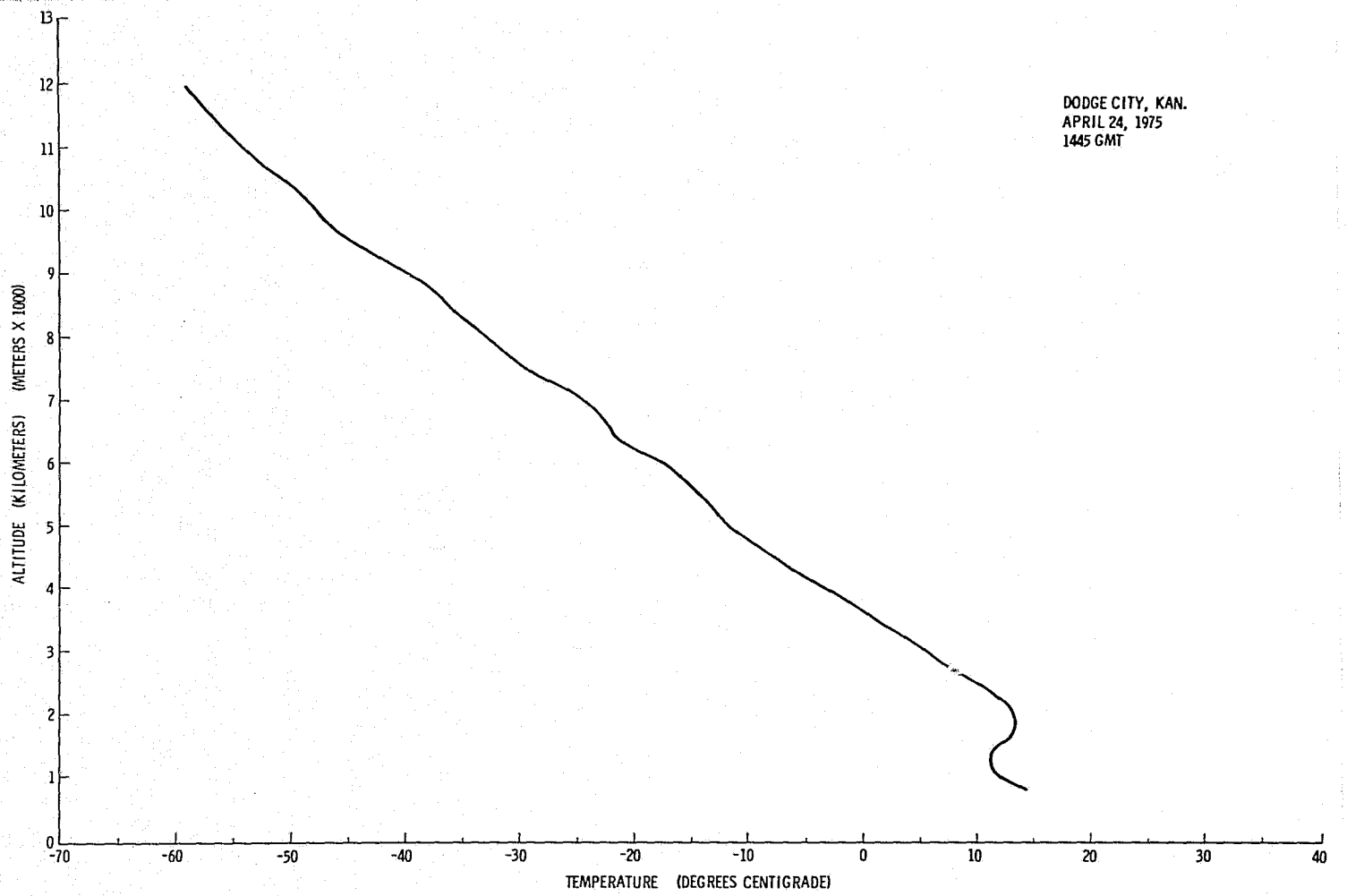

Figure A.13. Temperature profile for 1445 GMT, April 24, 1975, over Dodge City, Kansas.

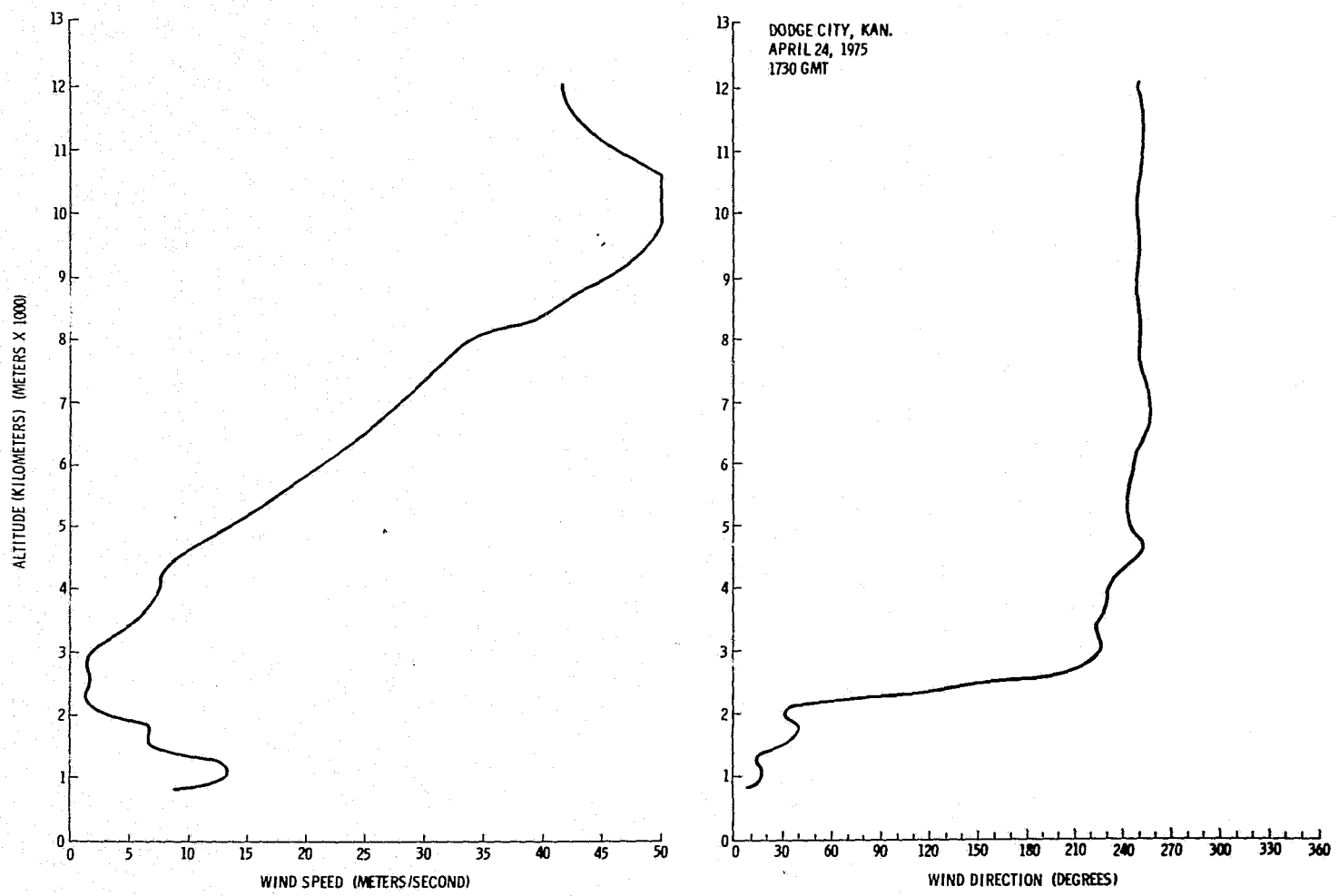

Figure A.14. Vertical wind profile for 1730 GMT, April 24, 1975, over Dodge City, Kansas.

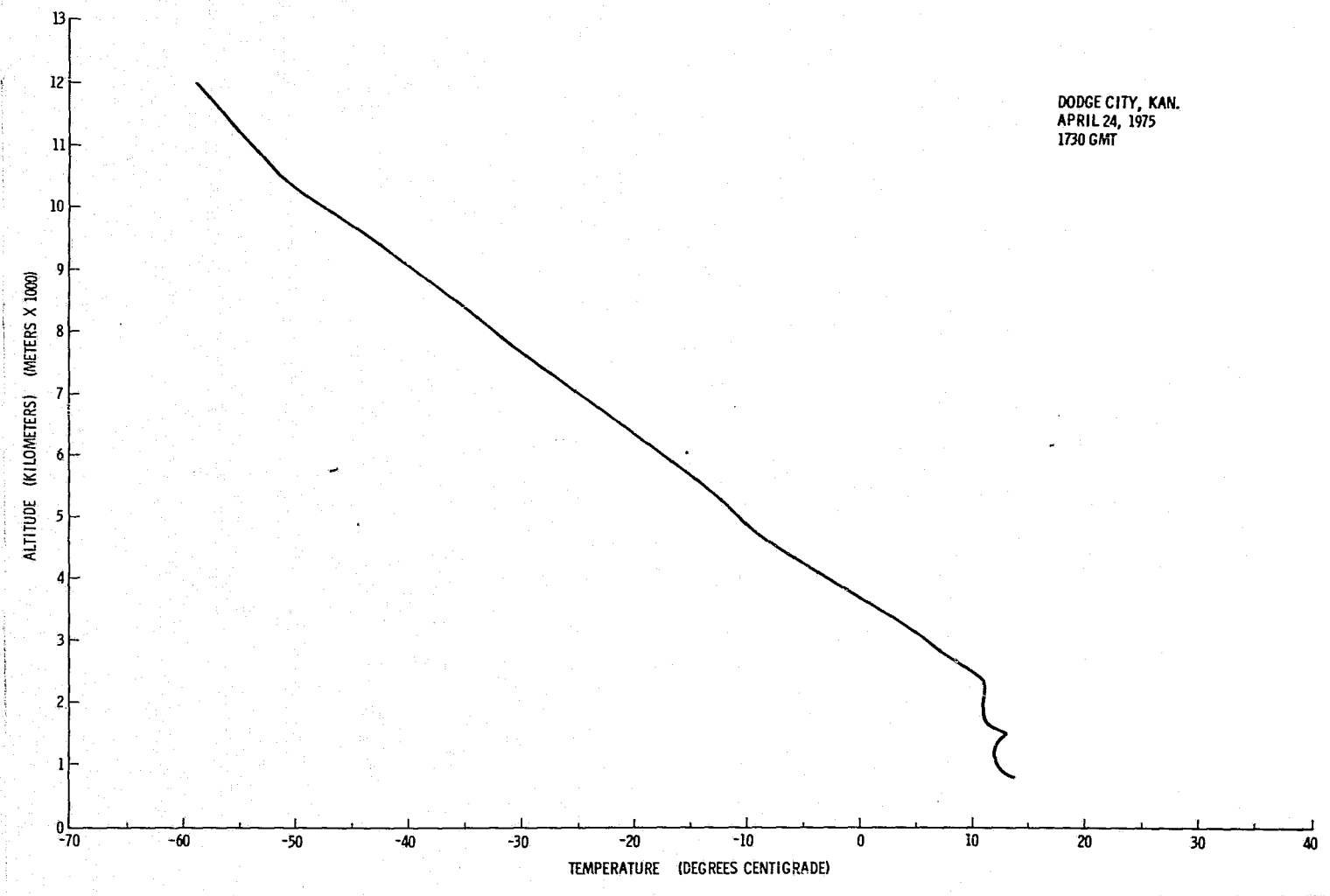

Figure A.15. Temperature profile for 1730 GMT, April 24, 1975, over Dodge City, Kansas.

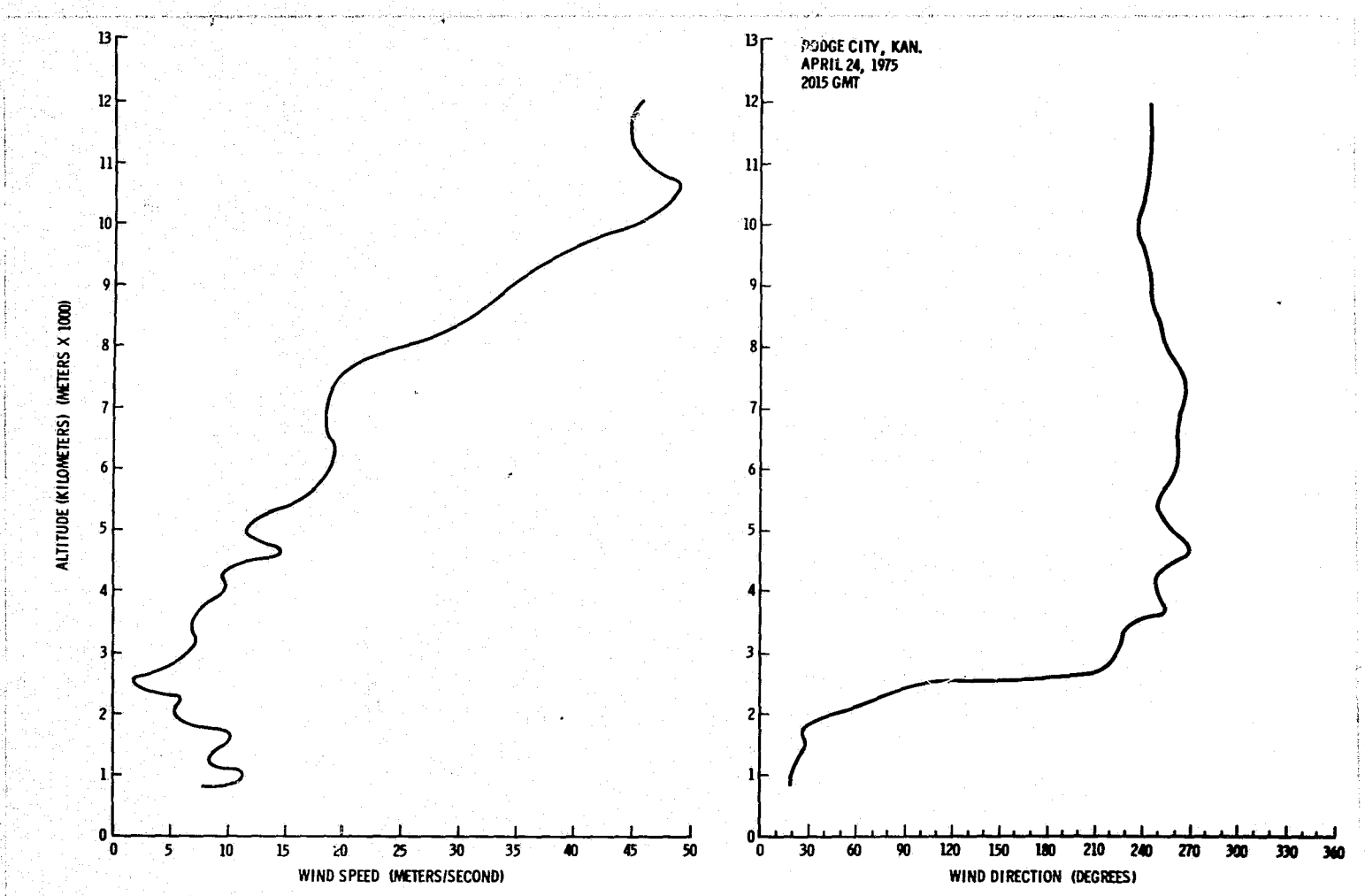

Figure A.16. Vertical wind profile for 2015 GMT, April 24, 1975, over Dodge City, Kansas.

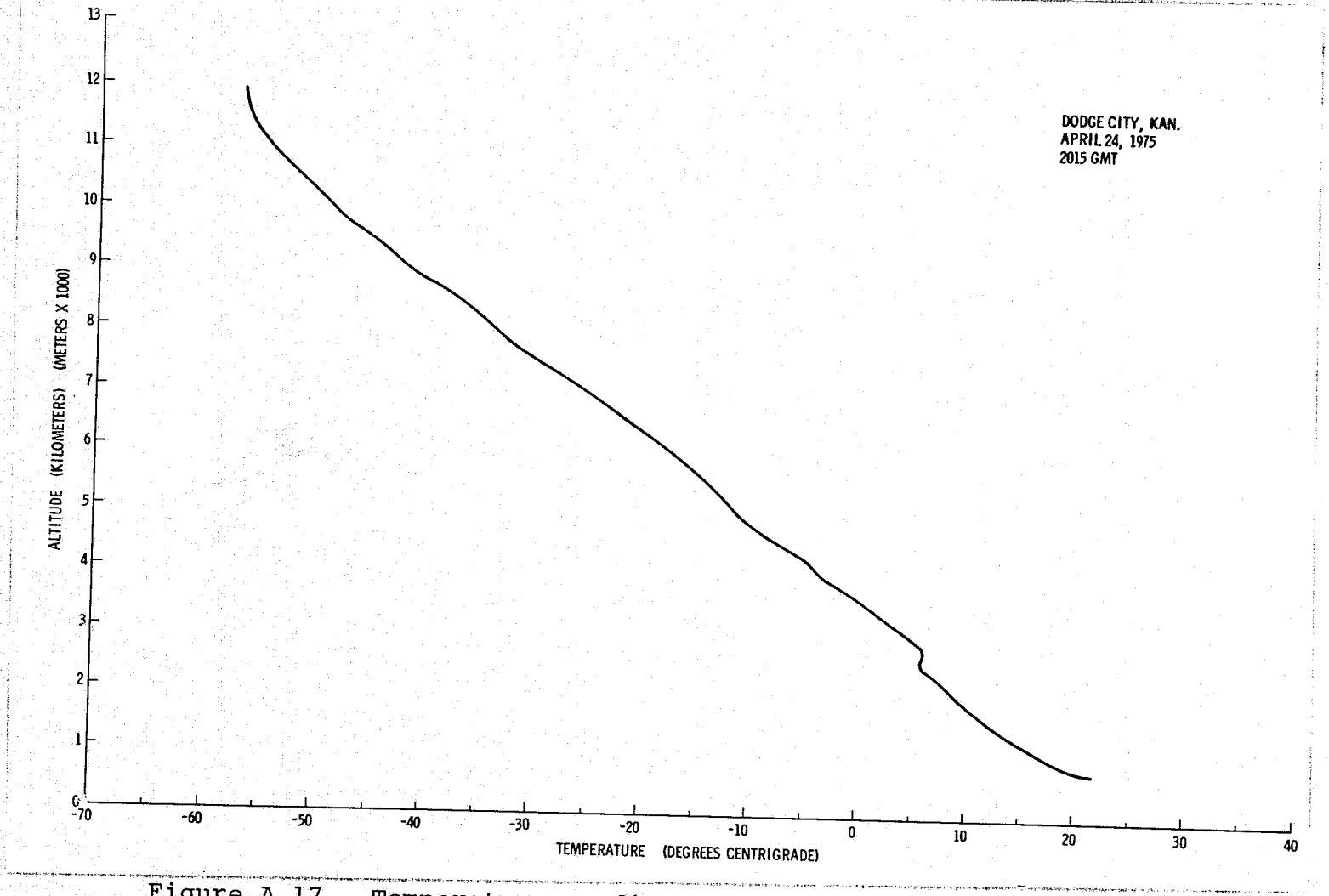

Figure A.17. Temperature profile for 2015 GMT, April 24, 1975, over Dodge City, Kansas.

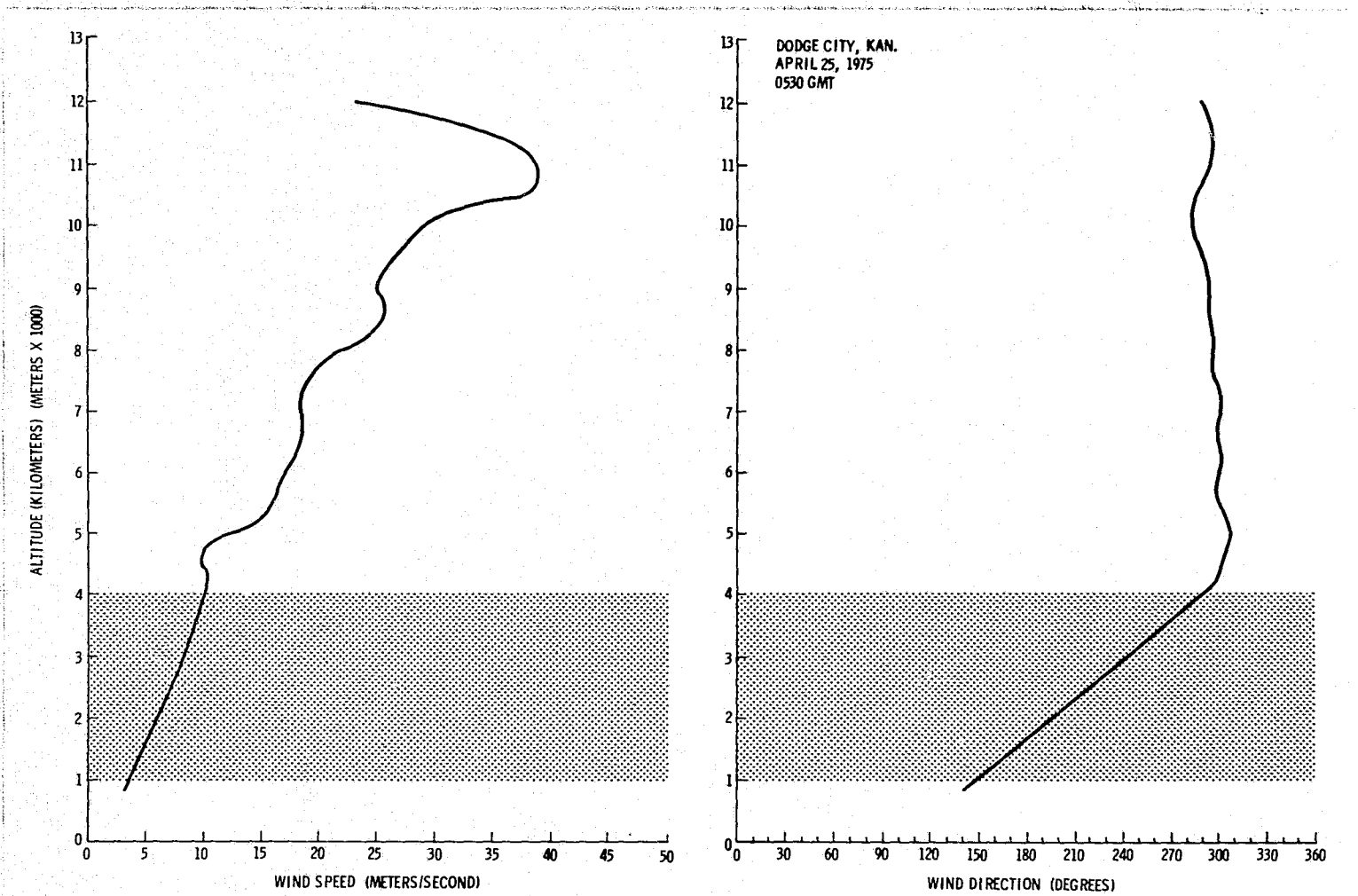

Figure A.18. Vertical wind profile for 0530 GMT, April 25, 1975, over Dodge City, Kansas.

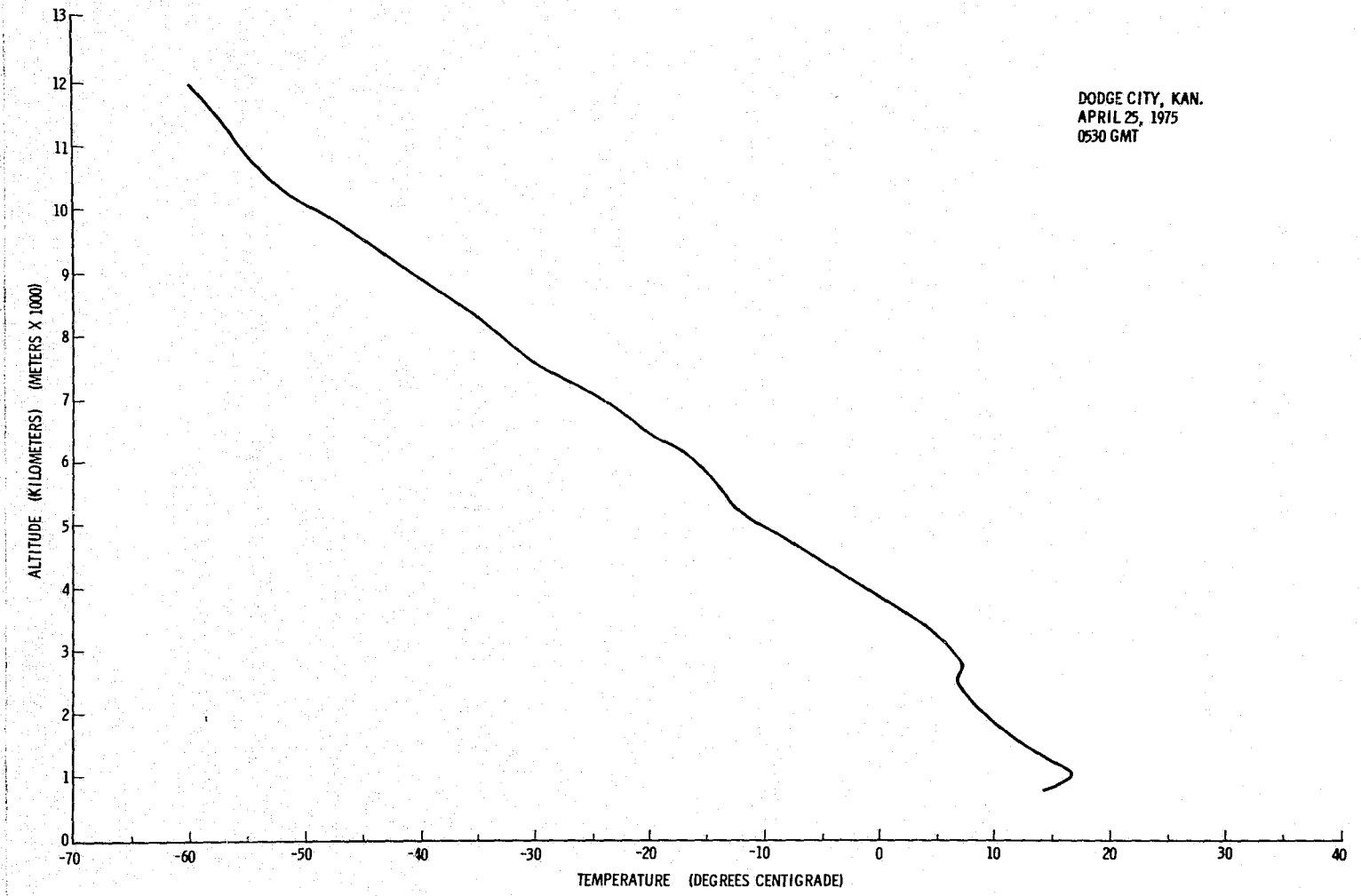

Figure A.19. Temperature profile for 0530 GMT, April 25, 1975, over Dodge City, Kansas.

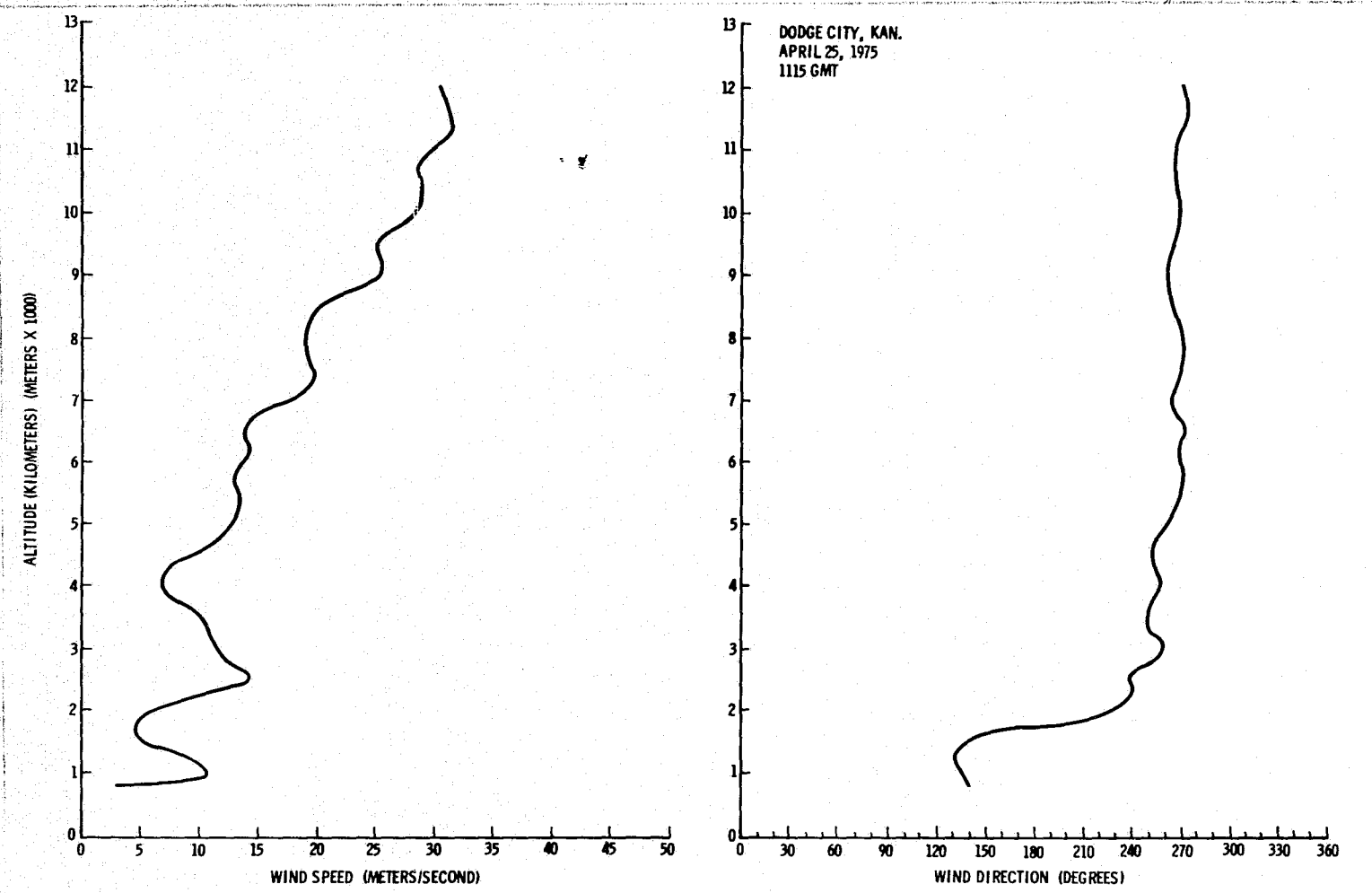

Figure A.20. Vertical wind profile for 1115 GMT, April 25, 1975, over Dodge City, Kansas.

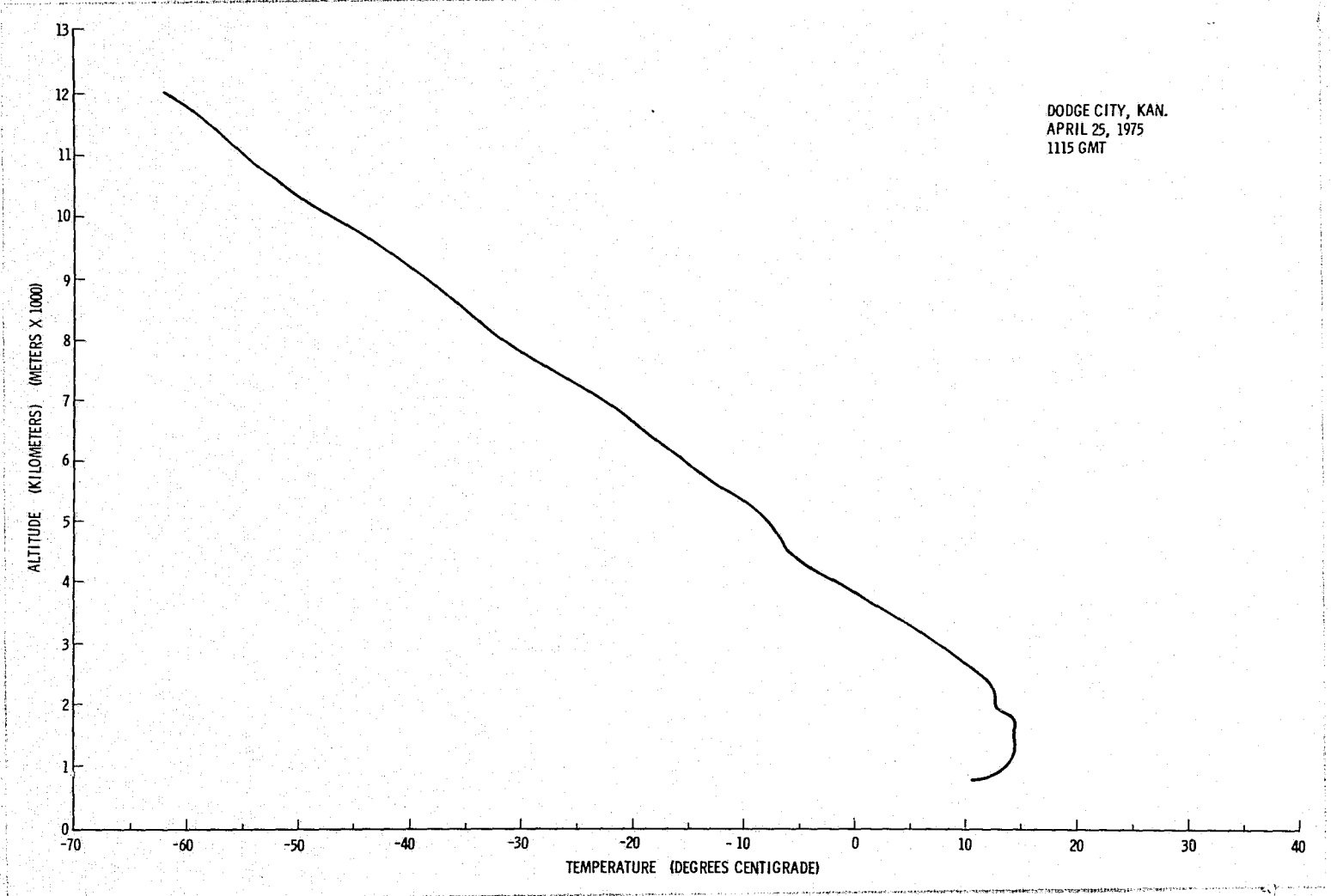

Figure A.21. Temperature profile for 1115 GMT, April 25, 1975, over Dodge City, Kansas.

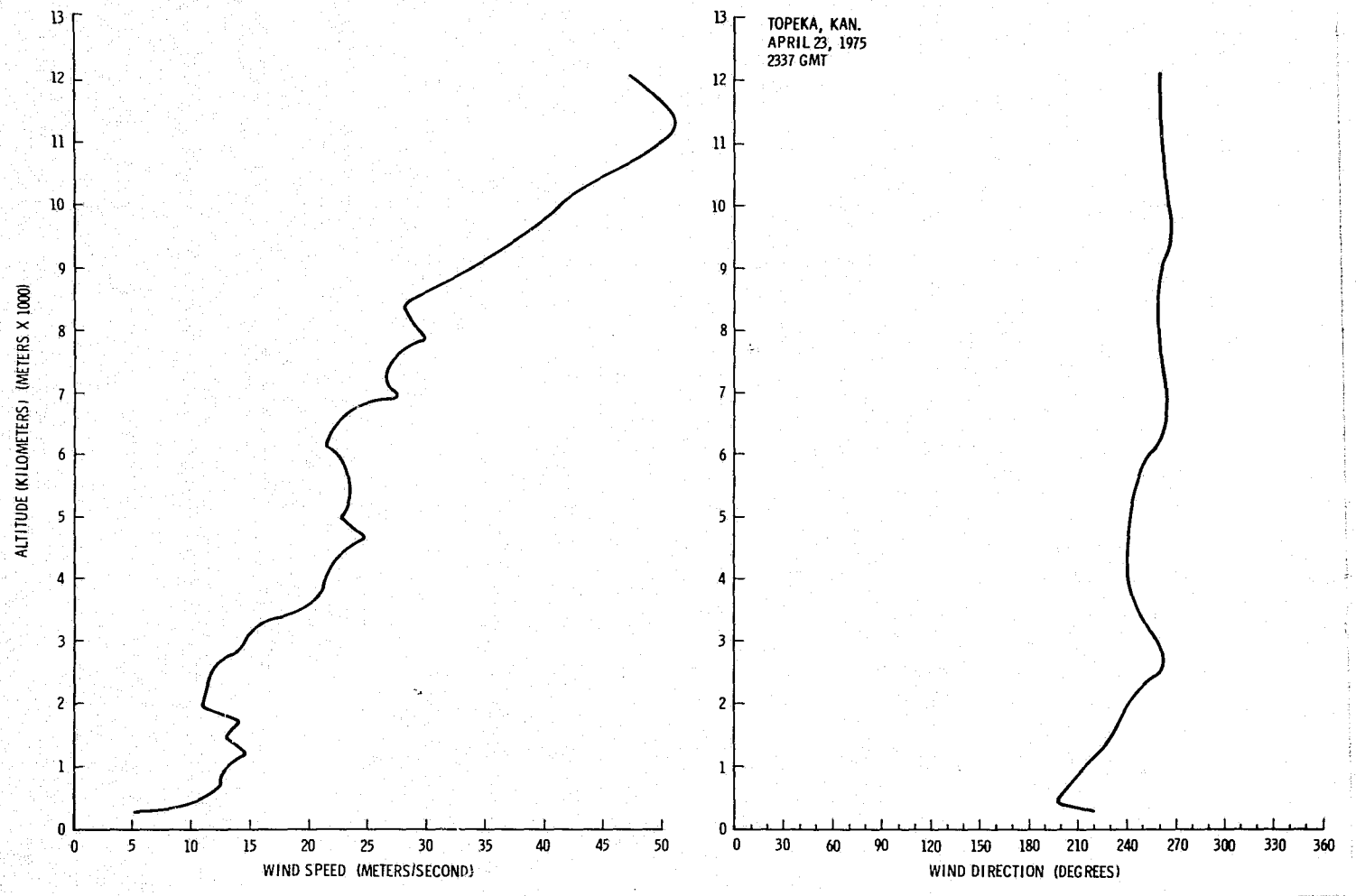

Figure A.22. Vertical wind profile for 2337 GMT, April 23, 1975, over Topeka, Kansas.

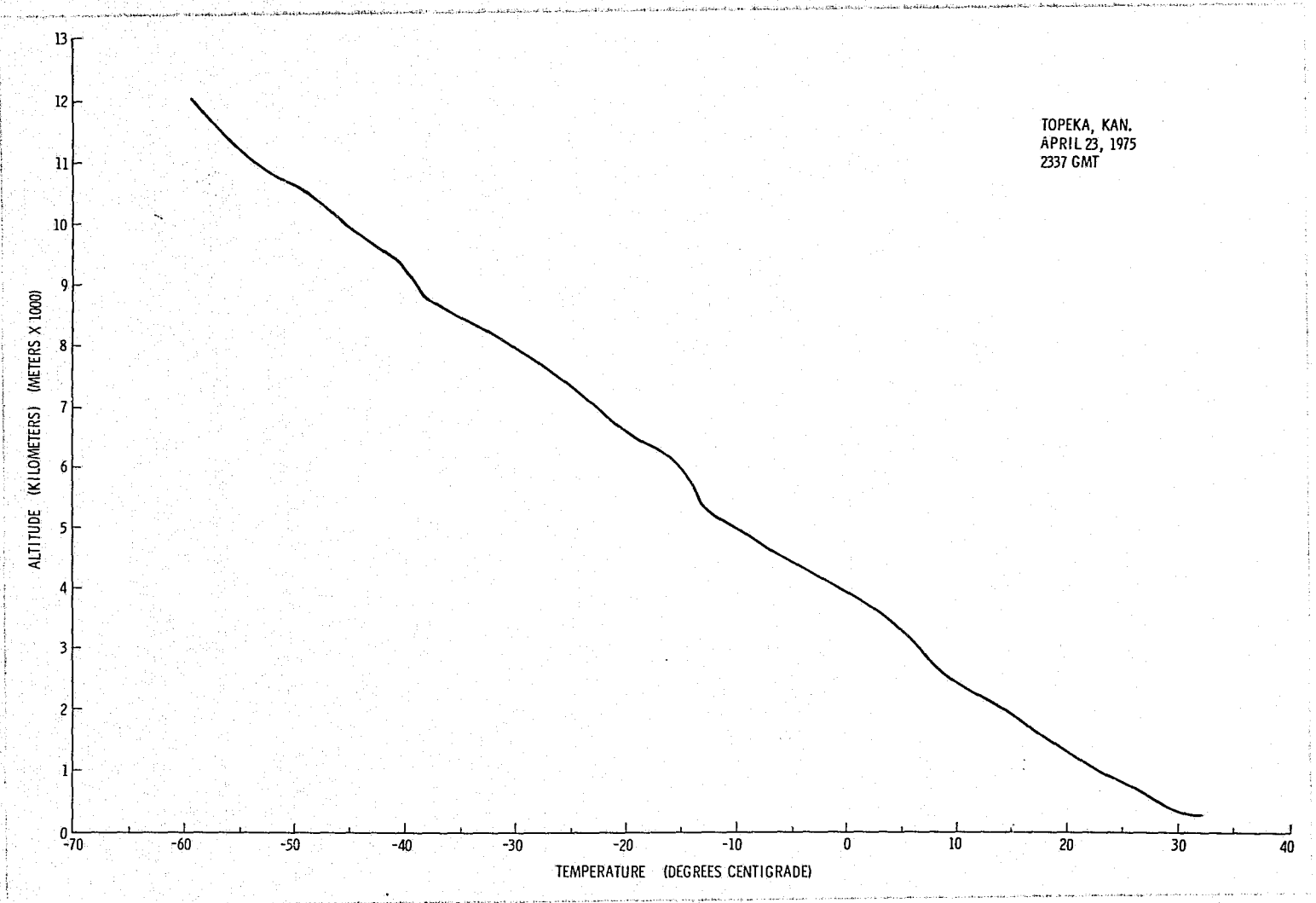

Figure A.23. Temperature profile for 2337 GMT, April 23, 1975, over Topeka, Kansas.

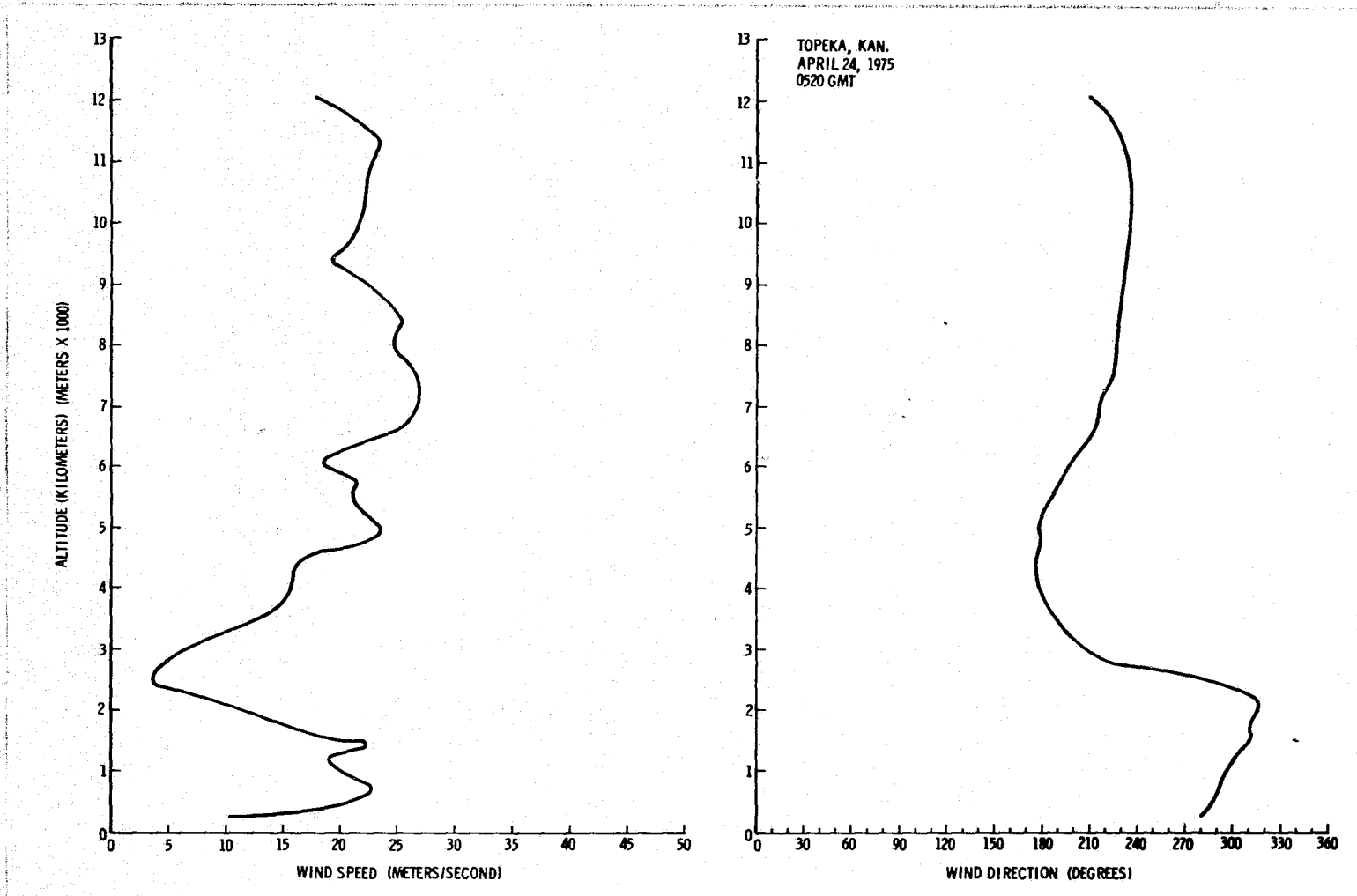

Figure A.24. Vertical wind profile for 0520 GMT, April 24, 1975, over Topeka, Kansas.

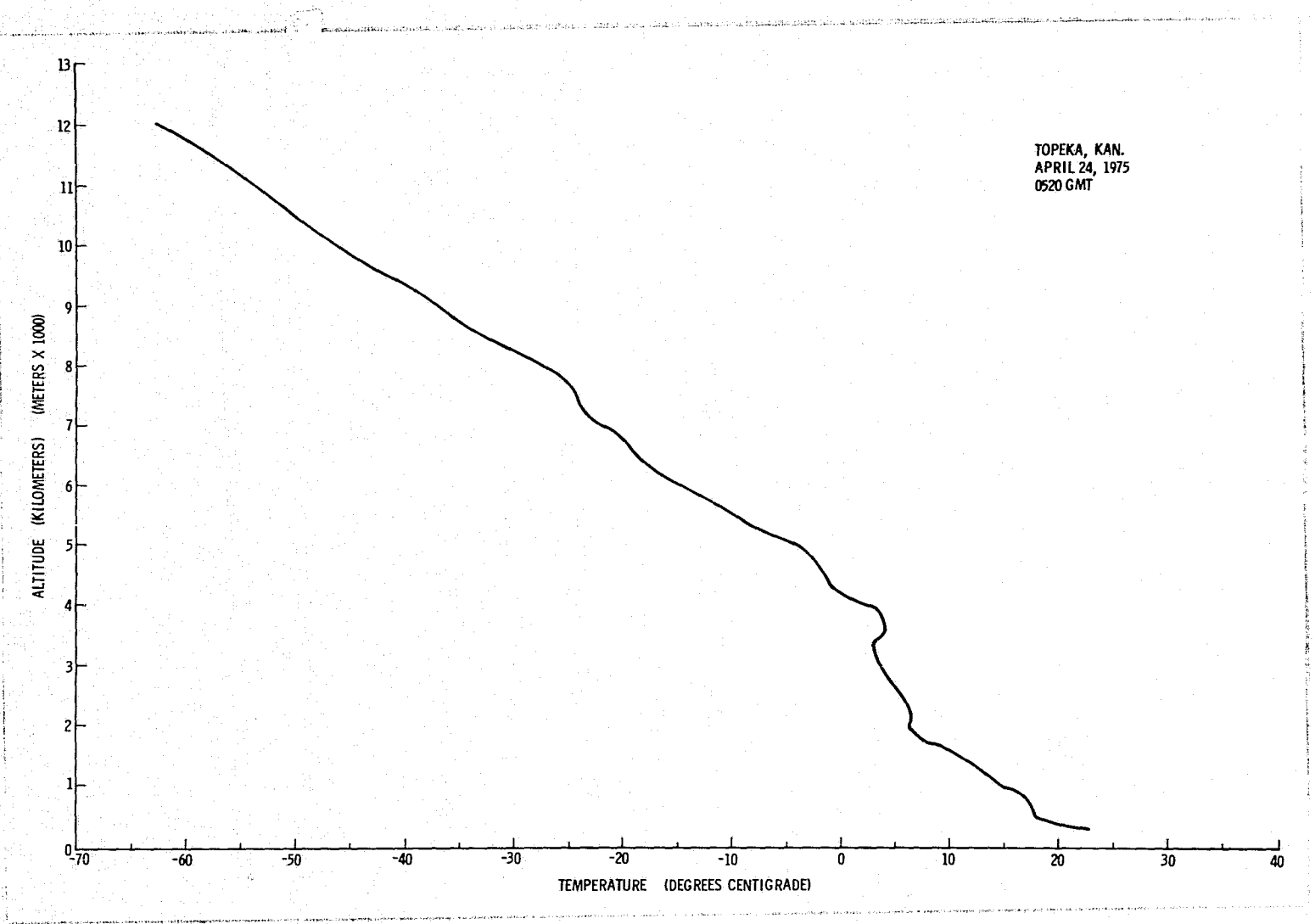

Figure A.25. Temperature profile for 0520 GMT, April 24, 1975, over Topeka, Kansas.

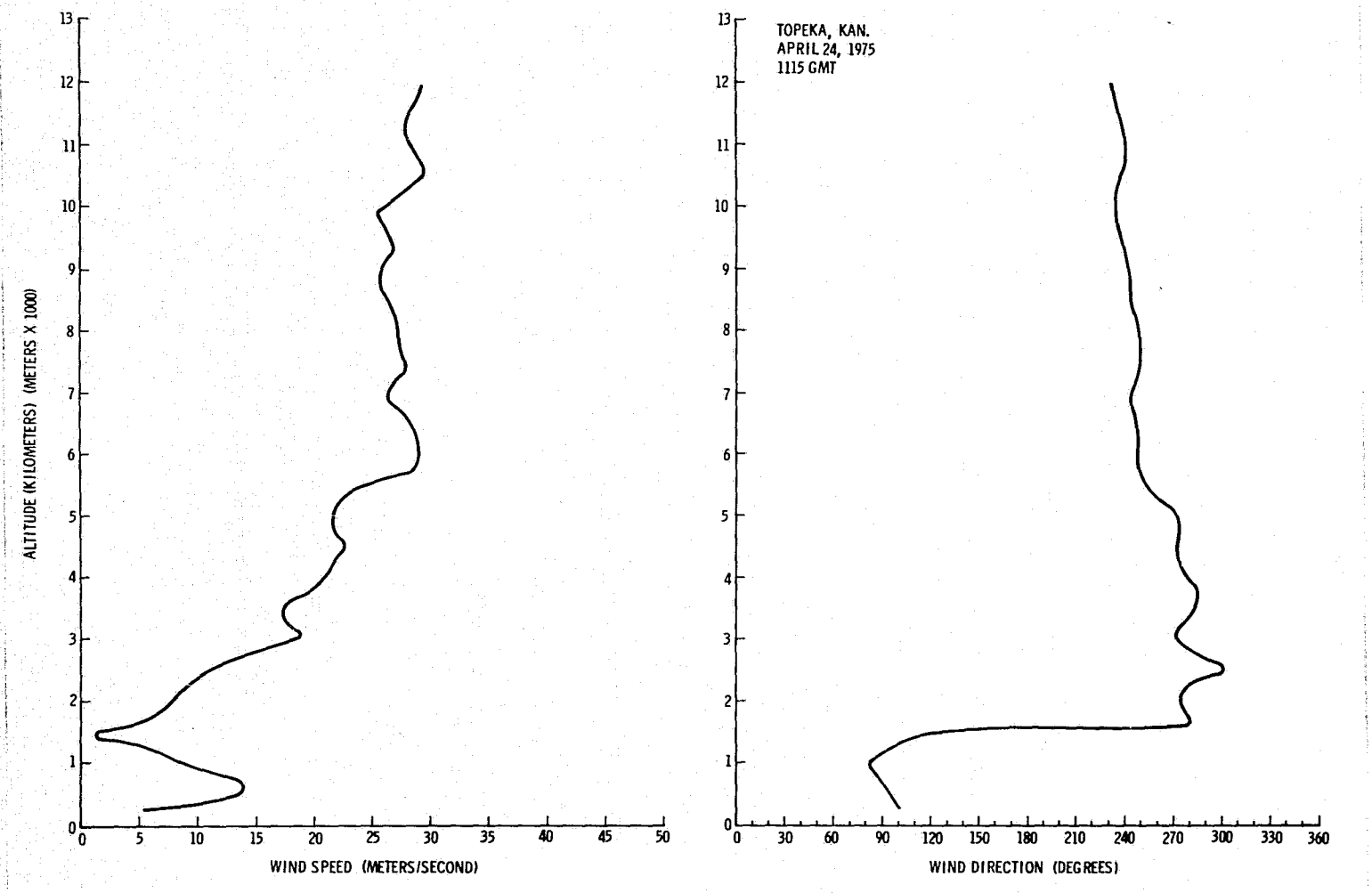

Figure A.26. Vertical wind profile for 1115 GMT, April 24, 1975, over Topeka, Kansas.

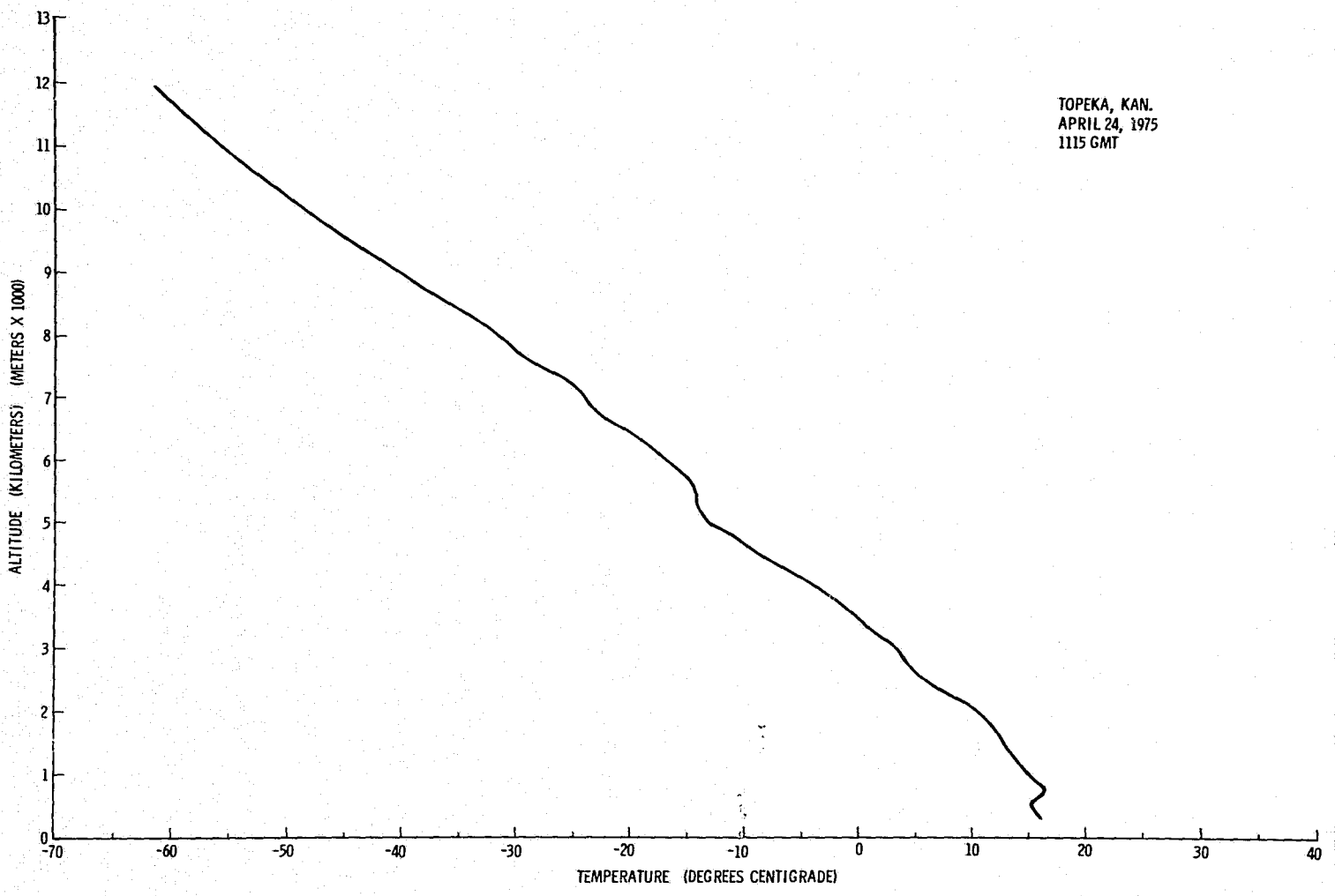

Figure A.27. Temperature profile for 1115 GMT, April 24, 1975, over Topeka, Kansas.

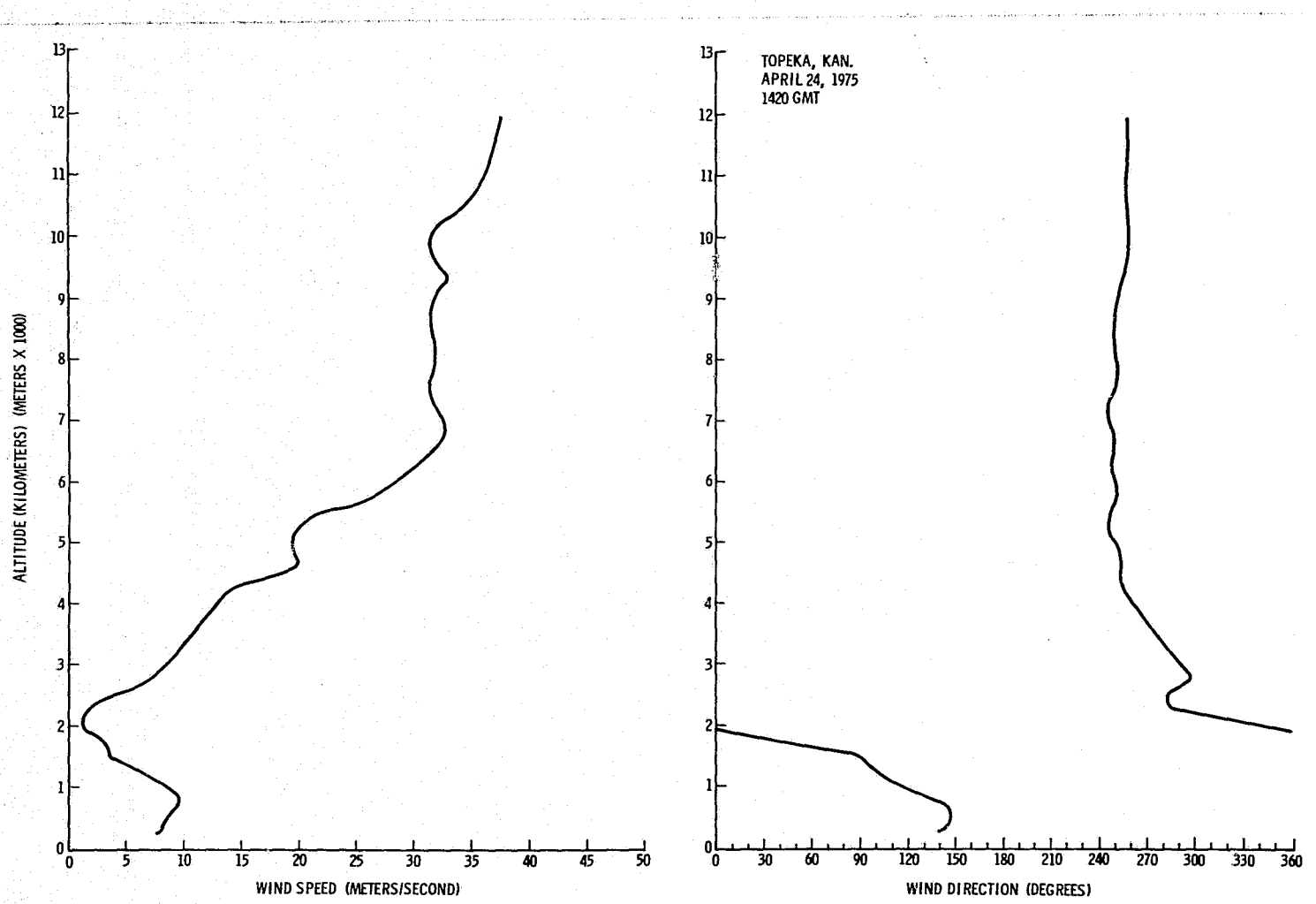

Figure A.28. Vertical wind profile for 1420 GMT, April 24, 1975, over Topeka, Kansas.

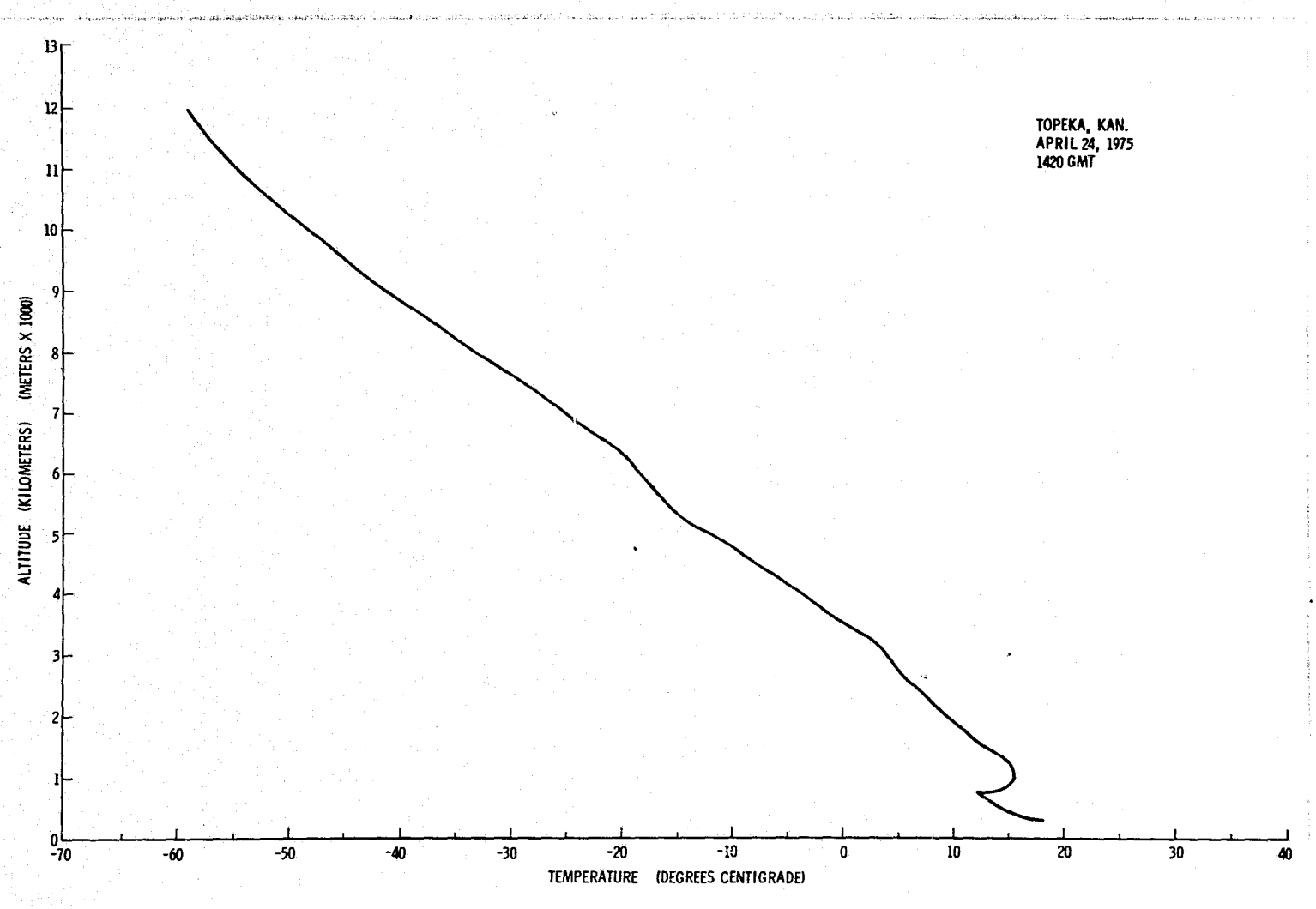

Figure A.29. Temperature profile for 1420 GMT, April 24, 1975, over Topeka, Kansas.

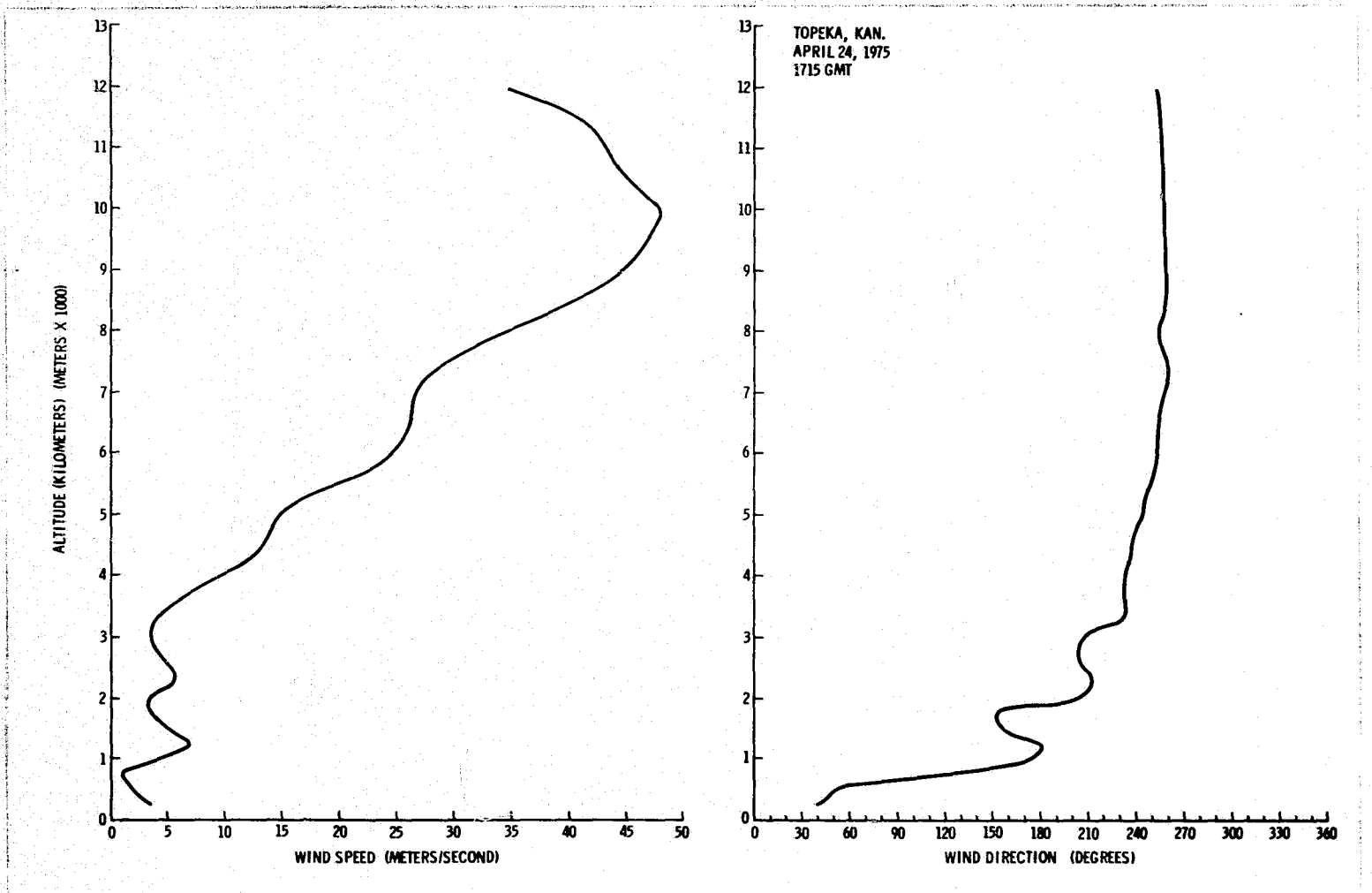

Figure A.30. Vertical wind profile for 1715 GMT, April 24, 1975, over Topeka, Kansas.

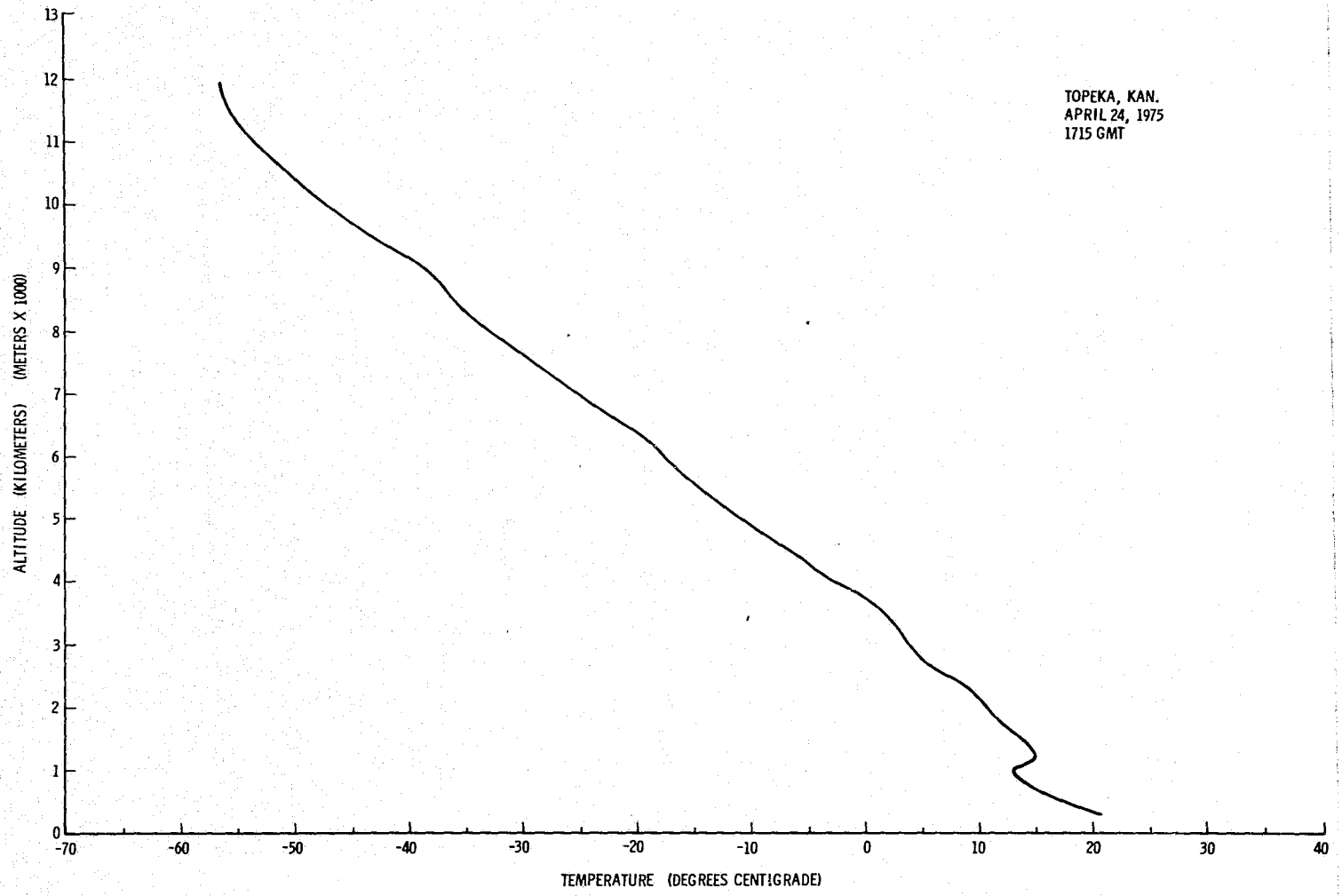

Figure A.31. Temperature profile for 1715 GMT, April 24, 1975, over Topeka, Kansas.

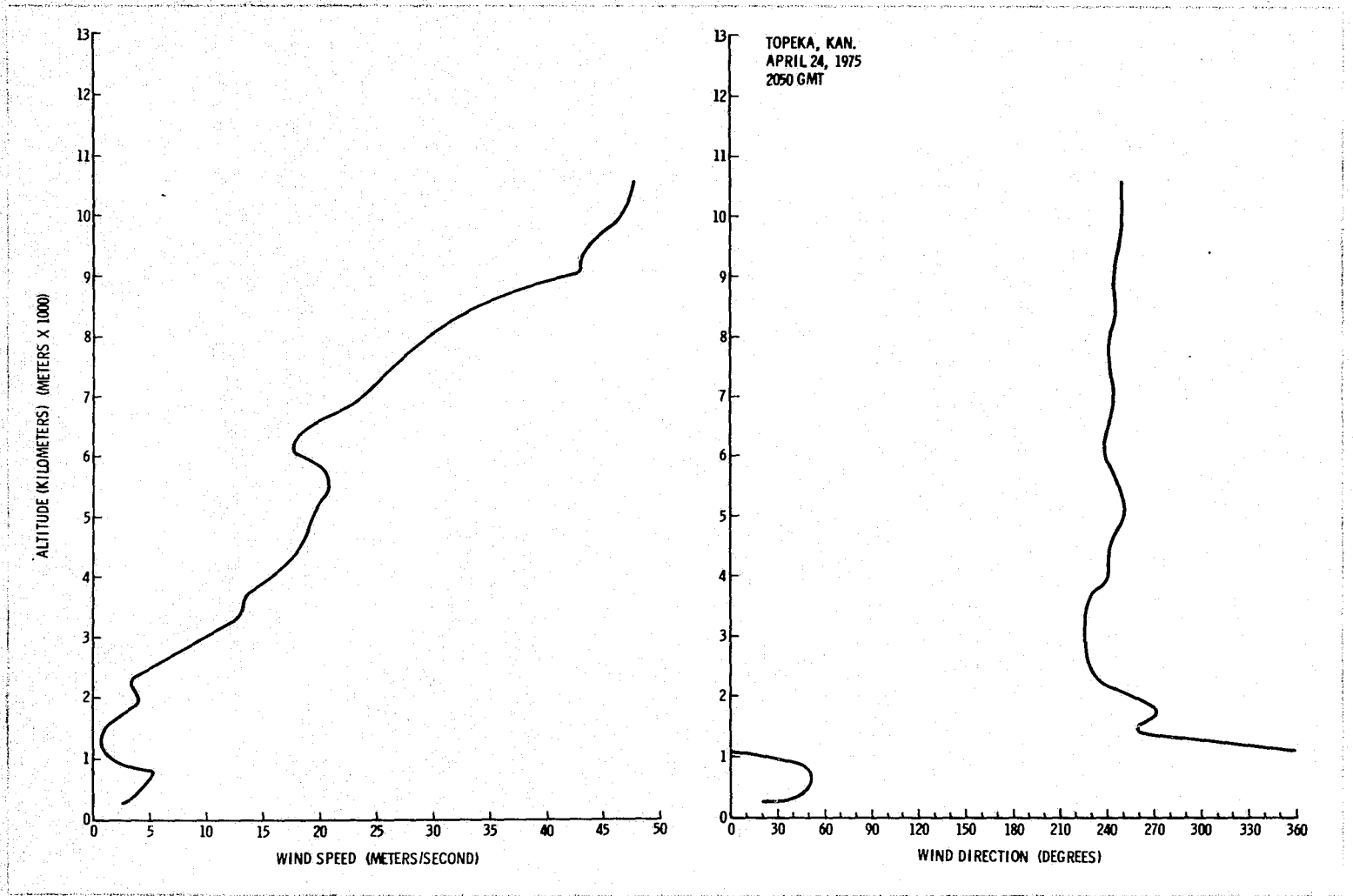

Figure A.32. Vertical wind profile for 2050 GMT, April 24, 1975, over Topeka, Kansas.

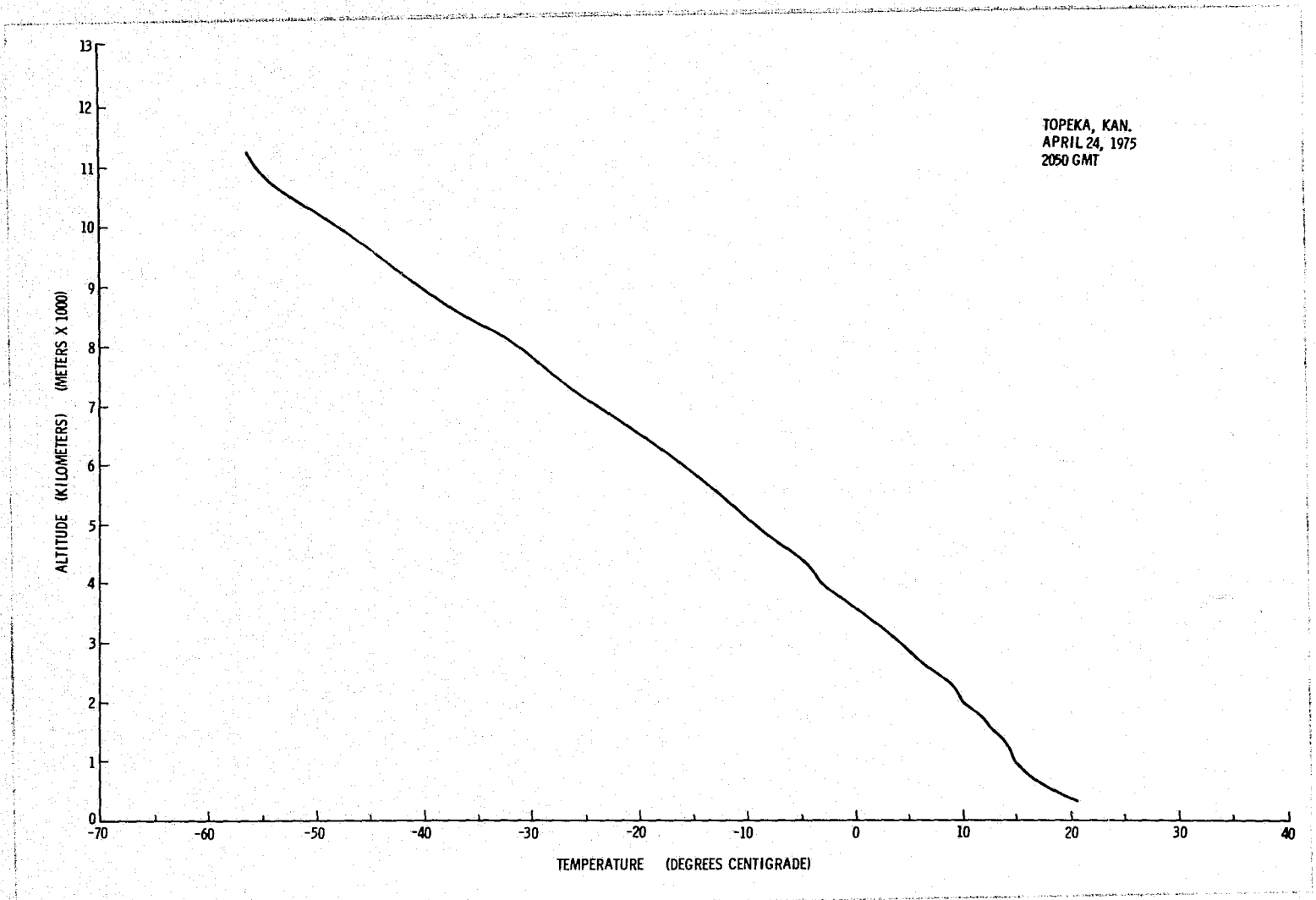

Figure A.33. Temperature profile for 2050 GMT, April 24, 1975, over Topeka, Kansas.

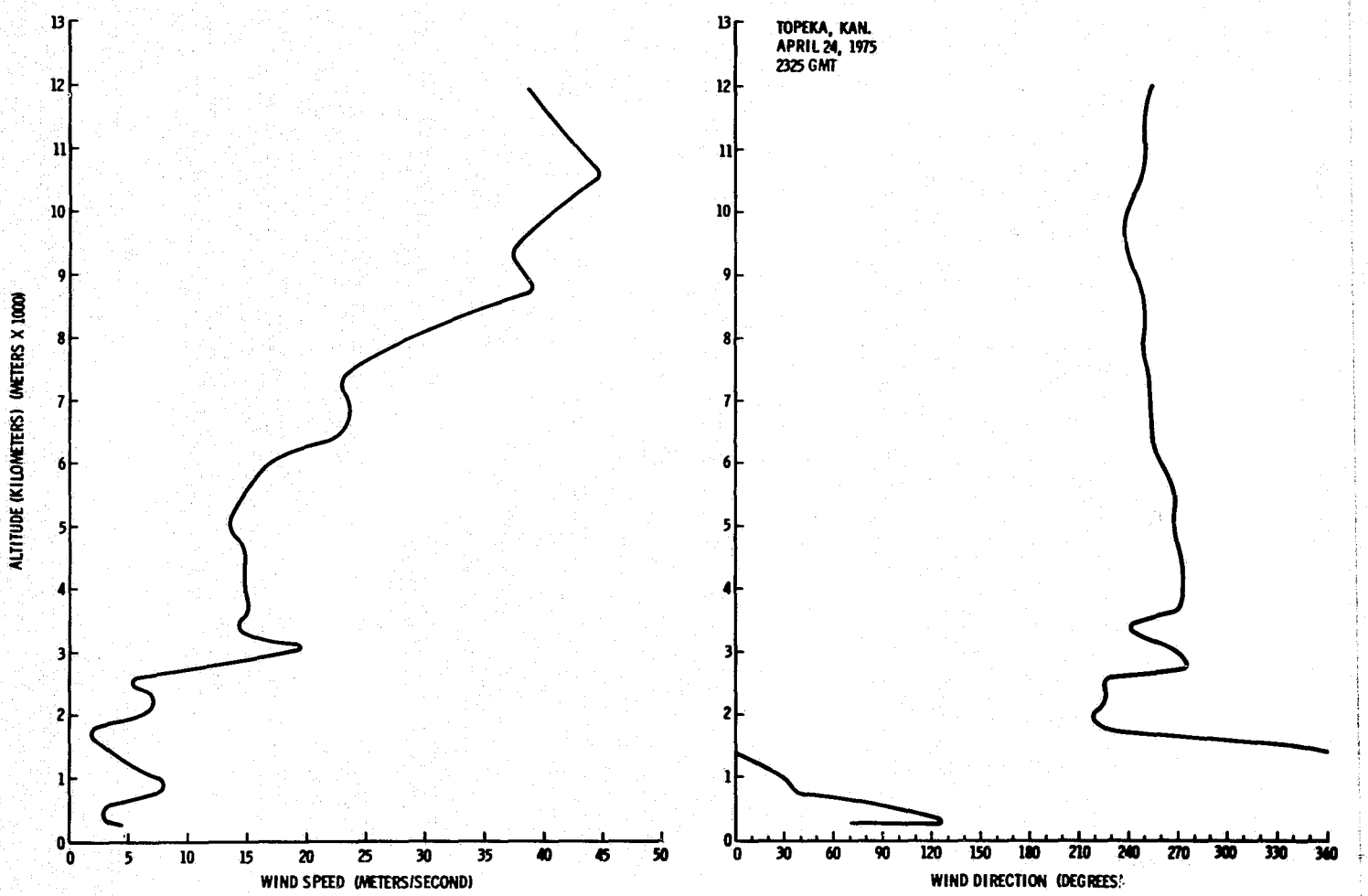

Figure A.34. Vertical wind profile for 2325 GMT, April 24, 1975, over Topeka, Kansas.

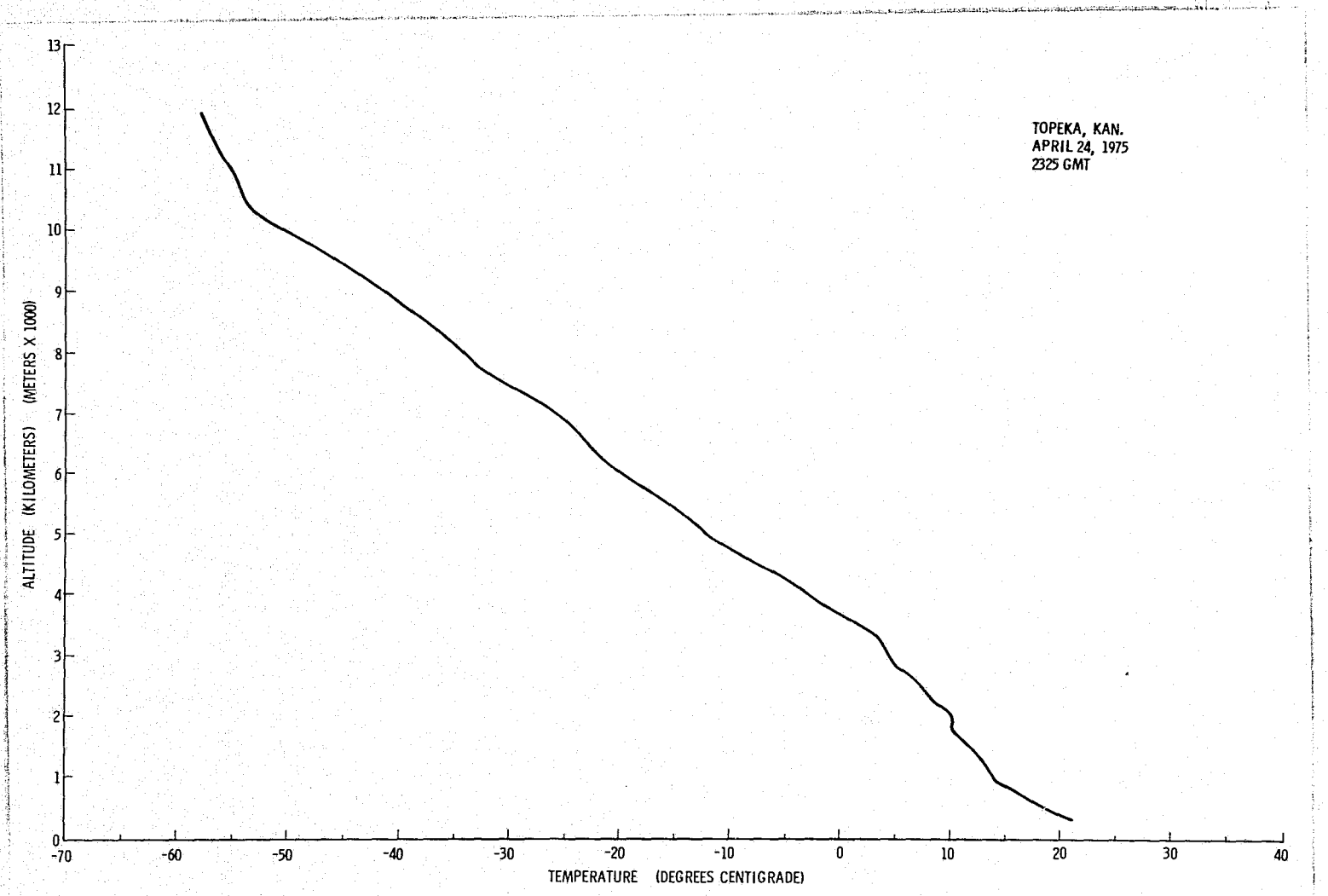

Figure A.35. Temperature profile for 2325 GMT, April 24, 1975, over Topeka, Kansas.

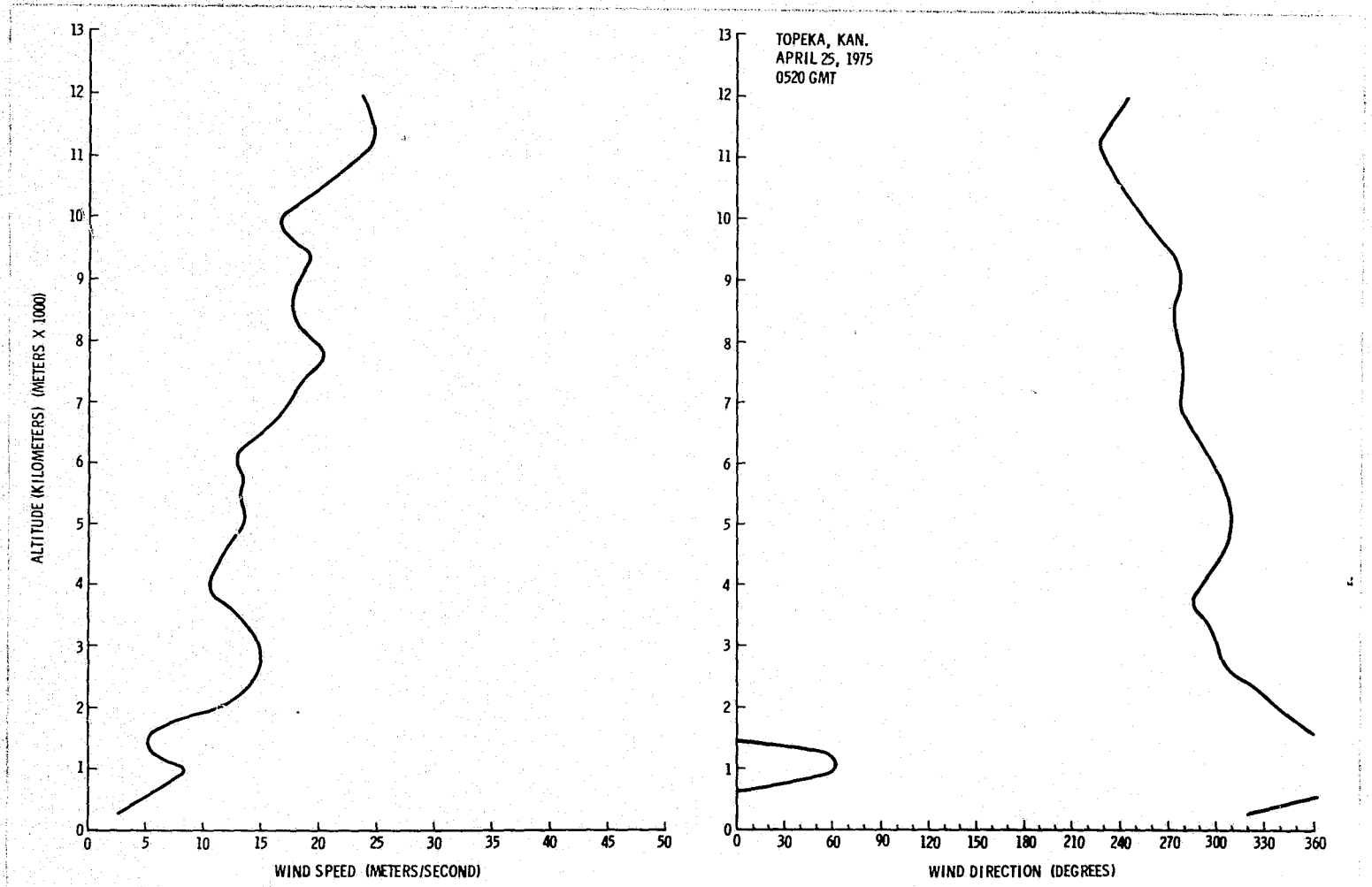

Figure A.36. Vertical wind profile for 0520 GMT, April 25, 1975, over Topeka, Kansas.

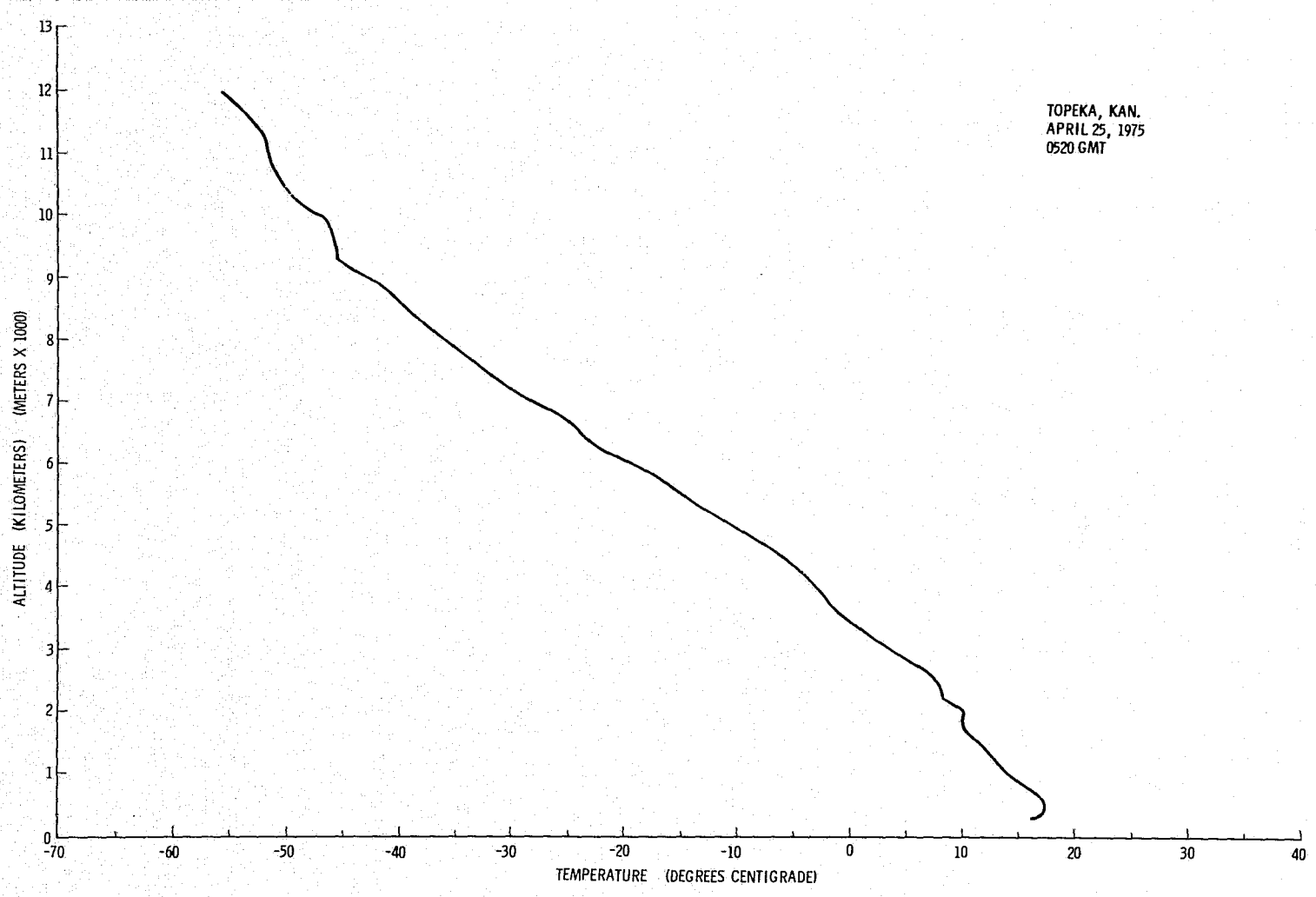

Figure A.37. Temperature profile for 0520 GMT, April 25, 1975, over Topeka, Kansas.

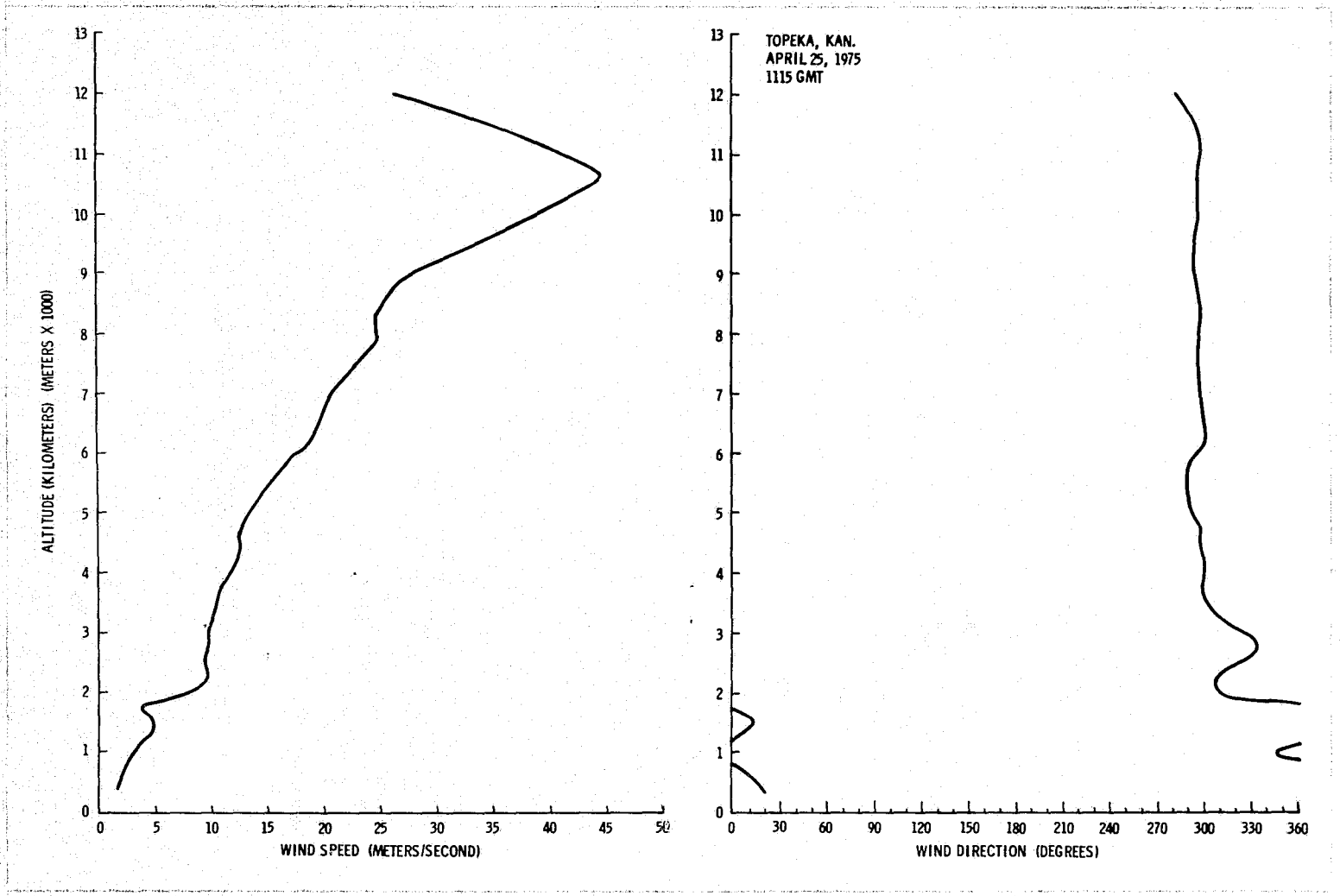

Figure A.38. Vertical wind profile for 1115 GMT, April 25, 1975, over Topeka, Kansas.

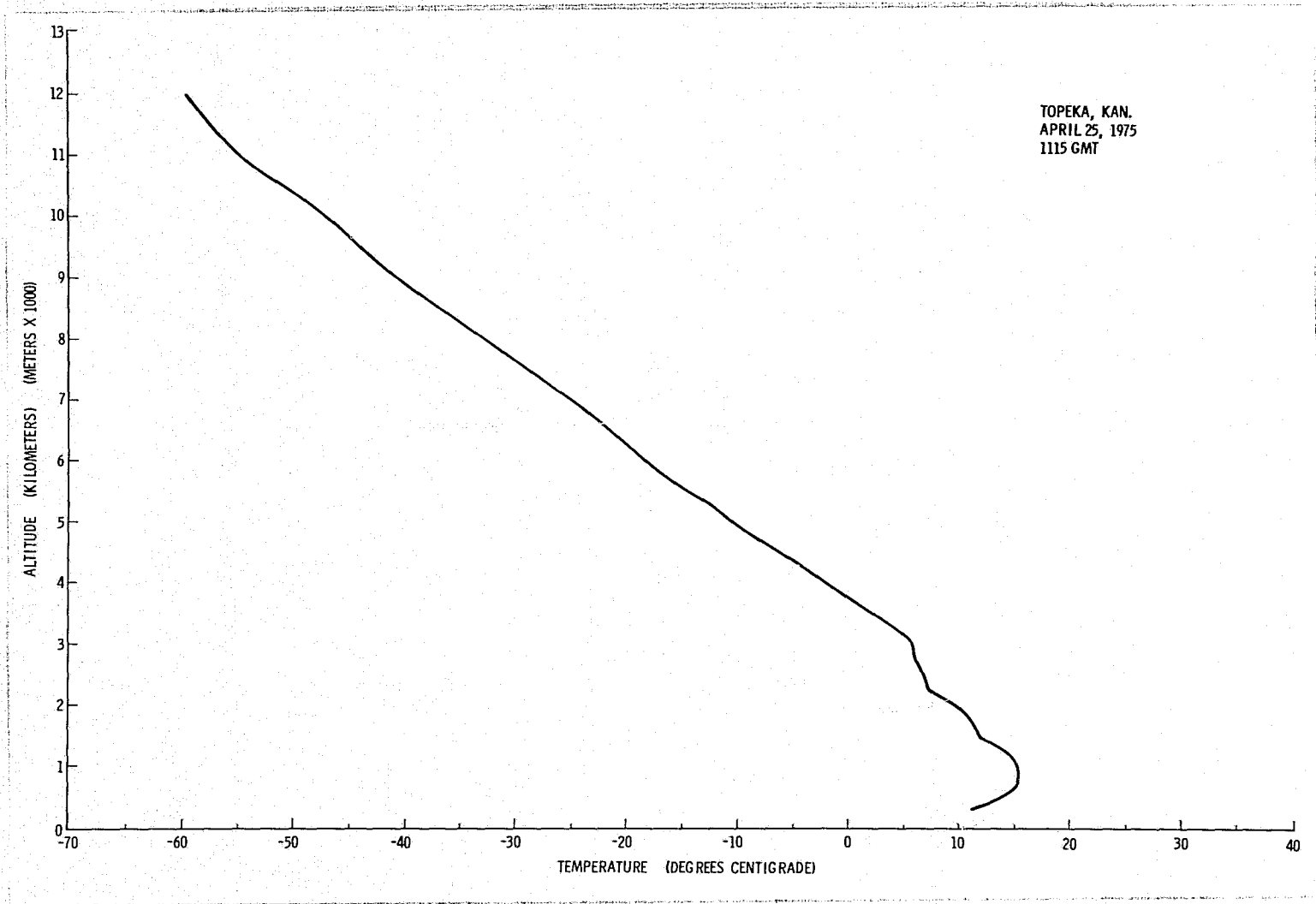

Figure A.39. Temperature profile for 1115 GMT, April 25, 1975, over Topeka, Kansas.

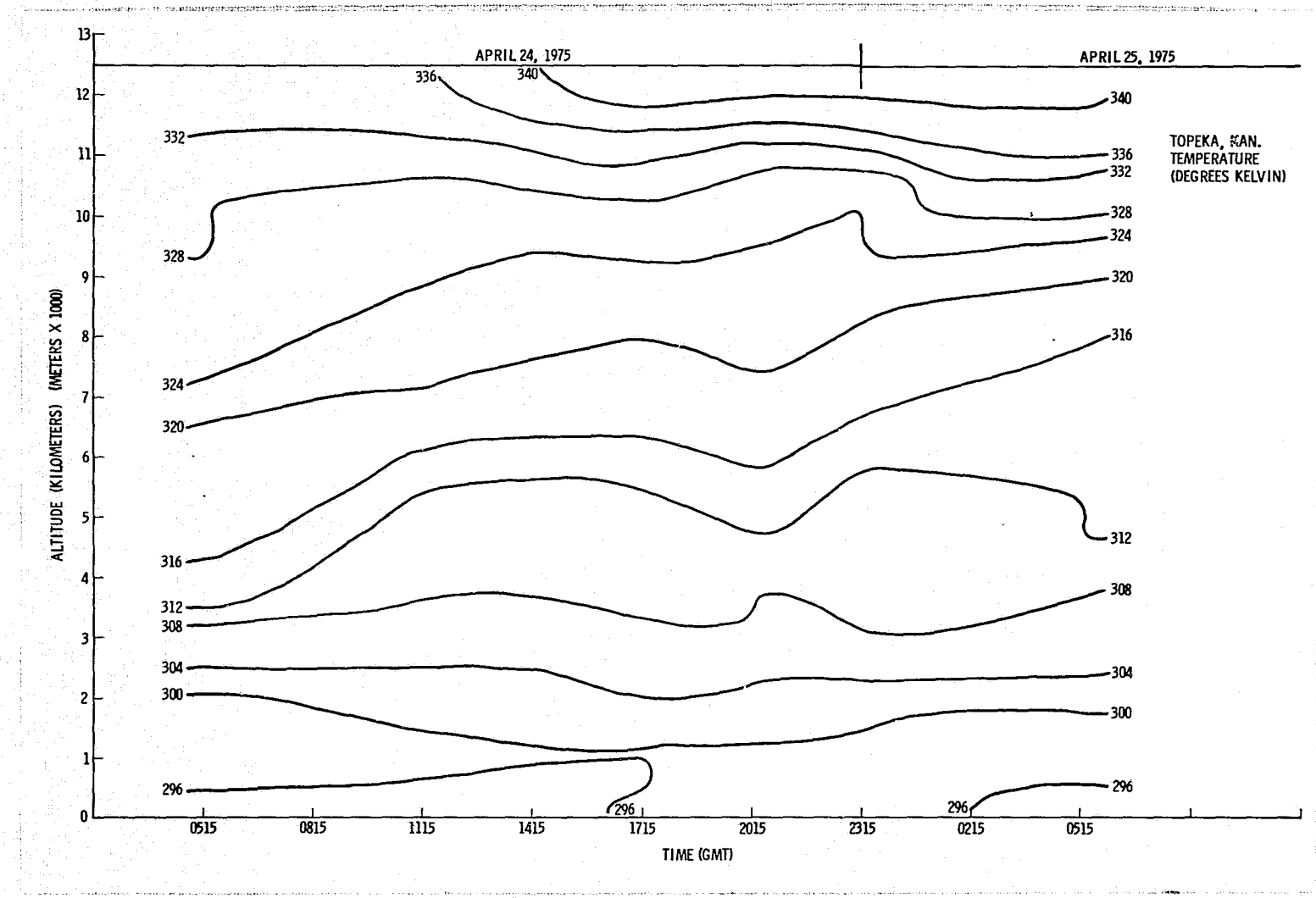

Figure A.40. Time cross section of temperature at Topeka, Kansas.

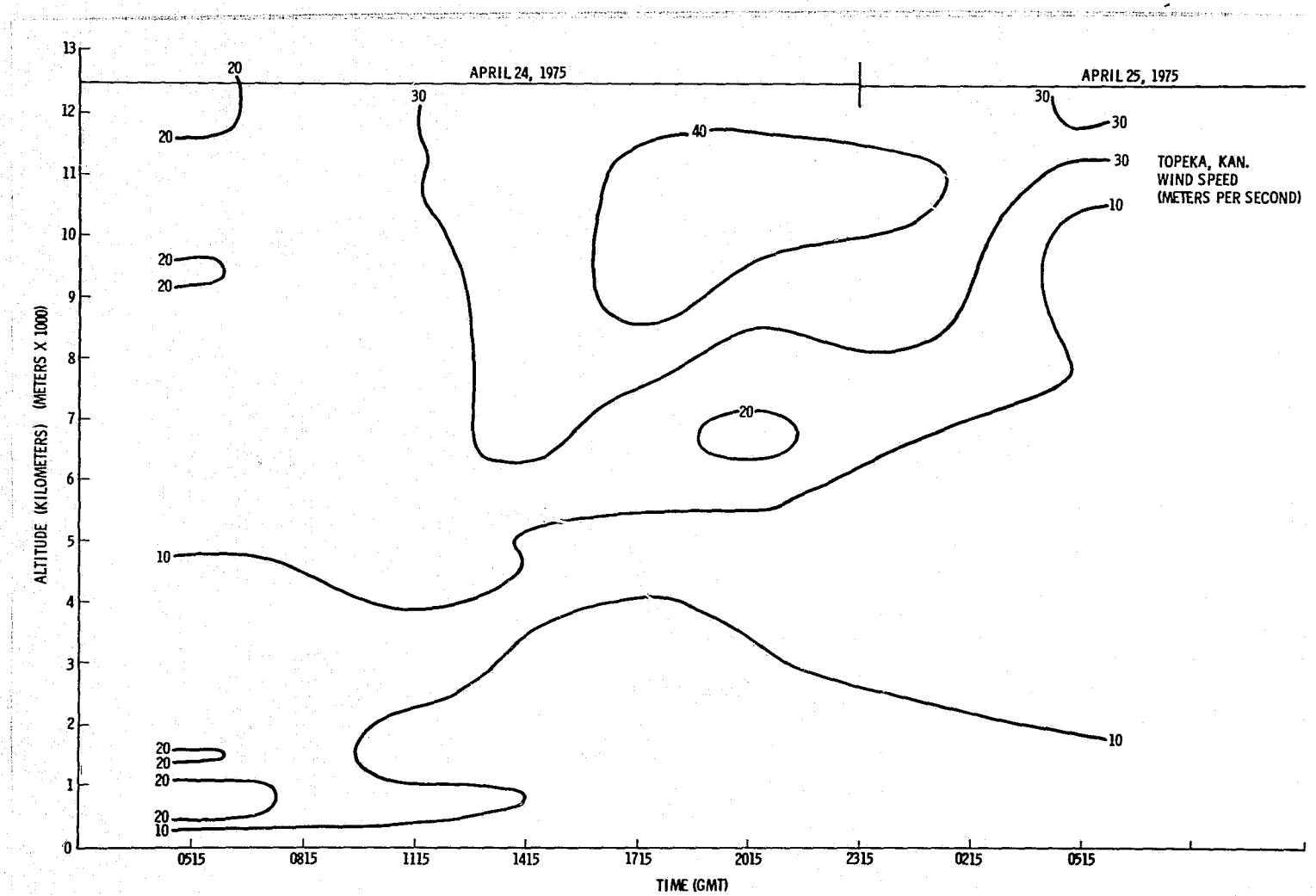

Figure A.41. Time cross section of wind speed at Topeka, Kansas.

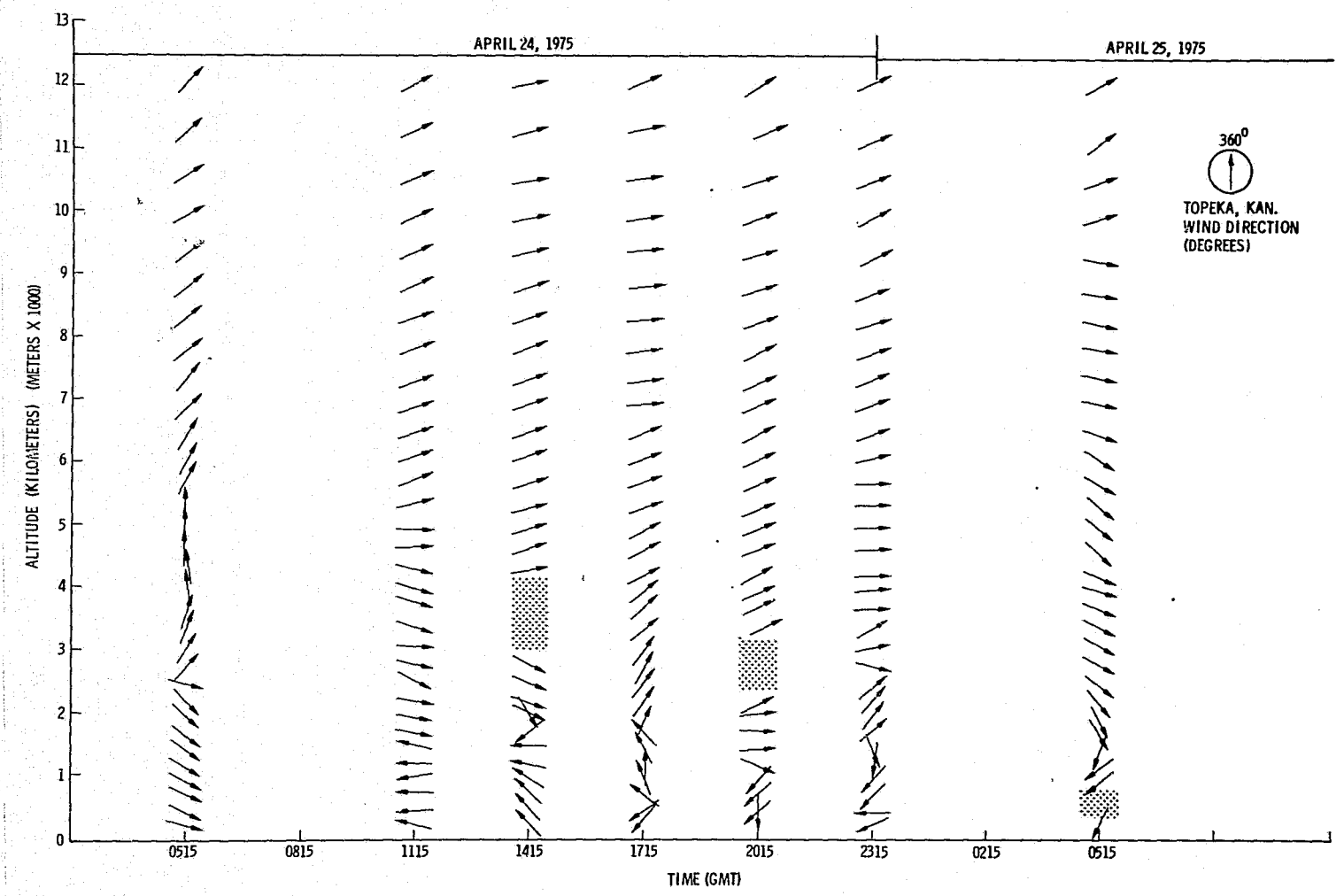

Figure A.42. Time cross section of wind direction at Topeka, Kansas.

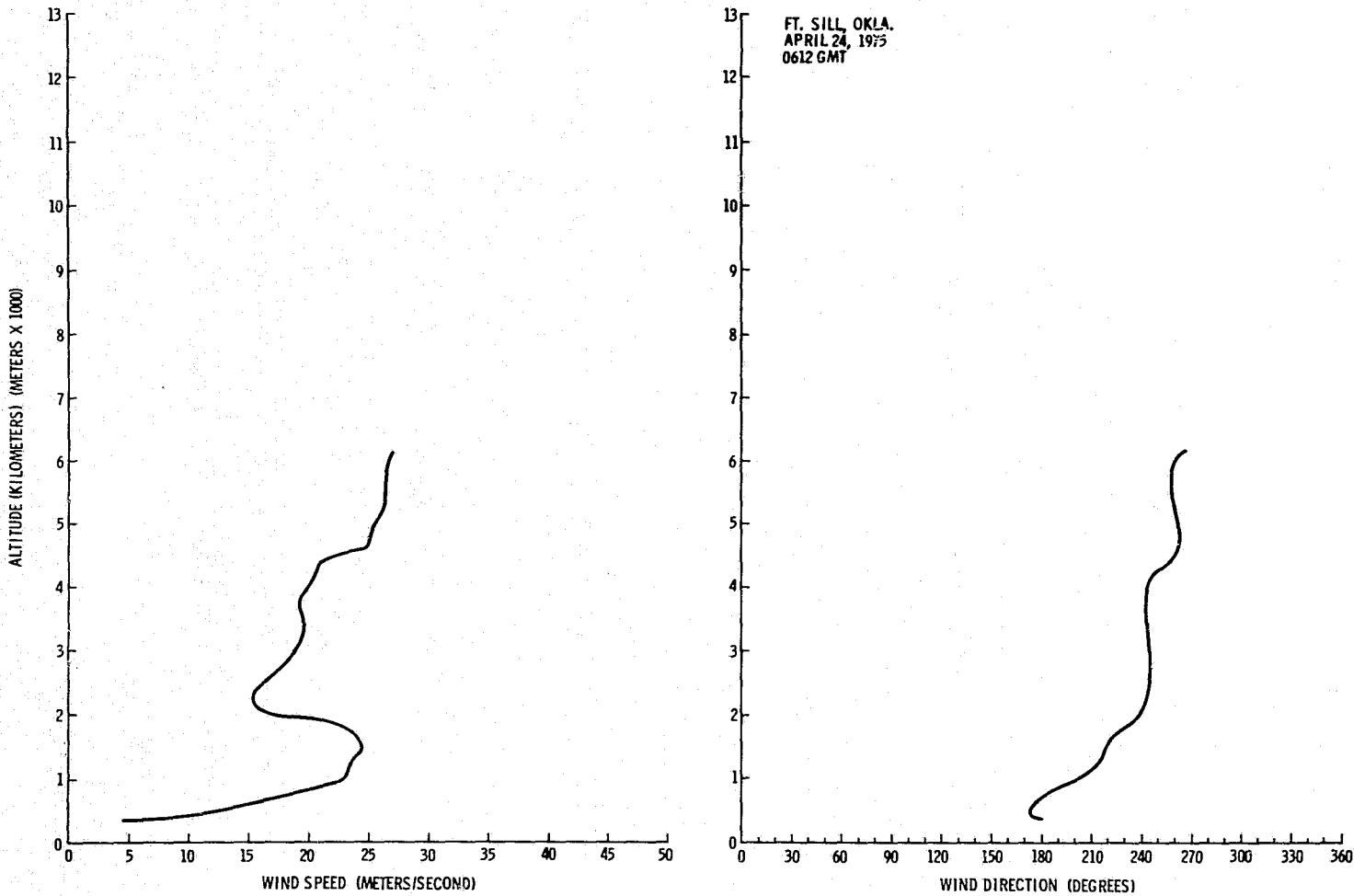

Figure A.43. Vertical wind profile for 0612 GMT, April 24, 1975, over Fort Sill, Oklahoma.

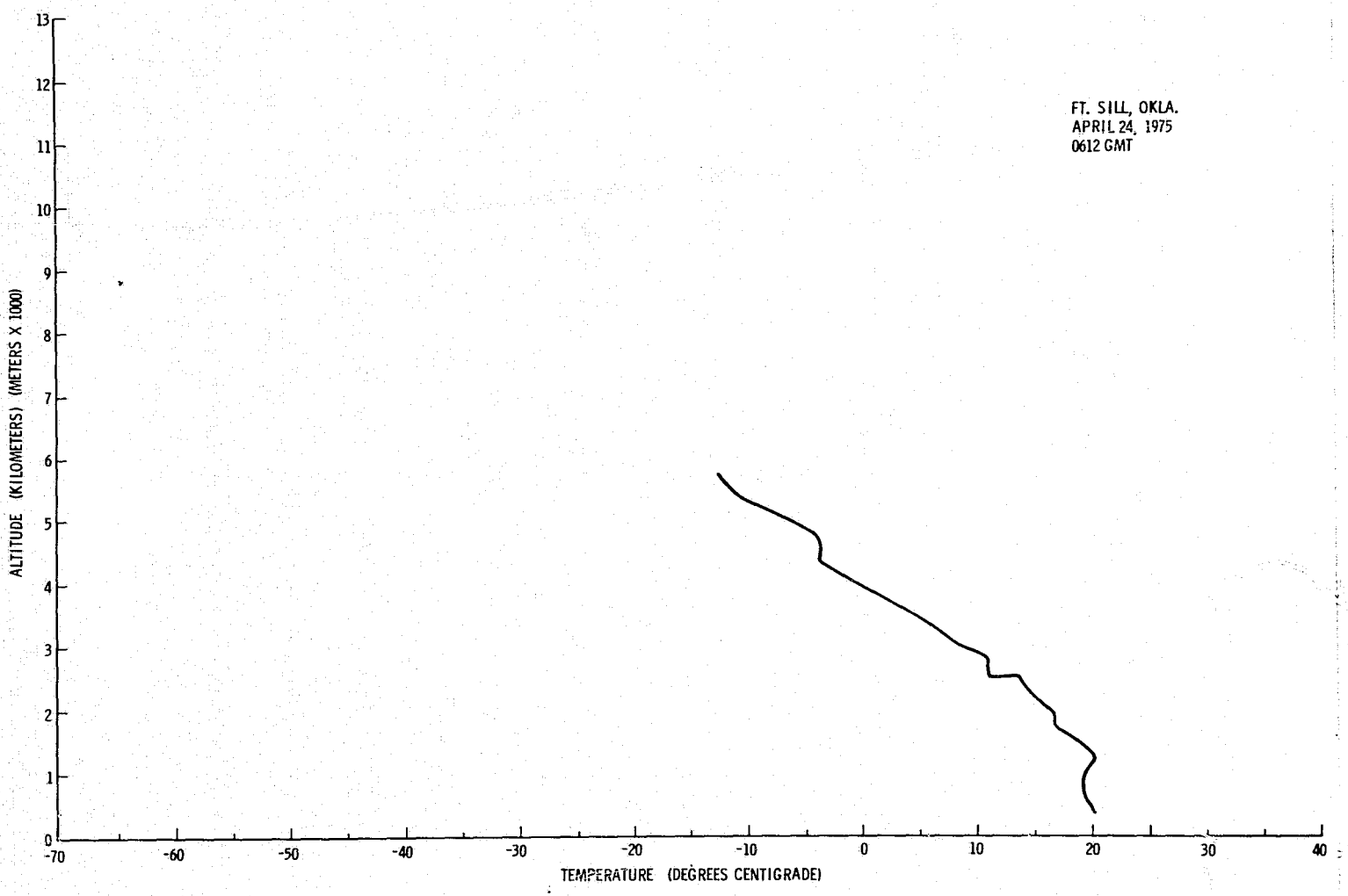

Figure A.44. Temperature profile for 0612 GMT, April 24, 1975, over Fort Sill, Oklahoma.

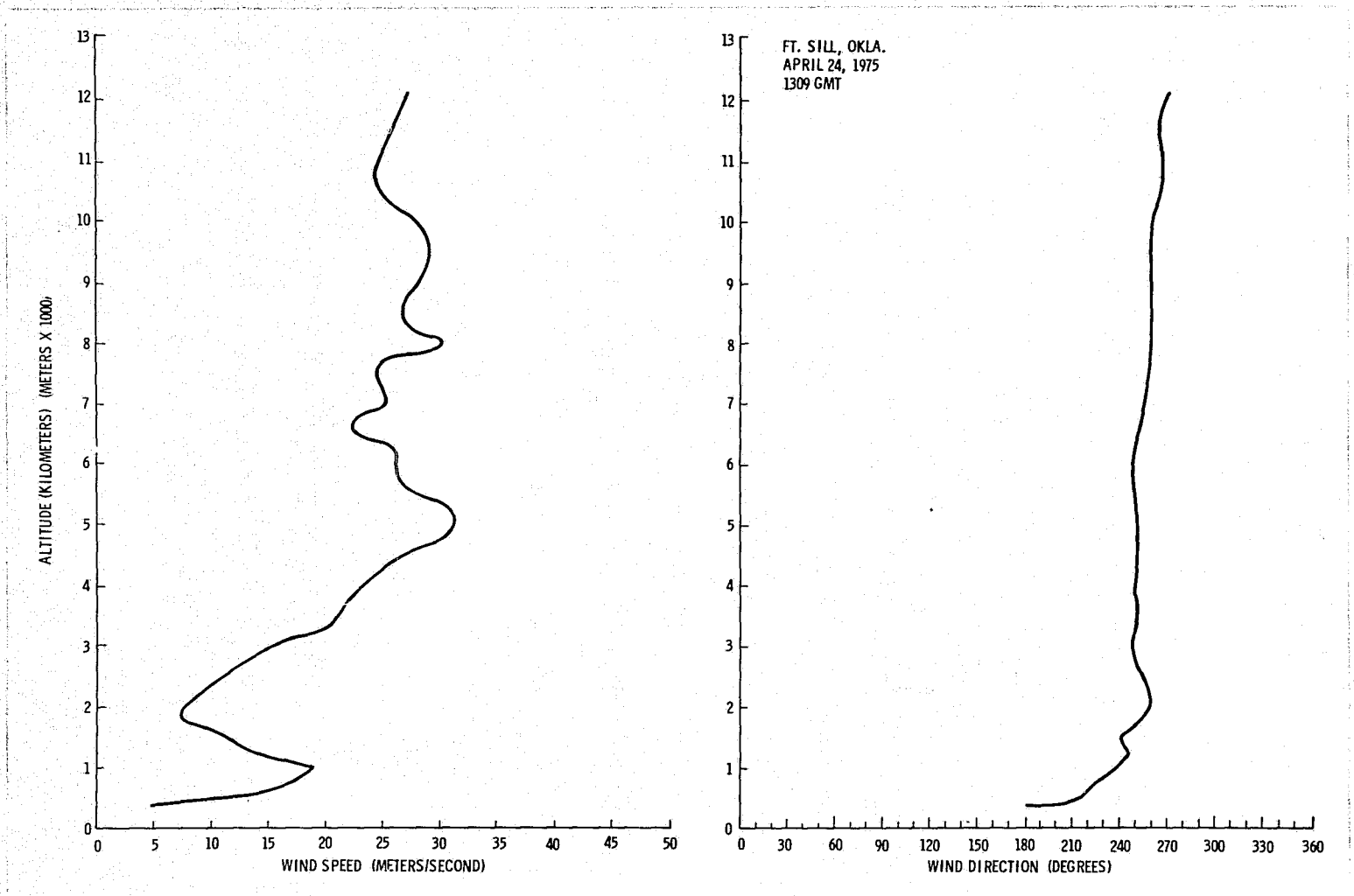

Figure A.45. Vertical wind profile for 1309 GMT, April 24, 1975, over Fort Sill, Oklahoma.

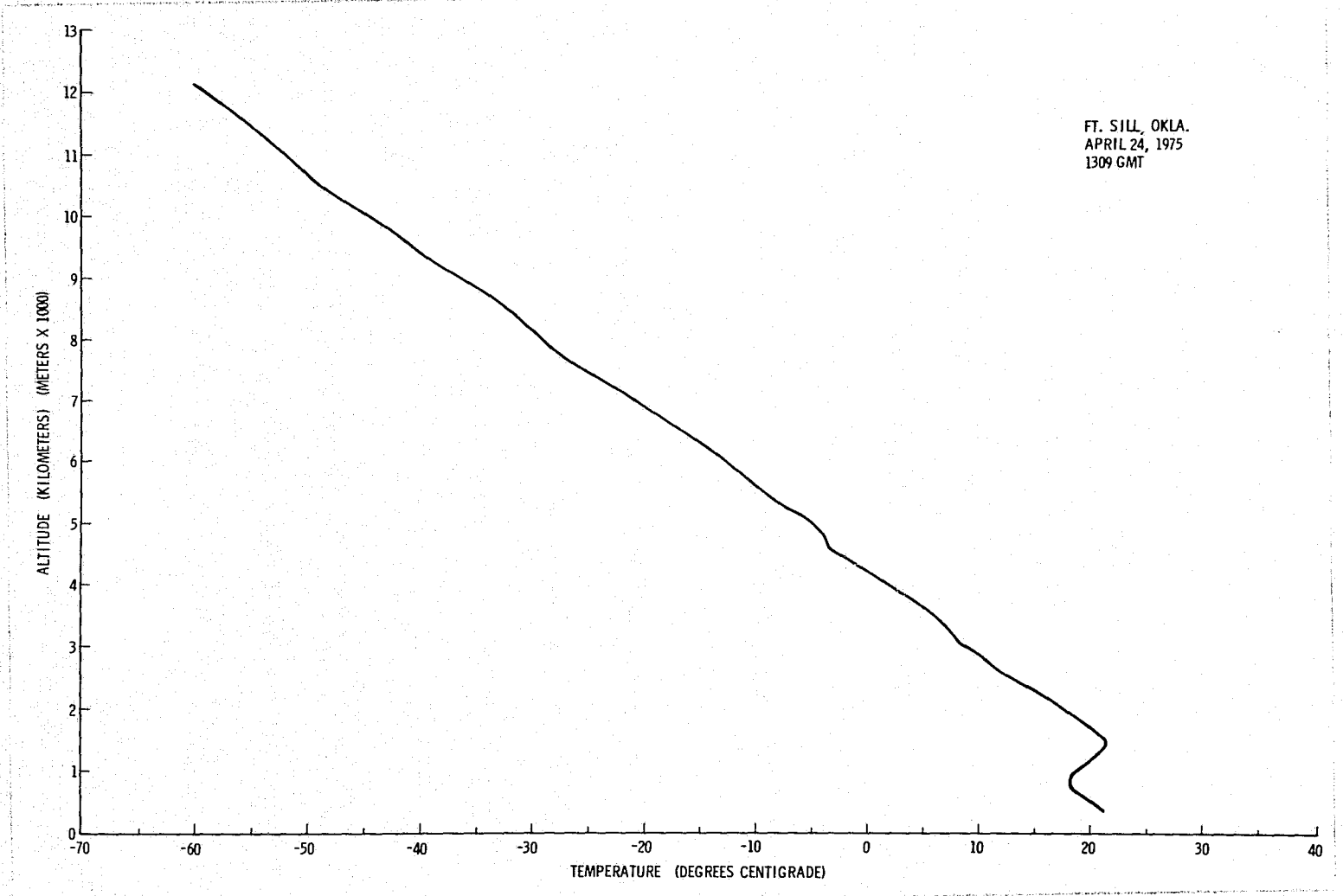

Figure A.46. Temperature profile for 1309 GMT, April 24, 1975, over Fort Sill, Oklahoma.

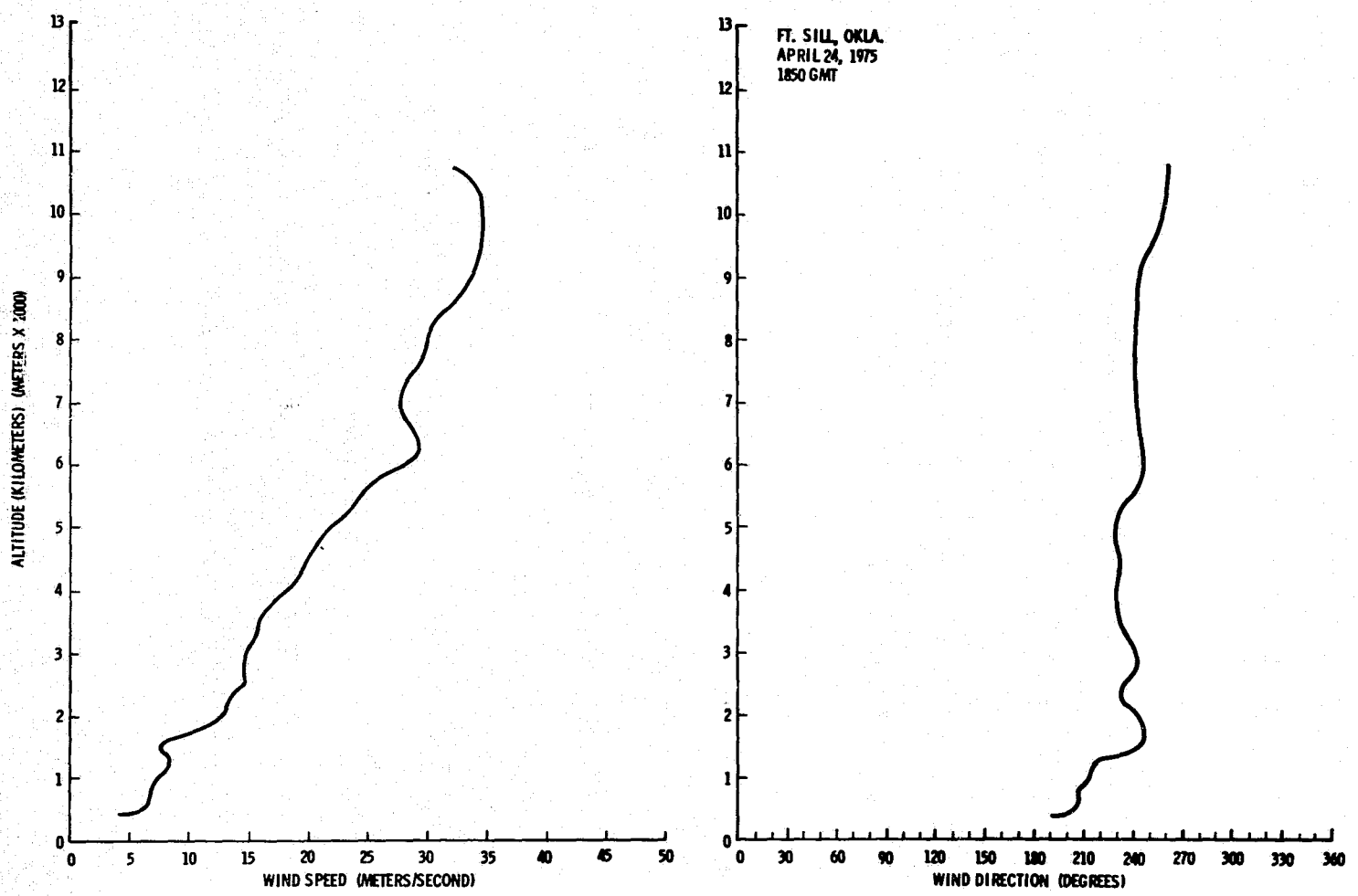

Figure A.47. Vertical wind profile for 1850 GMT, April 24, 1975, over Fort Sill, Oklahoma.

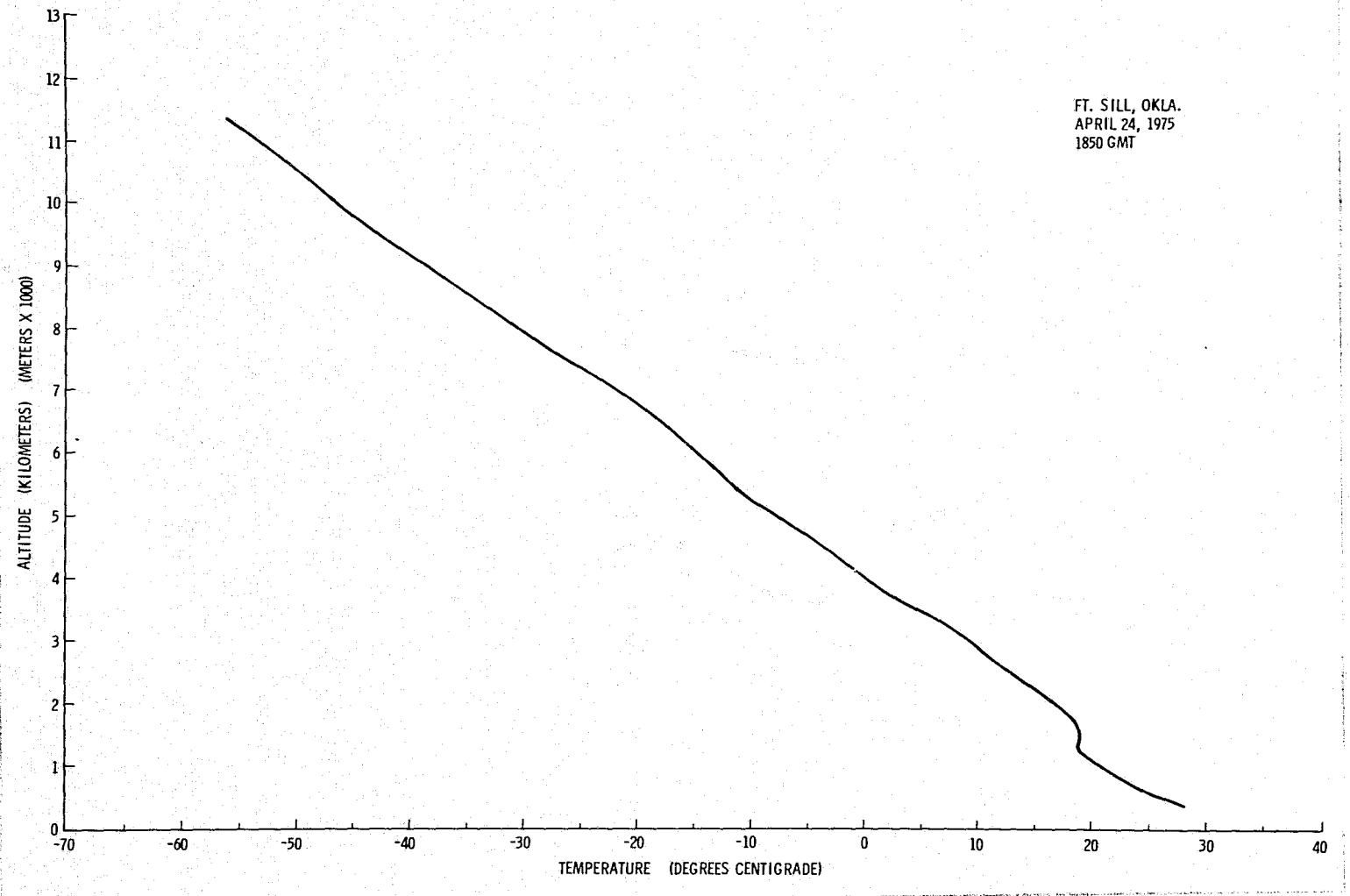

Figure A.48. Temperature profile for 1850 GMT, April 24, 1975, over Fort Sill, Oklahoma.

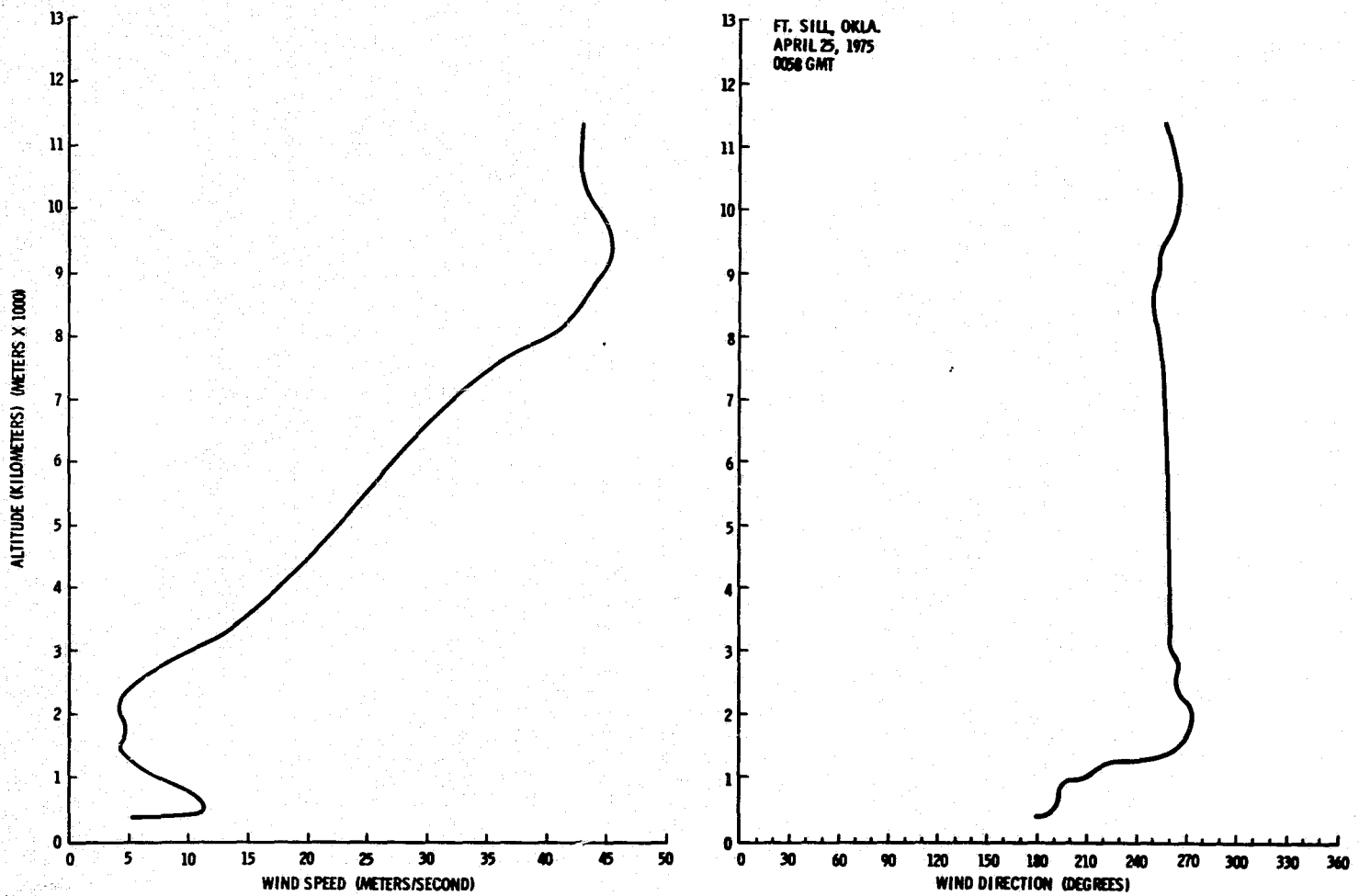

Figure A.49. Vertical wind profile for 0058 GMT, April 25, 1975, over Fort Sill, Oklahoma.

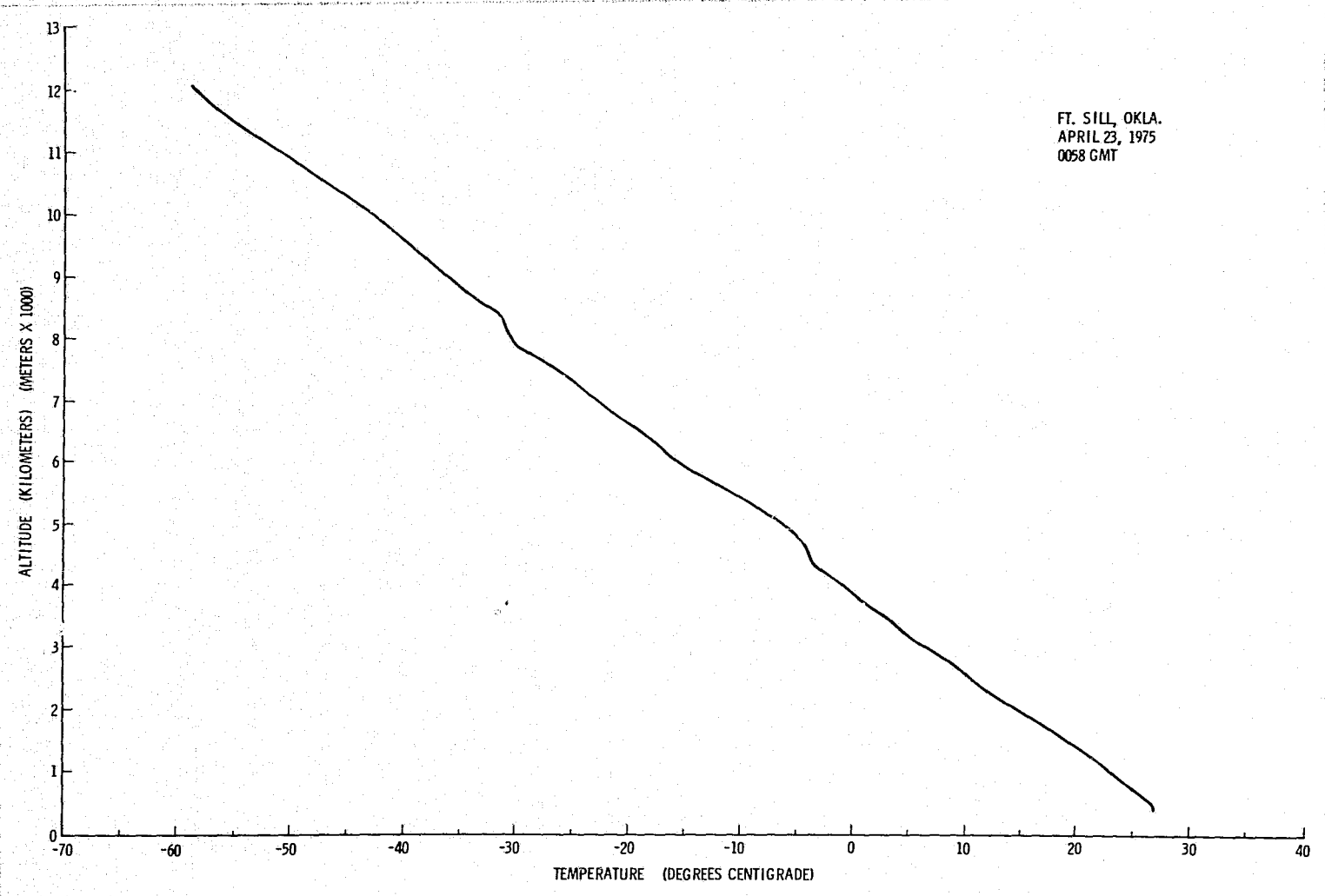

Figure A.50. Temperature profile for 0058 GMT, April 23, 1975, over Fort Sill, Oklahoma.

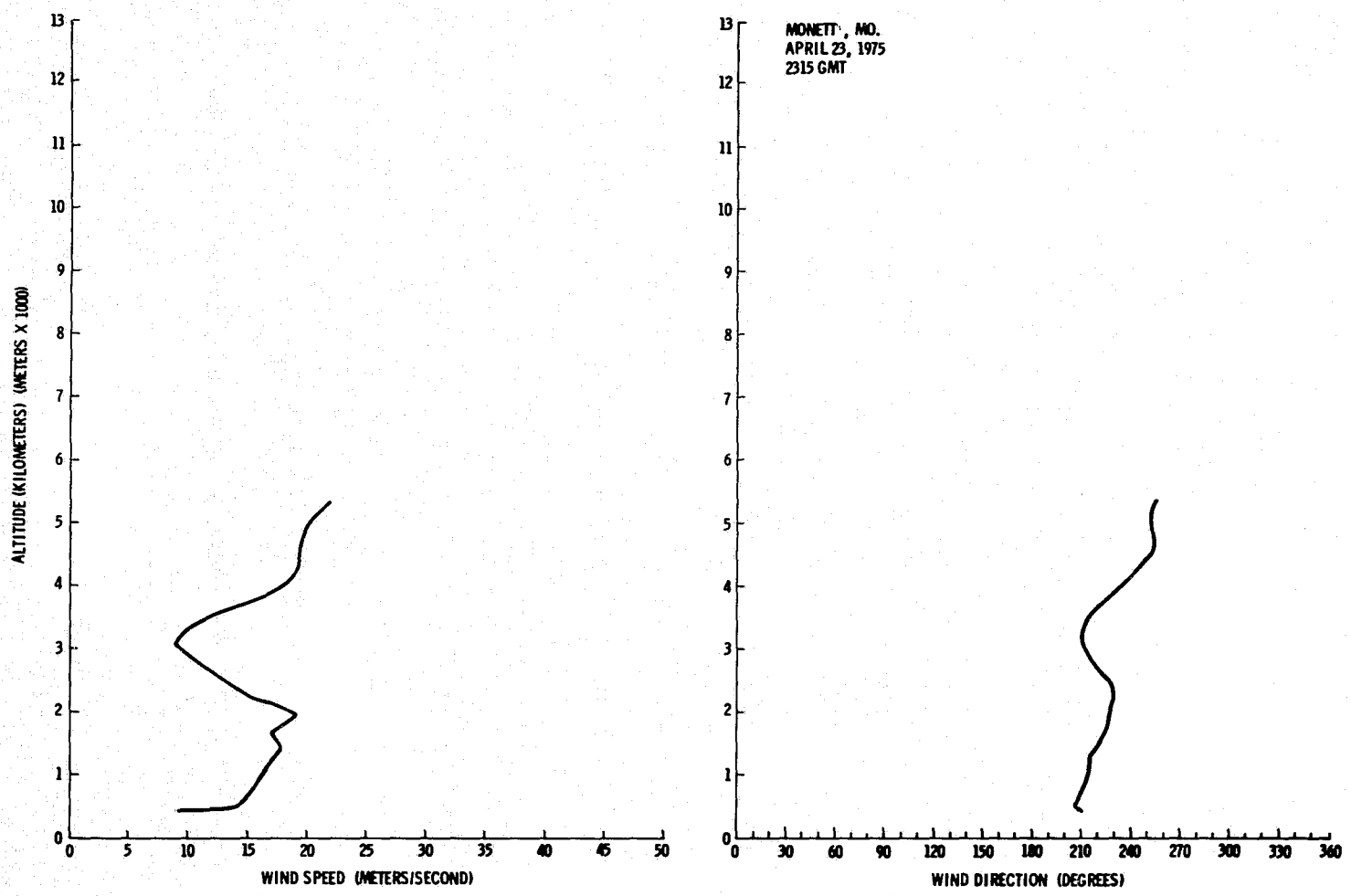

Figure A.51. Vertical wind profile for 2315 GMT, April 23, 1975, over Monett, Missouri.

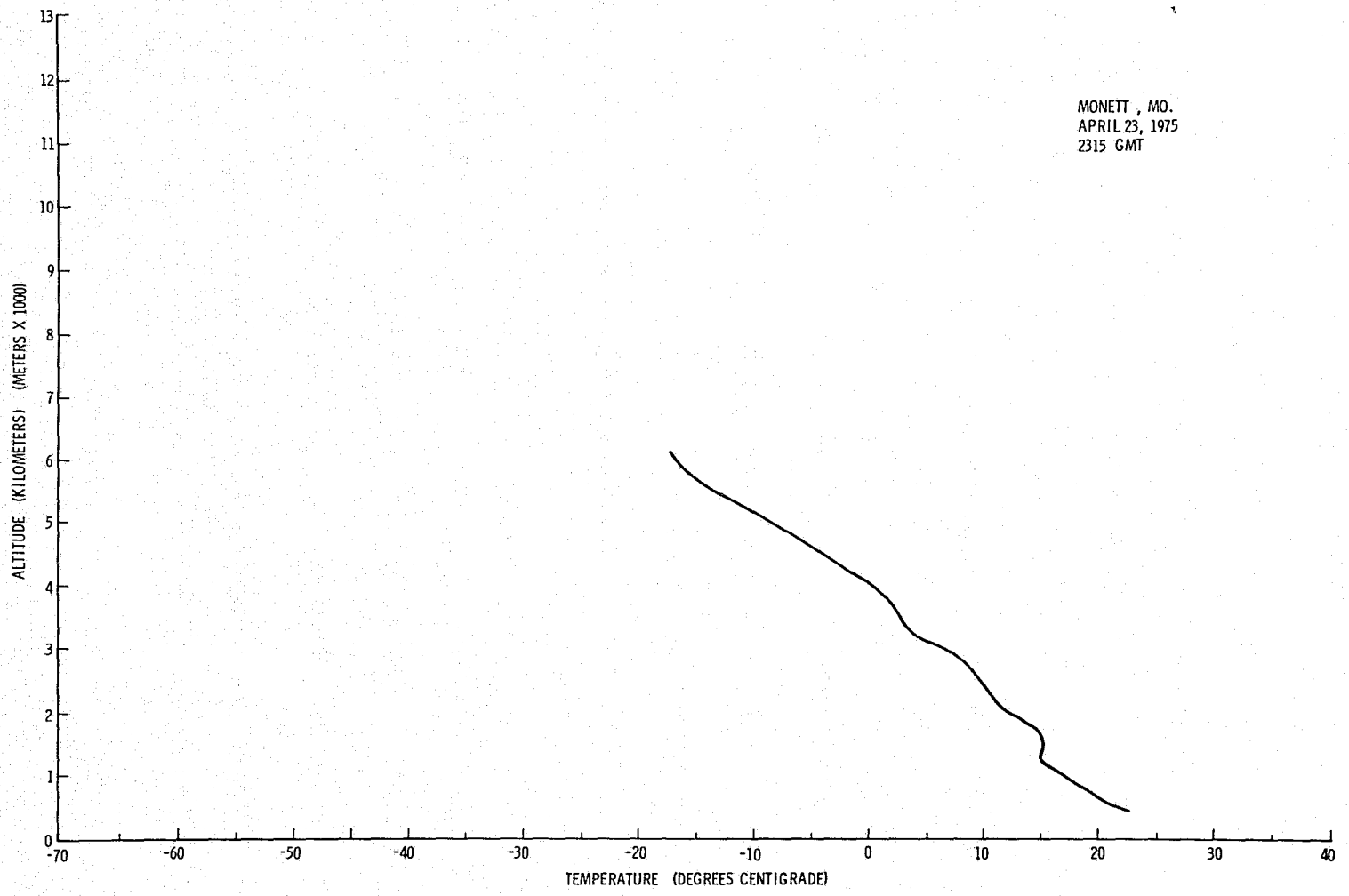

Figure A.52. Temperature profile for 2315 GMT, April 23, 1975, over Monett, Missouri.

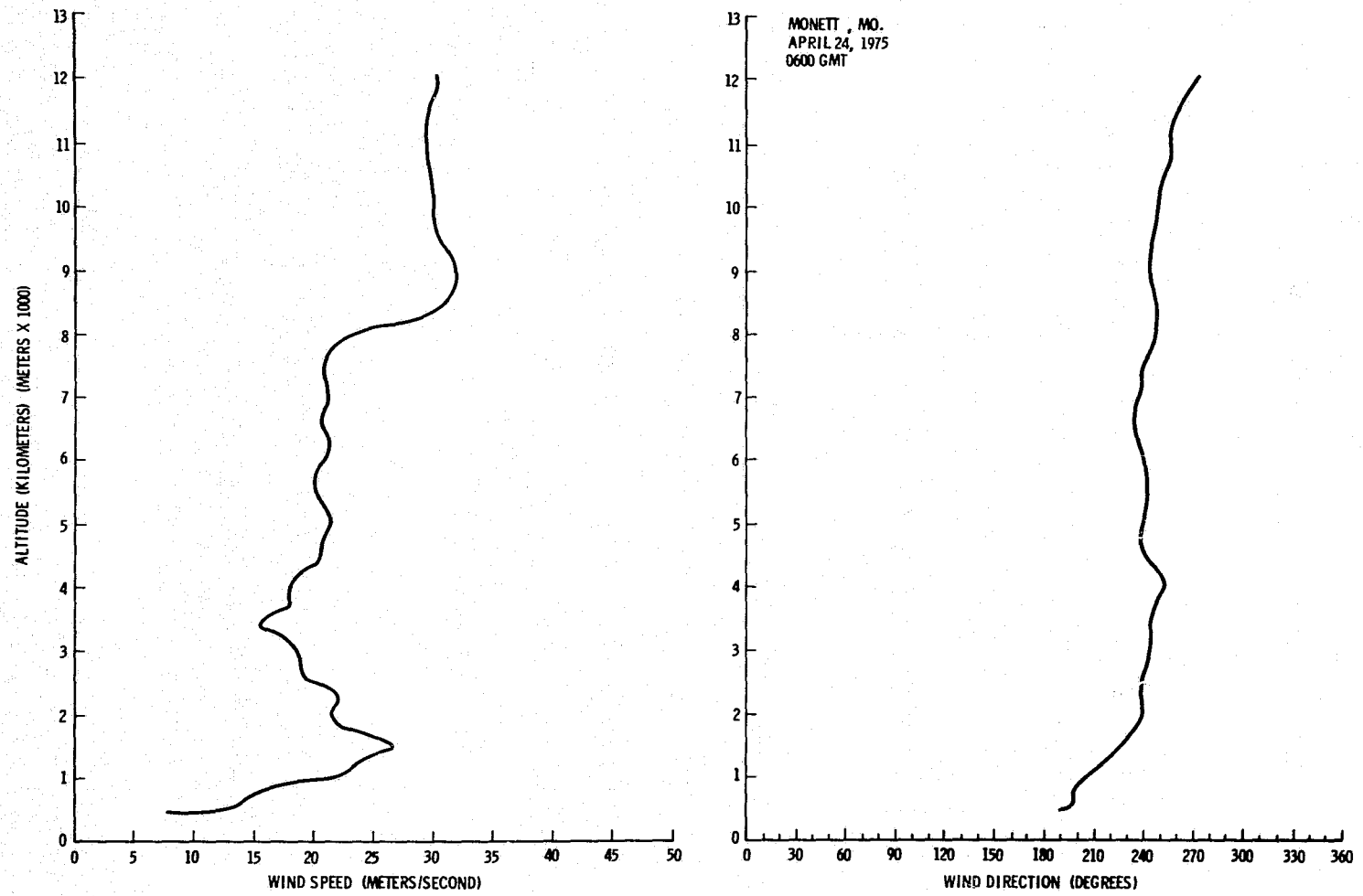

Figure A.53. Vertical wind profile for 0600 GMT, April 24, 1975, over Monett, Missouri.

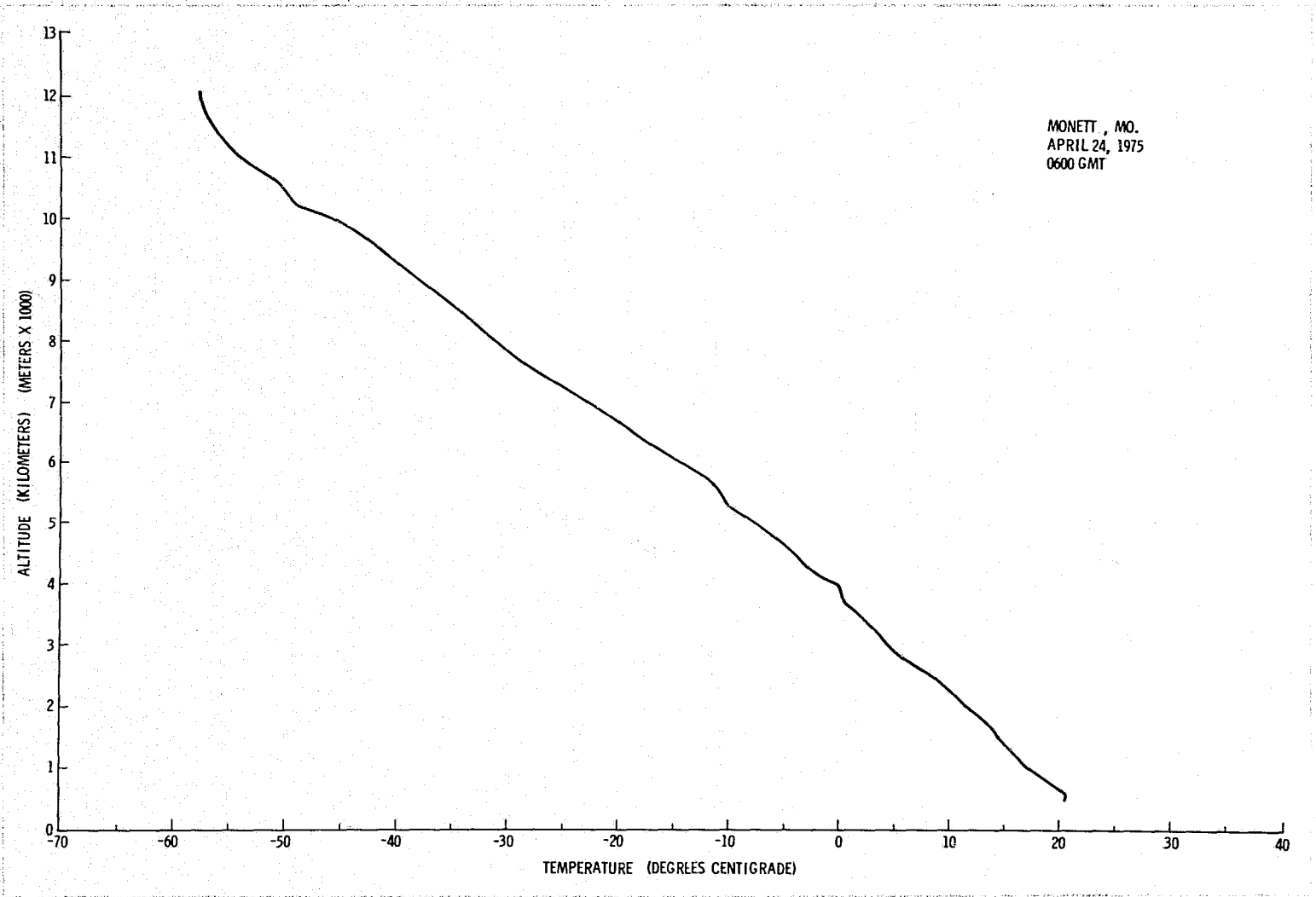

Figure A.54. Temperature profile for 0600 GMT, April 24, 1975, over Monett, Missouri.

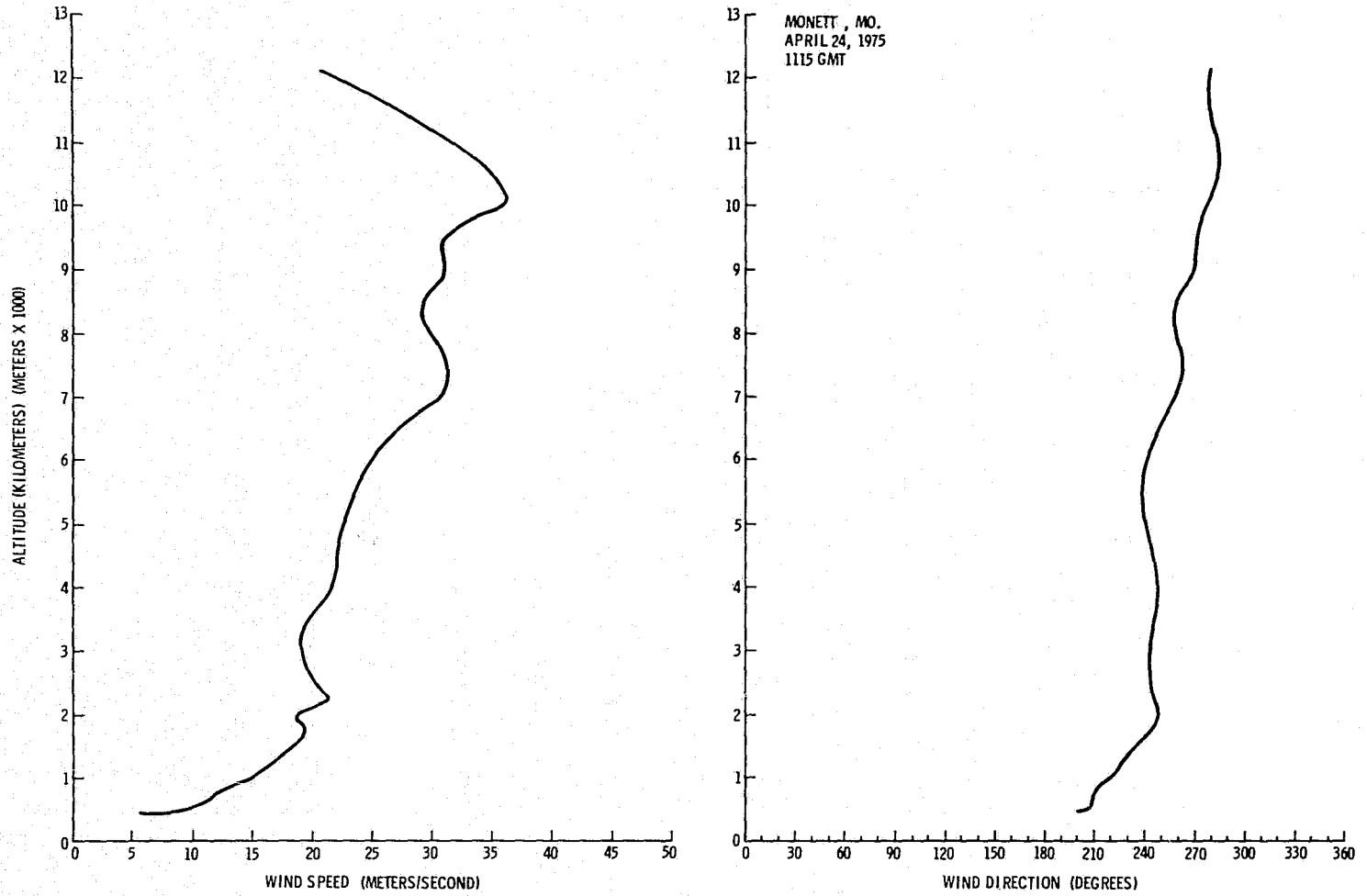

Figure A.55. Vertical wind profile for 1115 GMT, April 24, 1975, over Monett, Missouri.

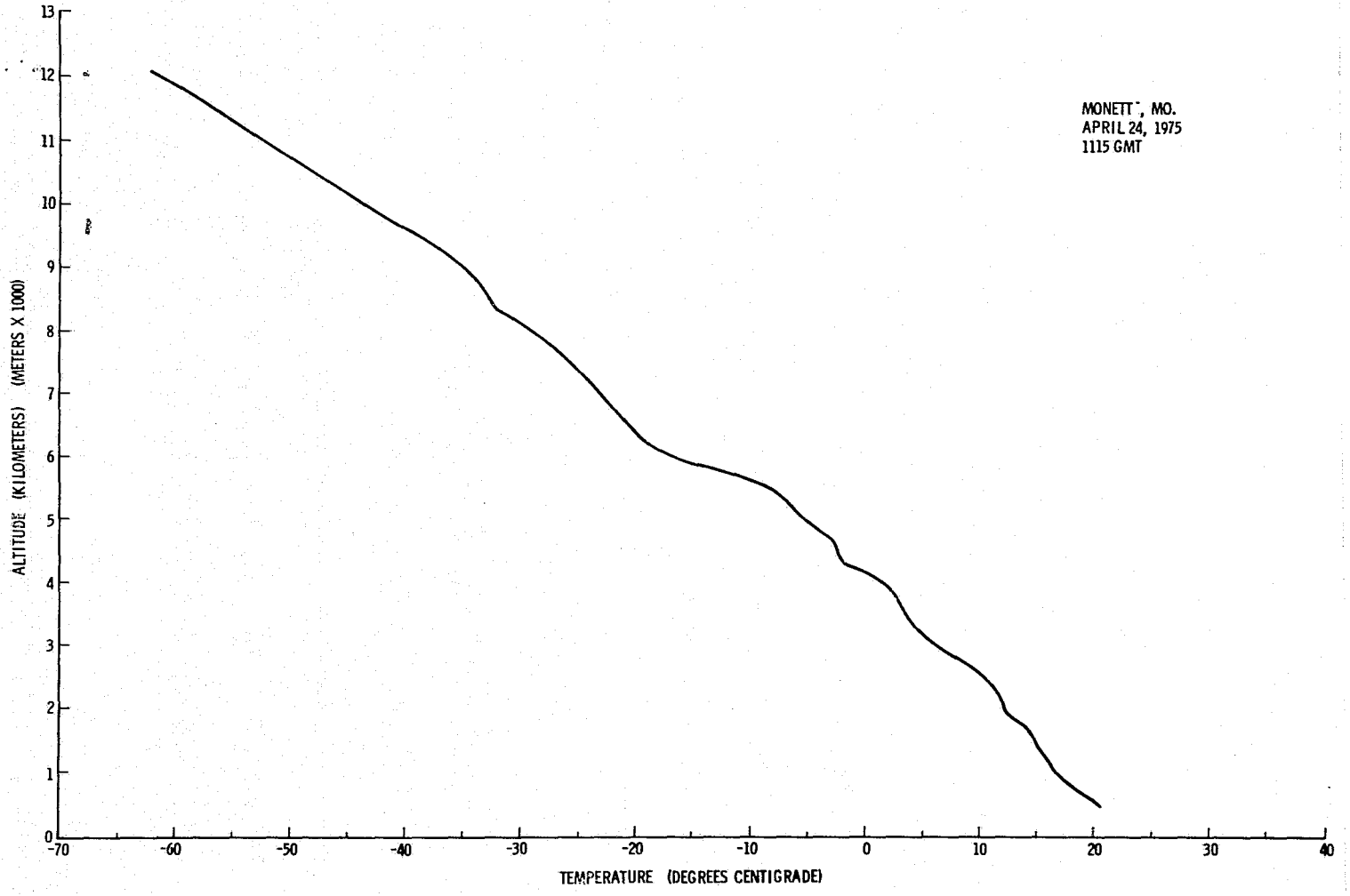

Figure A.56. Temperature profile for 1115 GMT, April 24, 1975, over Monett, Missouri.

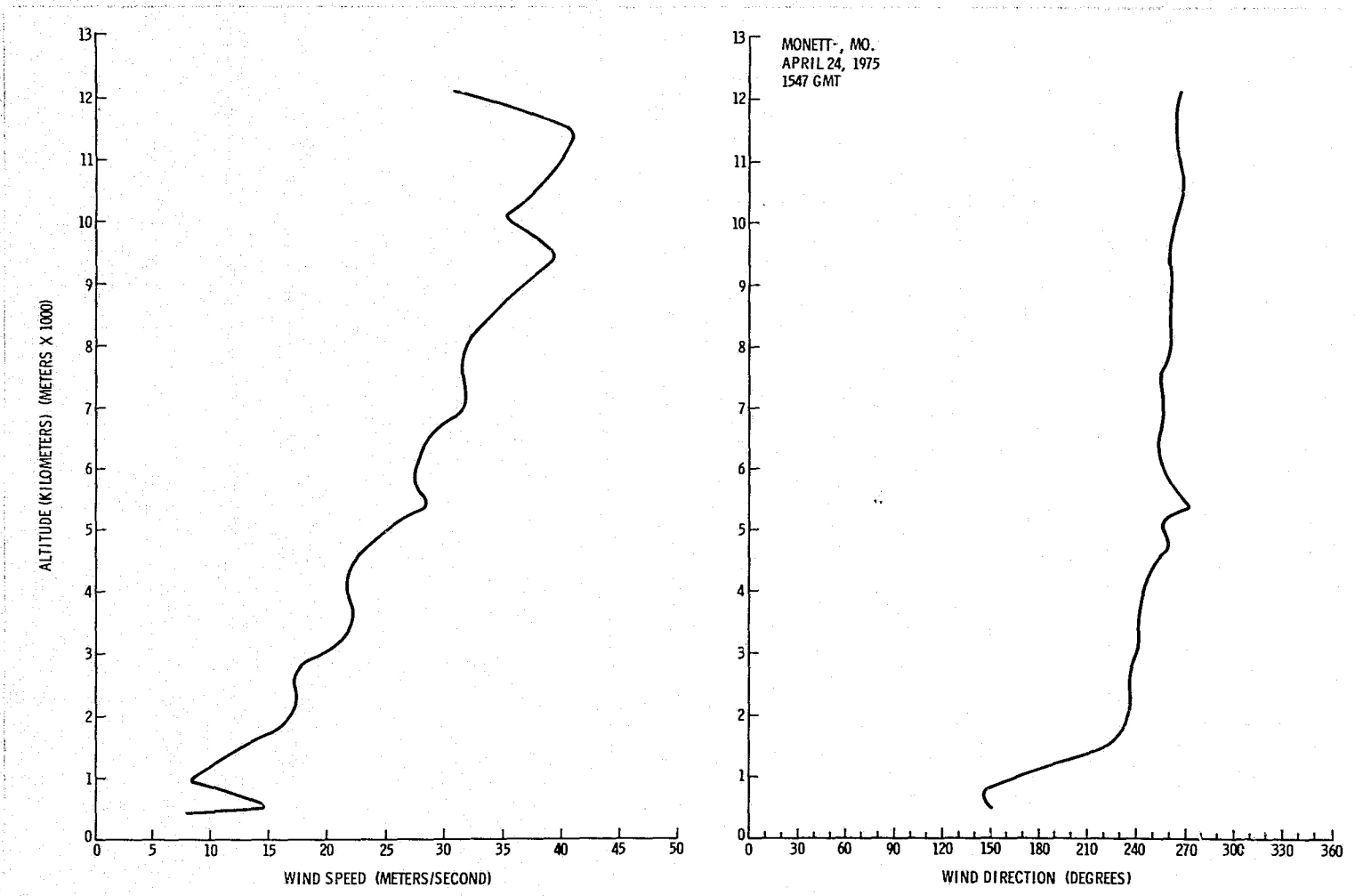

Figure A.57. Vertical wind profile for 1547 GMT, April 24, 1975, over Monett, Missouri.

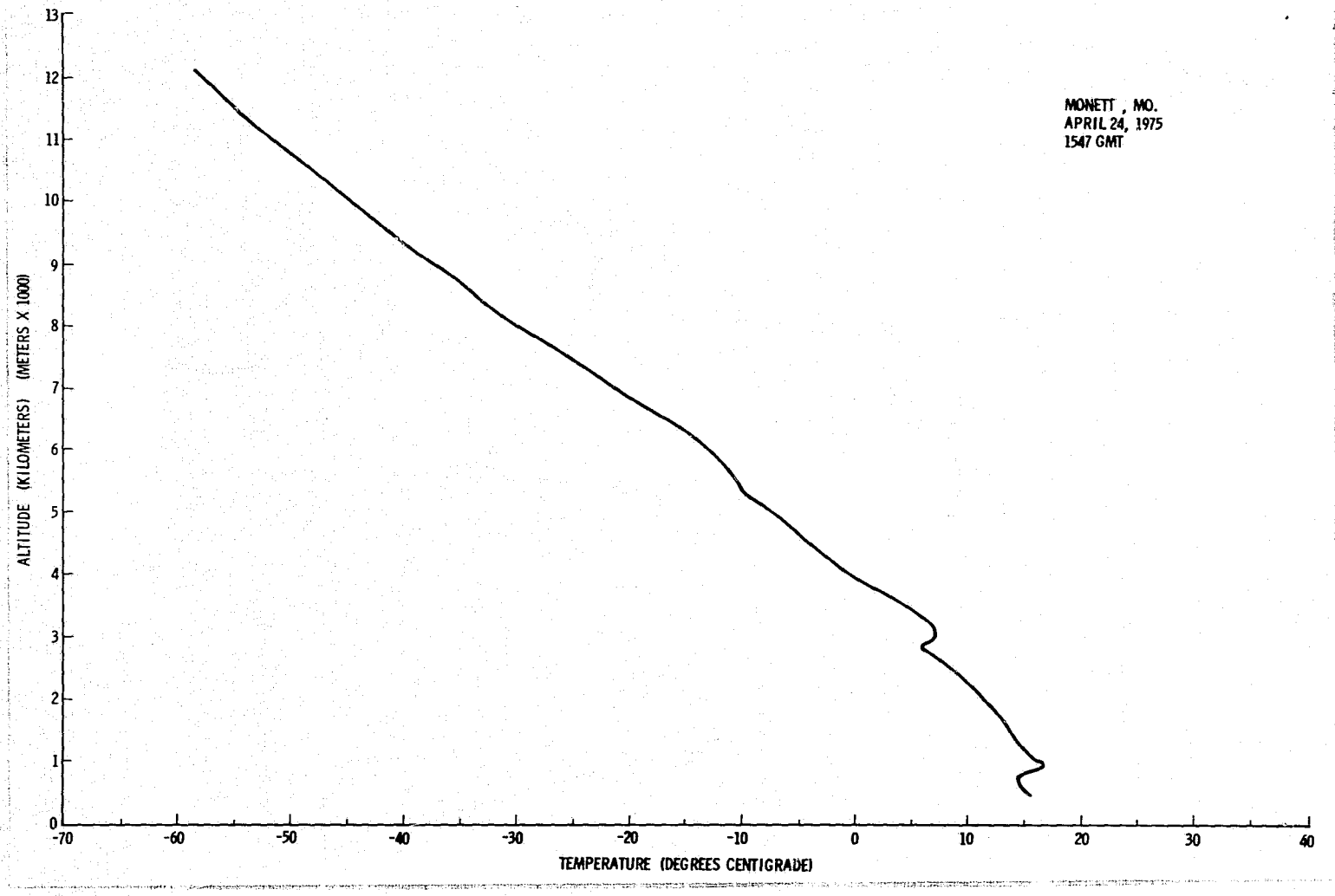

Figure A.58. Temperature profile for 1547 GMT, April 24, 1975, over Monett, Missouri.

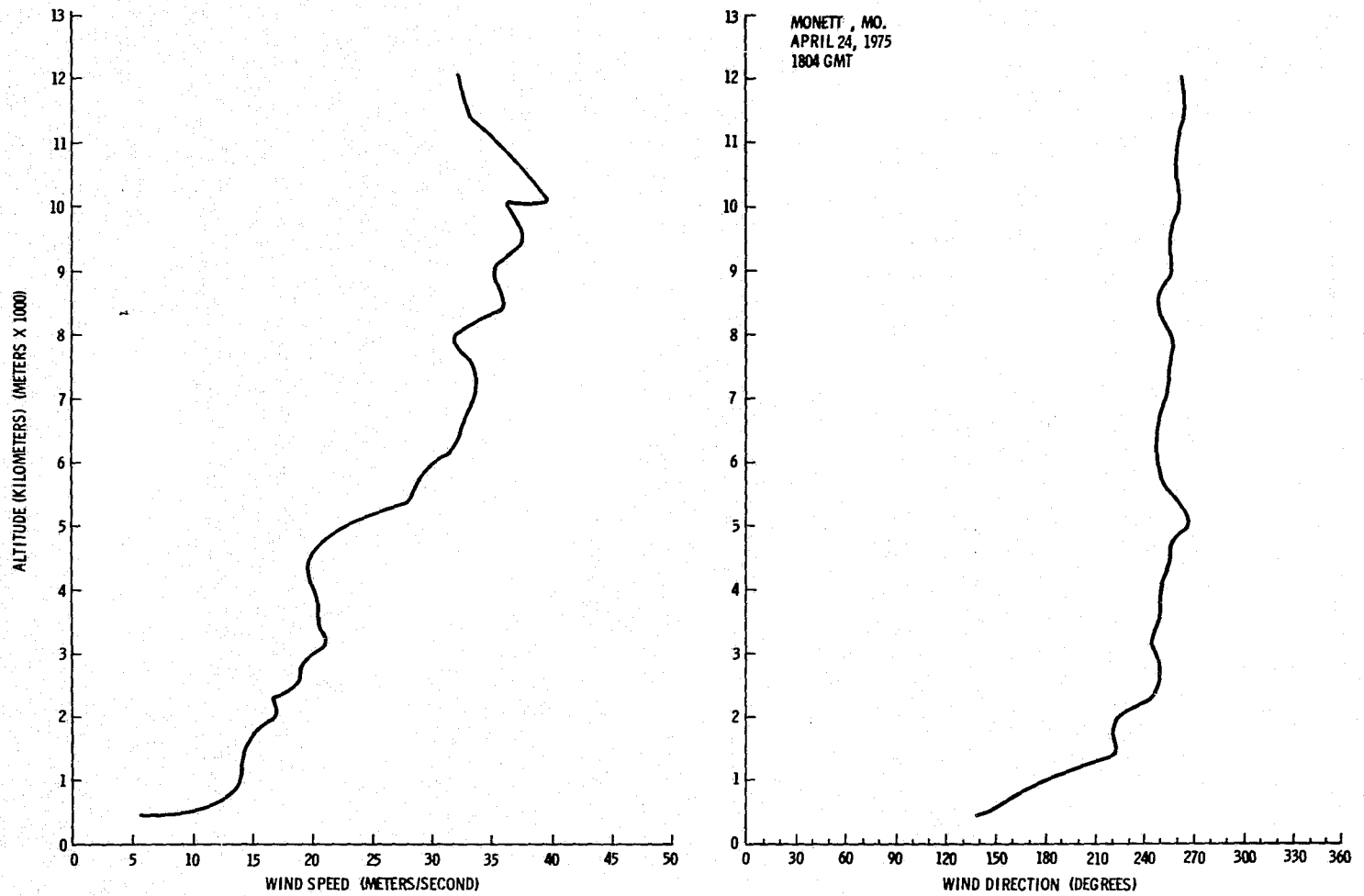

Figure A.59. Vertical wind profile for 1804 GMT, April 24, 1975, over Monett, Missouri.

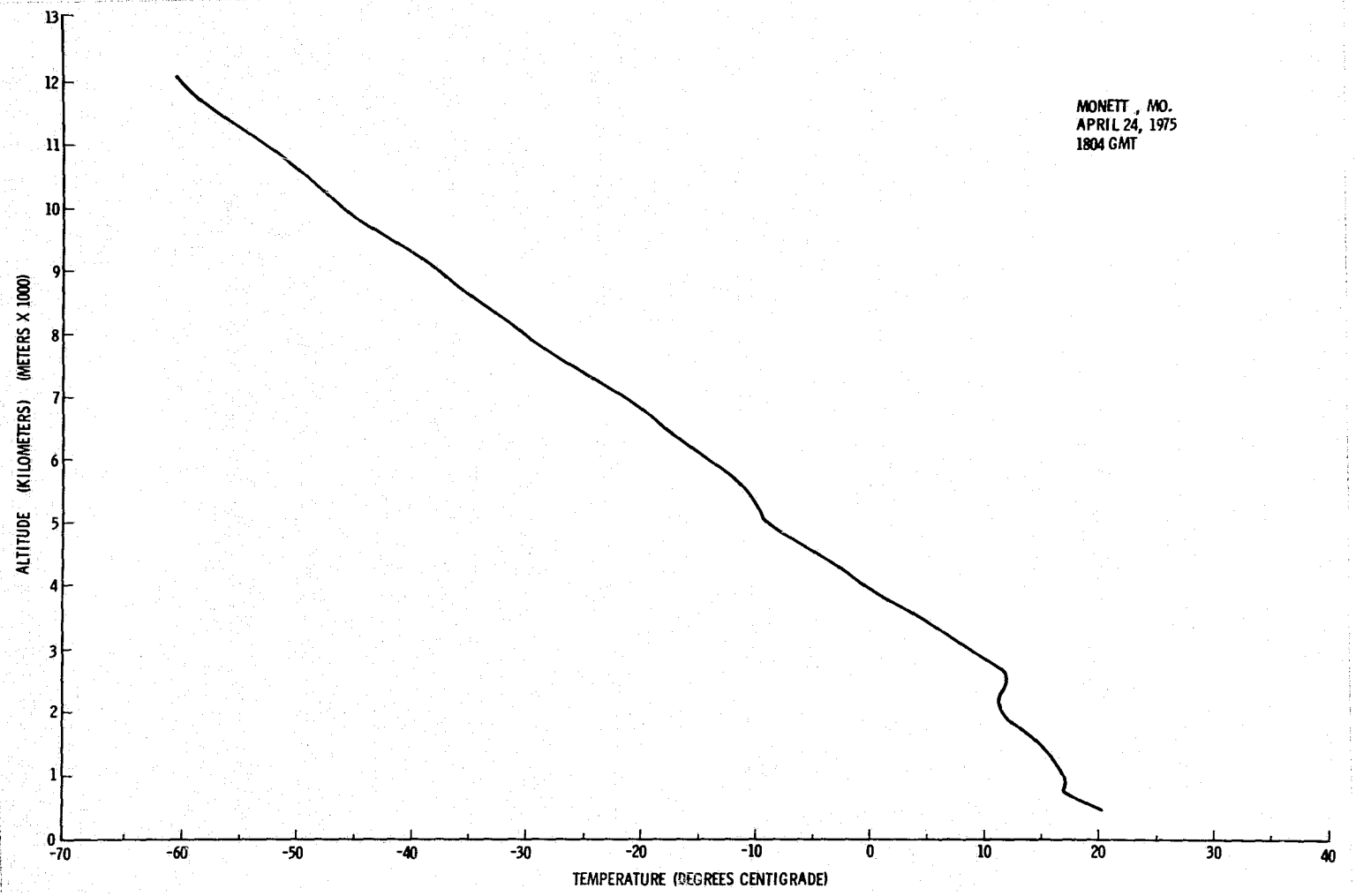

Figure A.60. Temperature profile for 1804 GMT, April 24, 1975, over Monett, Missouri.

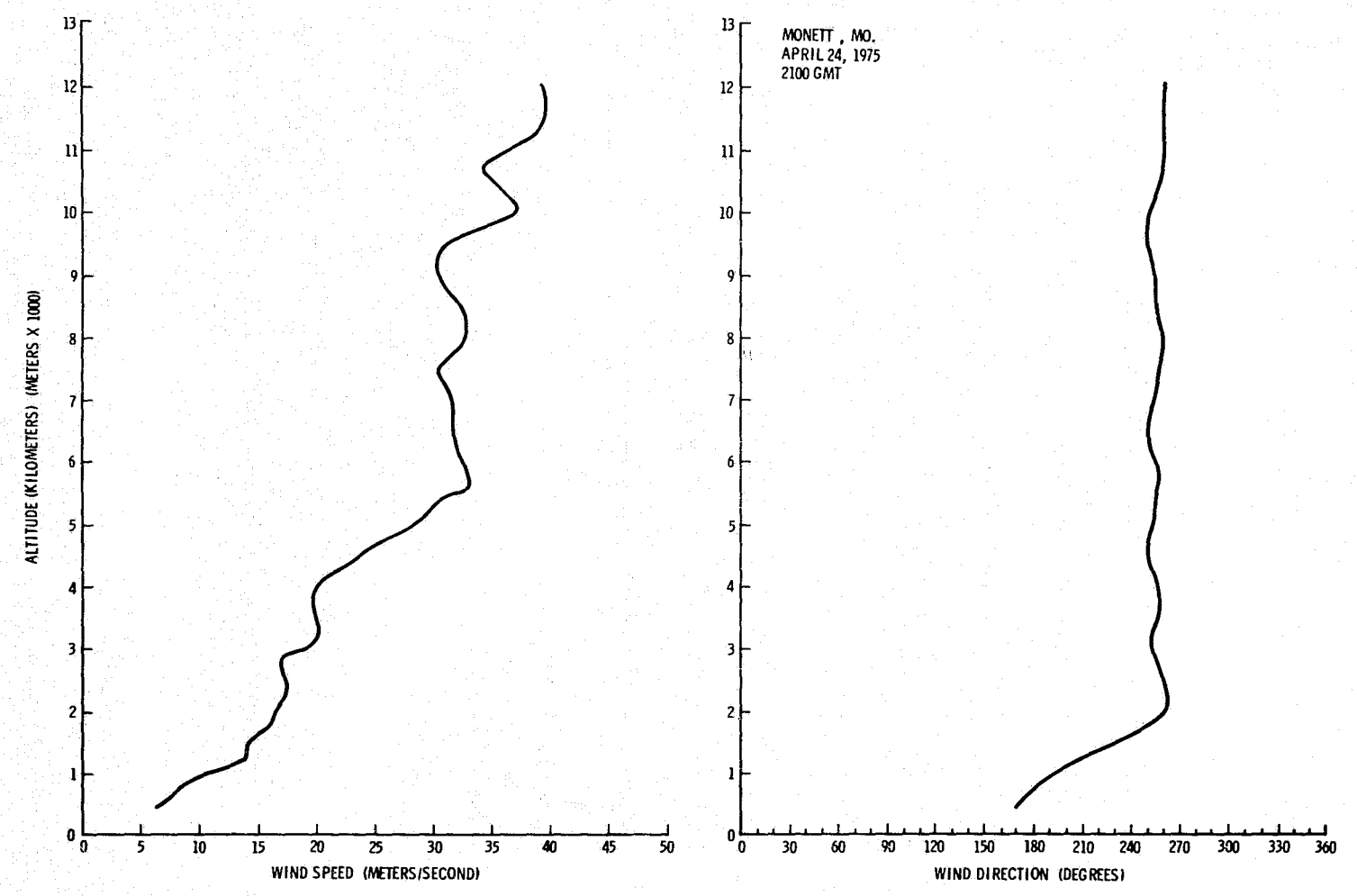

Figure A.61. Vertical wind profile for 2100 GMT, April 24, 1975, over Monett, Missouri.

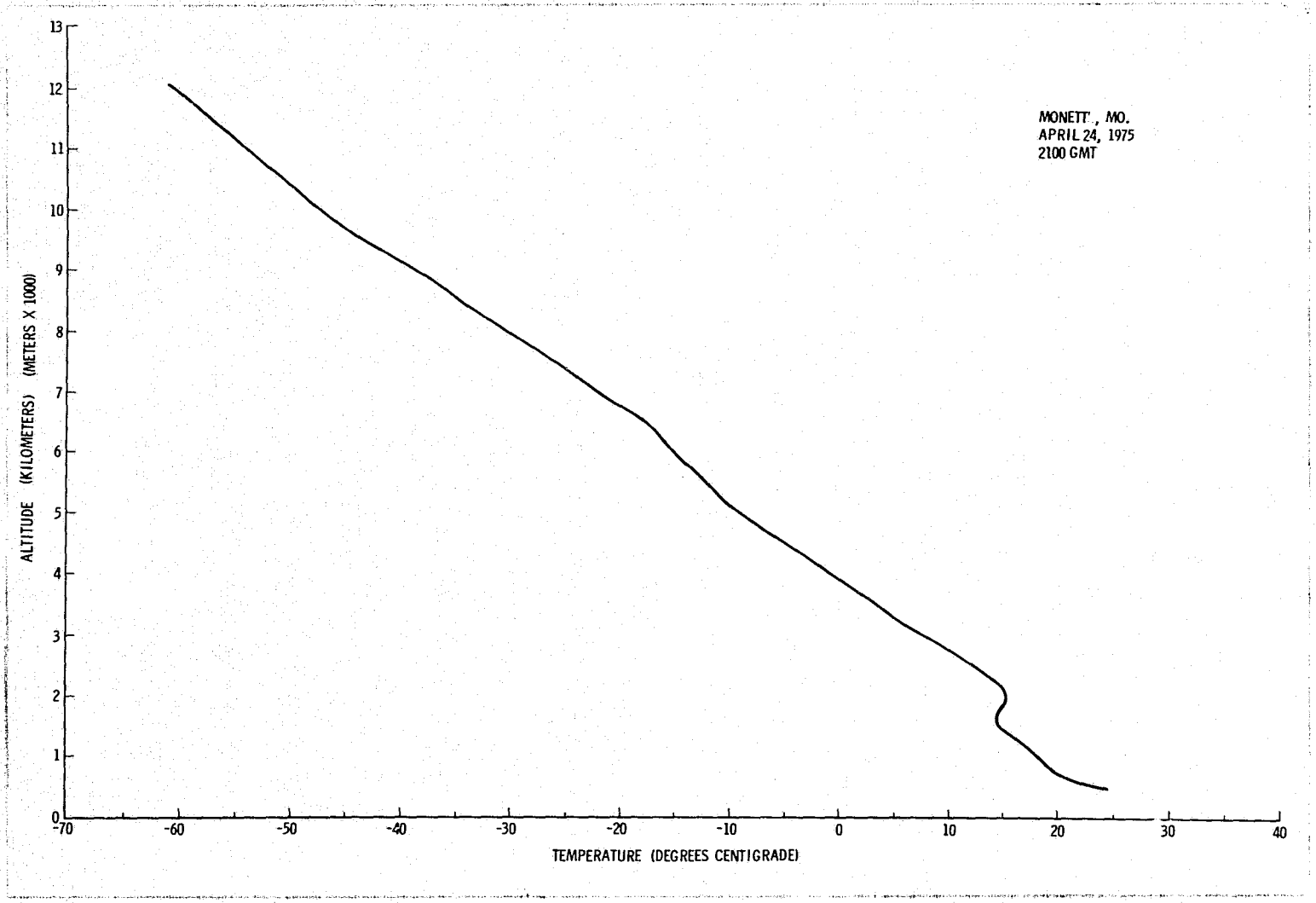

Figure A.62. Temperature profile for 2100 GMT, April 24, 1975, over Monett, Missouri.

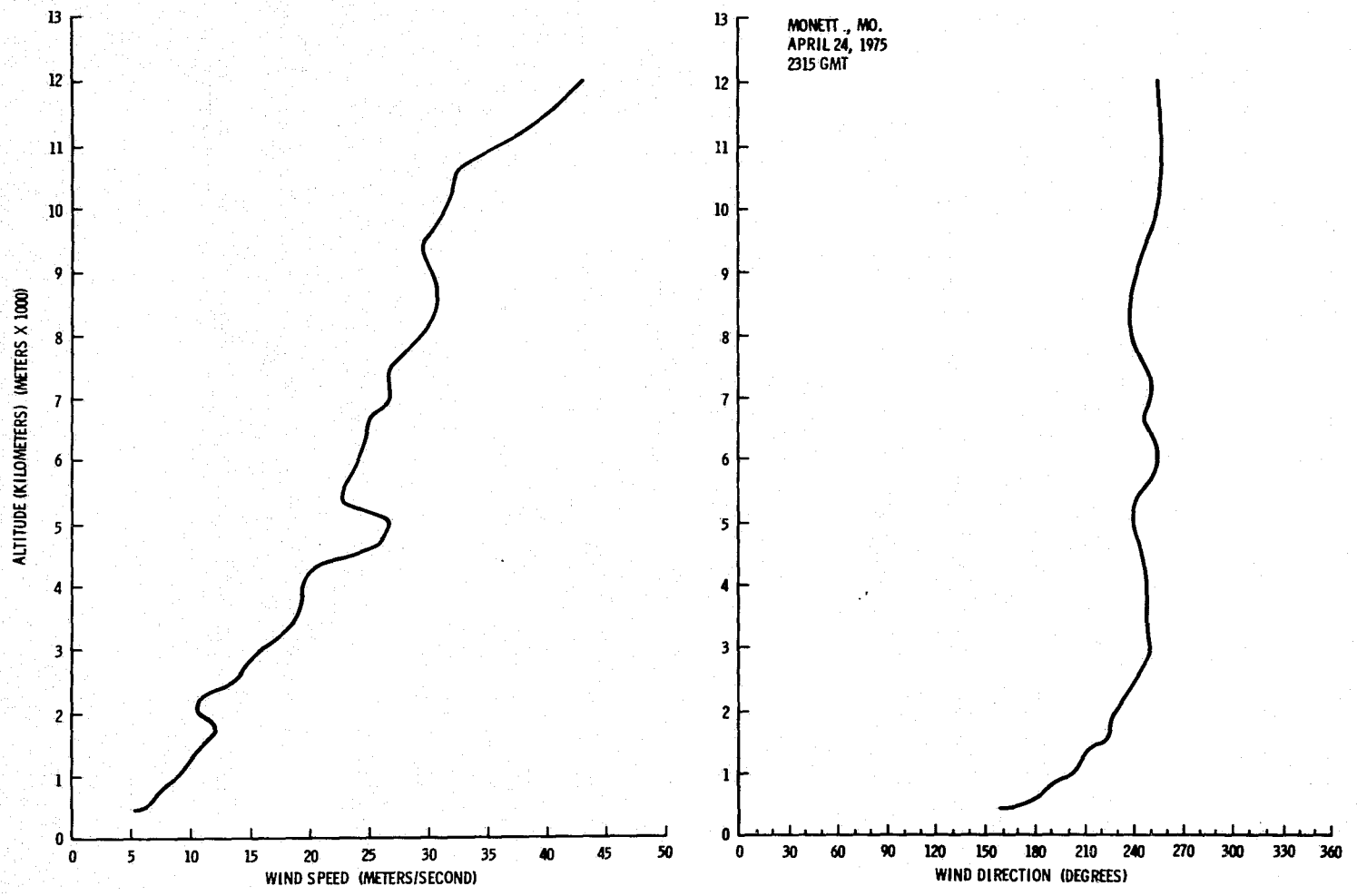

Figure A.63. Vertical wind profile for 2315 GMT, April 24, 1975, over Monett, Missouri.

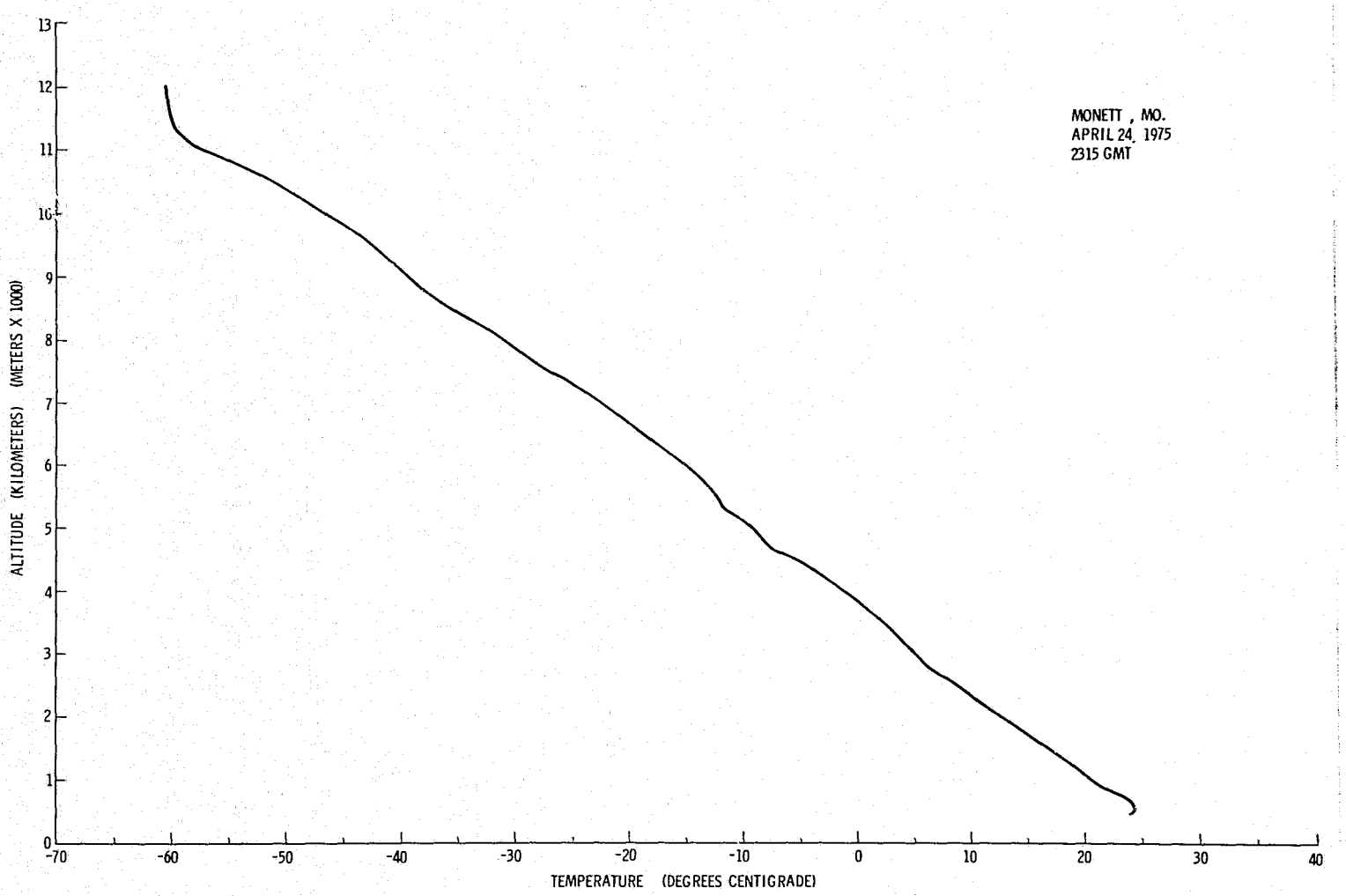

Figure A.64. Temperature profile for 2315 GMT, April 24, 1975, over Monett, Missouri.

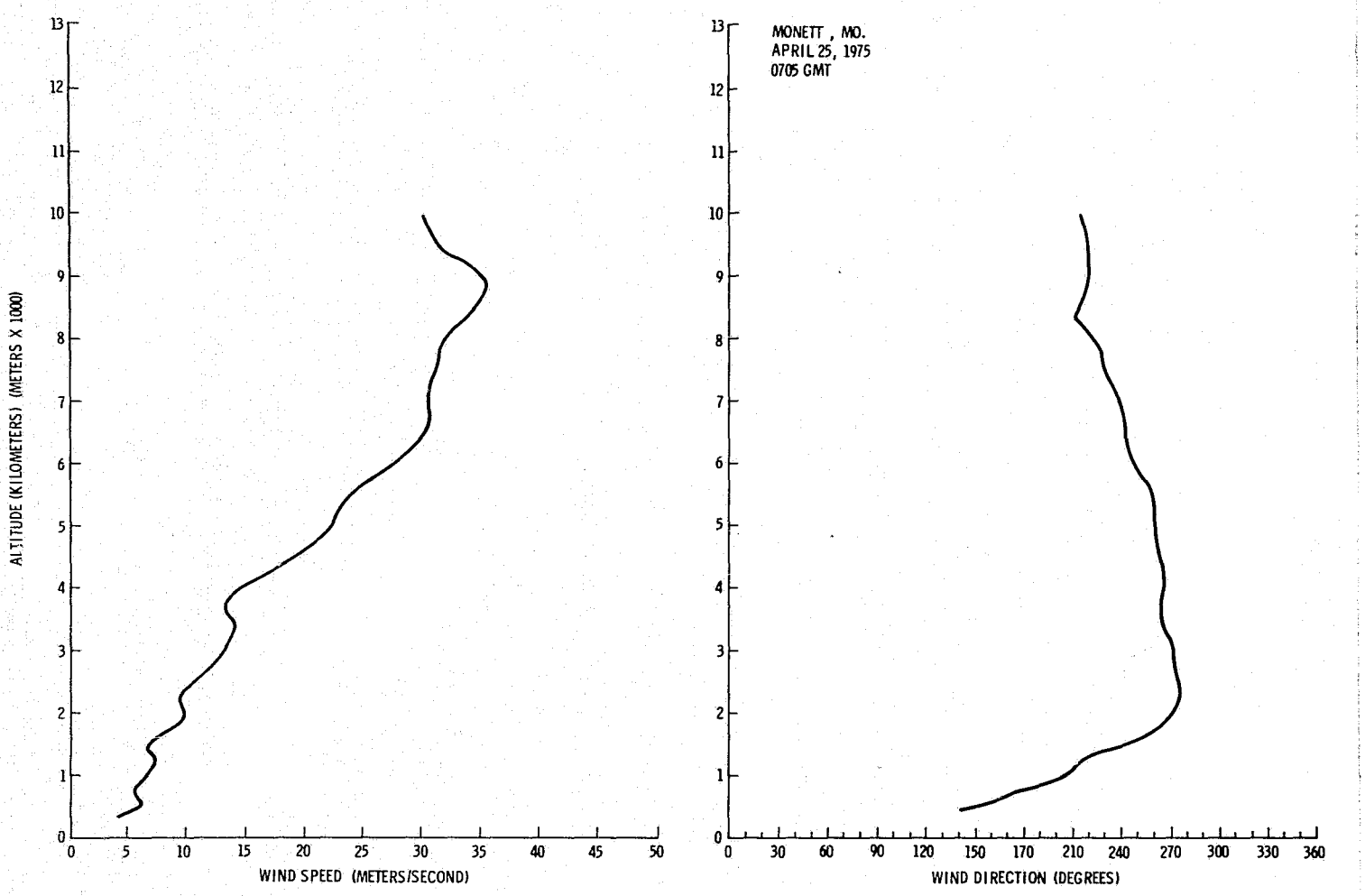

Figure A.65. Vertical wind profile for 0705 GMT, April 25, 1975, over Monett, Missouri.

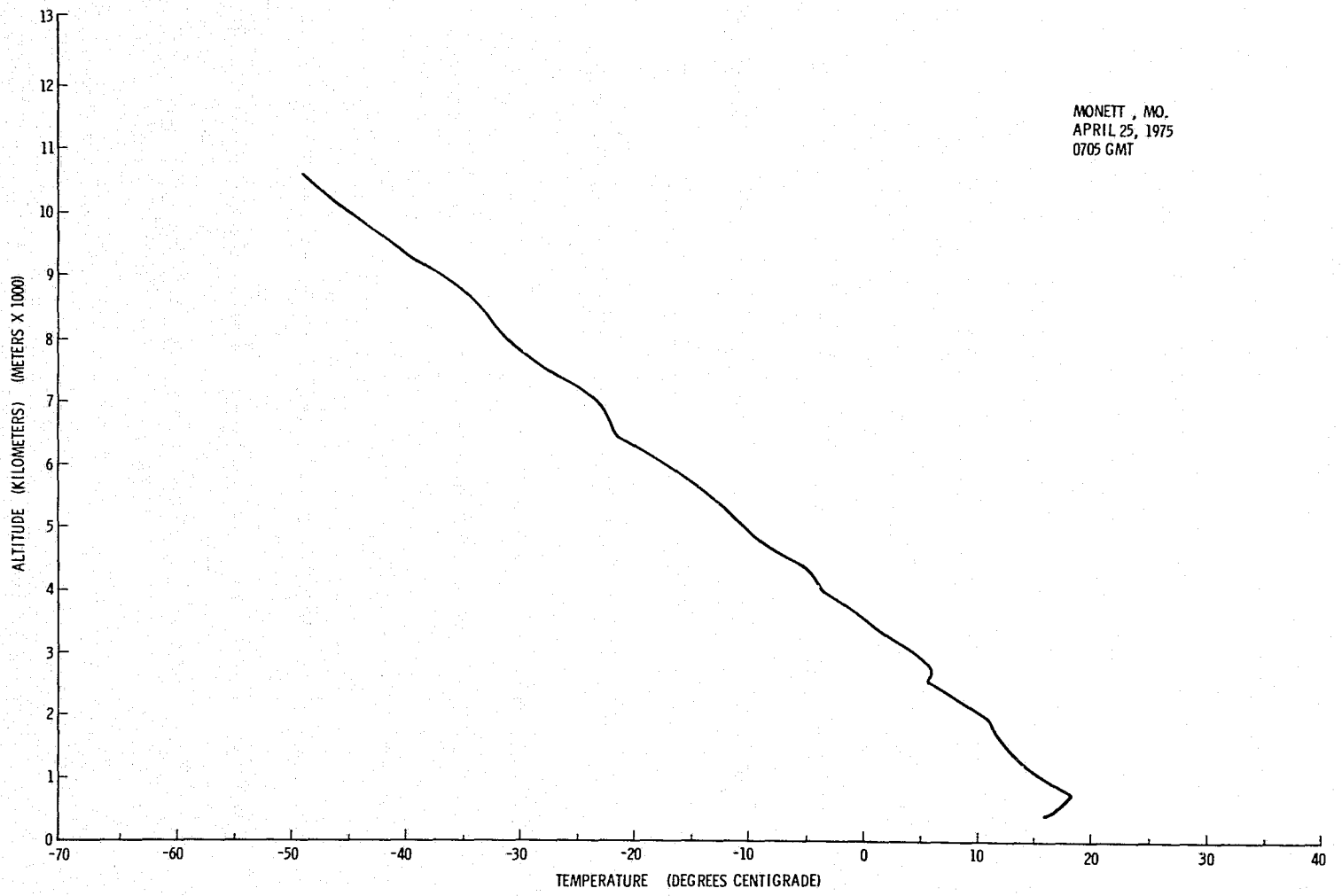

Figure A.66. Temperature profile for 0705 GMT, April 25, 1975, over Monett, Missouri.

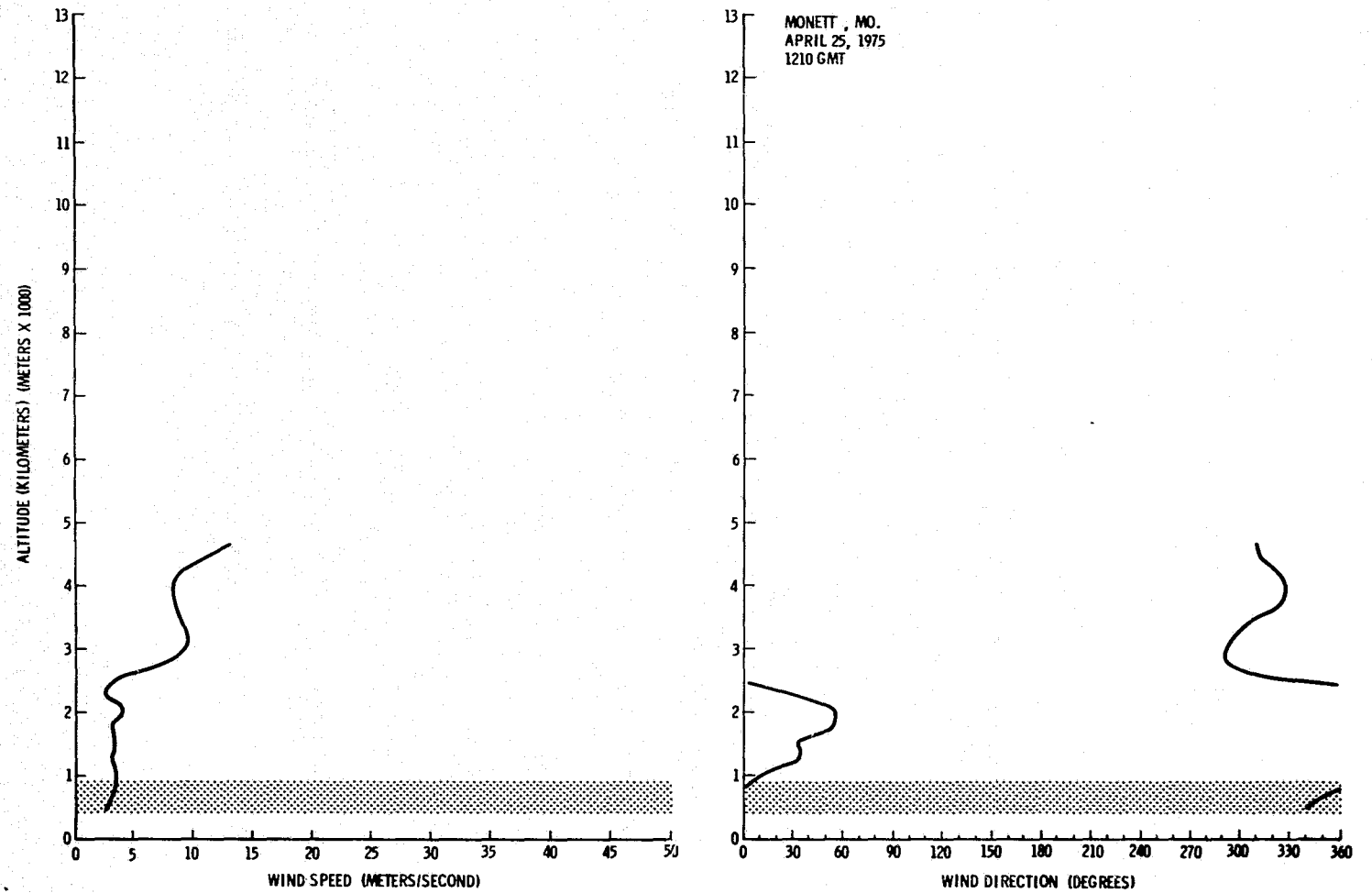

Figure A.67. Vertical wind profile for 1210 GMT, April 25, 1975, over Monett, Missouri.

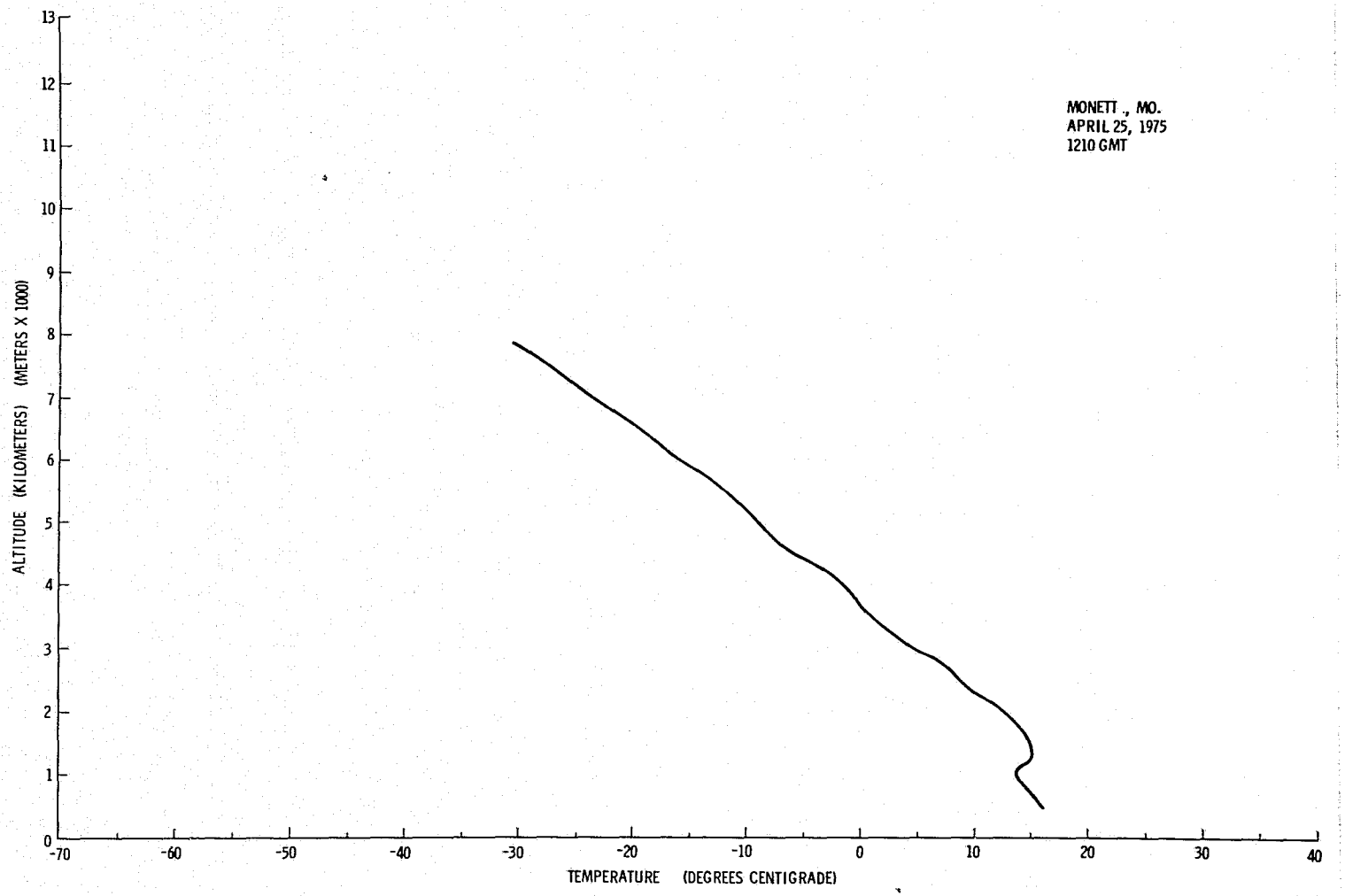

Figure A.68. Temperature profile for 1210 GMT, April 25, 1975, over Monett, Missouri.

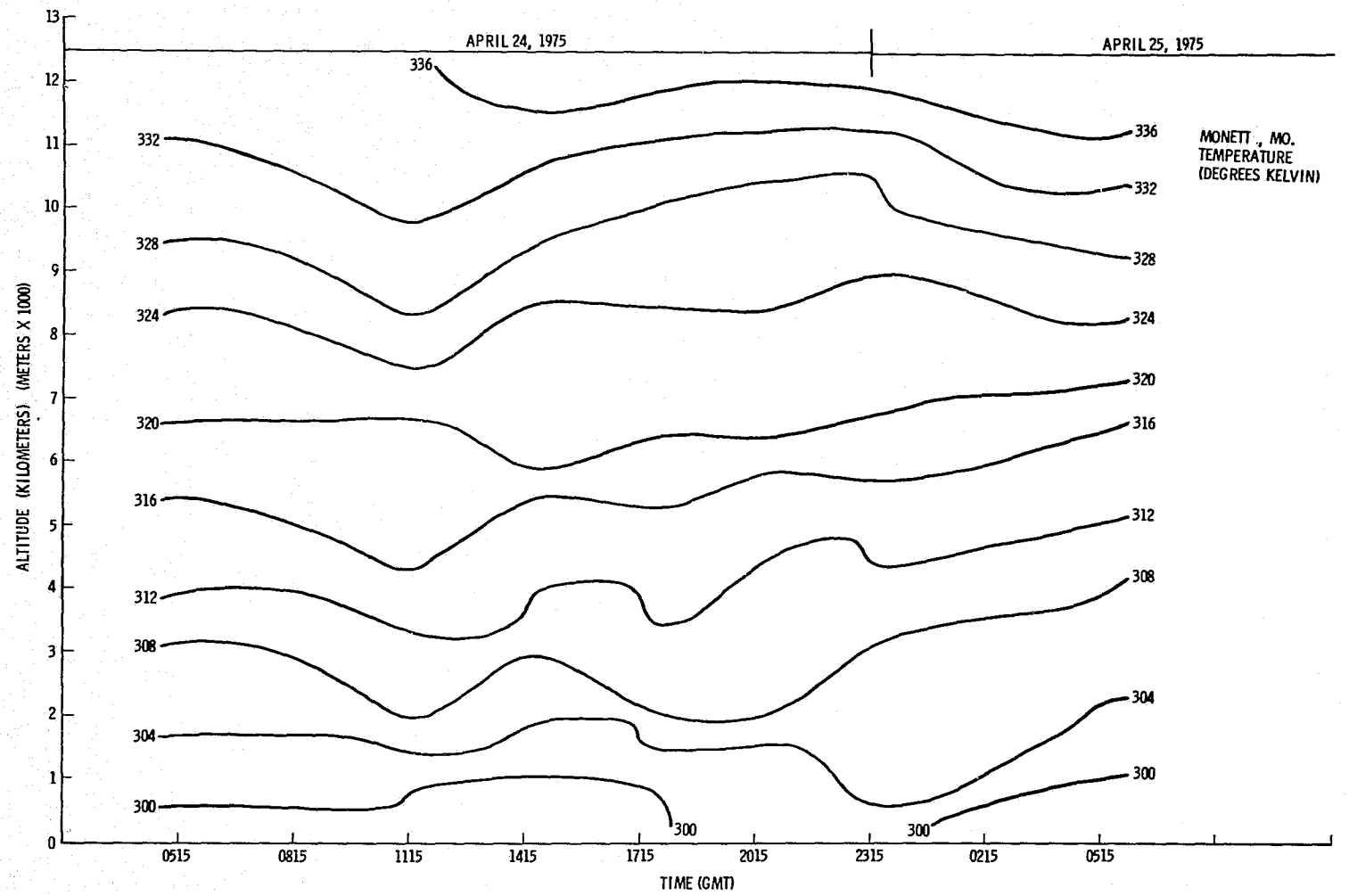

Figure A.69. Time cross section of temperature at Monett, Missouri.

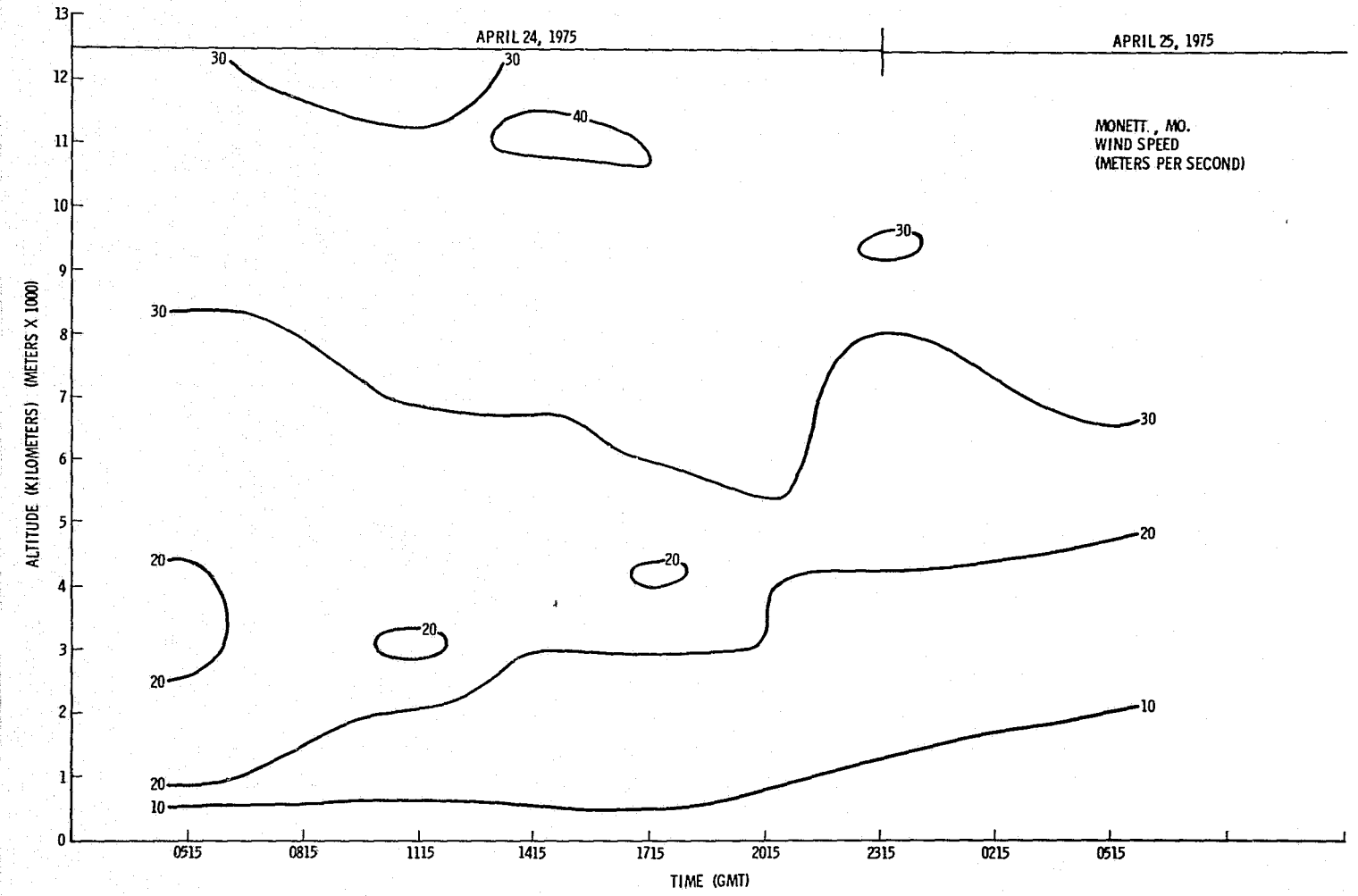

Figure A.70. Time cross section of wind speed at Monett, Missouri.

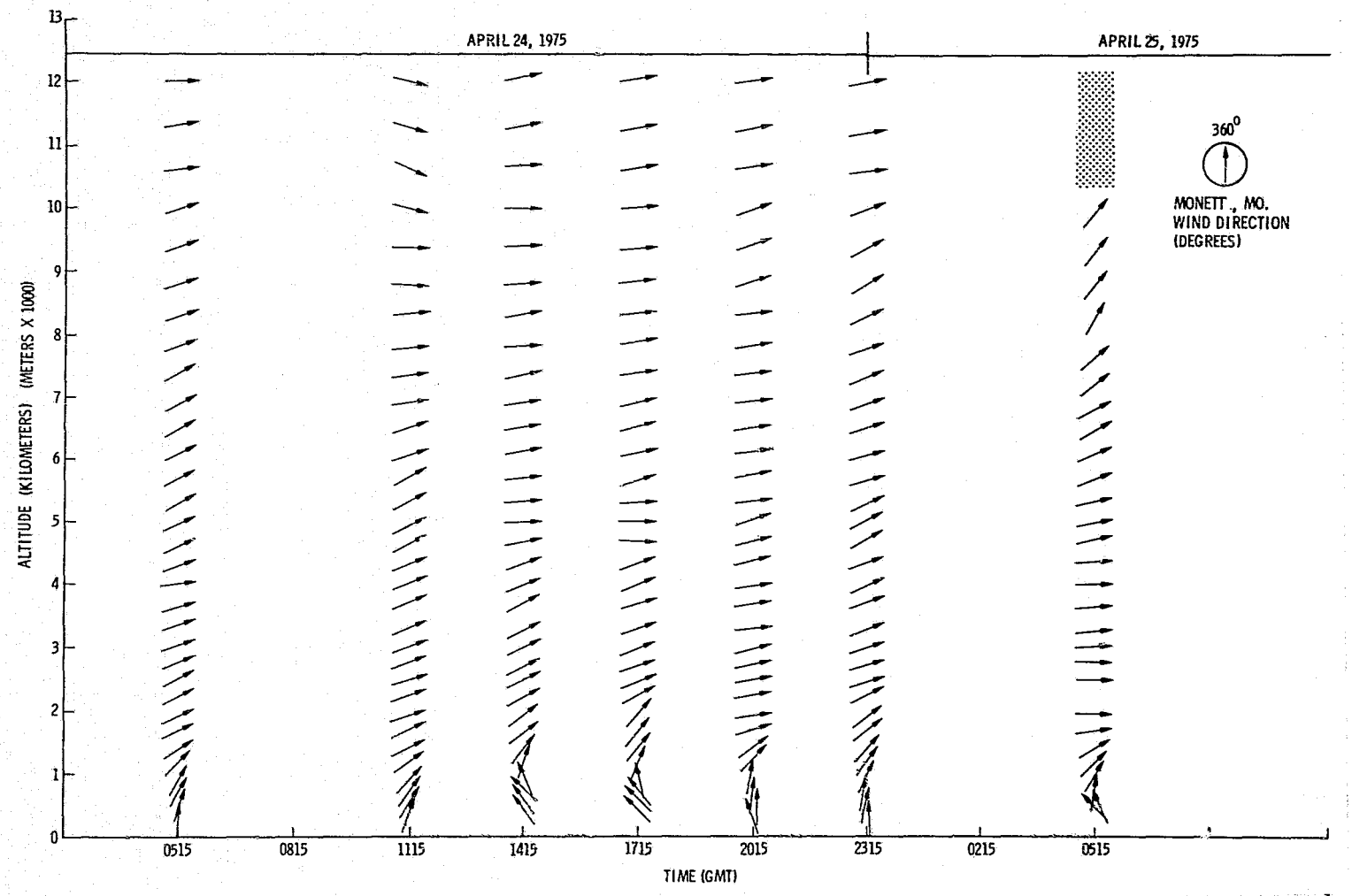

Figure A.71. Time cross section of wind direction at Monett, Missouri.

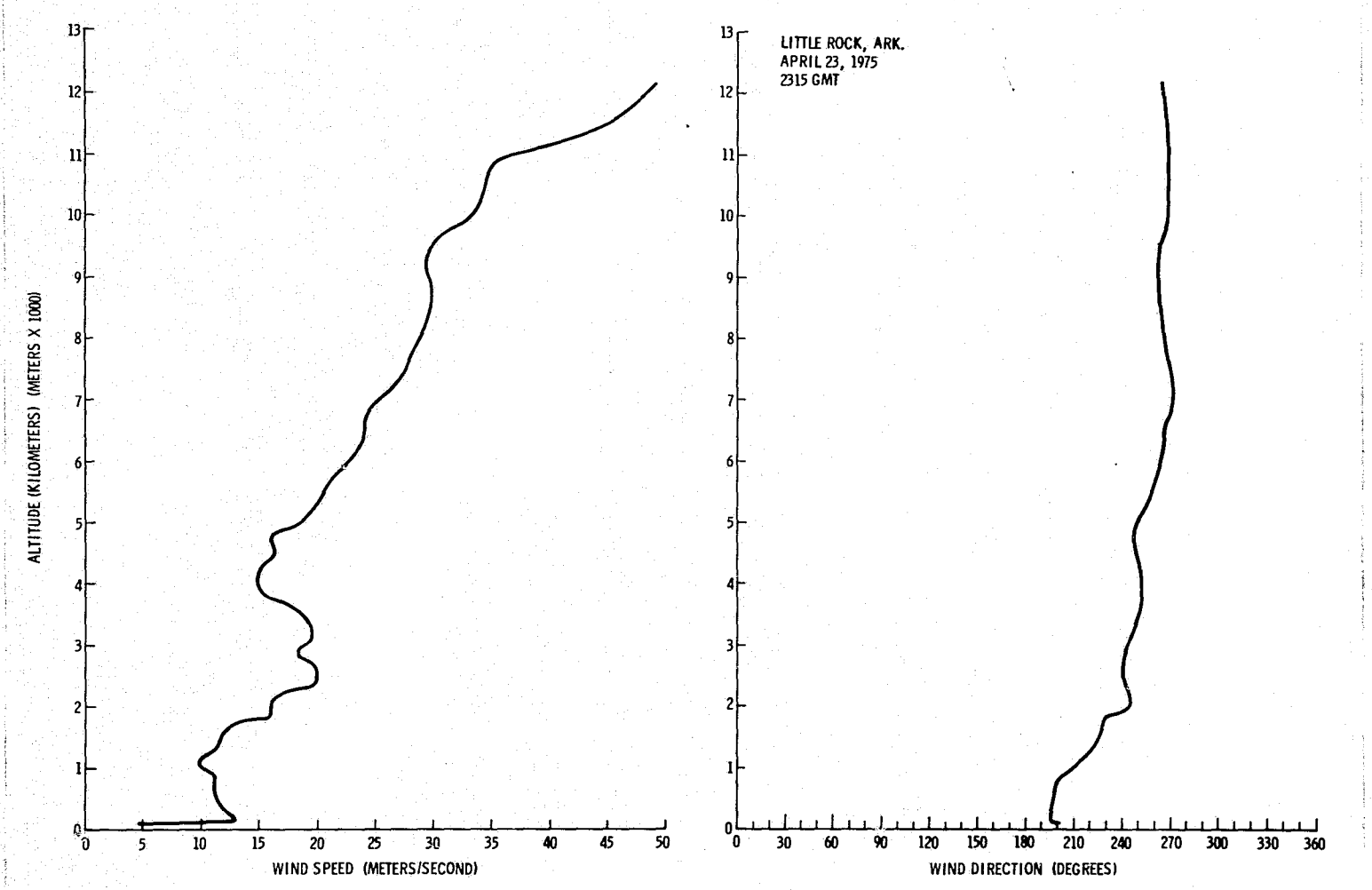

Figure A.72. Vertical wind profile for 2315 GMT, April 23, 1975, over Little Rock, Arkansas.

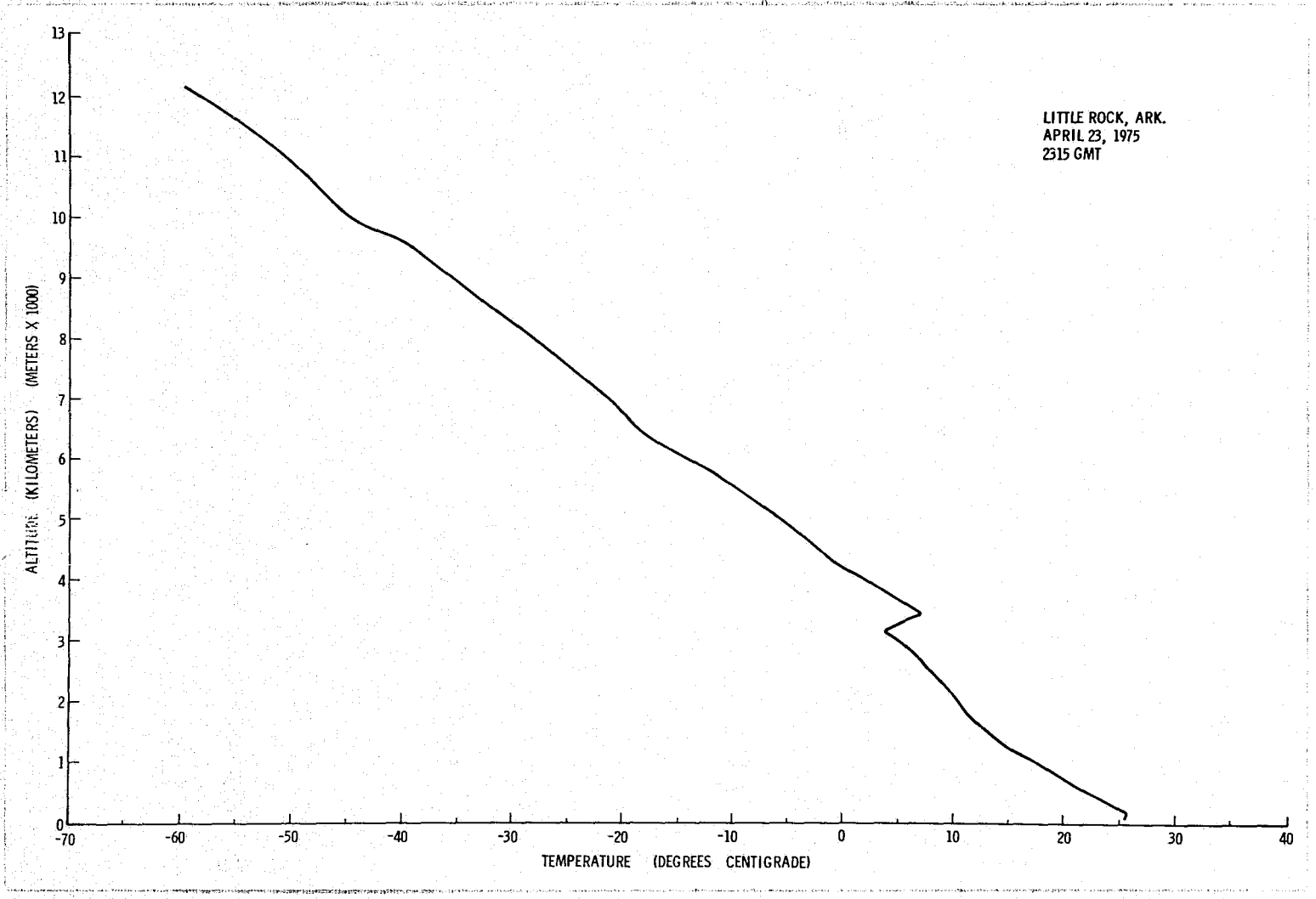

Figure A.73. Temperature profile for 2315 GMT, April 23, 1975, over Little Rock, Arkansas.

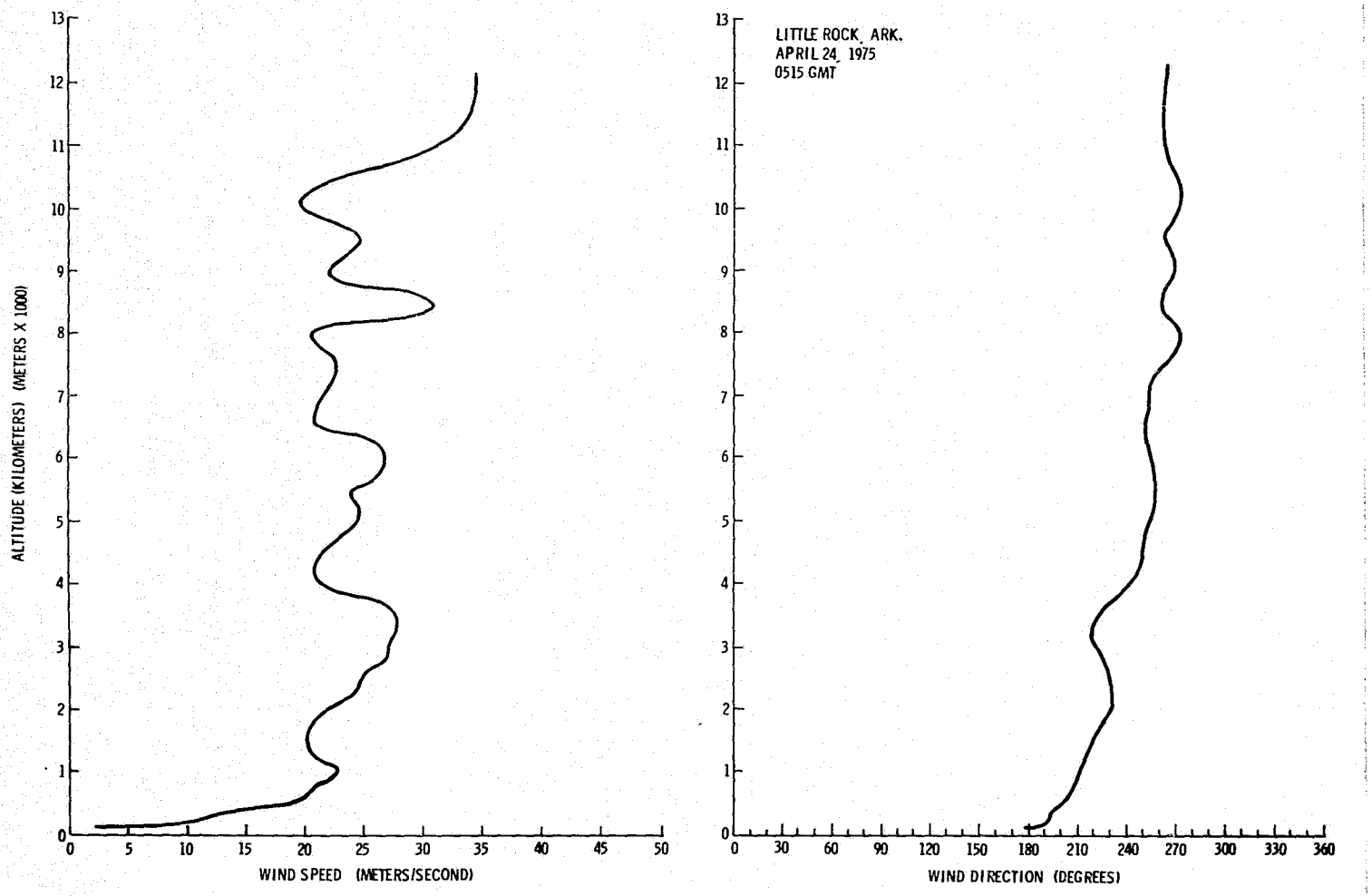

Figure A.74. Vertical wind profile for 0515 GMT, April 24, 1975, over Little Rock, Arkansas.

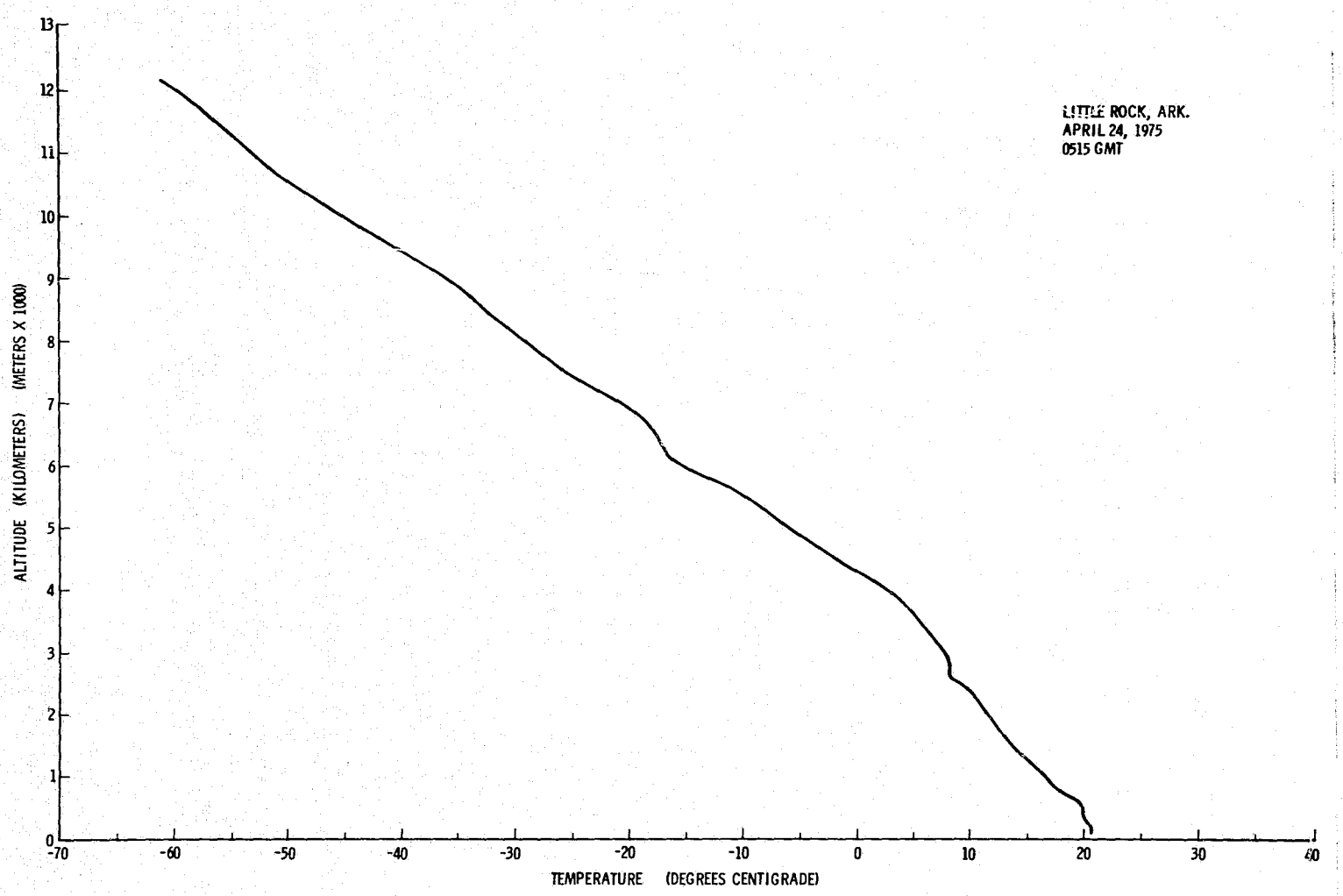

Figure A.75. Temperature profile for 0515 GMT, April 24, 1975, over Little Rock, Arkansas.

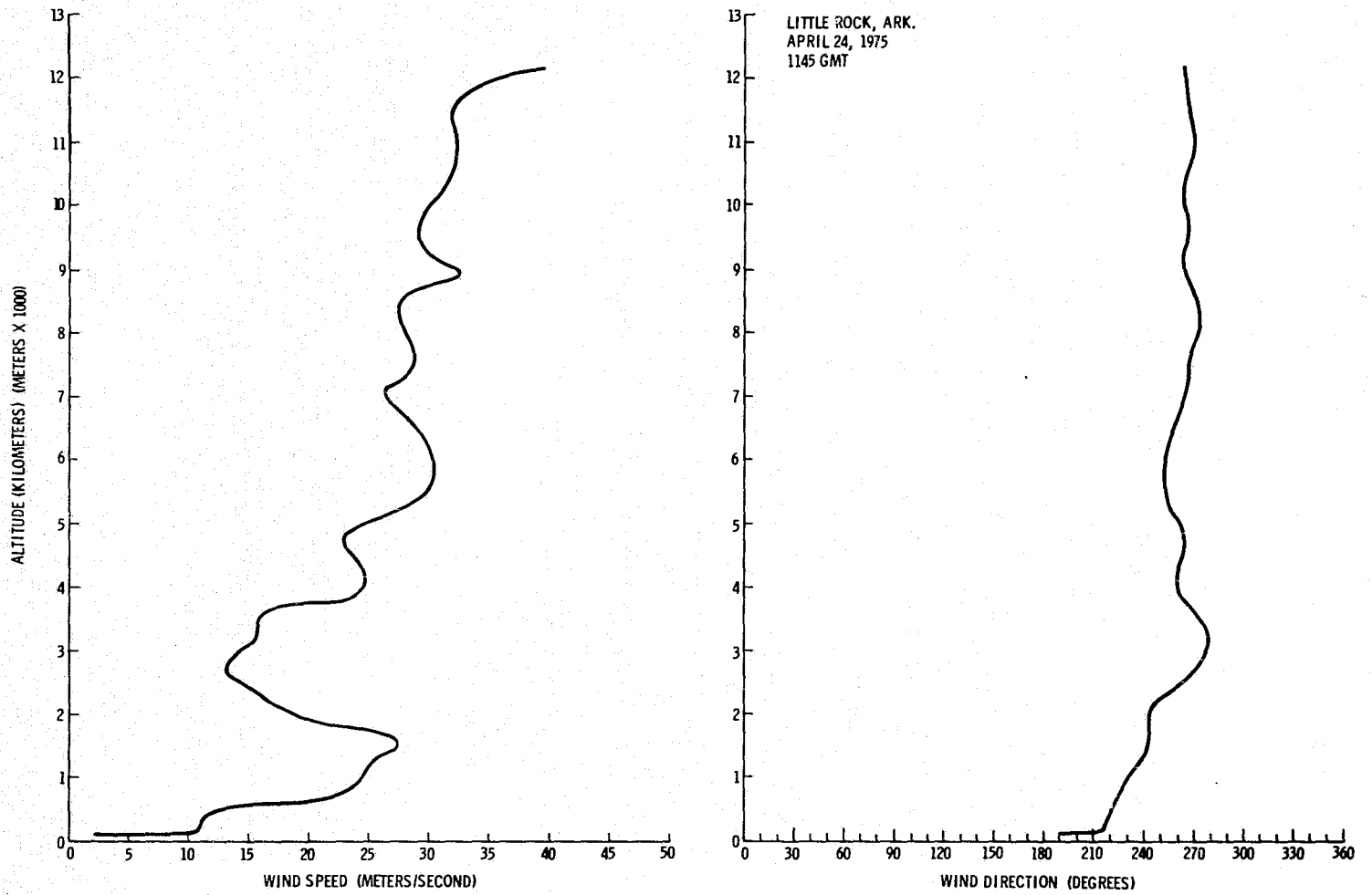

Figure A.76. Vertical wind profile for 1145 GMT, April 24, 1975, over Little Rock, Arkansas.

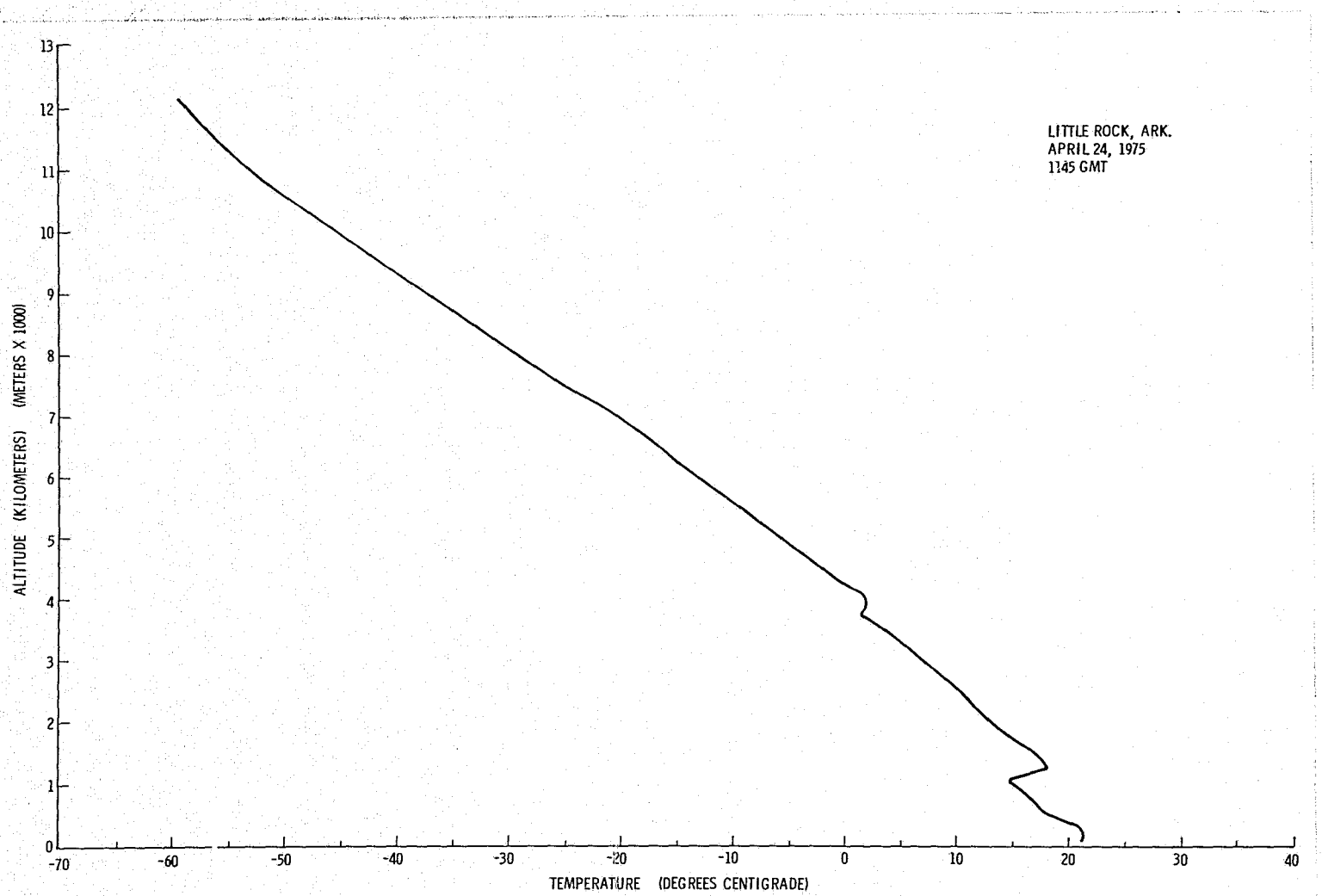

Figure A.77. Temperature profile for 1145 GMT, April 24, 1975, over Little Rock, Arkansas.

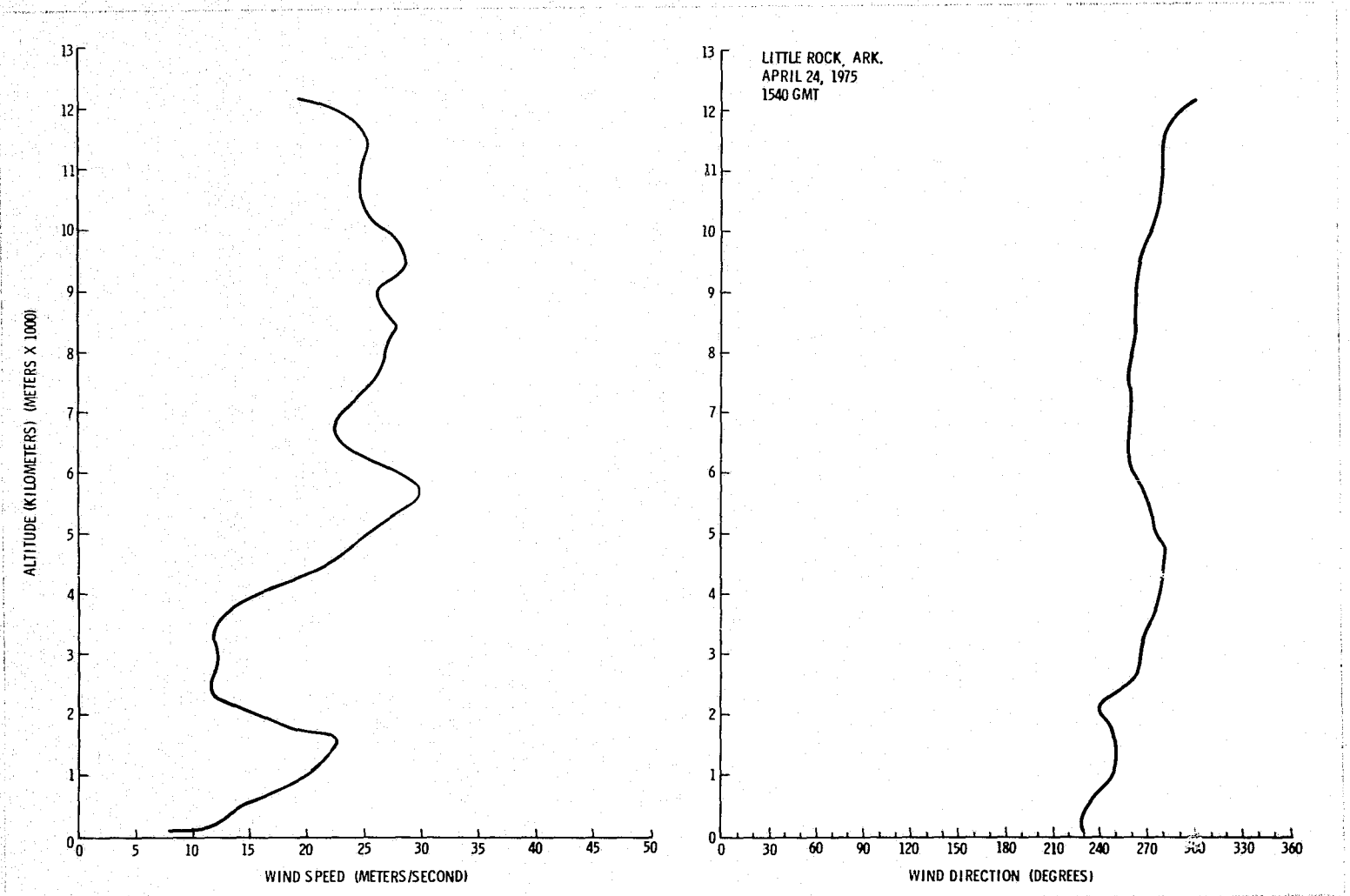

Figure A.78. Vertical wind profile for 1540 GMT, April 24, 1975, over Little Rock, Arkansas.

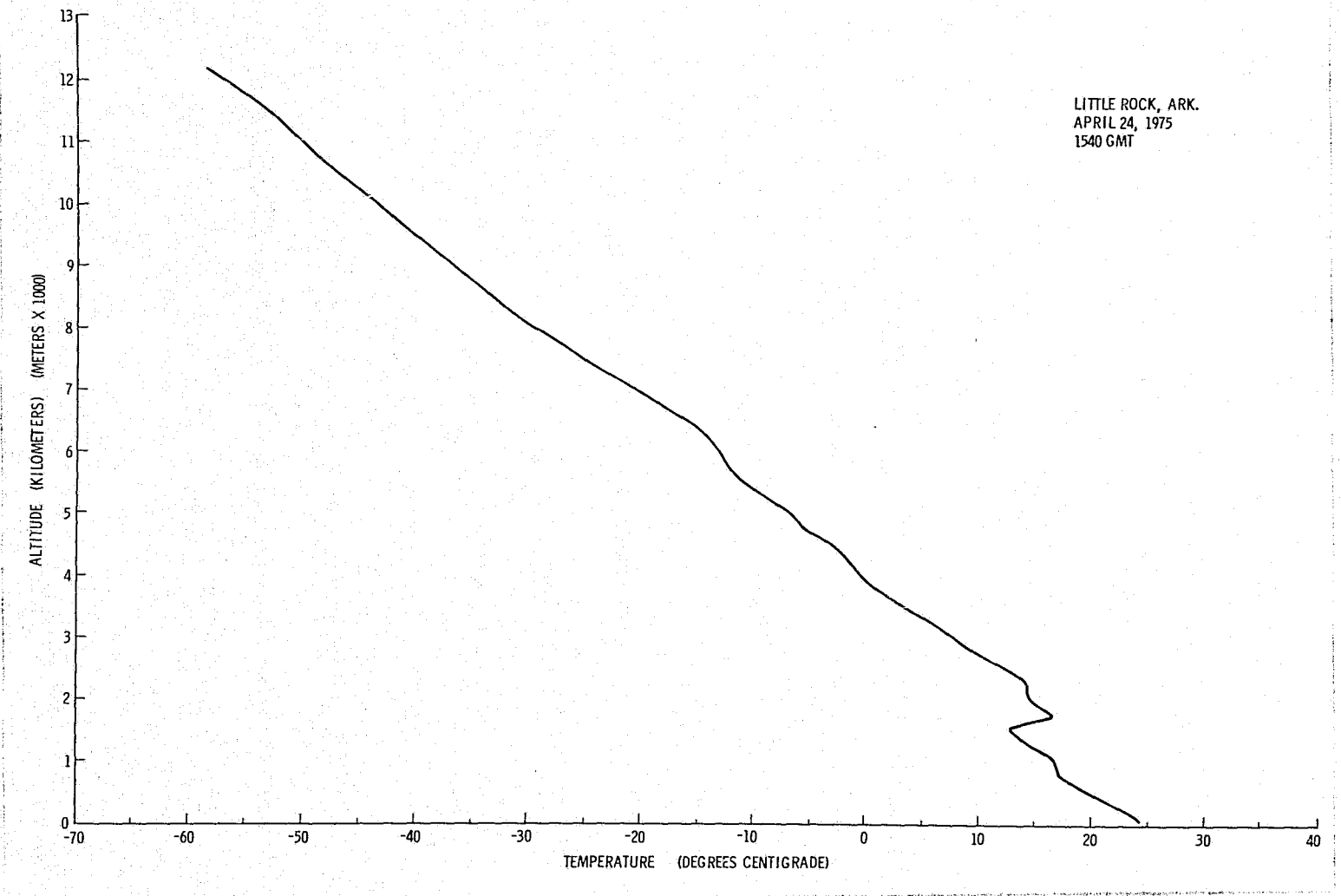

Figure A.79. Temperature profile for 1540 GMT, April 24, 1975, over Little Rock, Arkansas.

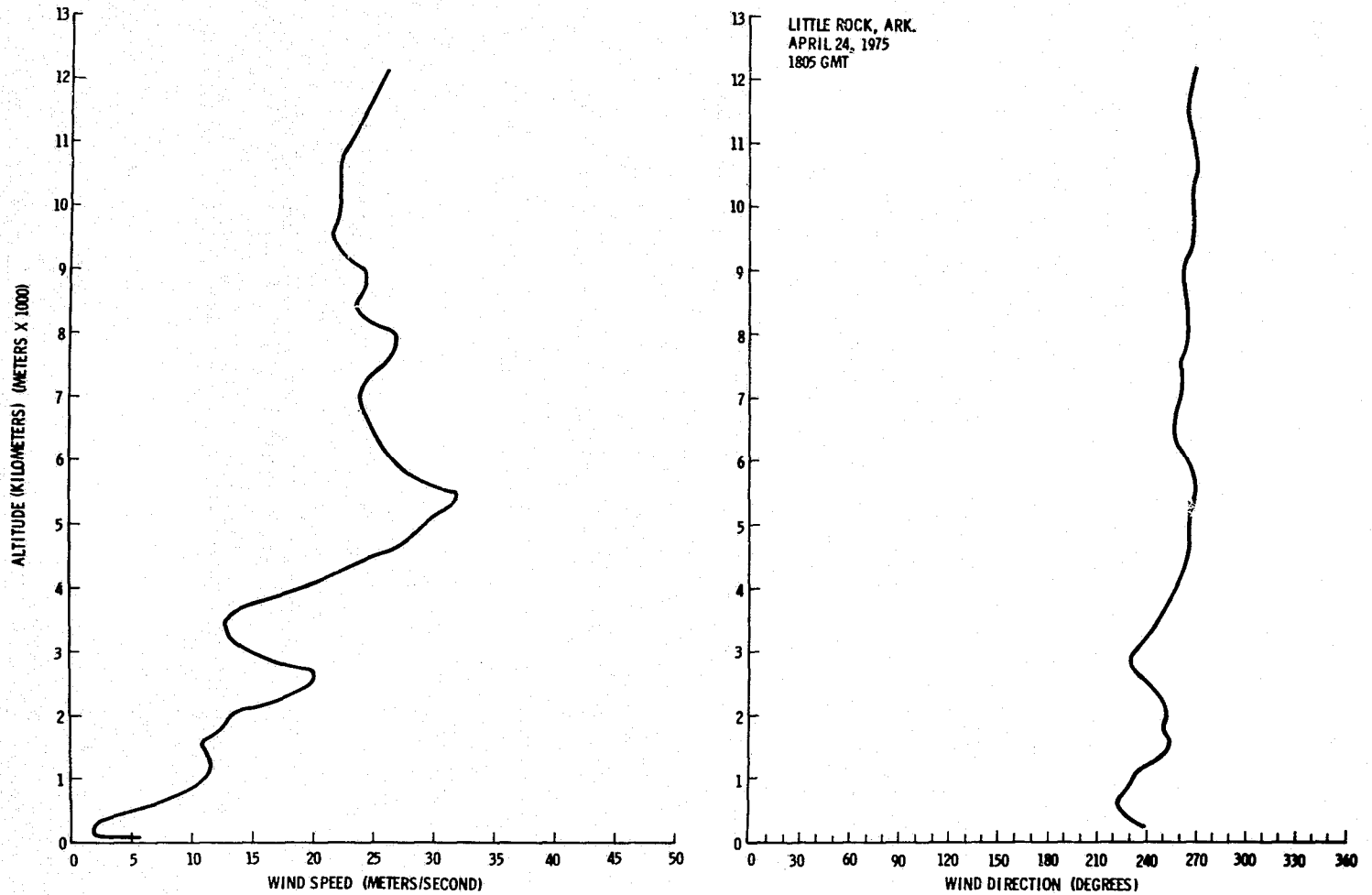

Figure A.80. Vertical wind profile for 1805 GMT, April 24, 1975, over Little Rock, Arkansas.

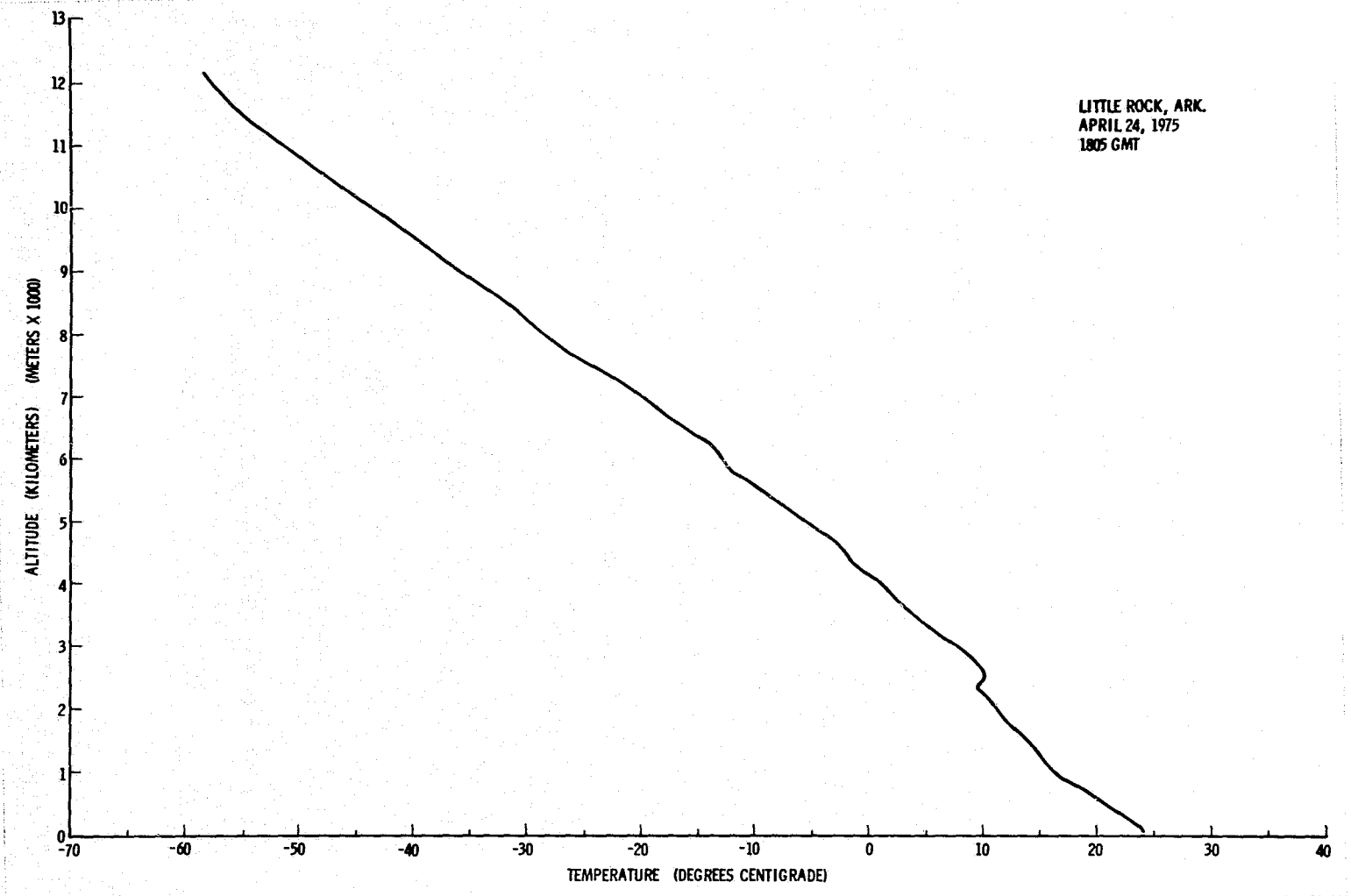

Figure A.81. Temperature profile for 1805 GMT, April 24, 1975, over Little Rock, Arkansas.

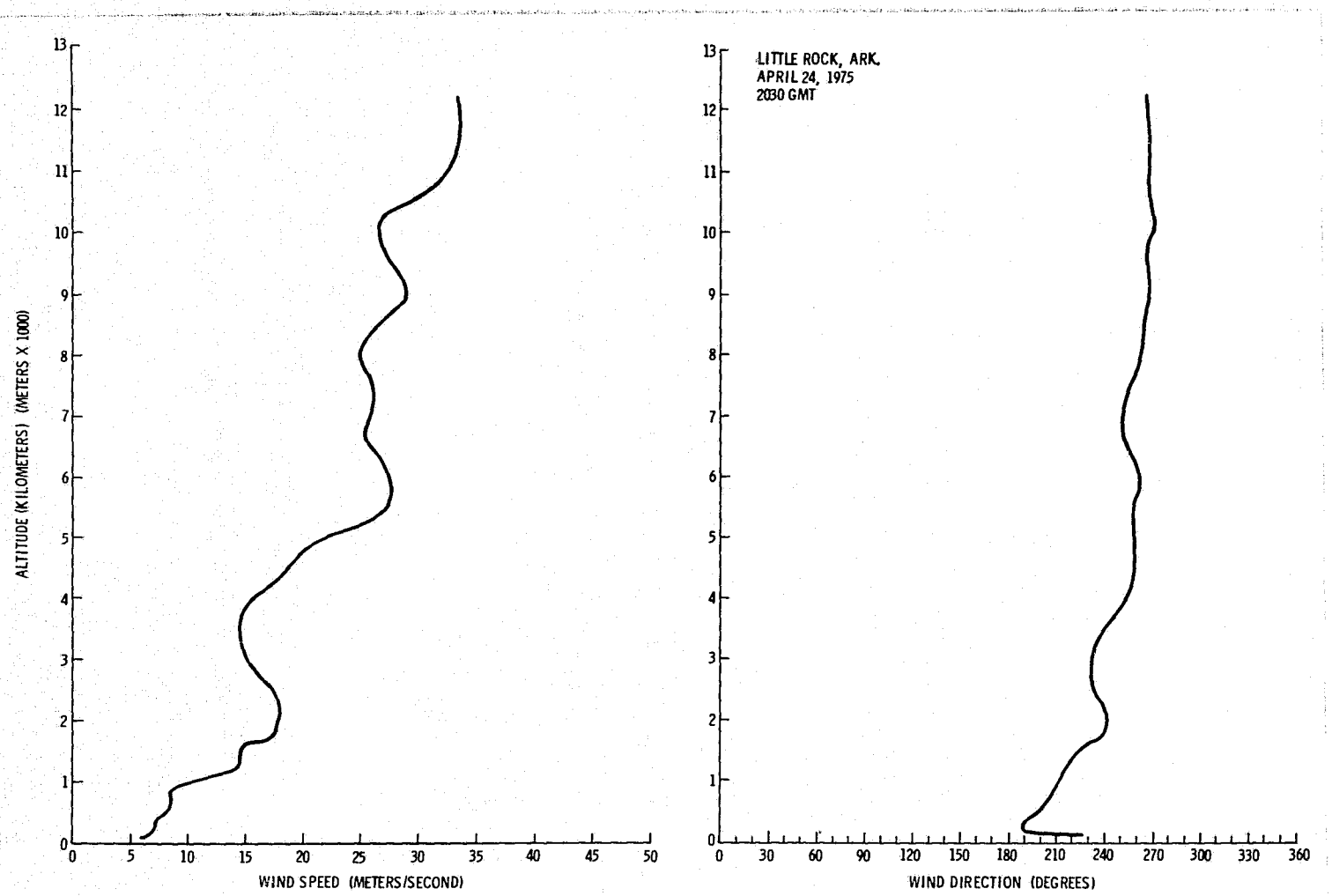

Figure A.82. Vertical wind profile for 2030 GMT, April 24, 1975, over Little Rock, Arkansas.

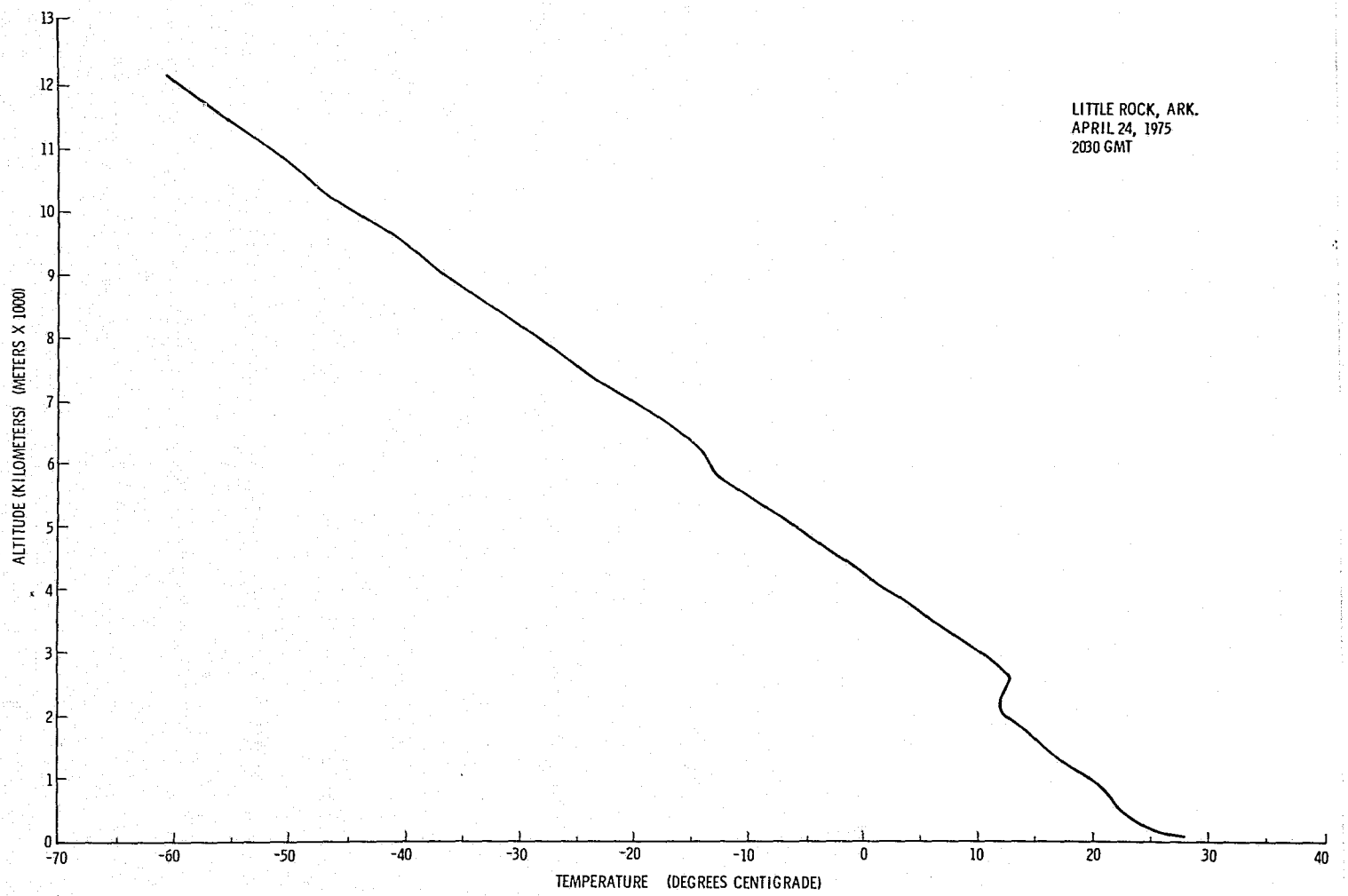

Figure A.83. Temperature profile for 2030 GMT, April 24, 1975, over Little Rock, Arkansas.

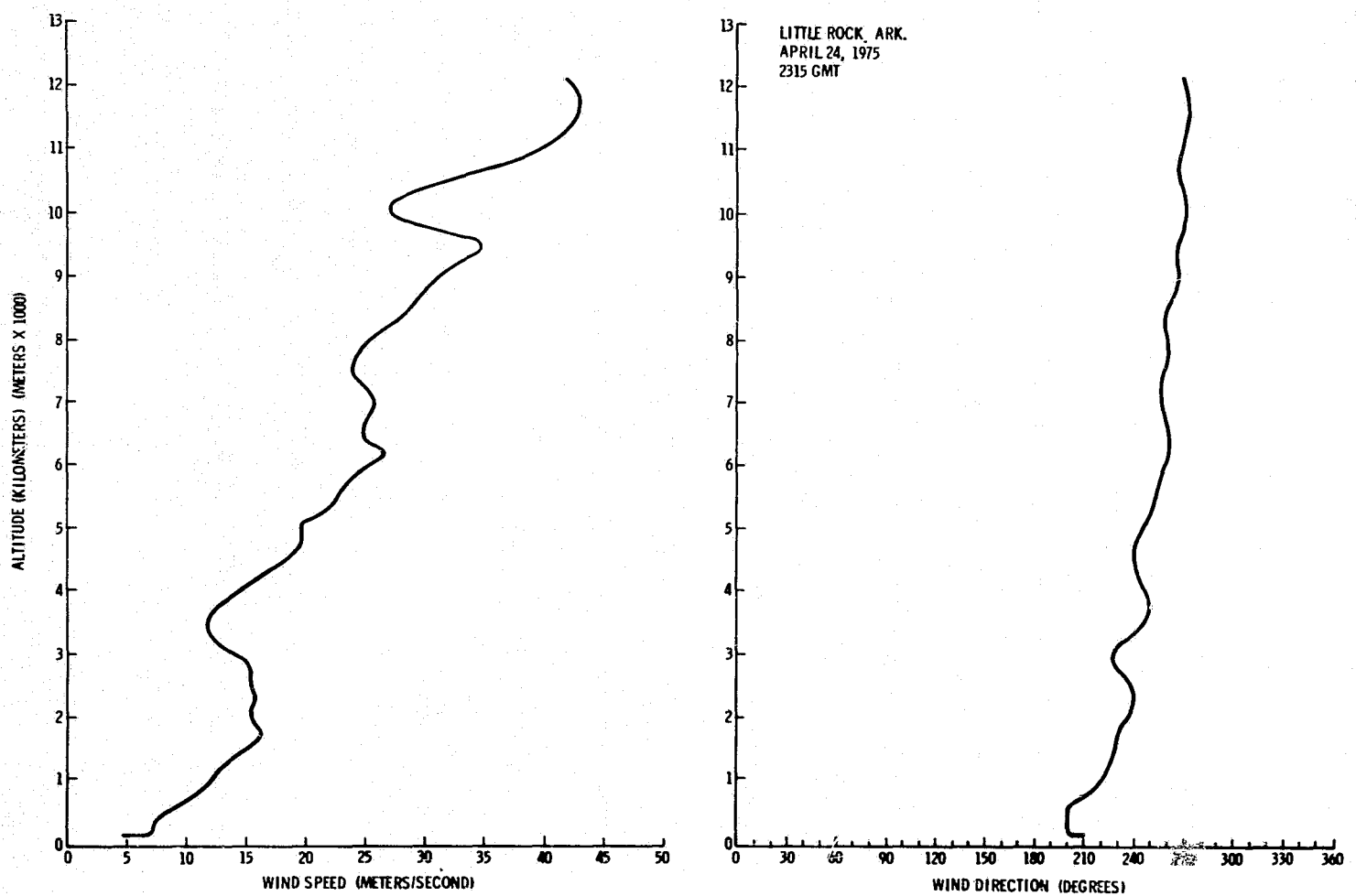

Figure A.84. Vertical wind profile for 2315 GMT, April 24, 1975, over Little Rock, Arkansas.

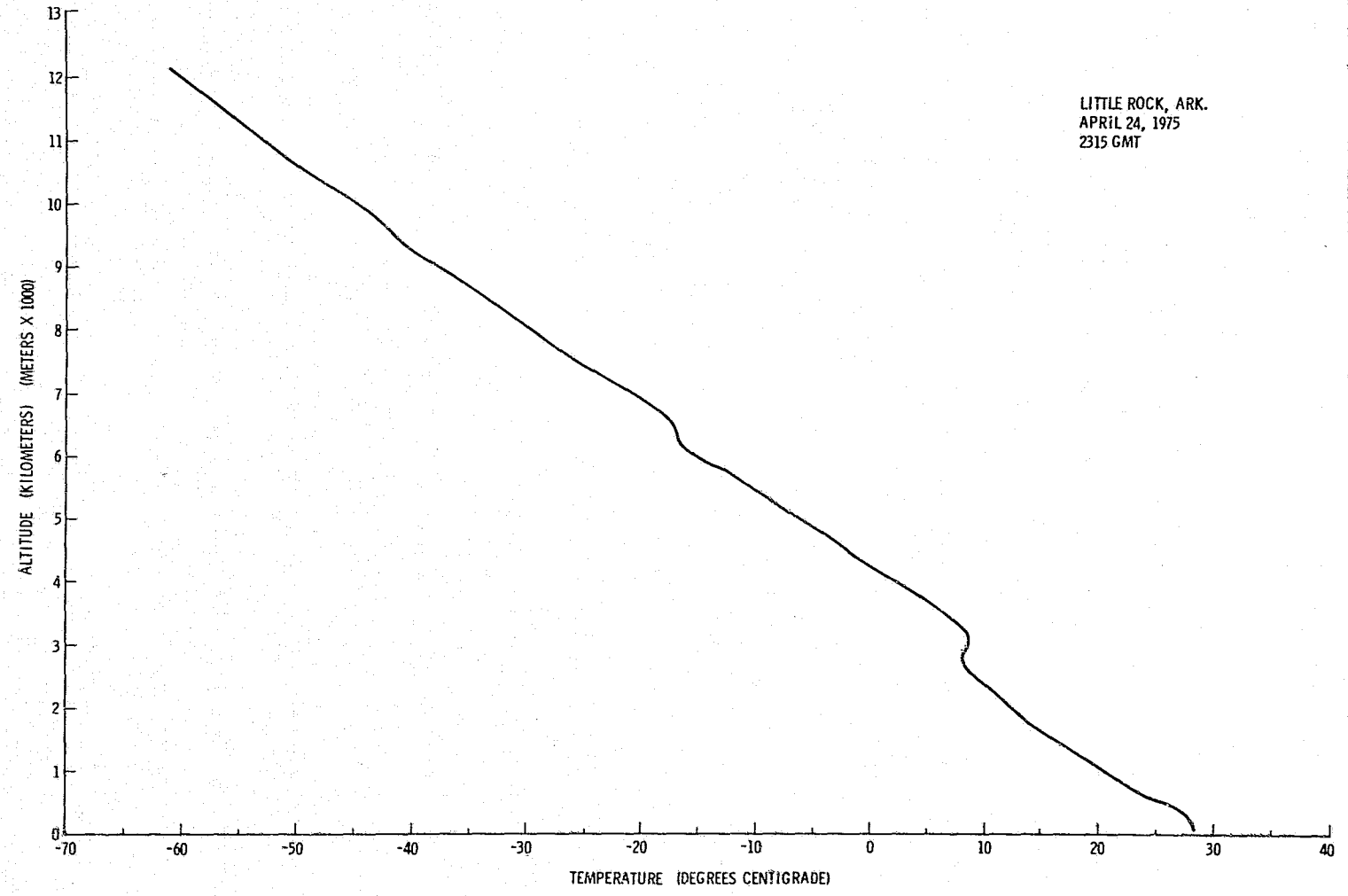

Figure A.85. Temperature profile for 2315 GMT, April 24, 1975, over Little Rock, Arkansas.

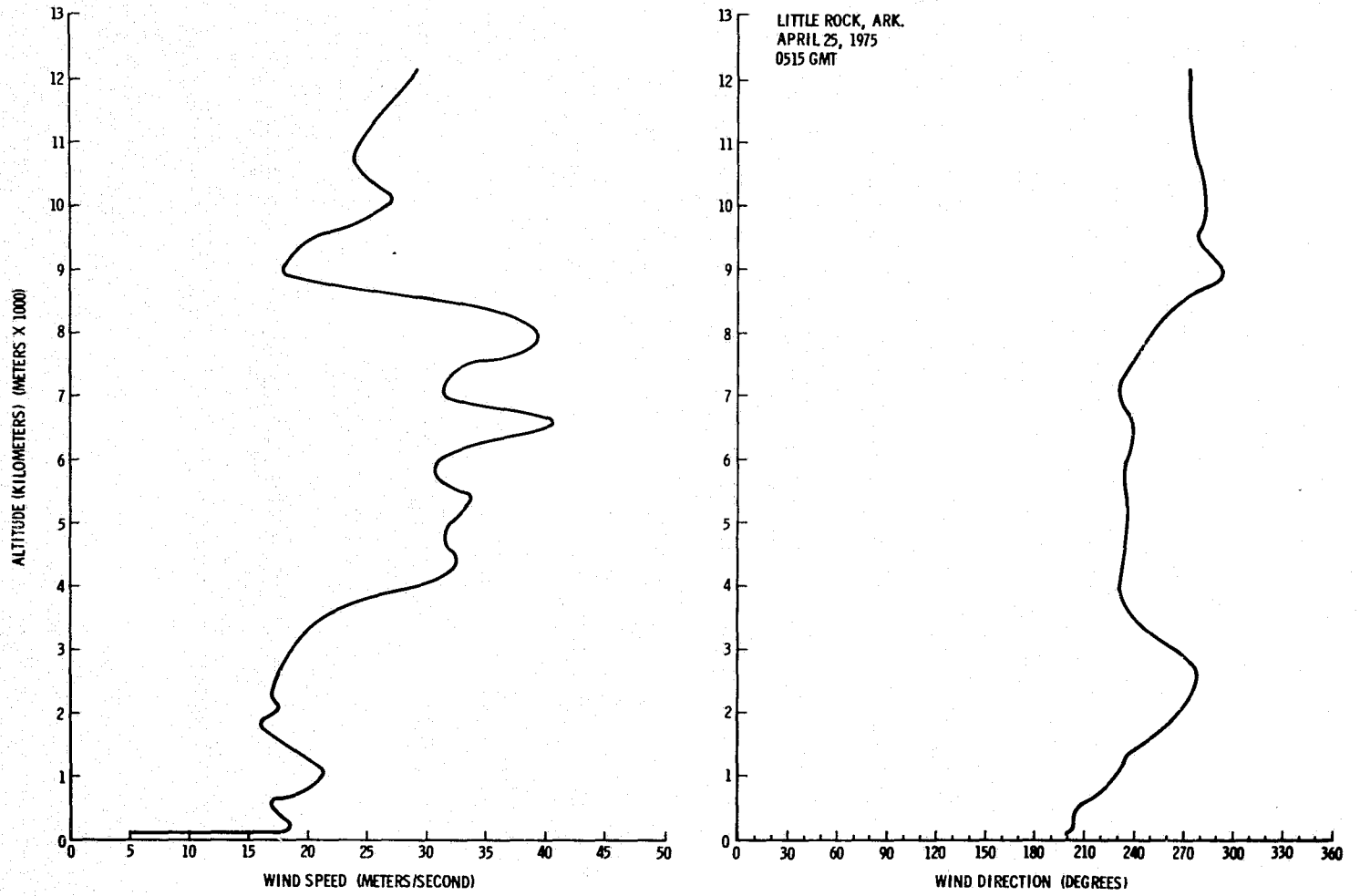

Figure A.86. Vertical wind profile for 0515 GMT, April 25, 1975, over Little Rock, Arkansas.

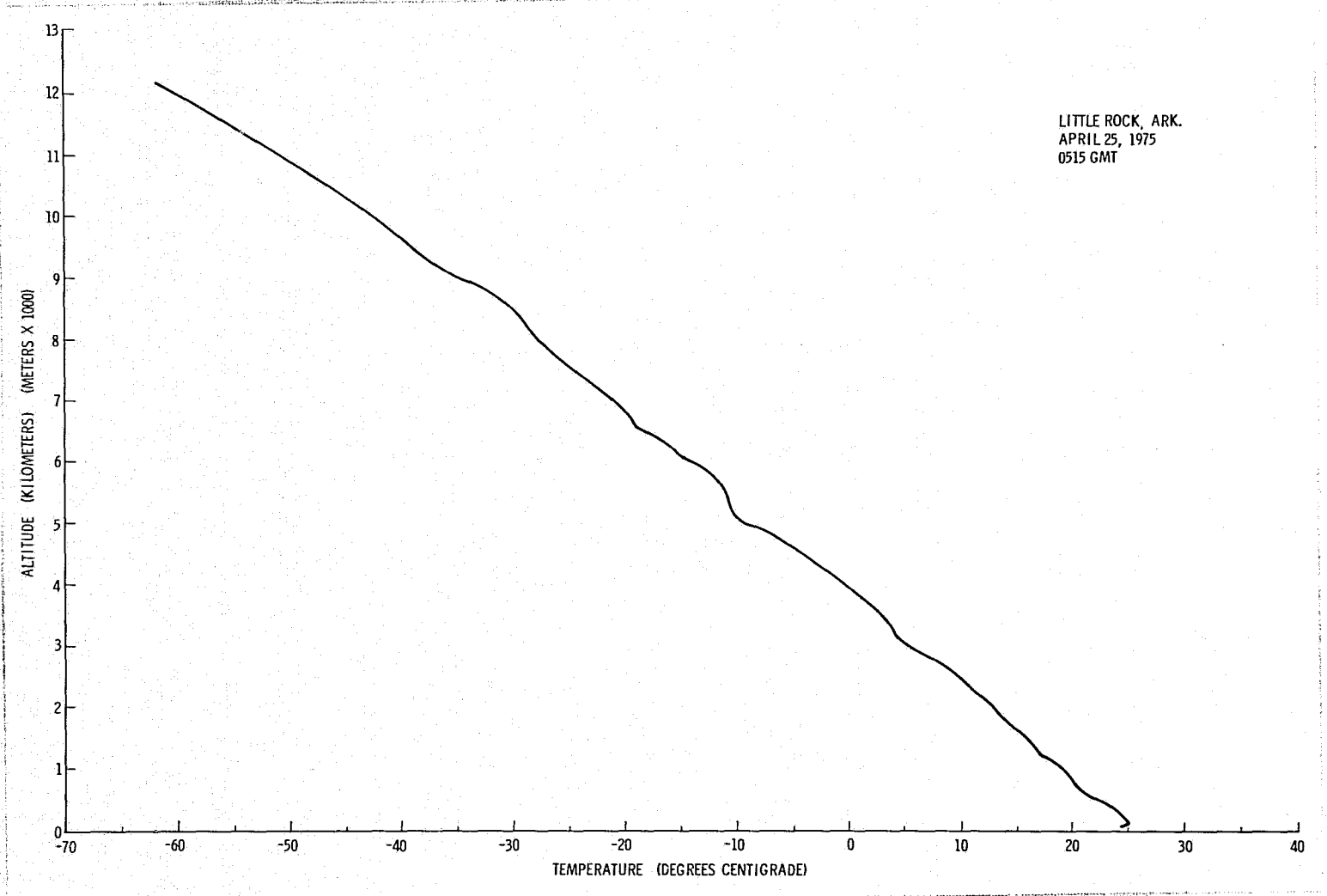

Figure A.87. Temperature profile for 0515 GMT, April 25, 1975, over Little Rock, Arkansas.

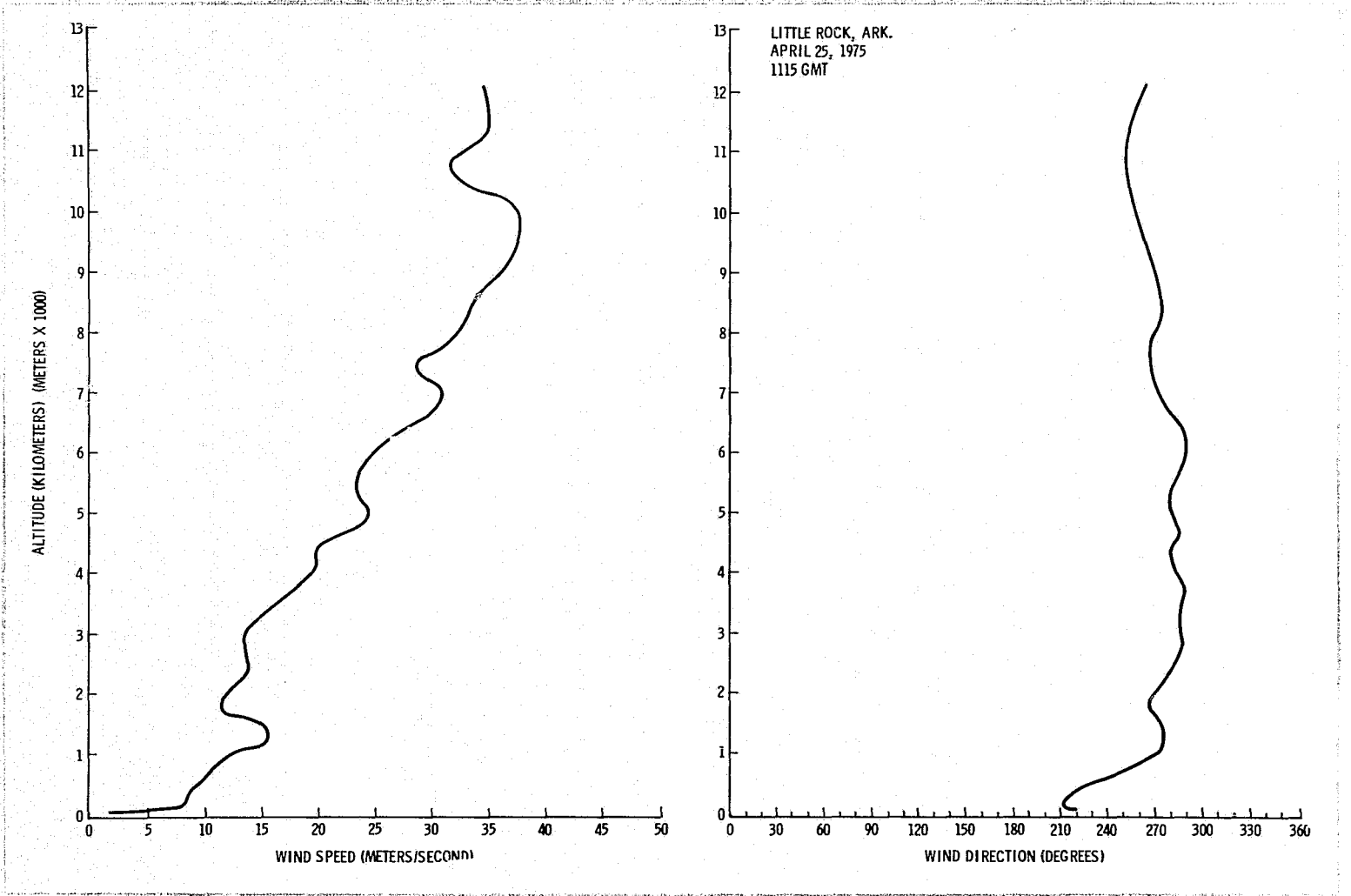

Figure A.88. Vertical wind profile for 1115 GMT, April 25, 1975, over Little Rock, Arkansas.

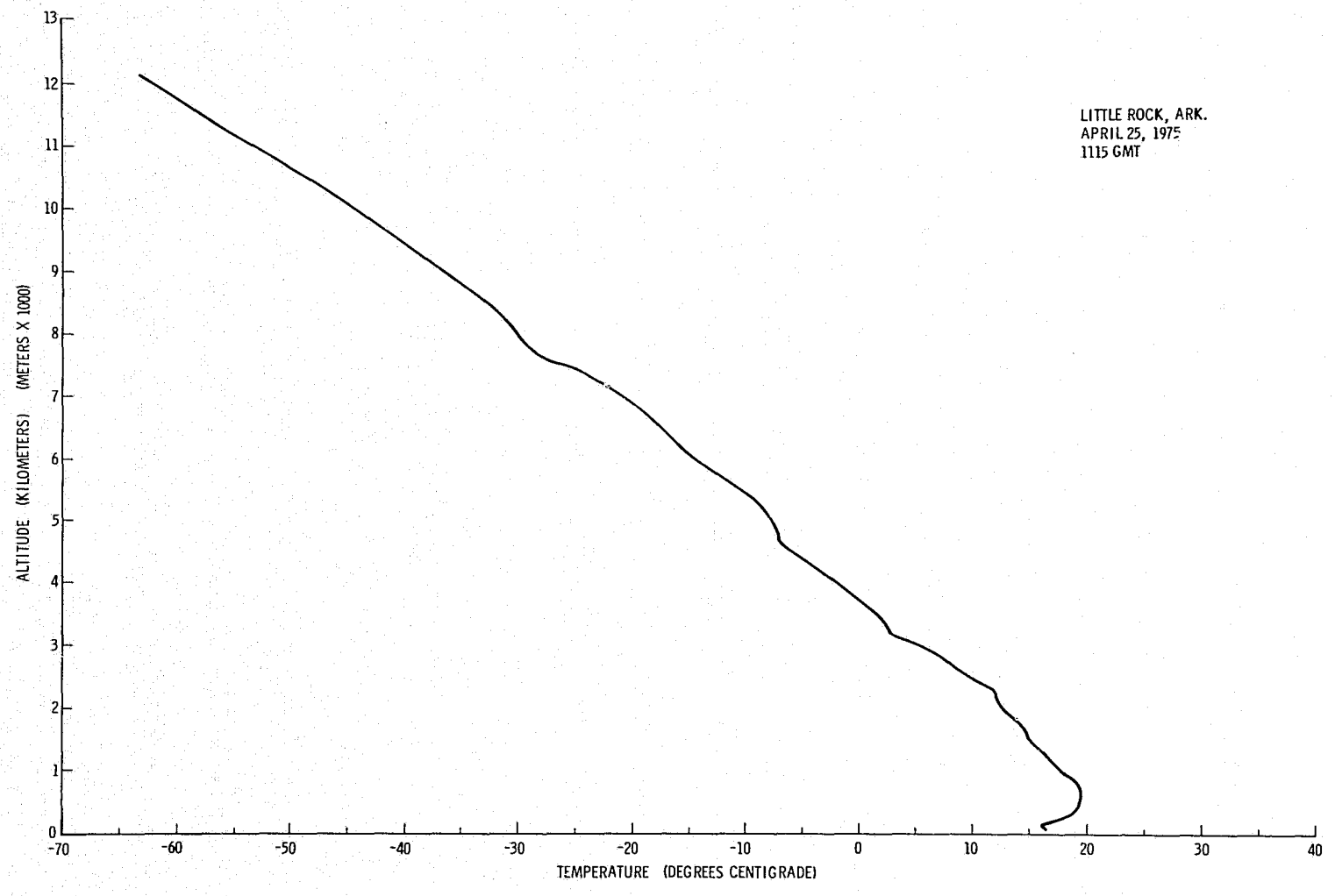

Figure A.89. Temperature profile for 1115 GMT, April 25, 1975, over Little Rock, Arkansas.

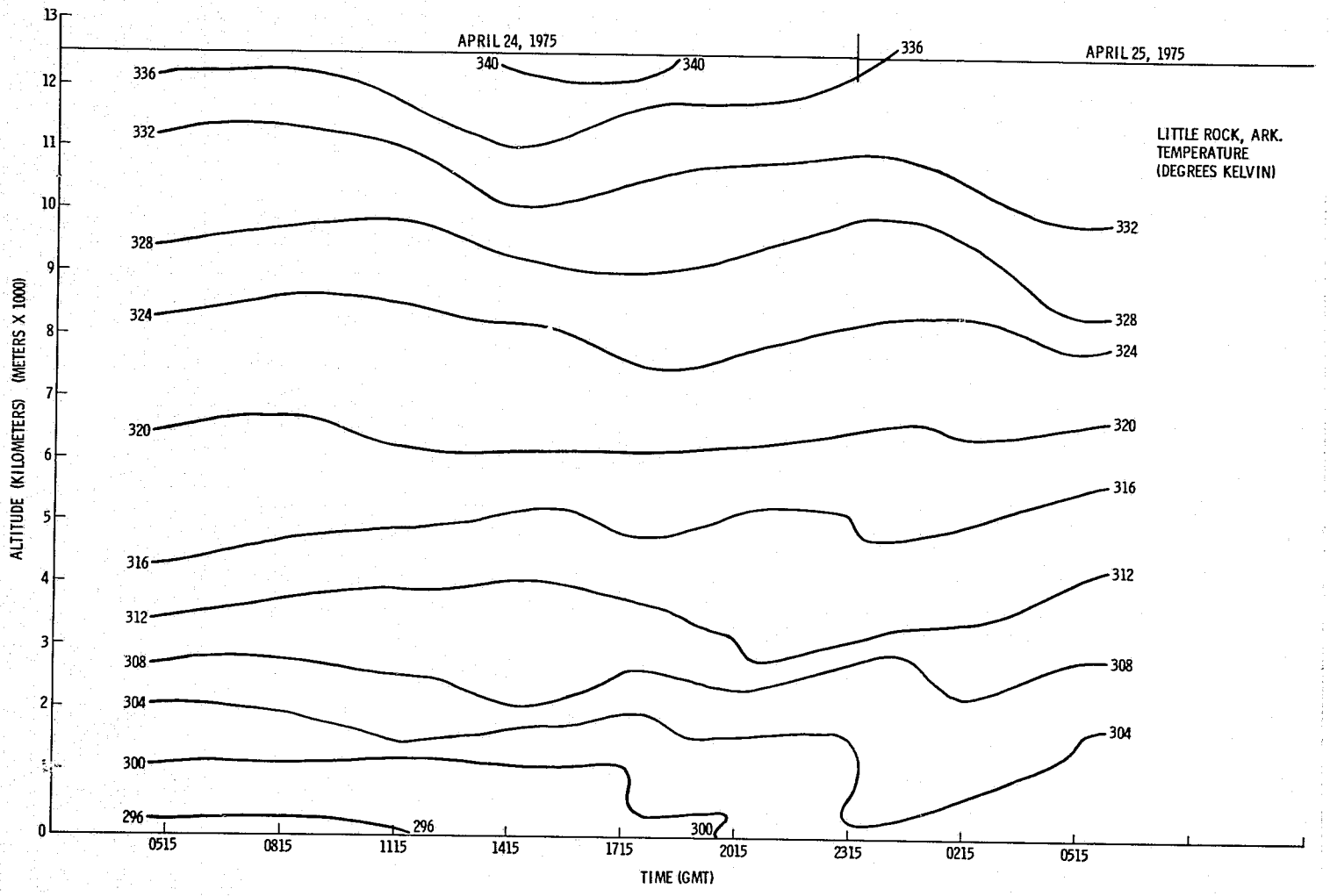

Figure A.90. Time cross section of temperature at Little Rock, Arkansas.

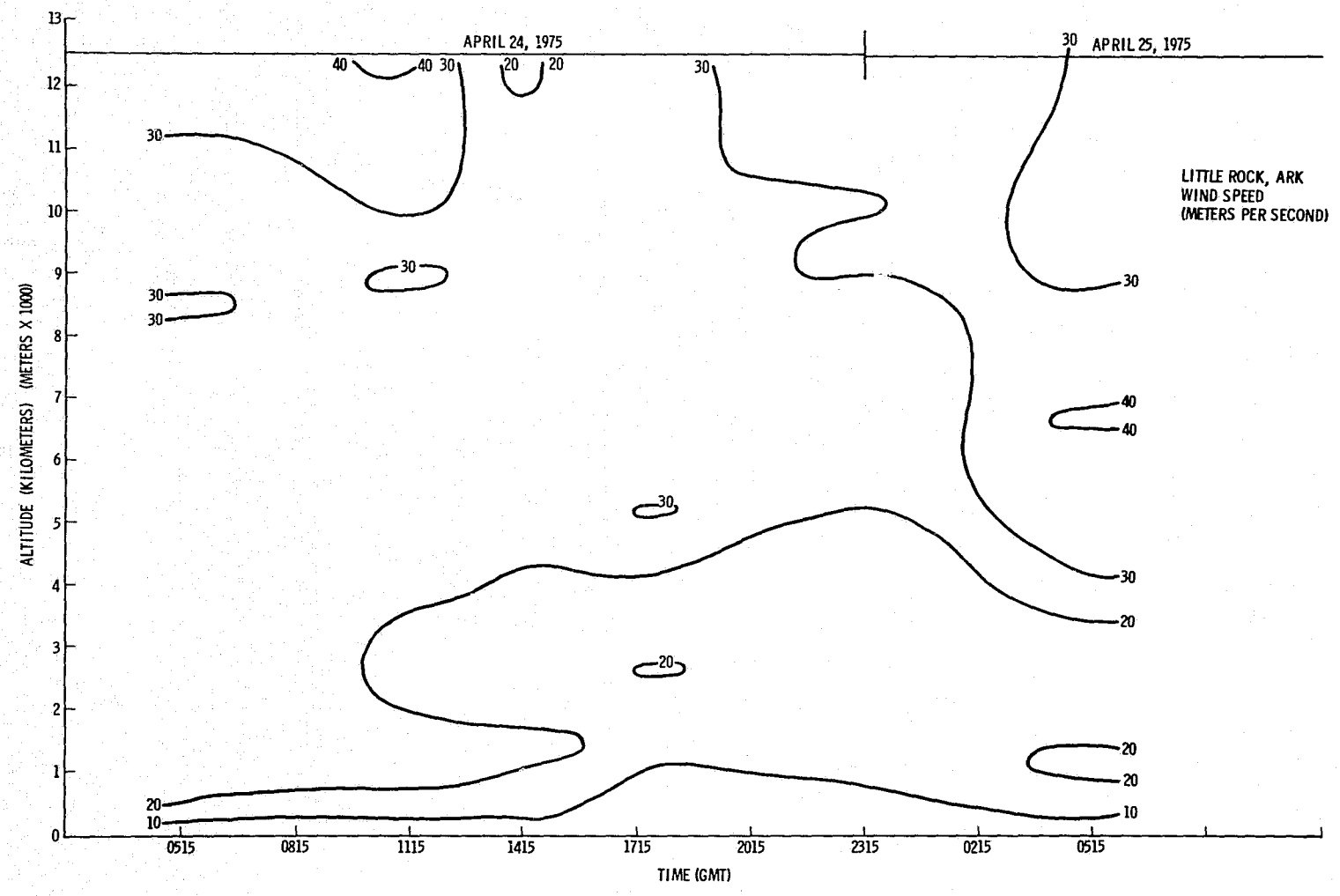

Figure A.91. Time cross section of wind speed at Little Rock, Arkansas.

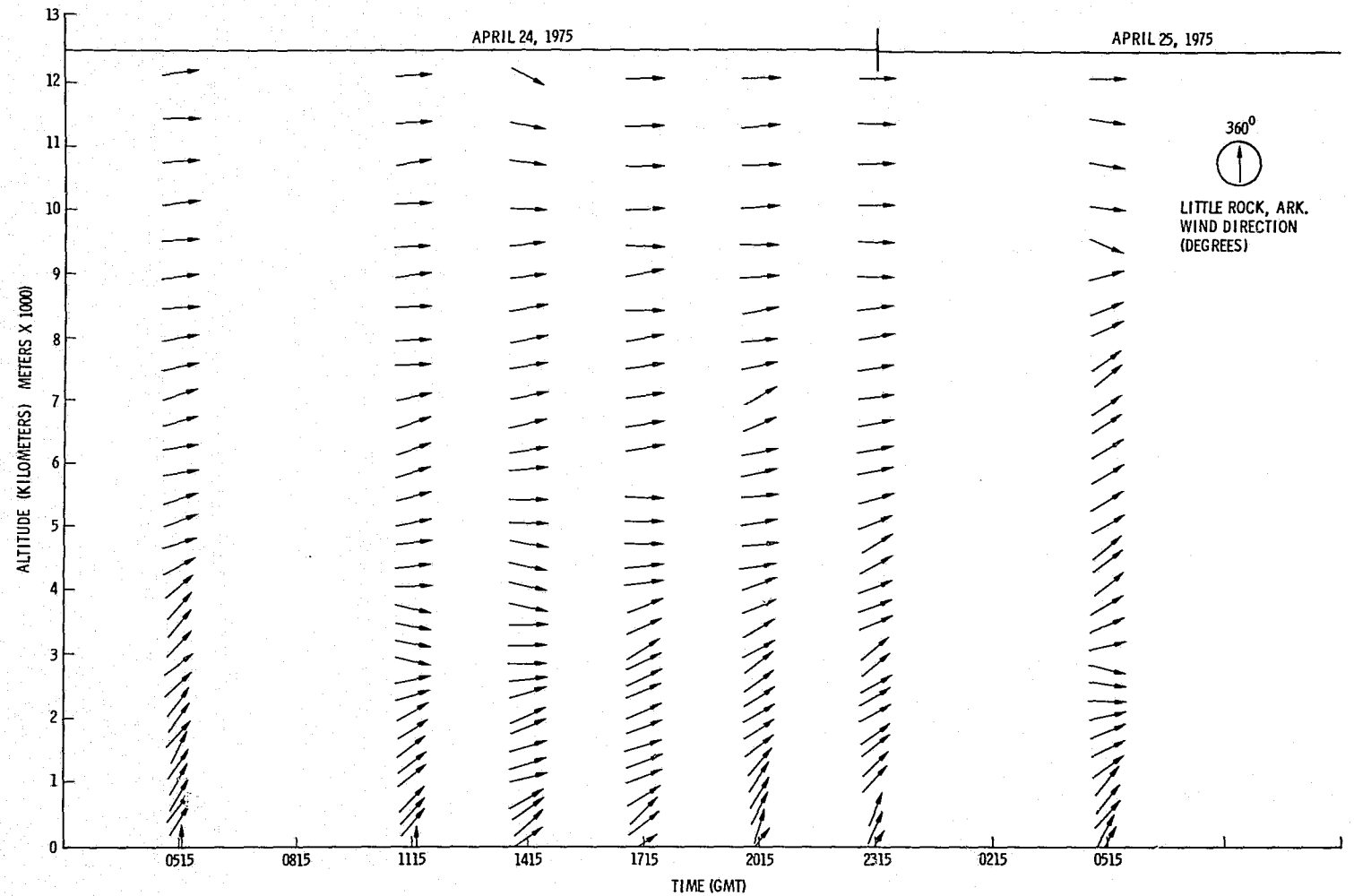

Figure A.92. Time cross section of wind direction at Little Rock, Arkansas.

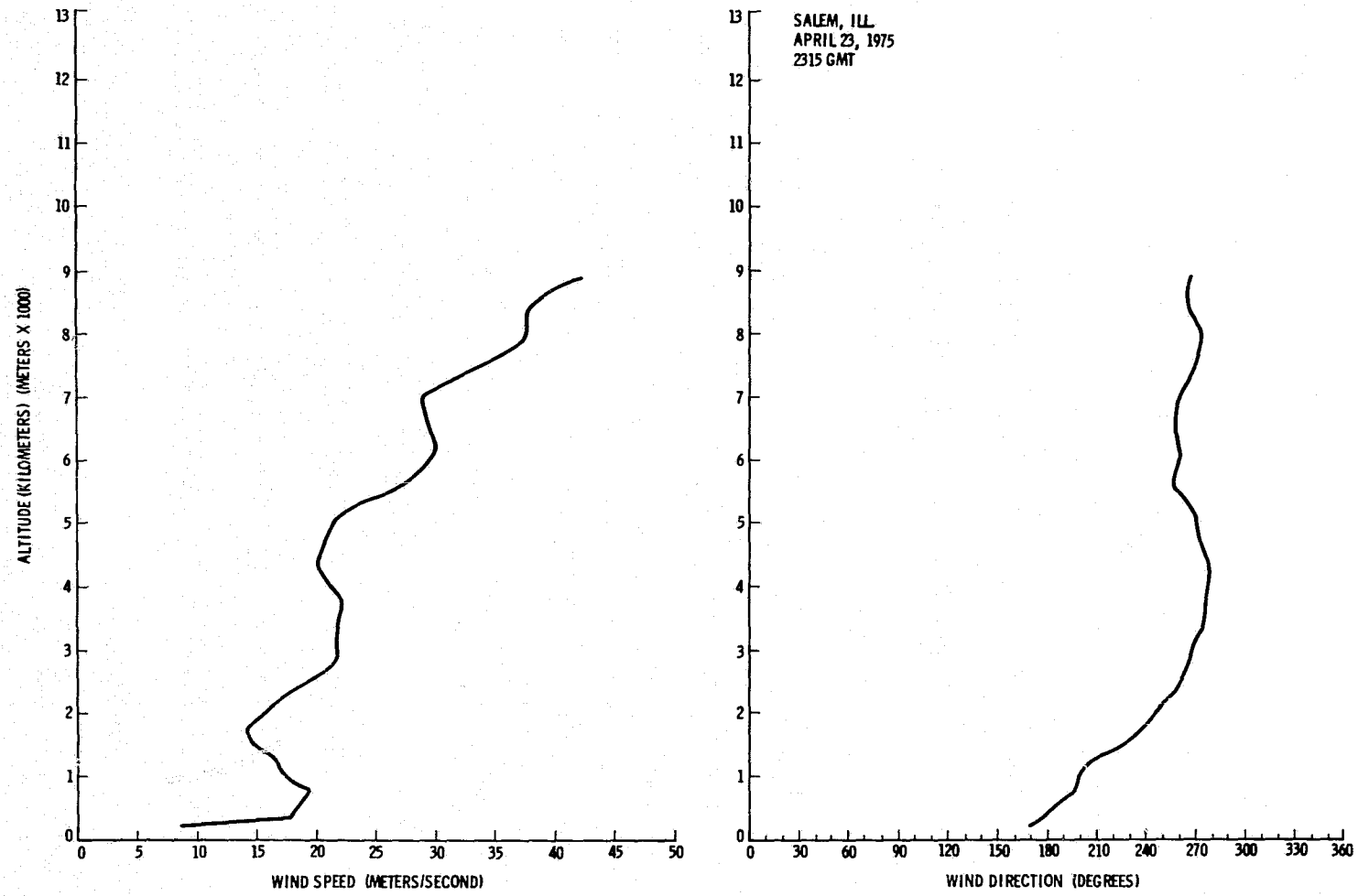

Figure A.93. Vertical wind profile for 2315 GMT, April 23, 1975, over Salem, Illinois.

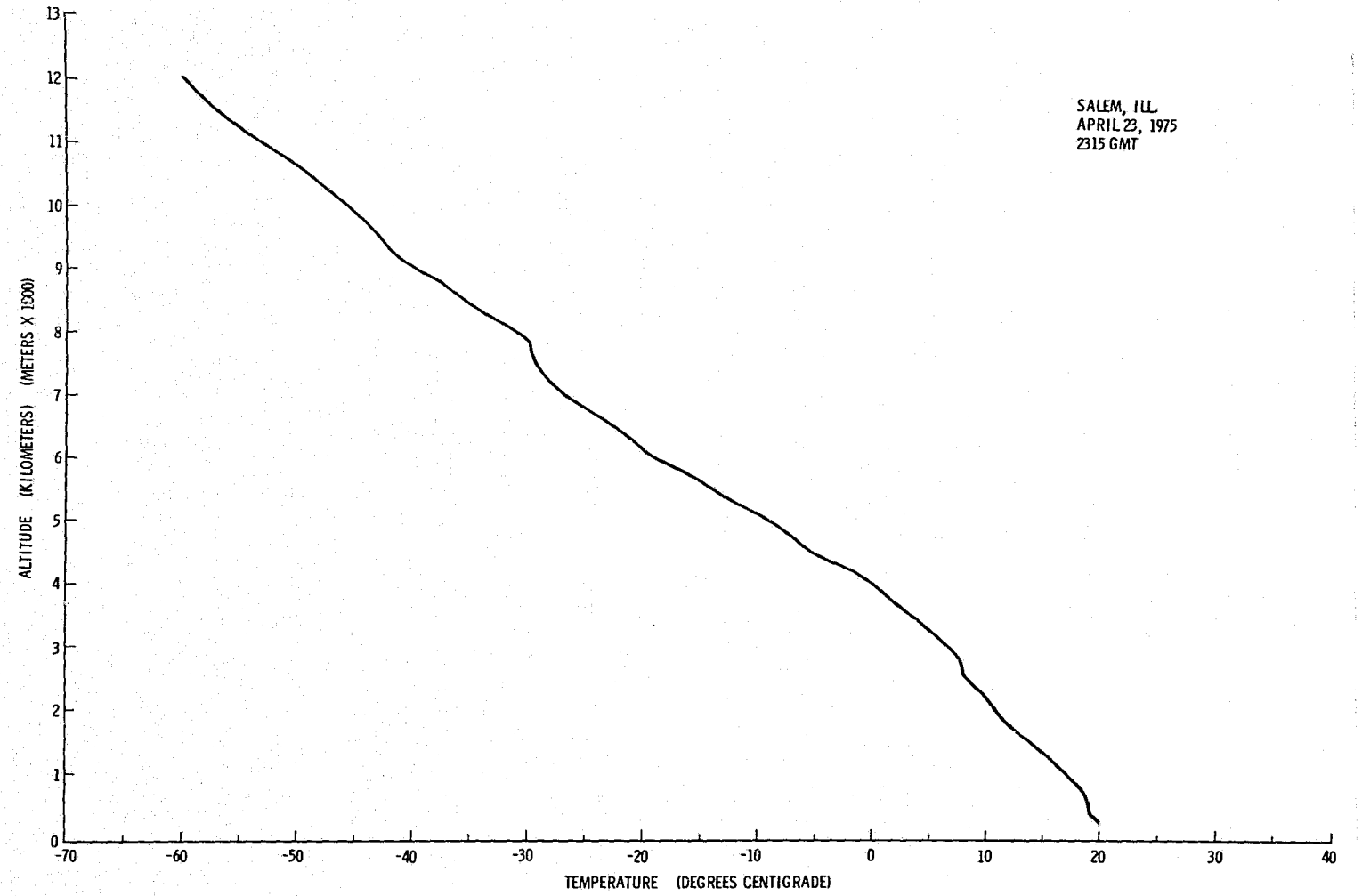

Figure A.94. Temperature profile for 2315 GMT, April 23, 1975, over Salem, Illinois.

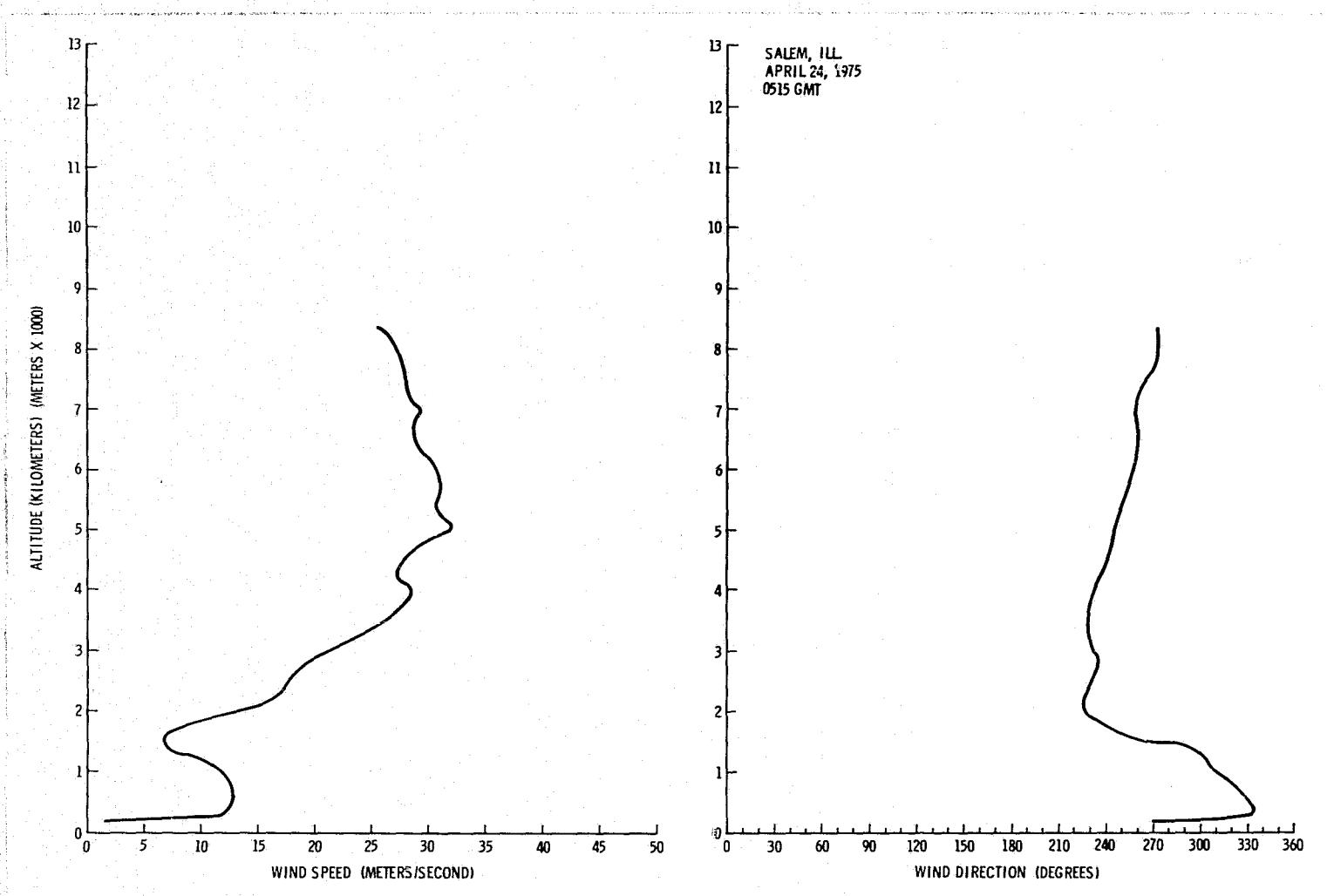

Figure A.95. Vertical wind profile for 0515 GMT, April 23, 1975, over Salem, Illinois.

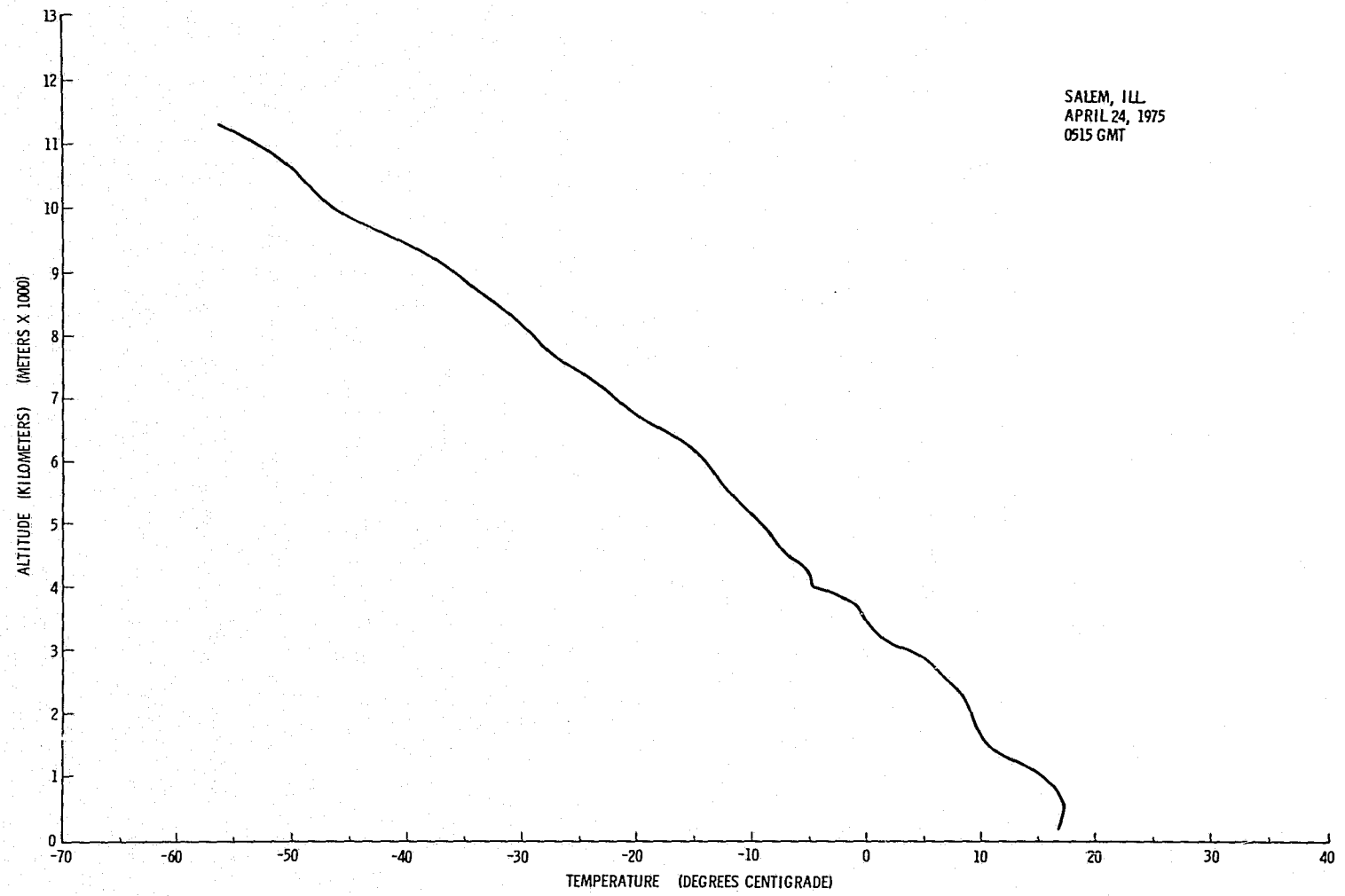

Figure A.96. Temperature profile for 0515 GMT, April 24, 1975, over Salem, Illinois.

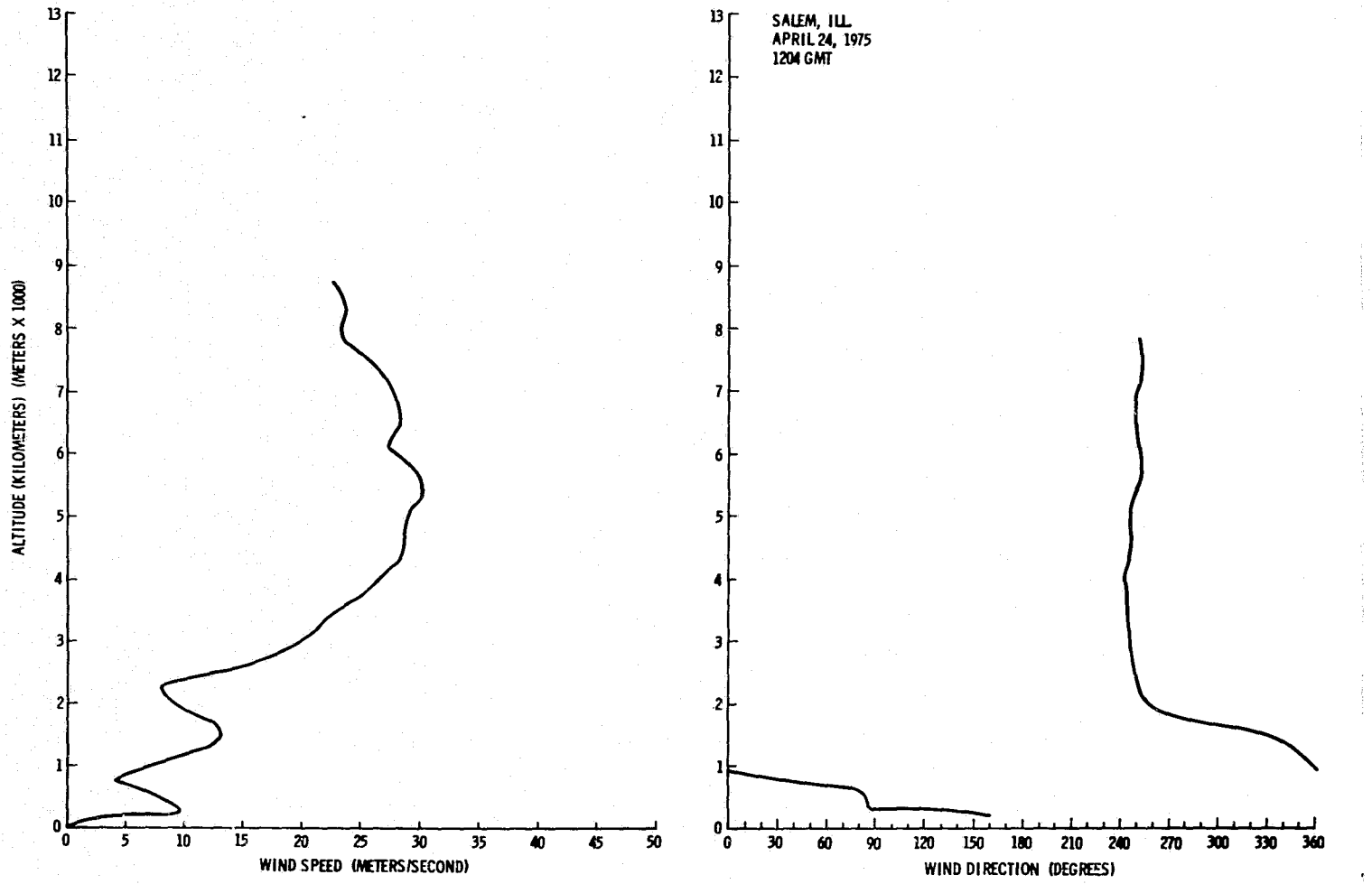

Figure A.97. Vertical wind profile for 1204 GMT, April 24, 1975, over Salem, Illinois.

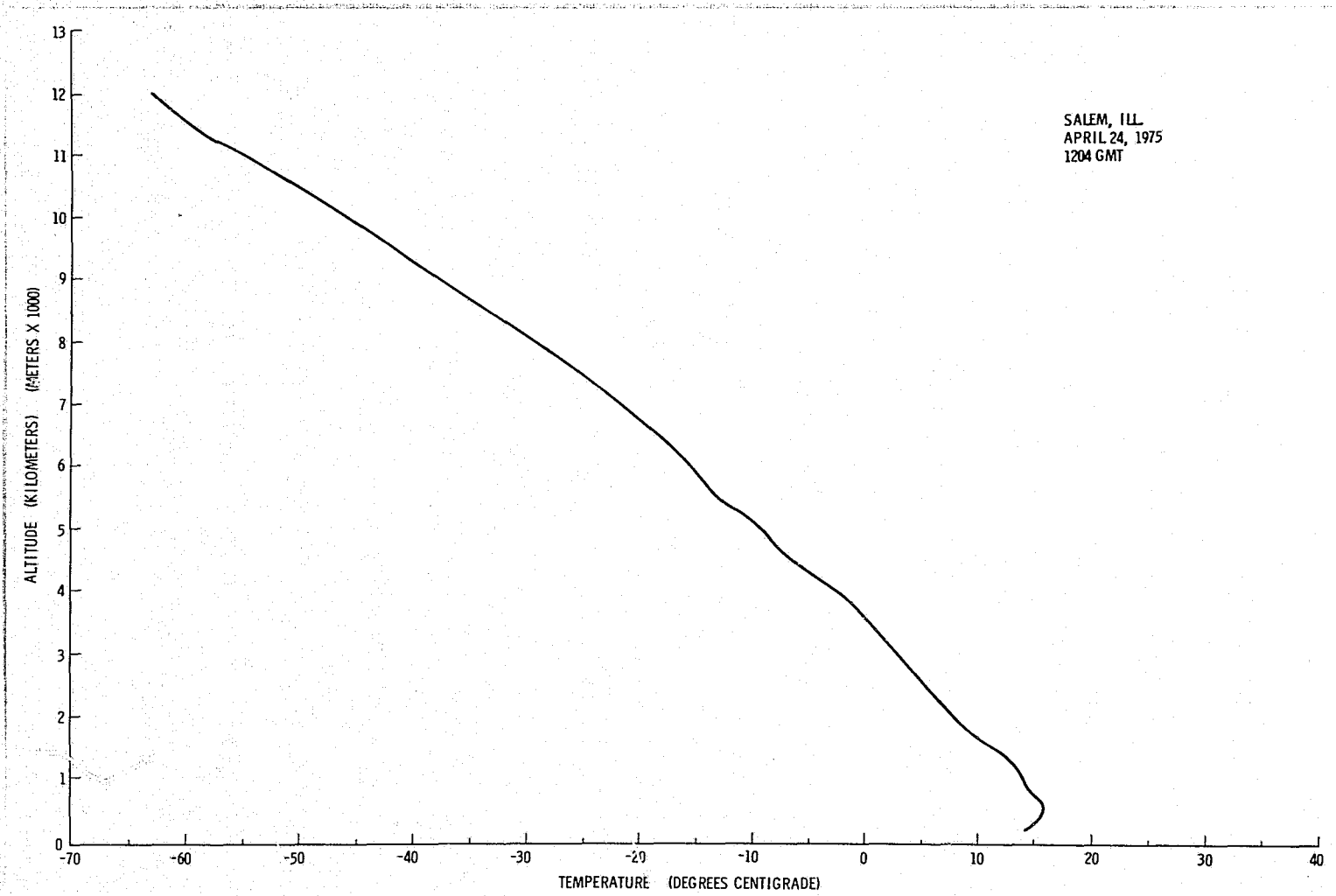

Figure A.98. Temperature profile for 1204 GMT, April 24, 1975, over Salem, Illinois.

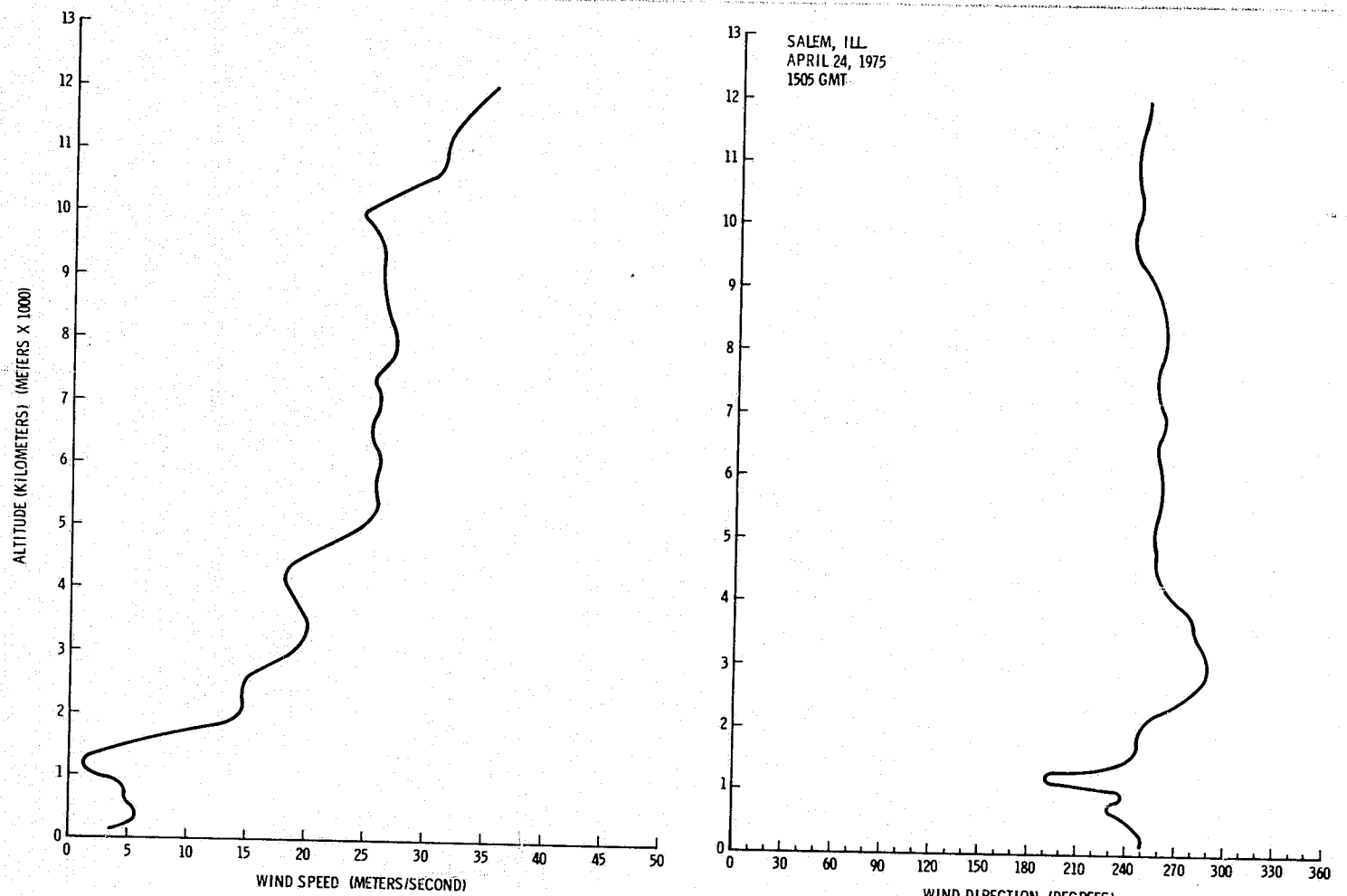

Figure A.99. Vertical wind profile for 1505 GMT, April 24, 1975, over Salem, Illinois.

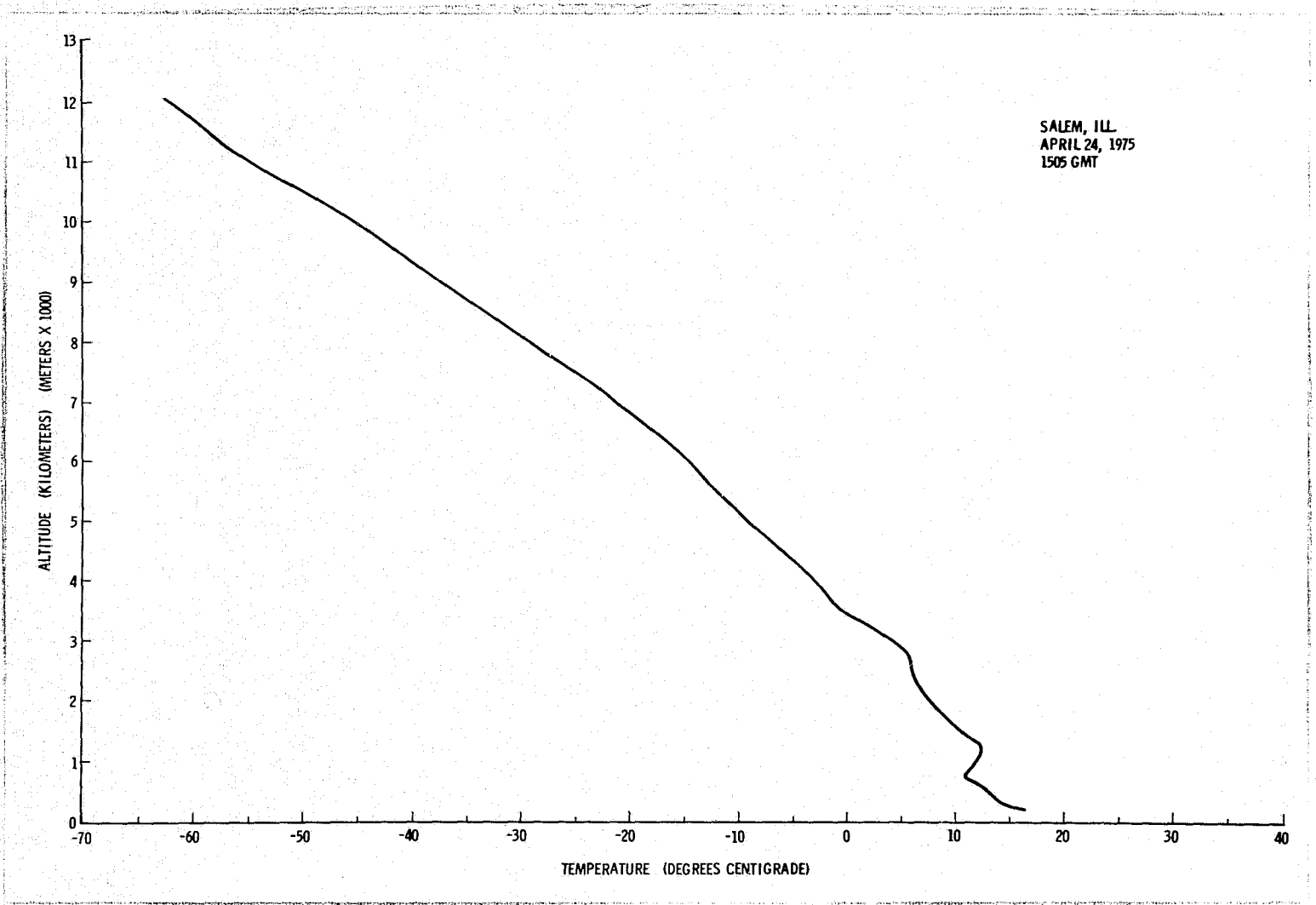

Figure A.100. Temperature profile for 1505 GMT, April 24, 1975, over Salem, Illinois.

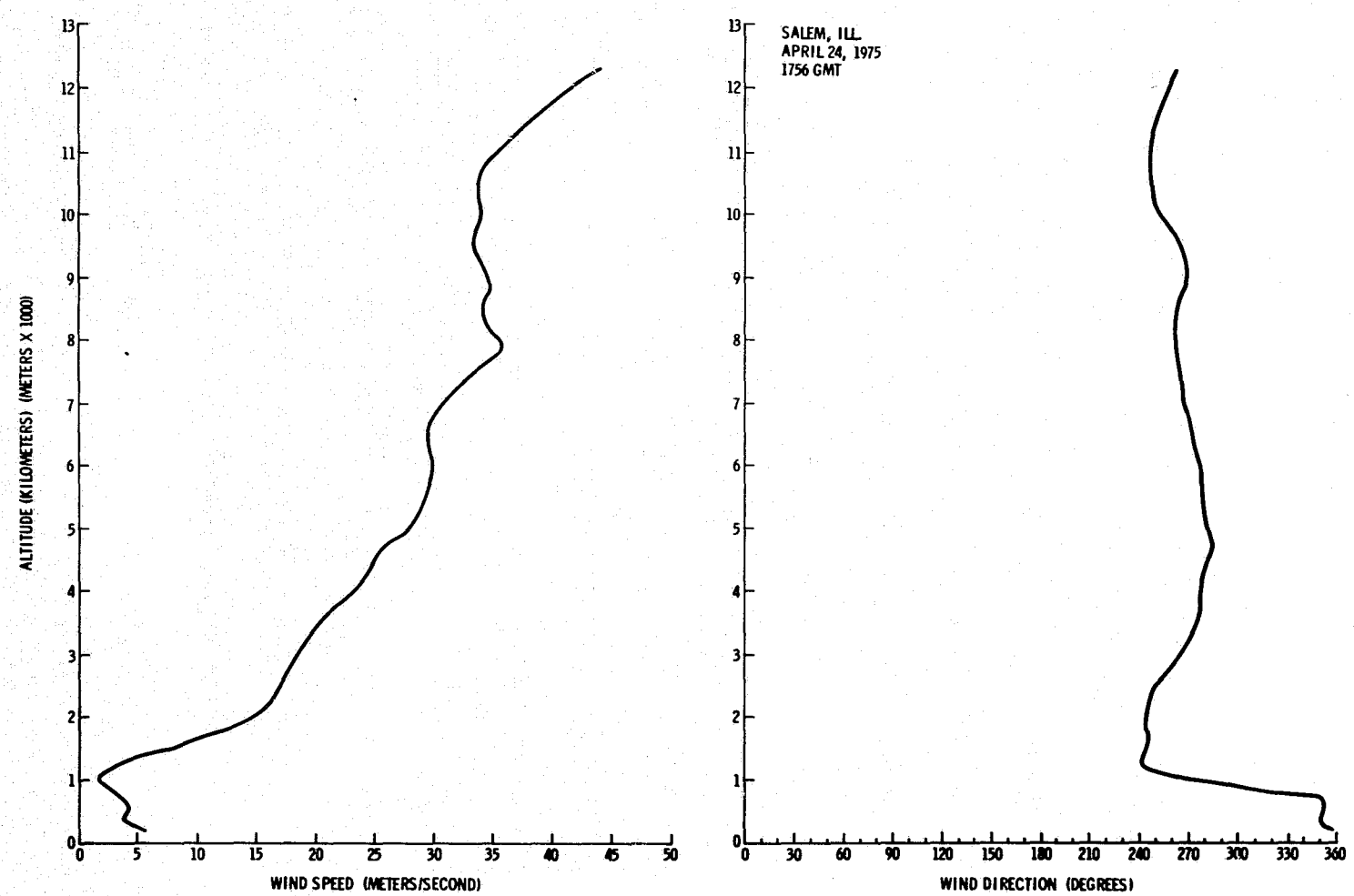

Figure A.101. Vertical wind profile for 1756 GMT, April 24, 1975, over Salem, Illinois.

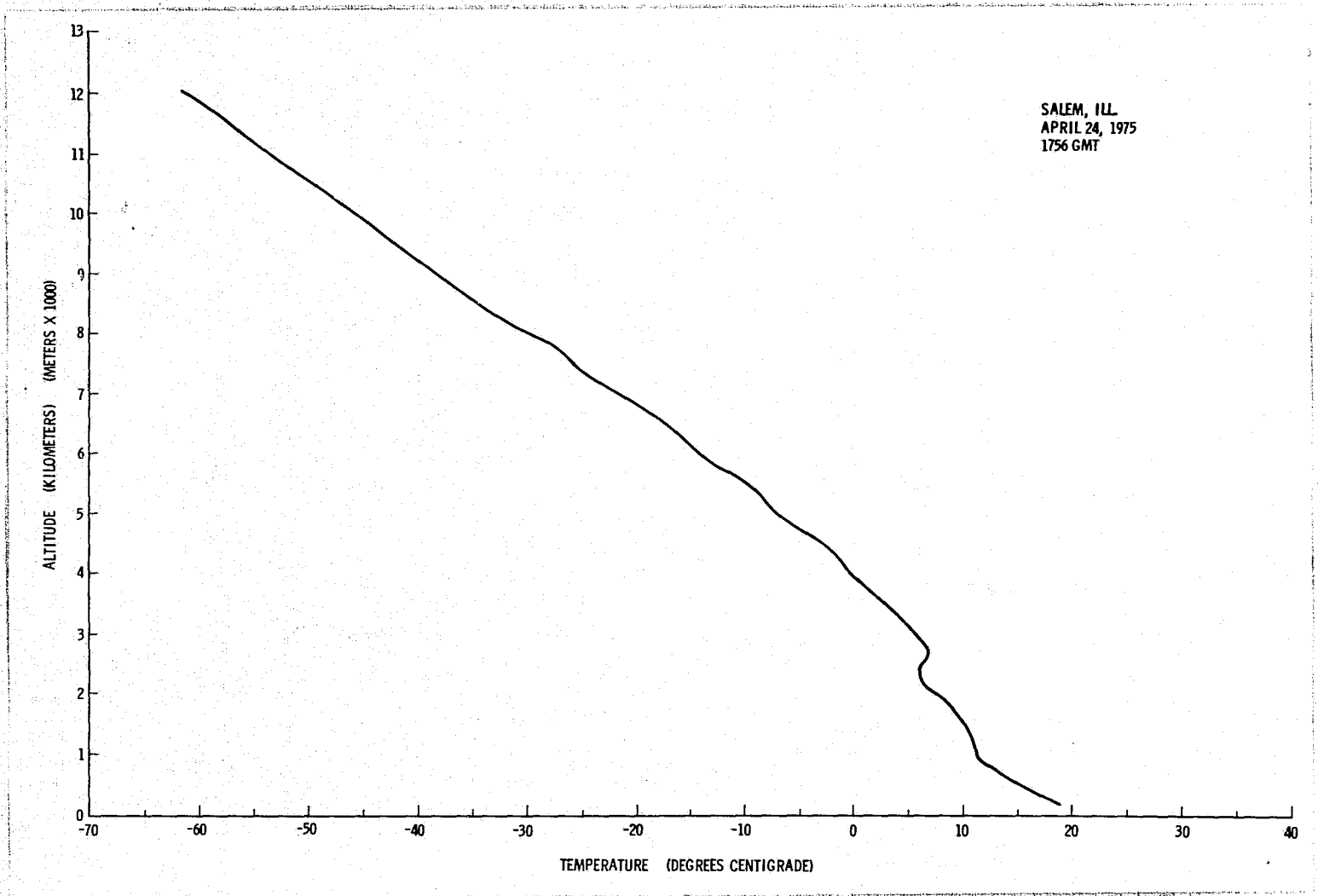

Figure A.102. Temperature profile for 1756 GMT, April 24, 1975, over Salem, Illinois.

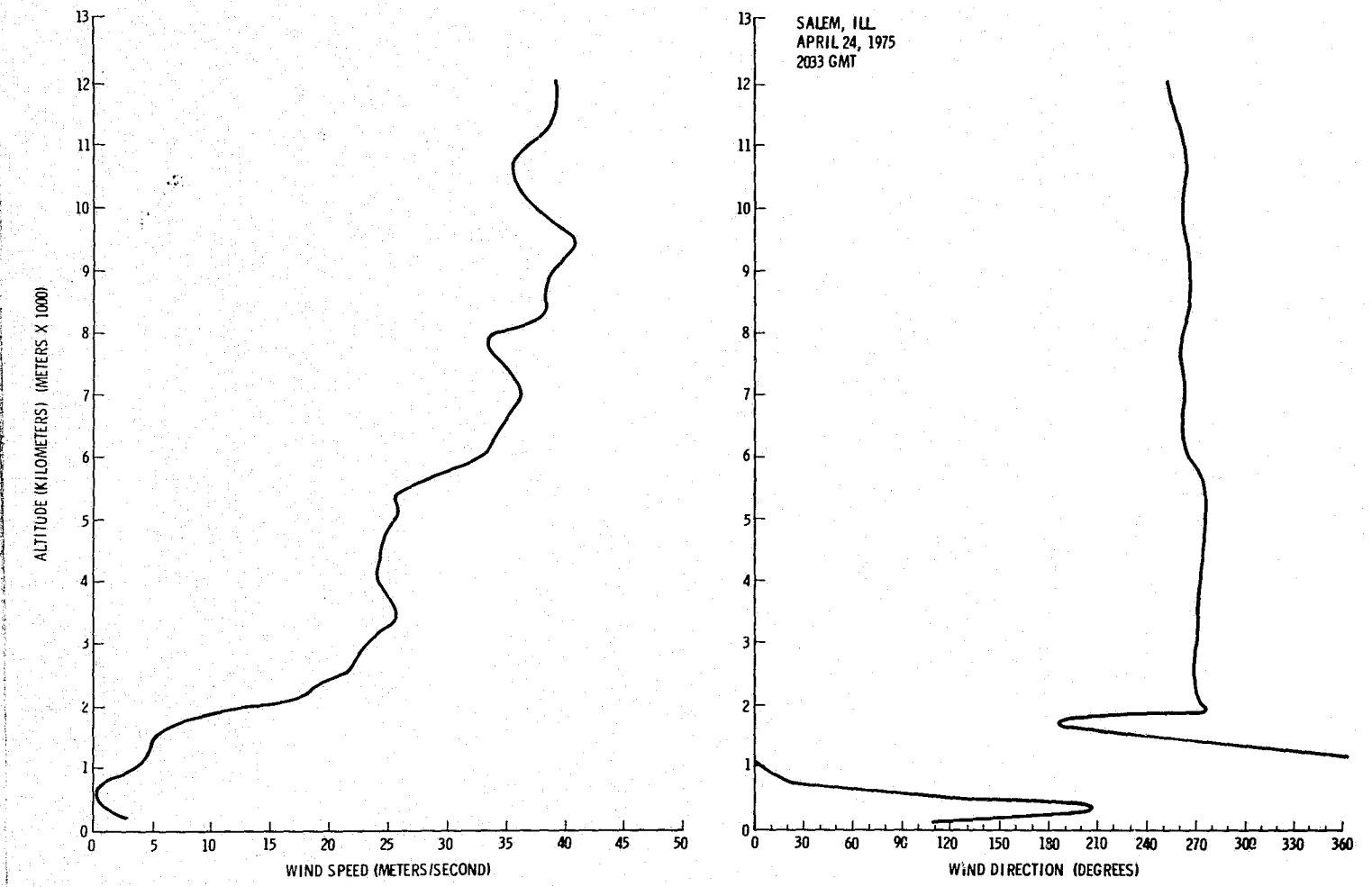

Figure A.103. Vertical wind profile for 2033 GMT, April 24, 1975, over Salem, Illinois.

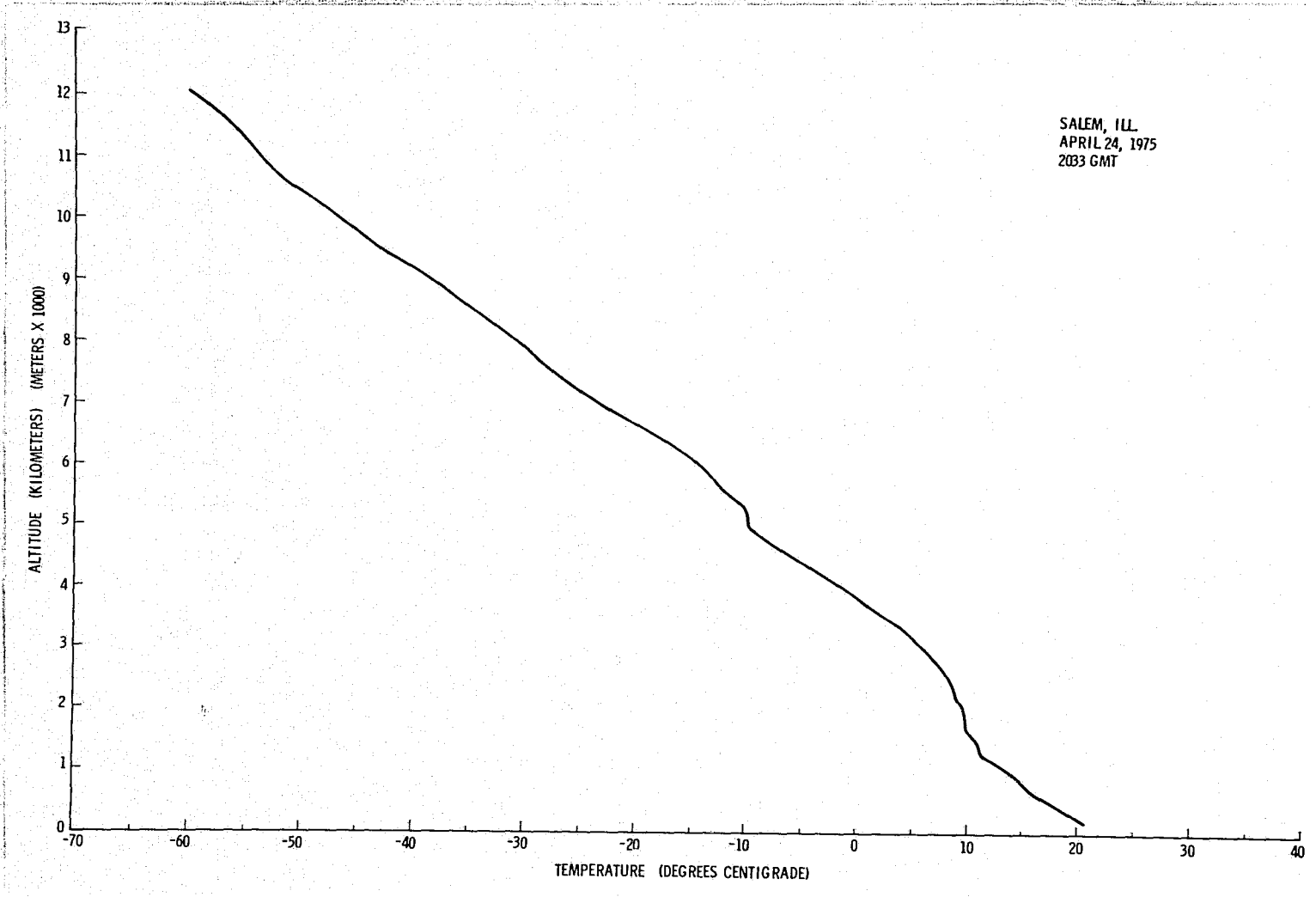

Figure A.104. Temperature profile for 2033 GMT, April 24, 1975, over Salem, Illinois.

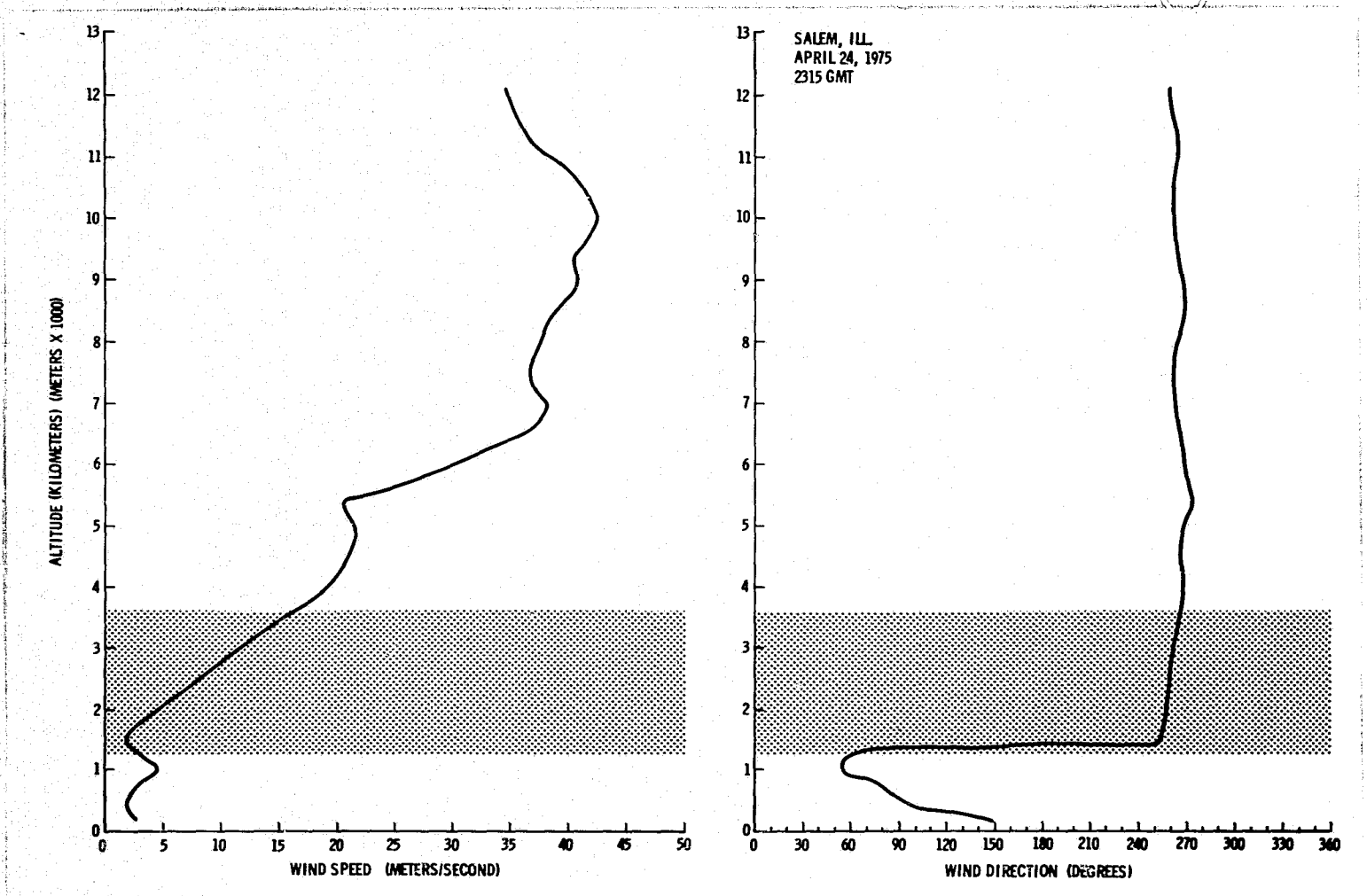

Figure A.105. Vertical wind profile for 2315 GMT, April 24, 1975, over Salem, Illinois.

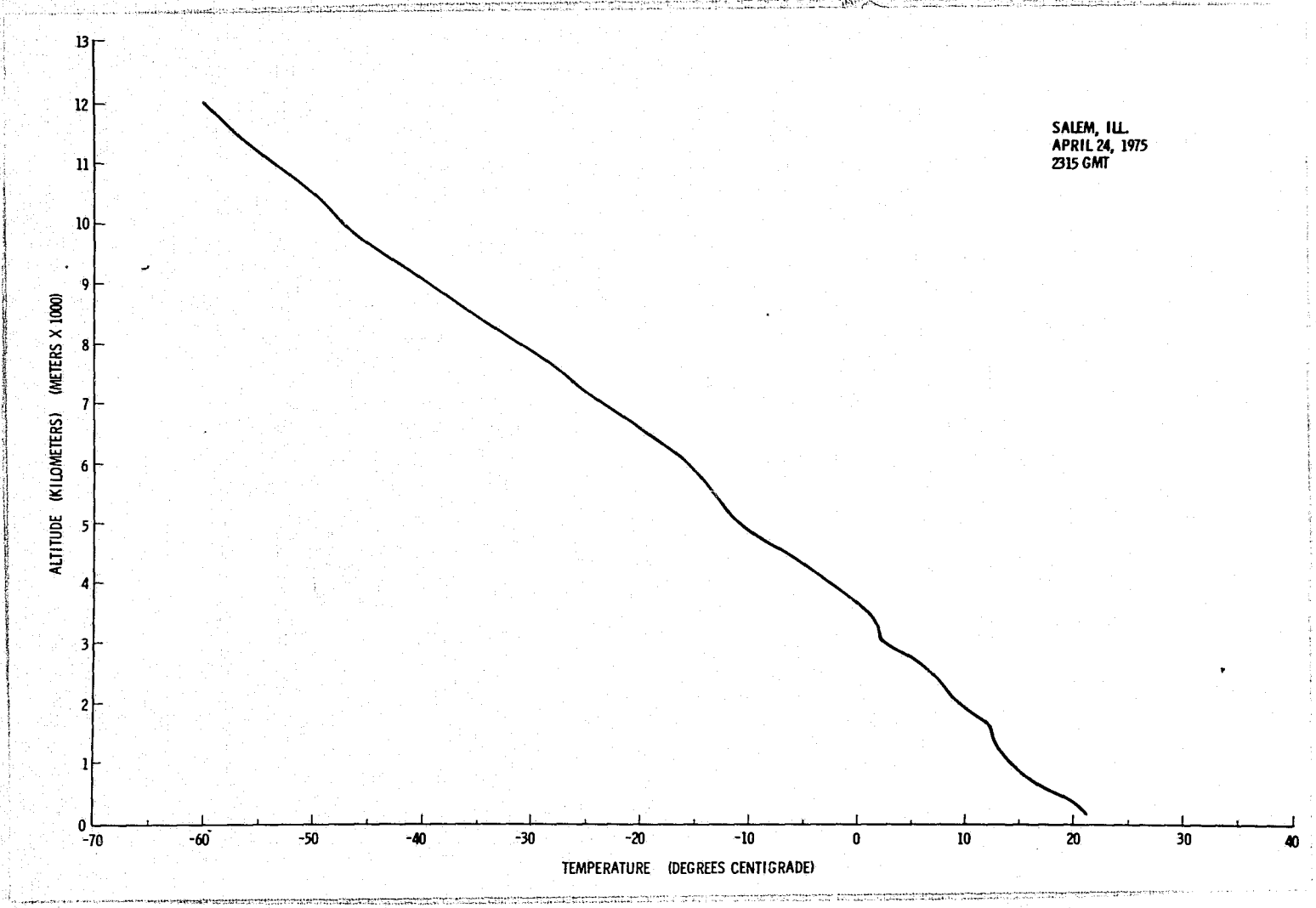

Figure A.106. Temperature profile for 2315 GMT, April 24, 1975, over Salem, Illinois.

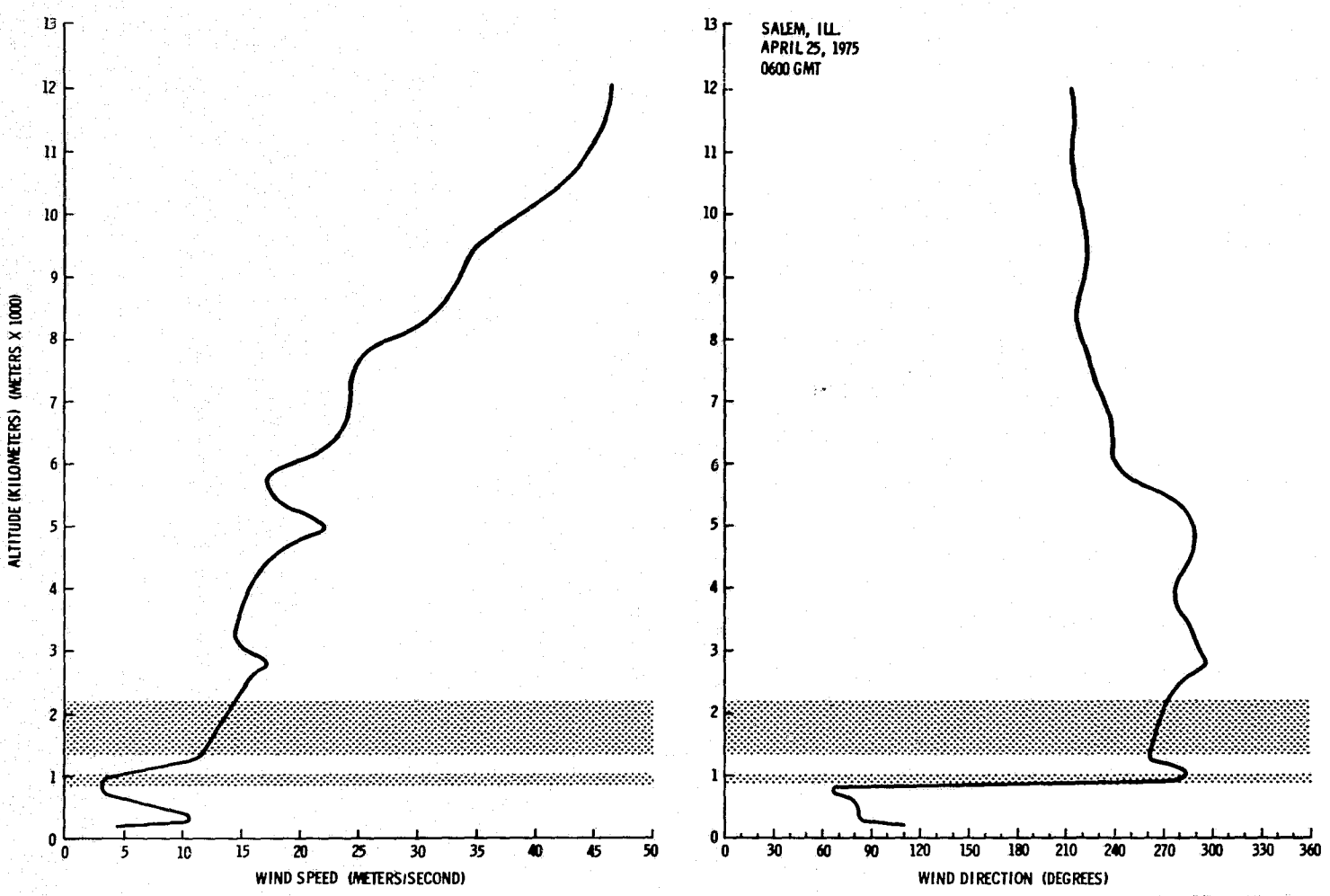

Figure A.107. Vertical wind profile for 0600 GMT, April 25, 1975, over Salem, Illinois.

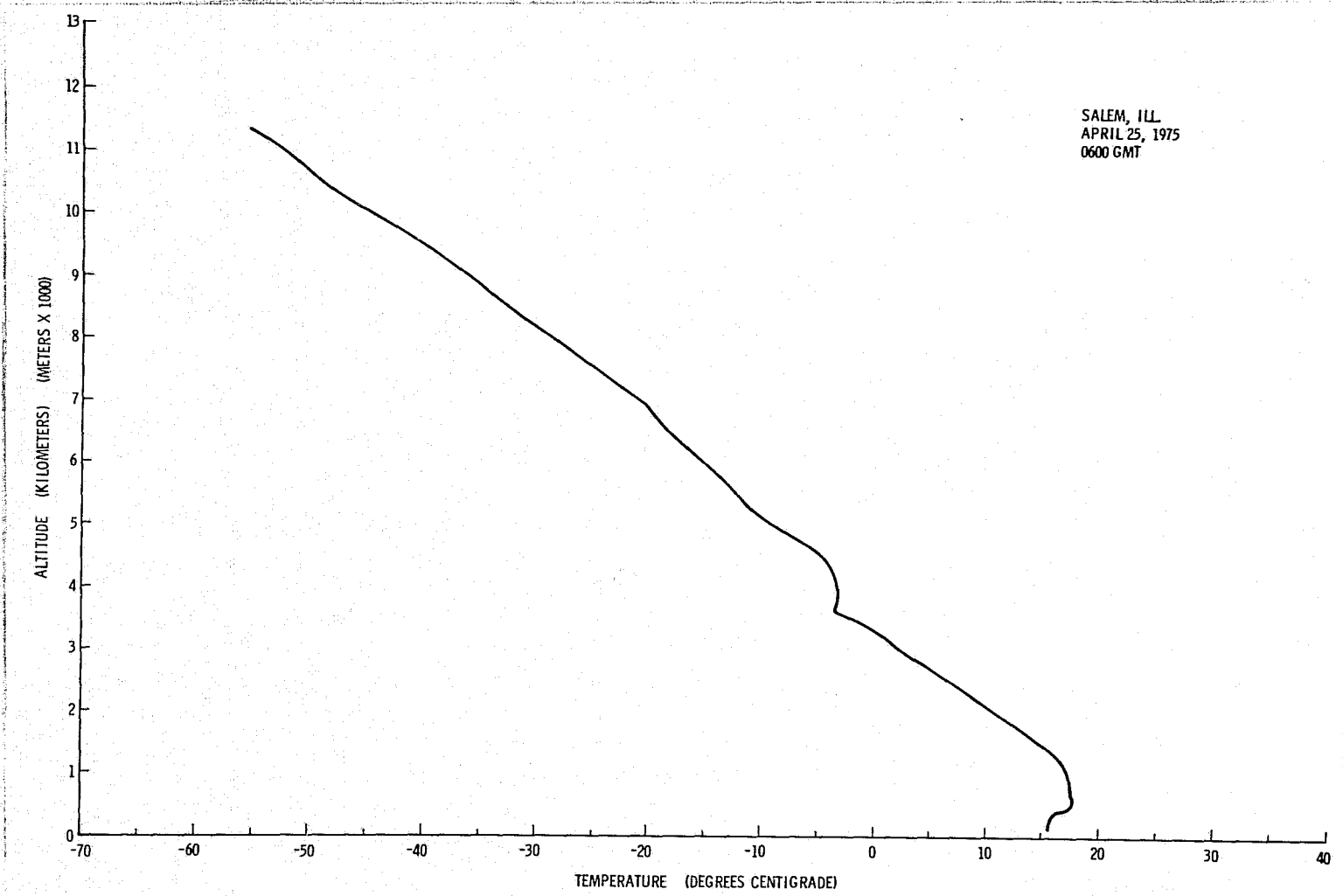

Figure A.108. Temperature profile for 0600 GMT, April 25, 1975, over Salem, Illinois.

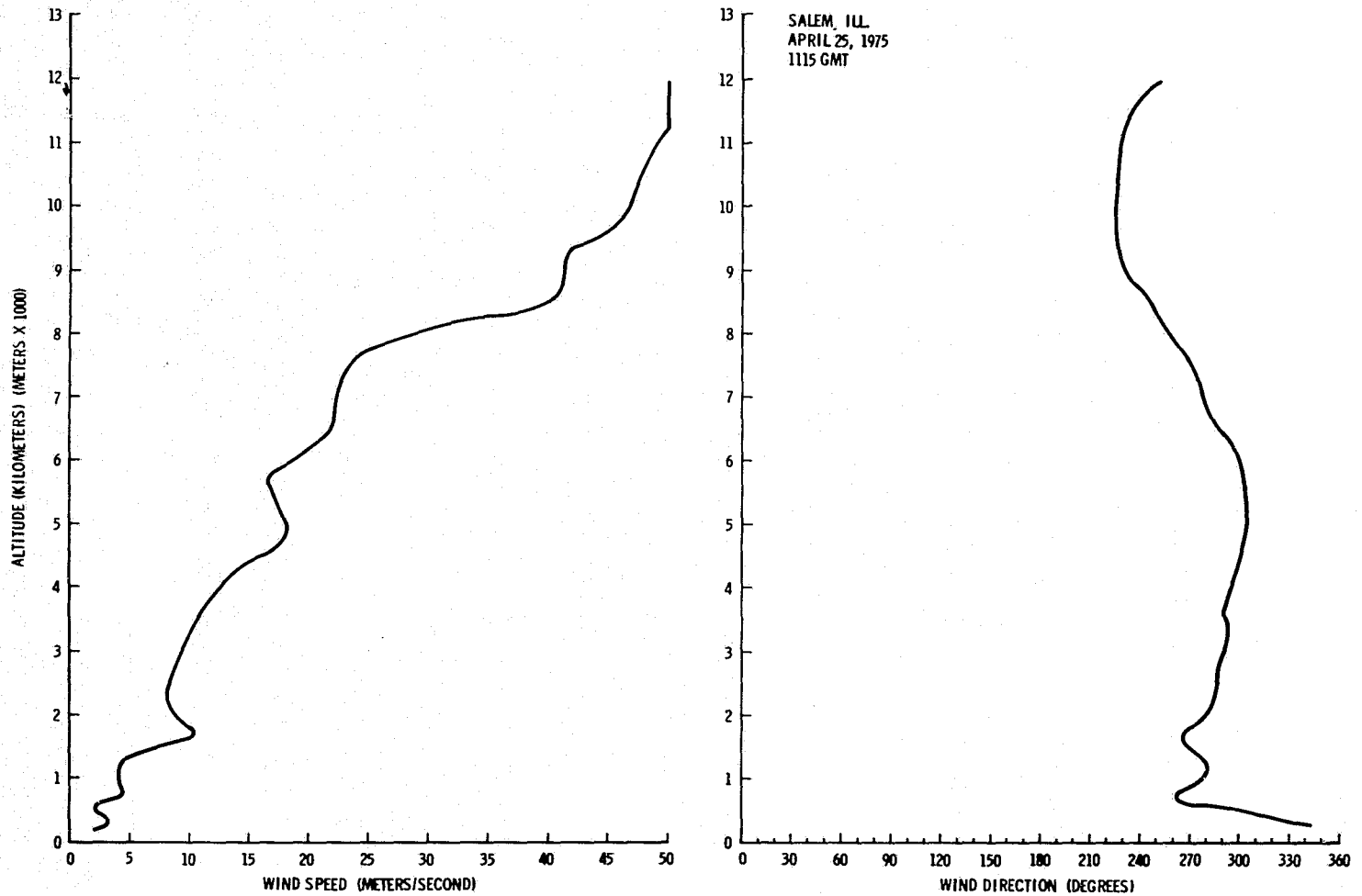

Figure A.109. Vertical wind profile for 1115 GMT, April 25, 1975, over Salem, Illinois.

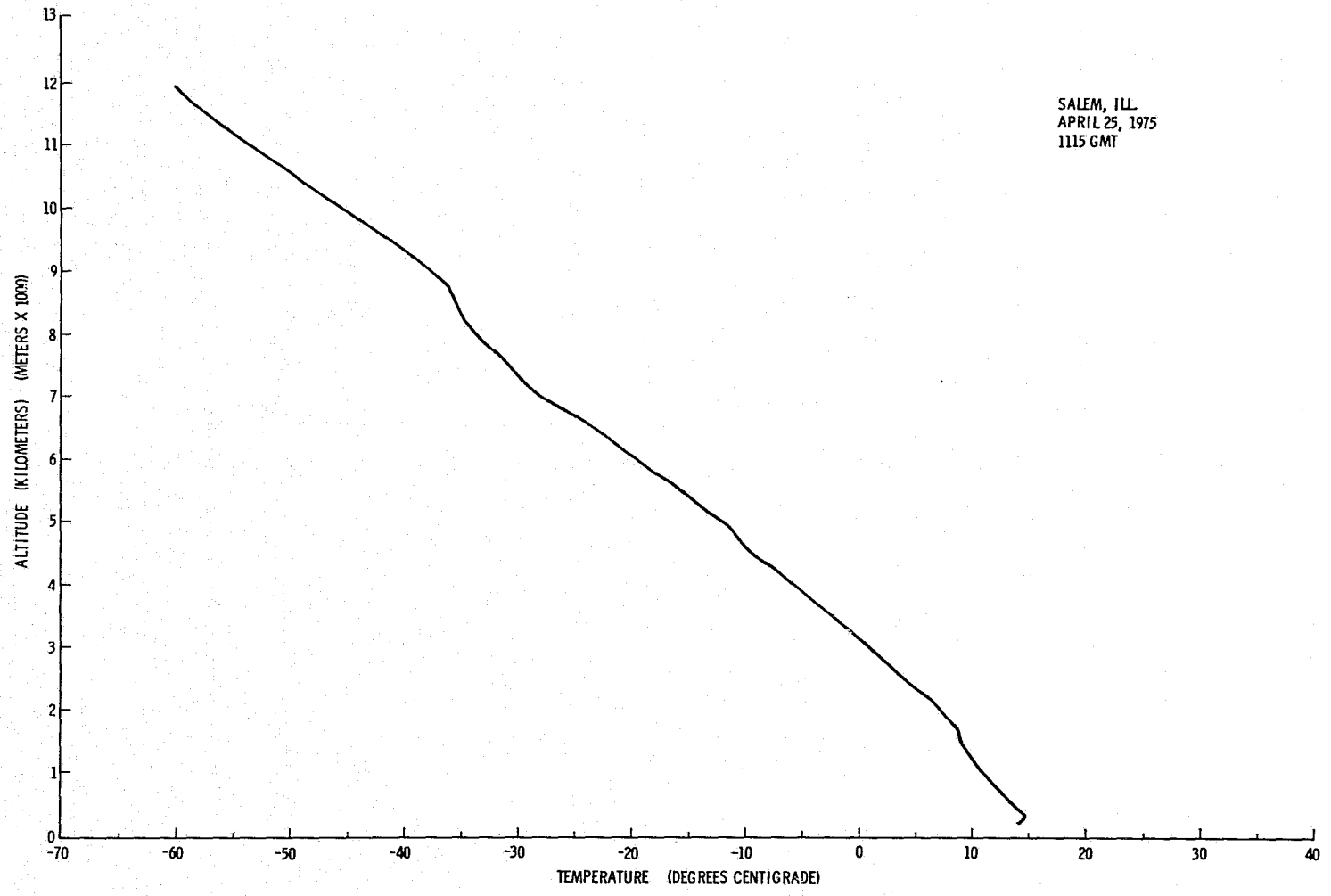

Figure A.110. Temperature profile for 1115 GMT, April 25, 1975, over Salem, Illinois.

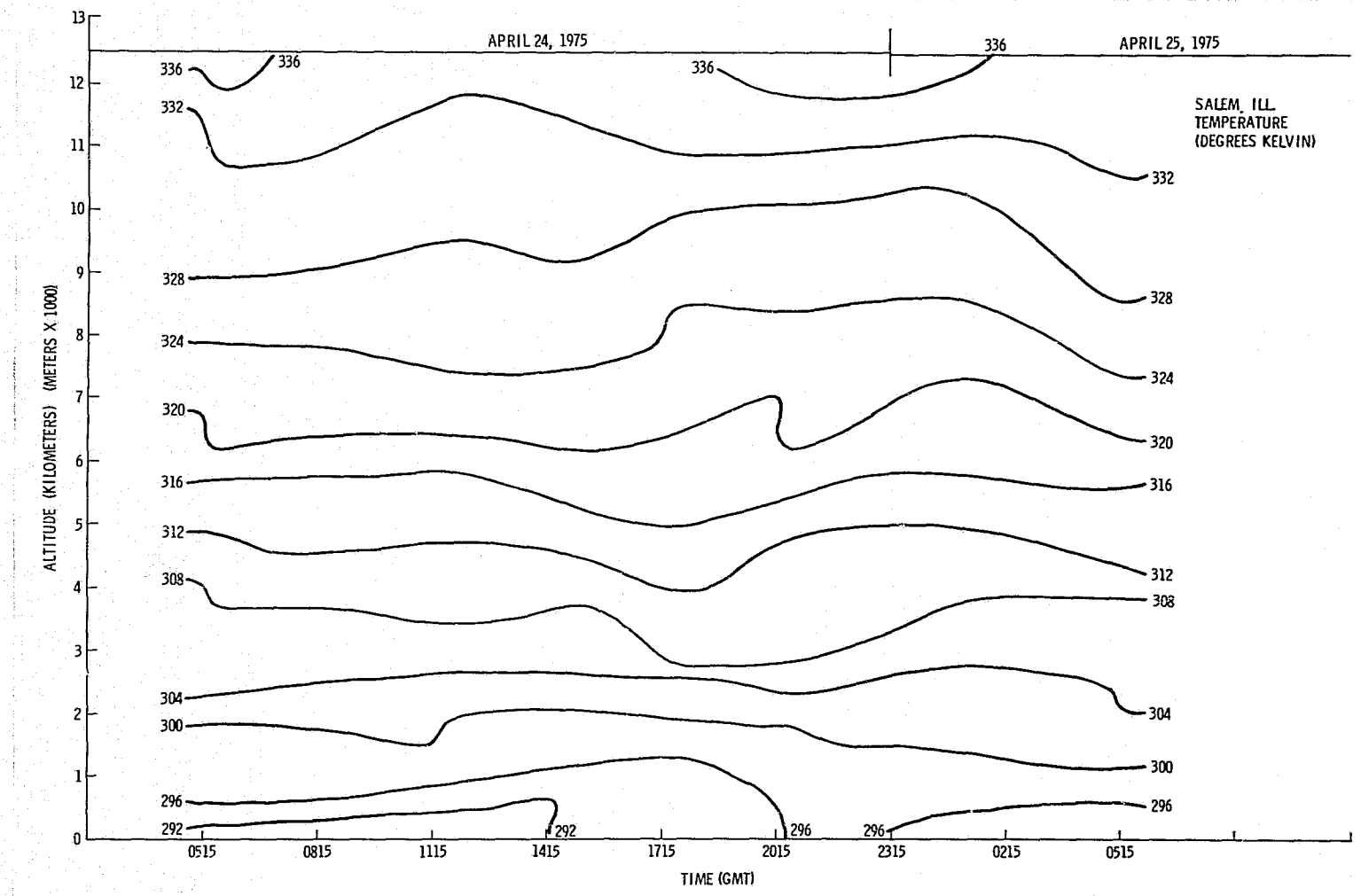

Figure A.111. Time cross section of temperature at Salem, Illinois.

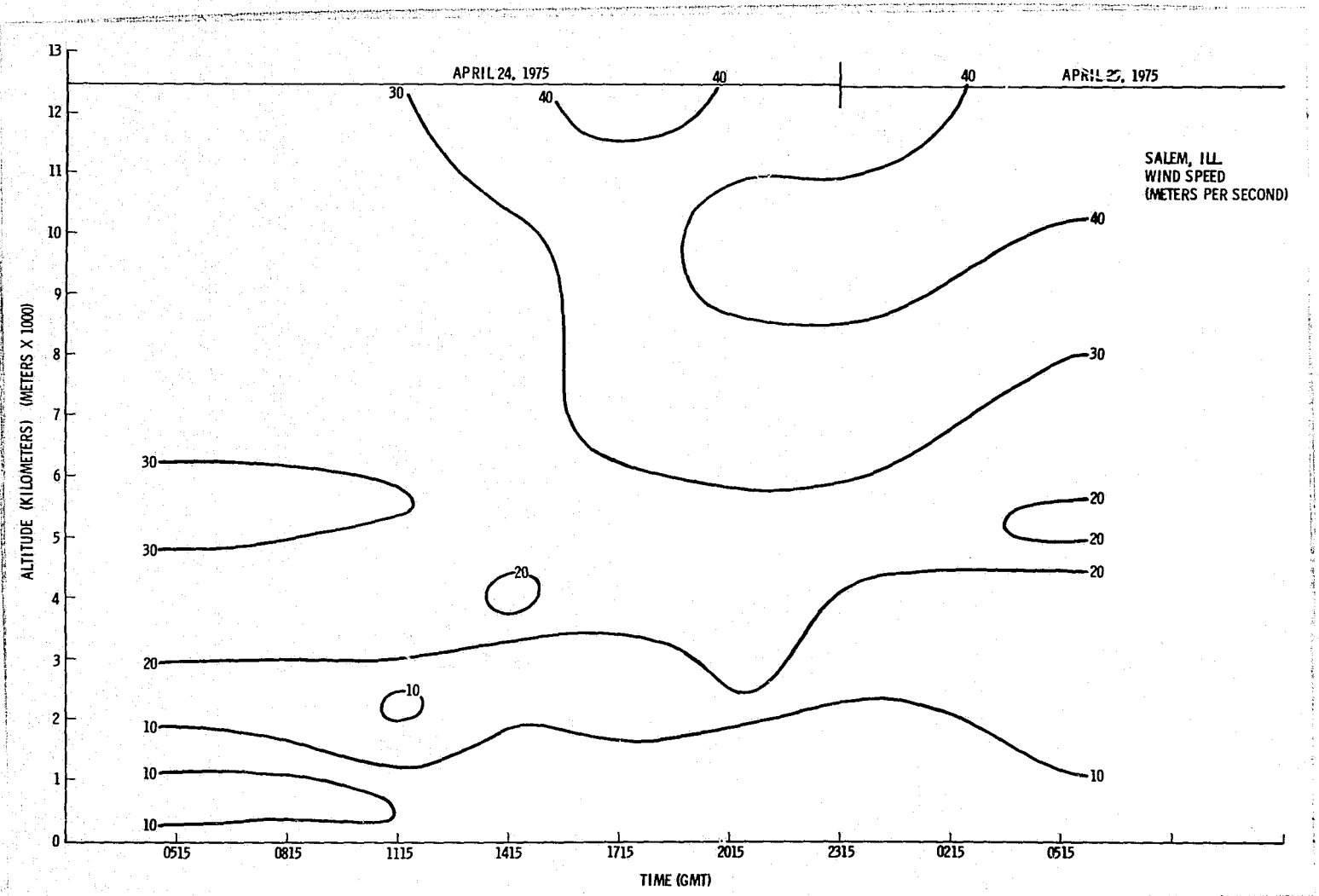

Figure A.112. Time cross section of wind speed at Salem, Illinois.

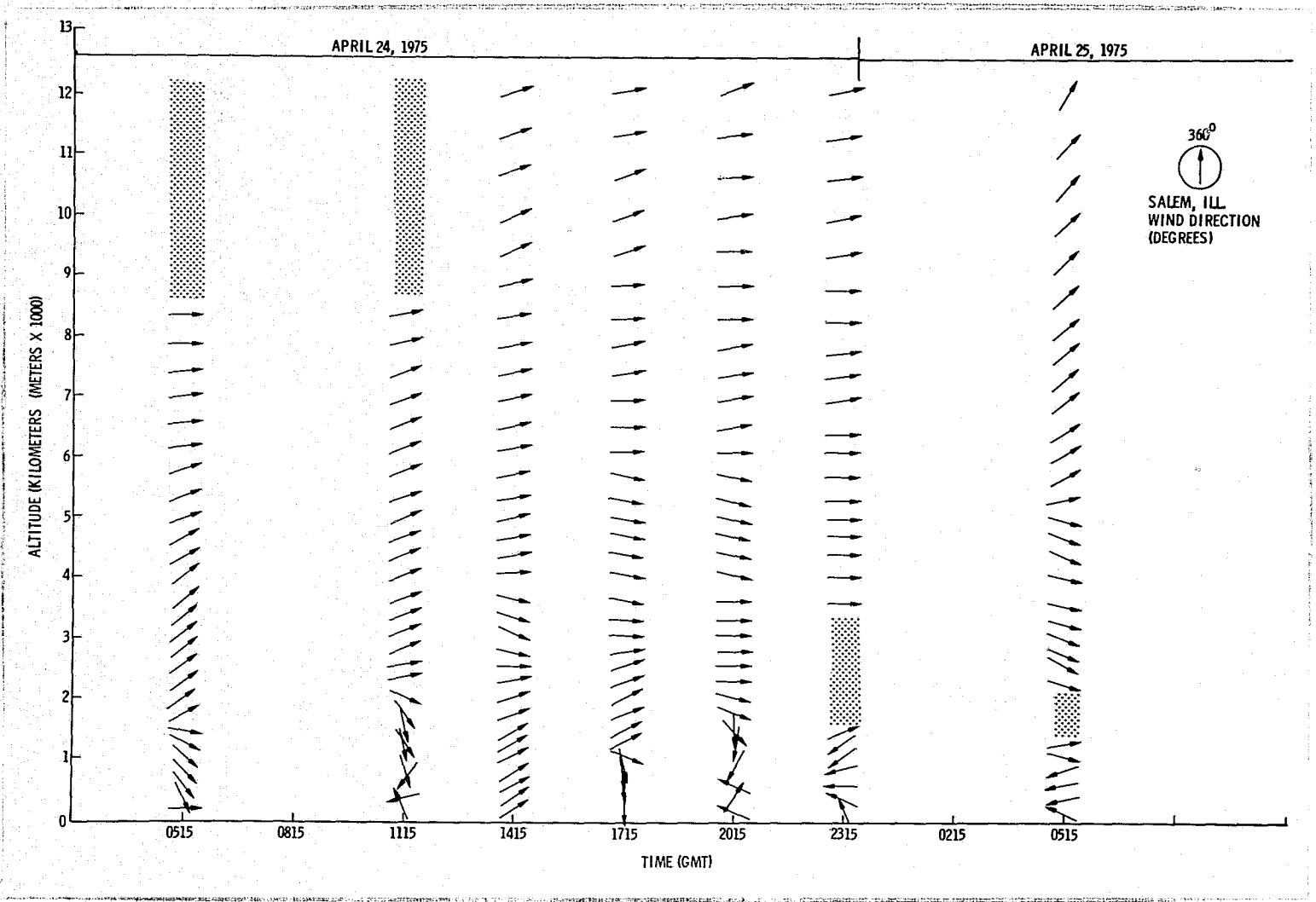

Figure A.113. Time cross section of wind direction at Salem, Illinois.

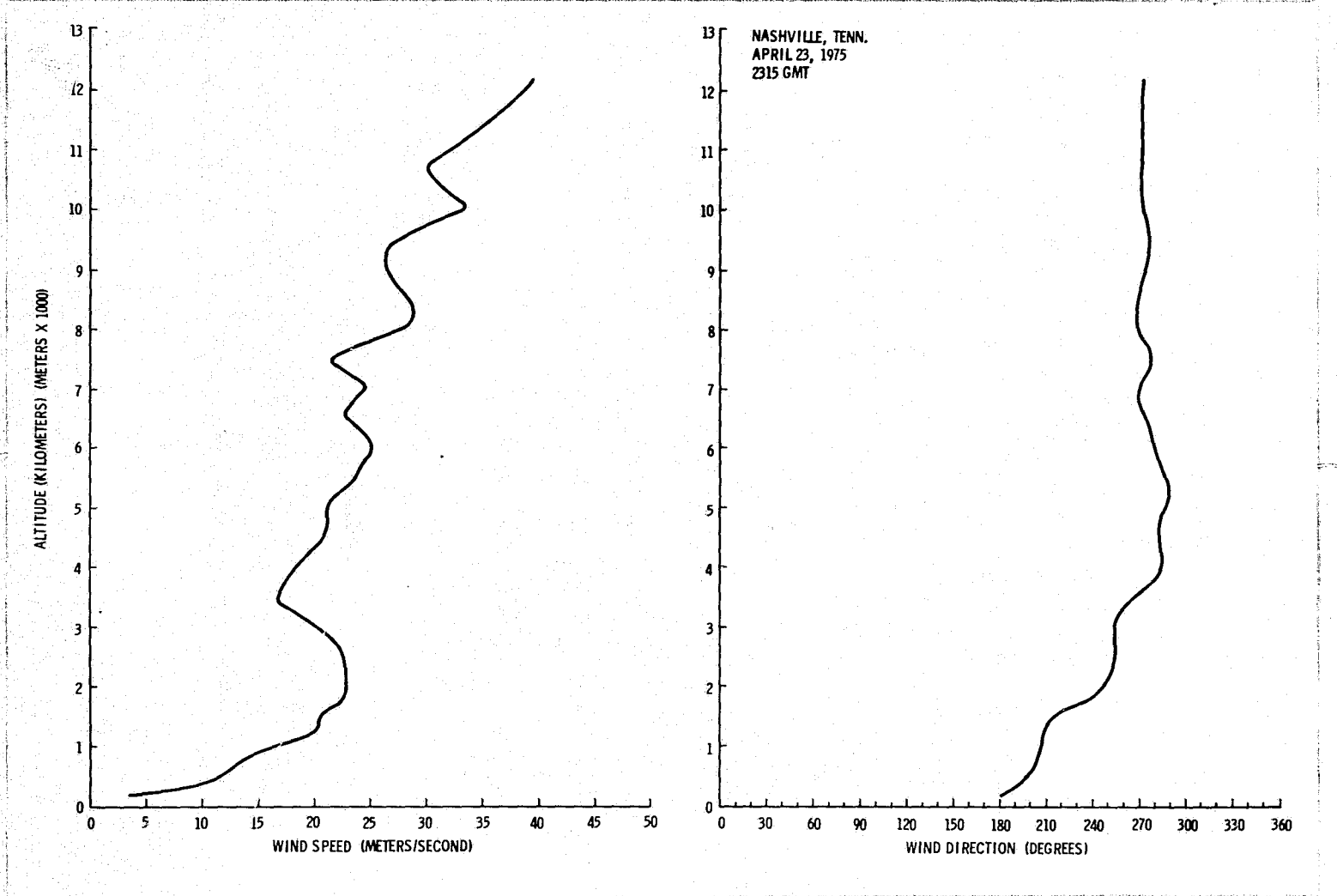

Figure A.114. Vertical wind profile for 2315 GMT, April 23, 1975, over Nashville, Tennessee.

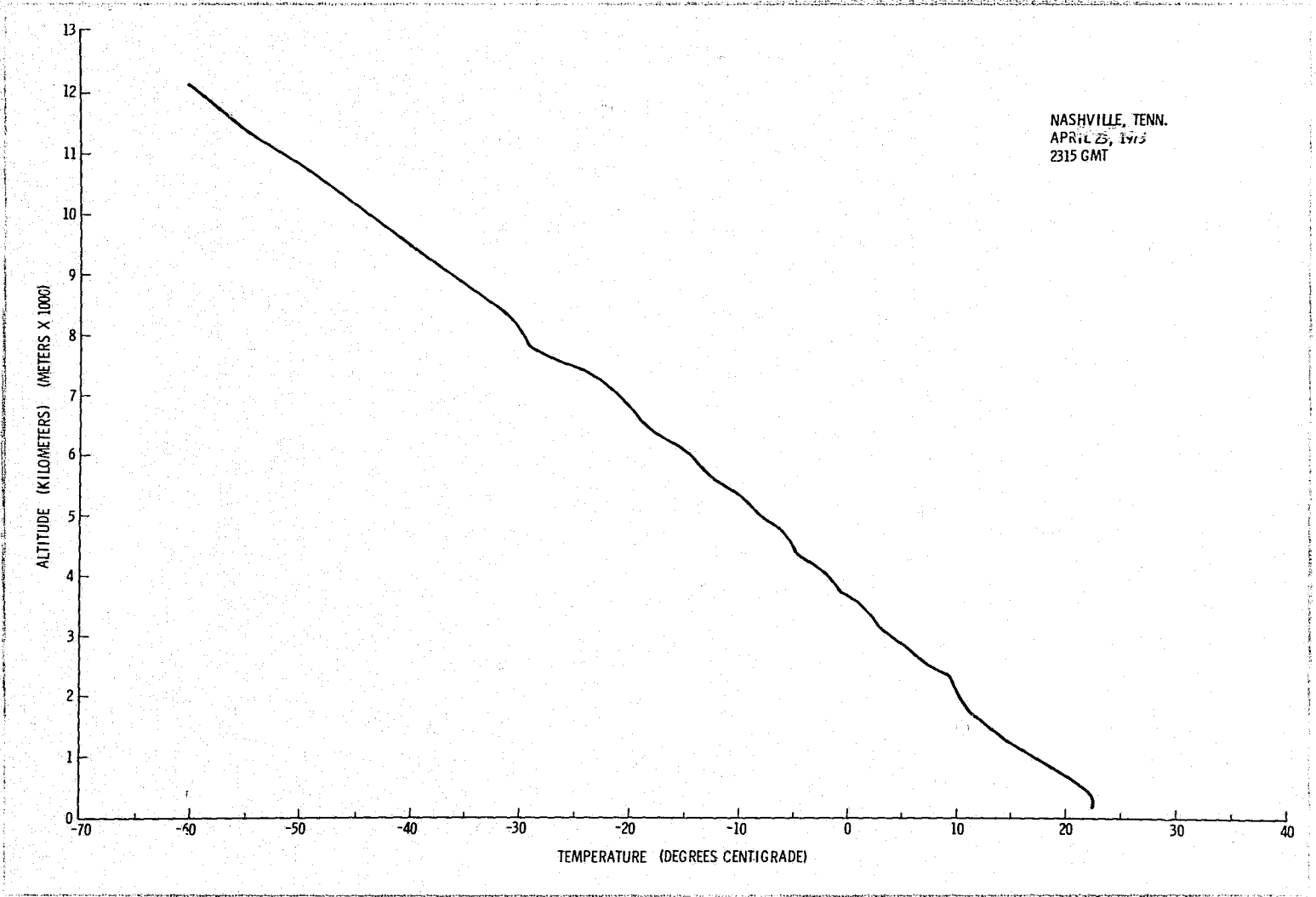

Figure A.115. Temperature profile for 2315 GMT, April 23, 1975, over Nashville, Tennessee.

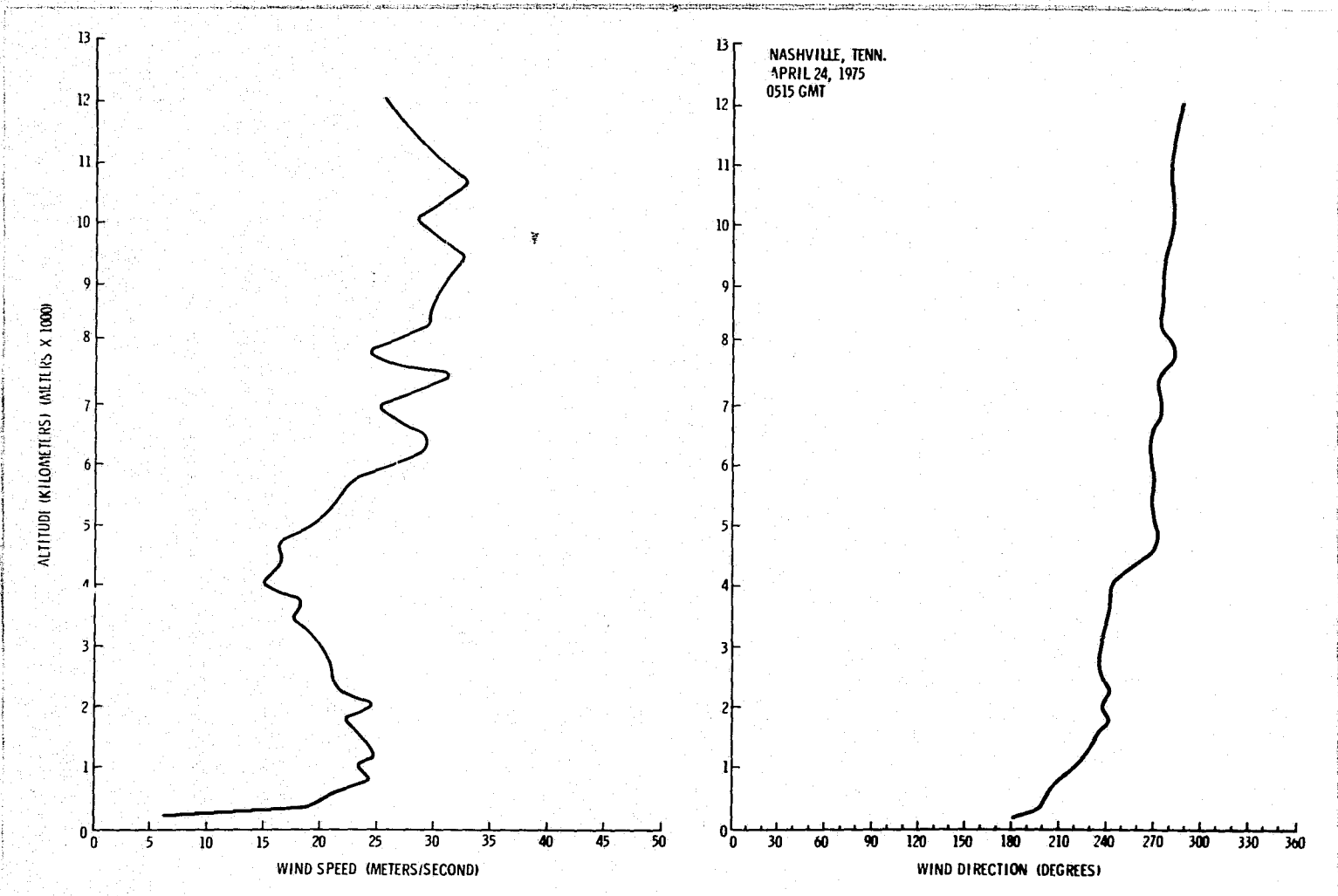

Figure A.116. Vertical wind profile for 0515 GMT, April 24, 1975, over Nashville, Tennessee.

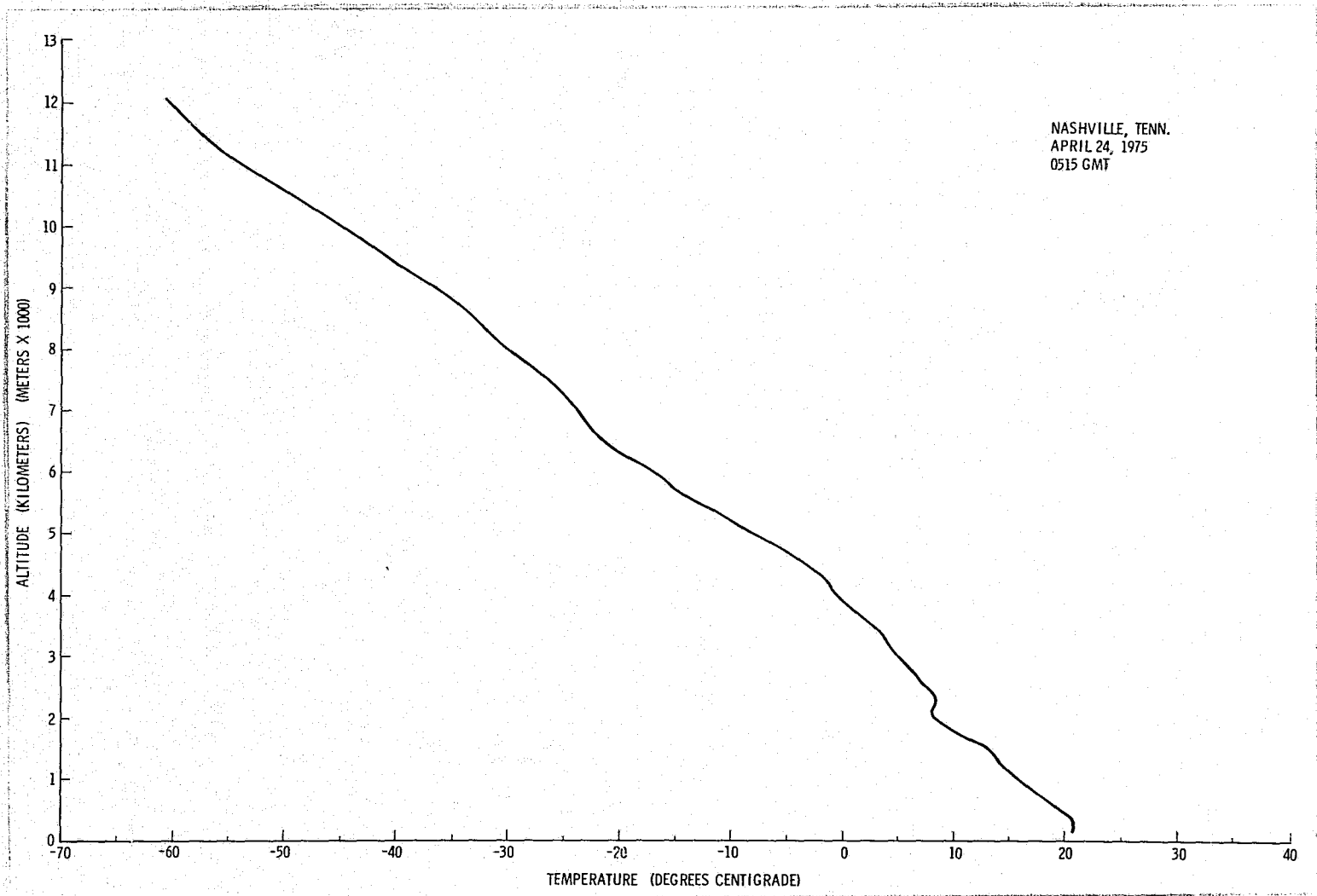

Figure A.117. Temperature profile for 0515 GMT, April 24, 1975, over Nashville, Tennessee.

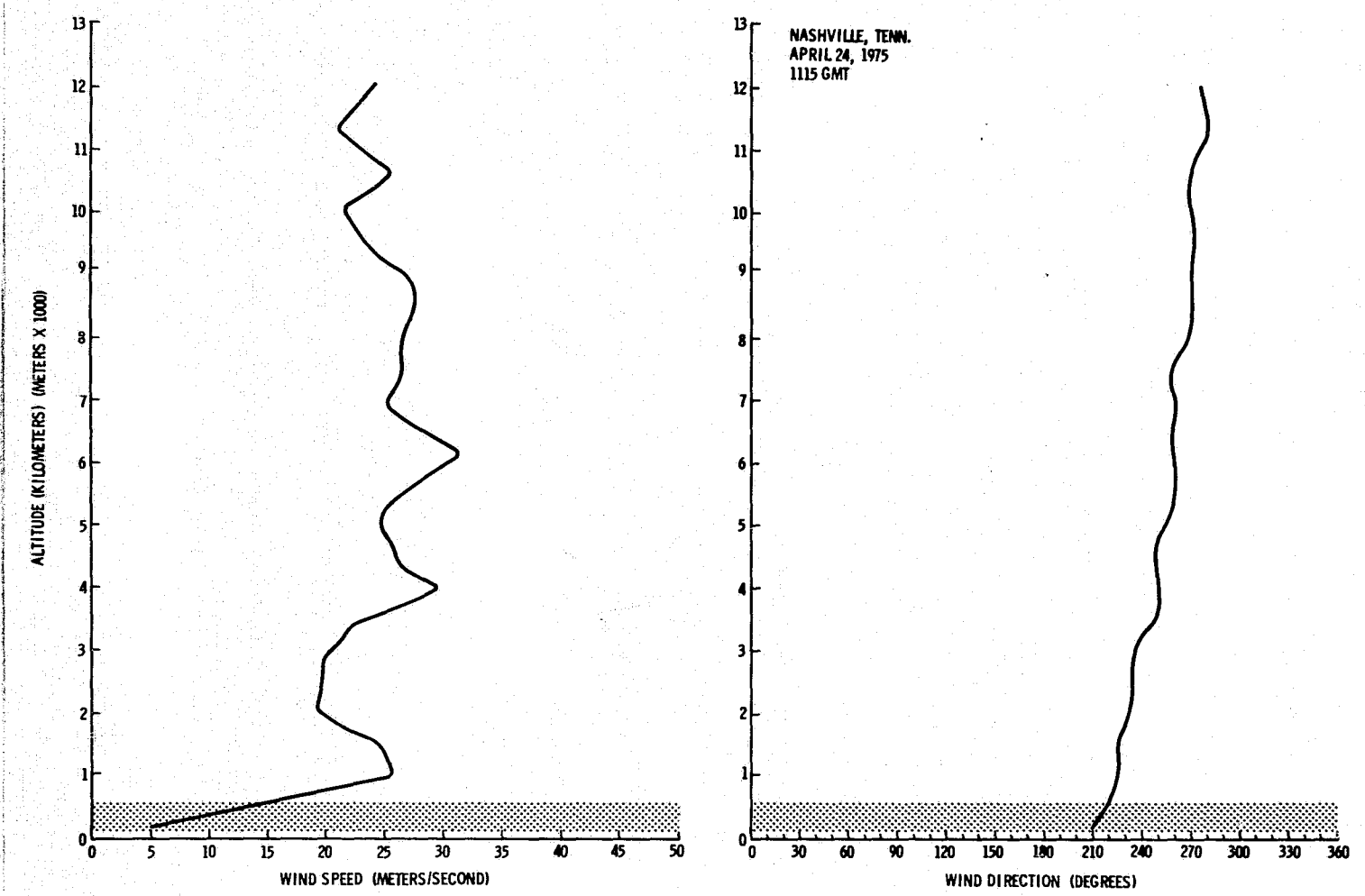

Figure A.118. Vertical wind profile for 1115 GMT, April 24, 1975, over Nashville, Tennessee.

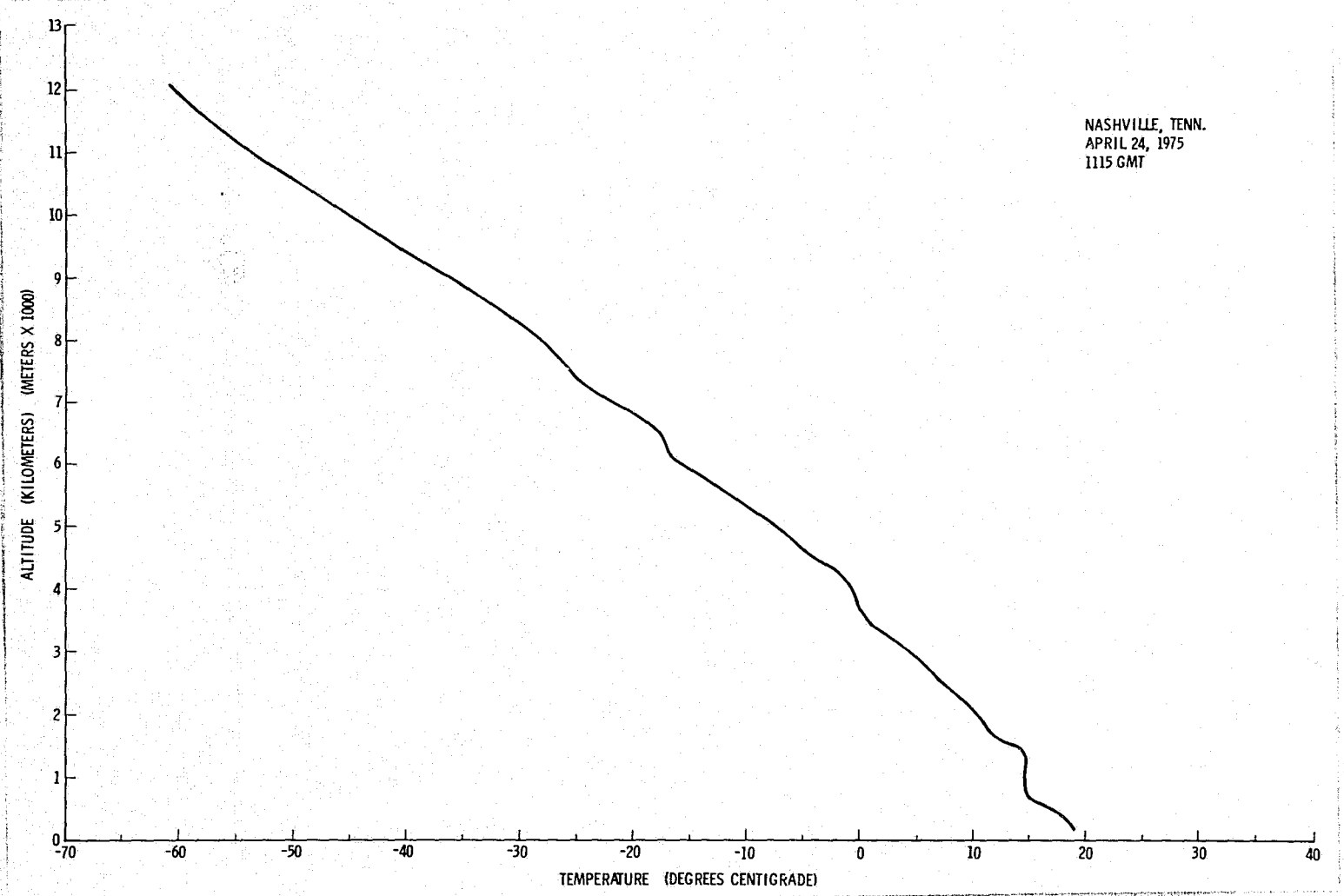

Figure A.119. Temperature profile for 1115 GMT, April 24, 1975, over Nashville, Tennessee.

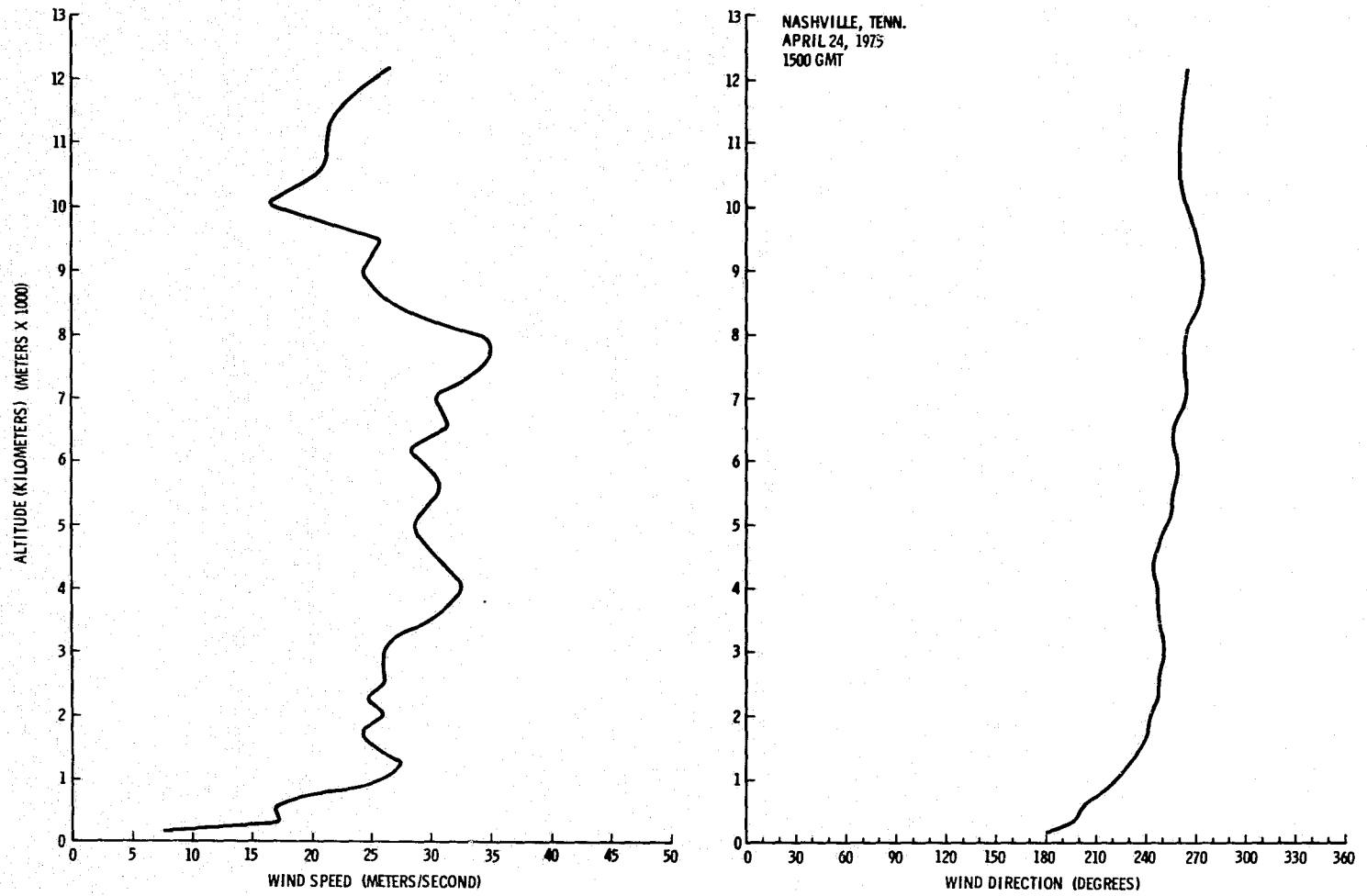

Figure A.120. Vertical wind profile for 1500 GMT, April 24, 1975, over Nashville, Tennessee.

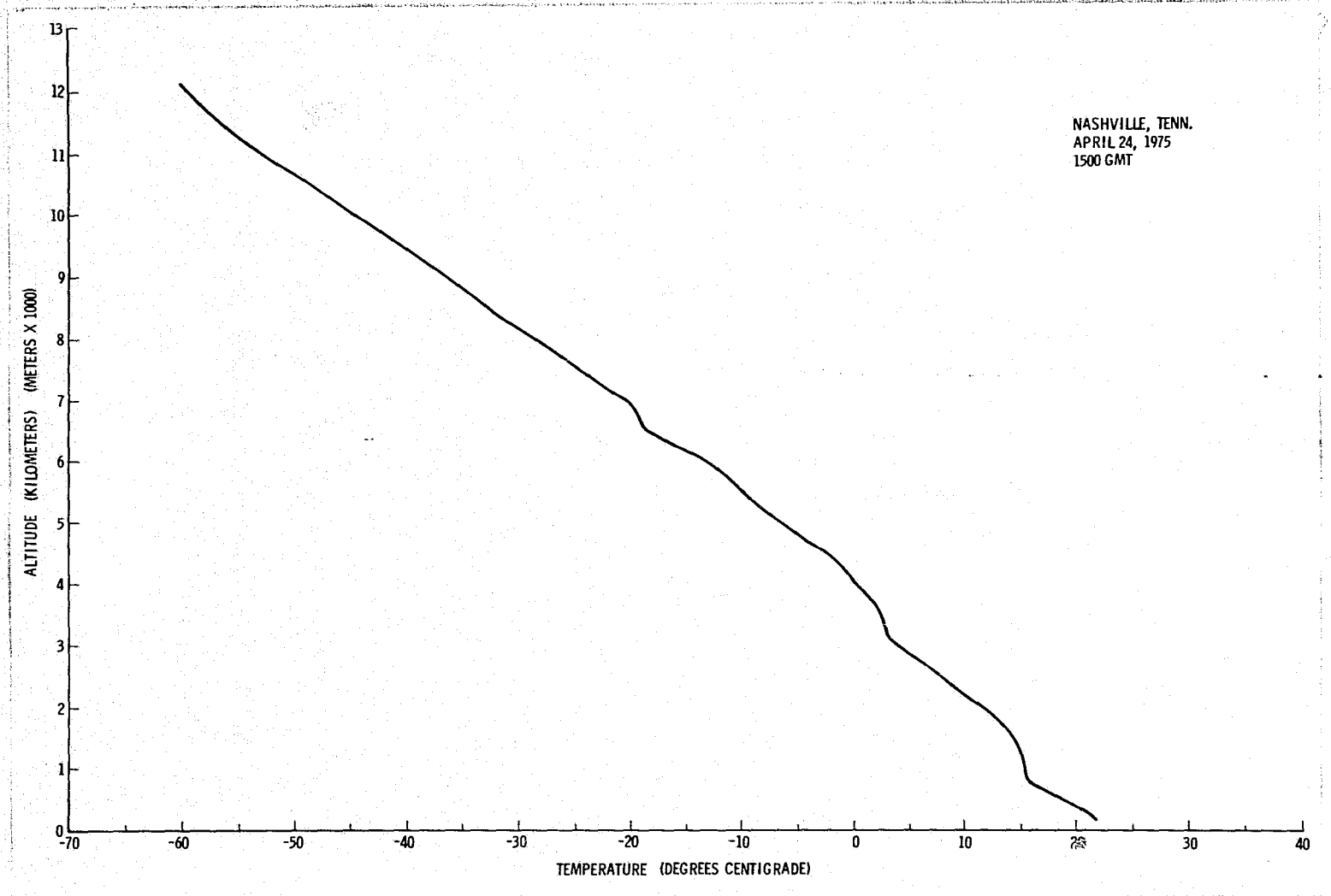

Figure A.121. Temperature profile for 1500 GMT, April 24, 1975, over Nashville, Tennessee.

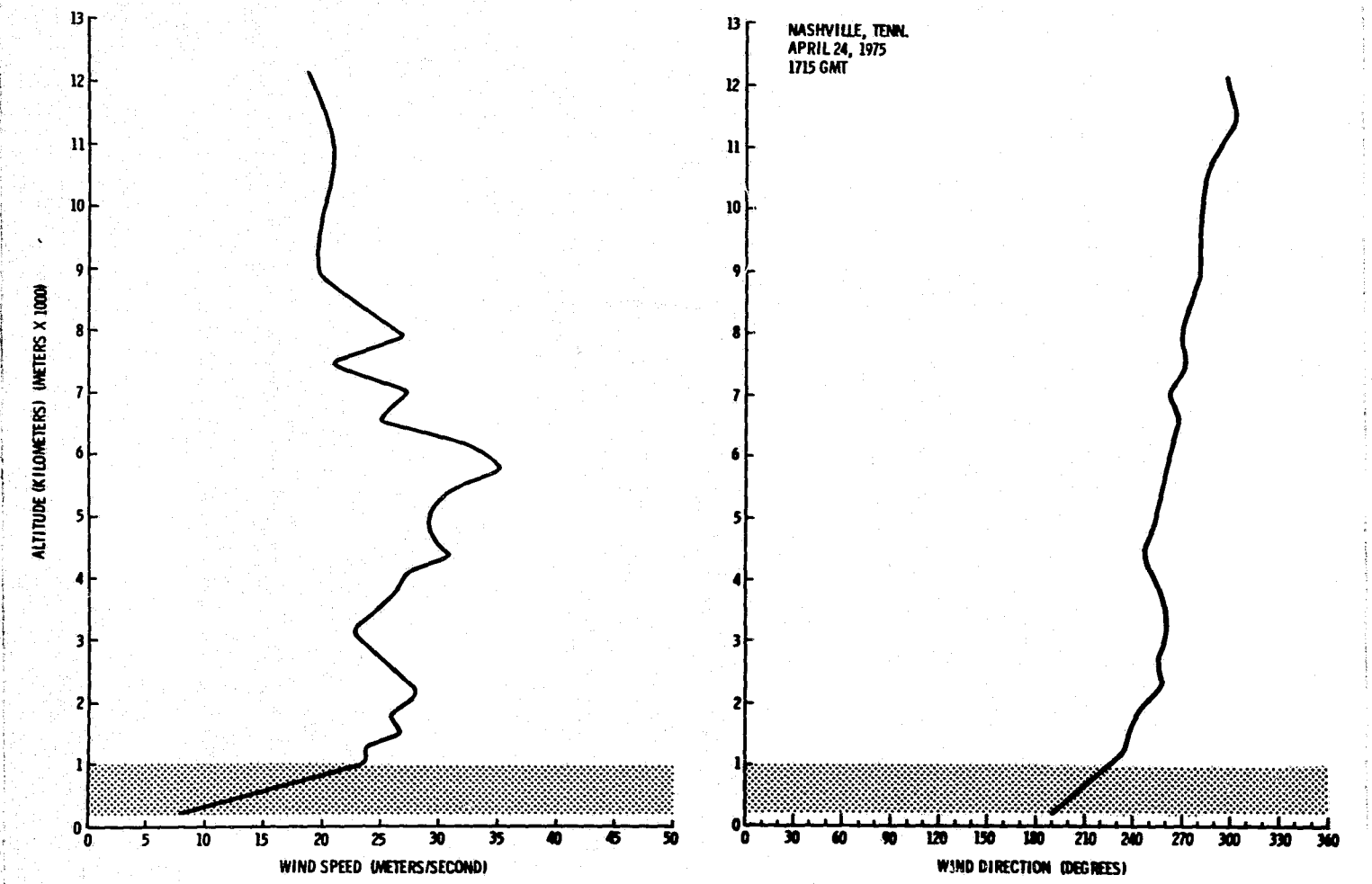

Figure A.122. Vertical wind profile for 1715 GMT, April 24, 1975, over Nashville, Tennessee.

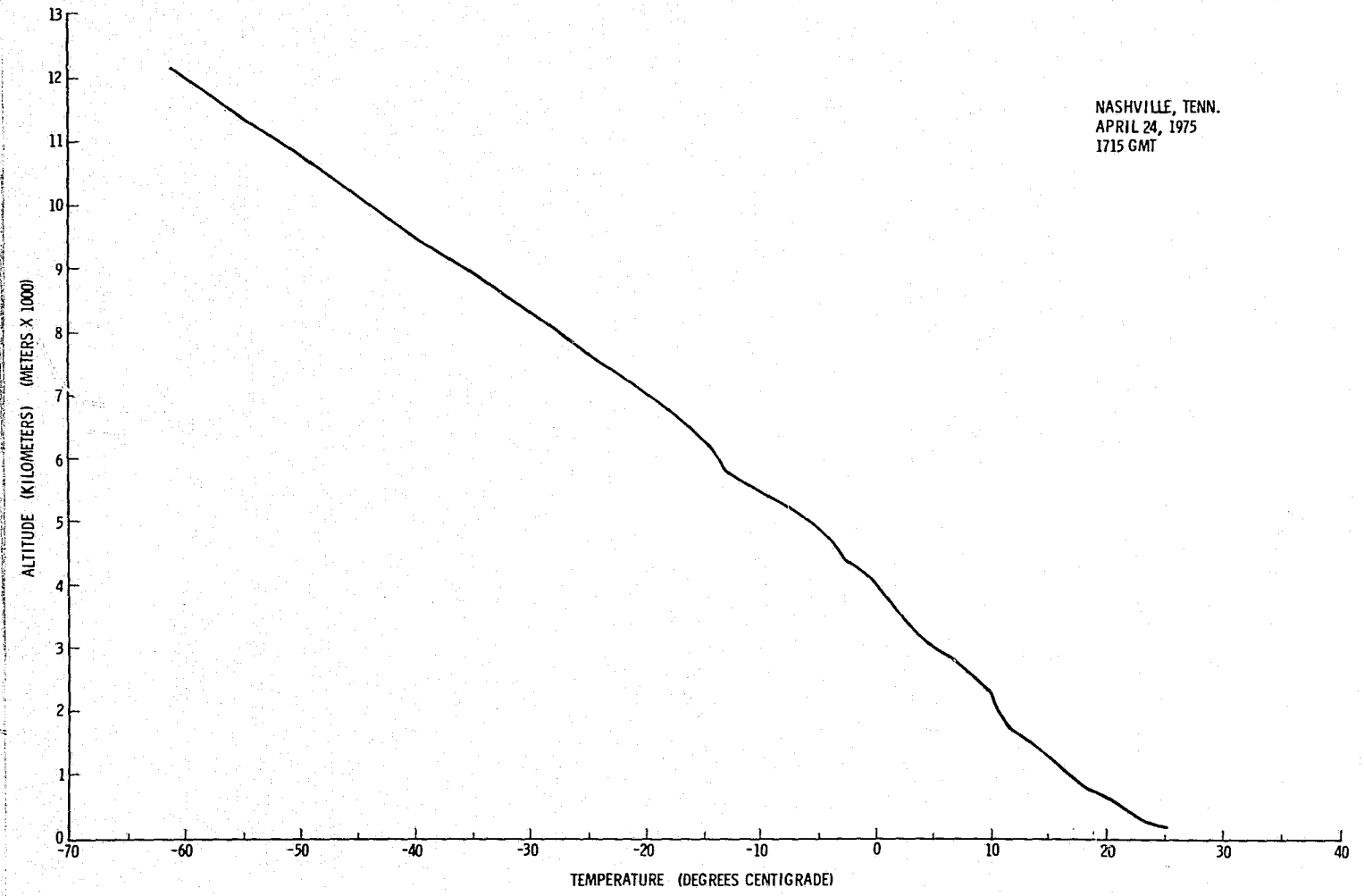

Figure A.123. Temperature profile for 1715 GMT, April 24, 1975, over Nashville, Tennessee.

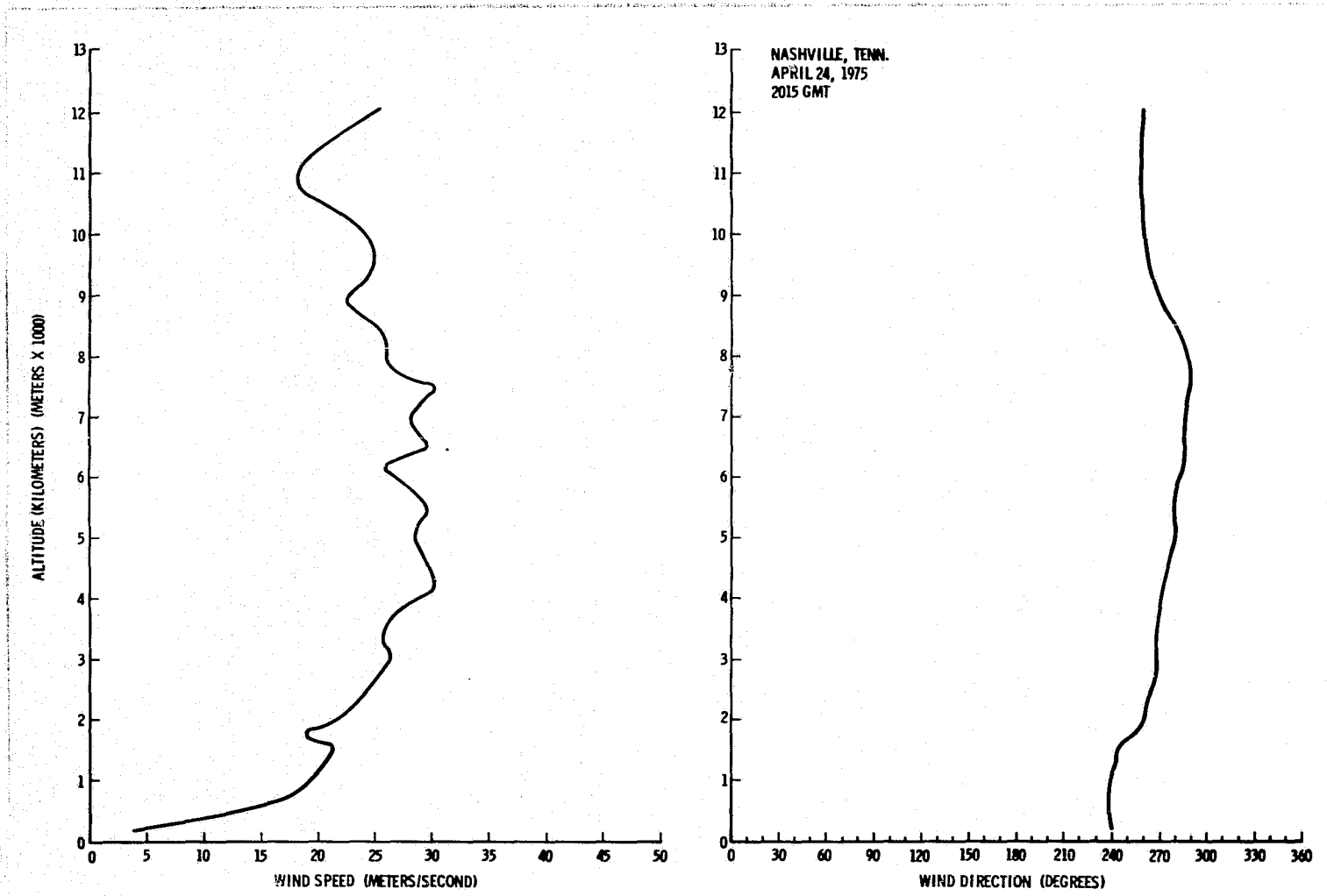

Figure A.124. Vertical wind profile for 2015 GMT, April 24, 1975, over Nashville, Tennessee.

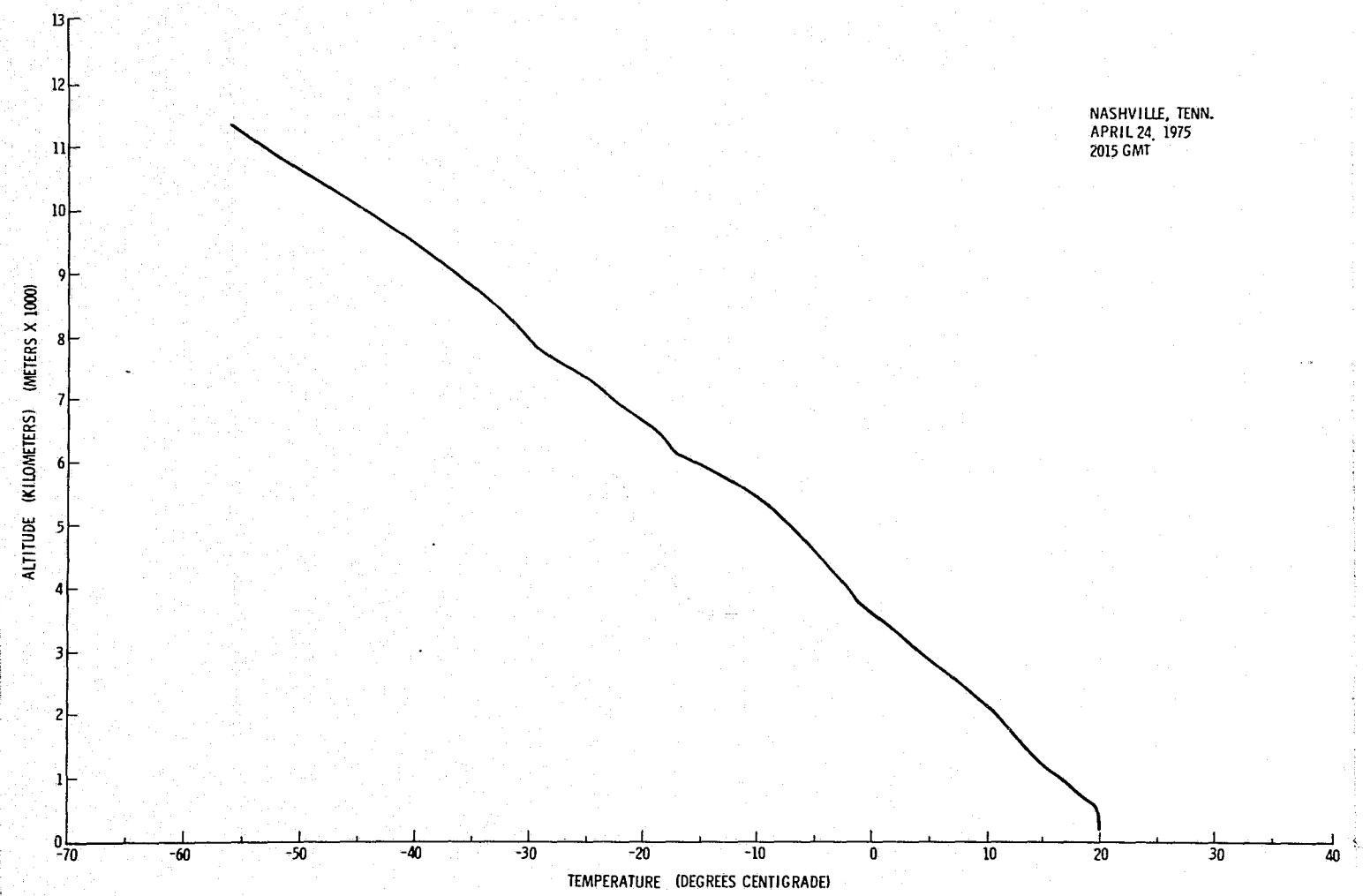

Figure A.125. Temperature profile for 2015 GMT, April 24, 1975, over Nashville, Tennessee.

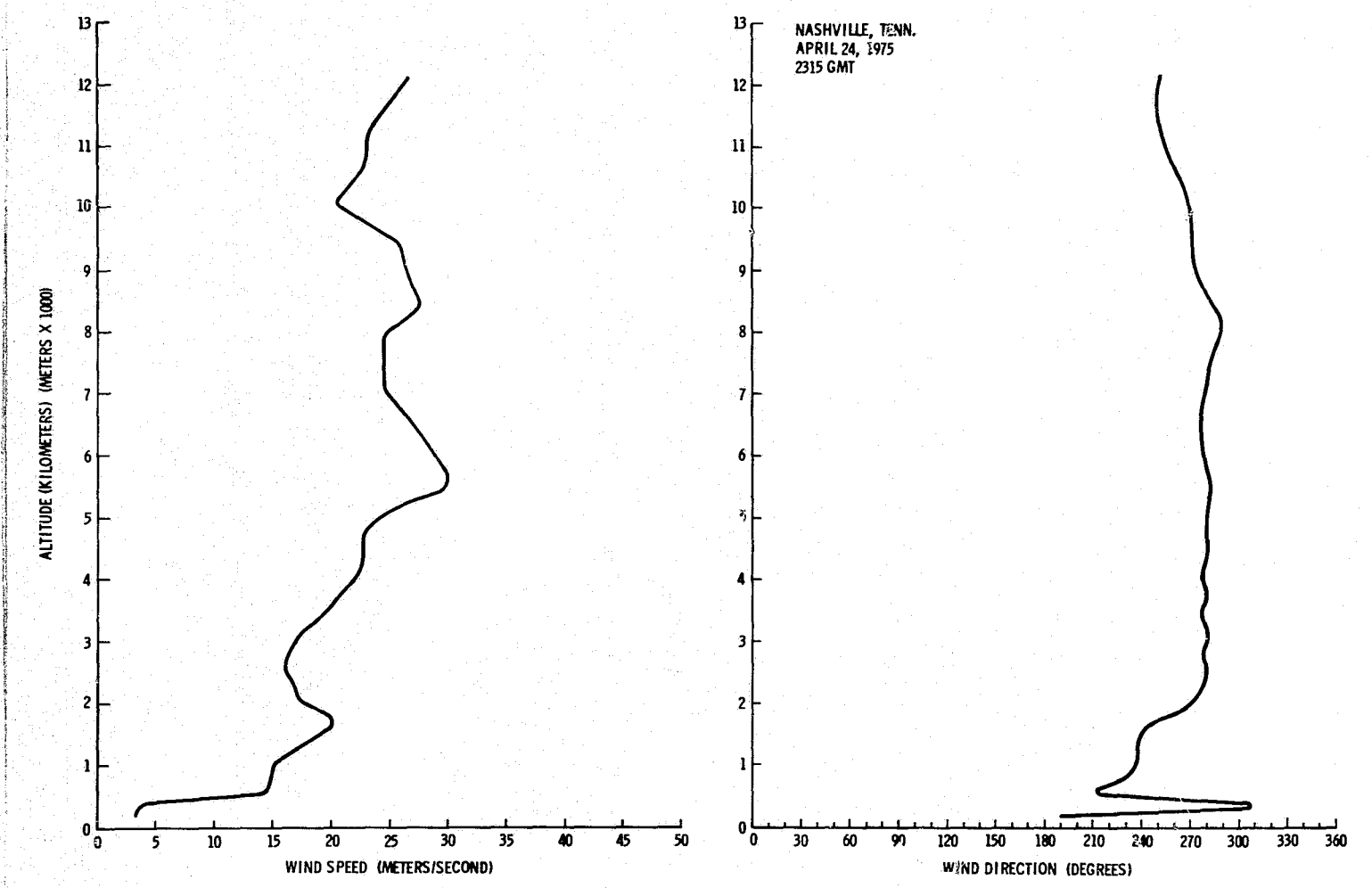

Figure A.126. Vertical wind profile for 2315 GMT, April 24, 1975, over Nashville, Tennessee.

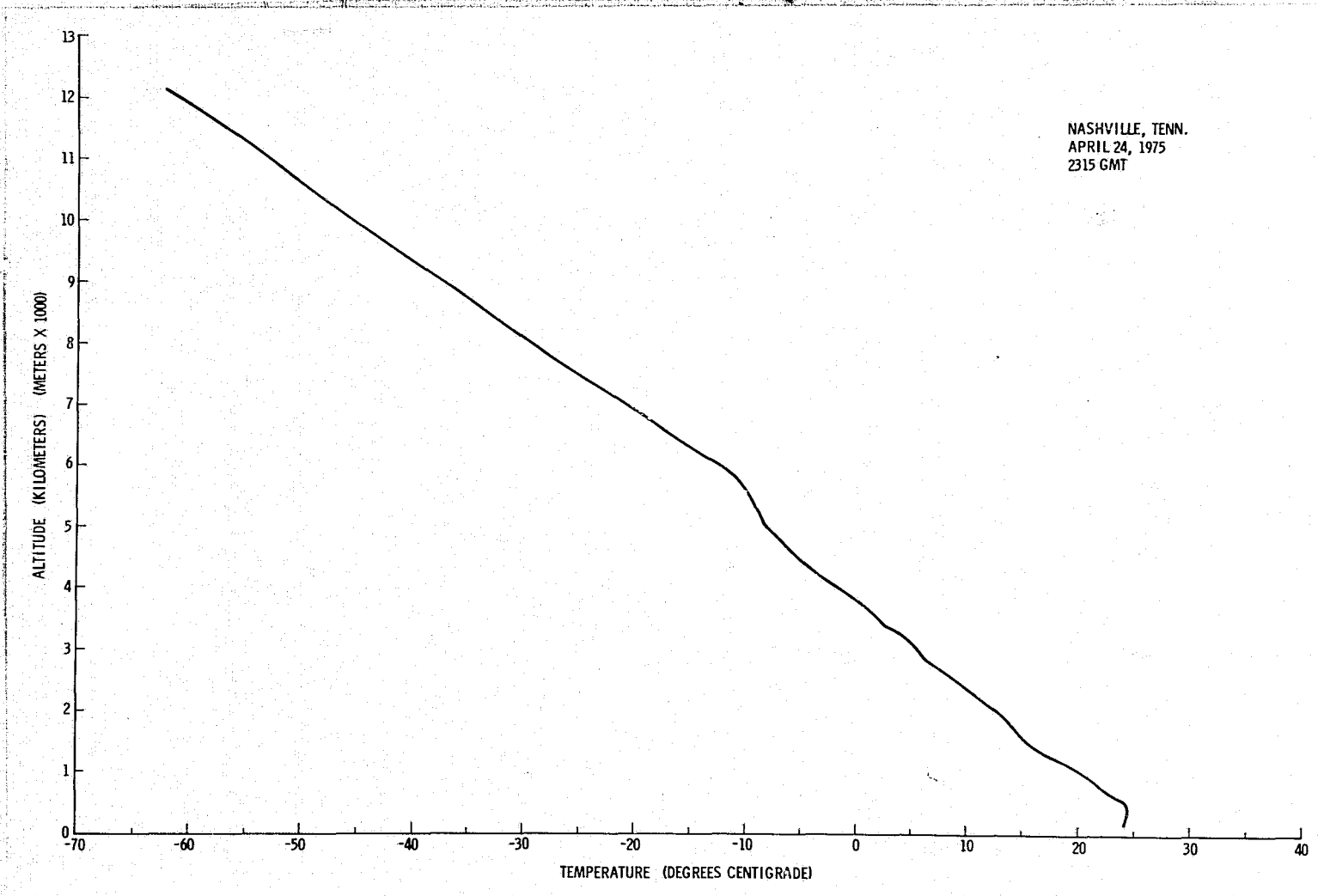

Figure A.127. Temperature profile for 2315 GMT, April 24, 1975, over Nashville, Tennessee.

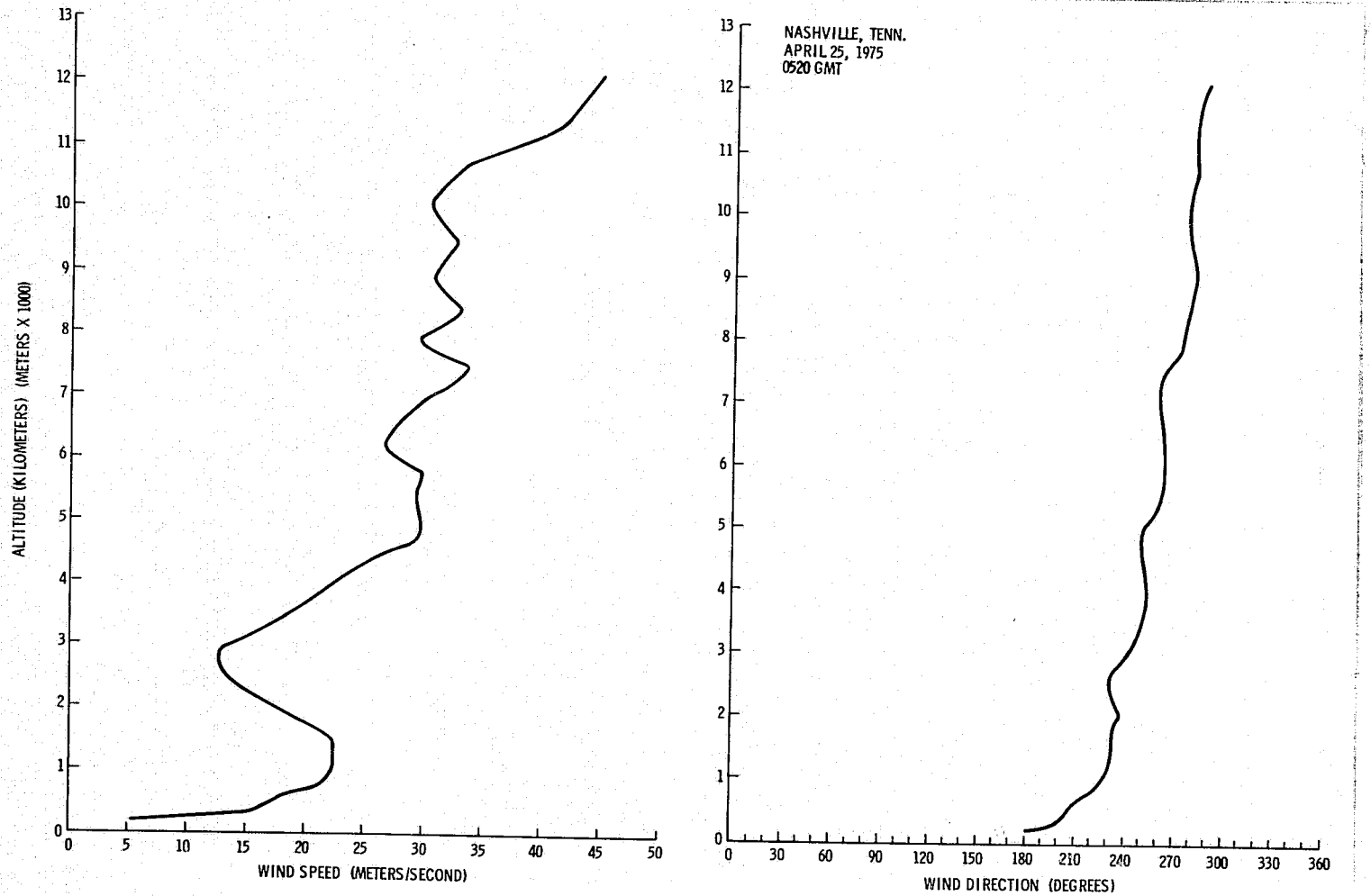

Figure A.128. Vertical wind profile for 0520 GMT, April 25, 1975, over Nashville, Tennessee.

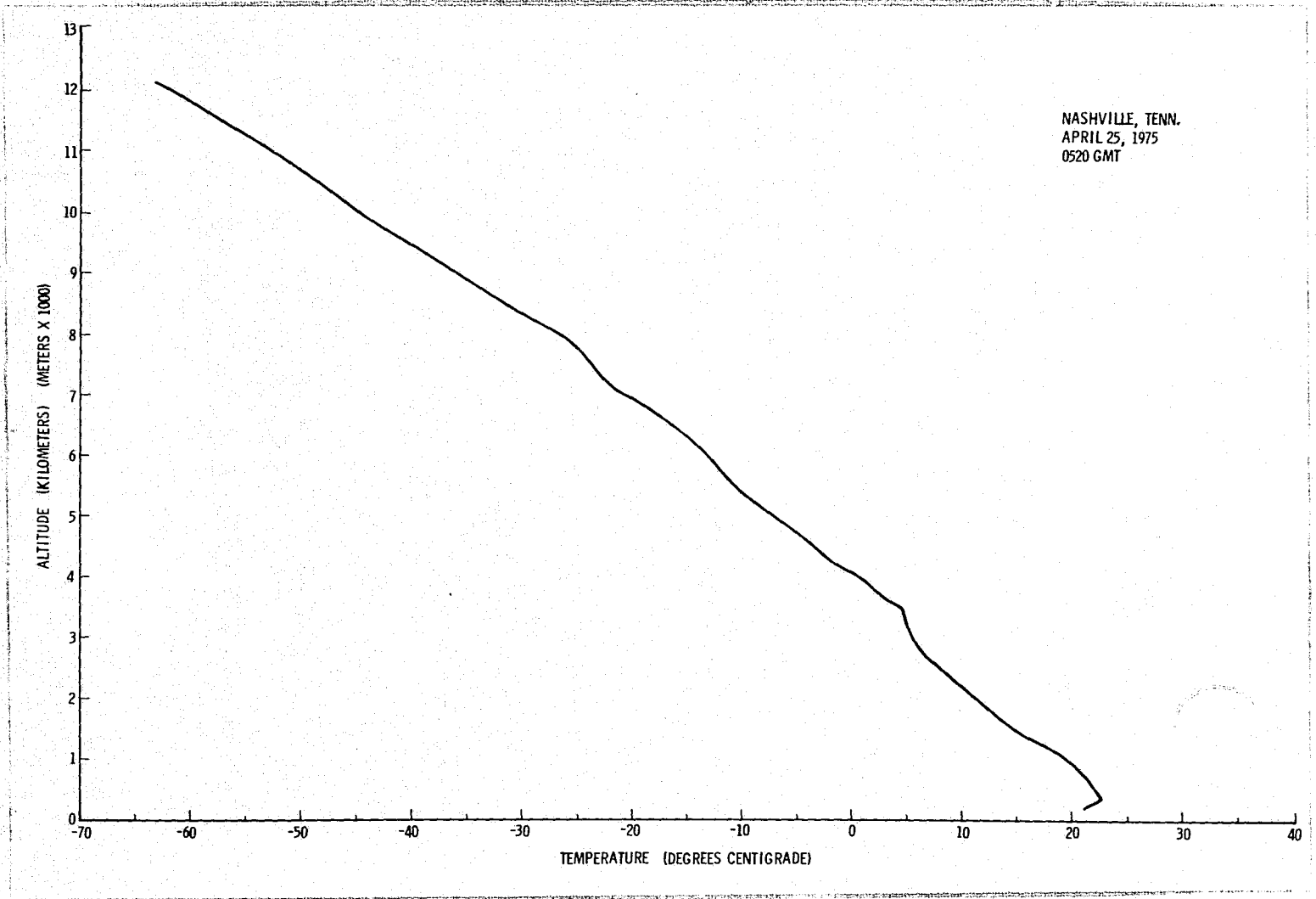

Figure A.129. Temperature profile for 0520 GMT, April 25, 1975, over Nashville, Tennessee.

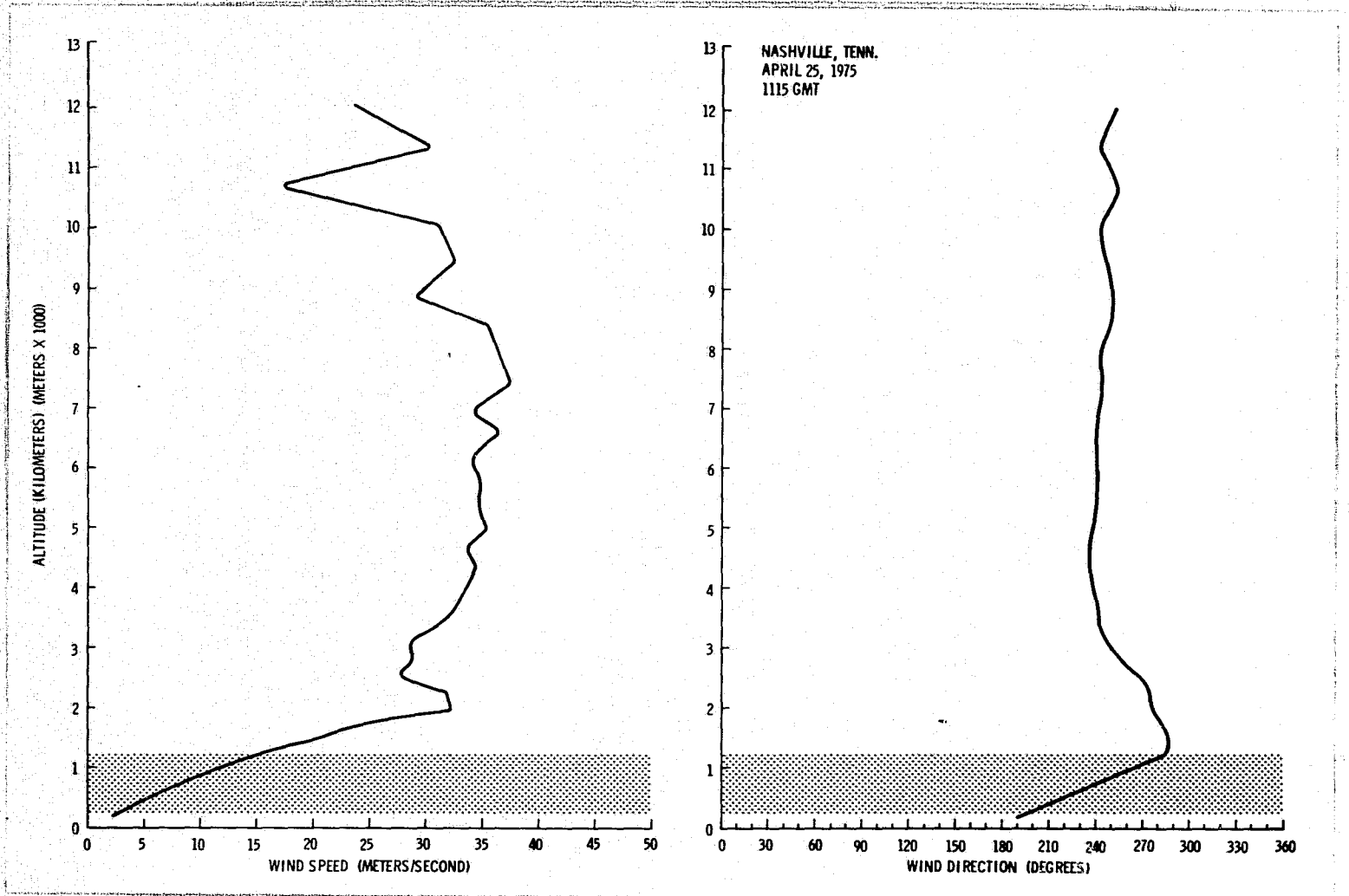

Figure A.130. Vertical wind profile for 1115 GMT, April 25, 1975, over Nashville, Tennessee.

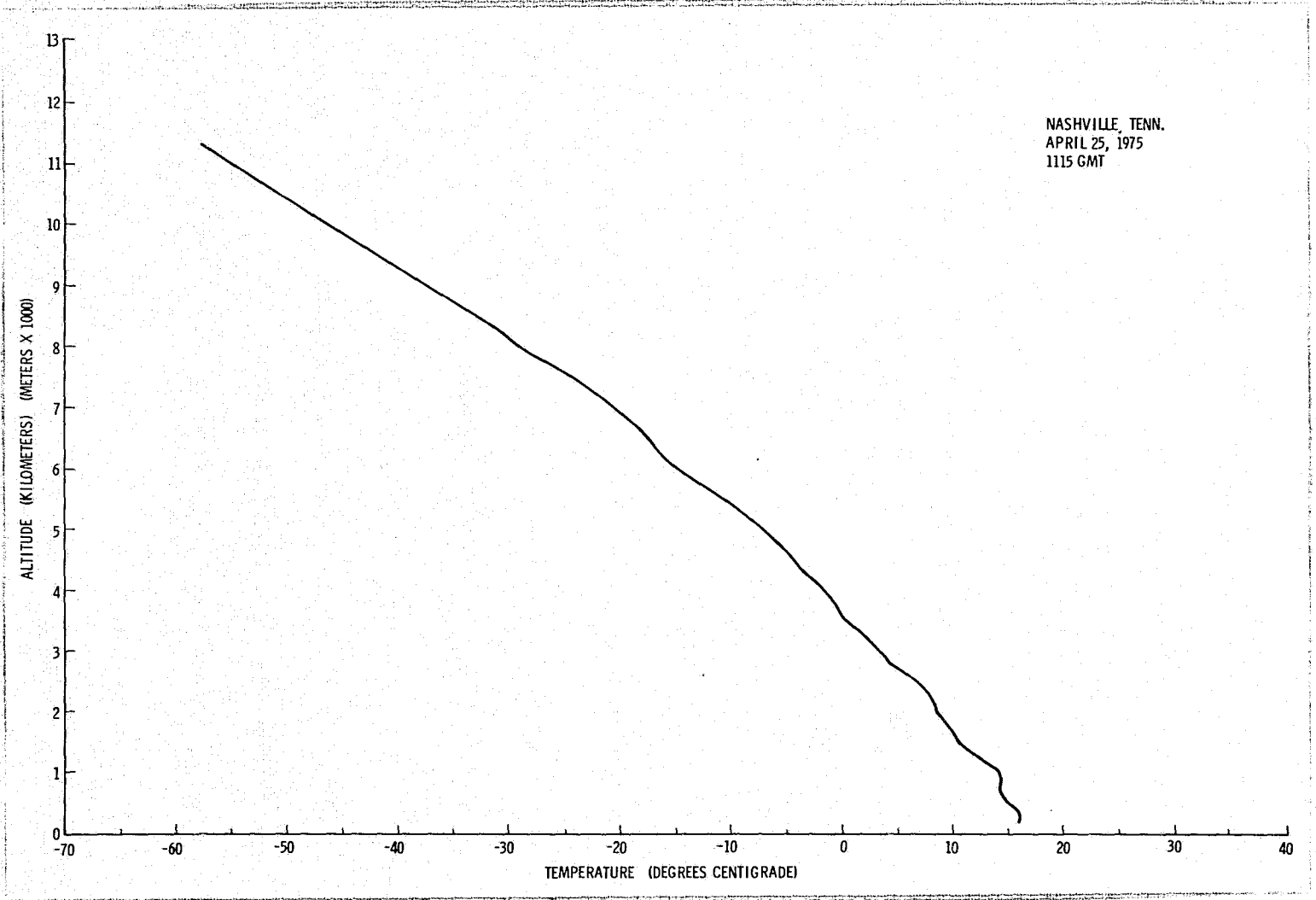

Figure A.131. Temperature profile for 1115 GMT, April 25, 1975, over Nashville, Tennessee.

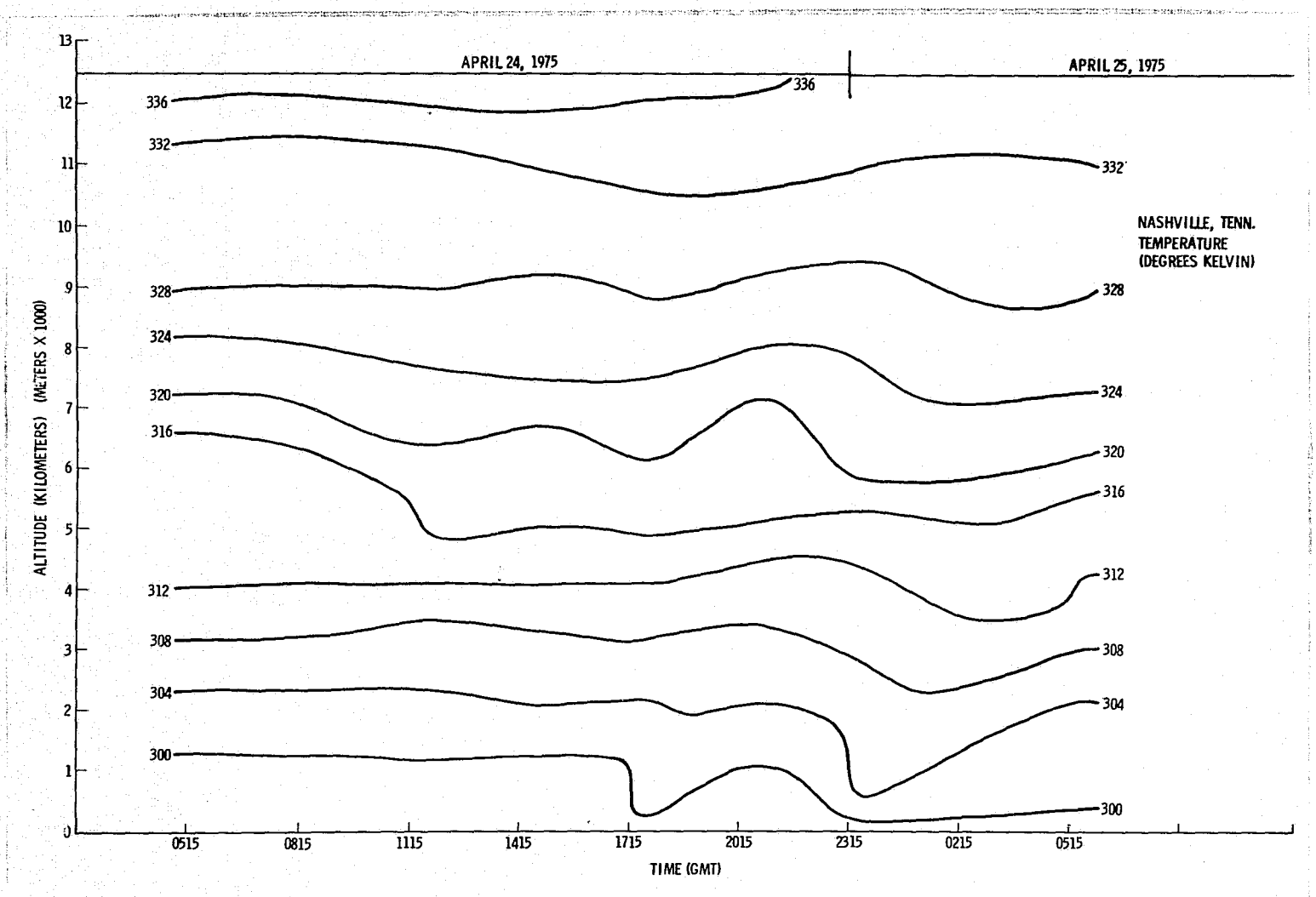

Figure A.132. Time cross section of temperature at Nashville, Tennessee.

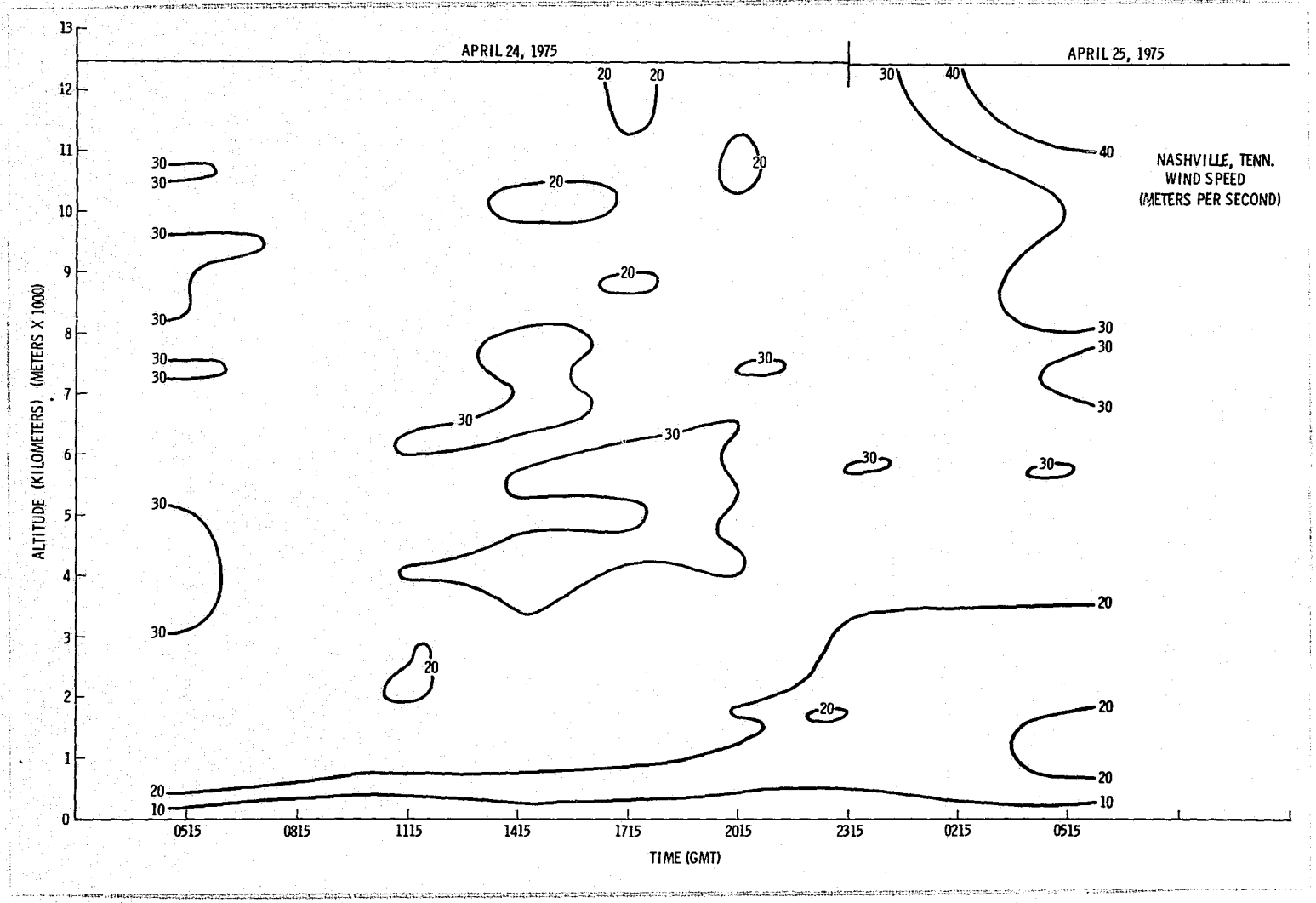

Figure A.133. Time cross section of wind speed at Nashville, Tennessee.

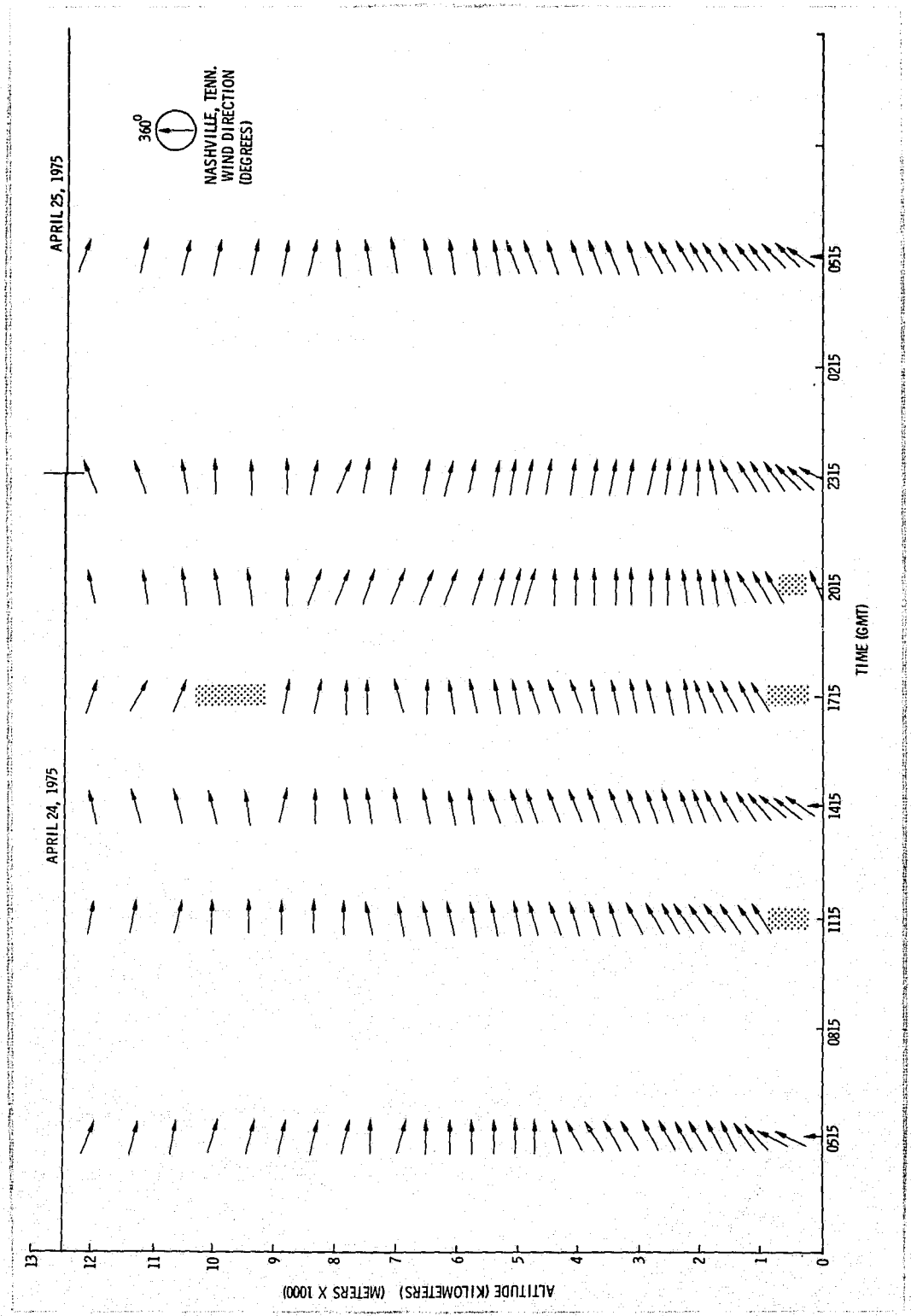

Figure A.134. Time cross section of wind direction at Nashville, Tennessee.

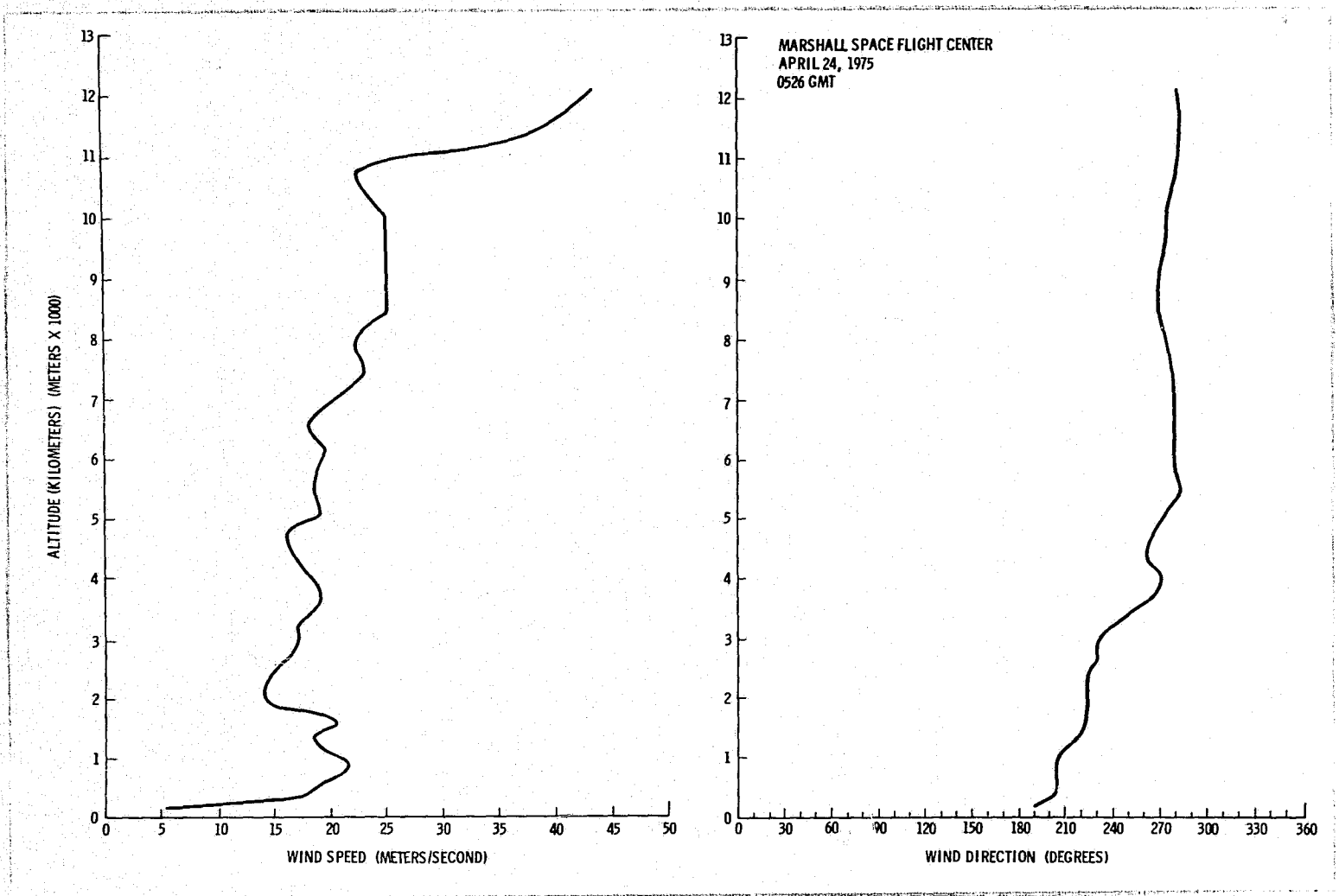

Figure A.135. Vertical wind profile for 0526 GMT, April 24, 1975, over Marshall Space Flight Center, Alabama.

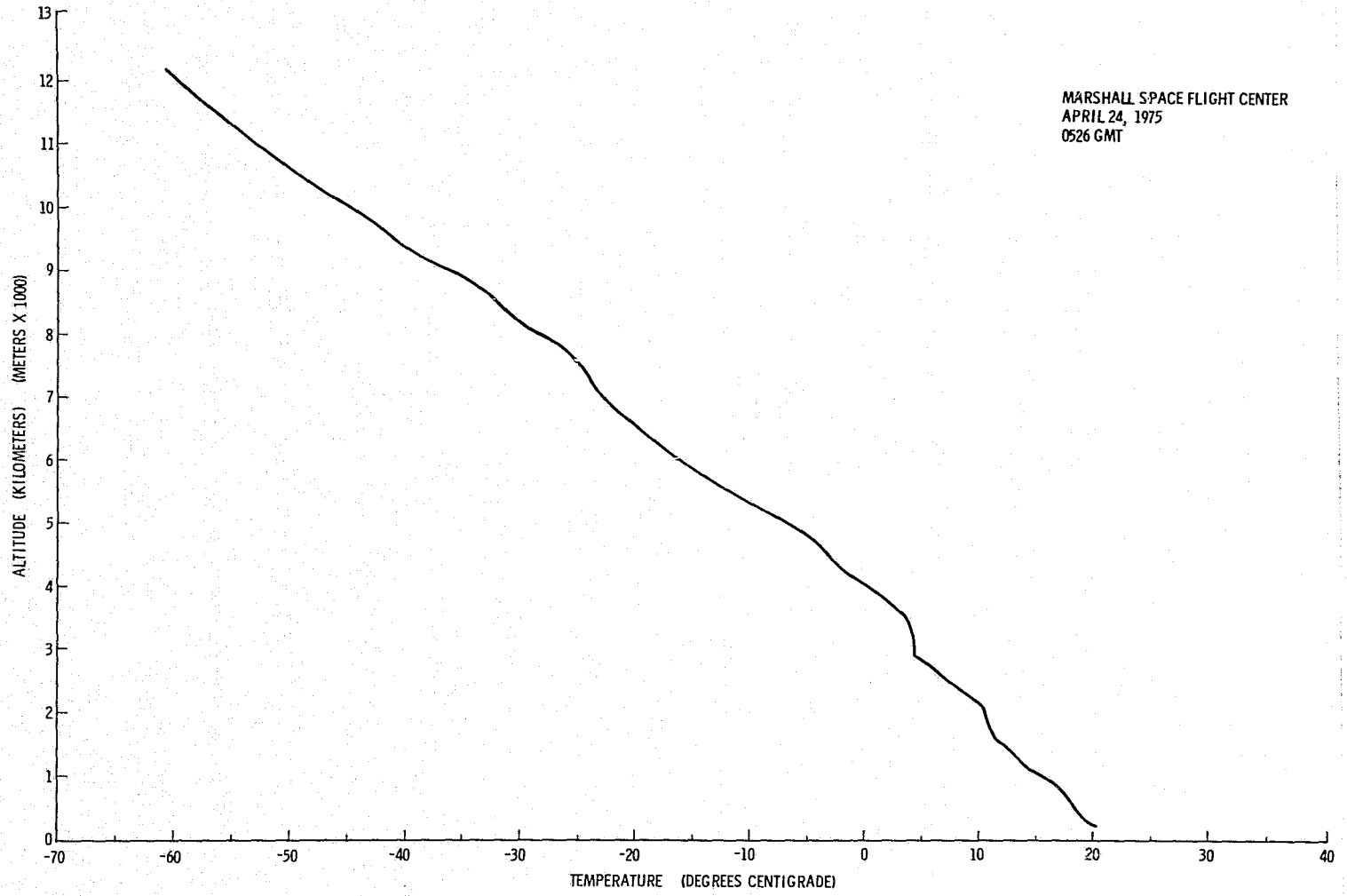

Figure A.136. Temperature profile for 0526 GMT, April 24, 1975, over Marshall Space Flight Center, Alabama.

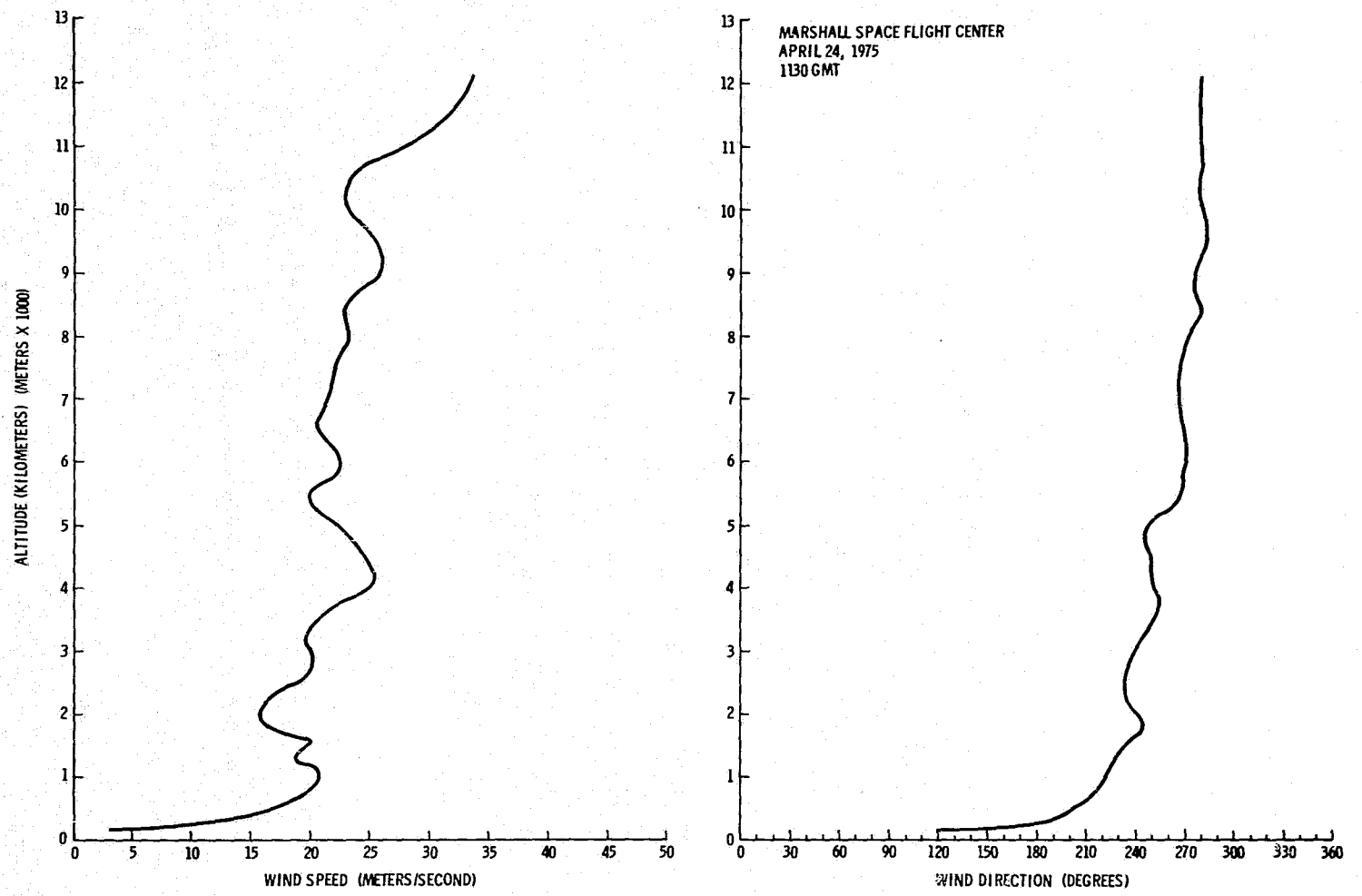

Figure A.137. Vertical wind profile for 1130 GMT, April 24, 1975, over Marshall Space Flight Center, Alabama.

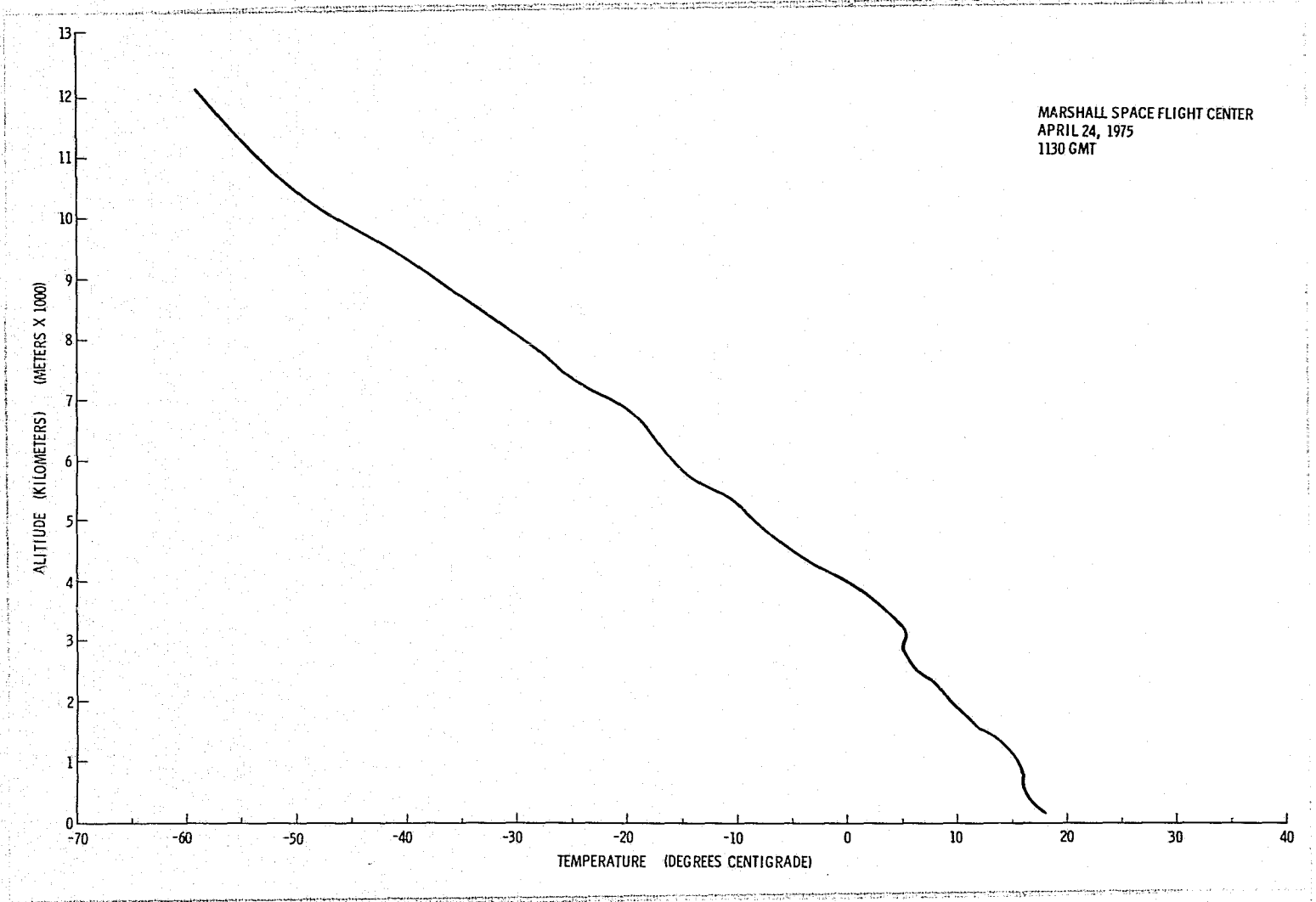

Figure A.138. Temperature profile for 1130 GMT, April 24, 1975, over Marshall Space Flight Center, Alabama.

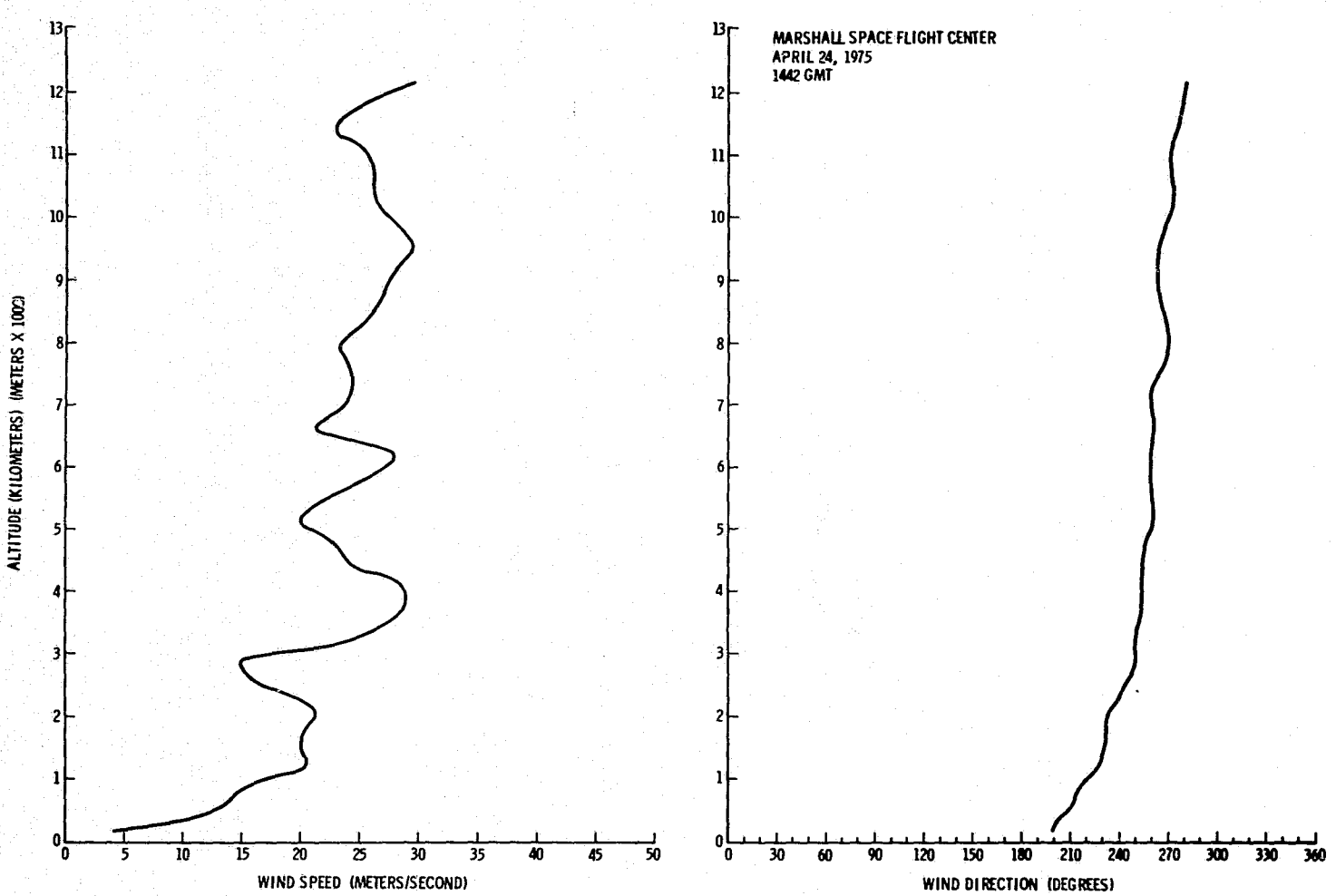

Figure A.139. Vertical wind profile for 1442 GMT, April 24, 1975, over Marshall Space Flight Center, Alabama.

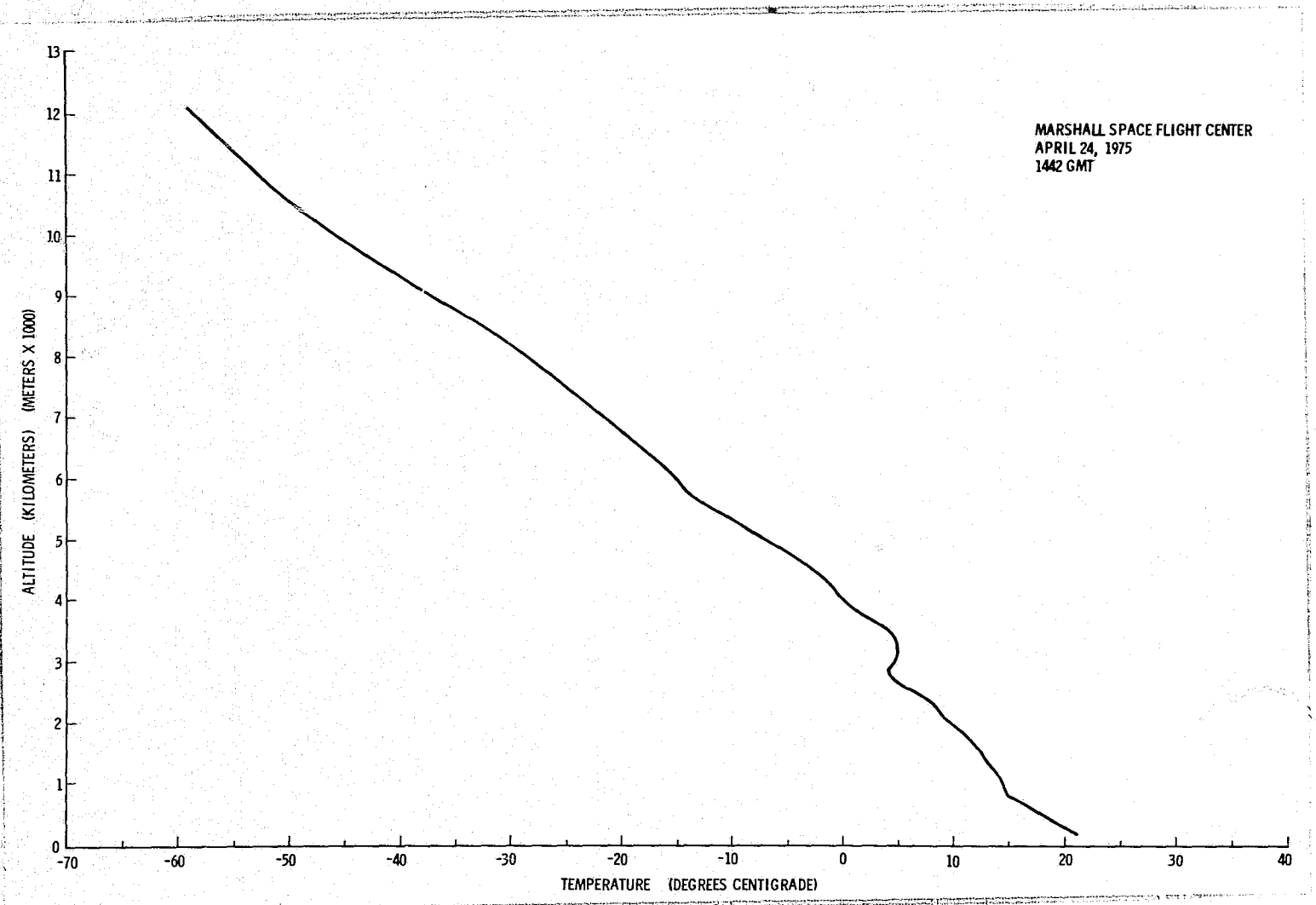

Figure A.140. Temperature profile for 1442 GMT, April 24, 1975, over Marshall Space Flight Center, Alabama.

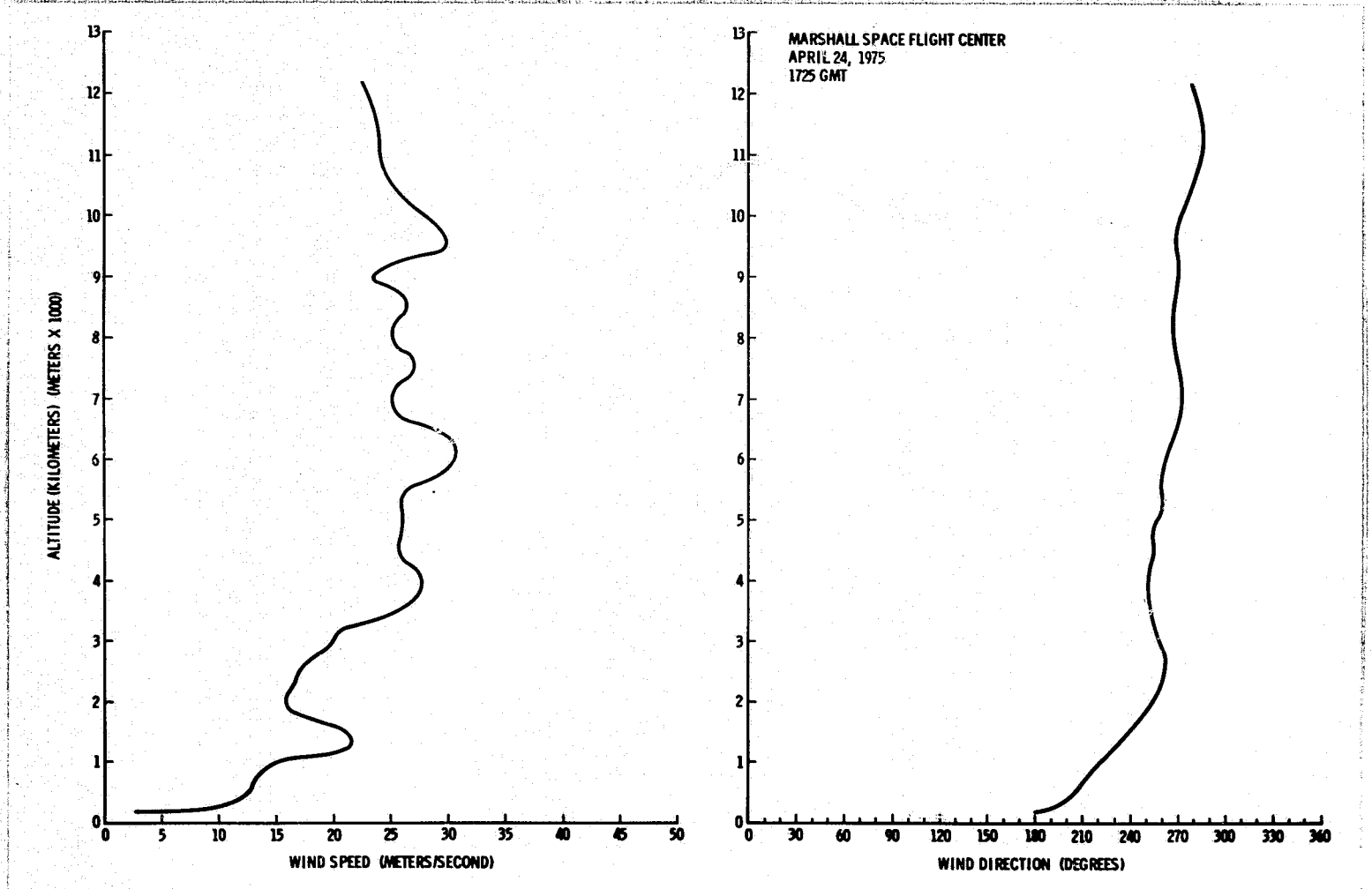

Figure A.141. Vertical wind profile for 1725 GMT, April 24, 1975, over Marshall Space Flight Center, Alabama.

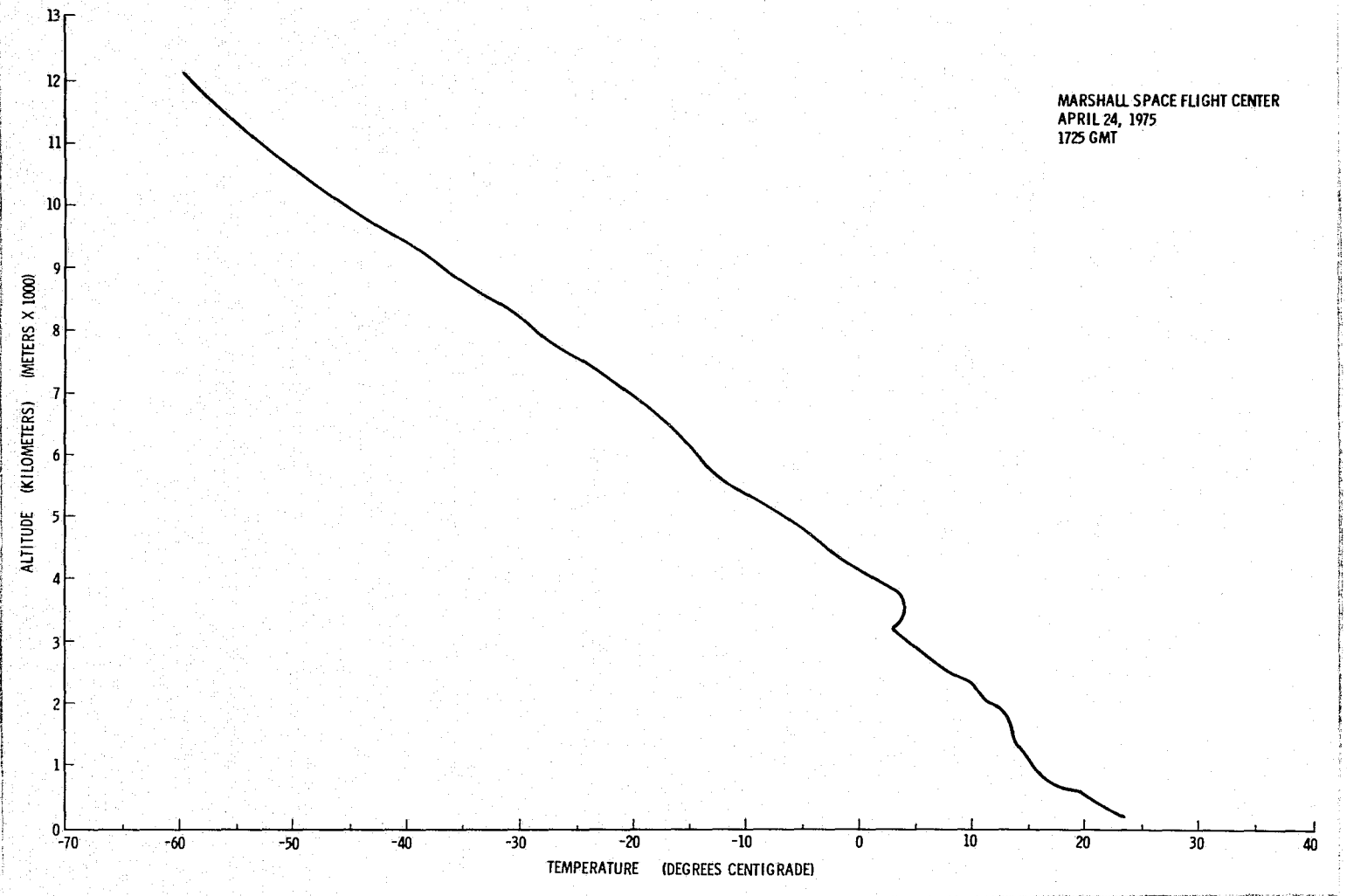

Figure A.142. Temperature profile for 1725 GMT, April 24, 1975, over Marshall Space Flight Center, Alabama.

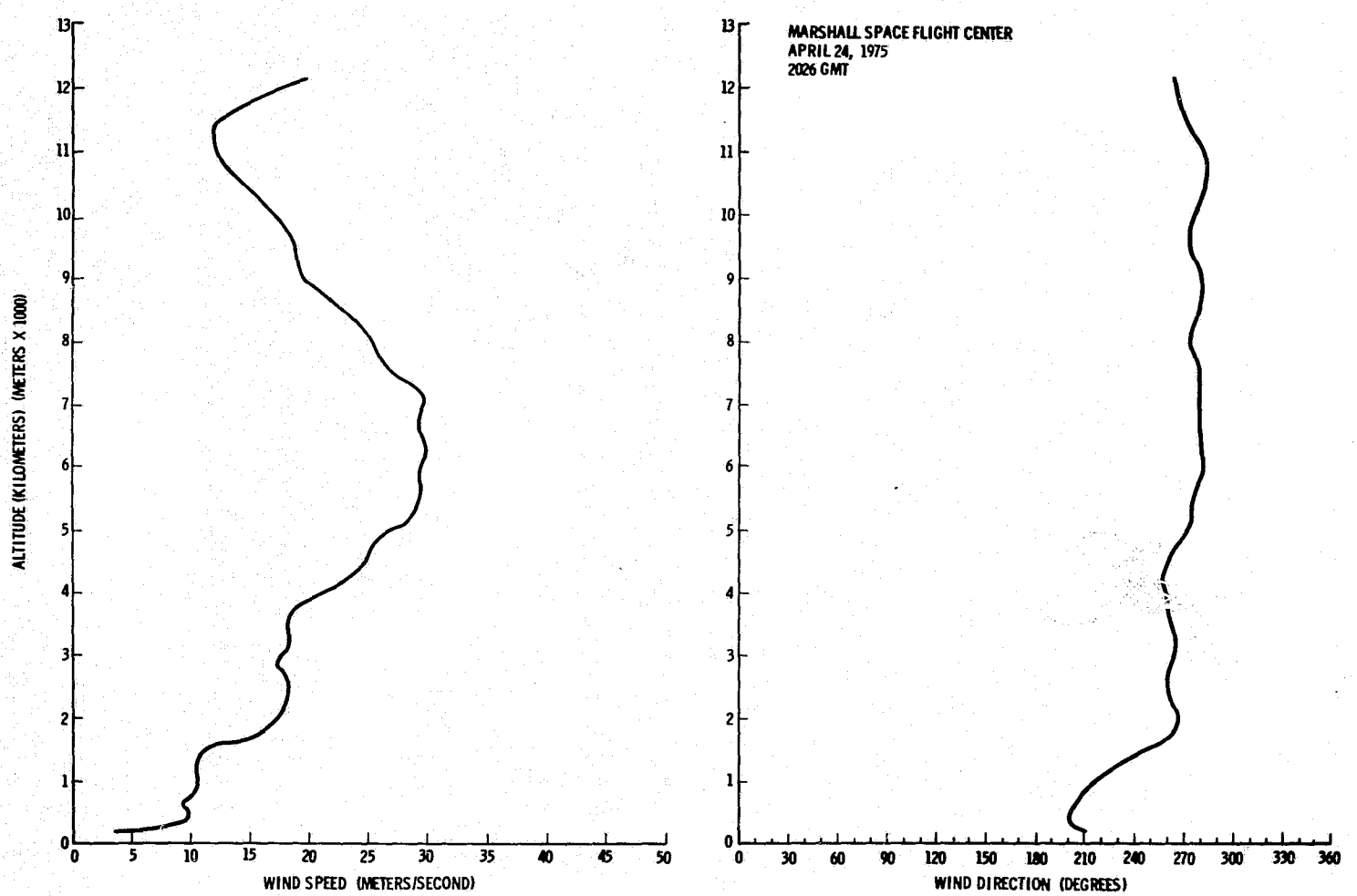

Figure A.143. Vertical wind profile for 2026 GMT, April 24, 1975, over Marshall Space Flight Center, Alabama.

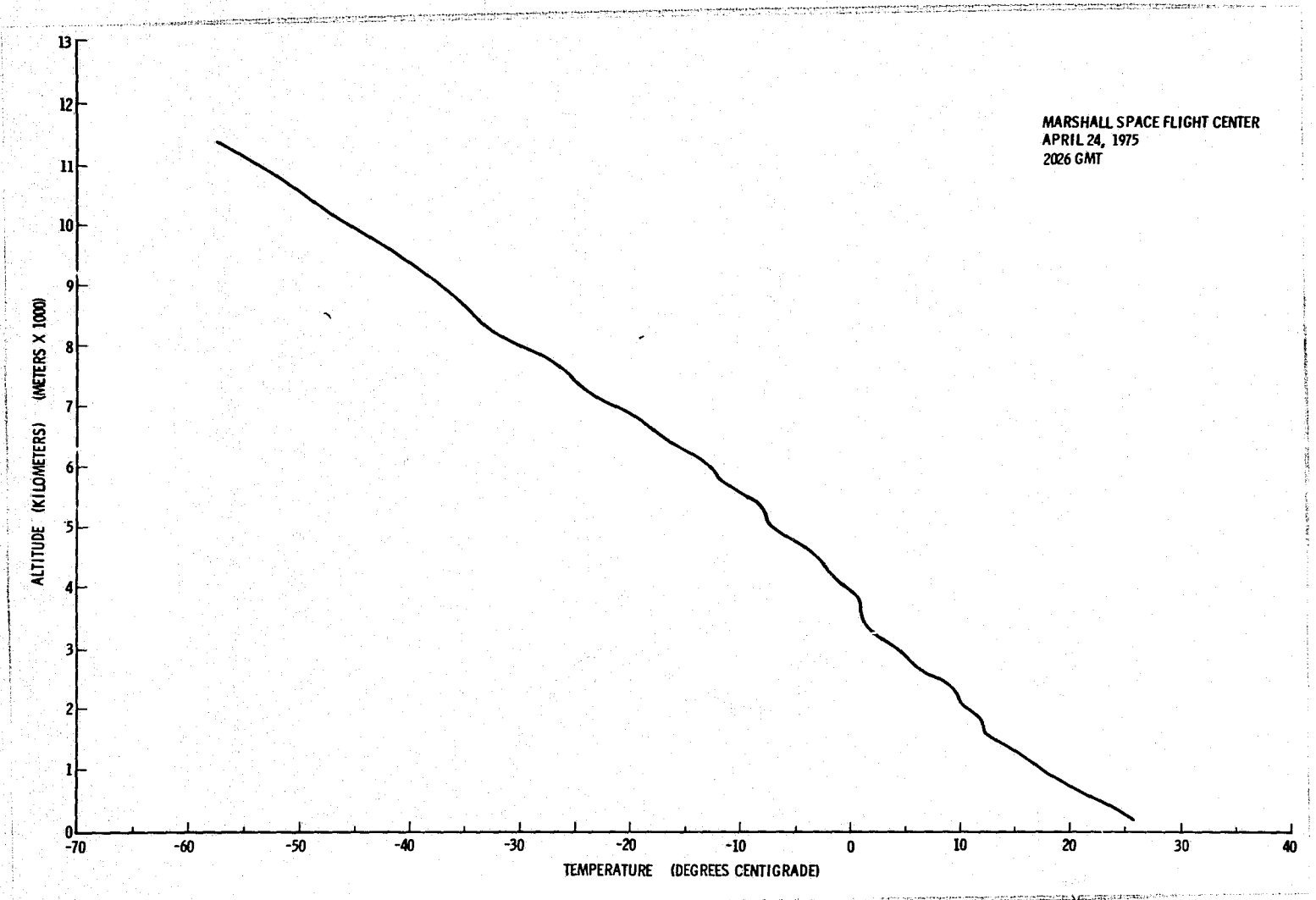

Figure A.144. Temperature profile for 2026 GMT, April 24, 1975, over Marshall Space Flight Center, Alabama.

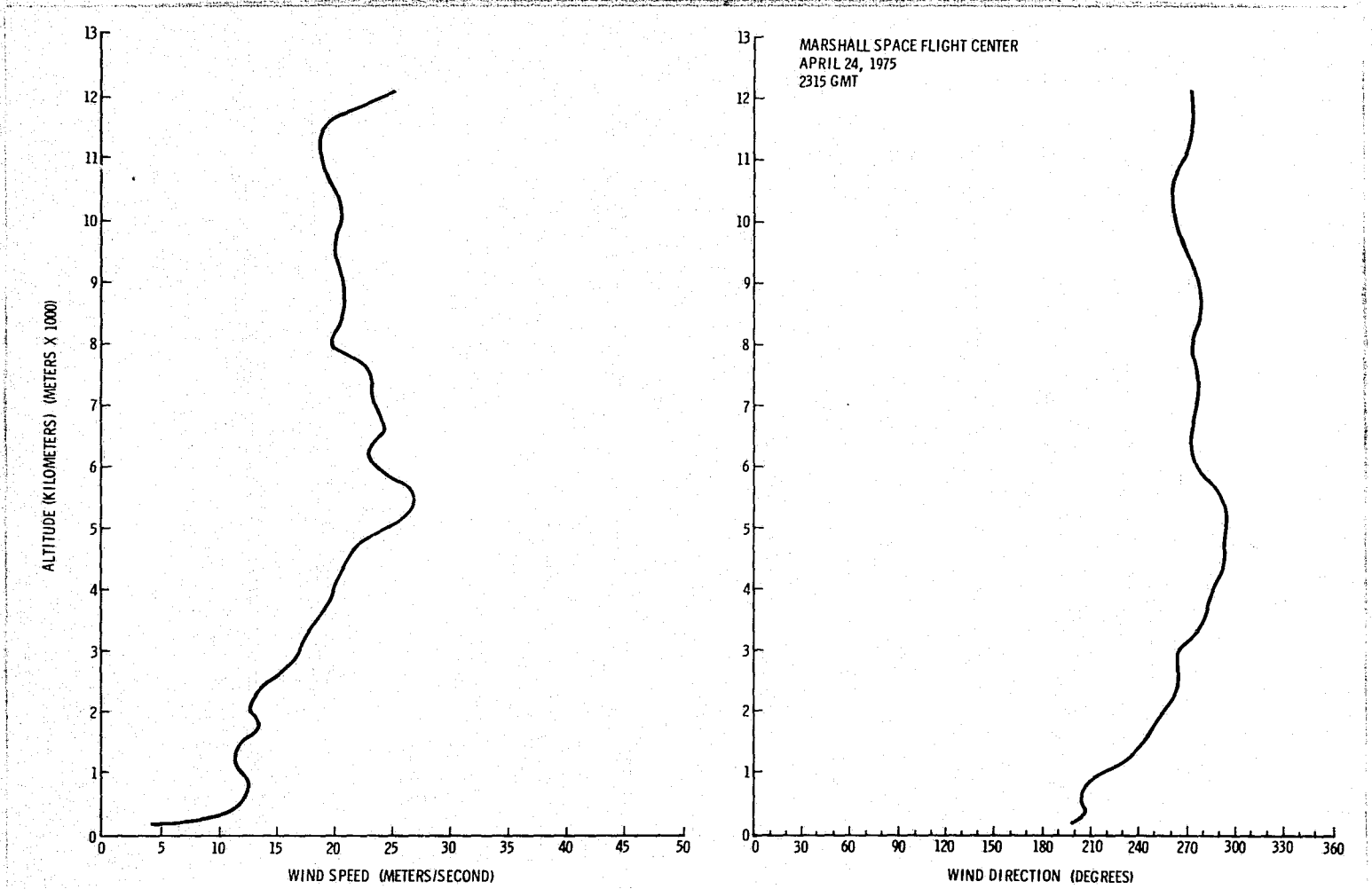

Figure A.145. Vertical wind profile for 2315 GMT, April 24, 1975, over Marshall Space Flight Center, Alabama.

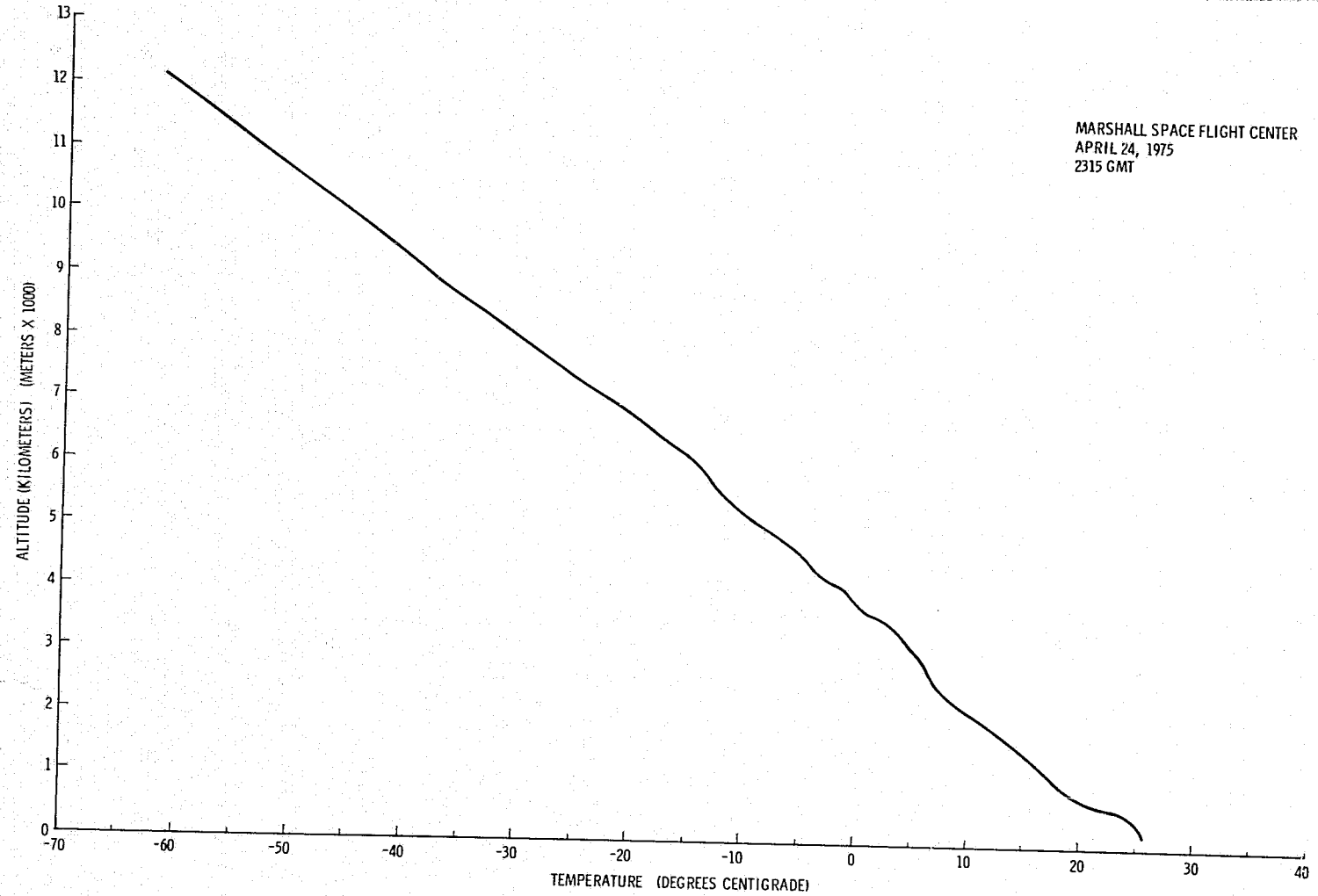

Figure A.146. Temperature profile for 2315 GMT, April 24, 1975, over Marshall Space Flight Center, Alabama.

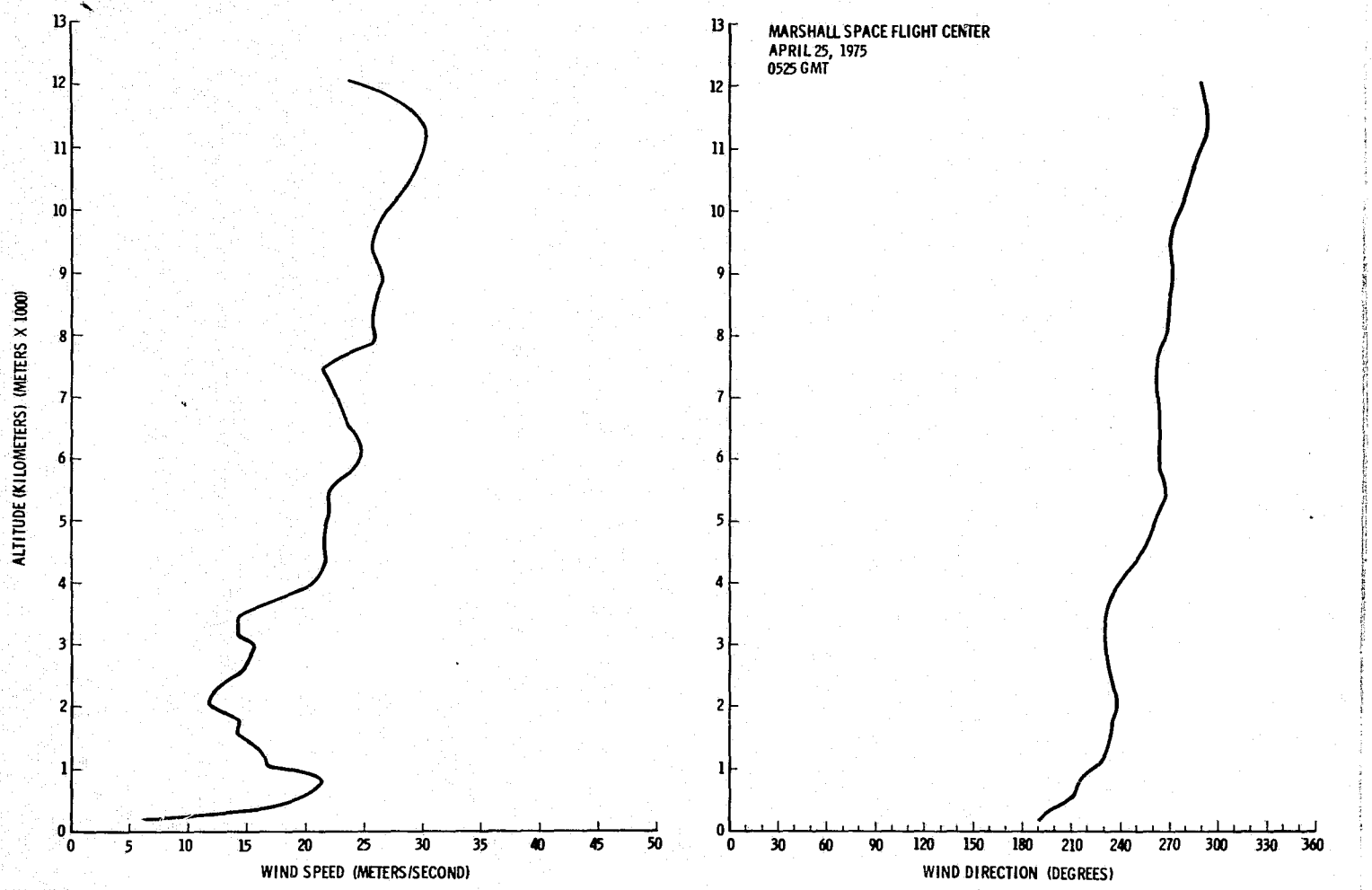

Figure A.147. Vertical wind profile for 0525 GMT, April 25, 1975, over Marshall Space Flight Center, Alabama.

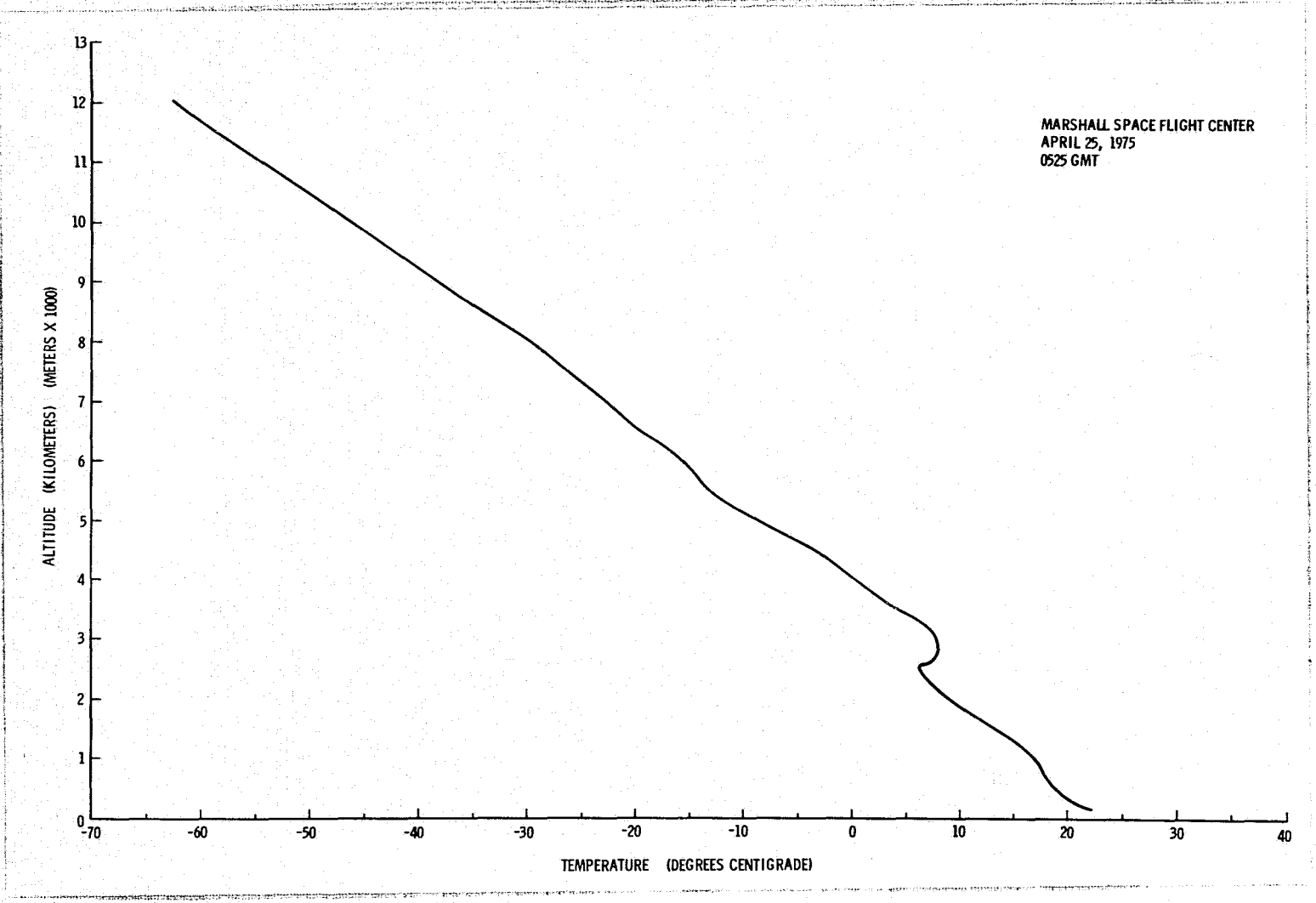

Figure A.148. Temperature profile for 0525 GMT, April 25, 1975, over Marshall Space Flight Center, Alabama.

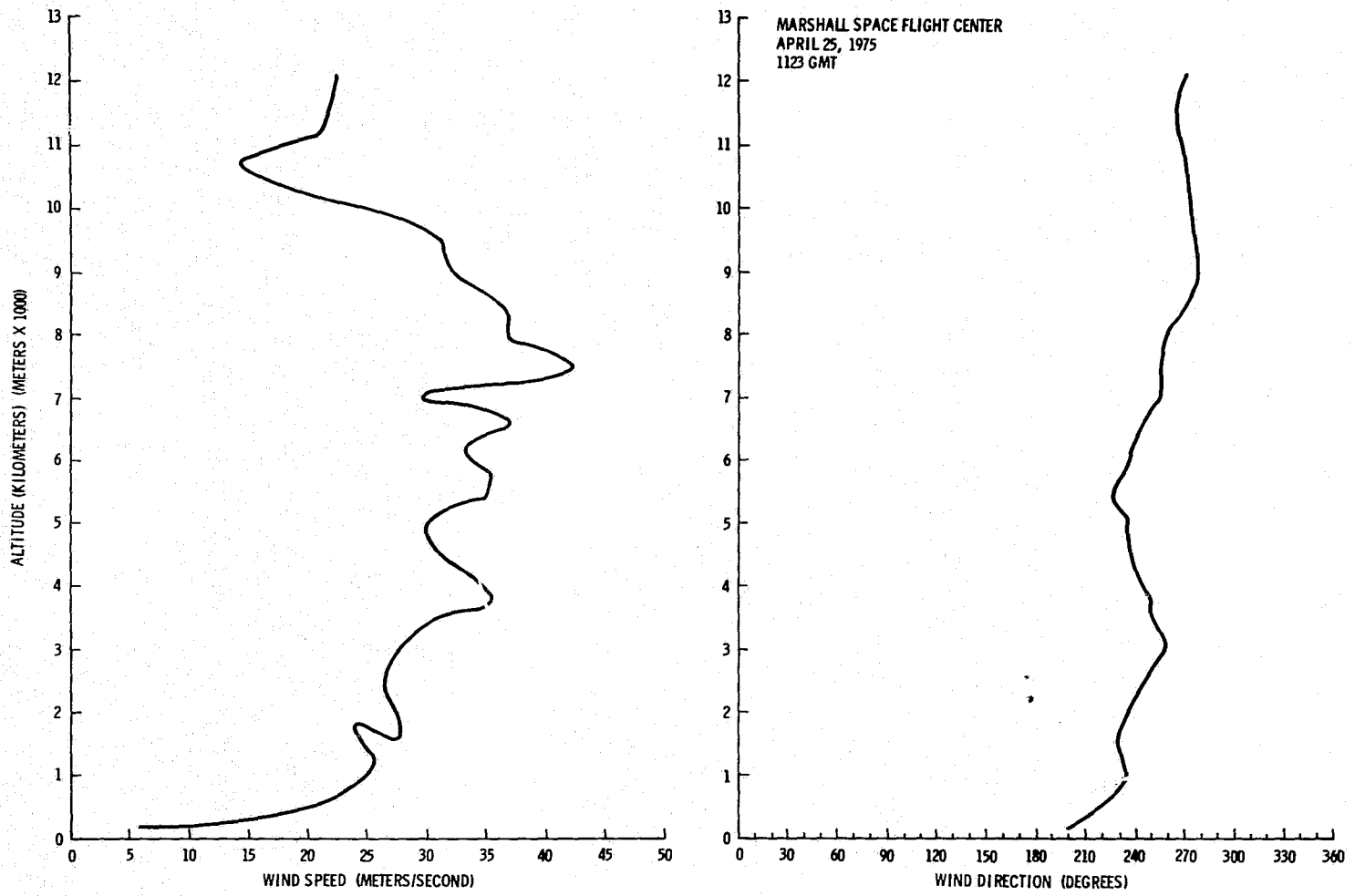

Figure A.149. Vertical wind profile for 1123 GMT, April 25, 1975, over Marshall Space Flight Center, Alabama.

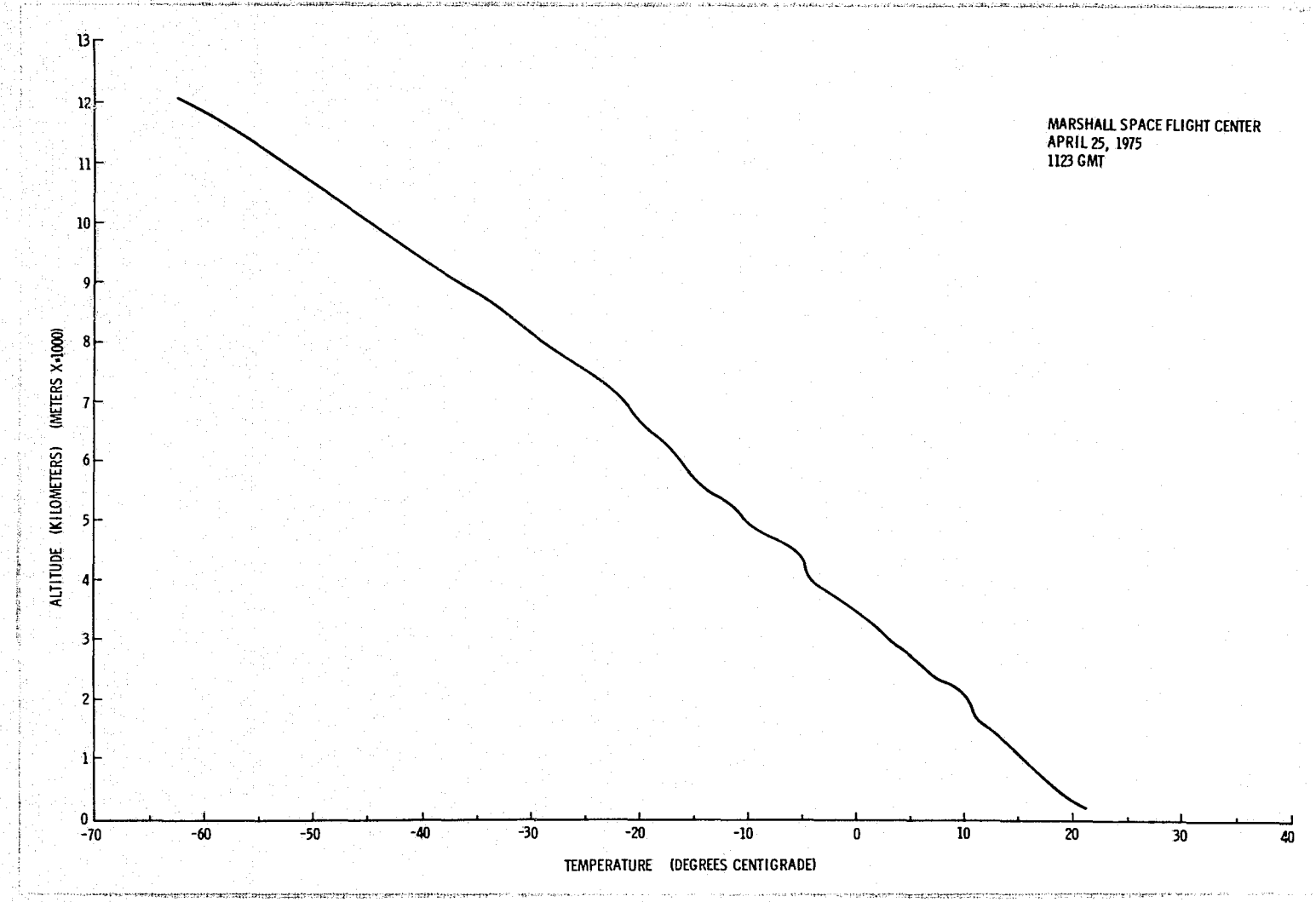

Figure A.150. Temperature profile for 1123 GMT, April 25, 1975, over Marshall Space Flight Center, Alabama.

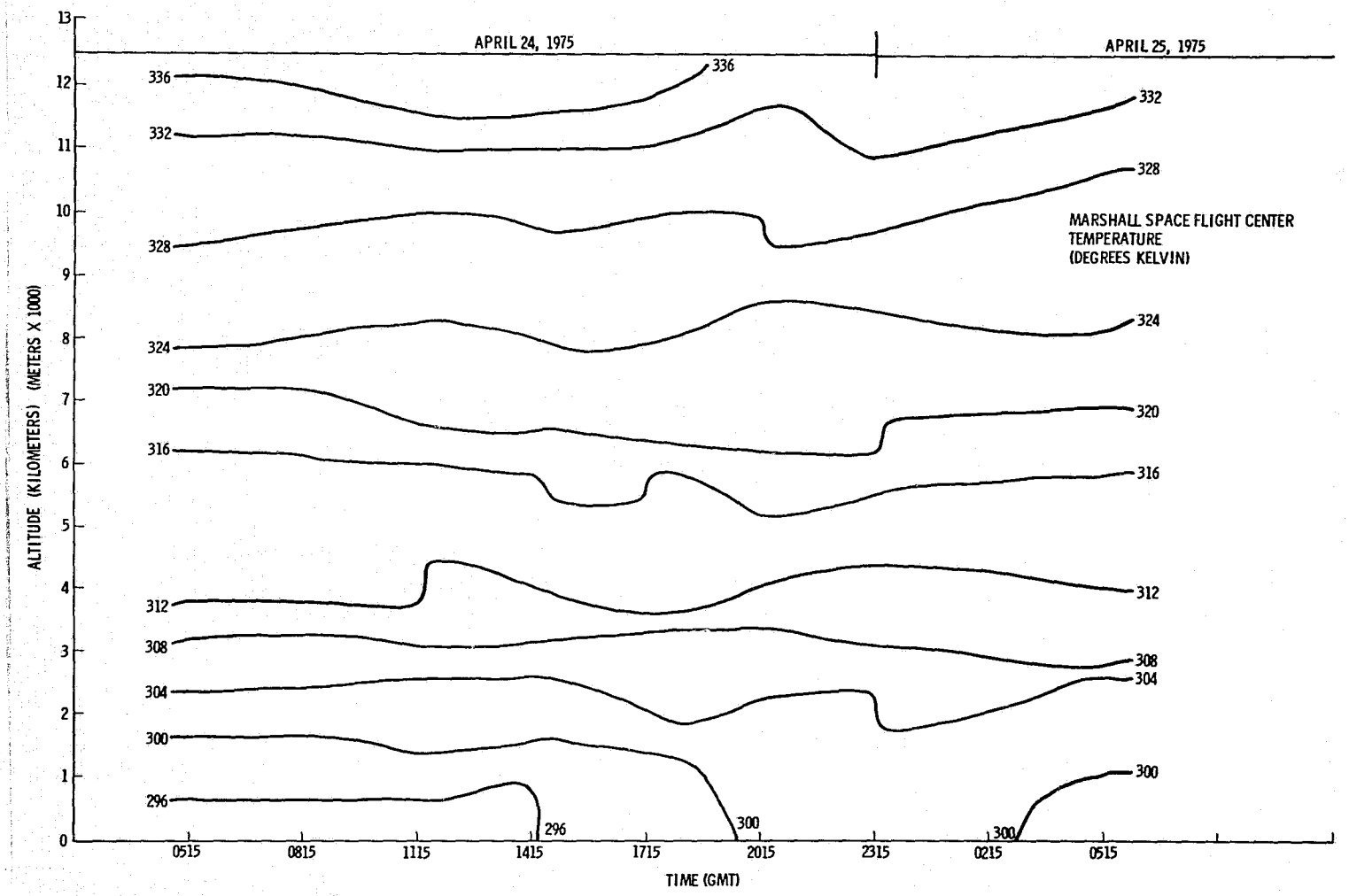

Figure A.151. Time cross section of temperature at Marshall Space Flight Center, Alabama.

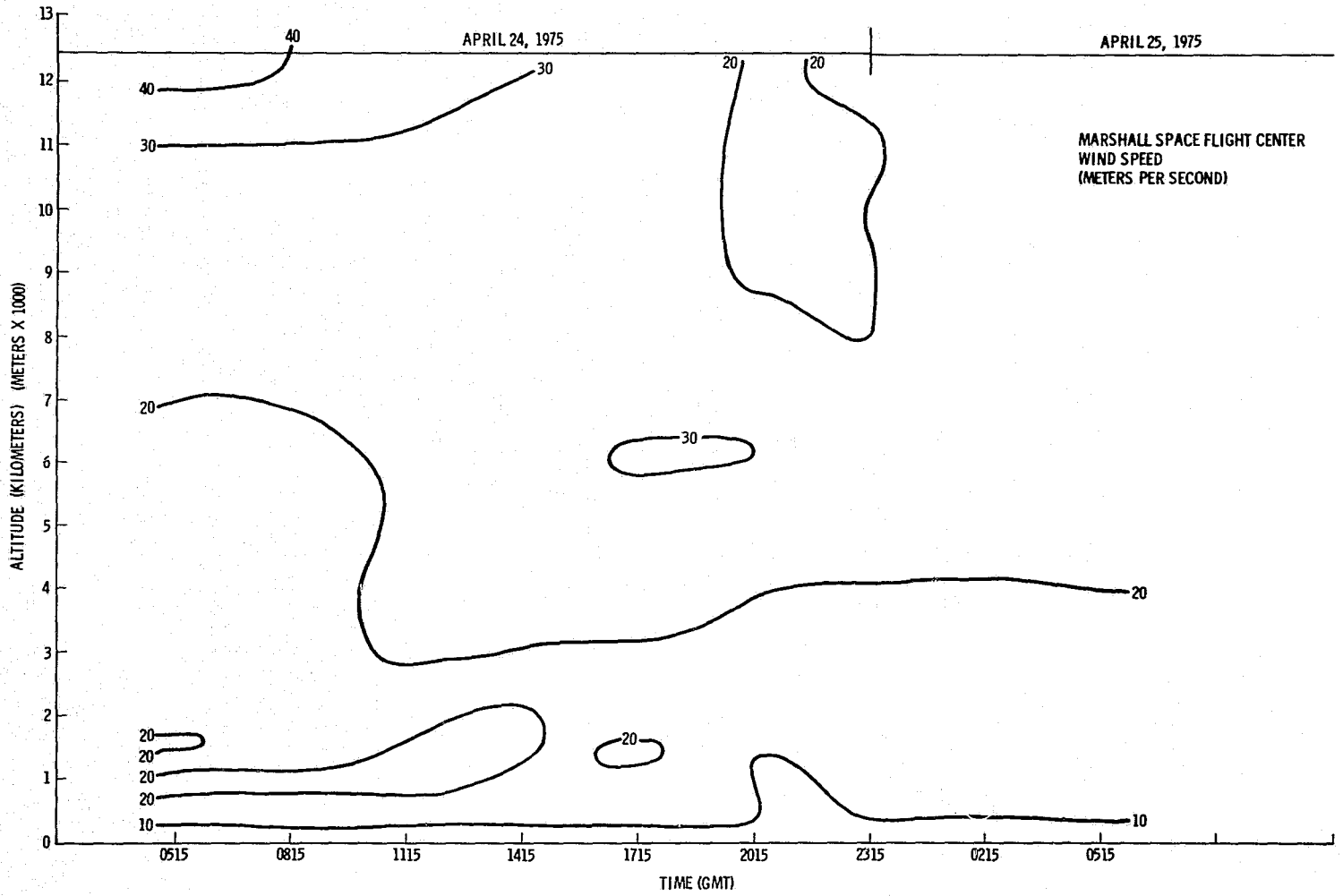

Figure A.152. Time cross section of wind speed at Marshall Space Flight Center, Alabama.

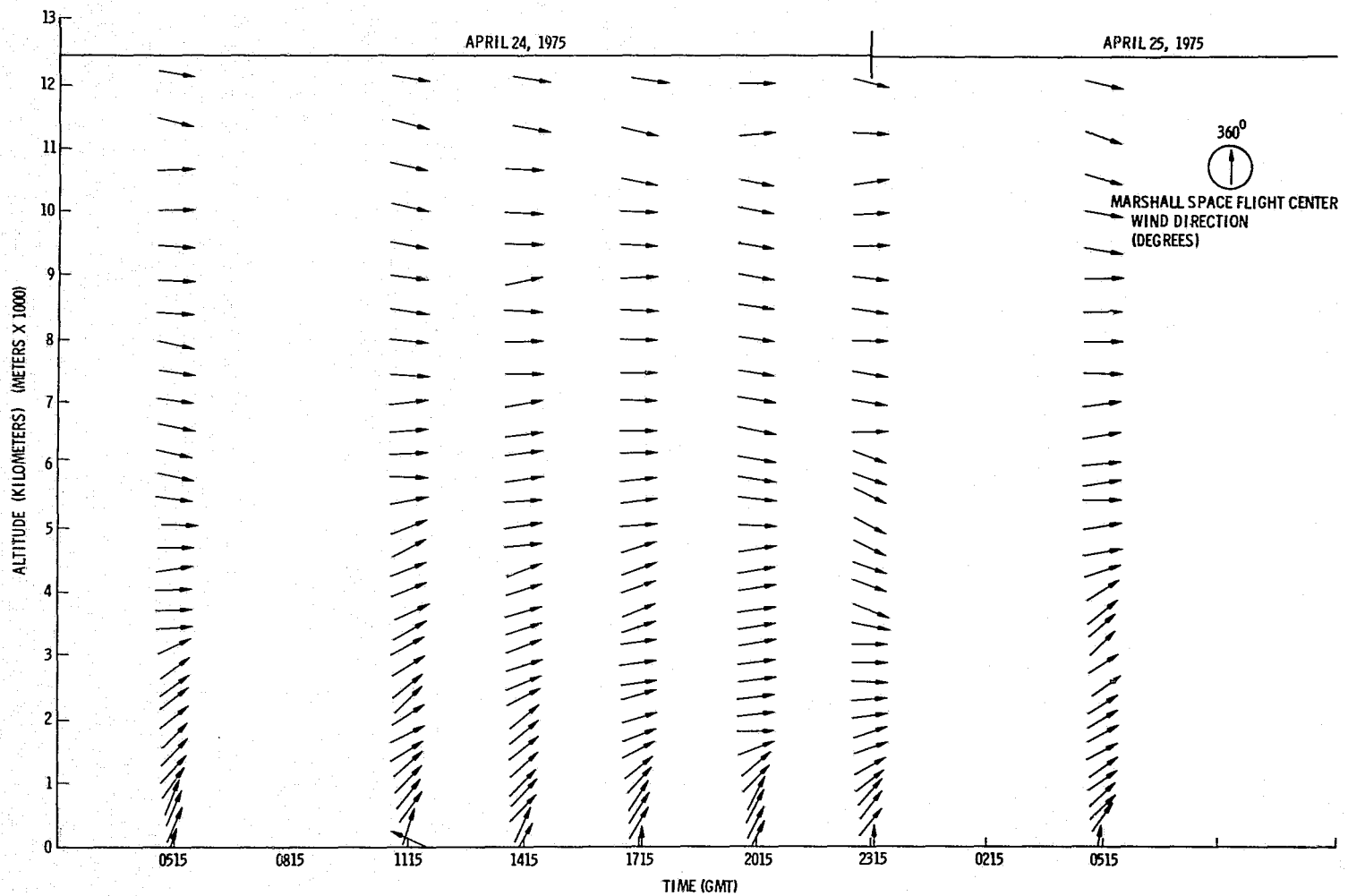

Figure A.153. Time cross section of wind direction at Marshall Space Flight Center, Alabama.